Experimental and numerical investigation of thermomechanical couplings and energy balance in metallic polycrystals

Rian Seghir

N° d'ordre : 181

ECOLE CENTRALE DE LILLE

THESE

présentée en vue
d'obtenir le grade de

DOCTEUR

en

Spécialité : Mécanique

par

Rian SEGHIR

DOCTORAT DELIVRE PAR L'ECOLE CENTRALE DE LILLE

Titre de la thèse :

Experimental and numerical investigation of thermomechanical couplings and energy balance in metallic polycrystals

Étude expérimentale et numérique des couplages thermomécaniques,
et bilan d'énergie au sein des polycristaux métalliques

Soutenue le 27 mars 2012 devant le jury d'examen :

Rapporteurs	*Mme Wiera Oliferuk, Professeur, Polish Academy of Sciences*
	Mr Samuel Forest, Directeur de recherche CNRS, Mines ParisTech
Président du jury	*Mr André Chrysochoos, Professeur, Université de Montpellier II*
Examinateurs	*Mr Xavier Feaugas, Professeur, Université de la Rochelle*
	Mr Patrick Villechaise, Directeur de recherche CNRS, ENSMA Poitiers
	Mr Jean-François Witz, Ingénieur de recherche CNRS, Ecole Centrale de Lille
Directeurs de thèse	*Mr Eric Charkaluk, Chargé de recherche CNRS, Ecole Centrale de Lille*
	Mr Philippe Dufrénoy, Professeur, Université de Lille 1

Thèse préparée au Laboratoire Mécanique de Lille – UMR CNRS 8107

Ecole Doctorale SPI 072 (Lille I, Lille III, Artois, ULCO, UVHC, EC Lille)
PRES Université Lille Nord-de-France

Contents

Acknowledgments

Je tiens tout d'abord à remercier Mme Wiera Oliferuk, professeur à l'académie des sciences de Pologne, et M. Samuel Forest, Directeur de Recherche au CNRS, d'avoir accepté de se constituer rapporteurs de ce manuscrit, d'en avoir parcouru les moindres détails et d'avoir fourni ce long travail d'analyse critique. Celui-ci ayant à mon sens grandement enrichi ma soutenance ainsi que les discussions qui ont suivi. Je remercie par la même occasion M. André Chrysochoos, Professeur à l'Université de Montpellier II, qui m'a fait l'honneur d'être le président de jury, M. Xavier Feaugas, Professeur à l'Université de la Rochelle et M. Patrick Villechaise, Directeur de Recherche au CNRS, avec qui j'ai eu grand plaisir à échanger tout au long de cette séance de "torture amicale" qui restera à jamais gravée comme un grand moment dans mon esprit.

Je tiens ensuite à remercier tout particulièrement M. Jean-François Witz, pour les réflexions, les idées et l'aide qu'il m'a apporté durant ce travail de thèse, donnant à celui-ci une teinte et un relief tout à fait particuliers. Je n'oublie bien évidement pas non plus son soutien moral et sa présence au quotidien.

Il m'aurait été également impossible de faire aboutir, ni même de débuter ce travail de thèse, sans la base de donnée extremement riche sur laquelle j'ai pu m'appuyer. Je tiens donc à remercier Mlle Laurence Bodelot, Maitre de Conférence à l'école polytechnique, avec qui j'ai pu à de nombreuses reprises échanger tout en m'appuyant sereinement sur son travail exceptionnel. Je remercie aussi, M. Patrick Villechaise, M. Laurent Sabatier, Ingénieur de Recherche au LMGC de Montpellier, M. Ahmed El Bartali, Maitre de Conférence au Laboratoire de Mécanique de Lille, M. François Lesaffre, technicien à l'école centrale de Lille, et M. Jeremie Bouquerel, Maître de Conférence à l'ENSCL, pour leurs contributions diverses relatives aux données expérimentales, leurs traitements et leur compréhension.

Cela me permet de remercier par la même occasion toute l'équipe de recherche "Micro-mécanismes de déformation, d'endommagement et de fatigue" du Laboratoire de Mécanique de Lille avec qui j'ai cohabité et travaillé pendant un peu plus de 3 années. Je pense aux thèsards, au technicien, aux Maîtres de Conférence et aux Professeurs grâce auxquels j'ai pu m'enrichir.

Enfin, je tiens à remercier tout particulièrement mes deux encadrants, M. Eric Charkaluk, Chargé de Recherche au CNRS et M. Philippe Dufrénoy, Professeur à l'Université de Lille 1, qui ont tout d'abord su croire en moi. Ils ont su chacun à leur manière me guider, m'épauler, me stimuler et me porter pendant plus de 3 ans. Je n'oublierai jamais tous ces échanges, ces questionnements et surtout ces derniers instants de pure rédaction et de correction, où plus que l'ambition de réussir, c'est votre confiance, votre soutien et votre travail de correcteur acharné qui m'a permi de conclure.

Je conclus par ce remerciement à mes proches, mes parents qui m'ont toujours poussé à réaliser mes rêves et mon amie Dorothée qui n'a pas cessé de croire en moi et qui m'a supporté à chaque instant. Merci vraiment.

General introduction

The fatigue of metals occurs under cyclic loadings and is the consequence of cracks nucleation and growth until the complete failure of the concerned structure. This research area, opened under industrial auspices after the tragic railway disaster of the Paris-Versailles train in 1842 (see [Smith 1990] for an historical exhaustive description of this accident), remains nowadays an important industrial problem which concerns macroscopic components and structures. The design of such industrial parts require physically based crack initiation criteria compatible with structural computation based, for example, on the Finite Element Method (FEM). The main difficulty to build such criteria is that the crack initiation mechanisms take place at a microscopic scale. In fact, it is now well known that the metals fatigue is essentially associated to the gliding of dislocations and the creation of slip bands which characterize irreversible damaging mechanisms at the grains scale. A review of these mechanisms can be founded for example, in the monograph of [Suresh 1998], in the pioneering works of [Mughrabi 1983], in the papers of [Magnin 1984a, Magnin 1984b] or in the recent synthesis of [Lukas 2001, Lukas 2002, Lukas 2004]. Even if elementary mechanisms have been extensively studied, the complete understanding of the transition from cyclic plasticity to the deformation localization and the crack initiation remain an open problem. As the principal mechanisms responsible of the fatigue damage, i.e. the cyclic plasticity and the crack initiation and growth, are irreversible ones, a dissipative framework could be an alternative way to address this question. In this way, a first major contribution is actually due to Dillon [Dillon 1962b, Dillon 1962c, Dillon 1963a, Dillon 1966] in a series of experiments on the cyclic torsion of copper and aluminum tubes. In [Dillon 1963a], one of his major observations is that the thermoplastic coupling during a cyclic torsion test induces a positive dissipation which conducts to a constant increase of the temperature. This certainly inspires the principle of the self-heating tests developed in the recent years. The first detailed approach was certainly proposed by [Luong 1995, Luong 1998] and enables the determination of the fatigue limit by using infrared thermography technique. He shows that the change in the dissipative behavior corresponds to the transition between unlimited and limited endurance in the fatigue life. Following this paper, numerous studies were realized to verify this relation on different materials: Fargione et al. tested different steels [Fargione 2002] and Krapez and Pacou, several aluminum alloys and steels [Krapez 2002]. A more formal discussion associating fatigue and temperature variations can be founded in the works of Boulanger, Doudard and Berthel [Boulanger 2004b, Doudard 2005, Berthel 2008]. However, all these tests and measures remain at a macroscopic scale and do not give information on this transition between diffuse and localized plasticity and finally crack initiation.

In order to improve such energetic approach, it could be interesting to analyze other localization process and the chosen way to analyze them. An instructive case is the Lüders bands occurring during the tensile loading of soft steel specimens, as it is studied since more than a century. As for the fatigue, this phenomenon has been first studied by metallurgists (see Jaoul [Jaoul 1965] for an historical overview) in order to understand the origin of this macroscopic localization process. As it concerns plastic deformation and stability, mechanicians proposed different approach in order to predict such phenomena. One can cite Hill [Hill 1958], Drücker [Drücker 1951], Rice [Rice 1976]. Even

if Lüders's bands appearance and propagation are not currently completely understood, the study of this phenomenon is relatively direct as it is a macroscopic one. Lüders's bands have then been studied from a dissipative point of view in order to understand the storage and the release of deformation energy during the deformation process [Oliferuk 1985, Louche 2001, Ait-Amokhtar 2008]. It is shown that the beginning of the localization (location and time) corresponds on the one hand to a maximum value of the stored energy and, on the other hand, the energy release beginning. Similar works were also done for the study of adiabatic shear bands under dynamic loadings [Rittel 2010, Rosakis 2000].

Then, it could be interesting to follow the same way for the fatigue study: can fatigue be resume to a storage/unstorage mechanisms at the microstructural scale? Is the stored energy evolution a good indicator of the localization process? Does the crack initiation correspond to an energy release? Such questions require (1) to work at the grain scale and (2) to propose a compatible modeling framework. These questions are challenging ones. Therefore one proposes first to follow recent studies conducted on oligo- and polycrystals under tensile loadings at small strain levels. Even if the plastic mechanisms will not be the same under monotonic loadings, the objective is to develop a complete experimental and modelling framework which could be transfer, in the future, to the fatigue mechanisms study.

This thesis is in the continuity of Bodelot's work [Bodelot 2008, Bodelot 2009] who proposed a new experimental setup for fully-coupled thermal and kinematic in-situ measurement used at the grain scale of a AISI 316L stainless steel under tensile loading. The main objectives will be:

- to develop relevent microstructural analyses
- to study the thermomechanical couplings during the transition from an heterogeneous elasticity to the beginning of microplasticity in a diffuse form and then to a localized one
- to establish first microstructural energy balances
- to develop the associated modeling framework in order to access to unmeasurable internal variables

After an introduction about strain localization, stored energy and dissipation, this work is divided in three main parts. First, the test, the material and the experimental techniques are presented. The microstructure after the test is analyzed through EBSD, profilometry, micrography with a particular development dedicated to the activated slip systems automatic analysis. A particular focus is done on the calibration of the infrared camera and the treatment of the thermal fields. Then, the next part is dedicated to the analysis of the thermomechanical fields. A specific technique is proposed in order to project the experimental calibrated fields on the microstructure. Then, inter- and intragranular thermomechanical couplings can be investigated and experimental energy balances are realized. Finally, polycrystal aggregate computations are conducted in order to estimate internal variables and to realize numerical energy balance in a complementary way in order to establish a real models-experiments dialog.

Introduction: strain localization, stored energy and dissipation

Contents

0.1 Localization of the deformation in polycrystals

Every industrial materials such as composites, metals, polymers ... as well as geophysic material such as minerals, ices ... are heterogeneous a in mechanical point of view. They are constituted by elementary components such as a matrix, reinforcements for composites, grains for polycrystals ... which have different intrinsic behavior. As a consequence, every macroscopic loading, even homogeneous, applied on the boundaries of the structure, leads necessarily to a heterogeneous distribution of stresses and strains within the material. This heterogeneity is linked to complex interactionq between elementary constituents which react fidderently to the macroscopic loading.

The heterogeneity of the deformation in metallic polycrystals has been widely studied and modeled since many decades and one can cite, for example, the pioneering works of Schmid, Sachs, von Mises and Taylor [Schmid 1924, Sachs 1928, von Mises 1928, Taylor 1938]. Henceforth, it is well known that the inhomogeneous deformation is leaded, within polycrystals, by the properties and interactions of its grains, i.e individual crystal with continuous orientation. First, they vary widely in size, from 10^{-7} to 10^{-3} m, and in orientation. Secondly, grains are anisotropic in both elastic and anelastic domains, due to the atomic arrangement within individual crystal lattice (BCC, FCC, HCP ...). Thus, this local gradient of mechanical properties triggers inhomogeneous deformations at different scales and at different loading states, leading in some cases to strain localizations and to the failure. The description of the origins and development of heterogeneities from diffused to localized deformation have been

notably described and synthesized in [Kocks 1981]. Furthermore, considerable works also focused on the intragranular nature of the deformed state, especially intragranular misorientations [Hughes 1997] and their prediction [Butler 1989]. It is currently well known that there is a wide range of internal length scales, from nanometers to millimeters, at which the microstructure and its associated mechanical fields are heterogeneous during deformation (see figure 1 (a)).

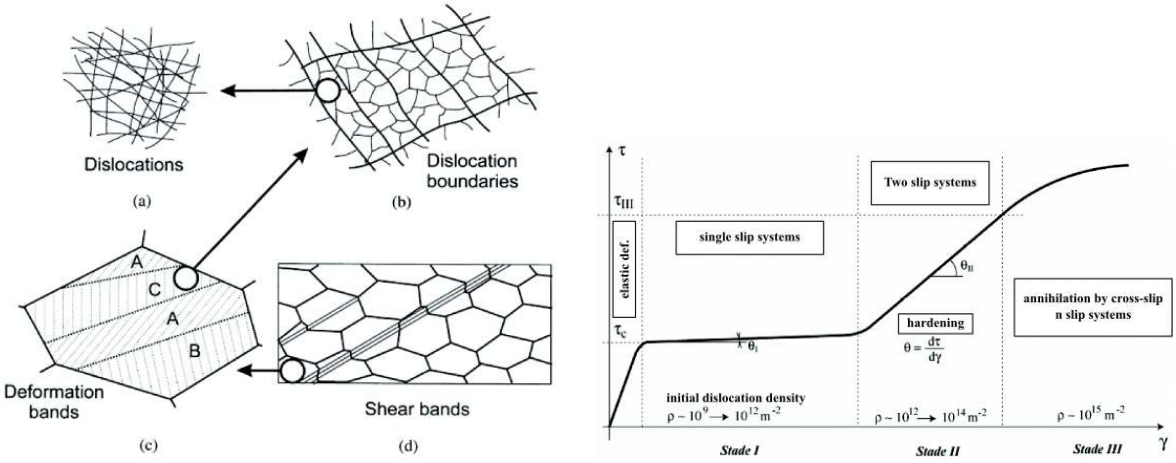

(a) (b)

Figure 1: The hierarchy of microstructure in a polycrystalline metal deformed plastically. (a) Dislocations, (b) dislocation boundaries, (c) deformation and transition bands within a grain, (d) specimen and grainscale shear bands [Humphreys 2004, Abrivard 2009]

Initially each grain deforms elastically in an anisotropic way while the resolved stresses on every slip systems of each crystals (material points) remain lower than a threshold value called the Critical Resolved Shear Stress ($CRSS$). It correspondss to the plastic criterion of Schmid and Siebel [Schmid 1924]. The CRSS is related to the crystalline structure as well as any material defects and varies notably as a function of the temperature. Many authors have experimentally investigated its initial value as well as its evolution within single crystals of aluminium, gold, silver, copper, nickel, etc. A large review of results could be found in [Jaoul 1965] nevertheless its measurement within polycrystal is still a challenging topics since it relates to the determination of a local flow stress.
Once the CRSS is reached, local plasticity occurs by shear on specific atomic planes relative to the rest of the crystal. The polycrystal undergoes elasto-plastic inhomogeneous field included also gradient of plasticity at intragranular domain and over grain boundaries. The heterogeneous intragranular plastic slip-activity leads to a non-uniform dislocation distribution then produces cells or subgrains. It corresponds to the picture 1 (a)$^{(b)}$ and (a)$^{(c)}$. The clear observation of an inhomogeneous deformation field in polycrystals has been particularly emphasized by Barrett *et al.* [Barrett 1948] and Boas *et al.* [Boas 1948]. At this stage of deformation, the material requires complex internal stress fields to ensure the compatibility condition between individual crystals and its intensity globally increases with the

mechanical heterogeneity of the material.
The compatibility condition between crystals has been introduced by von Mises [von Mises 1928]. It could be summarized as follow: five independent crystallographic systems are required to accommodate any strain gradient at grain boundary. This transition from single to multiple shear, accompagning the deformation observed in Face-Centered Cubic material is presented in figure 1 (b) [Abrivard 2009] and corresponds to a change in hardening process of the material. One classically denotes three stages of deformation noted I, II and III. As the shear strain γ increase, dislocations ρ are produced and different kind of systems are successivelly activated from easy plastic slip to cross-slip. In this context, intragranular subdomains can rotate independently to accommodate the inhomogeneous imposed strain at grain boundaries.
Then, depending on the loading case, i.e. quasi static, monotonic, cyclic or dynamic, plastic instabilities occur and slip bands cross the grain boundaries. These instabilities leads to damaging strain localization phenomena either at microscopic scale (some grains) notably under cyclic loading at low strain levels or at macroscopic scale (the structure) such as in monotonic test with high strain levels. Under cyclic loadings the localization phenomenon is characterized by Persistent Slip Band (PSB) where slip bands cross grain boundaries in a limited region. Even if this phenomenon has been studied for a long time [], it is not yet a mastered problem. Indeed, many question remains about the progressive transition from elasticity, intragranular plasticity, over grain localization and failure [], especially the plasticity transfer from grain to grain leading to PSB. Concerning macroscopic localizations, the three main plastic instabilities or plastic flow localization are described for example in [Needleman 1988]: Lüders bands, necking of specimen and shear band. The last one corresponds to the phenomenon observed in figure 1 (a)$^{(d)}$. It is currently known that the lattice reorientation during the deformation is one important parameter which promotes localized shearing, nevertheless a variety of softening mechanisms can act to promote localization [Chang 1981].

At the very beginning of the last century, the mechanisms of hardening, visible in figure 1 (b), accompanying the material deformation (cold work) was not clearly understood. Various explanations were proposed to explain the observed phenomena, especially the fact that with the amount of plastic deformation, necessary forces to deform the material also increase. One hypothesis was the appearance of phase change processes at the crystal planes where slipping occurs during the deformation. According to this hypothesis, currently known as being false, Farren and Taylor decided to investigate the variation of latent energy of the material during deformation in [Farren 1925]. It has opened the way to a new manner to investigate the material deformation and hardening: the energy point of view. In the continuity of the pioneers works of Taylor and co-workers [Farren 1925, Taylor 1934, Quinney 1937] many authors have then investigated the material from the energy point of view [Michell 1952, Gordon. 1955, Dillon 1962a, Bever 1973, Chrysochoos 1985, Oliferuk 1985].
more recently, as the diffused or localized inelastic phenomena triggers a dissipation and a temperature increase of the specimen many works have been devoted in the analysis and the detection of macroscopic localization phenomena within metallic materials. For exemple, ***necking*** [Wattrisse 2002, Chrysochoos 2009], ***Lüders bands*** [Louche 2001], ***Portevin-Le Chatelier*** (PLC) [Ait-Amokhtar 2008, Ranc 2008], ***dynamic shear bands*** [Guduru 2001, Padilla 2011], ***dynamic deformation*** [Zehnder 2000]

and ***fatigue localization*** [Boulanger 2004a, Morabito 2007, Berthel 2008]. In addition, it is henceforth well-known that during cold-working, most of the plastic work reappears in the form of heat whereas a certain proportion remains latent in the material and is associated with microstructure changes, including mainly dislocations elastic energy. An extensive review of the early work within this field was published by Bever *et al.* [Bever 1973]. From the works of Louche in [Louche 1999] one knows, at least under monotonic test, that the macroscopic energy stored within the material always reaches a maximum before the appearance of macroscopic damaging phenomeon such as necking.

Thus, the latent or stored energy and the dissipation are an alternative view of plastic deformation which focusses one one hand, on the energy related to its intrinsic constituants (dislocation, defects) and on the other hand on the bulk and local sign of plasticity flow. The next sections present the origin of energy storage and different means developped during the last century to estimate this quantity.

0.2 Energy storage, unstorage and dissipation

During plastic deformation, and resulting in part from plastic sliding, defects are multiplied throughout the metallic material. When the metal is plastically deformed by cold working processes, i.e an unstable deformation process, it is generally characterized by:

- a permanent deformation after removing stress,
- a work hardening, i.e an increase in resistance to further deformation,
- the ability to theses effect to be partly or wholly vanished under certain conditions, including a minimum temperature,

Therefore, a variety of defects could be produced. Plastic deformation occur, raising the overall energy of the "system" by such defects production. This change in internal energy is traditionnally called "Stored energy of cold working". It has been investigates early in [Farren 1925] and [Bever 1973] presents a wide overview. An essential characteristic of this elastic energy is that it is not released after removal of the loading. It allows notably to clearly distinguish the stored energy of cold working from the macroscopic elastic strain energy. Nevertheless, this stored energy could be released through three distinct microstructure evolution processes: recovery, recrystallization and grain coarsening. These processes are presented in figure 2.

1. recovery: the system minimizes its energy by rearranging the dislocations into subgrain structures,
2. grain coarsening: grains increase their size to decrease the total grain boundary area, therefore reducing their associated energy,
3. recrystallization: process by which deformed grains are replaced by a new set of undeformed grains that nucleate and grow until the original grains have been entirely consumed. These nuclei finally lead to a new grain structure (see figure 2 from [Resk 2010]). Recrystallization is

usually accompanied by a reduction in the strength and hardness of a material and a simultaneous increase in the ductility. It explains notably why the control of such process is crutial for metallurgical industries.

As a consequence, the stored energy of cold working is a "latent" energy within the deformed metal, and changes are mainly caused by the generation, motion and annihilation of dislocations and/or other defects. Thus, "the process of energy storage, [within a metal], is a macroscopic manifestation of [its] microscopic activities" [Oliferuk 1995]. It characterizes its current microstructural state, its deformation history, and the future one since it contains the needed energy for further crystallographic transformation, for exemple recrystallisation, and drives the kinetics of grain or subgrain boundaries. As expressed in [Doherty 1997], "the entire recrystallization process is latent in the deformed state".

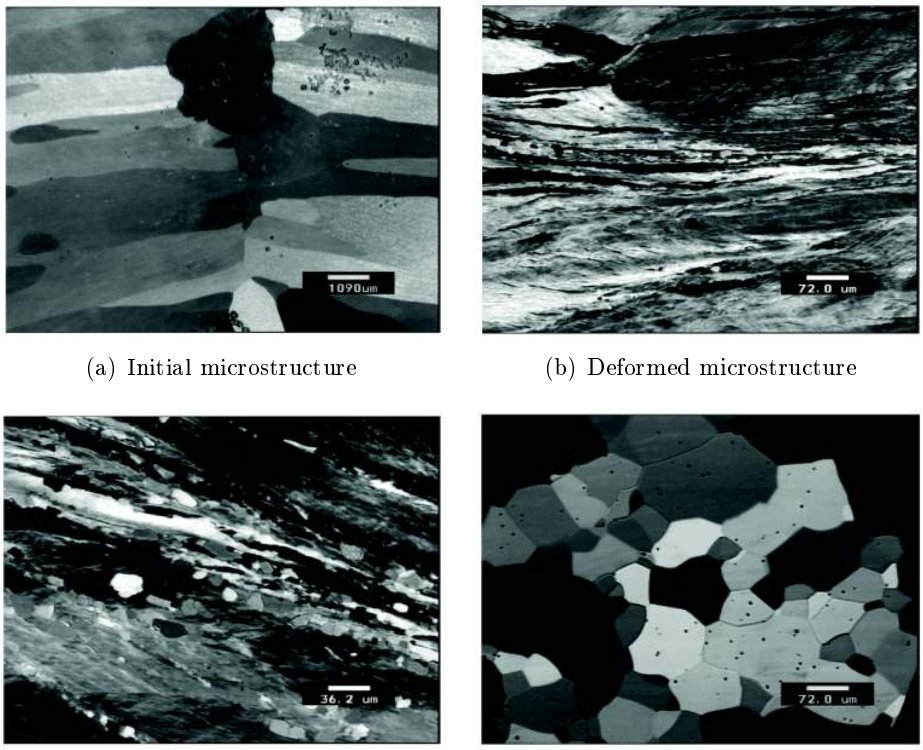

(a) Initial microstructure (b) Deformed microstructure

(c) Nucleation (d) Recrystallized microstructure

Figure 2: Exemple of recrystallization phenomenon extracted from [Resk 2010]

The dissipation is in opposite the part of energy directly released during inelastic phenomena and which do not act in the deformation process, at least under cold working conditions. The bulk or local temperature variation reflect its activity.

In conclusion, the temperature and the dissipation evidence, in real time, where and when diffused or localized anelastic phenomena occur and the stored energy characterizes the deformation state, and potentially predict where and when the threshold must appear.

0.3 Measurement techniques of stored energy

We have briefly seen the physical significance of stored energy and its intrinsic connection with mechanisms of deformation and any transformations acting within the polycrystal up to its ultimate state. One proposes here a none exhaustive overview of main techniques which have been developped during the last century to access to this quantity. We have seen that the lattice transformation leads to energy storage and unstorage and that the thermomechanical behaviour of the specimen is then affected. So, in a general way, the stored energy can be measured by a calorimetric approach, or it can be estimated through relationships between the stored energy and microstructural parameters or between the stored energy and stress flow. One proposes to decompose approaches in three categories:

1. ***The microscopic approach***, where the stored energy is estimated from the physical origin of energy storage, i.e dislocation network or other defects, grain boundary misorientations and more generally crystal lattice transformation [Rajmohan 1997a, Gerber 2003, Choi 2004, Benzerga 2005, Hazra 2009]. In this case one only have access to the estimated storage mechanism and this approach is generally limitated to micromechanical studies.

2. ***The bulk approach***, where the stored energy is estimated from the energy balance, i.e the difference between provided plastic energy to the system and the dissipated one into heat [Farren 1925, Dillon 1962a, Chrysochoos 1989a, Hodowany 2000, Louche 2001, Doudard 2004, Berthel 2007b, Dumoulin 2010]. This approach generally consists in a macroscopic point of vue of plasticity mechanisms. In this case, the estimated energy includes energy due to dislocations, point defects and/or their clusters, boundaries and associated internal stresses but cannot distinguish each of their mechanisms.

3. ***The multiscale approach***, where authors are interested in both micromechanism of plasticity and macroscopic (homogenized) energy balance [Michell 1957, Clarebrough 1958, Bailey 1960, Bever 1973, Oliferuk 1985, Oliferuk 1993, Oliferuk 2001, Oliferuk 2009, Saai 2010].

Let us first basically describe some thermomechanical power. Notice that the detailed establishement of heat equation is done in appendix A.1. The mechanical power W provided to the specimen during deformation can be decomposed into an elastic power W_e and an anelastic one W_p. The anelastic power W_p can also be separated into a power dissipated in form of heat Q and a residual part W_s stored in the material.

$$W = W_e + W_p = W_e + Q + W_s \tag{1}$$

W_s is classically assumed as being only a small energy amount stored in the material.

0.3.1 The microscopic approach

Since these techniques have not been used in this work, one only focuses on main ways. Interested readers could refer to the recent publications.

To our knowledge, 4 local experimental techniques have been used to access to the stored energy:

- ***From microhardness***. This technique uses the linear dependence between the slope of the stress-strain curve $\frac{d\sigma}{d\varepsilon}$ and the rate of energy stored $\frac{\partial E_s}{\partial E_w}$ where σ is the stress, ε the strain, E_s the stored energy and E_w the expended one. This observation was originally done by [Hort 1907]. It is currently assumed that there exists a factor K such as:

$$E_s = K\left(\sigma^2 - \sigma_0^2\right) \tag{2}$$

  In [Hazra 2009], authors used this empirical law as well as the relationship between approximate flow stress (σ) and Vickers microhardness (HV) such that $\sigma \approx HV/3.67$. This technique accounts for the stored energy due to dislocations only.

- ***From Electron-Back Scattering Diffraction*** (EBSD) (see chapter 1.1). In [Choi 2004] three differents methods to estimate the energy stored in a cold-rolled specimen of low carbon steels from a classical EBSD analysis are summarized:

  - ***The intragranular misorientation***. This technique presupposes that the dislocations are arranged in low-energy dislocation boundaries. Thus the energy per unit area of dislocation boundary can be estimated from the angular misorientation across the boundaries. The EBSD technique provides a measurements of these low-angle boundaries.
    It is classically assumed that the energy is mainly stored in metals in the form of dislocations. Basically it is assumed that $E_s = \rho E$ where ρ is the total dislocation density, and E the energy per unit length of dislocation line. The low-energy dislocation boundaries could be estimated from angular misorientation across the boundaries, notably by the Read-Shockley equation (see eq. 6 [Read 1950]). The stored energy due to dislocations takes therefore the following form [Godfrey 2005]:

$$E_s = S_v\gamma + E\left(\rho_0\right) \tag{3}$$

    where S_v is the area per unit volume of boundary, γ the energy boundary per unit area and $E\left(\rho_0\right)$ is a contribution from individual dislocations in the volume between the dislocation boundaries. Note that this contribution is frequently neglected as well as the contribution to the stored energy from the original high-angle grain boundaries in the undeformed material [Godfrey 2005, Choi 2004, Huang 1999].
    Subgrain structures noted i are considered, i.e intragranular subdomain separated by a low-angle boundary greater than a threshold angle noted $\Delta\theta$. The equivalent circle diameter of region i, noted D_i and the mean misorientation $\Delta\theta_i$ is known. Then assuming that the intragranular stored energy is entirely due to the subgrain boundary energies, γ_i, and that

the boundary energy is only a function of the boundary misorientation $\Delta\theta_i$, i.e notably none dependent on boundary type (tilt and twist), the mean stored energy within each subgrain i could be extracted from the following equation system [Humphreys 1995]:

$$E_s^i = S_v^i \gamma_i \tag{4}$$

$$S_v^i \approx \frac{3}{D^i} \tag{5}$$

$$\gamma_i(\Delta\theta_i) = \begin{cases} \gamma_m \frac{\theta_i'}{\theta_i^*}\left(1 - ln\left(\frac{\theta_i'}{\theta_i^*}\right)\right) & \text{if} \quad \theta_i' < \theta_i^* \\ \gamma_m & \text{if} \quad \theta_i' \leq \theta_i^* \end{cases} \tag{6}$$

with $\theta_i' = |\Delta\theta_i|$ for $0 \leq |\Delta\theta_i| \geq \pi$ and $\theta_i' = 2\pi - |\Delta\theta_i|$ for $\pi \leq |\Delta\theta_i| \geq 2\pi$. θ_i^* and γ_m are the values of misorientation and boundary energy when the boundary becomes high angle, commonly 15^o. In [Murr 1975], γ_m is estimated about 0.324 $J.m^{-2}$.

It is important to keep in mind the whole set of assumptions done for the stored energy estimation and potential errors; in [Godfrey 2005] theses points are explored in details. It underlines that only Geometrically Necessary Dislocations ($GNDs$) are taken into account and not the Statistically Stored ($SSDs$) ones. Consequently, the stored energy must be underestimated. It provides an explanation of the deviation from the stored energy level measured from calorimetric analysis.

– ***The Pattern or Image Quality***. When a lattice is distorded by crystalline defects such as dislocations or sub-grain boundaries, the Kikuchi Pattern[1] in E.B.S.D. analysis will also be distorded [Zhou 2007]. It consequently exhibits a lack of clear contrast in every diffracting bands from crystallographic plane. It leads to a drop in Image Quality factor. The E.B.S.D. procedure will be discussed in more details in chapter 1.1. According to this fact, some authors tried to exhibit a relation between Image Quality factor which is proportionnal to the sharpness of the Kikuchi pattern and to the presence of crystallographic defects and/or dislocations [Wu 2005]. The stored energy takes in Choi work has the following form:

$$E_s \propto H_i = \alpha\left[1 - \frac{Q_i - Q_{min}}{Q_{max} - Q_{min}}\right] \tag{7}$$

where Q_i is Image Quality for the site i, Q_{min} and Q_{max} are minimum and maximum pattern quality of the aggregate respectively, H_i is proportionnal to the opposite of normalized Image Quality and E_s proportionnal to H_i. Nevertheless, it is important to remind that it is somewhat not fined to say that EBSD can measure dislocation or plasticity or stored energy. Instead, EBSD measures the effects of plasticity upon the crystallite lattice in the form of lattice bending ($GNDs$), lattice imperfection ($GNDs$ and $SSDs$) and also rotation caused by the elastic deformation which is pratically always neglected and hardly distinguishable. In addition, as precised in [Choi 2004], the Image Quality could be drastically affected by

[1] Seishi Kikuchi and Shoji Nishikawa discovered the fundamental diffration on which the EBSD is based in 1928

experimental procedure such as specimen preparation, consequently, used as a metric for a quantitative stored energy measurement remains questionnable.

- ***The granular orientation***. From the knowledge of the macroscopic stress tensor Σ applied to a specimen, the macroscopic strain tensor E, the granular orientation and assuming a scale transition assumption it is possible, for exemple, to access to numerical Taylor factor field within each grain. In [Rajmohan 1997a], the existence of a correlation between Taylor factor and stored energy in 80% cold-rolled IF steel sheet is reported. Thus assuming such a dialogue between model, experiment and empirical laws, some authors tried to estimate the mean granular stored energy [Choi 2004].

- ***From X-ray or neutrons analysis***. This technique take profits of the changes in crystal lattice structure during deformation. After the discovery of X rays, it has been shown that highly deformed materials keep their crystal structures (revealed by the Debye-Scherrer ray) "almost" unchanged. This slight change in crystal structure is now called "the analysis of diffraction profiles". The enlargement of diffraction profiles may result from the size of the diffracting crystals and the microscopic heterogeneity of deformation. From a theoretical point of view, all contributes to crystal defects enlargement profiles. Krivoglaz [Akrivoglaz 1969] divided all the defects into two classes as a function of the range of their strain fields: class I defects at long range, causing crystallographic disturbances at long range (for example: dislocations, coherent precipitates, interfaces in multilayer materials, etc..) and defects class II short-range, i.e. point defects, inclusions or precipitates, etc... Stored energy is then estimated using the Stibitz relationship [Hazra 2009] by correlating it with the mean relative change in lattice spacing such that:

$$E_s = \frac{3}{2} E \frac{(\Delta d/d)^2}{1+2\nu^2} \tag{8}$$

where E is the Young modulus, ν the Poisson's coefficient and $(\Delta d/d)$ is the relative change in lattice spacing. As X-ray are notably affected by state of surface specimen, similar works has been done, using neutrons diffraction method since neutron penetrates through the bulk of the specimen. Such technique has been used for exemple in [Rajmohan 1997a, Rajmohan 1997b, Monnet 2009, Hazra 2009]

0.3.2 The bulk approach

This section presents the main methods used during the last century to achieve the in-situ energy balance of specimens submitted to different types of loading as well as main associated errors. Interested reader could find a very exhaustive overview of calorimetric analysis performed to access to the stored energy in [Bever 1973]. This way takes profit of the thermodynamical aspect of deformation processes, notably the first law of thermodynamics:

$$E_s = \Delta E = Q + W \tag{9}$$

where ΔE is the change in internal energy of the body, Q the energy exchanges in form of heat (assumed as being positive if absorbed) and W the mechanical work (positive if given to the body). Notice that considering an homogenous material with an ideal plastic behavior, i.e elastic perfectly plastic, $Q = -W$ and $\Delta E = E_s = 0$. The whole mechanical work is converted into heat. Nevertheless, as no metal is ideally plastic, following this thermodynamic approach, the stored energy measurement requires the measurement of mechanical work and the heat. Bever decomposes measurements techniques in two main methods:

1. ***The single-step methods***: this a bulk measurement performed during the test. During deformation, force-displacement data as well as temperature variation are measured to estimate mechanical work and heat. Farren and Taylor [Farren 1925] have used this method in the earliest stored energy investigation. Figure 3 (a) presents pioneer results concerning β ratio, i.e the ratio of instantaneous stored power on the total done, for a twistted pure copper specimen [Taylor 1934] and a stretched rod of metal (Farren and Taylor [Farren 1925]). Authors emphasize the fact that β is nearly constant up to $\frac{ND}{l} = 1$ and then it rapidly decreases up to a saturated state. They evidenced that latent energy, which could retained within a material subjected to cold working, may not increase indefinitely. Notably for a twisting loading, a stage could ultimately be reached when no further latent energy could be absorbed. From these results, many author have successfully used this technique.

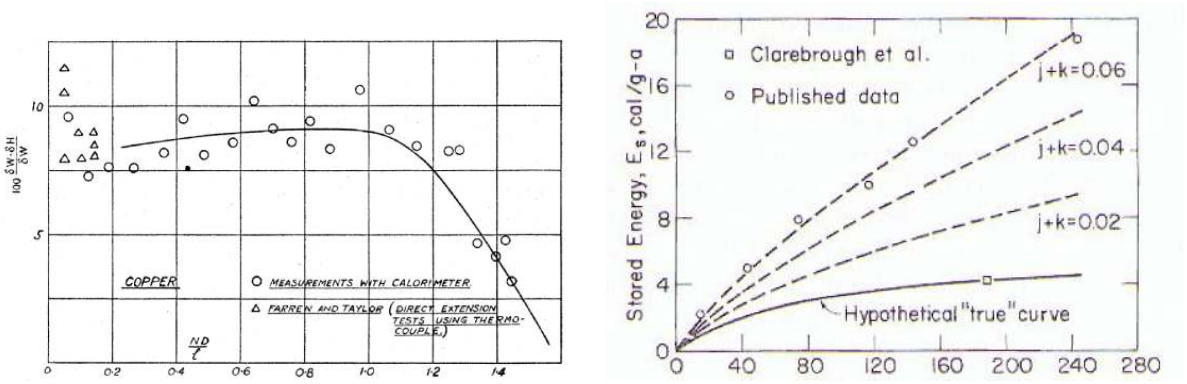

(a) β in % (b) E'_s

Figure 3: (a) Percentage of work done which remain latent in pure copper specimen subjected to plastic twisting [Taylor 1934] and (b) effect of systematic errors in the value of heat and work on typical published values obtained by single-step method of measuring the stored energy [Bever 1973]

One of the main problem concerning this technique is that the work done and the heat are measured by different techniques, with different systematic errors which do not cancel each others. An illustration of such a problem is proposed in [Bever 1973]. It comes from the fact that work and heat do not differ by more than 10% because of the low level of stored energy traditionnally observed in metals. Consequently an "high degree of absolute accuracy" on each quantity is

crutial. If one assumes that work W differs from the measured one W' by a small amount jW and the true heat Q also differs from the measured one Q' by a small amount kQ, the estimated E'_s follows the evolutions presented in picture 3 (b). Figure 3 evidences the fact that, from 0 to 6% of systematic error on work and heat measurement leads to a large error in E_s estimation as well as a significant change of curve shape.

2. ***Two-step methods***: in a first step, a classical mechanical test is performed on a specimen, and in a second step the stored energy is measured. This procedure takes profit of irreversibility of storage mechanism expected under some specific conditions. Indeed, once the specimen has been loaded, the stored energy remains latent in the material. It is then possible to measure the energy released when annealing conditions, notably thermal conditions, are applied. Bever decomposes this method in two parts:

   - ***Annealing methods***:
     - ***Anisothermal annealing***: the deformed material and a standard one (previously annealed) are separatly heating continuously, usually at a constant rate. The power necessary to maintain the same rate of rise of temperature in each specimen is measured. It is expected that the power needed for the deformed specimen will be less since the stored energy gradually releases. The power difference ΔP is therefore proportionnal to the released energy. Figure 4 (a) presents results extracted from Clarebrough's works who has originally developped the method. It also evidences a point which has been already discussed in previous sections: resistivity and hardness are also parameters which are stored energy dependent.

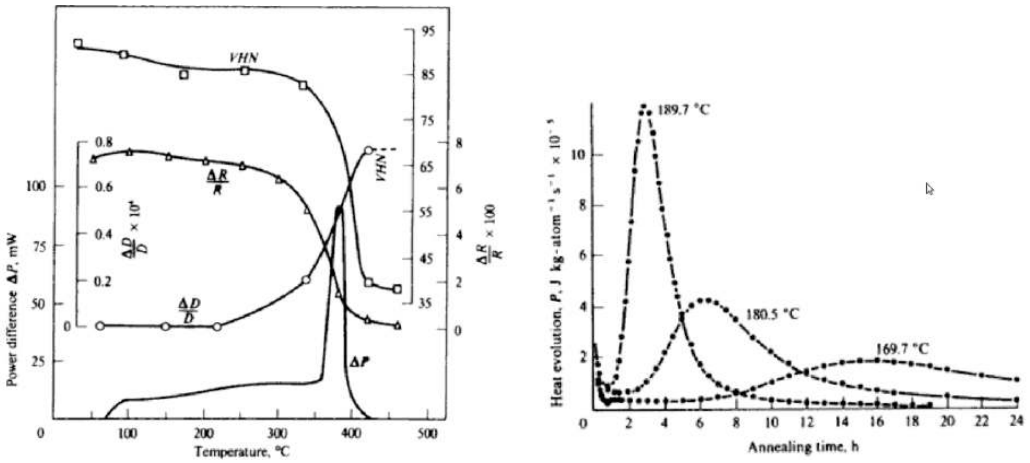

(a) (b)

Figure 4: (a) Release of stored energy, plotted as power difference ΔP, from commercial copper deformed 33% in tension at room temperature. (VHN) Changes in hardness, (R) resistivity and (D) density (after Clarebrough, Hargreaves and Loretto 1963) and (b) isothermal release of stored energy from 99.999% copper deformed 30% elongation in tension, at room temperature [Gordon. 1955]

- ***Isothermal annealing***: the deformed material is placed in a constant-temperature calorimeter and the effect of energy release is observed as a function of time. Gordon [Gordon. 1955] designed a microcalorimeter able of holding temperature variations to within 10^{-4} ^{o}C. Figure 4 (b) shows results using a 99.999% purity copper specimen after 30% elongation in tension for different annealing temperatures. One observes here the wide influence of temperature on the rate of stored energy released and probably also on the rate of energy storage.
- ***Reaction methods***: here, a cold-worked specimen and an annealed one react with a solvent (working substance) in a calorimeter. The released energy is obtained by difference between heats of reaction.

Bever [Bever 1973] summarizes previous methods by one sentence: the "single-step method determines the difference in internal energy [whereas] the two-step method determines the enthalpy difference between cold-worked and the standard state".

Historically, such energy balances have been developped in parallel of kinematic and thermal measurement techniques. Nevertheless, whatever the technology, current energy balance are still achieved following these pioneering works. The whole set of works performed are not detailed here. Nevertheless, table 1 summarizes main steps in technique developpements and increasing knowledges about the well known β ratio.

The following indexes refer to the table 1:
(1) means that the β ratio tend toward zero.

(2) In [Chrysochoos 1985], the heat Q dissipated is estimated solving the heat equation introduced in appendix A.1. Indeed, InfraRed thermography allows the estimation of surface specimen temperature and thus doesn't allow a direct measurement of heat compared to calorimeter. Solving the heat equation leads necessarily to make some assumptions concerning unknown quantities, such as the temperature in volume for exemple. The InfraRed thermography principle is detailed in appendix C.

(3) In [Oliferuk 1993], the heat Q dissipated is estimated on the basis of the Joule-Lenz effect. The temperature variation during deformation is simulated by means of controlled-resistance heating of an unstrained sample with an electric current. Since the simulation and the loading are conducted under identical geometrical and environnement conditions, the dissipated heat Q corresponds to the amount of electric power supplied to the sample during simulation. This technique allows the experimental estimation of dissipated power from the specimen temperature avoiding to solve the heat equation (see appendix A.1).

(4) In [Berthel 2007b] or [Berthel 2008], the heat source fields are obtained by InfraRed Thermography and associated kinematic field are registered simultaneously by means of Digital Image Correlation. Recovering the local displacement field allows solving the heat equation in its local form in every material point of the studied area and at each time increment. The Digital Image Correlation technique

is detailed in appendix B.
One could notably note from [Oliferuk 1993], that the stored energy ratio on the expended energy reaches a maximum about 40% before decreasing toward a saturated state at ≈25%.Mechanisms associated to this change in storage rate will be developped in the next chapter.

references	material	loading	techniques	β ratio(%)
[Farren 1925]	steel copper aluminium	monotonic tension	thermocouple	13.5 9.5 7
[Taylor 1934]	copper decarburised mild steel	monotonic twist	calorimeter	8.3→(1) 0 9.2→0
[Dillon 1962a]	aluminium	cyclic twist	thermocouple	23.08
[Chrysochoos 1985]	duralumin XC38 steel A316L	monotonic tension	microcalorimeter IR thermography(2) IR thermography	 50-60→≈20 (9% of strain)
[Oliferuk 1993]	austenitic steel	monotonic tension	IR thermography and electrical power(3)	0→35-45→25 (20% of strain)
[Berthel 2007b]	DP600 steel	symmetric fatigue test	IR thermography and DIC(4)	

Table 1: Improvement of measurement techniques for energy balance achievement from thermocouple to InfraRed thermography.

One observes from [Farren 1925] to [Berthel 2008] that techniques to achieve the energy balance has envolved. One passes from 0 dimensionnal approach (bulk heat, displacements, forces measured as a scalar global quantity) to 2 dimensionnal approach (strain fields, thermal fields). Nevertheless stress field remains a tricky problem since, as the stored energy, it is an internal variable. It is not measured and could be only estimated. Consequently, excepted for stress, one has currently access to gradients and localizations of each measured quantity. The current studies take profit of an additionnal point: the resolutions of cameras used within kinematic and thermal measurements are currently enough significant to provide fields of which the scale is close to the one of the microstructure and of the deformation mechanisms. This convergence between plasticity mechanism scale and measurement resolution is presented in section 0.4.2. The next section deals with the multiscale approach.

0.3.3 The multiscale approach

The way that we called "multiscale" is related to studies where authors systematically tried to link the macroscopic energy balance and the plasticity mechanisms. These authors have consequently mixed techniques of thermal or heat measurement and microscopy. This way allows the dialogue between two fields within mechanic of materials: crystallographic and Continuum Thermodynamics points of vue. It takes profit of a quantitative measurement of global stored energy at macroscopic scale and a fine description of microscopic plasticity mechanisms. Different great results have been underlined from this dialogue, and some of them are pointed here:

- ***The influence of the loading path***: This point has been already underlined from the pioneering works of Taylor and Quinney in [Taylor 1934]. Comparing the energy stored during a monotonic tension test in [Farren 1925] and during a monotonic twist in [Taylor 1934], authors underlined that a monotonic tension test provides to the material only a very small fraction of latent energy which it could stored compared to the twist loading for an equivalent cold-work. Thirty years later, Clarebrough published in [Clarebrough 1955] results confirming this point. Results are presented in picture 5.

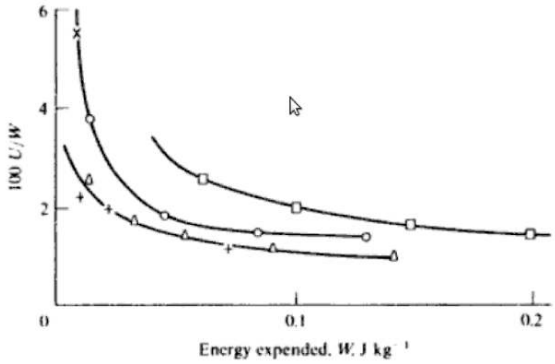

Figure 5: Percentage of energy stored (U) as a function of the work of deformation (W) in $J.kg^{-1}$ for various metals and methods of working. □=nickel, torsion; ○=arsenical copper, torsion ; ×=arsenical copper, tension; △=pure copper, torsion; +=pure copper, compression. [Clarebrough 1955]

Every material appears to tend toward a saturated state, in terms of stored energy. But depending on the loading, and consequently on the microscopic activated mechanisms, the rate of storage is more or less significant. The more complex is the working process, the higher will be the initial rate of storage. This point make sens compared to studies [Clarebrough 1958, Oliferuk 1995] concerning the influence of grain size, for exemple.

- ***The grain size***: the influence of grain size on mechanical behavior of metal has been widely investigated. Currently, the grain size effect is frequently summarized by the following sentence: "smaller is stronger". In 1958, considerable divergence of opinion exists as to the exact influence of

grain size, so Clarebrough has investigated the grain size influence, notably on stored energy and hardeness [Clarebrough 1958]. Pure bar of copper has been submitted to tensile and compression test and stored energy as well as hardness have been measured. In the present case, the heat measurement was performed by the global anisothermal two-step method. Figure 6 (a) presents his results.

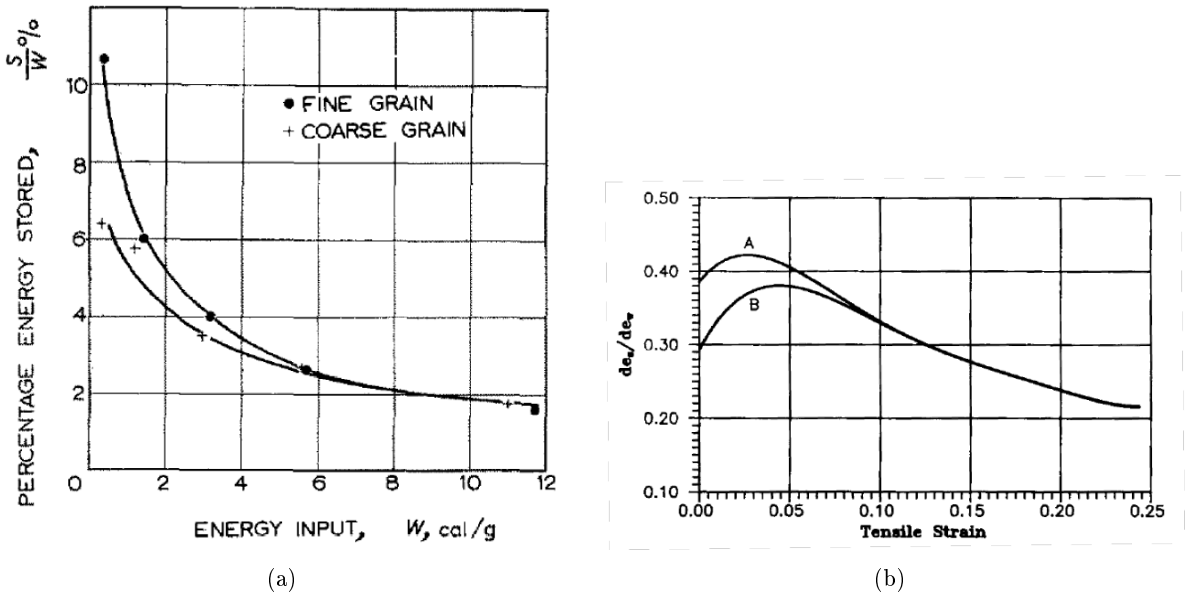

(a) (b)

Figure 6: (a) Percentage of energy storage as a function of energy expended in deformation for specimens of copper: • fine-grained ($30\mu m$) and + coarse-grained ($150\mu m$) [Clarebrough 1958]. (b) Dependence of $\frac{de_s}{de_w}$ (ratio of rate of storage on rate of expended energy) vs strain for A fine-grained ($8\mu m$) and B coarse-grained ($80\mu m$)[Oliferuk 1995]

His conclusion was that at low strain, fine grain structures ($30\mu m$) stores more than coarse grain ones ($150\mu m$), but as the strain increases this difference disappears. The author explain this observation by the following fact. At low strain, the major obstacle to slip within the crystal is grain boundary. When the strain and hardening occur, dislocation flow grows from boundary to center of grain in a high hardening rate process. Then, obstacles to dislocation movement become more and more closely spaced leading to the activation of cross slip process which is a lower rate hardening phenomenon. It explains why smaller grain structure, where grain boundaries are closer to each others, store more rapidely than higher ones. Oliferuk confirms this analysis in an austenitic steel [Oliferuk 1995]: in a first stage the rise of storage rate is due to the heterogeneity of strain field and stress localization at grain boundary where easy dislocation source are widely produced. Then, they propagate through the grain until the interaction between them becomes too much stronger. It corresponds to a maximum in storage rate (see figure 6 (b)). Finally, low energy dislocation structure are produced in aggreement with the principle of energy minimiza-

tion. The author adds that the decrease in ratio of storage rate on expended work rate means an increase of dissipation which is totally in line with the plastic phenomena occuring in this stage, i.e cross-slip and dislocation annihilation, micro shear banding [Oliferuk 1996]... Figure 6 (b) presents the corresponding results. Readers could underline the same influence of grain-size on initial storage rate, and strain level when a maximum is reached. Note that in [Oliferuk 1995], a higher storage of energy in smaller polycrystal grains is founded contrary to [Clarebrough 1958]. Nevertheless, this point must be compared to the uncertainty of measurement which is relatively high at the end of test.

- ***The chronology of elasto-plastic mechanisms contributions to stored energy***: from contribution of Ashby [Ashby 1970] one knows that dislocation density, in metal, could be classified into two categories: Statistically Stored Dislocations ($SSDs$) and Geometrically Necessary Dislocations ($GNDs$). $GNDs$ are distinguished from $SSDs$ as they are only present in regions of non-homogeneous plastic deformation to accommodate geometric incompatibilities or strain-gradients. Therefore, $GNDs$ are essentially localized in grain boundaries where the lattice discontinuity is found. One the contrary, $SSDs$ are inherently present in a homogeneously deforming material, where they accumulate by randomly trapping other moving dislocations. As theses dislocations move in a closed environnement, two kind of interaction between them can be distinguished: short range interactions between $SSDs$ and $GNDs$ densities giving rise to the slip system resistance, and long range interactions arise from the repulsive nature of the dislocation induced stress fields. Oliferuk [Oliferuk 1996] evidenced, as already partially discussed in [Bever 1973] and in other works, a linear relationship between the square of flow stress and stored energy during monotonic tensile test on stainless steel material. She emphasized the fact that a linear relationship exist only after a maximum in energy storage rate was reached (see figure 6 (b) and figure 7 (a)). It was underlined that, this result agrees with a well known empirical dependence $\sigma^2 \propto \rho$, where ρ is the total dislocation density. So $E_s \propto \sigma^2 \propto \rho$ is verified only in the stage where ratio of stored energy rate on rate of expended energy decrease. In a first stage of plastic deformation an additionnal mechanism of storage is consequently present. In [Oliferuk 2004], performing test on pre-strained specimen in loading direction (L), in transversal direction (T) and on standard specimen (0) of stainless steel, the author evidenced the fact that such maximum in $\frac{de_s}{de_w}$ curve do not exist on further response of (L) specimen. Actually, the (L) specimen, has already accomodated strain field at grain boundary for the imposed loading. It confirms that the first stage in plastic deformation associated to a rise in $\frac{de_s}{de_w}$ curve is associated to micro-stresses (internal stresses) resulting from the polycrystalline nature of the material, notably from differently oriented adjacent grains.

The conclusion is that the storage of energy includes contributions of internal stresses (elastic accomodation at grain boundary) and dislocation flow. In a first stage, depending notably on grain size the internal stresses, i.e. microstructural texture, dominates (from 0 to $\approx 4.5\%$ in [Oliferuk 1996]) then dislocation flow becomes prominent and the stored energy depends linearly on it.

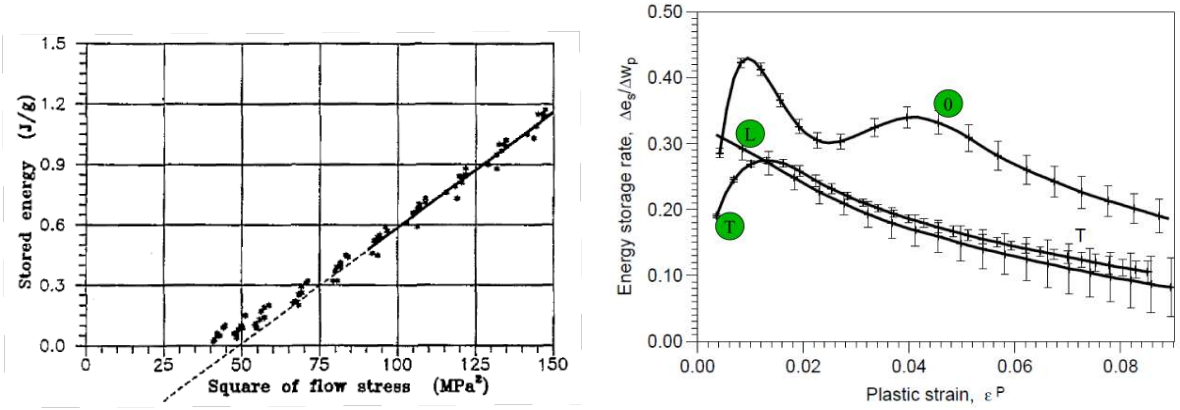

(a) (b)

Figure 7: (a) Stored energy as a function of flow stress square during uniaxial tension of an austenitic steel. The measurements were performed on eight samples (average grain diameter = 80 μm) [Oliferuk 1996] and (b) The energy storage rate $\frac{de_s}{de_w}$ as a function of the plastic strain ε^p for the L, T and 0 samples. The mean square deviation is marked [Oliferuk 2004]

Two conlusions could be put in light regarding the stored energy and the temperature:

- The stored energy, even at macroscopic scale, is intrinsically linked to microstructural transformations. It includes the influence of grain size, material properties, internal elastic stresses or plasticity and allows an analysis of the appearance and magnitude of each anelastic mechanisms. One understands consequently, the importance of the dialogue between thermodynamic and crystallography. Understanding the variation of rate of storage or unstorage (release), their thresholds as well as the anelastic mechanisms that develop, is an opened way on new energy based criteria [Chrysochoos 1989b, Vincent 2008].

- In parallel, as a dissipative phenomenon, the scenario of strain localization within material can also be understood regarding to local variation of temperature, in a first step. This point is in the continuity of some works [Wattrisse 2002, Louche 2005, Ait-Amokhtar 2008, Ranc 2008, Padilla 2011, Rittel 2010, Maynadier 2011a] where authors have tried to track signs of macroscopic strain localization using infrared thermography.

Many other contributions have been provided by many authors, concerning the link between electrical resistivity, density, hardeness, metal identity (additive elements) and stored energy. A wide description

of litterature on this field was published in [Bever 1973].
Nevertheless, one of the main problem in the dialog between thermodynamic and crystallography is the difference of scale. Indeed, to our knowledge, no energy balance has been performed at grain scale of fully polycrystal, even if some recent studies has been performed on bicrystals or oligocrystals (< 10 grains) (see section 0.4.2). Thus, it is necessary to converge toward the grain scale.

0.4 Dissipation and storage at granular scale

0.4.1 Questioning point

The principle of Infrared Thermography as well as Digital image correlation are introduced in appendix C and B respectively. Let us first introduce a questioning point. One has seen along the last chapter that the main avantage of the thermodynamic approach compared to the microscopic one is that the energy storage measurement is quantitative. Indeed, microscopic approach necessarily assumes a model, analytic and empirical laws to recover stored energy from measurement of lattice transformation, rotation, dislocation pattern, which are "difficult to verify unambiguously". This point has been notably treated in [Miroux 1999]. Nevertheless one understand from appendix C and B, that this point is not clearly verified anylonger when one desires to go down in scale using thermodynamic approach. Indeed, contrary to calorimetry which allows a direct access to global dissipated energy (macroscopic scale), the thermal measurement, performed by InfraRed camera do not. Thermal measurements firstly ask many hard metrological questions, still unsolved in some cases, and secondly require to solve the heat equation to recover dissipative sources and stored ones. It remains nevertheless the only way to access to heat source fields. The next section discusses the recent results.

0.4.2 Scale convergence

The convergence between deformation mechanism scale and infrared thermography scale is possible thanks to the improvement of technology as well as the constant improvement of knowledges concerning microstructural transformations.

- ***The grain growth***. Knowledges concerning microstructure transformations relate to the management of grain growth in metallic polycrystals. Many authors have studied this point, for exemple [Stanley 1969, German 1978, Atkinson 1988], notably in the case of austenitic stainless steel. Currently, it allows creating microstructures matching imaging systems capabilities.

- ***The limit of the IR imaging***. In situ full-field thermography is commonly used as experimental tool thanks to recent improvements of detectors, size of the focal plane pixel array, and capture rate. Most of recent works employed a spatial resolution which range from 100 to 500 $\mu m/pixel$ and a frame rate on the order of 10 to 100 Hz. Nevertheless, much higher frame rate fullfield thermography (on the order of 1000's of Hz) has been used to observe variation of temperature during split-Hopkinson pressure bar (SHPB) compression [Guzmáin 2009] and dynamic fracture [Zehnder 2000] experiments. Nevertheless such frequency of measurement implies a compromise on the spatial resolution (64x16 pixels and 8x8 pixels, respectively). More recently,

in [Padilla 2011] a spatial resolution of $8\mu m/pixel$, over a 320x256 pixel array of InSb detectors combined with a measurement frequency of 157 frames/s has been reached. In this case, the focal plane array infrared camera used to observe the deforming sample is a Stress Photonics model DT 1550 (Stress Photonics, 2008) combined with an IR transmissive two-position zoom lens.

To our knowledge, during the last 4 years, 3 studies were truly interested in the convergence between the scale of deformation mechanisms, the grain, and the infrared scale measurement for energy balance. These experiment are briefly introduced here, with main corresponding results (experimental setup are not detailed in this part but will be in chapter 2.1). Notice that the Quantitative Infrared Thermography at granular scale requires to follow every material points along their deformation path as well as their associated temperatures. Thus it requires to couple kinematic and thermal measurements. Different techniques could be used. More details about the principle of such measurements are presented in chapter 2.1. Finally note that each study has been done under monotonic tension test.

Bodelot *et al.* proposed a new experimental setup for fully-coupled thermal and kinematic in-situ measurement used at the grain scale of a AISI 316L stainless steel [Bodelot 2008, Bodelot 2009, Bodelot 2011]. It couples Digital Image Correlation (see appendix B) and InfraRed Thermography (see appendix C).

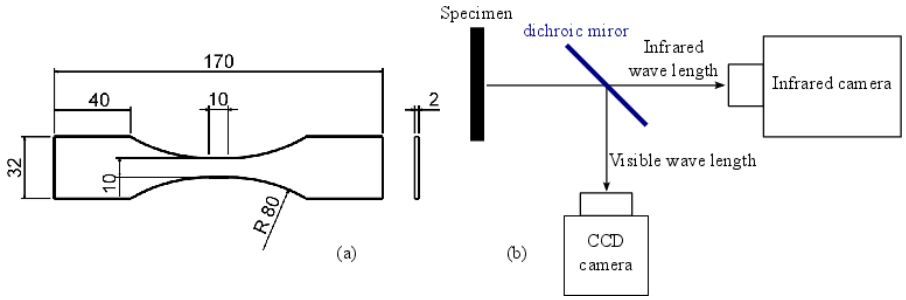

Figure 8: Scheme of the experimental setup used in [Bodelot 2011].

One avantage is the very low diffusivity of the material, allowing the observation of low temperature variations, i.e. low plastic off-sets. The authors combine both kinematic and thermal measurements by means of a dichroïc miror which transmits IR wavelength and reflect visible ones. It allows observing simultaneously the same specimen surface with both cameras. Resulting datas are fully-coupled insofar as both fields correspond to the same zone (5x5 mm^2), at the same time, expressed in the undeformed configuration and the spatial resolutions achieved in strain measurements as well as in temperature measurements are suitable to give meaningful data at the scale of the grains of the studied material. Figure 8 presents the scheme of the experimental setup and table 2 summarizes main specificities of the experimental setup.

	Visible measurements	InfraRed measurements
camera	Jai CV-M4+ CCD	Cedip Jade III MW
frequency of measurements	7 Hz	140 Hz
tracking and imaging system coupling	DIC	dichroïc miror
resolution	90 $\mu m/px$	104 $\mu m/px$
uncertainty	0.1 %	30 mK
material	AISI 316L stainless steel	
mean grain size and number	118μm - 1776 grains	

Table 2: Main specificities of the experimental setup used in [Bodelot 2011]

Additional details about this work are given in chapter 2.1. Different, monotonic and cyclic tests have been performed. One of them, presented in figure 9, allows the observation of the localization of temperature due to microplasticity within a A316L specimen submitted to a monotonic tensile test up to 270 MPa of nominal stress. The micrography of surface specimen is superimposed and allows distinguishing the microstructure.

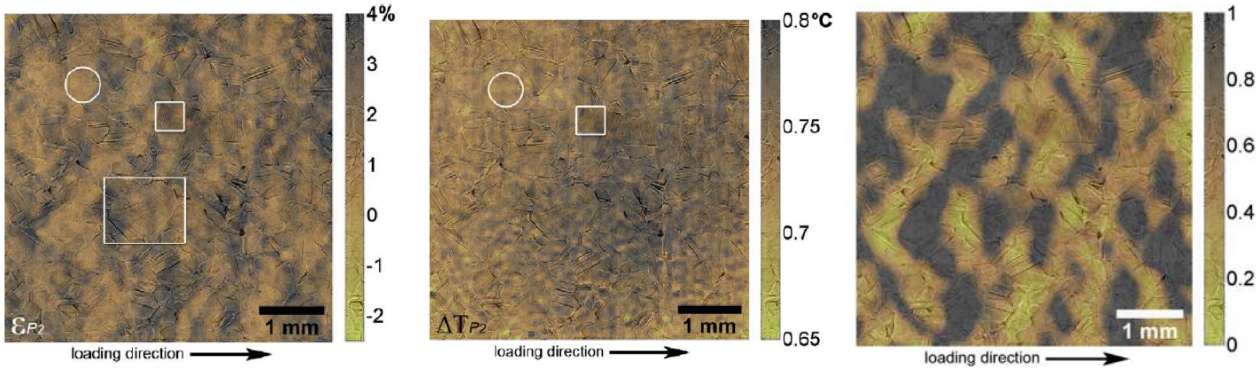

(a) ε_{axial} (b) θ (c) β

Figure 9: Case of the 5x10^{-3} s^{-1} monotonic tensile test. (a) Axial strain field in the loading direction over the 5x5 mm^2 ZOI at 268.9 MPa ($R_e^{0.2\%} = 223$). (b) Field of variation of temperature from the initial equilibrium at same instant. (c) First estimation of the differential β ratio ($\beta = \frac{\text{intrinsic dissipation}}{\text{plastic work}}$) field during linear hardening [Bodelot 2011]

Fields reflect the early plastic localization of heat within a polycrystal aggregate composed of more 1776 grains. Figures 9 points here the complexity of a thermomechanical analysis of deformation processes. Indeed, in figure 9 (a), one observes that many regions localize strain level over 4% nevertheless, only one specific regions seems to dissipated and conduct heat through the material (see figure 9 (b)). It points the local and cumulative aspect of strain over the deformation path while the

temperature is instantaneous and space dependent. Thus it reflects the current heated region as well as the propagation of this heat through the material. One observes in figure 9 (b) a clear link between an apparent very deformed region and the thermal localization. Figure 9 (c) presents first differential β ratio estimation, i.e. the fraction of plastic energy converted into heat. The heat equation is solved using adiabatic conditions as well as the assumption of neglectable elastic strains. One observes that heavily marked zones (by slip marks) exhibit a low β ratio meaning that a great part of the locally expended energy has been stored into microstructural changes while in others the plastic work is highly dissipated into heat.

In parallel, works of Saai *et al.* [Saai 2007, Saai 2010] propose a similar investigation on Al bi-crystals submitted to monotonic tension test. It couples grid method (used for exemple in [Delaire 2000]) and InfraRed Thermography.

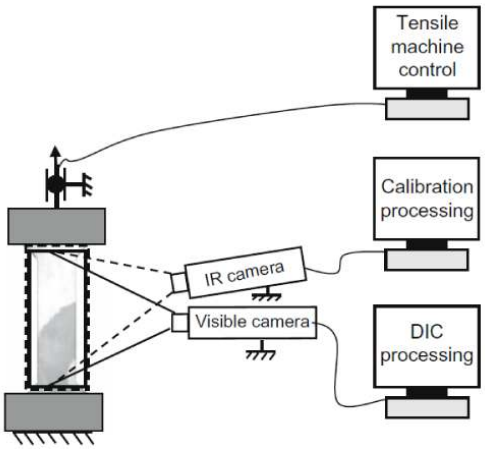

Figure 10: Scheme of the experimental setup used in [Saai 2010].

The aluminium has the avantage to be a good candidat for large grain growth nevertheless its diffusivity is very high making more complex the observation of slight variation of temperature, i.e small plastic off-set. Works focus on different aspects: (1) the implementation of physic mechanisms of storage and unstorage in crystalline plasticity framework and Finite Element method, (2) the fully-coupled measurement of in-situ kinematic and thermal fields and (3) the experimental achievement of energy balance. Figure 10 presents the scheme of the experimental setup. Notice that in the setup, the IR camera is slightly tilted to allow the simultaneous observation of the surface specimen by both IR and CCD camera. The use of this technique was made possible by the macroscopic aspect of the microstructure. Table 3 summarizes main specificities of the experimental setup.

	Visible measurements	InfraRed measurements
camera	Hamamatsu	Cedip Jade III MW
frequency of measurements	4.5 Hz	20 Hz
tracking and imaging system coupling	grid method	tilted camera
resolution	360 $\mu m/px$	170 $\mu m/px$
uncertainty	0.1%<u<0.8%	20 mK
material	A1050 Aluminium	
mean grain size and number	>10 mm - 2	

Table 3: Main specificities of the experimental setup used in [Saai 2010]

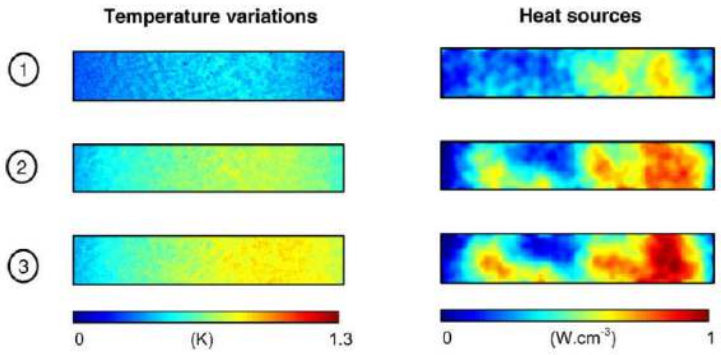

(a) θ (b) $\dot{\phi}$

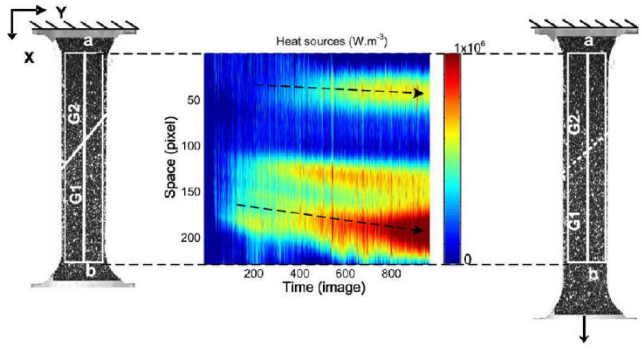

(c) $\dot{\phi}$

Figure 11: Case of the 1.1x10^{-2} s^{-1} monotonic tensile test. (a) thermal field and (b) heat source field (mW.mm^{-3}) at different loading levels respectively (1) 3.7 mm, (2) 8 mm and 12 mm of grip displacement from top to bottom (specimen gauge-section 31 mm). (c) Temporal evolution of heat source profile along the line a-b (W.m^{-3}) [Saai 2010]

Figures 11 (a) and (b) present the thermal and thermomechanical heat sources fields at different loading levels. Heat sources are estimated from filtered experimental surface temperature and the assumption of homogeneous temperature along the thickness of specimen. The successive fields allow the observation of the zones where local plasticity develops preferentially. Figure 11 (c) presents the time variation of the heat source profile along the line a-b. Figure 11 (a) emphasizes the fact that the temperature is a degraded form of the heat source which has made it. Although the temperature is an instantaneous sign of anelastic phenomena in terms of localization and appearance nevertheless it remains a weak quantity due to conduction, convection, radiation. Indeed, one clearly observes the wealth information provided by thermomechanical heat sources (see figure 11 (b)), especially about the magnitude of the observed mechanisms. According to heat sources in figure 11 (b), the plasticity localizes firstly in the center of the grain G_1 which has the higher Schmid factor (0.49) then propagates up to the boundary, finally over a certain macroscopic deformation, plastic slip occur within the grain G_2. The heat source allows in the present work following the elasto-plastic path of both grains. Notice, the heat source ranges from 0 to 1 mW.mm^{-3} at ≈20 % of strain.

More recently, Badulescu *et al.* [Badulescu 2011] couple the grid method and Infrared Thermography to investigate the plastic deformation within a multicrystal (6 grains) of aluminium.

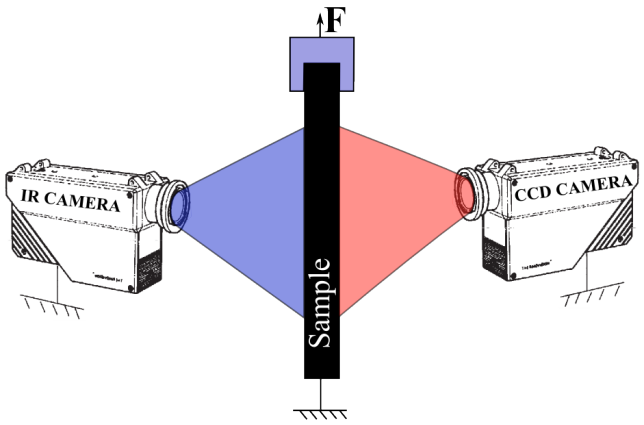

Figure 12: Scheme of the experimental setup used in [Badulescu 2011].

Taking profit of a flat specimen with columnar grains, IR measurement is performed on one face while kinematic is performed on the other. Figure 12 presents a scheme of the experimental setup and table 4 summarizes its main specificities.
One observes within figure 13, at ≈5% of axial strain, the difference of temperature from the initial state, the heat source, the variation of deformation around the considered instant and finally the variation of β ratio from 0 to ≈6 % of external loading. One observes simultaneously the localization of the temperature, the axial strain and the heat source within both grain 4 and 5. The present work underlines consequently a clear link between the kinematic activity of grains and their thermal response.

	Visible measurements	InfraRed measurements
camera	SENSICAM	Cedip Jade III MW
frequency of measurements		
tracking and imaging system coupling	grid method	dual-face
resolution		
uncertainty	0.01%	20 mK
material	Commercial pure aluminium	
mean grain size and number	>5 mm - 7	

Table 4: Main specificities of the experimental setup used in [Badulescu 2011]

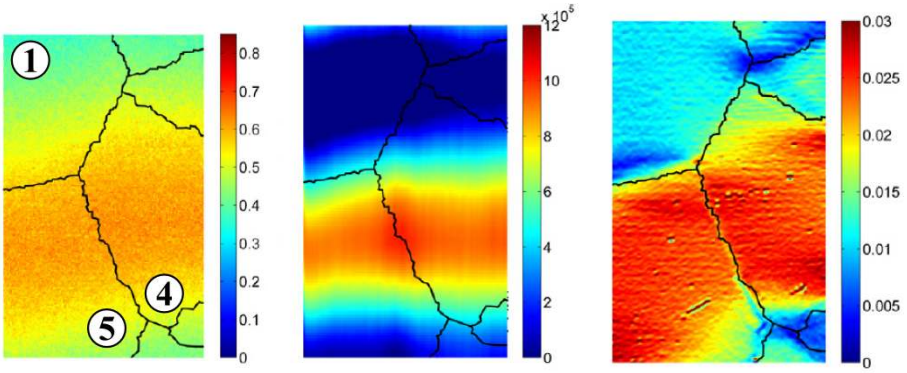

(a) θ (b) $\dot{\phi}$ (c) $\Delta\varepsilon_{axial}$

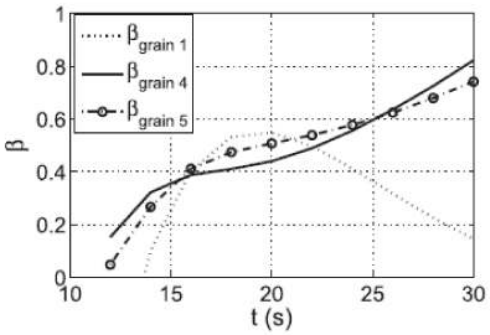

(d) β

Figure 13: Case of 85N.s^{-1} monotonic tensile test. (a) Temperature difference($\theta = T - T_0$), (b) Heat source d (W.m^{-3}), (c) $\Delta\varepsilon_{axial}$ (from t=26 to t=28s) at 27s (≈5%) of axial strain. (d) Variation of β ratio up to ≈6% of axial strain [Badulescu 2011]

One also observes a clear discontinuity of strain field from grain to grain as well as the localization of heat source at interface between grain 4 and 5. Consequently, it demonstrates the first order role playing by the grain boundary network in the mechanisms of localization of deformation and energy. Figure 13 (b) points in addition that a factor ten exists on heat source between low strained grains, high strained grains and grain boundaries. It confirms the great necessity to base energy criteria of localization on such local investigations. Finally, figure 13 (c) presents the variation of β ratio within grains noted 1, 4 and 5. One observes that from 0 to 20s ($\approx$3% of axial strain) each grain has almost the same ratio of dissipated energy on expended one. It reaches 50%. Then grain 1 exhibits a drop of β ratio while both other increase. It is in aggreement with its lower strain level presented in figure 13 (c). Nevertheless, it is important to note that the β ratio does not provide any information about the absolute value of the dissipation, it only reflects the variation of the ratio of the dissipated energy on the expended one. Thus the ratio necessarily requires the observation of a complementary field (such as the strain field) in order to be discussed unambiguously.

0.5 Conclusion

As during quasi-static loading with high or low strain variations or dynamic ones, the crack initiation always results from a mechanism of localization, the understanding of the localization process is a key feature for many industrial problems. A possible way to track and to analyze these localization processes is the thermal and energy analysis, taking profit of the dissipative aspect of every anelastic phenomena. These phenomena can be followed and analyzed by means of the temperature resulting from dissipation but also by means of the latent energy, i.e. the one which is not dissipated. From the pioneering works of Taylor and co-workers, energy balances have been done at macroscale, and more recently at the sample scale thanks to the InfraRed Thermography. In this way, localization phenomena at the scale of the samples have been widely investigated. In parallel, many authors studied the stored energy at the crystal lattice and the dislocation scales.

Currently, the necessity to deal with very local phenomena of localization such as the ones occuring in fatigue, and the increasing miniaturization of industrial components leading to a convergence between the structure and the microstructure scale, require a convergence between classical energy balance investigations and the scale of the deformation mechanisms. Few works have really been done on this topic and the great majority have been performed on bi-crystals or oligocrystals of aluminium.

In the continuity of the introduced works, our study aims at investigating the thermomechanical couplings as well as the ability to perform mesoscopic energy balance within a metallic true polycrystal aggregate (thousand of grains) submitted to low strain levels. This loading type allows investigating the strain levels occuring in fatigue, i.e. ± 1 % even if it is clear that plastic mechanisms are different. Our study relies on works of Bodelot [Bodelot 2008], where the in-situ measurements of kinematic and thermal fields were done during a monotonic tension test up to 2.5% of plastic strain on a A316L stainless steel.

This study is firstly based on different tools: (1) a InfraRed metrology, (2) the multi-experiments and multi-fields couplings especially the material microstructure allowing an original treatment method of experimental data, (3) and a dialog between model and experiment allowing the validation of experimental data and the observation of hardly measurable fields. Secondly, the complementarity of crystallographic, kinematic, thermal and numeric field allow the investigation of microplastic phenomena, micro-strain localization, the thermomechanical coupling, the local flow stress and also the numerical and experimental mesoscopic energy balance.

Part I

Material, test and measurements

Chapter 1

Test and material

Contents

1.1 Material

This short section summarizes the main arguments which leaded to the choice of a specific material, considering the whole set of experimental constraints. Interesting readers could find more details in [Bodelot 2008]. As the final purpose is the study of microstructural thermomechanical couplings, three main constraints have to be underline:

1. **material diffusivity**: the thermal diffusivity is a measure of the rate at which a temperature disturbance propagates within a material. It is expressed by the relationship $\lambda = \frac{k}{\rho C_p}$, where k is the coefficient of thermal conductivity, ρ is the density, and C_p is the specific heat at constant

pressure. This thermal diffusivity must be as low as possible in order to limit a rapid diffusion of the heat generated by microstructural within the material.

2. **microstructure type**: a single phase material should be a better choice since thermal properties remain constant within the whole material. Then, material with cubic symmetry for example, leads necessarily to symmetric (isotropic) heat conduction tensor [Debreceni 1982]. Nevertheless, even in such case, a local anisotropy of thermal phenomena could be consider due to the polycrystalline nature of the material [Kapitza 1941, Jahanshahi 1966, Achenbach 1968].

3. **grain size**: the mean grain size must be in agreement with the spatial resolution of the considered measurement techniques, i.e more than 100 μm in the present case. The spatial resolution will be discussed in detail within chapter 2.1.

The table 1.1 proposes a comparative of thermal properties previously discussed, considering different metallic materials. It shows that different material are particularly suitable for such thermomechanical analysis, notably the AISI [1] 316L stainless steel and different nickel-based superalloys. Considering also the wide bibliography dealing with AISI 316L stainless steel [German 1978, Chrysochoos 1989b, Oliferuk 1995, Feaugas 1999, Feaugas 2003, Lee 2003] as well as the relative simplicity of grain size control by heat treatment, this steel was chosen by Laurence Bodelot, as being one of the best compromise. Its chemical composition and mechanical properties are shown in tables 1.2 and 1.3. One could note, a posteriori, that performed such thermomechanical study with a based-nickel alloy such as Inconel 625 would be sensibly better.

Metal	density ρ ($kg.m^{-3}$)	specific heat C_p ($J.kg^{-1}.K^{-1}$)	conductivity K ($W.m^{-1}.K^{-1}$)	diffusivity α x10^{-5} ($m^2.s^{-1}$)
Silver	10,500	230	418	17.1
Copper	8,940	380	389	11.4
Aluminium	2,700	860	200	8.6
Brass	8,500	370	100	3.3
Nickel (pure)	8,902	440	90.7	2.31
Steel (0.1%C)	7,850	490	46	1.2
Titanium (pure)	4,506	520	21.9	0.94
Steel AISI 316L	8,000	500	15	0.38
Udimet 720 (Alloy based-nickel)	8,080	420	13	0.38
Inconel 625 (Alloy based-nickel) [www.aviationmetals.net/inconel.php]	8,440	410	9.8	0.28

Table 1.1: thermal properties of different metals at 20^oC [Bodelot 2009]

[1] American Iron and Steel Institute

C	Cr	Ni	Mo	Mn	Si	N	P	S
≤0.03	16 to 18	10 to 14	2 to 3	≤2	≤0.75	≤0.1	≤0.045	≤0.03

Table 1.2: Composition ranges for 316L stainless steel (in mass percentage)

E (MPa)	R_e 0.2% (MPa)	R_m (MPa)	A (Elongation at Break) (%)	Z (striction coefficient) (%)
186,000	261	582	53	80

Table 1.3: mechanical properties for a standard 316L stainless steel

Bone shaped flat samples 2 mm thick (Figure 1.1) have been heat treated under air for 2 h at 1,200^{o}C and immediately water-quenched in order to grow the grain size up to the desired one, i.e more than 100 μm. They have then been mechanically polished up to a 1 μm diamond finish on the studied face. The mean grain size of the heat-treated material is 118 μm (results coming from E.B.S.D analysis including twin boundaries) thus matching the spatial resolution capabilities of measurement techniques. Spatial resolution of imaging system will be treated in chapter 2.1

1.2 Monotonic tensile tests

Different tests have been performed within the PhD work of Laurence Bodelot [Bodelot 2008]: 2 monotonic tensile tests and 2 cyclic tests performed under two different strain rate conditions, about 5x10^{-3} and 5x10^{-4} s^{-1} respectively. Nevertheless, within the present work, the database and results concerning only one monotonic tensile test will be consider. This choice has been done by considering the relatively low temperature variation leaded by fatigue test ($\Delta T \approx$150 mK) compared to monotonic one ($\Delta T \approx$1000 mK) compared to the uncertainty of measurement. Nevertheless, the developed strategy is compatible with other test conditions and results.

Finally, the chosen test consists in an monotonic tensile test performed on an electro-mechanical Instron 4508 machine. It is displacement controlled at a corresponding quasi-static strain rate of 5x10^{-3} s^{-1} and up to a stress of 270 MPa; the highest strain rate has been chosen in order to maximize the plastic dissipation. The associated final mean strain is 2.5%.

Figure 1.1 presents the specimen dimensions as well as the micrography of the specimen gauge section performed after the test. One can identify four regions within the specimen surface: the red one which corresponds to the area observed by the infrared camera (for thermal measurements), the blue one which corresponds to the area observed by the C.C.D. camera (for kinematic measurements), the yellow one which corresponds to the area analyzed by E.B.S.D. (for the grain boundaries network determination and the crystallographic orientations identification) and finally the white one which corresponds to the area analyzed by profilometry (for out-of-plane displacements measurements). Then,

all the results presented in this work, i.e displacements, strains, temperature, profilometry ... will be those of a 5mm × 5mm common zone of interest located in the center of the gauge zone (see figure 1.1).

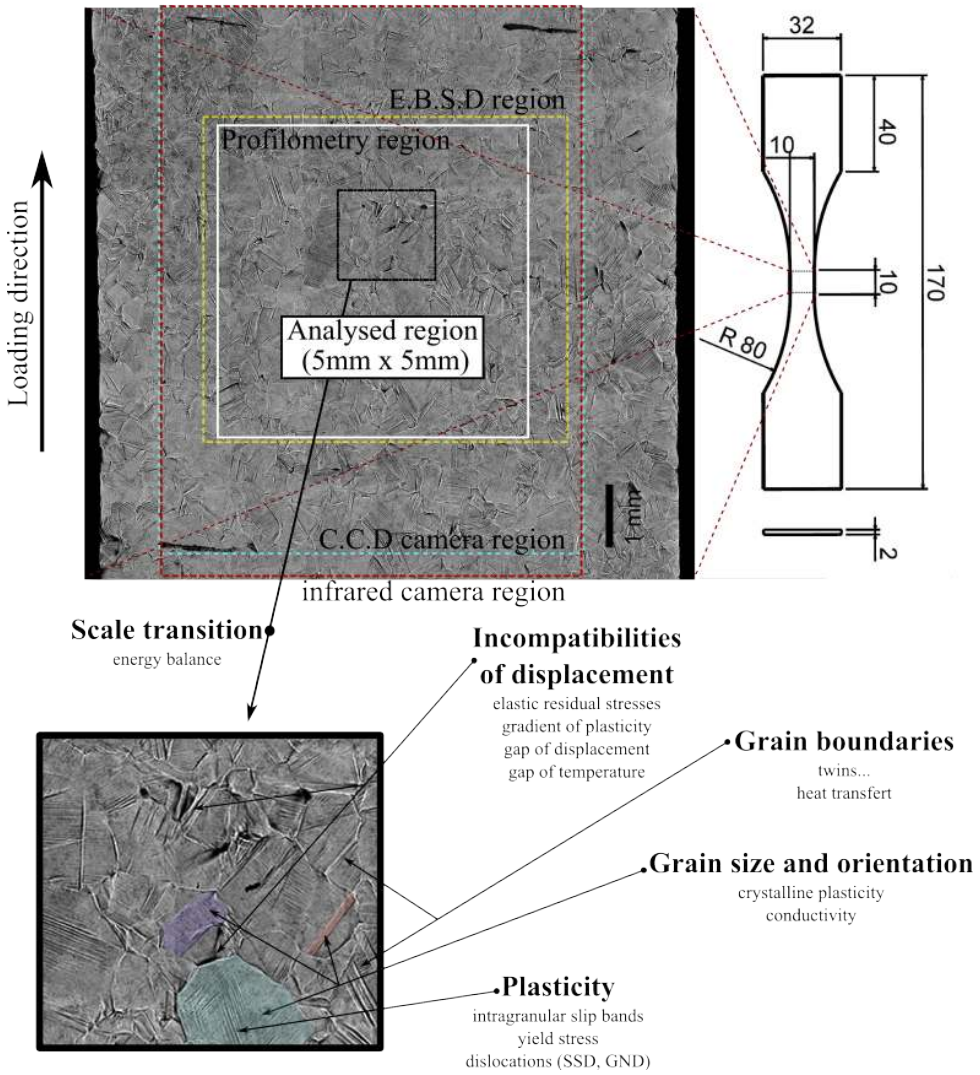

Figure 1.1: dimensions of the tested specimen and details on the studied area within its gauge section

Focusing on this central zone ensures, among others, to limit any distortion effects affecting the images as well as of any boundaries effects appearing during the following computations. Figure 1.1 also presents a zoom within the studied area. Some keywords underline briefly the complexity of deformation mechanisms developed on the material surface. To analyze such deformation mechanisms, some elements are required:

- a basic abseil on plastic mechanisms within polycrystalline materials. This point will be treated in section 1.3.1.
- a grain boundary network and orientations analysis. This point will be solved by a classical E.B.S.D. technique introduced in section 1.3.3.
- an identification procedure of the plastic slip marks on the specimen surface after the test. Classically, this time consuming operation is performed manually. An automatic procedure developed during this work is proposed in section 1.4.1.

1.3 Plasticity and crystallography

In this section, a general plasticity framework is first detailed. A second part deals with crystallographic aspects of plasticity in Face-Centered Cubic (F.C.C.) materials. Finally, the theoretical link between slip marks observations and crystallographic activated slip systems is also introduced.

1.3.1 Origins of plasticity

When a metallic material undergoes a loading such as the level is greater to its yield stress, plastic deformations occurs. The origin of the plastic strain is essentially the creation, the movement and the interaction of dislocations within crystalline structures. One consequence of these dislocation movements within grains is the appearance of slip bands on the material surface (see figure 1.2).

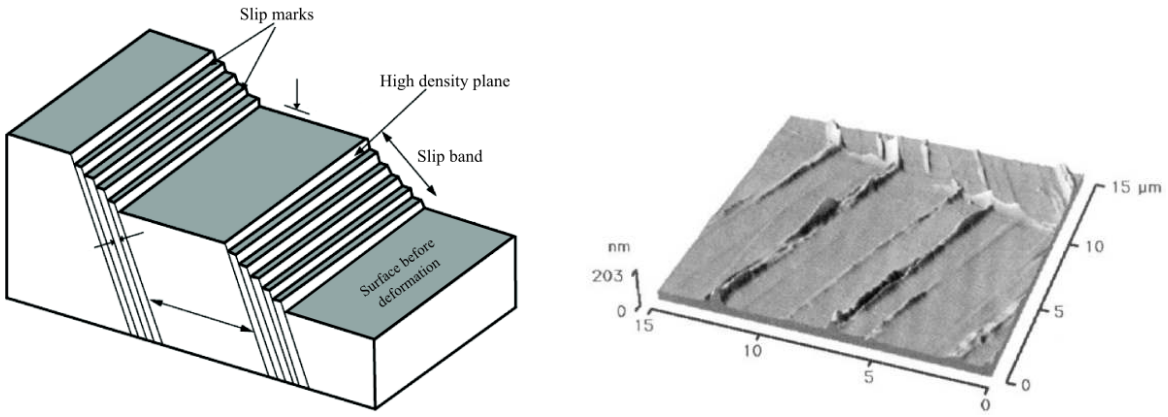

(a) (b)

Figure 1.2: (a) schema of the crystal surface exhibiting slip-marks groupped in slip-bands. (b) AFM images performed in contact mode on a AISI 316L stainless steel subjected to 5000 cycles (LCF) of symmetrical uniaxial test ($\frac{\Delta\varepsilon^p}{2} = 2\text{x}10^{-3}$)[Villechaise 2002]

A slip line or mark is the extremity of a stair generated by the appearance of a gliding dislocation on the surface. It corresponds to a relative displacement between tow parts of the crystal following

a particular plane and direction. Crystallographic directions as well as crystallographic planes are fictitious lines and planes related to the atoms of a crystal (see figure 1.3). Some directions and planes have a higher density of atoms and these particular planes have an influence on the behavior of the crystal, particularly on plastic deformation. Indeed, dislocation glide occurs preferentially along higher density planes and the perturbation carried by the dislocation (Burgers vector) is along a dense direction. This phenomenon comes from a minimization of the deformation energy since the shift of one atom in a more dense direction requires a smaller distortion of the crystal lattice. The combination of a high density plane and a high density direction constitutes slip systems which are currently well known for a large range of crystalline structure (*C.C.*, *F.C.C.*, *H.C* ...). The shear stress on this slip system is called Resolved Shear Stress (*RSS*) and its threshold, the Critical Resolved Shear Stress (*C.R.S.S.*). The following section deals with the particular case of F.C.C. structure.

1.3.2 Crystallographic slip systems within F.C.C. structure

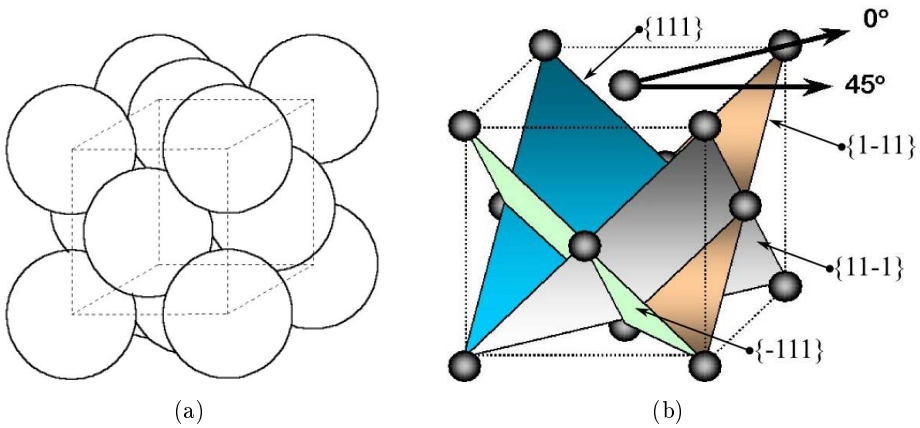

Figure 1.3: (a) F.C.C. crystal and its 4 preferential slip systems

Figure 1.3 presents a schema of F.C.C. crystal with fictitious crystal boundaries in dotted line and its four high density slip planes. Within F.C.C structure, at room temperature, dislocation could principally move along 4 planes of {111} kind. Within each plane, 3 possible directions of <110> type exist. Finally, in a F.C.C. grain there is 12 slip systems of {111}<110> type. These slip systems are recalled in table 1.4.
As there is a limited number of slip systems within F.C.C. structure, there is a limited number of possible slip mark orientations on surface specimen due to the movement of such planes. It is currently well known that there is a basic geometrical relation allowing to make the link between slip marks orientation from the loading direction Y and the effective activated slip system.

Slip planes	slip directions						Slip systems		
A: (-111)							A_2	A_3	A_6
B: (111)	1	2	3	4	5	6	B_2	B_4	B_5
C: (111)	[011]	[0-11]	[101]	[-101]	[-110]	[110]	C_1	C_3	C_5
D: (111)							D_1	D_4	D_6

Table 1.4: Schmid and Boas notation for slip system 111<110>

Three elements are necessary for the slip systems identification:

- the rotation matrix R between the global reference system (specimen reference) and the local reference system (crystal or grain reference).
- the angle of each possible slip marks (associated to each slip system) compared to the loading direction Y and the angle of the effective ones.
- the Schmid factor μ for each slip system. This element only allows the determination of the slip direction within the three possible ones effectively activated in the slip plane. Indeed, slip mark orientation does not provide any information to discriminate the effective direction.

Let us consider the triplet (X, Y, Z) as the specimen reference system and (X', Y', Z') the granular reference one. Y is the loading direction, Z the normal of the specimen surface and X completes the direct orthogonal trihedral and represents the transverse direction. Then (ϕ_1,Φ, ϕ_2) are the three Euler's angles defined on figure 1.4.

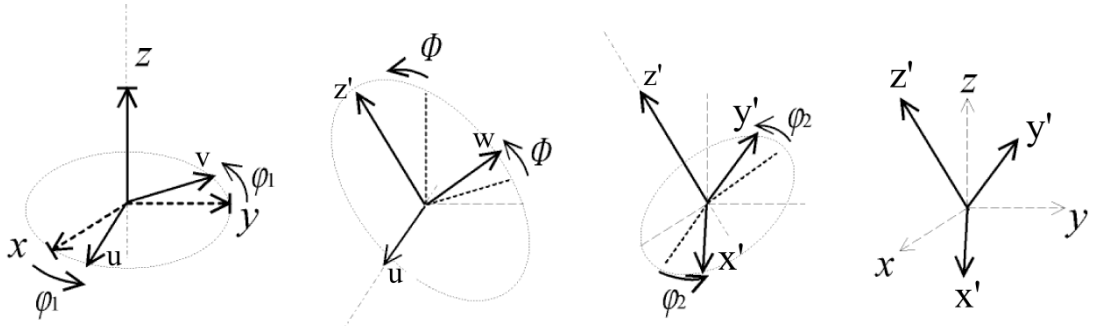

Figure 1.4: Euler's angle (ϕ_1,Φ, ϕ_2) according to Bunge notation [Bunge 1982]

Considering the following notation:

$$\left(\begin{array}{cccccc} C_1 & S_1 & C & S & C_2 & S_2 \end{array} \right) = \left(\begin{array}{cccccc} cos(\phi_1) & sin(\phi_1) & cos(\Phi) & sin(\Phi) & cos(\phi_2) & sin(\phi_2) \end{array} \right)$$

the equation which define the transition between the local coordinate system and the global one is

expressed as a function of the rotation matrix noted $\mathbf{R}$:

$$\begin{bmatrix} X' \\ Y' \\ Z' \end{bmatrix} = \underbrace{\begin{bmatrix} C_2C_1 - S_2CS_1 & C_2S_1 + S_2CC_1 & S_2S \\ -C_2CS_1 - S_2C_1 & C_2CC_1 - S_2S_1 & C_2S \\ SS_1 & -SC_1 & C \end{bmatrix}}_{\mathbf{R}} \begin{bmatrix} X \\ Y \\ Z \end{bmatrix} \tag{1.1}$$

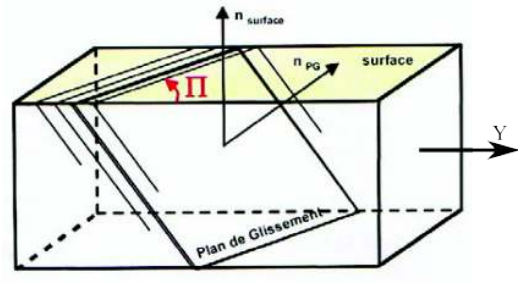

Figure 1.5: schema of Π angle between slip marks and loading direction Y

Figure 1.5 defines the angle Π between slip marks and the loading direction Y. In the present case, $n_{surface} = Z$. n_{pg} is the normal direction to the slip plane, known for each slip plane in the granular reference system (see table 1.4). It is expressed in the global one thanks to the equation 1.1 and the triplet (ϕ_1,Φ, ϕ_2) defined for each grain. Based on simple geometrical observation, the Π angle is defined as follows:

$$\cos(\Pi) = \frac{\left(\boldsymbol{n}^*_{\boldsymbol{pg}} \wedge \boldsymbol{Z}\right).\boldsymbol{Y}}{\left\|\boldsymbol{n}^*_{\boldsymbol{pg}} \wedge \boldsymbol{Z}\right\| \left\|\boldsymbol{Y}\right\|} \tag{1.2}$$

with $\boldsymbol{n}^*_{\boldsymbol{pg}} = \mathbf{R}\boldsymbol{n}_{\boldsymbol{pg}}$. As four dense planes are able to activate plastic gliding within FCC structure, the relation 1.2 allows the identification of four potential surface slip-mark orientation for a given crystal. A systematic comparison between effective slip-mark observed on specimen surface and the fourth potential ones allows the determination of effective activated slip planes. Interested readers could find more details about these crystallographic parameters within [Mineur 2000, Sabatier 2002].

This practical introduction on plasticity mechanisms has briefly pointed the kinematics and the origins of plastic gliding. A deeper focus on key features to observe plasticity appearance has been given. Especially, relations which relate surface slip mark orientations and slip system activity has been underlined. The section 1.4.1 will propose an automatic determination of these activated slip systems.

1.3.3 Principle of the E.B.S.D. analysis

The Electron Backscatter Diffraction (E.B.S.D.) technique[2] associated to Scanning Electron Microscope (S.E.M.) provides quantitative microstructural information about the crystallographic nature of metals, minerals, semiconductors, and ceramics. It reveals grain size, grain boundaries, grain orientations, textures and phases of the sample. The spatial resolution depends on the S.E.M. resolution, but for modern Field Emission S.E.M. (FE-SEMs), 20 nm grains can be measured with a reasonable accuracy. The macroscopic sample size is dependent on the ability of the SEM's stage and chamber to orient a sample at 70^o tilt at an appropriate working distance, usually in the range 5 to 30 mm.

EBSD operates by arranging a flat, highly polished sample at a specific angle to the incident electron beam (see figure 1.7 (a)).

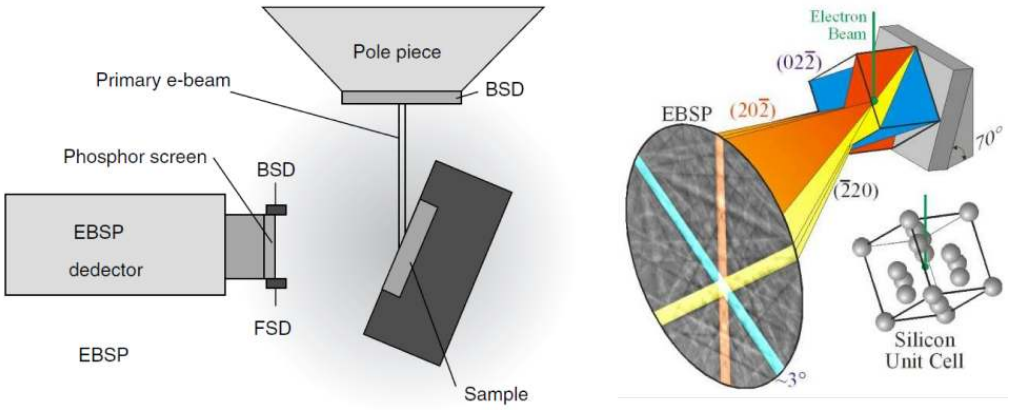

Figure 1.6: Schematic arrangement of sample orientation in the SEM and electron interaction with crystalline material [Zhou 2007]

With an accelerating voltage of 10-30 kV associated to a 1-50 nA incident beam, electron diffraction occurs from the incident beam point on the sample surface. With a stationary beam, an EBSD pattern emanates spherically from this point (see figure 1.7 (b)). When the primary beam interacts with the crystal lattice, low energy loss backscattered electrons are channeled and are subjected to path differences that lead to constructive and destructive interferences. If a phosphor screen is placed at a short distance from the tilted sample, in the path of the diffracted electrons, a diffraction pattern can be seen (see figure 1.7 (b)). Bands which are visible within EBSD pattern are called Kikuchi bands[3]. Specialized computer software analyze the EBSD by detecting a number of Kikuchi bands using an optimized Hough transform. With a priori information about the candidate phases under the beam, the software determines all possible orientations with each phase and reports the best fit as the

[2] this section is inspired by [Zhou 2007]

[3] Seishi Kikuchi and Shoji Nishikawa have discovered the fundamental diffraction principle at the origin of the EBSD technique in 1928

identified phase and orientation. When its orientation and phase are known the EBSD is considered indexed.

1.4 Microstructural analysis of the tested specimen

This part deals with the signs of plastic phenomena observed on the specimen surface after the test. As presented in the previous section, the specimen has been subjected to a monotonic tensile test with a constant strain rate of 5x10$^-$3 s^-1 up to 270 MPa and 2.5% of plastic strain. The purpose of this section is to analyze these signs and their link with the material crystallography. Firstly, E.B.S.D. results are introduced, i.e grain sizes and orientations, texture effects.... Then, two ways to reveal indicators of the deformation localization are introduced. One one hand, the quantification of the local misorientation between grains thanks to E.B.S.D. analysis is presented as well as the associated results. Then, an original texture image analysis is introduced in order to characterize the slip marks observed on the specimen surface after the test.

1.4.1 Texture, grains sizes and orientations

E.B.S.D. analysis was performed in collaboration with Patrick Villechaise within ENSMA[4] in Institut Pprime at Poitiers. The Scanning Electron Microscope is a Jeol 6100 with a conventional electron gun operating at 25kV and a $\approx 1nA$ probe current. Data come from the O.I.M.[5] analysis system provided by TSL. The pitch of measurement is 20 μm (size of the EBSD grid).

Picture 1.7 presents E.B.S.D. field: (a) the 1^{st} Euler angle ϕ_1, (b) the 2^{nd} Euler angle Φ and (c) the 3^{rd} one ϕ_2 in the triplet (ϕ_1,Φ,ϕ_2) which characterize the 3D orientation of each grain in a global system reference. Note that these pictures present the mean grain orientation per grain. The figure 1.7 (d) presents the maximum Schmid factor, μ_{max}, computed for the presented loading direction as follow. For every grains, let n_k be the unit slip plane normal vector, v_s the unit slip direction vector, k the considered system ($k = i \dots 12$ in FCC structure), σ the axis of the external load, and $\bar{\bar{\mu}}_k$ the Schmid tensor. It is a third order tensor (dimension = 3x3x12). Slip systems k have been already presented according to the Schmid and Boas notations in Table 1.4. According to the Schmid theory (see 6.5), the Schmid tensor is expressed as followed:

$$\mu_{ijk} = \frac{1}{2}\left(\left(n^i \bullet v_j\right)_k + \left(v^j \bullet n_i\right)_k\right) \qquad \text{with } (\bullet) \text{ the tensor product} \tag{1.3}$$

Then, assuming that the granular loading is collinear to the external one (uniaxial assumption within the single crystal) and exploiting the Schmid principle expressing that the plastic shear occurs first on

[4]Ecole Nationale Supérieure de Mécanique et d'Aerotechnique
[5]Orientation Imaging Microscopy

the maximum Schmid factor system, one can express μ_{max} as follows:

$$\mu_{max} = \max_{k} (\mu_{kij} \bullet \sigma_{ij}) \quad with \quad \sigma = \begin{pmatrix} 1 & 0 & 0 \\ 0 & 0 & 0 \\ 0 & 0 & 0 \end{pmatrix} \tag{1.4}$$

($\bullet$) is here the double-contracted tensor product.

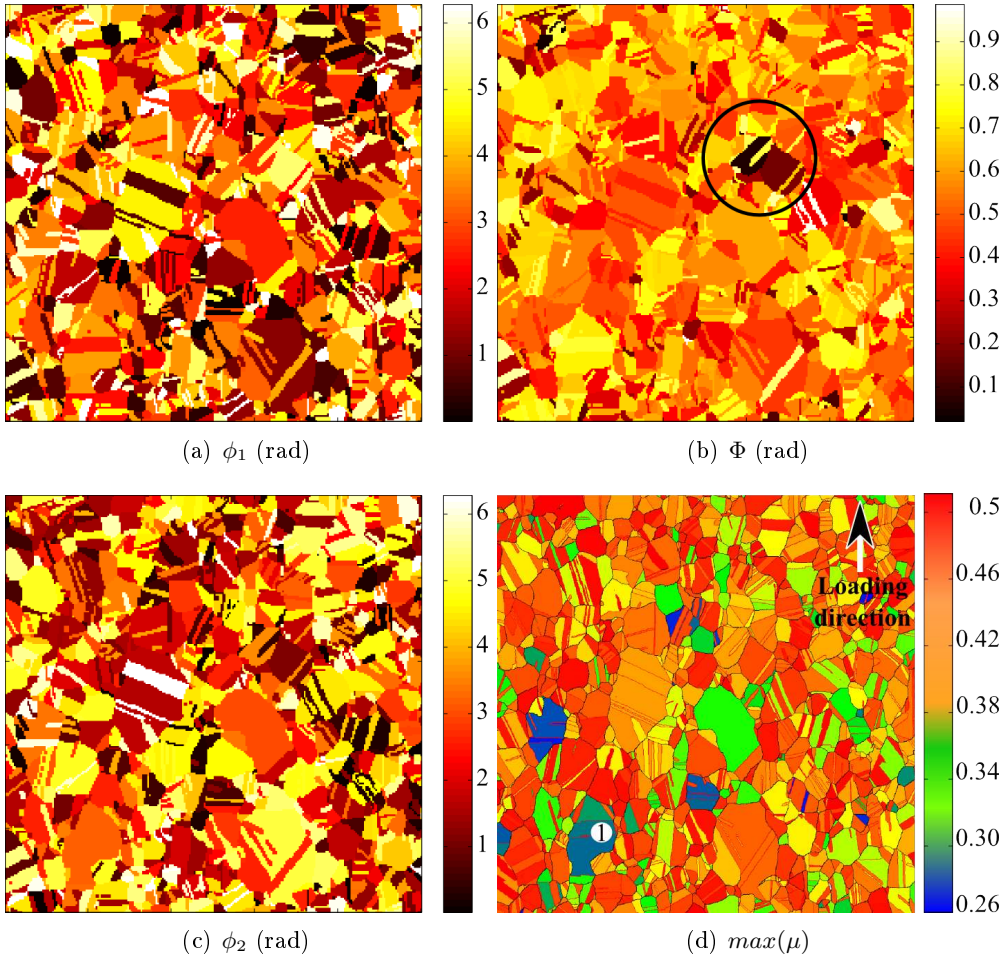

(a) ϕ_1 (rad) (b) Φ (rad)

(c) ϕ_2 (rad) (d) $max(\mu)$

Figure 1.7: triplet ((a) ϕ_1, (b) Φ, (c) ϕ_2) provided by E.B.S.D analysis (in *rad*) and (d) maximum Schmid factor

Figure 1.7 (d) shows that the mean maximum Schmid factor is 0.44 and evidences that the major part of the studied area exhibits a maximum Schmid factor higher than 0.45 even if some grains exhibit very low maximum Schmid factor, notably the region denoted 1. According to the Schmid principle this region is expected to undergo lower plastic strains. Focusing on figures 1.7 (a), (b) and (c) one

observes that Φ_1 and Φ_2 are distributed between 0 to 2π. In comparison, Φ ranges (by definition from 0 to π) from 0 to 0.9 radians. It is quite uniform and relatively low, especially for a string of grain located in the black circled region. These grains have thus a lattice which is in the plane, i.e only rotate about <001> axis. In addition, according to pole figures (not presented here), the microstructure exhibits a classical Goss texture, i.e {101}[111]. Nevertheless the maximal texture factor remain low (i.e. 3.7).

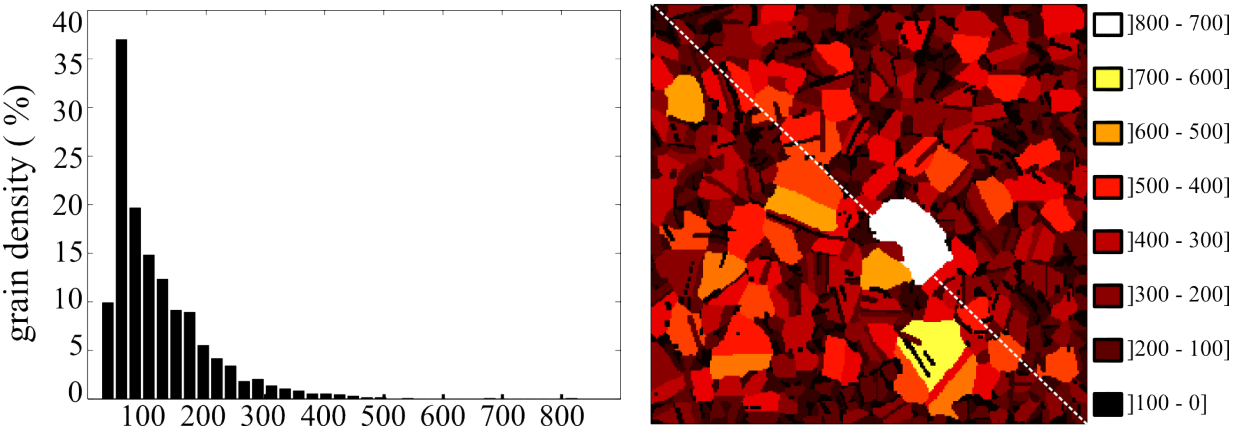

(a) grain diameter in μm (b) grain diameter in μm

Figure 1.8: (a) distribution of grain diameter function of grain density and (b) mean grain diameter field per range

The microstructure of the central $5mm \times 5mm$ area is composed by 1776 grains with a mean grain size equal to 118 μm (based on the diameter approximation). Picture 1.8 presents (a) the distribution of grain size within the studied area and (b) the spatial location of each diameter range. In addition, table 1.5 precises statistics about grain size considering on one hand the percentage of grain and on an other hand the percentage of surface occupied by grains. One could note, according to table 1.5, that 60.7 % of grains have a diameter lower than 100 μm[6], nevertheless, one could see that these 60.7 % of grains only represents 15.1 % of the studied are. Then, more than 84 % of the central area exhibits significant grains in terms of size and, in particular, $\approx$20 grains have a diameter higher than 400 μm. In figure 1.8, one can also note that grain size is statistically lower ($95\mu m$) above the white dotted line than below ($141\mu m$). This phenomenon is probably due to the the water quenching process used on the specimen before the test. As there is a direct link between the grain size and material properties [Hall 1951], one can suppose that this will have an impact on thermomechanical analysis.

[6] the fullfield measurement resolution is $104\mu m$ (see next chapter)

Ranges	[0-100[	[100-200[	[200-300[	[300-400[	[400-500[	[500-600[	[700-800[
% of grain	60.7	25.7	8	2.4	0.9	0.2	0.1
number of grain	1113	457	143	43	16	3	1
% of surface	15.1	32.6	28	16.1	4.6	1.4	2.2

Table 1.5: statistic of grain size

In conclusion, the analyzed area of the specimen is representative of a polycrystal ($\approx$ 1700 grains). The grain diameter ranges from $20\mu m$ to more than $800\mu m$. Moreover, more than 80% of the gauge surface is composed by grains with a diameter higher than $100\mu m$. The material does not exhibit a real crystallographic texture but exhibits a macroscopic area where grains are statistically smaller. Finally, some singular values within second Euler angle, and maximum Schmid factor have been underlined. Theses regions should be analyzed in depth in order to underline possible interaction with deformation processes.

1.4.2 Misorientation

The purpose of this section is to determine the misorientation field of the tested specimen, i.e. the mean angular deviation between one grain and its neighbors. As it has been introduced in the previous section, the grain orientation could be defined by a triplet of Euler angles (ϕ_1, Φ, ϕ_2). Nevertheless, there is no uniqueness of Euler angle triplet to characterize the rotation which allows passing from the global reference system to the crystalline one. The deviation from one grain to its neighbors or to the global reference system could not be trivially found. This section is inspired by [Guilhem 2011].

Let us define the orientation matrix $\mathbf{g}$, i.e the operator which provides vectors expressed in the basis β_0, from vectors expressed in the basis β_1.

$$\beta_0 = \mathbf{g}.\beta_1 \tag{1.5}$$

with, from equation 1.1:

$$\mathbf{g} = \begin{pmatrix} C_2C_1 - S_2CS_1 & C_2S_1 + S_2CC_1 & S_2S \\ -C_2CS_1 - S_2C_1 & C_2CC_1 - S_2S_1 & C_2S \\ SS_1 & -SC_1 & C \end{pmatrix} \quad \text{and} \quad \begin{cases} C_1 = cos(\phi_1) & S_1 = sin(\phi_1) \\ C = cos(\Phi) & S = sin(\Phi) \\ C_2 = cos(\phi_2) & S_2 = sin(\phi_2) \end{cases} \tag{1.6}$$

One considers two crystals A and B, their orientation matrix $\mathbf{g}_A$ and $\mathbf{g}_B$ and their local basis β_A and β_B respectively. The misorientation matrix between β_A and β_B, denoted $\mathbf{g}_{A/B}$ is defined as follow:

$$\beta_B = \mathbf{g}_{A/B}.\beta_A \tag{1.7}$$

and takes the form:

$$\mathbf{g}_{A/B} = \mathbf{g}_B.\mathbf{g}_A^T \tag{1.8}$$

In order to obtain the misorientation angle from this matrix, one uses the invariance property of the matrix trace:

$$\theta_{A/B} = arccos\left(\frac{tr\left(\mathbf{g}_{A/B}\right) - 1}{2}\right) \tag{1.9}$$

$\theta_{A/B}$ could be called the absolute misorientation between basis β_A and β_B. Nevertheless, it is important to underline the difference between the absolute misorientation of two basis and crystalline misorientation. The second one is more restrictive. Indeed, in the case of a crystalline structure, for example F.C.C., crystalline lattice possesses 24 symmetries associated to 24 symmetry operators $\mathbf{O}_i$. These 24 operators are recalled within appendix F. That means that different absolute misorientation could actually be related to the same crystalline one. To take into account these symmetries, one applies the symetry operator $\mathbf{O}_i$ to $\mathbf{g}_A$ and $\mathbf{O}_j$ to $\mathbf{g}_B$. Equation 1.10 becomes:

$$\mathbf{g}_{A^i/B^j} = \mathbf{O}_j\mathbf{g}_B.\mathbf{g}_A^T\mathbf{O}_i^T \tag{1.10}$$

and the crystal misorientation angle corresponds to the minimal value within the following set of possibilities:

$$\Delta\theta_{A/B} = \min_{i,j}\left[arccos\left(\frac{tr\left(\mathbf{g}_{A^i/B^j}\right) - 1}{2}\right)\right] \tag{1.11}$$

Note that, under such symmetries, the misorientation ranges finally from 0 to 62.8^o.

Within the following analyses, two kinds of misorientation are considered. The first one corresponds to the systematic misorientation between every couple of neighboring grains. It is called "systematic mutual misorientation". The second one corresponds to the mean misorientation per grain relative to the set of its neighbors. For the second case, the set of neighboring grain relating to grain i are considered and the crystal misorientation angle is calculated between the grain i and the entire set of neighbors. Finally, the mean misorientation weighted by the grain boundary length related to each grain interface is computed. The entire procedure has been implemented under the ***MATLAB*** software.

Figure 1.9 (a) presents the distribution of both misorientation distributions as well as the well known crystal misorientation distribution calculated for an untextured material by Mackenzie [Mackenzie 1958]. If one observes the systematic mutual misorientation distribution (red one), one observes that $\approx 30\%$ of granular misorientations are 60^o whereas misorientations between 10 and 60^o are almost equally distributed, even if a slight increase of density is observed at higher level of misorientation. That means

that for every grain, a large variety of misorientations with neighbors exist and that a large amount of grain exhibit at least one 60^o misorientation on a part of its grain boundary.

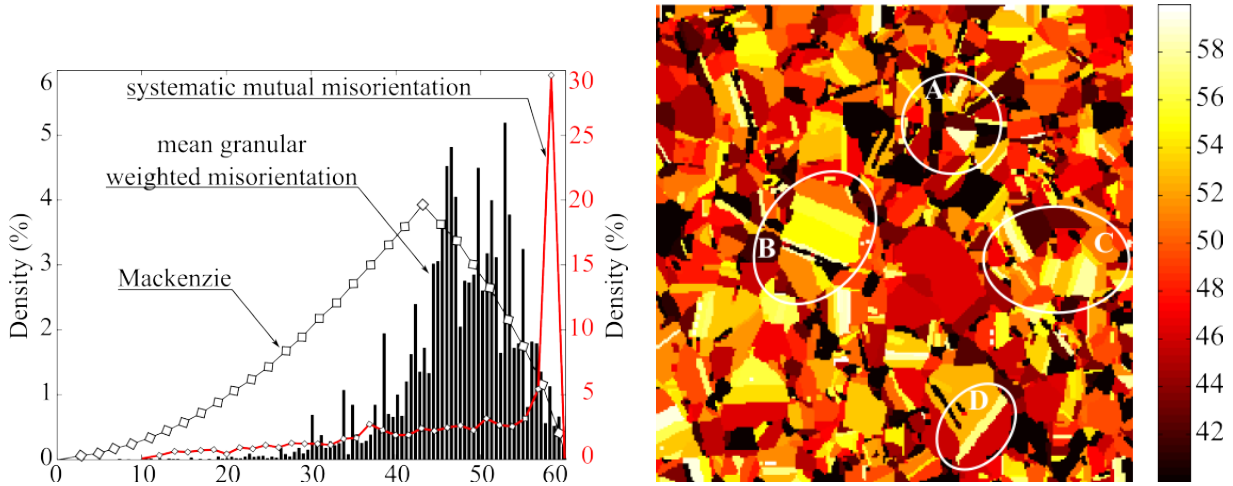

(a) $\Delta\theta_{A/B}$ in degree (b) $\Delta\bar{\theta}_{A/B}$ in degree

Figure 1.9: (a) distribution of two kind of misorientation compared to the untexturel material reference distribution coming from [Mackenzie 1958] and (b) mean granular weighted misorientation field

The distribution of mean granular weighted misorientation shows that an important density of grain possesses a misorientation relative to their neighbors between 45 and 55^o when for others, the misorientation decreases exponentially up to 10^o. The distribution exhibits a similar shape compared to the Mackenzie distribution. Nevertheless, in the studied case, the peak is higher and only a few grains are subjected to a low misorientation. Figure 1.9 (b) presents the field of mean granular weighted misorientation. One could note that many significant grains (in term of diameters) present intense misorientation ($> 55^o$), notably the regions denoted B, C and D. These areas will be discussed in further sections. The misorientation appears to be randomly distributed. The region denoted A is underlined in order to introduced the comparaison with figure 1.1. Indeed, the more strained area within the studied region seems to be the area where a focus is performed. This observation is leaded by intense contrast (deformation) appearing at boundary of grain within the focused region. Such intense grain boundary deformation are probably leaded by incompatibilities of strain field from grain to grain. nevertheless, the misorientation field doesn't exhibit a very specific localisation of high misorientations within this domain. Excepted within the triangular grain of region A which exhibit very intense deformation in figure 1.1.

1.4.3 Profilometry and grain boundaries (GBs)

In order to obtain information about the granular out-of-plane displacement during the tensile test, the topography of the specimen surface has been measured. After testing, the coating has been

removed by plunging the sample into an ultrasonic bath first with acetone and then with alcohol. Next, profilometric analysis has been performed on a Wyko NT 9300 (Veeco) profilometer with a $5\mu m$ step. In addition some areas have been analyzed with a $1\mu m$ finer step. Figure 1.10 present the results. As the specimen surface was originally perfectly flat and polished up to $1\mu m$ diamond finish, one could assume that the following topography only results from out-of-plane plastic strain.

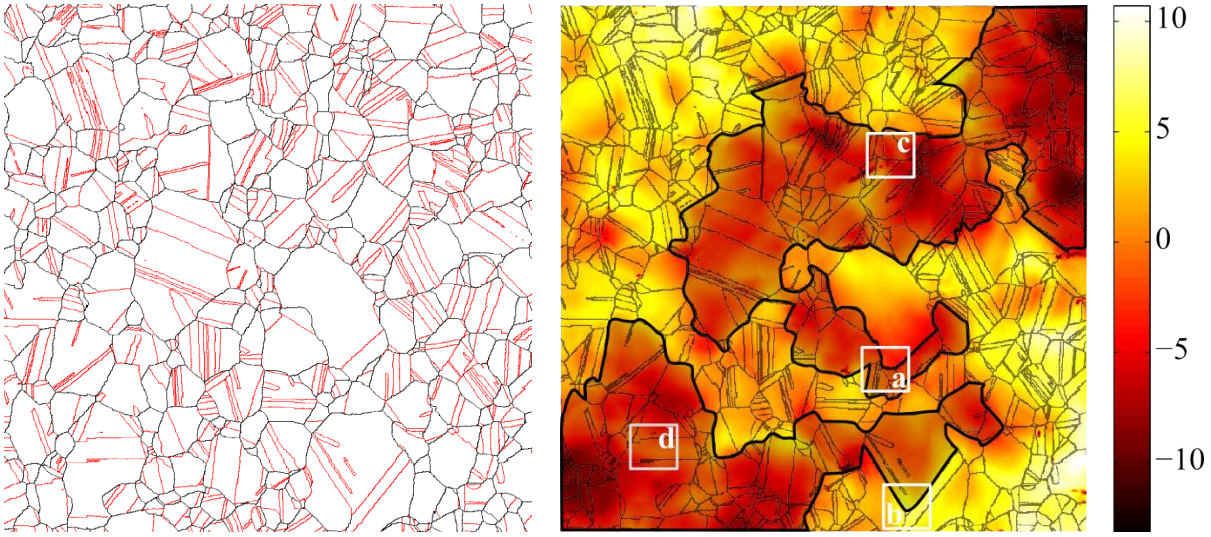

(a) (b)

Figure 1.10: (a) grain boundary pattern and type and (b) profilometry of specimen surface performed after test

Figure 1.10 (a) present the grain boundary pattern, pointed out the difference between "ordinary" boundaries and "special" ones. Black lines show High Angle Grain Boundaries ($HAGBs$), i.e where the misorientation ranges from ≈ 10 to 180^o whereas red ones show twin boundaries (Σ_3), i.e where lattices are related by a 60^o rotation about the <111> crystal direction. It is traditionally denoted <111><60^o>.

Within the Coincidence Site Lattice framework (CSL), grain boundaries are classified by a Σ value, which gives the reciprocal density of lattice points that are coincident in the two adjacent grains [Sutton 1995]. Moreover, lower is the Σ value, lower is the boundary energy. Twin boundaries (Σ_3) are consequently called low-energy boundaries. Within FCC material the frequency distribution of "special" grain boundaries is dominated by Σ_3 interfaces.

In the present case, the occurrence of Σ_3 interfaces is significant due to the initial heat treatment performed for the grain growth. Indeed, during grain growth, the internal energy of the material is minimized in two ways: (1) by decreasing the total grain boundaries, (2) by transforming high-energy

boundaries in low-energy ones, especially Σ_3. Here, 57% of grain boundaries are Σ_3 ones[7]. One can also note that, if one does not consider Σ_3 boundaries, the mean grain size passes from 118 μm to 237 μm with a quasi perfect equiaxed shape (equiaxiality ratio = 0.51). In figure 1.10(b) the grain pattern is superimposed on the profilometric analysis. One observes that the relief ranges from -12μm to 11μm. Consequently the specimen gauge surface passed from an initial variation of topography close to 1μm to more than 20μm during the tensile test. It reflects an important plastic activity of the free surface. The mean value of the field is 0.45μm.

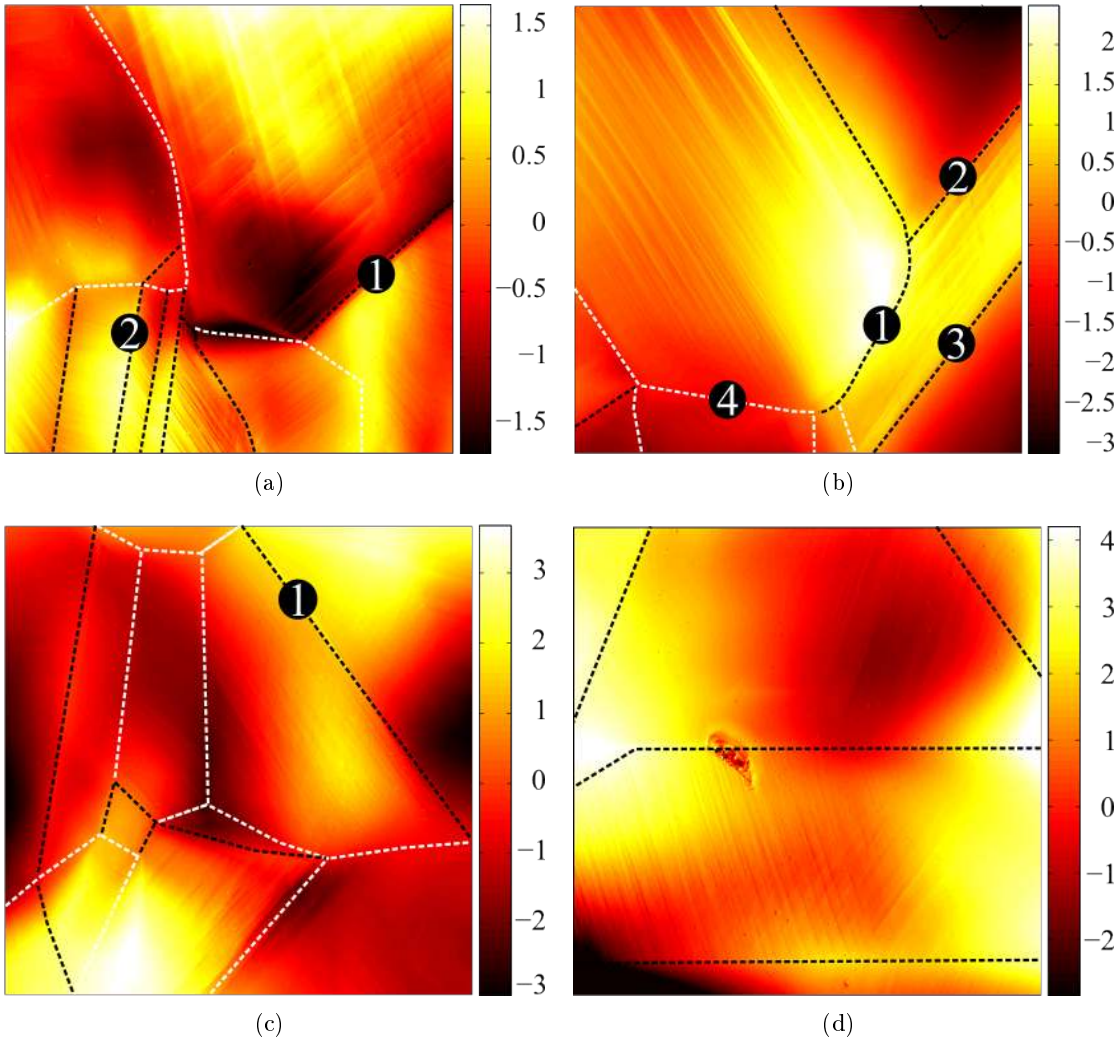

Figure 1.11: zoom on 4 zones refered in figure 1.10

If one considers the mean value ≈ 0 as the reference, i.e the intruded volume is equal to the extruded

[7]Ordinary GBs length = 62.86 cm - Σ_3 GBs length = 36.36 cm

one, the field exhibits that some large domains (surrounded by thick black line) "plunged inside" the material whereas the rest of specimen have emerged from the surface. This profilometry field seems to emphase a concrete link between the grain boundary pattern and the surface topography. Indeed, out-of-plane displacement discontinuities are widely connected to grain boundary network and reach $10\mu m$ in some areas. Obviously this value is directly connected to the resolution.

Then, figure 1.11 from (a) to (d) presents a focus on 4 regions surrounded by white squares within the previous figure 1.10. Note that each field has its own colormap. Grain boundaries are pointed by dotted lines: white ones are High Angle Grain Boundaries ($HAGBs$), and black ones are Σ_3 interfaces. Firstly, as already pointed out, one can observe on these figures 1.11 that the grain boundary plays a significant role with the surface relief. Indeed, one observes, notably within (a), (b), (c) that the surface topography is well associated to grain domains and lead to very different relief from grain to grain. Inside grains, especially within (a) and (b), one observes also significant out-of-plane displacements related to plasticity: extruded straight lines, corresponding to high out-of-plane displacements, which are associated to plastic slip plane activity. The Σ_3 interfaces exhibit a very specific relief: they concentrate the deformation or lead to a significant displacement gap.

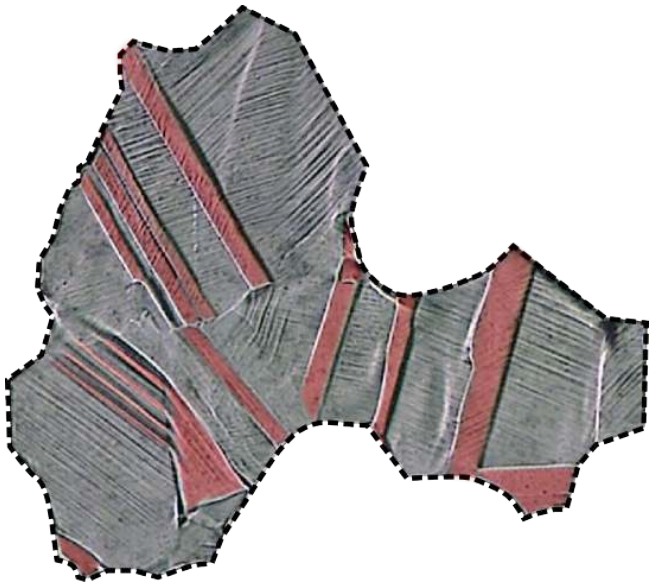

Figure 1.12: micrography of the specimen surface, performed after test. Focus on a significatively twinned region. Twins (Σ_3 interfaces) are red colored

In figure 1.11 (a), one observes at Σ_3 interfaces, noted 1, that a $3\mu m$ gap of out-of-plane displacement is present from one grain to the other one, where in parallel other Σ_3 interfaces localized a significant relief. Similar observations could be pointed out within picture 1.11(b). Σ_3 interfaces, noted 1, localized the highest level of relief, 2 and 3 a significant gap of displacement (from 3 to 4.5 μm) whereas the ordinary boundary, noted 4 for example does not presents any specific variation of

relief. This singularity of Σ_3 interfaces could also be observe directly within the micrography of surface specimen.

Figure 1.12 presents a focus on a significantly twinned region. Twins (Σ_3 interfaces) are pointed in red. One observes intense contrasts at each Σ_3 boundaries which reflect an intense out-of-plane step from grain to grain. This point is in line with the present profilometry analysis, especially within figure 1.11 (b). This phenomenon appears within the whole micrography and emphasis an important kinematic degree of freedom of Σ_3 interfaces, notably along the direction normal to the surface specimen.

The topography of the specimen after the test has been investigated as well as the presence of twin Σ_3 boundaries within the analyzed region. The specimen, originally polished up to $1\mu m$ diamond finish, exhibits a variation of topography close to $20\mu m$ which reflects a significant out-of-plane activity of the free surface. An intrusion/extrusion phenomenon appears a macroscopic scale boundaries of each macro domain are clearly related to grain interfaces. It reveals a significant freedom degree of grain boundary, at least on free surface. Finally, very intense displacement gap at grain boundaries and/or significant relief localization have been related to Σ_3 boundaries which represent 57% of total grain boundary length.

1.4.4 Slip-system identification by Radon transform

1.4.4.1 Introduction

As introduced earlier, interesting information about the deformation process and the plastic strain localization can be done by analyzing the surface specimen micrography after the test. One has first to identify in each grain the number of activated slip systems and their associated orientation. Then, one has to count the number of slip-marks. It provides information about the plastic process intensity [Perrin 2010]. Note that these analysis are traditionally manually performed [Villechaise 2002, Bridier 2005, El Bartali 2009]. This process is excessively time consuming especially when the objective is the analysis of a wide region of a polycrystal (>1500 grains). This part presents an original developed technic to automatically identify:

1. the intragranular number of activated slip-systems
2. their associated orientation
3. their associated slip-systems
4. the intragranular mean density of slip-mark
5. the intragranular mean slip-mark thickness
6. the intragranular mean inter-slip mark distance

These informations are crucial in order:

- to know the activated slip systems in every grain in order to confront the results to the Schmid theory, on the one hand, and to kinematic measurements, on the other hand. The micrography analysis provides the final state while the intragranular shear strain is expected to provide the the slip-system activation chronology.

- to compare the experimental slip-system activation and the numerical one in order to evaluate the ability of the simulation to render the local crystallographic kinematic.

- to compare slip-mark densities and experimental dissipation and stored energy values.

This question consists actually in the analysis of image texture and many methods are based on the gradient of the picture gray level according to the fact that the main texture orientation is perpendicular to the image gradient [Rao 1990]. An other technique is widely used in mechanical field to extract linear pattern from a picture: the Radon or Hough transforms. One can cite some applications: (1) ***E.B.S.D. analysis*** to extract straight line orientation from the Kikuchi pattern to recover the orientation of the crystallographic plane which is diffracting [Zhou 2007], (2) ***Dislocation boundary alignment*** within Transmission Electron Microscopy analysis to identify the orientation of Geometrically Necessary Boundaries (GNBs) or dense dislocation walls induced by deformation [Winther 2004], (3) ***Auto-detection of wood texture orientation*** in order to quantitatively analyze texture pattern [Hai-peng 2005]. Other methods have been used for similar applications but more appropriate to unknown pattern, for example to build the anisotropy tensor of fibrous materials, like glass wool, by determining the local fiber orientations [Bergonnier 2005, Witz 2008].

1.4.4.2 Historical of the Radon transform and application in tomography

In 1917, Joseph Radon showed that using X rays passing through a material in every direction allows accessing to the plane integral of its density distribution. Thus, to recover the 3 dimensional material density passes through an inversion formula of an integral transform, now called the Radon transform. The formula is a key ingredient in Computerized Tomography, and constitutes therefore a mainstay of medical imaging as well as many other remote imaging sciences. As presented in picture 1.13, the tomography principle is to observe the interior structures of objects by collecting a set of X-ray intensity attenuation of this object through all possible lines.

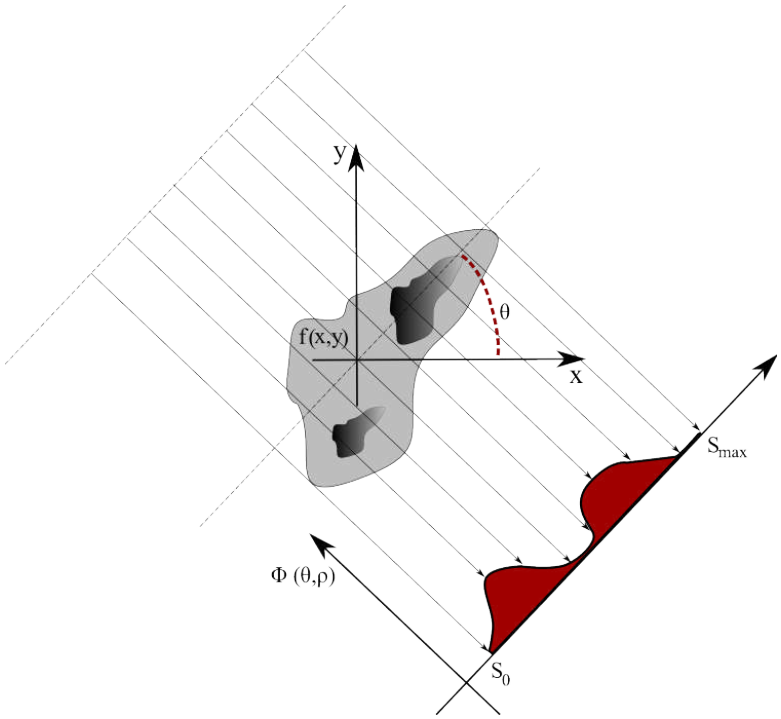

Figure 1.13: Principle schema of tomography

If f represents an unknown density function of the interior of the object, the collected set of X-ray intensity attenuation constitutes the radon transform of function f. Tomography is therefore a reconstruction problem based on inverse Radon transform.

1.4.4.3 Application to straight lines

An other application of the Radon transform is to detect features within a two-dimensional image, in particular, straight lines. The Radon transform computes projections of an image matrix along specified directions. It is defined as:

$$R(\theta,\rho) = \int_{-\infty}^{+\infty} f(\rho \cdot cos(\theta) - s \cdot sin(\theta), \rho \cdot sin(\theta) + s \cdot cos(\theta)) \cdot ds \tag{1.12}$$

where

$$\begin{Bmatrix} \rho \\ s \end{Bmatrix} = \begin{Bmatrix} cos(\theta) & sin(\theta) \\ -sin(\theta) & cos(\theta) \end{Bmatrix} \begin{Bmatrix} x \\ y \end{Bmatrix} \tag{1.13}$$

Figure 1.14 presents a black line within a white domain. θ is the incline angle and ρ the smallest distance of the coordinate system to the origin.

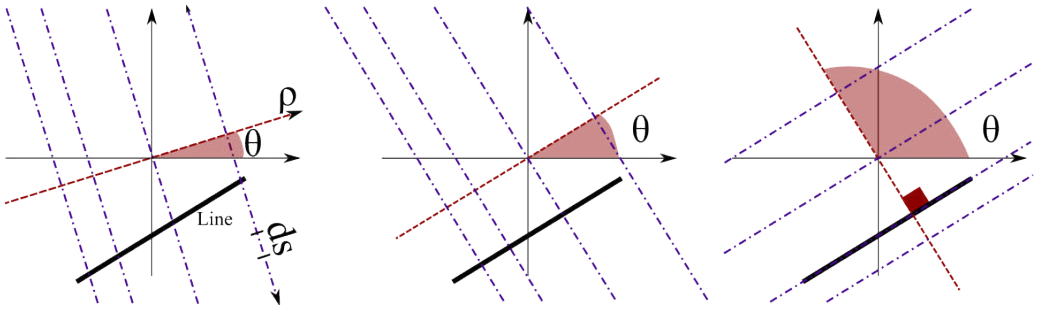

Figure 1.14: principle shcema

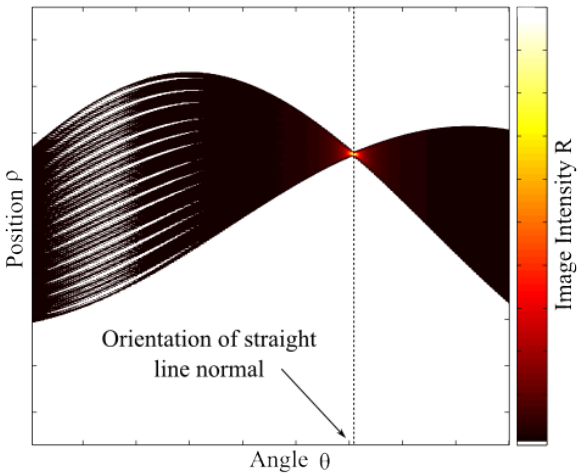

Figure 1.15: Sinogram

The Radon operator maps the spatial domain $f(x, y)$ to the projection domain $R(\rho, \theta)$ performing a line integral for each couple (ρ, θ). The Radon transform for a large number of angles is often displayed as an image called sinogram (see figure 1.15). It is the plot of ρ function of θ. A very bright spot is found in the sinogram and the intensity of this spot represents the line integral through the image $f(x, y)$ obtained for the line with a slope $\theta - \frac{\pi}{2}$ with the abscissa direction and located at a ρ distance from the origin. A simple thresholding algorithm could then be used to pick out the line parameters. The Radon transform appears consequently as a perfect tool for slip-marks detections, since the micrography of specimen surface is actually a straight lines field.

1.4.4.4 Application to micrography and slip marks analysis

Of course, the problem is more complex when patterns are composed by many crossing rough lines as on a micrography. In such case, it is complicated to extract from the sinogram the orientation and the position of each slip-marks individually. Picture 1.16 (a) and (b) illustrates this point. Figure 1.16 (a) presents a cropped area of the micrography. This region is composed by a main grain surrounded by

many others. Many slip-marks are observed as well as a large range of slip-mark orientations. Picture 1.16 (b) presents the associated sinogram. One observes bright spots where the line integral, at fixed ρ and θ, is the highest. Two angular domains reveal bright spots: from -60 to -40 and from 10 to 60 degrees.

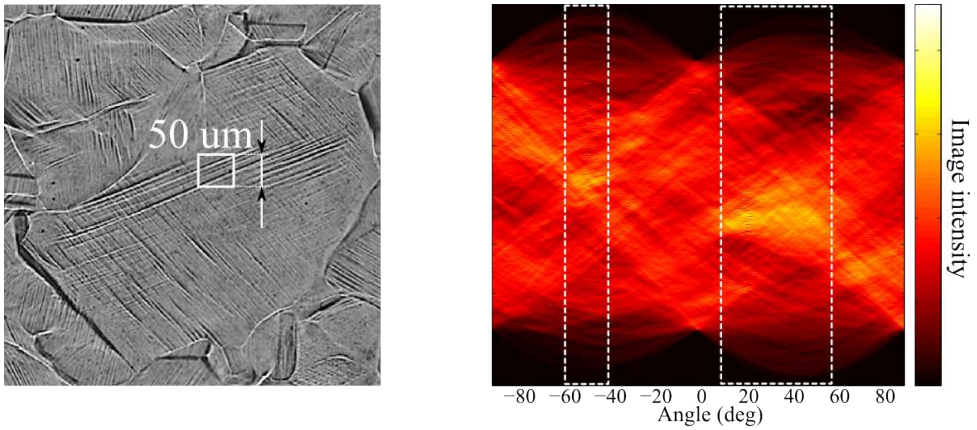

Figure 1.16: (a) micrograph (b) Radon transform

Thus the sinogram reveals that some linear patterns have an angular orientation included within these domains. Nevertheless the link between slip-marks number, orientation and sinogram is not trivial in this case. Moreover no discrimination exists between grain boundary marks and slip marks. Within the present micrography, the GBs are more contrasted and will lead to significant line integrals. The simplest way to extract slip-marks characteristics seems consequently to work on sub-domains.

- a first possibility is to use the natural granular partition, i.e to perform analysis on each grain. The technique requires the a priori knowledge of the microstructure (EBSD analysis) as well as a thresholding algorithm able to extract from the sinogram many orientations. Indeed each grain could contain from 0 to 3 and more slip-bands as well as a large number of slip-marks. Nevertheless, this technic would be the more efficient in term of calculation time since it depends linearly on the grain number. Moreover a discrete counting of slip-marks by grain is possible.

- a second way is the one used by [Bergonnier 2005], i.e to work on sub-domains associated to a regular mesh. Sub-domains must be enough large to account for a representative image texture and enough small to contain a unique main texture. The main advantages are the simplicity of the thresholding algorithm which only need to extract one orientation by sub-domain, i.e the one which exhibit a peak within the sinogram. Moreover the user does not need any a priori knowledge about the microstructure. The main disadvantage is the time calculation which depends on the sub-domain size. Note in our case that an appropriate sub-domain size is up to 10 time lower than the grain size which imply to perform up to 100 times more Radon transform per grain. Then, only the main orientation will be extracted from domains where multiple slip-marks cross

each others. Finally, working on discrete sub-domains allows only an estimation of slip-mark density by sub-domain and then per grain and not a quantitative counting of each slip mark.

The application developed within this work, called ***SlipEx*** for Slip-mark EXTraction (see Appendix E), is based on the second method. This choice has been done regarding to the relative simplicity of the implementation. As only one micrography is analyzed within the present study, there is no need to be time efficient. Nevertheless, in order to analyze a large number of micrographies, the first method should be considered. It uses iterations on crossing sub-domains, in order to improve the resolution, until obtaining a slip mark orientation full-field. The procedure as well as user's arguments are presented in appendix E. One just explain here the main steps, the user's parameters as well as a short example.

In this way, let us consider a very local crop of this micrography. It corresponds to the white bordered region on figure 1.16 (a). Within this example the sub-domain size has been chosen equal to 50x50μm^2. The algorithm of slip-mark orientation detection is composed by two steps and two specifics methods have been chosen with two representations of the micrography: the original one (see figure 1.17 (b)) and its edge detection (see figure 1.17 (a)).

Note that the edge detection field is obtained thanks to the the Matlab function ***EDGE***. Both representations are used as one observes in figure 1.17 (b) that both line integrals through the picture, noted 1 and 2, lead more or less to the same intensity. This is due to the slip-mark thickness and leads to an uncertainty θ_{err} on the slip-mark orientation estimation. Performing the same line integral on the edge map (see figure 1.17 (a)) removes any uncertainty on slip-mark orientation since the pattern is not slip-mark thickness dependent. Nevertheless, counting the number of slip-marks or estimating the slip-mark thickness is much more complicated from the edge map since the field does not contain any information about the localization of intra and inter slip-domain. The figure 1.17 (c) presents the sinogram of 1.17 (a) and (b) respectively. According to the right part of picture 1.17 (c), 4 slip marks are detected. According to the left part of picture 1.17 (c), slip-band makes precisely an angle of 22^o with the loading axis. According to the right part of picture 1.17 (c), the slip mark size is almost uniform ($6.5\mu m$) and the mean distance between them is $\approx 12.5\mu m$. Note that these values are necessarily affected by the original micrography resolution. In the present study, the micrography resolution is 3661x3661 pixels with a pitch of 1.4 μm. To summarize, the figure 1.17 (c) evidences that the "edges method" (Radon transform performed on edge map of micrography) is more precise on slip-mark orientation whereas the "raw method" (Radon transform performed on raw micrography) is more appropriate for a simple and quick slip-mark number and thickness identification. Thus, the best incline is found with the "edges method". Once the precise main sub-domain texture orientation is found, θ, with the help of the matlab function ***MAX***, the Radon transform is performed on raw micrograph at θ. Other statistic are then extracted.

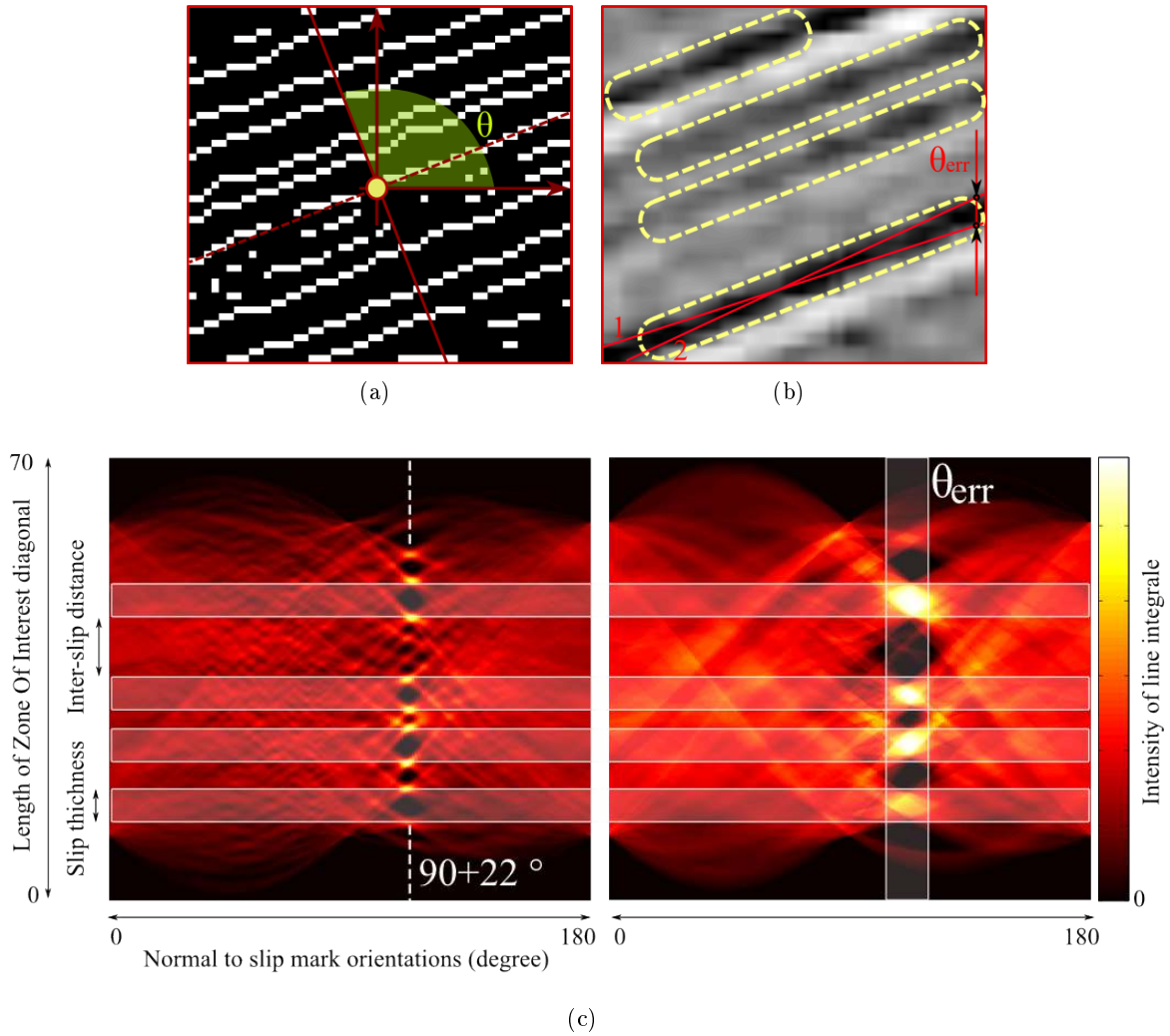

Figure 1.17: (a) raw micrograph (b) Sinogram from binarised micrograph (c) Sinogram from micrograph edges

The efficiency of the proposed method is really difficult to quantitatively estimate. Indeed no objective and automatic way exists to identify potential mistakes excepted the one by one comparison with grain micrography. It will be done in the next section. Nevertheless one proposes here to observe one big grain composed by many twins to evidence the accuracy of the results. This grain is interesting since three different slip systems are activated, and the density of slip mark is clearly not uniform. This grain is shown on picture 1.18. One could see on the micrography that a large region is crossed by parallel slip planes whose the marks on the surface make an angle of 69^o with the abscissa. The rest of the grain exhibits slip marks at 35^o and -35^o. Note that most regions where slip marks are observed with an inclination of $\pm 35^o$ exhibit low slip marks density. Both other pictures present respectively

the relative slip-mark density and the absolute value of slip-mark incline.

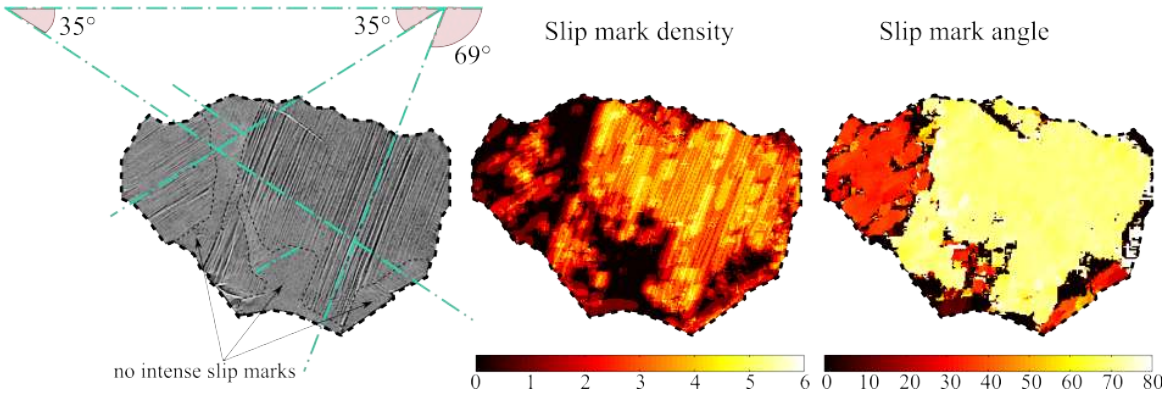

Figure 1.18: (a) zoom on grain composed by some twins

One clearly observes that regions where no slip mark are identified are connected to micrography as well as high density regions. Concerning the incline, three main domains are visible and correspond to the micrography. Note that more noisy results are observed within regions where a lower density of slip mark exist. The combination of angle and density map is consequently required to well define the slip mark orientation. Thus, a denoising procedure of the slip-mark incline is performed with the help of the slip-mark density field. Practically, every regions where the slip-mark density is lower than a parameter C are not considered. Then, using a loop on grains, an intragranular segmentation is performed to extract the effective intragranular number of systems and their associated orientation.

This point requires a deeper explanation. Let us consider, for example, the main grain introduced within picture 1.16 (a). The distribution of slip-mark inclines within the grain is presented in figure 1.19. It corresponds to the mean slip-mark incline for every sub-domain contained within the considered grain. The signal is composed by two main slip-mark orientations within the grain. These orientations are visible within picture 1.16 (a). In a theoretic case, the distribution is reduced to 2 dirac: the first one at 21^o and the second one at -46^o. The density of each of them must represent the intragranular surface slip bands density occupied respectively by the first and the second slip-systems. In practice, one observes that orientations are distributed around a mean orientation. Orientations which are far away from peaks are potential errors within incline identification, probably due to a low intensity of slip-marks or cross-slips. Other orientations can deviate from peaks because of the uncertainty of incline measurement, especially when the sub-domain is very small. The goal is consequently to extract from this raw distribution, the number of slip-systems (here 2), their associated slip-domain or slip-bands and remaining domain where no relevant results are founded.

In order to solve this problem, a convolution product is used with a Gaussian function, i.e to filter the raw distribution by using of Gaussian kernel whose standard deviation corresponds to an angular margin, D, for the slip-band detection. A convolution is an integral that expresses the amount of

overlap of a function g as it is shifted over another function f. It is defined over a finite range $[0, t]$ by:

$$[f * g](t) = \int_0^t f(\tau)\, g(t-\tau) \cdot d\tau \tag{1.14}$$

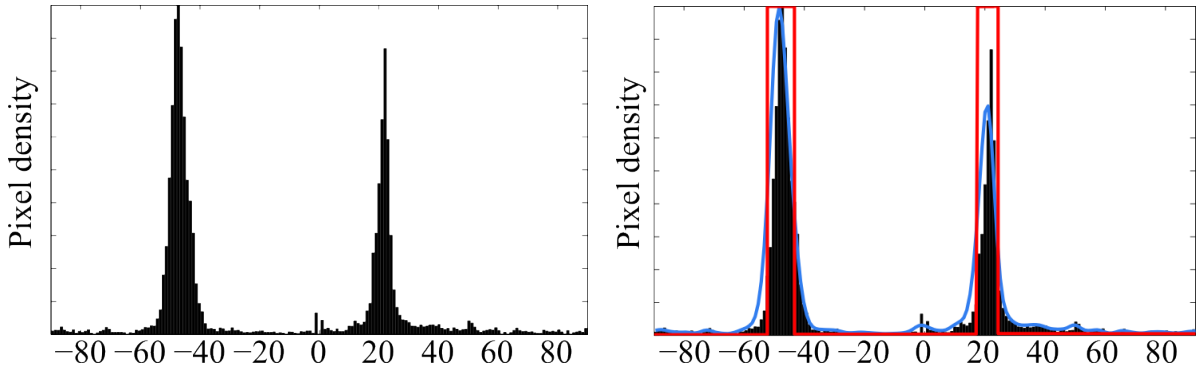

(a) slip-mark incline in ^{o} (b) slip-mark incline in ^{o}

Figure 1.19: (a) distribution of slip-mark inclines of each sub-domain containing within the main grain introduced in figure 1.16 (a). (b) Superimposition of the convolution product between the distribution and a gaussian function as well as the final segmentation

	action	variables		results
Step 1	loop on n sub-window	$\boldsymbol{A} = 25px$ sub-window size (px)	$\boldsymbol{B} = 20px$ sub-windows superposition (px)	•raw slip-mark incline field •relative slip-mark density field •mean slip-mark thickness field •mean inter slip-mark distance field
Step 2	loop on m grains for intragranular segmentation	$\boldsymbol{C} = 10\%$ minimal relevant slip-mark density for denoising	$\boldsymbol{D} = 5^o$ angular margin for slip-bands segmentation	•intragranular segmentation •intragranular number of slip-system •mean statistics per slip-bands
Step 3	loop on m grains for system detection	$\boldsymbol{E} = 5^o$ angular margin for system identification		•intragranular slip-systems

Table 1.6: ***SlipEx*** steps and variables

Blue curve in figure 1.19 (b) presents the convolution product between the raw incline distribution

and the Gaussian function whose standard deviation is equal to 4^o. Finally, a thresholding is performed. Let μ be the mean value, σ the standard deviation of the Gaussian distribution. Every pixel included within $\mu \pm 2\sigma$ are attributed to its associated slip-band, the incline of each peaks is extracted and remaining pixels are considered as bad pixels. 1.19 (b) presents, in red, the final segmentation.

Finally, according to the equation 1.2 previously introduced, as well as to the knowledge of grain domains, grain orientations and loading directions, it is possible to perform a systematic comparison between the set of intragranular possible slip-marks and the effective ones, measured thanks to radon transform and intragranular segmentation. Two successive criteria are applied. First, the difference between theoretical and effective slip-mark incline must remain lower than a user's parameter E. It allows to reduce the set of possible candidate. Then the system whose Schmid factor is the highest is conserved. Table 1.6 summarises steps of Slip-system extraction and focus on user's parameters.

1.4.4.5 Method efficiency

To estimate the benefit of the implemented procedure in term of slip-systems detection and then to deal with slip-system statistics, 55 grains have been manually studied within the microstructure and compared to the ***SlipEx*** routine results (see figure 1.20). The analyzed grains are surrounded by black dotted line. Red, white and blue lines correspond, within ***SlipEx***, to single, double and triple shear per grain respectively. Lines allow to compare the slip-system solution and the effective slip-marks. In the 55 slip systems presented here, 5 mistakes could be identified corresponding to 9% error. These errors are pointed with the help of exclamation mark in vicinity of the bad or missing system. According to the picture 1.20 and within a larger investigation not presented here, two kinds of mistake have been identified:

- not sufficiently marked systems appearing within small regions are sometimes forgotten. It represents 33% of the errors.

- the grain boundary exhibits an intense contrast (out-of-plane displacement, strain localization) and then, the grain boundary incline is a good candidate for slip system identification; the grain boundary mark could be identified as a slip-system. It represents 67% of errors.

Concerning the first point, it has to be balance by the micrography resolution as well as the eye capabilities. The resolution of micrography is in our case 3661x3661 pixels with a pitch of 1.4 μm. To increase this resolution will improve such results. Note that in many cases, it is extremely difficult to identify each slip system even with eyes. For the second point, the human eye doesn't make mistake since the image contrast is very singular at grain boundary. This point could be improved if the other proposed method of analysis is used, i.e the one which loop on grain domains instead of regular mesh. Nevertheless a complementary grain contour crop algorithm, depending notably on the grain size, has to be developed. Finally one could note that no wrong slip-system identification has been observed. That means that slip-marks orientation are well captured.

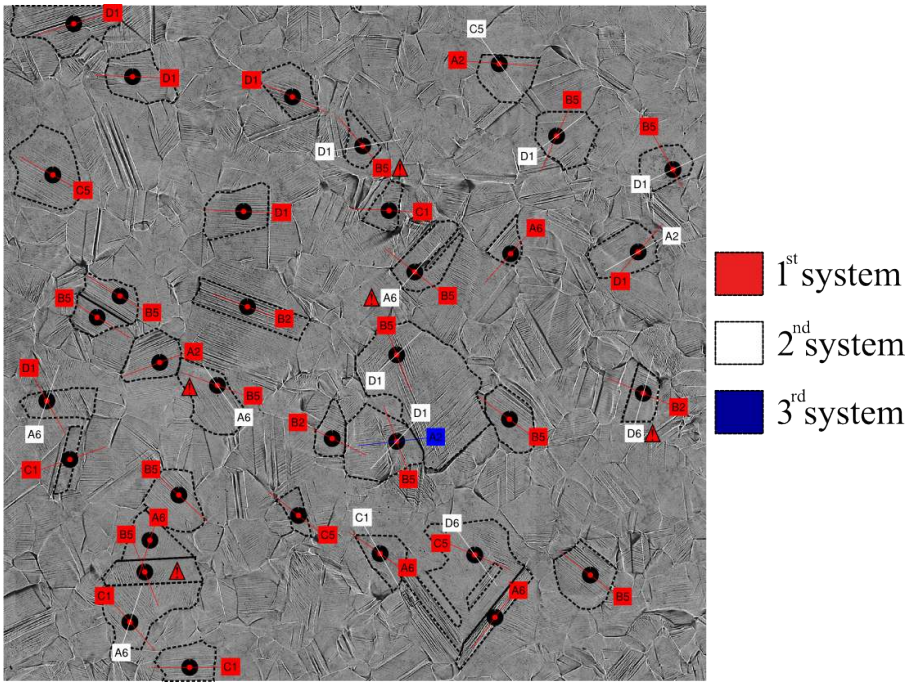

Figure 1.20: Comparison between effective slip-marks and slip-systems solution coming from ***SlipEx***

1.4.4.6 Statistics and stage of deformation

Picture 1.21 from (a) to (d) present the slip-mark incline as well as the slip-mark density field and their respective distributions. Data are averaged per slip-band. One observes a variation of slip mark incline which ranges from -90 to 90^o compared to the loading direction (see figure 1.21 (b)). The distribution of absolute value of incline (see picture 1.21 (c)) evidences 5 main slip-band orientations: (1) at 22^o, (2) at 36^o, (3) at 49^o, (4) at 70 ^{o} and (5) at 87 ^{o}. Considering a margin of $\pm 2^o$ these main inclines represent about 50% of slip-marks. The slip-mark density field is here saturated between 15 and 45% in order to underline contrasts. Note that the relative slip-mark density corresponds to the mean slip-mark density per slip-bands area normalized by the maximal slip-mark density of the field. One observes a very heterogeneous slip-mark density pattern. Some large regions where the slip-density is about 15% and lower are surrounded by white circles. This contrast of slip-mark density can be interpreted as a qualitative representation of the plastic strain field. In agreement with this natural assumption, one could already emphasis that white circled regions are expected to undergo few or no plastic strain whereas regions noted 1 or 2 for example are expected to undergo intense plastic strain level. This point will be further verified with the help of experimental strain field.

In this way, one can already pointed out an interesting point regarding to the comparison between topography of the surface specimen (see figure 1.10 (b)) and the relative slip-mark density field (see figure 1.21 (b)). Focusing on regions where few slip-marks are identified, notably the bottom of the

picture (white circled in 1.21 (b)), one observes that it is globally associated to a plateau of out-of-plane displacement located at $\approx -5\mu m$. A similar comparison could be done concerning a part of the top right area where the relative slip-mark density is very low and relief exhibits a large plateau. This point is notably in agreement with the fact that highly slip-systems crossed regions exhibit significant out-of-plane displacement as it has been underlined regarding to figures 1.11.

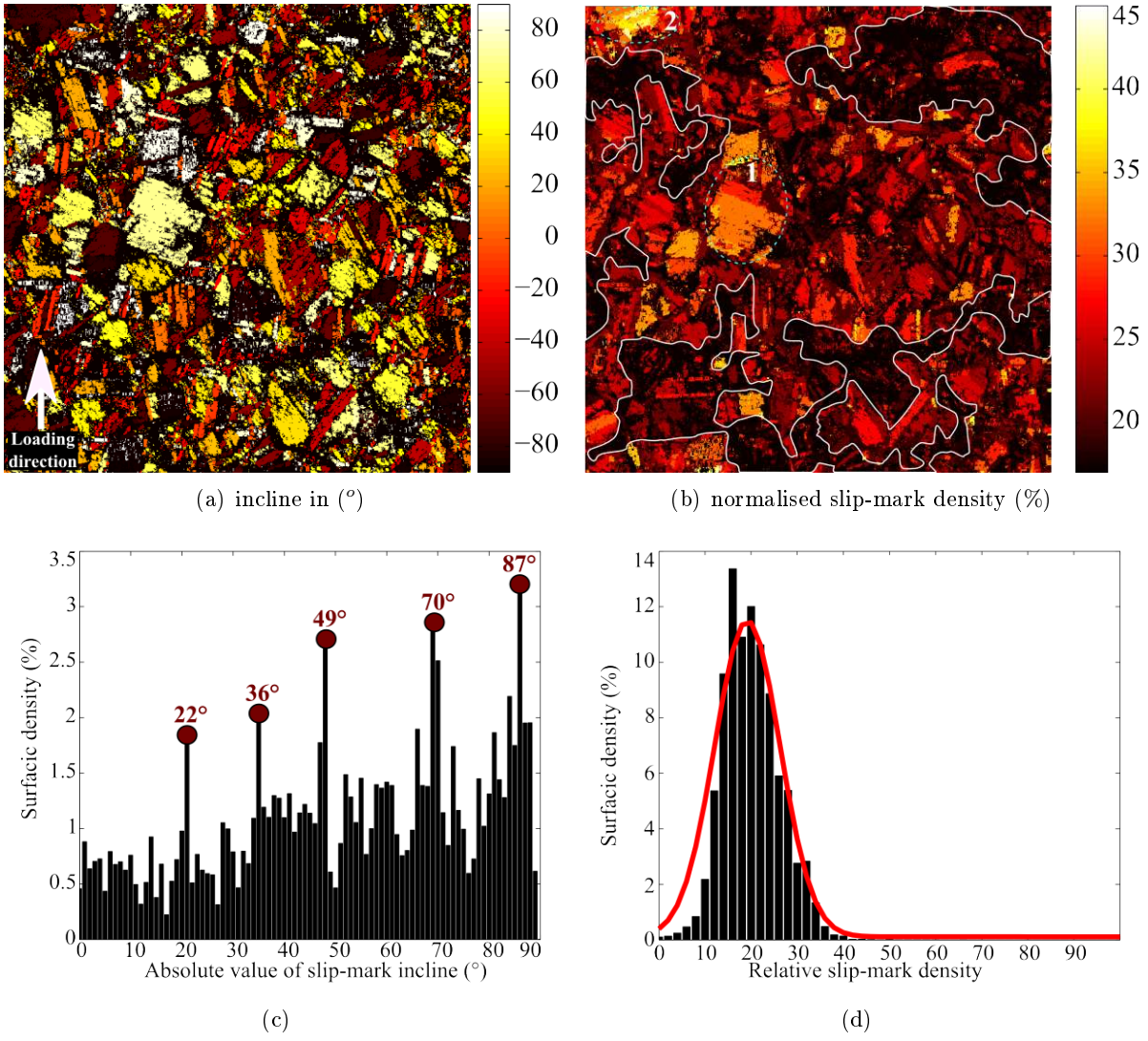

(a) incline in (°) (b) normalised slip-mark density (%)

(c) (d)

Figure 1.21: (a) angle of slip bands (b) slip band density

The distribution of relative slip-mark density (see figure 1.21 (d)) ranges obviously from 0 to 100% with a mean value equal to 19.2%. One could note that the distribution is a Gaussian centered around 19.2%. The superimposed red curve represents the best Gaussian fitting and its expression G is the

following:

$$G = Aexp\left(-\frac{(x-\mu)^2}{2\sigma^2}\right) \tag{1.15}$$

where the standard deviation σ is 7.1%, the mean value is μ and A is a constant equal to 11.4%.

The great heterogeneity of strain field within polycrystals has already been emphasis by many author and for a long time [Barrett 1948]. Considering the normalized density of slip-mark as being representative of plastic strain field, one could imagine that for a mean strain of $\approx 2\%$ the local plastic strain can range from 0 to 5% and up to 10% in very localized regions. In the same way, one could imagine that some macroscopic domains, surrounded by white line in figure 1.21 (b), undergo strains which vary between 0 and 1.5%.

Picture 1.22 (a) and (b) present statistics associated to activated systems.

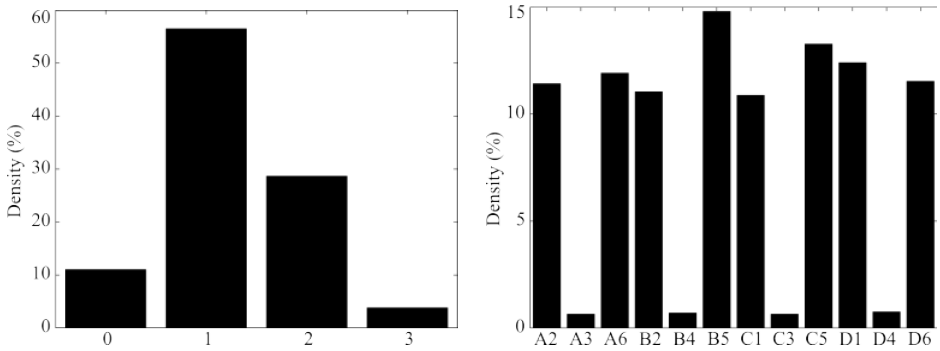

Figure 1.22: (a) Density of none, single, double and triple shear and (b) density of each of 12 potential slip-systems within F.C.C. structure

Figure (a) shows the density of grain which activate none, single, double or triple slip. Figure (b) shows the activated systems according to the Schmid and Boas notation (see table 1.4). Statistics show that 57% of grains exhibit single slip while 29% exhibit double slip. These statistics could be interpreted as a transition between stage I and stage II of the deformation process, i.e the deformation level when the specimen passes from mainly planar/single slip to mainly multiple and cross-slip. According to [Feaugas 2003] this transition is grain size dependent and occurs, in a A316L with a grain size of $\approx 107\mu m$ at ambiant temperature, at $\approx 290MPa$. According to the Hall-Petch law [Hall 1951] presented in equation 1.16 as well as to the variation of Hall-Petch parameters as a function of the plastic strain level within AISI A316L austenitic stainless steel presented in figure 1.23 (a) one could

estimate that the transition between stage I and stage II occurs in the present case (grain size $\approx 118\mu m$) at 285MPa. One recalls that the monotonic tensile test has been performed up to 2.5% of plastic strain and $270MPa$ of nominal stress. Thus, both the nominal stress level and the plasticity mechanisms evidence that the final state of the material is situated between the end of stage I and the beginning of the stage II.

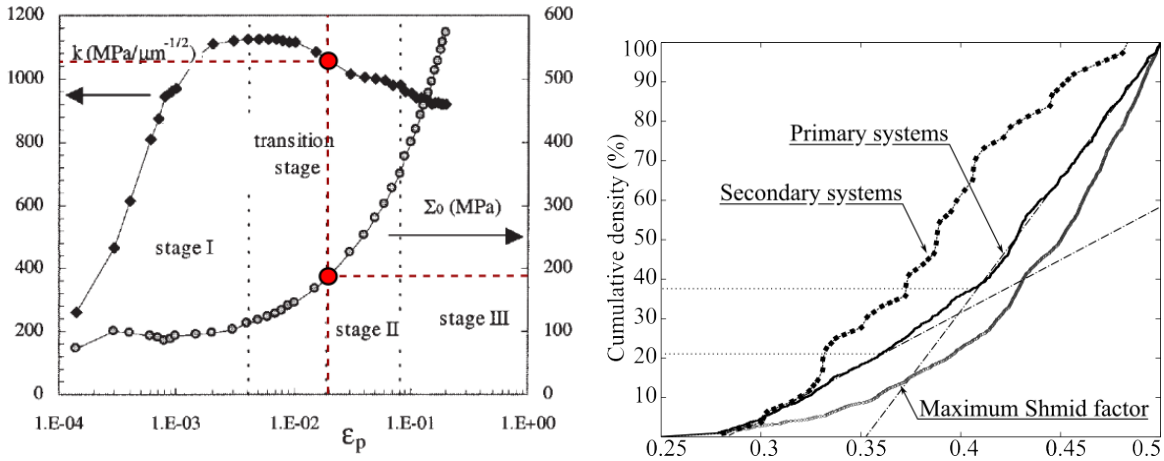

(a) (b) μ

Figure 1.23: (a) The dependence of the Hall-Petch parameters Σ_0 and k on plastic strain for austenitic stainless steel AISI 316L extract from [Feaugas 2003]. (b) Cumulative density of: Schmid factor within the primary identified system, the secondary identified one and maximum Schmid factor

$$\Sigma(\varepsilon) = \Sigma_0(\varepsilon) + k(\varepsilon)d^{-\frac{1}{2}} \tag{1.16}$$

where $\Sigma(\varepsilon)$ is the macroscopic stress flow, $\Sigma_0(\varepsilon)$ and k the Hall-Petch parameters function of strain and d the mean grain diameter. Moreover, one observes on the histogram 1.22 (b) that every slip-plane statistically contributes to the deformation process. One could note that the slip-plane B and its third direction B_5 is the predominant system since about 15% of plastic grain activate it. Others, first and third direction of each slip-plane are equitably activated ($\approx 12\%$). Note that the second slip directions, i.e A_3, B_4, C_3 and D_4 systems are statistically very few activated. They globally contribute up to 4%.

The figure 1.23 (b) presents the cumulative density of maximum Schmid factor as well as the cumulative density of Schmid factor identified on primary slip-system and secondary one. When multiple systems are activated, note that the primary system is the one which exhibits the higher Schmid factor. The secondary is the lower. In addition, the curve noted "primary system" includes, within its statistics, the contribution of every sheared grain whereas the one noted "secondary system" only include grains with double shear. Within this analysis only single and double shear are discussed.

One could first note that primary system does not correspond systematically to the highest Schmid factor. Indeed both curves are not superimposed. It underlines a significant activity of lower Schmid factor systems notably between 0.3 and 0.35. As the maximal Schmid factor "law" is based on stress uniaxiality hypothesis one first explanation could be the existancy of a significative local triaxiality of stresses. One could underline three trends: (1) from $\mu = 0.25$ to 0.36, from $\mu = 0.36$ to 0.41 and from $\mu = 0.41$ to 0.5. The first trend is associated to $\approx 21\%$ of sheared grain, the second one $\approx 17\%$ and the final one $\approx 62\%$. One could notice that identical μ domains partition where already found within the analysis the austenitic phase of Duplex steel [El Bartali 2009]. The only difference concerns the first trend where traditionnaly, a few percentage of grain are present. In parallele, the cumulative Shmid factor density within the secondary system appears to have a more or less constant trend from $\mu = 0.33$ to 0.48.

1.5 Conclusion

The specimen-gauge section of the material (A316L) tested by Bodelot has been investigated by meaning of different tools. (1) EBSD analysis has been performed in order to provide grain pattern as well as grain statistics, i.e grain size, morphology, texture, orientations ... (2) Profilometric analysis has been done in order to reveal the out-of-plane plastic activity as well as potential connections with the grain pattern. (3) Routines for misorientations fields an distributions calculation has been developped and results have been notably compared to untextured material. (4) Finally, an algorithm for automatic slip-system identification has been implemented under ***MATLAB*** software in order to understand which kind of plasticity mechanisms has been developped within the material.

In consequence one could underline that the studied specimen is representative of a real polycrystal since it contains a large variety of grain (1776 grains), with a large variety of shape and sizes (mean size is $118\mu m$). In parallele, grains are quite "large" since more than 84% of studied area is composed by grain of which the mean diameter is greater than $100\mu m$. This point will be very important for field measurements. The material is untextured in terms of orientation nevertheless it reveals a macroscopic region where grain size is statistically lower (95 and $141\mu m$). Then, the grain boundary network is made of 57% of twin Σ_3 boundaries. Its has been shown that free surface topography is grain boundary dependent ($\approx \pm 10\mu m$ of relief) and that Σ_3 boundaries play a very important role. Indeed, intense out-of-plane displacements as well as steps on free surface are widely related to twin Σ_3 boundaries. This point should necesserally have an impact on dissipative response of the material. Finally a very heterogeneous pattern of slip-mark density has been observed which is the sign of a very heterogeneous plastic strain field. Indeed, according to relative slip-mark density field a variation of plastic strain from 0 to 5 and locally 10% could be expected for a mean plastic strain of 2.5%. In addition large regions exhibit few slip-marks and are supposed to have a concrete impact on plastic strain and thus stored energy field for exemple. The microstructure exhibits mainly single and double shear (57 and 29% of active slips), it evidences that the material has been submitted to montonic tensile test up to the end of transition between stage I and II of deformation.

The specimen has been here investigated in a "material" way, i.e basing the underestanding of final plastic state on microstructural observations. The objective of the next chapter is to provide an other point of vue; the one of the thermomechanic, analyzing kinematic and thermal fields. The ultimate purpose is obviously the comparison between both ways, both observations by coupling measurements.

Chapter 2

Measurement techniques and metrology

Contents

In the previous chapter, material, tests, crystallographic information and different analysis of the plastic activity have been presented. Statistical informations are now available about grain size, grain orientation, mean grain misorientation, intragranular activated slip systems, relative density of slip marks etc. The current chapter concerns in situ full-field measurements. This is a complementary way to analyze plastic phenomena through a kinematic, a thermal and thermomechanical point of view. Notice that the whole calibration strategy and data treatments introduced here could also be found in [Seghir 2013].

As noticed in the general introduction, simultaneous measurements of thermal and kinematic necessary fields are complex as well as the whole necessary data treatments for energy balance achievement. Previous works on such experiments and treatments at a very local scale are very limited: (1) studies on a bi-crystal of an A1050 aluminum was published in [Saai 2010], (2) works on an oligocrystal (7 grains) of a commercial pure aluminium in [Badulescu 2011], and finally (3) analysis on a polycrystal (2000 grains) of AISI 316L stainless steel [Bodelot 2009, Bodelot 2011]. To our knowledge only four experimental techniques of in situ calorimetric measurements at such scale have been used during the last 3 years. These techniques will be detailed in the next section, but, regarding the literature, it is

important to notice that each of them introduces some specific constraints and limitations concerning the studied material and the fineness of the considered microstructure.

The lack of such studies could be explained by some reasons: while Quantitative Infra Red Thermography used on macroscopic uniaxial tests becomes to be mastered (for example [Chrysochoos 1989b]), the case of microstructural analysis still presents some difficulties due to the nature of the loading path and the heterogeneity of the material. One of the difficulties lies in the necessary tracking of a material point during the experiment in order to follow the temperature evolution of each of them. Classically, it is necessary to couple thermal (QIRT[1]) and kinematic fields measurements and to use an imaging method (DIC[2]) that solves the optical flow. It allows recovering a displacement field that matches the first image taken and then performing a "Lagrangian thermography" (the transport of I.R. fields in the initial configuration). However using such technique is not trivial and leads to new measurement uncertainties that must be quantified. Let us first propose a review of the main technique used to couple QIRT and DIC techniques.

2.1 Review of techniques

The constraint of QIRT and DIC seems to be opposite. This part presents several ways to succeed in such a coupling and tends to balance the advantages and the inconvenient of the different approaches.

1. ***two-faces measurements***: each imaging system (C.C.D. and I.R. camera) observes one face of the specimen (see figure 2.1 (a)). This technique was used for example used in [Badulescu 2011]. The main advantage of this technique is that QIRT and DIC constraints are separated. In the case of [Badulescu 2011], a thin, opaque and uniform black paint is sprayed onto one face to obtain a thermal emissivity close to 1 and a microgrid could be applied on the other face to recover displacement field. Note that the microgrid could be replaced by a speckle coating. Nevertheless it implies to dispose on the same microstructure on both faces which require columnar extruded grains through the thickness, assuming that the displacement field is representative of the other face. This technique seems therefore to be appropriate for thin specimens of single, bi or oligocrystals ($<$ 10 grains) but not for polycrystalline structures.

2. ***one-shot measurement***: a single I.R. camera is used to obtain both kinematic and thermal fields on a same surface over the exact same space and time discretization. In this case, the contrast of I.R. images due to heterogeneity of emissivity is exploited to perform D.I.C. analyses in order to obtain reliable displacement fields. This technique, called "One-shot Measurement", implies to add the temperature evolution in the optical flow resolution, thus to modify classical D.I.C. algorithm. It was recently introduced in [Maynadier 2011b]. The main advantages of this technique are first to avoid any bias in time and space matching between kinematic and thermal field and secondly to conduct to a relatively simple experimental implementation compared to other techniques. Nevertheless, it implies a strong limitation on spatial resolution as the pitch of the best I.R. camera pixel is currently about 10 times superior to the best C.C.D camera one.

[1] Quantitative InfraRed Thermography
[2] Digital Image Correlation

Thus, all local variations of kinematic and thermal field or discontinuities are smoothed before being analyzed. As regard of I.R. camera properties, this technique seems currently much more appropriate for aggregates whose grain size is greater than $200\mu m$ in the best case and does not take profit of the efficiency of C.C.D and I.R. cameras in terms of optical and infrared microscopy.

3. ***single-face measurement***: Both imaging systems (C.C.D. and I.R. camera) observe the same zone at the same instant. Two kinds of setup could be considered:

   - the introduction of an angle between I.R. and C.C.D. camera (see figure 2.1 (b)). This technique was successfully used in [Saai 2010]. Nevertheless this setup clearly introduces some distorsions in temperature field which must be corrected by taking into account the spatial resolution. Moreover using a high magnification lens, such as the G_1 lens[3], for infrared microscopy is impossible due to its small depth of field ($\approx 100\mu m$). Indeed, in this case, the angle imposed to the camera with respect to the normal of the surface sample would be lower than 1^o. In consequence, this technique seems much more appropriate for big grain structure, such as bi-crystals [Saai 2010] than in optical microscopy for many small grains.

   - the use of a dïchroic mirror (see figure 2.1 (c) and (d)). This technique has been used in [Bodelot 2009]. Thanks to its filtering properties, the dïchroic mirror transmits the infrared radiations towards the infrared camera, located in front of the sample and reflects the rest of the radiations, including the visible radiations, to the C.C.D. camera which is perpendicular to the sample surface. The main disadvantages of this setup the difficulties of implementation and the necessary experimental bias due to the mirror (transmission, reflections). Nevertheless, in this case, both arrays of detectors remain parallel to the image of the sample's surface avoiding to introduce any distortion in the measured fields.

In both cases, if a high and local temperature precision is required, a specific coating must be elaborated. It must be as much as possible homogeneous in the I.R. spectrum and heterogeneous in the visible one [Bodelot 2009]. For more precision, heterogeneous emission properties of coating must be identified.

[3]High magnification lens which provides a geometrical spatial resolution equal to the InfraRed Focal Plane Array (IRFPA) sensor size

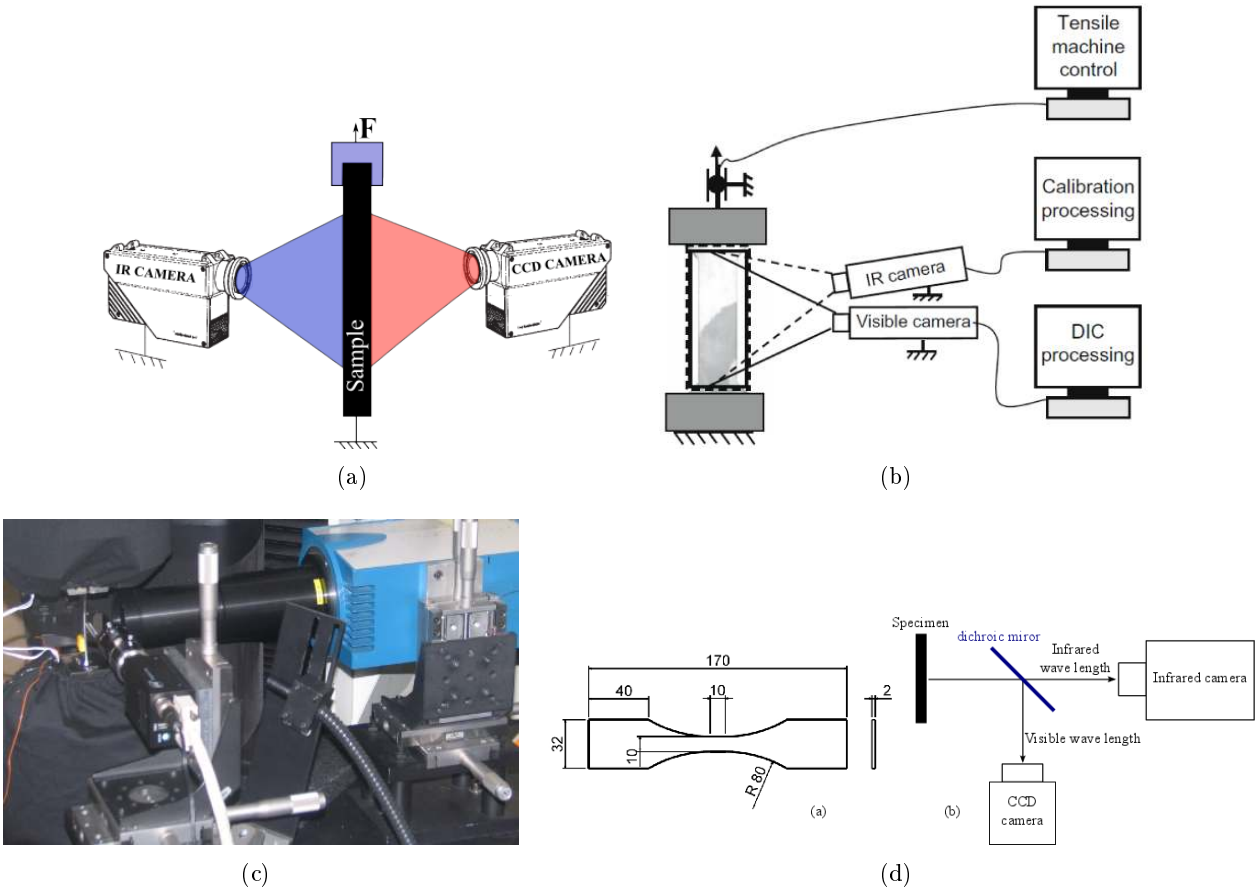

Figure 2.1: (a) Schema of bi-face QIRT and DIC measurement technique, (b) one-face experimental setup (from [Saai 2010]), (c) Experimental setup (from [Bodelot 2009]) and (d) its principle diagram

2.2 Focus on one "single-face" experimental setup

The main steps of fully coupled thermomechanical measurements used in [Bodelot 2009] are detailed and some assumptions, notably on the calibration procedure are discussed. Displacement fields are obtained thanks to DIC (Digital Image Correlation) performed with Correli^{LMT} developed at the "Laboratoire de Mécanique et Technologie" (LMT) of Cachan in France [Hild 2002]. Images of the deforming sample are grabbed thanks to a Jai CV-M4+ CCD camera. It is used with a Tamron 23FM50SP 50 mm lens and extension tubes, leading to a spatial resolution of 6.5x6.5 μm^2 per pixel and a field of view of 8.9x6.7 mm^2. Since the DIC computation is performed with 16x16 pixels subsets, the spatial resolution of the displacement and strain fields data is finally 104x104 μm^2. Temperature fields are obtained by IRT (Infrared Thermography). The sample is filmed by a FPA[4] Cedip Jade III

[4]Focal Plan Array

MWIR camera. It is used with a high magnification lens called G_1. The spatial resolution for the temperature fields data is 30x30 μm^2.

Different steps are necessary to obtain a fully coupled measurement of kinematic and thermal fields at the grain scale of a polycrystal. As many details about each step could be found in [Bodelot 2009], only the main features are recalled here.

1. Dichroïc mirror: a dichroic mirror is then located in front of the sample. Thanks to its filtering properties, it transmits the infrared radiation (wavelength between 2 and 6 μm) toward the infrared camera, located in front of the sample and reflects the rest of the radiation, including the visible radiation, to the CCD camera which is perpendicular to the sample surface. Arrays of each camera detectors remain parallel to the image of the sample surface avoiding any distortions in the measured fields.

2. Pixel to pixel calibration: providing that each detector of a FPA camera has its own behavior, each of them are calibrated regardless of neigbours in a defined range of temperature.

3. Coating: the keystone of the fully-coupled measurements lies in the coating applied on the sample and the difference in resolution of each camera. On the one hand, the coating exhibits a speckle aspect at a very fine scale, covering a wide range over the grey scale, which is required for the DIC computation. On the other hand, to perform IRT, this coating tends towards a high and uniform emissivity at the working scale, as close as possible to the one of the blackbody used for the calibration.

4. Lagrangian configuration: the thermal fields are measured on a deforming body. The DIC displacement data is therefore used to track the displacement of material points in order to express the temperature fields in the undeformed configuration.

Finally data presented in [Bodelot 2009] are fully-coupled insofar as both fields correspond to the same zone, at the same time, expressed in the undeformed configuration and the spatial resolutions achieved in strain measurements as well as in temperature measurements are suitable to give meaningful data at the scale of the grains of the studied material.

Nevertheless within this work, different assumptions have been done in order to recover thermal field expressed in Lagrangian configuration, notably concerning the noise treatment. The author underlines that the "measured" temperature of the sample is the sum of: (1) a fixe and unlocal thermal parasite signal, (2) a local parasite signal deforming with the sample and (3) a temporal noise. An additional noise come from the pixel to pixel calibration performed on a BlackBody [Berthel 2007a]. The solutions proposed in [Bodelot 2009] are now described.

- ***calibration***: the author has performed a pixel to pixel calibration in temperature. In this way she assumed the emissivity of the blackbody is 1. Actually, the used black body was a SR800 of CI Systems with a precision of $0.01^{\circ}C$ on $[0\ 125]^{\circ}C$ thermal range and has the following emissivity: 0.97±0.01. Traditionally, BlackBody emissivity is considered equal to 1 avoiding to take into account any reflection induced by the term $(1-\varepsilon)\Phi_{env}$ with Φ_{env} the environment flux

(see appendix C) and its heterogeneity is also neglected. Nevertheless, by tilting the BlackBody compared to IR camera and by blurring its radiation thanks to a gap from IR camera focal depth, it is possible to take into account its real mean emissivity, avoiding any reflections and smoothing any heterogeneities. Then in order to recover the surface temperature of the sample, the author has considered its mean emissivity. The author underlines, after the measurement of the coating emissivity distribution, that the emissivity values remain close to the mean one, i.e. 0.927±0.009, and, consequently, its spatial variation could be neglected. Note that this value comes from an indirect emissivity measurement technique as described in [Berthel 2007a] or [Poncelet 2007].

- ***fixed and unlocal thermal parasite signal***: the author associates this macroscopic thermal noise to reflexions leaded notably by the dichroïc mirror. This signal was identified, then approximated with the help to a 31x31 pixels rolling average and finally subtracted to each IR picture.

- ***local parasite signal deformed with the sample***: the author associates this signal to the emissivity variations on the surface specimen. Performing an average on 100 IR pictures of specimen during an unloading phase, the thermal influence of coating has been approximated and then subtracted to each IR picture. From this point the author does not deal any longer with absolute temperature T but with deviation of temperature from the initial state θ. In addition a smoothing of residual coating effect was performed assuming the mean value over a 3x3 pixels window.

- ***temporal noise***: the author solves this problem performing a rolling average every 11 data point of temporal signal and for each pixel.

Some improvements are proposed in this work: (1) the use of Correli^{Q4} [Hild 2008] instead of correli^{LMT} to remove some artifacts in displacement fields visible in [Bodelot 2008]. (2) The realization of the entire calibration procedure in flux. This limits the possible errors during the calibration procedure and conducts to an additive decomposition of the signal and the estimation of the emissivity field. Thanks to this emissivity field estimation the temperature naturally takes into account the "local parasite signal deforming with the sample". (3) Finally the noise associated to each material point of IR scenes is removed thanks to a low-pass filter. The outline of the next section is then the following:

1. every calibration which could be done in Eulerian configuration, i.e. fixed phenomena compared to IR camera, are done. One presents the pixel to pixel calibration in flux as well as the eulerian decomposition of global measured signal. The reflections are removed and the emissivity field is estimated.

2. the Digital Image correlation is presented and the "Lagrangian thermography" is introduced.

3. temperature is recovered thanks to IR scene expressed in Lagrangian configuration and emissivity field.

4. the noise is removed from the temporal evolution of each material point.

2.3 From raw data to thermomechanical ones

2.3.1 Eulerian thermal metrology

Following the thermal evolution of a material point during a mechanical loading is not a trivial task:

1. as introduced in appendix C, the infrared camera does not measure temperature but radiative flux and does not express it in physical units but in Digital Level (DL).
2. the measurement could be affected by optical distorsions.
3. each sensor of the IRFPA (Infrared Focal Plan Array) camera has its own dynamic and noise.
4. the relation between radiative flux and temperature depends on surface material properties of specimen as emissivity, diffusivity ...
5. external heat sources could dramatically affect the observed thermal scene.

It is therefore essential to establish a calibration strategy which minimizes the error at each step. This part focus on calibration steps which must be done in Eulerian configuration.

2.3.1.1 Calibration

Pixel to pixel

The infrared camera converts the received flux (emitted by an object) in DL (Digital Level). To convert it in physical units it is therefore necessary to calibrate each pixel/sensor of the IRFPA camera. A "flux calibration" method is proposed. Its principle is to determine, thanks to a least square method, the optimal function to pass from DL to flux emitted by the observed object ϕ at fixed integration time IT of the camera. Contrary to temperature calibration the function does not depend on the emissivity of the observed object. Finally, as each IRFPA sensor of the camera has its own dynamic, this calibration must be done for each detector (pixel to pixel calibration [Berthel 2007a]).

With the help of an extended BlackBody (BB) at different given uniform temperature T_k and the corresponding Digital Level (DL_i^k) of each pixel (i) of matrix sensor provided by the infrared camera, one could build each calibration curves. The procedure is performed according to the following equation:

$$\Phi\left(IT, T_k, i\right) = \sum_{u=1}^{p} \alpha_u \left(DL_k^i\right)^u \tag{2.1}$$

where coefficients α_u are determined by the least square method (see 3.3), p corresponds to the degree of the classically polynomial calibration law. Equation 2.1 is actually a system of k equations, for every calibration temperature T_k of BlackBody which must be minimized. In practice, in order to limit the temporal noise of each sensor, the calibration is done with the help of the mean field over 100 IR pictures.

In the present case, the minimization is performed thanks to Matlab. Picture 2.2 (a) presents the whole flux calibration function of the IRFPA camera sensors.

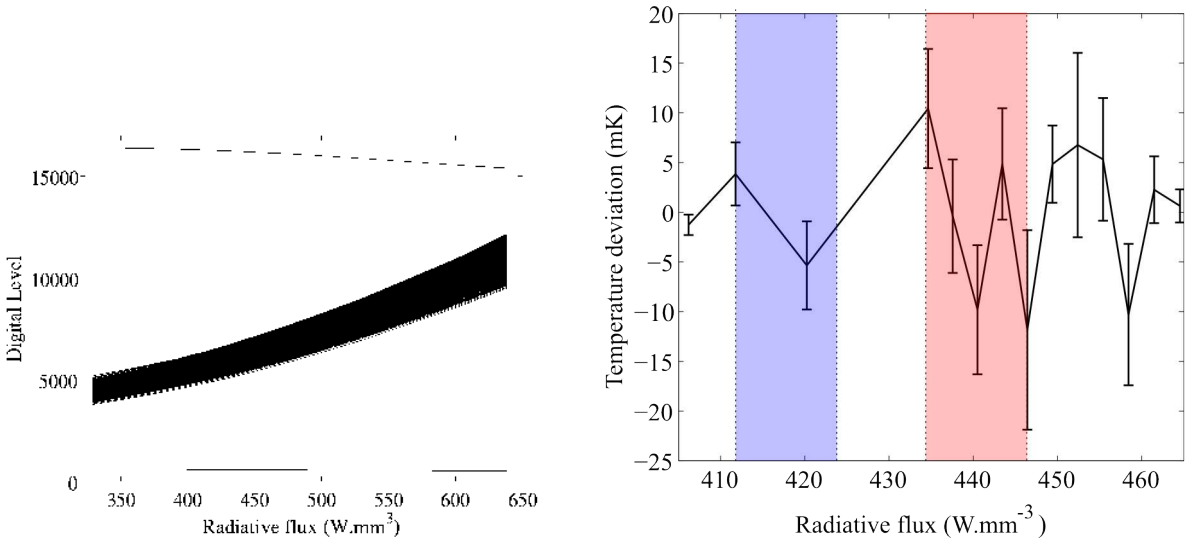

Figure 2.2: (a) 76800 flux calibration functions associated to each IRFPA sensors and (b) error between radiative and measured temperature (mK)

They consist of 6 order polynomial functions. One could note that most of the pixels constitute a set of curve with a maximum deviation of 3000 DL at a given homogeneous emitted flux and that some pixels have a flat response as a function of the flux. These pixels are considered defective and replaced by the mean value of their neighbors. Once each calibration function is determined, the corresponding thermal fields are calculated following the Boltzman law. It permits to determine the accuracy of the calibration (in mK).

$$\Phi = \varepsilon\sigma T^4 \tag{2.2}$$

where ϕ, ε, σ are in the present case, the flux radiated by the BlackBody at fixed temperature T, the uniform emissivity of the BlackBody ($\varepsilon_{\text{BB}} = 0.97$) and the Boltzmann constant $\sigma = 5.67032\text{x}10^{-8}$ respectively. Picture 2.2 (b) presents the mean and extreme deviation between the effective temperature of the BlackBody and the "measured" or calibrated one. It shows that the mean error within each pixel when the flux radiated by the object remains in the [405 - 465] $W.mm^{-3}$ domain fluctuates from -10 to 10 mK and that the absolute error is locally inferior to 30 mK. Note that such result remains valid under the presented flux domain regardless of any temporal noise. It is relatively important to note that the camera will now be calibrated for a specific range of flux and not for a range of temperature. Picture 2.2 (b) presents two domains: the blue one is the flux domain corresponding to the interval $[25^oC - 27^oC]$ assuming the mean specimen emissivity ($\varepsilon_s = 0.927$), the red one correspond

to the interval $[25^oC - 27^oC]$ assuming BlackBody emissivity ($\varepsilon_{BB} = 0.97$). Obviously, the interval $[25^oC - 27^oC]$ does not lead to the same range of flux, in the case of BlackBody or specimen, because of the difference of emissivity. It is therefore important to approach as close as possible specimen emissivity by an other measure to determine the appropriate range of flux calibratation especially in the case where the specimen emissivity is far from 1. An other possibility is to extend the calibration range otherwise calibration error dramatically increases over the calibration limit because of the polynomial fitting.

Considering the interval $[25^oC-27^oC]$ for specimen temperature variation during monotonic tension test [5] one could conclude that the present calibration remains valid for a coating emissivity which would range from 0.92 to 0.98 . This seems enough to take into account the effective emissivity distribution [Bodelot 2008].

Temporal noise

As previously introduced, the calibration function results from a mean field over 100 IR pictures of BlackBody regulated at different temperatures. Nevertheless, these functions are applied to each IR pictures of the specimen in order to follow its thermal behavior at the imposed measurement frequency (140Hz). Consequently, the effective measurement uncertainty will necessarily increase. To maintain this one under $30mK$ at a high measurement frequency and a high resolution, the pixel to pixel calibration is applied to each 100 IR scenes at a fixed temperature and then the maximal local deviation from the effective temperature is observed. Figure 2.3 presents the local maximal deviation from the effective temperature for different BlackBody temperatures and for different treatments: (1) black lined curve is the thermal deviation considering full frequency (140Hz) and full resolution, (2) black dotted curve is the one considering lower frequency (25Hz) and full resolution. (3) is finally the one considering low frequency (25Hz) and low resolution, i.e. average over 3x3 pixels. Note that a low frequency signal is obtained by using a low-pass filter in Fourier space.

Finally, previous works [Pron 2004] have shown that the resolution of an IR imaging system is not equal to the size of the area observed by the IRFPA pixel. The method used to determine the real measurement resolution, called SRF (Split Response Function), is described in [Pron 2004] and permits to affirm that for the CEDIP Jade III camera, a zone of interest of 3x3 pixel at worst is sufficient to capture 100% of emitted radiations. Taking into account this material constraint one knows that the minimal resolution provided by IR imaging system is 90x90 μm (3x3 pixels).
Then the figure 2.3 shows that when both constraints are verified the highest local deviation from effective temperature of BlackBody is at worst 30 mK. Note that the low-pass filter will be applied on Lagrangian signal and not directly on the Eulerian one. This point will be treated in 2.3.3.3.

[5] This interval has been verified a posteriori by thermocouple measurement

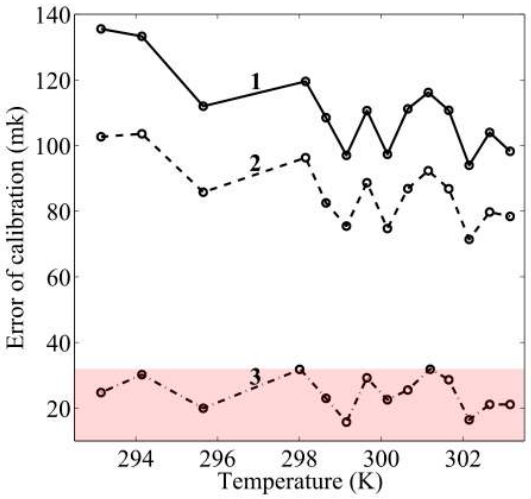

Figure 2.3: Error on calibration (mK) for different cases: (1) 140Hz and full resolution, (2) 25Hz and full resolution and (3) 25Hz and average over 3x3 pixels

This part has introduced the pixel to pixel calibration. This calibration has been done in flux, in order to be able to consider the effective emissivity of the BlackBody instead of 1, as usually done. 6^{th} degree polynomial function has been chosen to calibrate each pixel of the IRFPA matrix within the flux range [405 - 465] $W.mm^{-3}$. The minimization was performed considering an average IR field over 100 pictures in order to limit temporal noise effects. An uncertainty of 30 mK on fully resolved IR field was found. Then, in order to guarantee this uncertainty for no time averaged signal, two constraints has been considered: the first one concerns the reduction of signal frequency, the second the reduction of spatial resolution. Finally, the thermal signal must be considered as having a frequency of 25Hz, a resolution of 90x90μm^2 (3x3 pixels) and an uncertainty of $30mK$.

2.3.1.2 Flux decomposition

In order to perform real quantitative infrared thermography at local scale, two phenomena have to be taken into account. The first one is the necessary reflections which could appear even if the test is performed in a totally controlled environment. In the present case, the fully coupled measurement is performed thanks to a dïchroic mirror. It is unfortunately a preferential source of reflections. Considering the fixed I.R. camera, this first phenomena is Eulerian (reflection spots does not move when the specimen deforms). The second one is the spatial variation of emissivity and diffusivity due to the thermal and mechanical[6] properties of the coating. Considering the fixed I.R. camera, this phenomenon is Lagrangian (the "apparent emissivity" field moves and deforms with the specimen). Both have to be

[6] one deals hear with potential cracking of coating

removed before determining and then analyzing thermal fields. Nevertheless experimental evaluation of reflections and emissivity field is not trivial. The objective of this part is to show that both aspects could numerically be treated since they are not connected.

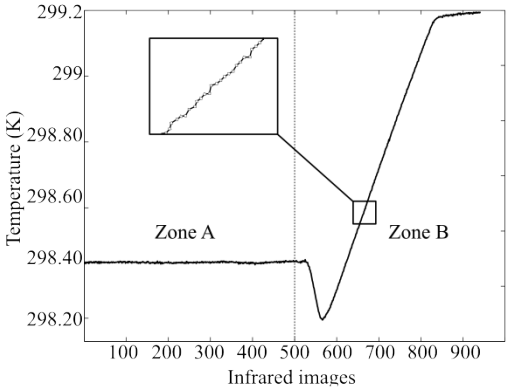

(a)

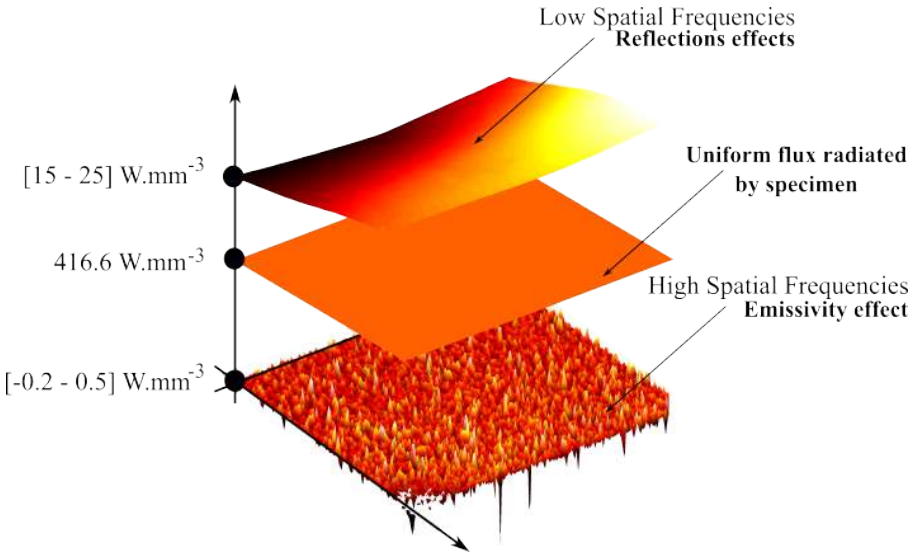

(b)

Figure 2.4: (a) Mean evolution over the specimen gauge section of temperature during monotonic tension test and (b) flux decomposition in Low spatial frequencies, High spatial ones and uniform one

Indeed, reflections and "apparent emissivity" affect the observed field at totally different spatial scale. A reasonable physical assumption is to consider that reflections affects the field in Low Spatial

Frequency (LSF) and are Eulerian whereas "apparent emissivity" field affects the observed field in High Spatial Frequency (HSF) and is Lagrangian (see figure 2.4 (b)). To treat both aspects, one focuses on a period A on figure 2.4 (a). During this period the specimen is around the thermal equilibrium, the specimen is unloading yet, thus its temperature is known and remains uniform. During this period the whole local and/or global spatial flux variation are linked to reflection (environment) and "apparent emissivity" (coating). figure 2.4 (a) part B presents the mean thermal response of the specimen during the tensile test.

Let us decompose the flux captured by IRFPA sensors. The flux measured by the infrared camera ϕ is the difference between the observed flux ϕ_{obs} and the flux radiated by camera IRFPA sensor ϕ_{cam} cooled at $T_{cam} = 77K$.

$$\left\{ \begin{array}{rcl} \phi & = & \phi_{obs} - \phi_{cam} \\ \phi_{obs} & = & \phi_{obj} + \phi_{refl} \\ \phi_{cam} & = & \sigma T_{cam}^4 \end{array} \right. \tag{2.3}$$

The observed flux ϕ_{obs} is the composition of two terms: the flux really emitted by the observed object ϕ_{obj} and some possible reflection fluxes ϕ_{refl} caused by external heat sources and the fact that the emissivity is not equal to one. In the case of gray body, the flux emitted by the object follow the Boltzman law as introduced in equation 2.2:

$$\phi_{obj} = \varepsilon_{obj} \sigma T_{obj}^4 \tag{2.4}$$

with ε_{obj} and T_{obj} are respectively the emissivity field and the temperature of surface specimen. Combining equations 2.3 and 2.4 one could write:

$$\phi = \underbrace{\varepsilon_{obj} \sigma T_{obj}^4}_{\text{(HSF,LSF)}} + \underbrace{\phi_{refl} - \sigma T_{cam}^4}_{\text{LSF}} \tag{2.5}$$

The main interest of this decomposition is to put in light the variables separation previously announced. Analyzing Low Spatial Frequency of ϕ by spectral decomposition, one could write:

$$\phi|_{LSF} = \bar{\varepsilon}_{obj} \sigma \bar{T}_{obj}^4 + \phi_{refl} - \sigma T_{cam}^4 \tag{2.6}$$

with $\phi|_{LSF}$ the measured flux without high spatial frequencies. High spatial frequency phenomena are assumed here if the spatial period is lower than $500\mu m$, i.e. lower than 10% of the picture. Within this assumption, LSF signal does not take into account any local variations. $\bar{\varepsilon}_{obj}$ is the measured mean emissivity of surface specimen (indirect emissivity measurement [Bodelot 2008]), $\bar{T}_{obj}$, the measured mean temperature (thermocouple) of surface specimen during part A (see figure 2.4). Picture 2.4 (b) presents the radiative flux decomposition introduced in equations 2.5. HSF signal fluctuates from -0.2 to 0.5 $W.mm^{-3}$; it results from the high frequency part of $\varepsilon_{obj} \sigma T_{obj}^4$ in eq. 2.5. LSF signal fluctuates from 15 to 25 $W.mm^{-3}$; it corresponds to ϕ_{refl} in eq. 2.5 and the constant signal corresponds to the

term $\bar{\varepsilon}_{obj}\sigma\bar{T}^4_{obj} - \sigma T^4_{cam}$ in eq. 2.6. Its value is 416.6 $W.mm^{-3}$.

Equation 2.6 leads to:

$$\phi_{refl} = \phi|_{LSF} - \bar{\varepsilon}_{obj}\sigma\bar{T}^4_{obj} + \sigma T^4_{cam} \tag{2.7}$$

Combining equations 2.7 and 2.5, it is possible to determine the "apparent emissivity" field of the specimen arround a thermal equilibrium.

$$\varepsilon_{obj} = \frac{\phi - \left(\phi|_{LSF} - \bar{\varepsilon}_{obj}\sigma\bar{T}^4_{obj}\right)}{\sigma\bar{T}^4_{obj}} \tag{2.8}$$

Classically, in coupled field measurement where an heterogeneous coating (for D.I.C) is necessary, emissivity is considered constant and homogeneous [Bodelot 2011, Dumoulin 2010]. Firstly, because it is not a so rude assumption in most cases and secondly, no direct and in situ method for emissivity field measurement of exists even if some authors try to obtain it by observing the specimen in two distinct spectral bands [Kasem 2010]. Finally, most Quantitative InfraRed Thermography analyses doesn't tend to access a such precise and local surface temperature. Thanks to the relation 2.8 one could build the temperature error field induced by the hypothesis of homogeneous emissivity. This error is corrected in the present case.

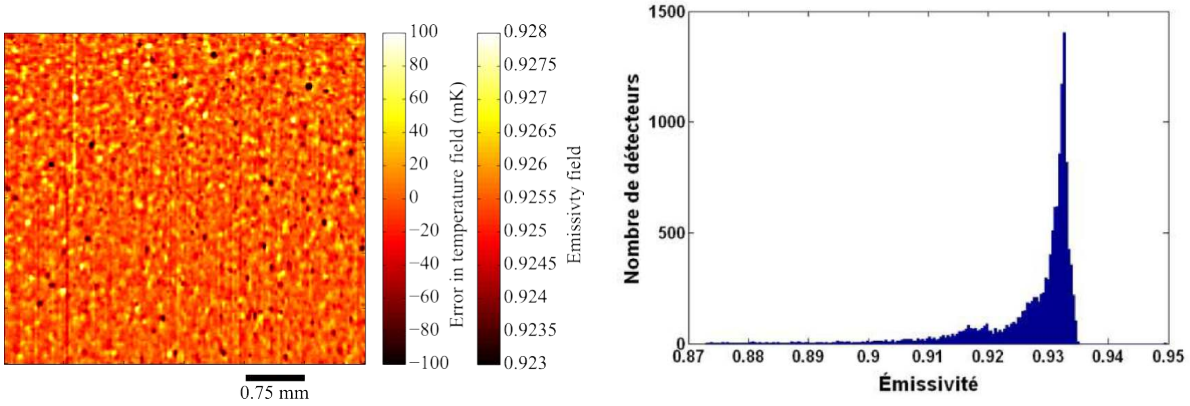

(a) (b)

Figure 2.5: (a) Temperature error field with homogeneous emissivity (0.927) considering non homogeneous emissivity field as reference and corresponding apparent emissivity field. (b) Emissivity of this coating measured in [Bodelot 2009]

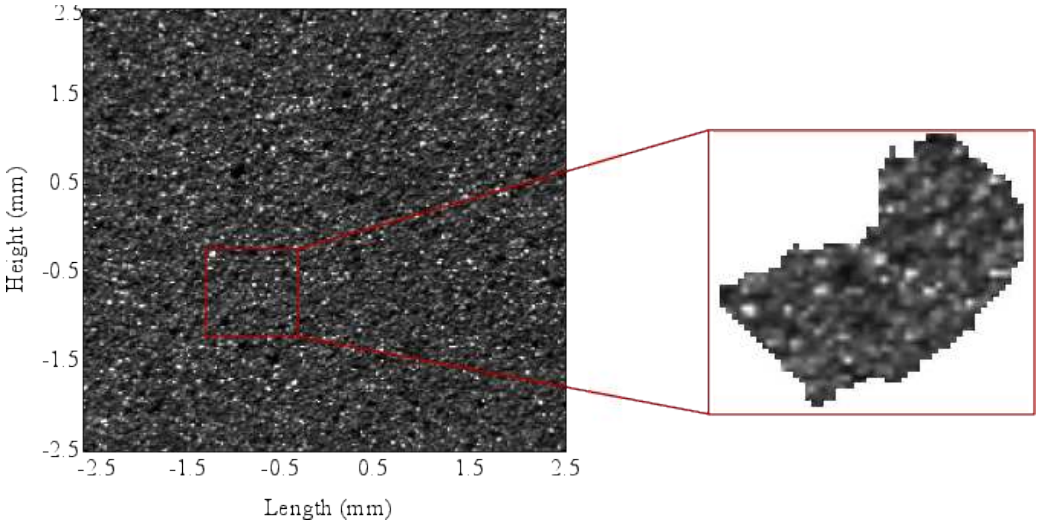

Figure 2.6: Coating in visible wavelength and zoom on a specific milimetric grain

Figures 2.5 (a) presents the temperature error field and the corresponding emissivity built from equation 2.8. Temperature error field is built from the difference between the field obtained with a uniform emissivity and the one obtained with the apparent emissivity map (see equation 2.8). One could note that the classical assumption of homogeneous emissivity leads here, to more than $200mK$ of thermal spatial noise which is clearly connected to the heterogeneity of coating of figure 2.6. Its mean value is null but it standard deviation is $23mK$. The built emissivity map permits to avoid this temperature error. Concerning the emissivity field (see 2.5 (a) 2^{nd} colorbar), it ranges from 0.92 to 0.93 with a mean value of 0.927 (experimental measure) and standard deviation of $1\text{x}10^{-3}$. Figure 2.5 (b) presents the emissivity distribution of coating measured by indirect method in [Bodelot 2009]. One could observe that it ranges from 0.875 to 0.935 and the standard deviation is $9\text{x}10^{-3}$. As regard to the experimental data provided by indirect emissivity measurement, one could conclude that the standard deviation of coating emissivity is underestimated even if the mean value is conserved. Nevertheless, the error on final thermal field is here locally reduced and it remains widely lower than the measurement uncertainty.

It is important to note that emissivity and diffusivity depend, in part, on the temperature of specimen. However the apparent emissivity field previously built does not take into account any variation of temperature since it is built around the equilibrium state. Nevertheless, the variation of temperature is, in the present case, i.e. monotonic tensile test up to 2.5% of mean axial strain, lower than 1K. Thus, one assumes a constant emissivity map during the test.

This part has introduced a way to decompose the flux radiated by the specimen. It has been assumed, during an unloading phase, that the radiative flux could be decomposed firstly, in a Low Spatial Frequency signal, associated to reflections. As this signal is Eulerian for the IR camera, it has been directly removed. A second part of the signal can be associated to High Spatial Frequencies, associated to heterogeneous emissivity effect. An emissivity map has then been established and compared to indirect measurement performed in [Bodelot 2008]. It has been evidenced that the built emissivity map underestimates the experimental standard deviation. Nevertheless, it permits locally to take into account a part of the specimen emission properties which clearly reduces errors due to uniform emissivity assumption. As this signal is Lagrangian for the IR camera, it needs material point paths to be applied. It will be done in further section.

2.3.2 Digital Image Correlation

Kinematic fields are here obtained from visible pictures taken by CCD camera, and thanks to Digital Image Correlation software Correli^{Q4} [Hild 2008]. The change in DIC software compared to Bodelot's works [Bodelot 2008] was justified on one hand by the appearance of some artifacts in the displacement field, clearly associated to the correlation method and, on the other hand, according to the Finite Element formalism which will facilitate a numerical/experimental dialog since displacement variation follow similar local shape functions. Other DIC softwares exist in the scientific community and could be also considered, for exemple: *Icasoft* [Mguil-Touchal 1997], *7D* [Vacher 2003], *Granu* [Brillaud 2002] ... but every software has its own performance and limits [Bornert 2009].
The principle of Digital Image Correlation is globally the same in every software. The basis of the algorithm is the comparison of two pictures of a same specimen area at two different states of the loading: a reference one and a deformed one. It is expressed as follows:

$$x_i - x_0 = u_0(A) \tag{2.9}$$

$$y_i - y_0 = v_0(A) \tag{2.10}$$

where A(x_i, y_i) are coordinates of point A in deformed configuration, A(x_0, y_0) are coordinates of point A in reference configuration and $\underline{U}_0^i(u_0^i(A), v_0^i(A))$ the axial and transversal displacements of a material point A expressed in the reference configuration. Obviously, specimen must exhibits a sufficient speckled texture in term of gray level. This speckle aspect could naturally exists on a material observed with high magnification [El Bartali 2009], but also be artificial as in the present case (see picture 2.6).

Figure 2.7 from (a) to (d) presents the reference picture of the specimen covered by its coating, displacement vectors $\underline{U}_0^i(u_0^i, v_0^i)$ superimposed on deformed picture and the displacement field u_0^i and v_0^i ones respectively.

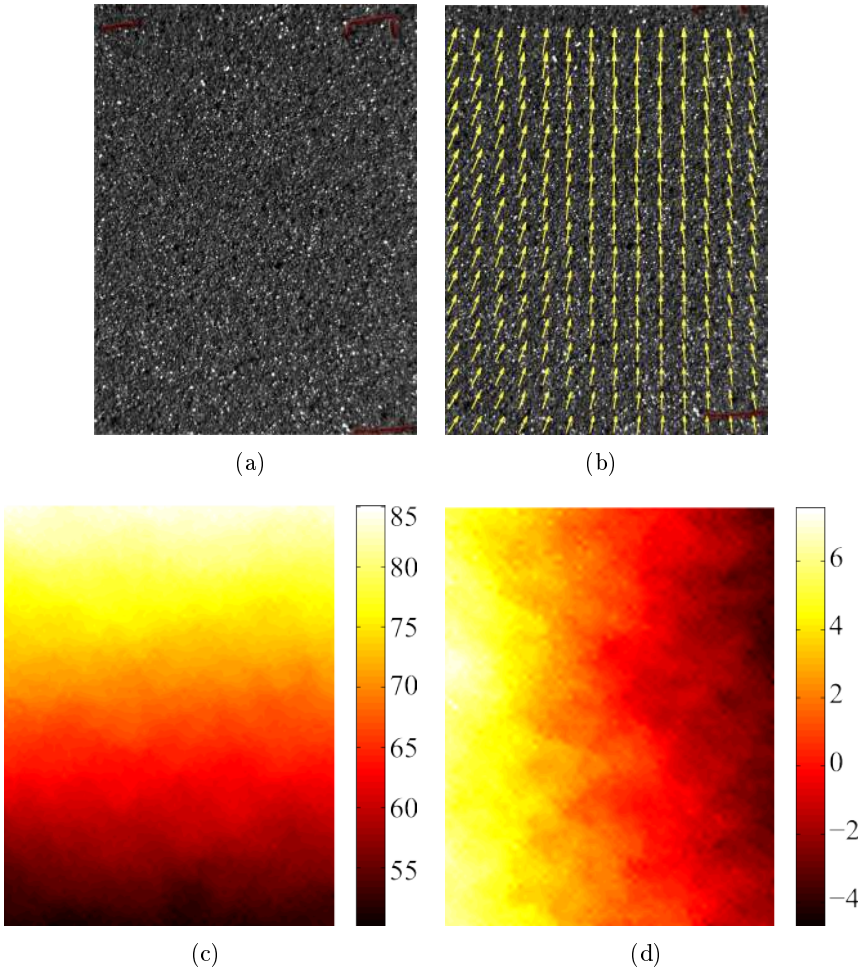

Figure 2.7: (a) reference picture of specimen gauge section covered by coating (b) displacement vectors $\underline{U}_0^i(u_0^i, v_0^i)$ superimposed on deformed picture, (c) vertical displacement field u_0^i and (d) horizontal one v_0^i (in pixels)

The principle of Digital Image Correlation is briefly introduced in appendix B, we only recall here mains results in term of resolution, uncertainty, and shape function.

- Correli^{Q4} assumes a bilinear kinematic within 4 nodes square elements. This is the kinematic classically assumed in Finite Elements where such elements are called $Q4P1$, i.e. 4 nodes elements using 1^{st} degree polynomials for interpolation functions.
- in line with [Bodelot 2008], 16x16 subset windows has been chosen as ZOI. Thus, the kinematic resolution is 104x104μm^2 since the imaging system provides initially a resolution of 6.5x6.5μm^2 per pixel.
- the uncertainty on displacement calculation for a given measurement and a given DIC software mainly depends on two points: (1) the coating, i.e. its random aspect and the grey level domain covered by it and (2) the ZOI size. Higher is the ZOI size greater is the accuracy but smaller is the resolution. The procedure for uncertainty estimation, in relation with the ZOI size and coating, already integrated in Correli^{Q4} has been used. Figure 2.8 (a) presents the systematic error on displacement as a function of the ZOI size and the coating presented in figure 2.6. The maximum of the error is obtained for a 0.5 pixel displacement. The systematic error, i.e. the mean error over each ZOI, is, in the case of 16x16 pixels, 6.24x10^{-4} pixels or 4.1x10^{-3} μm. Figure 2.8 (b) presents the uncertainty, i.e. the mean standard deviation over each ZOI, also function of ZOI size. The uncertainty of the kinematic measurement considering 16x16 pixels is consequently 5.72x10^{-3} pixels or 4x10^{-2} μm.

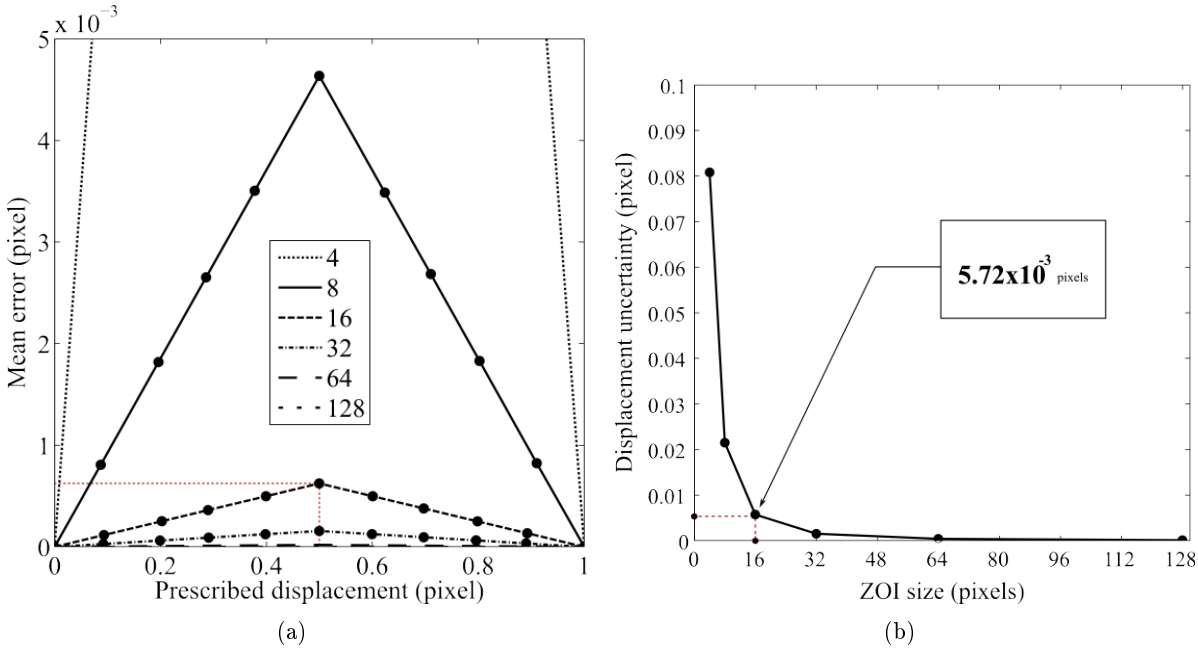

Figure 2.8: (a) systematic error on the pixel displacement function of ZOI size and (b) uncertainty of displacement function of ZOI size (both in pixel)

2.3.3 Lagrangian metrology and thermography

Radiative flux is expressed in the deformed configuration. However the emissivity map and kinematic fields are expressed in initial configuration. Thus, to determine thermal fields and to rely thermal evolution and microstructure for example, it is therefore necessary to follow then to move back radiative flux associated with each material points of the observed zone. It is realized thanks to DIC performed on CCD camera pictures. It constitutes the concept of "Lagrangian thermography". For this, a time and space matching between kinematic and thermal fields has to be done.

2.3.3.1 Time and space matching

Different fields in term of resolution, measurement frequency, ... have been used and table 2.1 summarizes some of their properties. Kinematic and IR measurement are first synchronized in space by using some marks on the specimen observable in visible as well as in invisible wavelength. This point is presented on pictures 2.9. It permits to rotate, translate and stretch fields in order to perfectly match each other at the initial instant. The time synchronization is realized thanks to the trig offset of each camera running at its own fixed frequency. In order to use a unique spatio-temporal mesh for any data, it is decided to take profit of the high resolution of E.B.S.D. field and the high frequency of IR camera. Thus one assumes a spatio-temporal interpolation of kinematic and IR field on:

- E.B.S.D. mesh for space

	Kinematic fields	IR fields	E.B.S.D. field	profilometry
field surface in mm^2	5x5			
resolution in μm^2	104x104	90x90	20x20	5x5
frequency in frame number	15	302	1	1

Table 2.1: Field of vue, resolutions and measurement frequency of kinematic, IR, E.B.S.D. and profilometry fields

- IR grid for time

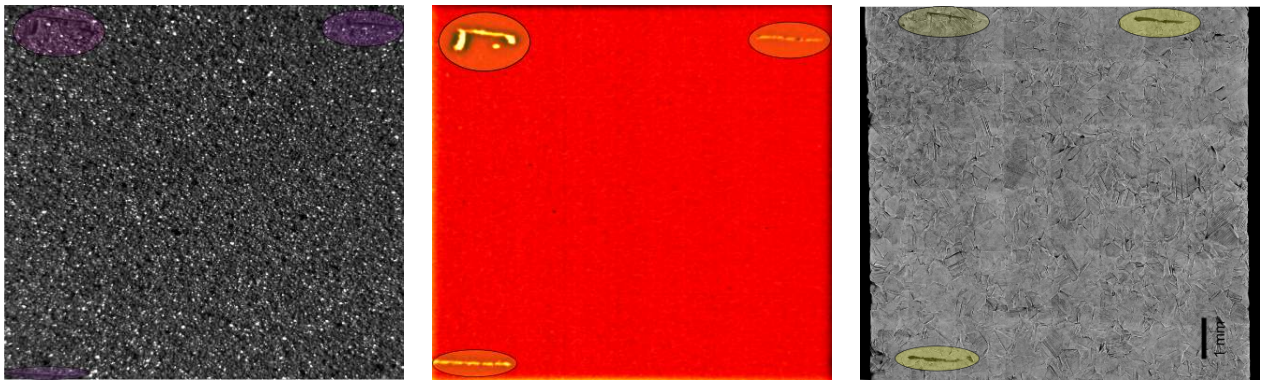

(a) (b) (c)

Figure 2.9: visualisation of marks on (a) optical pictures (CCD camera), (b) IR picture (IR camera) and (c) on micrography performed after test and removing of coating

It constitutes a trilinear interpolation (2D space, 1D time) of data which is realized under Matlab using the function *interp3*. Note that this procedure does not change the resolution of each quantity as they are only linearly interpolated on a unique reference mesh.

2.3.3.2 Lagrangian thermography

Figure 2.10 presents the principle of the Lagrangian thermography. $P_{IR,i}$ denotes a point in the infrared camera coordinate system expressed in current configuration, i.e. at time t_i, $P_{CCD,i}$ a point in the coordinate system of CCD camera in the same configuration. Note that $P_{CCD,0}$ and $P_{IR,0}$ are in the same coordinate system thanks to space and time synchronization and then spatio-temporal linear interpolation (see previous section). Then, the displacement between instant 0 and t_i, expressed in the initial configuration and denoted $\underline{U}_0^i$, could be directly applied to $P_{IR,i}$. Following equations 2.9 and 2.10, one obtains:

$$P_{IR,0} = P_{IR,i} - \underline{U}_0^i \tag{2.11}$$

Equation 2.11 must be applied to each material point $P_{IR,i}$ at each time t_i. Within the same framework, E.B.S.D. fields performed after test, i.e. euler angles in deformed configuration, is also transported from current to initial configuration. Finally, displacement, radiative flux, emissivity and E.B.S.D. fields are henceforth expressed in the same reference system.

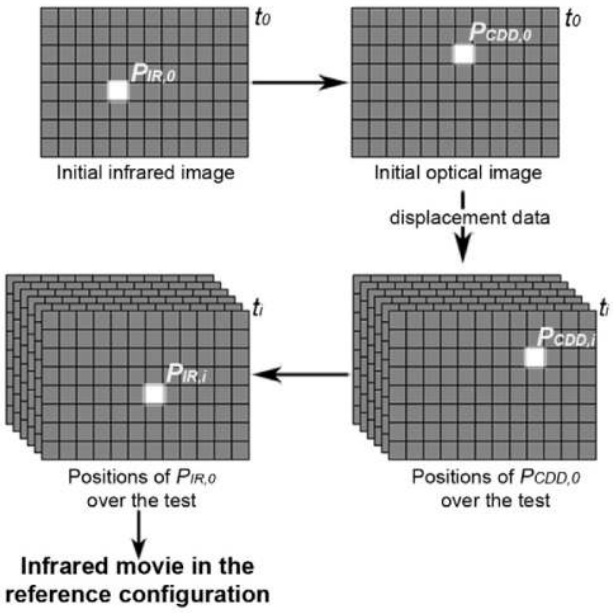

Figure 2.10: Principle of the algorithm used to follow material points in front of the infrared sensor and express the infrared fields in the undeformed configuration ("Lagrangian thermography") extract from [Bodelot 2011]

2.3.3.3 Time treatment

The time noise which appears in infrared fields (see figure 2.4) is mainly due to the variation of flux in the room during the test, and the intrinsic noise of each pixel. Thus it has to be removed before applying the emissivity correction and determining the temperature fields. Within Lagrangian thermography framework each material point is affected by the sensibility of each pixel along its deformation path. Thus, in order to perform a time smoothing with a physical sense, the treatment has to be done after the Lagrangian thermography on material points. Different kind of smoothing could be consider here:

- a polynomial function (6^{th} degree at least) could be considered. It represents quite well the drop and then the increase of temperature but not the initial and final evolutions (see figure 2.4). Moreover every quick variation of radiative flux are removed. The consequence is a global uniformity of the thermal response.
- a function which includes a physical sense could be considered. It supposes to assume a constitutive law and to perform an identification with the help of the strain field providing by DIC.

- a classical low-pass filter could be applied in order to remove high time frequency in Fourier space.

As already introduced in section 2.3.1.1, a low-pass filter cutting frequencies strictly higher than $25Hz$ has been chosen. Such low pass filter guarantee the thermal uncertainty. Picture 2.11 presents the raw and smoothed radiative flux evolution of one of the material points within the center zone of the specimen. One observes that main variations of radiative flux are conserved.

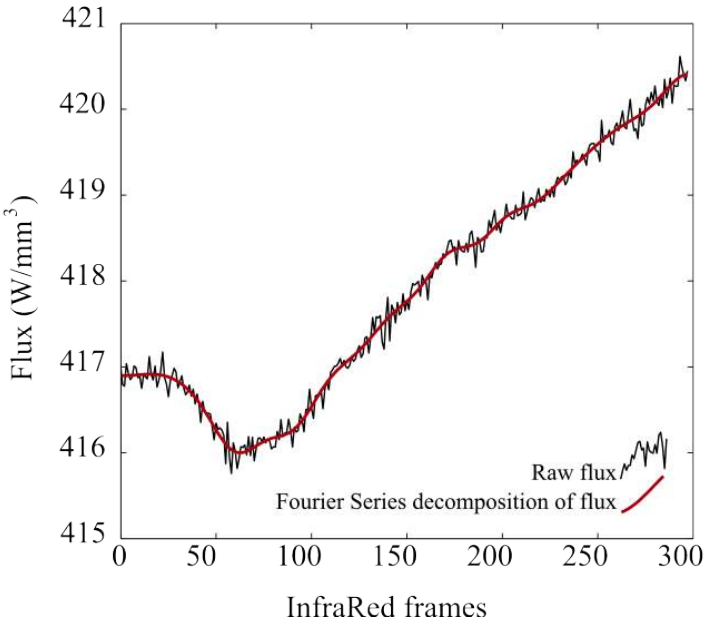

Figure 2.11: Raw and time smoothed ($>25Hz$) radiative flux of one material point within the center zone of specimen gauge section

2.3.3.4 Apparent emissivity correction

In section 2.3.1.2 a local spatial variation of flux response was identified on unloaded specimen. The nature of this flux distribution has been quantified and attributed to emissivity distribution due to the coating. Then, in section 2.3.3.2, Lagrangian thermography has been performed on IR scene in order to express both fields in same initial configuration. Now, the apparent emissivity correction can be applied on the whole IR scene to finally express from ϕ_{obj} the effective surface temperature of specimen.

$$T_{obj} = \left(\frac{\phi_{obj}}{\sigma \varepsilon_{obj}}\right)^{\frac{1}{4}} \tag{2.12}$$

with ε_{obj} introduced in section 2.3.1.2. The calibrated thermal scene expressed in undeformed configuration will be analyzed in the next section thanks to microstructural data.

2.4 Conclusion

In this chapter, the entire metrological procedure to obtain in-situ fully-coupled kinematic and thermal fields expressed in the undeformed configuration has been introduced. A special attention to the decomposition of measurement errors in an Eulerian part related to the sensor dynamic, an Eulerian part related to reflections due to the environnement and the experimental setup and a Lagrangian part related to the intrinsic emission properties of the surface specimen has been done. The metrological procedure has been applied to Digital Levels and Gray levels frames registered by IR and CCD camera respectivelly within [Bodelot 2009]. Table 2.2 and the figure 2.12 present respectively, the characteristics of calibrated data such as resolutions, uncertanties, fields of view... and a schematic representation of the entire work done within this part.

	Kinematic fields	IR fields	E.B.S.D fields	Profilometry
matrix of sensors (pixels)	1368x1024	320x240	250x250	1000x1000
geometrical spatial resolution (μm^2)	6.5x6.5	30x30	20x20	5x5
field of view (mm^2)	8.9x6.7	9.6x7.2	5.5x5.7	5x5
frequency (Hz)	7	140		
final resolution (μm^2)	104x104	90x90	20x20	20x20
final analysed zone (mm^2)	5x5			
final frequency (Hz)	7Hz	25Hz		
uncertainty	$0.04\mu m$	$30\ mK$		
spatio-temporal grid for coupling	250x250 pixels and 302 frames			

Table 2.2: Resolution and uncertainty of fully coupled measurements

Nevertheless, notice that two questionning points have not been treated within this chapter: (1) the inter-dependency of each sensor within the matrix sensor and (2) the influence of dïchroic mirror. Both relate to the reliability of measurements. One has to admit firstly, that it is very complicated to quantify the impact of possible electrical transferts from one pixel to its neighbours. According to Cedip, a space between each sensor ensure the well electric insulation and one assumes that the average over 3x3 pixels region allows to neglect this point. Secondly, using a dïchroic mirror to perform infrared measurement is not so usual. One could cite in other applications works of [Bendada 2004] and [Ranc 2008]. The transmission curve of dïchroic mirror mainly depends on the wave length of emitted radiations [Gaussorgues 1989] moreover the considered dïchroic mirror transmits 60 to 80% of IR radiations of which the wave length ranges from 2 to 6 μm (include in Mid-wavelength infrared) and totally reflects others wavelength. Nevertheless the signal reduction induced by transmission properties is taken into account at best by performing the calibration of camera IRFPA sensors in the

experimental conditions, i.e. the calibration is done with the black body located as the specimen and using the dichroic mirror.

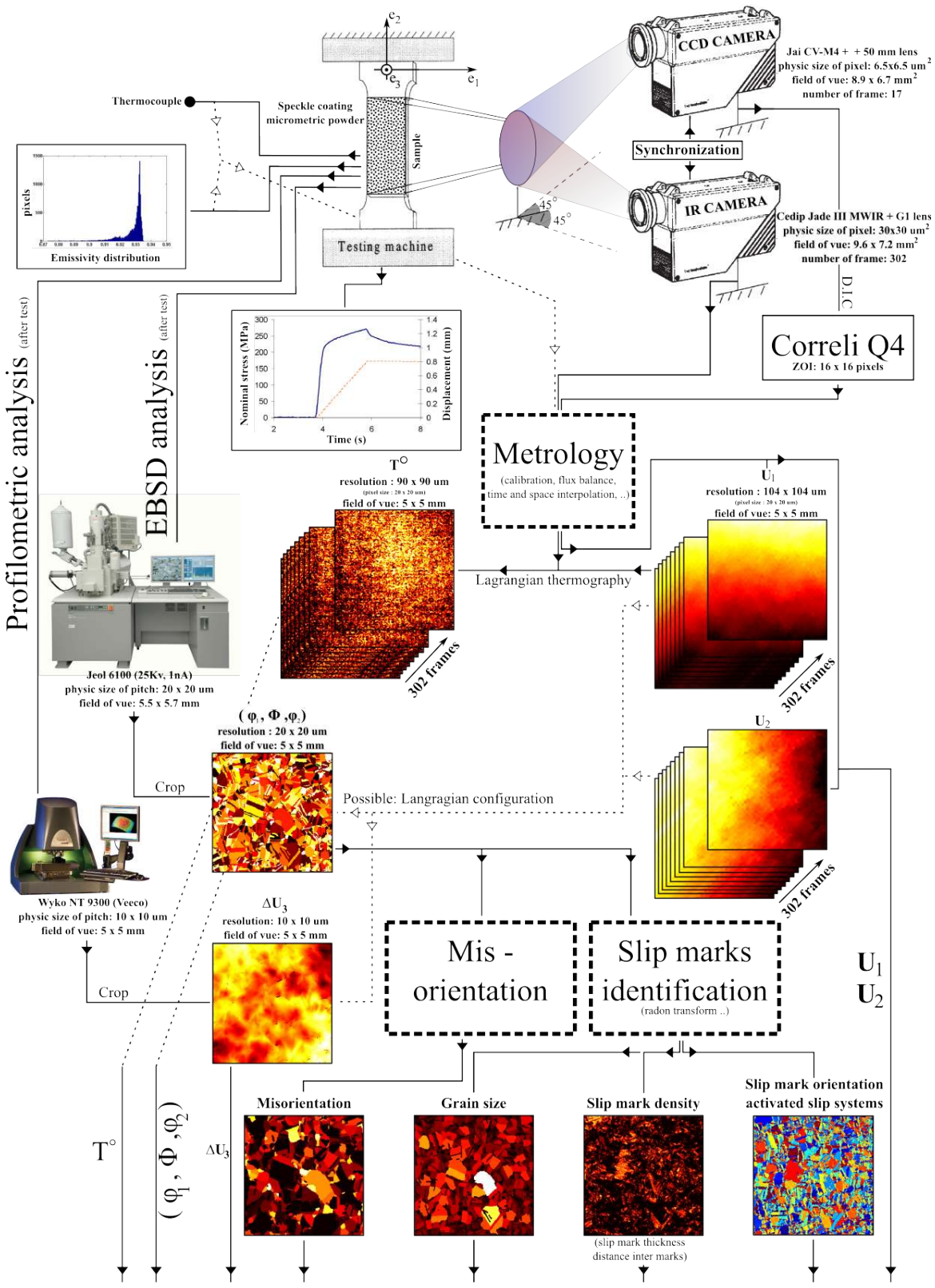

Figure 2.12: Schematic representation of the work done in this part from the raw measurements of Bodelot's works [Bodelot 2008]

Part II

Local analysis of thermomechanical couplings

Chapter 3

Fullfield projection on crystallographic base

Contents

In the previous part, an experimental strategy has been proposed in order to obtain fully coupled calibrated fields at local scale. This procedure conducts to the specific properties summarized in the table 3.1.

Here, gradients of displacements (strain fields) are calculated by a direct finite difference approximation which clearly amplifies the noise and gives a poor result as presented on figure 3.1 (b). To avoid this phenomenon, many differentiation algorithms have been developed in the literature, notably assuming larger smoothing domain than one pixel and its neighbors. However, calculating heterogeneous strain fields from a noisy displacement data over an arbitrary geometry is still a challenging topic, in particular when the size of the smoothing domain could reveal or remove the desired data. The same results are observed on temperature and flux quantities. In this case, derivative effects are amplified since flux correspond in part to $div\,(\boldsymbol{grad}\,(T))$. Thus, as derivative operators are highly sensible to spatial variation, noisy component of calibrated field do not have to be derived.

	Spatial resolution (μm)	Time resolution (Hz)	Measurement Uncertainty (mK) - (μm)
Temperature	90x90	25	30
Displacement	104x104	7	0.04

Table 3.1: Summary of measurement capabilities

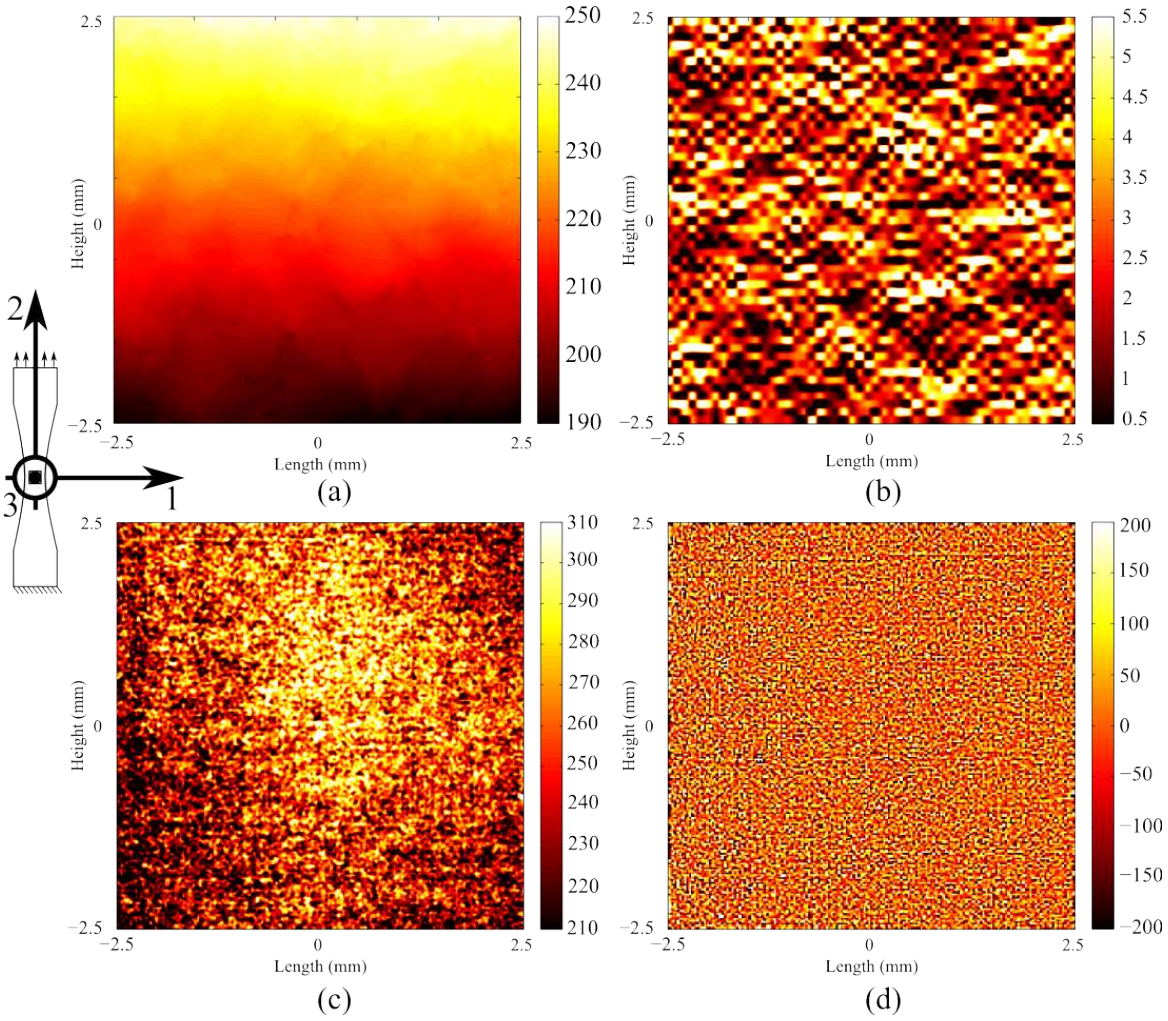

Figure 3.1: (b) Strain (%) and (d) flux (W/mm^3) expressed in the sens of finite difference from (a) axial displacement (μm) and (c) surfacic temperature (mK)

Nevertheless, the quantities of interest are often not the primal ones, i.e. displacement and temperature, but dual ones, i.e. strains and fluxes. In this way ,fields have to be derived. Figure 3.1 (a), (b), (c) and (d) present calibrated fields ((a) axial displacement, (c) temperature) and the dual ones

((b) strain (E_{22}) and (d) flux ($\Delta^2 T$)).

This chapter proposes an original method to project primal fields on a set of continuous and smooth spatio-temporal domain. This technique is based on the assumption that surface measured fields are representative of the surface microstructure, i.e. surface temperature and displacement fields are related on first order more to surface grain than to grains in depth. This is due in part to the deformation mechanisms which are much more limited in depth than on a free surface. In this way, displacement and thermal fields could be projected on the surface grain structure obtained by the EBSD. This technique will be first detailed. Then, the relevance of such projection will be studied and, finally, analytic derivative operators will be presented. Notice that the whole procedure to obtain an analytic expression of exerimental displacement, strain and thermal fields through the surface microstructure knowledge could be found in [Seghir 2012b].

3.1 A natural smoothing domain

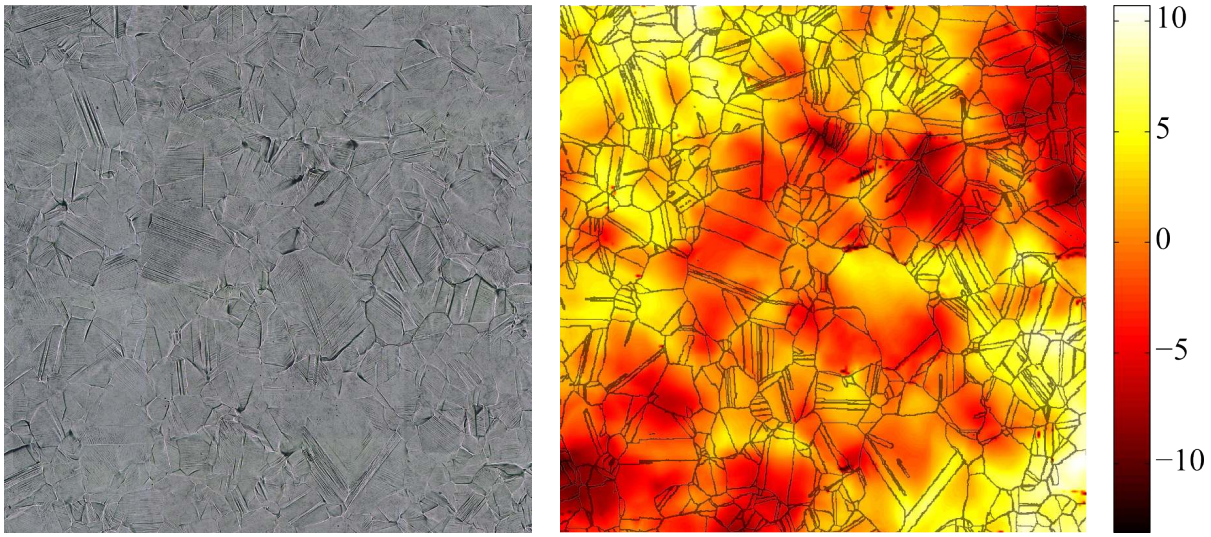

(a) (b)

Figure 3.2: (a) micrography of gage section of specimen taken after tensile test (b) profilometry (μm) taken in same conditions

Different ways could be considered to improve data treatment and, in particular, their derivation: 1) a reduction of the spatial noise by a smoothing technique in the Fourier space [Louche 1999], 2) the approximation of the strain tensor within a domain Ω thanks to a surface integral on $\partial\Omega$ [Allais 1994], where $\partial\Omega$ describes the boundaries of the domain Ω. In this particular case, when Ω is the domain occupied by a given grain of the microstructure, the surface integral on $\partial\Omega$ represents the mean strain

over this grain, 3) a smoothing operation on the displacement and temperature fields over a rectangular window by least square minimization of a high-order polynomial [Berthel 2007a]. In these different techniques, one can note that the high-frequency parts of information are also eliminated and this is particularly harmful in the case of highly heterogeneous fields.

In this work, it is proposed to use the complementary EBSD field in order to project the initial measurements on the microstructure. In fact, the EBSD data provide the boundaries of each grain within the analyzed central area. The grain (or twin) boundary network constitutes a natural partition between intra and intergranular domains and it is well known that grain and twin boundaries highly participate to the deformation accommodation processes. This aspect is comforted by the profilometric analysis which has been previously presented. Figure 3.2(b) presents the out-of-plane displacement field obtained after the test which exhibits out-of-plane displacement variations of approximately $20\mu m$ over the whole 5 mm $\times$ 5 mm central area. By comparing this field with the microstructure on figure 3.2 (a), a more precise analysis shows that the more important displacement gradients are localized around grain and twin boundaries where high strain incompatibilities are observed after the test. Then, it appears unjustified to smooth the displacement field over grain boundaries as obtained by a classical D.I.C. technique (see figure 3.3, at the top). Such approach leads to a significant underestimation of the localization processes. Here, thermal and kinematic discontinuities will be assumed at GBs, as schematically represented on the bottom of the figure 3.3.

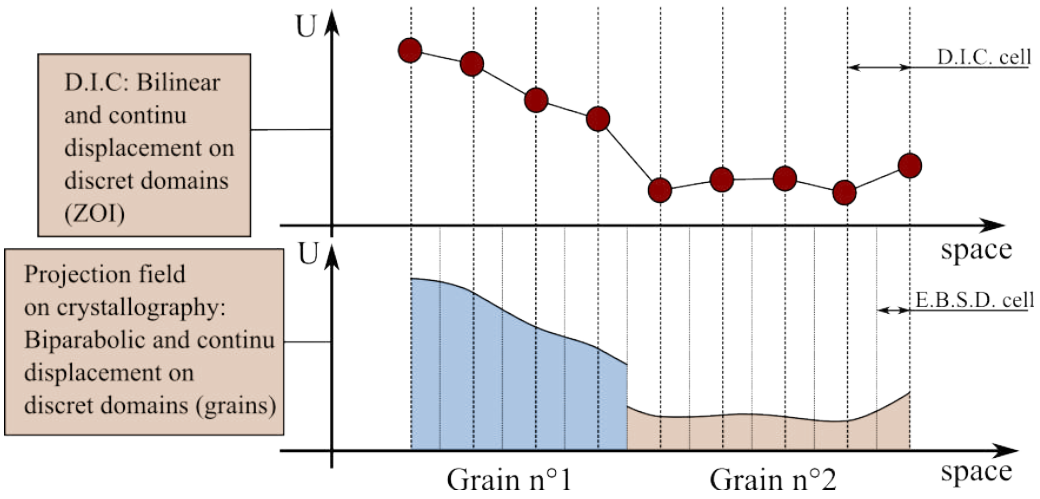

Figure 3.3: How pass from D.I.C to field associated to grain structure

3.2 A projection basis

This projection operation requires to choose a granular projection basis. This choice is based on different elements: (1) the ability to render the global shape of the observed thermomechanical fields within each grain, (2) its implementation facility within a least square minimization, i.e. a problem

with separable variables. As it can be observed on temperature field, for example, on picture 3.5 (b), extremely local phenomena occurs within each grain which are probably associated to slip bands activation. Nevertheless, as a first step, it seems relevant to only focus on a global response of each grain assuming a simplified intragranular basis, simple polynomial functions for example. In this way, figures 3.5 present projected field on polynomial functions within one specific grain. Pictures ((a) and (b)) present calibrated fields (axial displacement field on left column and temperature field on the right one), (c) and (d), projected fields on a first degree polynomial basis (see 3.3), figures 3.5 (e) and (f) present projected fields on a second degree polynomial basis but without the coupled terms XY and finally, (g) and (h) correspond to a full second degree polynomial basis (see 3.3). One can note that each field conserves the mean quantity thanks to the least square method and therefore it is consistent to perform such a mesoscopic analysis of thermomechanical fields. Nevertheless, it is important to remark that the degree of the polynomial function imposes the possible order of derivation. Consequently, it will be impossible to deal with fluxes if the order is inferior to 2. Equation 3.3 presents the general expression of the tested functions.

$$A^g = (A_0 \quad A_1 \quad A_2 \quad \dots \quad A_n) \tag{3.1}$$

$$N = \begin{pmatrix} 1 & X & Y & X^2 & Y^2 & XY & \dots & X_n \end{pmatrix} \tag{3.2}$$

$$F = \sum_{k=1}^{m} A_k^g N_k^T \tag{3.3}$$

with A^g a set of constant associated to each grain, N the shape function and F the interpolated function.

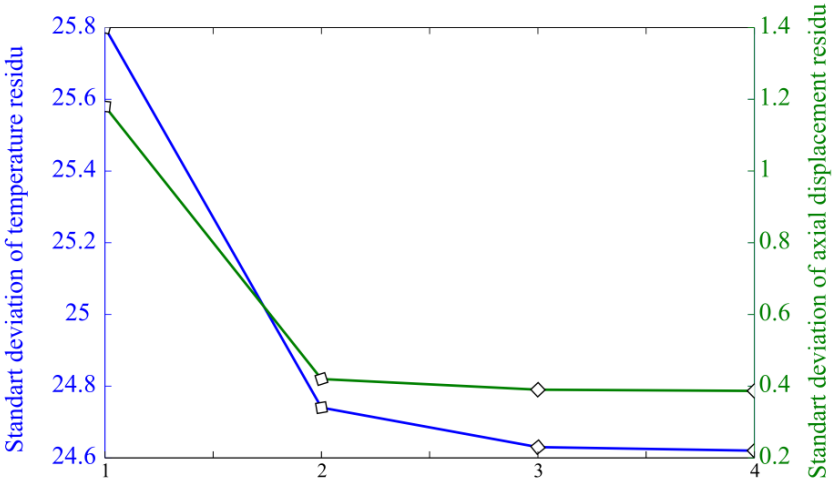

Figure 3.4: Standard deviation of residu field within the global gage section of specimen for different degre of polynomial base funtions

Figure 3.4 presents the standard deviation of the full-field residual quantities within the gauge section of the specimen for different polynomial function degrees. Step 1,2,3 and 4 represent respectively a zero degree, a first degree, a partial second and a full second degree polynomial function. One can observe on step 1 that the standard deviation of the global residual field is 1.18 μm and 25.8 mK on axial displacement and temperature fields respectively. This means that even if displacement and temperature are considered constant per grain, standard deviations do not exceed the uncertainty of measurement (0.04 μm on displacement and 30 mK on temperature). Then we can observe that higher is the degree of the function, smaller is the standard deviation. Nevertheless no significant improvement could be found over a 2nd degree polynomial function.

Then, pictures 3.5 present results on a particular grain. First, note that both experimental fields (see 3.5 (a) and (b)) exhibit very intense local gradients which are notably smoother on displacement field. This is partly due to of the measurement methods as the displacement field has already been projected on a Finite Element mesh within the D.I.C. method whereas on temperature field, each detector of IRFPA sensor matrix camera provides is own response regardless of their neighbors.

One can simply observe on the projections, that (1) the displacement field exhibit a smooth circular gradient from the right side to the left one, which is in very good agreement with the original results and (2) the temperature field exhibits a kind of large hot band from right bottom to left top which is also in relative good agreement with the original temperature localization.

Taking into account the relative simplicity of such polynomial functions and its ability, in the present case, to render displacement and thermal fields, a full second degree polynomial function appears to be the more appropriate. Then, the consequences of such a second-order polynomial projection technique are the following:

1. **Granular treatment**: grain boundaries represent a natural discontinuity network within the polycrystal: kinematic and thermal continuities are not ensure on these boundaries. For displacements, this is comforted by the profilometric analysis (see figure 3.2) and for temperature, this is justified by some studies on the Kapitza effect [Kapitza 1941]. Therefore, to take into account grain boundary discontinuities and the proposed treatment enables a better estimation of the local gradients and conducts to the definition of a projection domain in which the interpolated functions fit at best the whole set of intragranular experimental data. Moreover, intragranular quantities can be derived in a simple analytical way.

2. **Biparabolic displacement field**: in the present case, the main plastic deformation mechanism is the slip activation on particular slip system. Then, displacement fields within each grain and at each time increment are projected on a biparabolic base and, as strain is calculated from the displacement gradient, we implicitly assume here a bilinear strain field within grain. Figure 3.6 presents in a schematic way the relevance of such an hypothesis. We observe on the left side a grain which exhibits parallel slip marks on its surface, and, on the center of the picture, the schematic representation of the shear strain component of the total strain tensor on its surface.

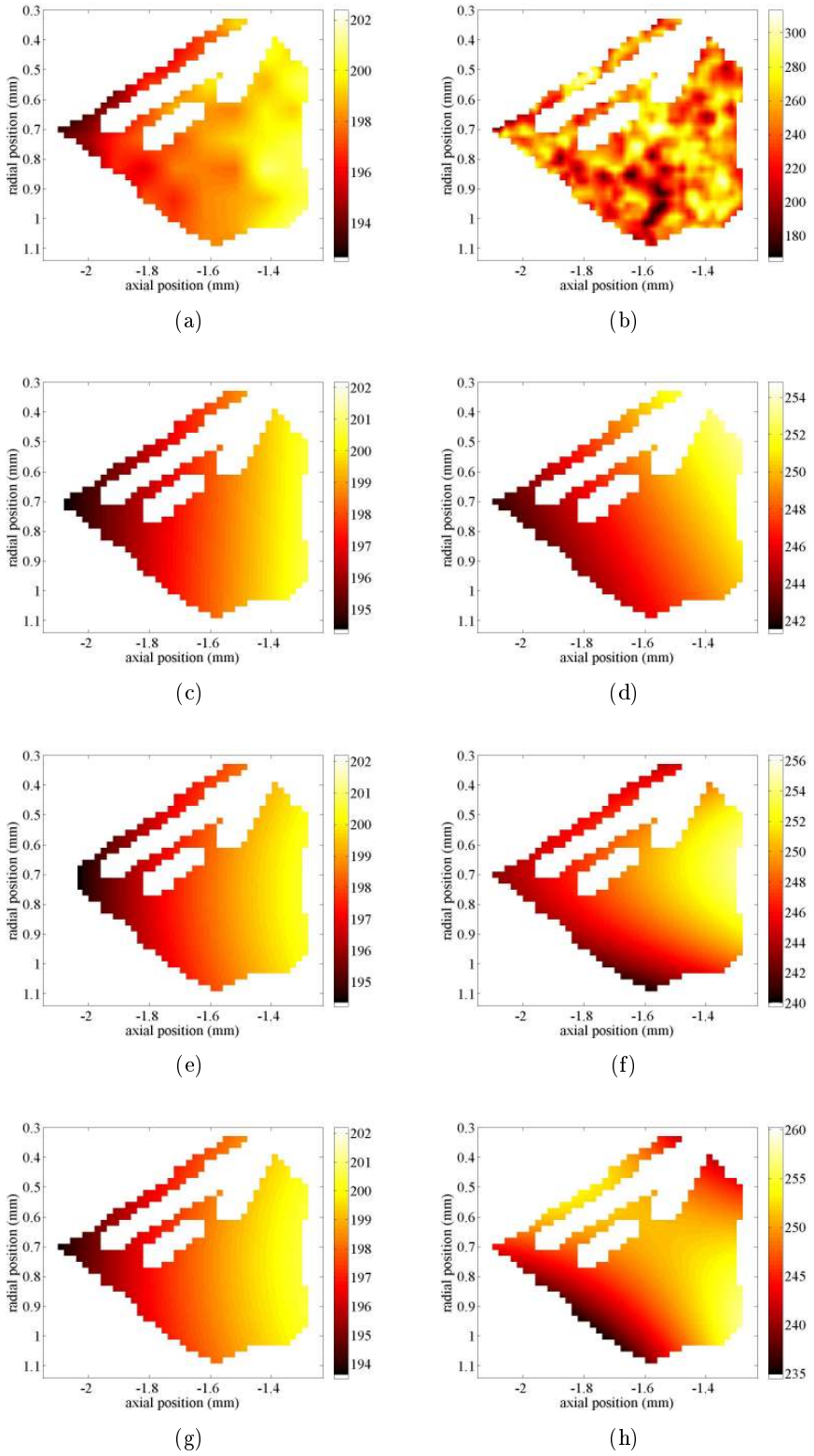

Figure 3.5: Projection of axial displacement (μm) and temperature (mK) field on polynomial bases: (a) and (b) calibrated fields, (c) and (d) order 1, (e) and (f) order 2 partial (without crossing terms), (g) and (h) order 2 full

Assuming a bilinear displacement field conducts to replace the true shear strain component by a plane whose isovalues are oriented in the slip direction as presented on the right side of the figure 3.6. As ms more than 60% of the grains of the 5 mm × 5 mm central area exhibit a single slip system activation, this assumption is relatively consistent even if it certainly conducts to more important errors where multiple slip systems activation is observed. The knowledge of the analytic expression of the in-plane displacement field $\underline{u}(x, y)$ within each grain allows an analytic derivation and the local estimation of each plane component of strain tensor, i.e. ε_{11}, ε_{22}, ε_{12} as well as the in-plane component of the spin tensor w_{12} which can be determined by with $\mathbf{F} = \frac{1}{2}\left(\text{grad}(\underline{u}) + {}^{T}\text{grad}(\underline{u})\right)$, $\varepsilon = \frac{1}{2}\left(\mathbf{F} + {}^{T}\mathbf{F}\right)$ and $\mathbf{w} = \frac{1}{2}\left(\mathbf{F} - {}^{T}\mathbf{F}\right)$. Moreover, this assumption leads also to a significant variables reduction: 6 parameters per grain at each instant which represents 12000 variables per field instead of 62500.

3. **Biparabolic thermal field**: as conductive fluxes are calculated from the temperature Laplacian, uniform conductive exchanges within grain at each instant are implicitly assumed through this hypothesis. As every local heat sources initiated within the grain are quickly uniform due to conductive phenomenon, it is therefore assumed that conductive exchanges are instantaneously uniform within the grain and on its boundaries. Then, as for displacement fields, thermal field can be analytically derived.

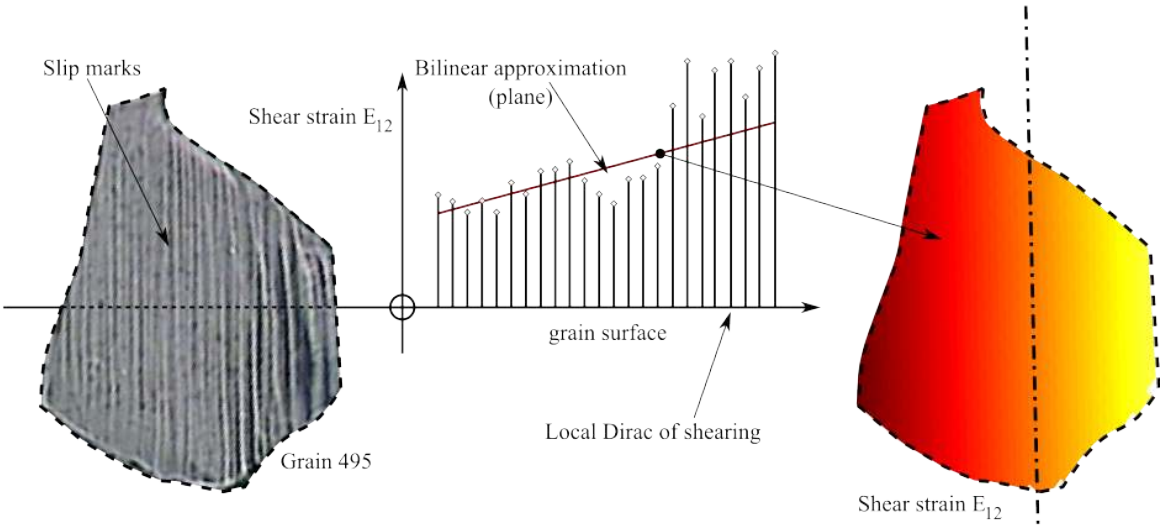

Figure 3.6: schematic interpretation of bilinear strain tensor whitin grain

It has to be pointed out that no data is lost in this projection procedure. The whole decomposition is additive. Residual fields between initial fields and projected one are complementary and can be separately analyzed (see section 3.4).

3.3 Least-squares method

In order to determine the polynomial parameters set for all the analyzed zone, a least-square method is used and, with the same previous notations (see equation 3.3), one could express this problem as:

$$\begin{aligned} E_{A^g} &= \min_{A^g} \sum_{i=1}^{n_g} \left[F(x_i, y_i) - Z(x_i, y_i)\right]^2 \\ &\text{or} \\ E_{A^g} &= \min_{A^g} \sum_{i=1}^{n_g} \left[\sum_{k=1}^{m} \left(A_k^g N_{ik}^T\right) - Z_i\right]^2 \end{aligned} \tag{3.4}$$

with Z_i the measured quantity at the position (x_i, y_i). Note that the least-squares minimization is performed within each grain (A^g parameters vector). For each coordinates vector (x_i, y_i), i range from 1 to n_g with n_g the number of element within the considered grain g and k represents the number of parameter to identify; $m = 6$ in the case of biparabolic function. By differentiation, one obtains:

$$\frac{\partial E}{\partial A^g} = 0 \tag{3.5}$$

$$2\sum_{i=1}^{n_g}\sum_{k=1}^{6}\left[\left(A_k^g N_{ik}^T - Z_i\right) N_{ik}\right] = 0 \tag{3.6}$$

which leads to a system of 6 linear equations in A_k^g which could easily be solved:

$$\sum_{i=1}^{n_g} \begin{bmatrix} 1 & x_i & y_i & x_i^2 & y_i^2 & x_i y_i \\ x_i & x_i^2 & x_i y_i & x_i^3 & x_i y_i^2 & x_i^2 y_i \\ y_i & y_i x_i & y_i^2 & y_i x_i^2 & y_i^3 & x_i y_i^2 \\ x_i^2 & x_i^3 & x_i^2 y_i & x_i^4 & x_i^2 y_i^2 & x_i^3 y_i \\ y_i^2 & y_i^2 x_i & y_i^3 & y_i^2 x_i^2 & y_i^4 & x_i y_i^3 \\ x_i y_i & x_i^2 y_i & x_i y_i^2 & x_i^3 y_i & x_i y_i^3 & x_i^2 y_i^2 \end{bmatrix} \begin{bmatrix} A_0^g \\ A_1^g \\ A_2^g \\ A_3^g \\ A_4^g \\ A_5^g \end{bmatrix} = \sum_{i=1}^{n_g} \begin{bmatrix} Z_i \\ x_i Z_i \\ y_i Z_i \\ x_i^2 Z_i \\ y_i^2 Z_i \\ x_i y_i Z_i \end{bmatrix} \tag{3.7}$$

The resolution provides the least square based-solution in every point (x_i, y_i) within the grain g, noted: $Z_i = A_0^g + A_1^g x_i + A_2^g y_i + A_3^g x_i^2 + A_4^g y_i^2 + A_5^g x_i y_i$.
The least square problem is solved in all the grains corresponding to the central 5 mm x 5mm area and at each time increment. Then, the whole thermomechanical scene projected on the microstructure as well as the whole residual thermomechanical one are obtained.

3.4 Field decomposition

In this section, projected field as well as residual ones are presented and discussed.

3.4.1 Displacement fields

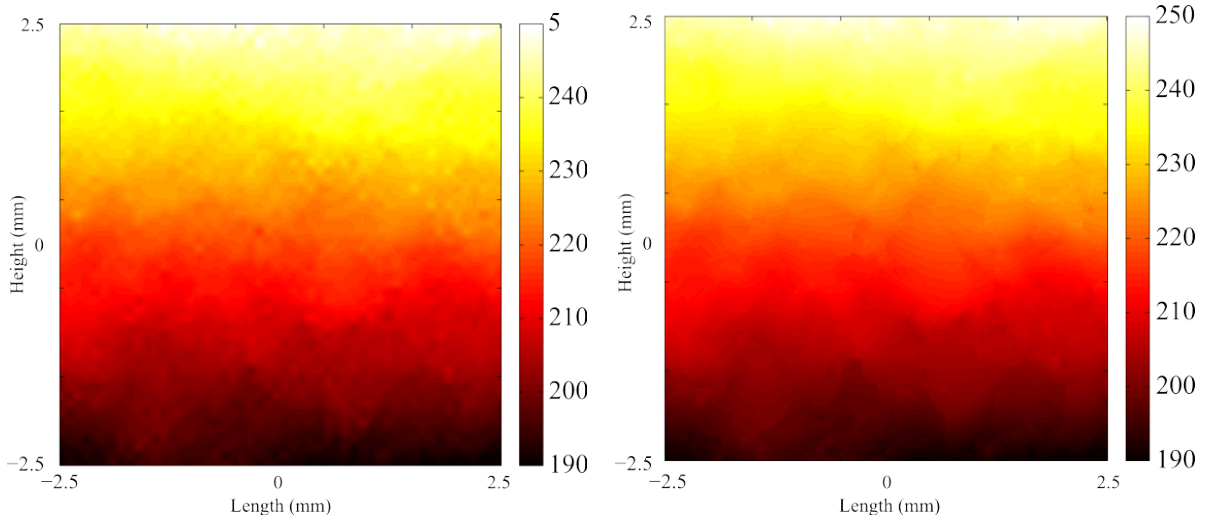

(a) (b)

Figure 3.7: Comparison between (a) original axial displacement field and (b) projected one (μm) both at 250 MPa of nominal stress

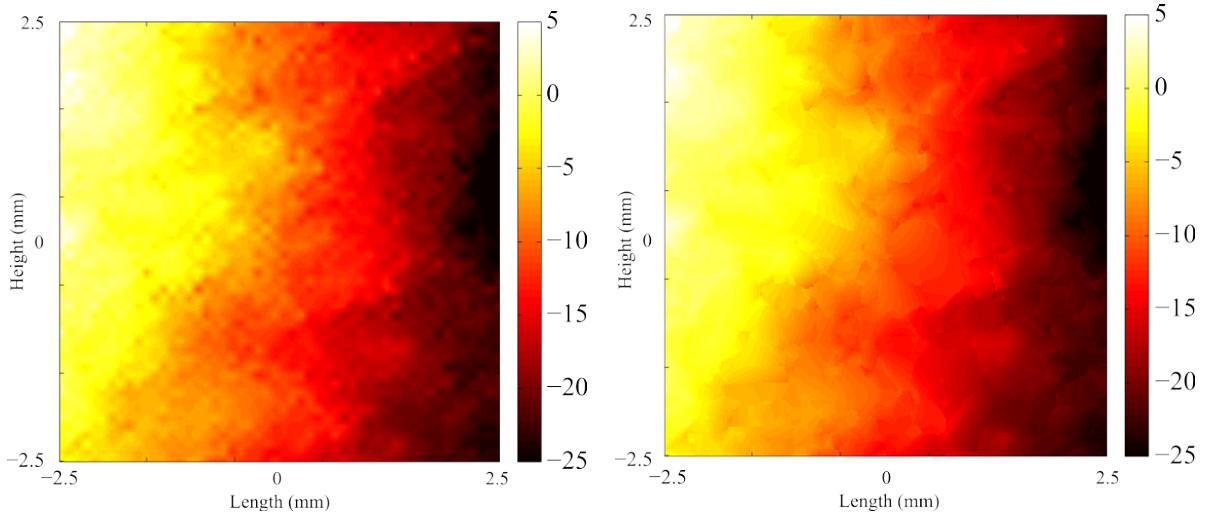

(a) (b)

Figure 3.8: Comparison between (a) original transversal displacement field and (b) projected one (μm) both at 250 MPa of nominal stress

Figure 3.7 and 3.8 presents a comparison between the original displacement field (a) and the projected one (b) at a 250 MPa nominal stress, respectively the axial one and the transverse one. One could observe that the projected fields are smoother than the original ones and that original the local displacement gradients are actually associated to the microstructure, particularly on the transverse displacement field. This is due on the one hand to the intensity of displacement which is 10 times less significant within transverse field and, on the other hand to the loading direction. Indeed, as the test is a uniaxial monotonic tensile test, the displacement is quite linearly progressive in the loading direction, whereas it is much more leaded by the heterogeneous microstructure in the transverse direction.

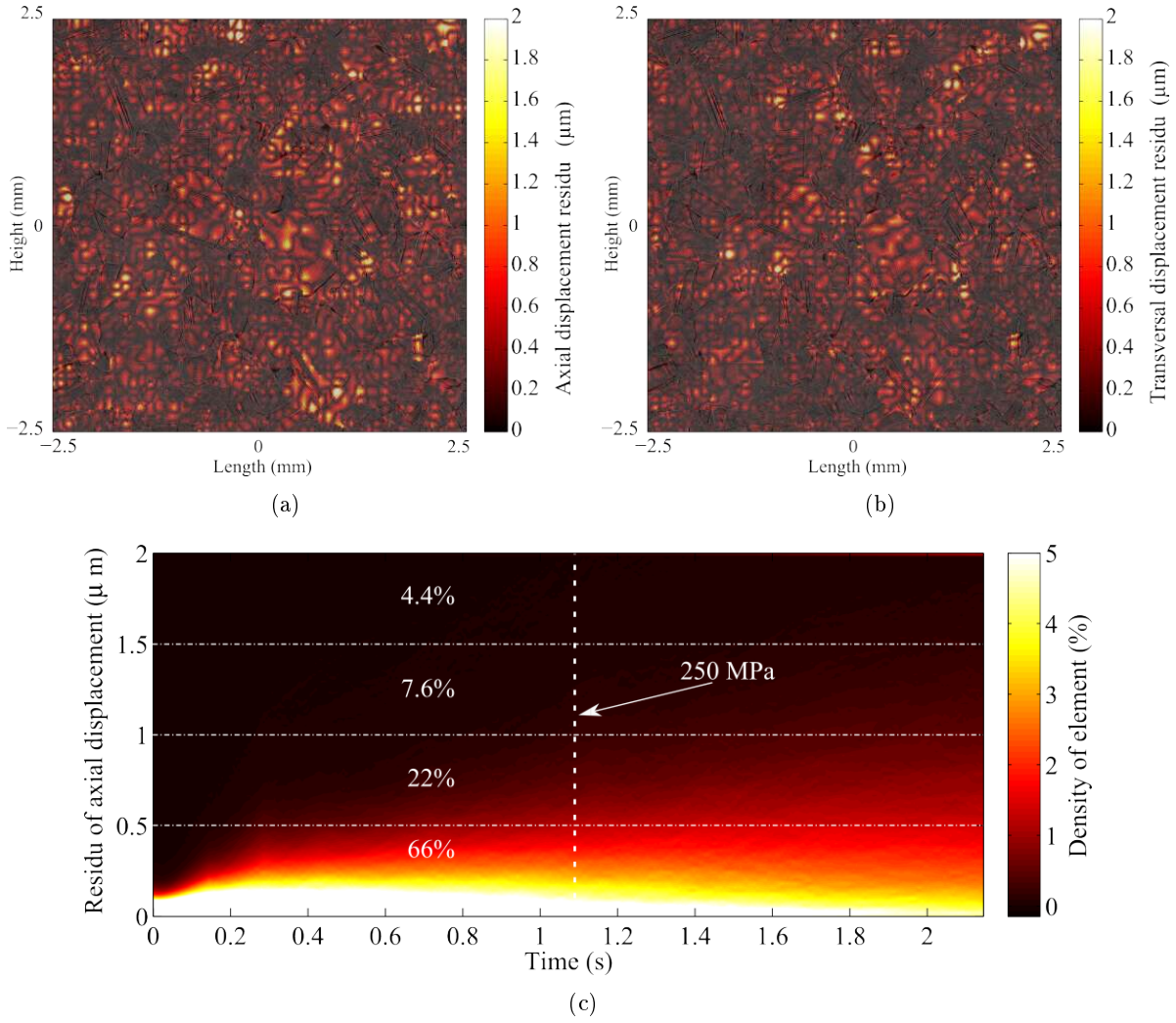

Figure 3.9: Absolute value of residual field of displacement (μm) (a) axial direction (U), (b) transverse one (V) both at 250 MPa of nominal stress and (c) axial direction during time

Figure 3.9 (a), (b) present the absolute residual displacement field for a 250 MPa nominal stress, respectively in the loading direction and in the transversal one. One could observe on figure 3.9 (a) and (b) the superimposition of the surface micrography and the residual displacement field: the highest residual levels are not located on grain boundaries. Figure 3.9 (c) presents the distribution of the absolute residual axial displacement at each time increment. As previously pointed out in section 3.2, one could observe that the residual values do not exceed $2\mu m$ and for more than 95% of the elements, the residual value is lower than the measurement uncertainty. Note on figure 3.9(c) that, on the one hand, higher is the loading higher is the residual values, and on the other hand, the displacement residual values describe a Gaussian distribution whose standard deviation do not exceed $0.5\mu m$. In order to understand the origin of the highest residual displacements, some particular grains are analysed in figure 3.10.

Even if the figure 3.10 shows that it is not simple to correlate residual displacement values and deformation mechanisms developed within grains, some highest residual spots could be correlated with slip system interaction in intragranular domain as well as in vicinity of grain boundary which can particularly observed within grain (b) on picture 3.10. This millimeter grain exhibits two slip systems with some specific interaction areas circled by white dotted lines. In theses regions, the residual values are more important compared to the rest of the grain. This is also the case on both sides of each slip marks set (white dotted box) where very high material discontinuities can be observed after the test. Then, it seems that this residual displacement field is not enough significant to affect to relevance of the projected displacement field in each direction, and no direct link between plasticity mechanisms and this field can be draw except in very specific cases.

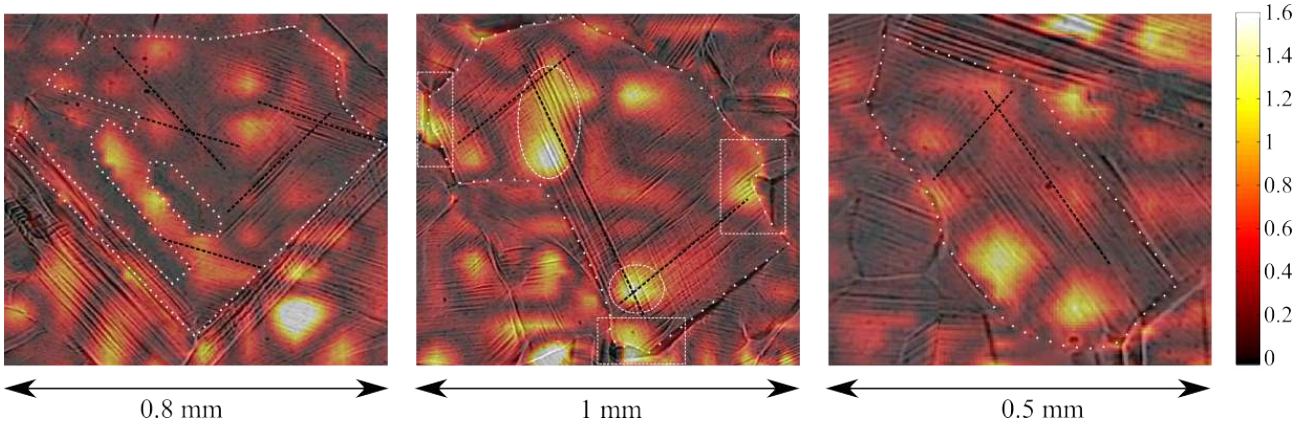

Figure 3.10: Superimposition of absolute value of axial displacement residual field (μm) within different grains at 250 MPa of nominal stress and micrography

3.4.2 Thermal fields

Figure 3.11 (a) and (b) present the original temperature field and the projected one at a 250 MPa nominal stress.

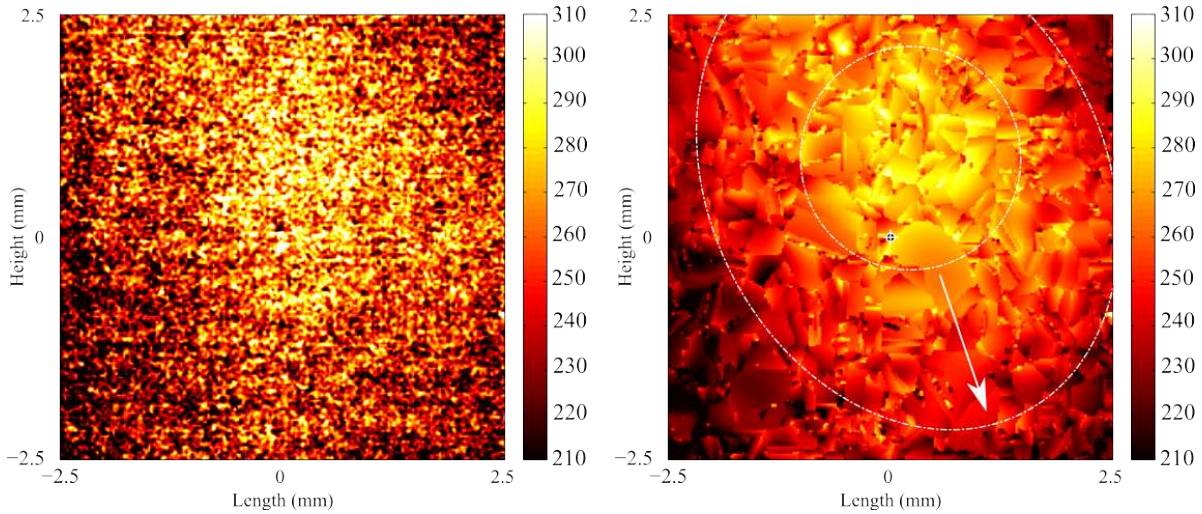

Figure 3.11: Comparison between (a) original temperature field and (b) projected one (mK) both at 250 MPa of nominal stress

One can clearly observe a smoothed field on figure 3.11 (b) where the contribution of each grain to the global field can now be identified and measured. It exhibits a 100 mK thermal gradient from a specific area to the gauge section borders which clearly reflects a conductive phenomenon from the center circle to the specimen border. Note that the hot region is not centered within the gauge section which is certainly the sign of a thermal localization due to the microstructure and not tp the specimen geometry. One can also underline some thermal grain discontinuities, which are very clear on some grain boundaries, notably around the big center one.

Figure 3.12 (a) and (b) present full scale temperature residual values and over measurement uncertainty residual values respectively for a 250 MPa nominal stress. 3.12 (c) presents the distribution of absolute residual temperature at each time increment. One could observe on 3.12 (c) that the residual values range from 0 to 100 mK during the test and that about 75% of elements exhibit residual values lower than the measurement uncertainty. Note that the standard deviation on temperature residual values is almost constant (24mK), i.e. no link between the loading level and the residual field. Figure 3.12(a) shows a randomly distributed residual field where the major part is inferior to measurement uncertainty as shown on figure 3.12(b).

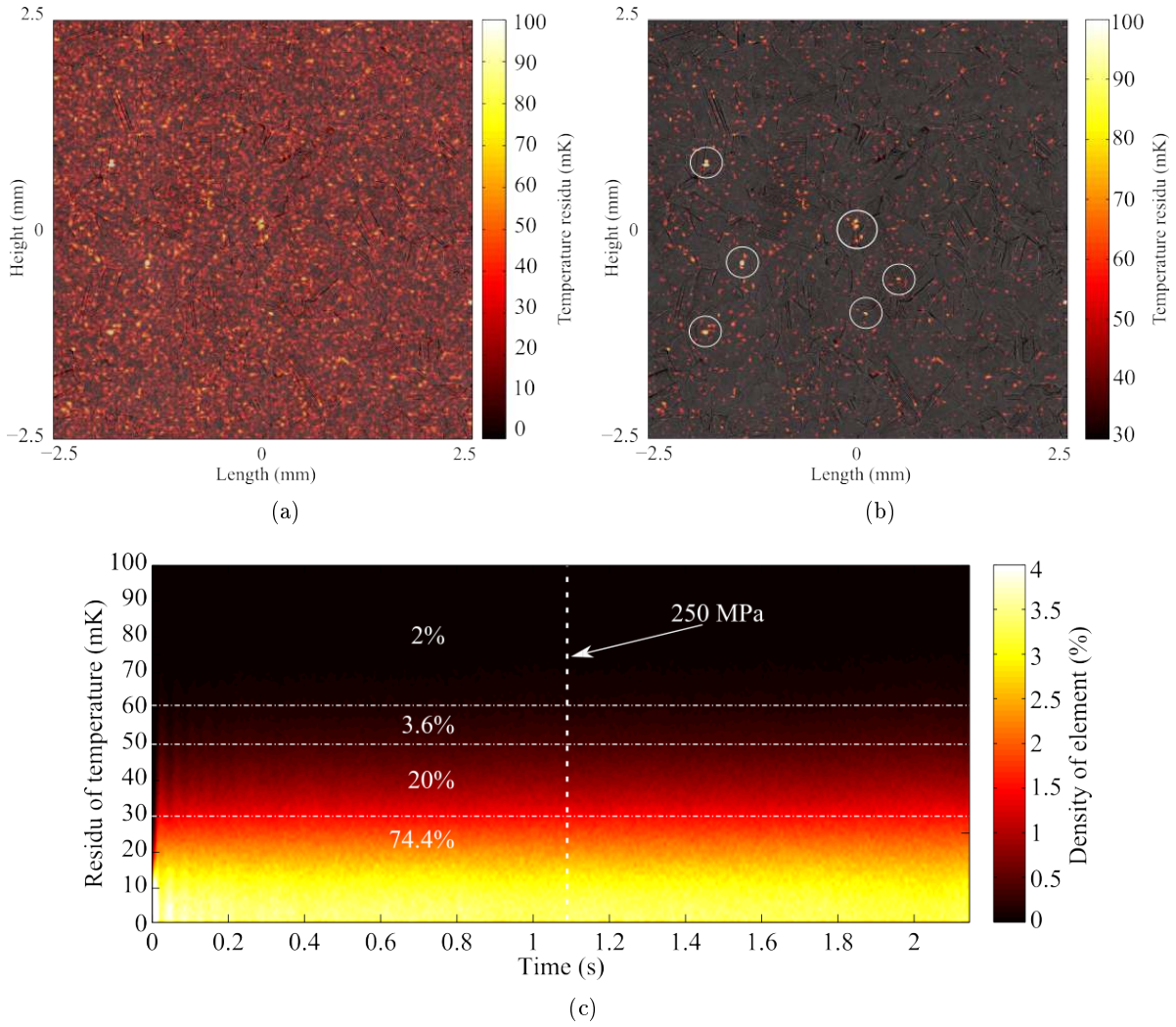

Figure 3.12: Absolute value of residual field of temperature (mK) (a) full colormap (U), (b) over measurement incertanty both at 250 MPa of nominal stress and (b) full during time

No link seems to exist between the microstructure and the hot residual spots. This residual field is certainly associated to coating effects (cf. 3.13) which are not entirely removed during the calibration method. Then, the projection technique on biparabolic basis per grain do not affect the field relevance and, on contrary, it seems to make the thermal scene more realistic removing measurement artifacts.

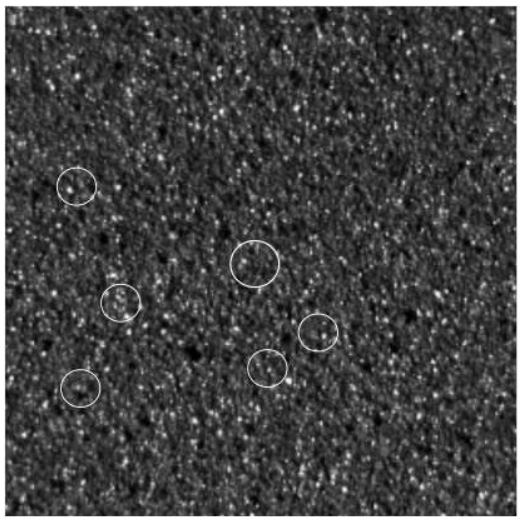

Figure 3.13: Coating

3.5 Differentiation operators

3.5.1 Mechanical operators

Considering a material point $M(x_i, y_i)$ within a specific grain g and its parameter set A^g at a fixed time t, the analytic derivative form of a function Z_i is expressed as follows:

$$\begin{bmatrix} \dfrac{\partial Z_i}{\partial x} \\ \dfrac{\partial Z_i}{\partial y} \\ \dfrac{\partial^2 Z_i}{\partial x^2} \\ \dfrac{\partial^2 Z_i}{\partial y^2} \end{bmatrix}_t = \begin{bmatrix} A_1^g + 2A_3^g x_i + A_5^g y_i \\ A_2^g + 2A_4^g y_i + A_5^g x_i \\ 2A_3^g \\ 2A_4^g \end{bmatrix}_t \tag{3.8}$$

Thne, the deformation gradient tensor $\mathbf{F}$ in every material point $M(x_i, y_i)$can be simply derived from the axial and transversal analytic displacement gradients:

$$\begin{pmatrix} F_{11} & F_{12} & F_{13} \\ F_{21} & F_{22} & F_{23} \\ F_{31} & F_{32} & F_{33} \end{pmatrix}_t = \begin{bmatrix} \dfrac{\partial U_i}{\partial x} & \dfrac{\partial U_i}{\partial y} & * \\ \dfrac{\partial V_i}{\partial x} & \dfrac{\partial V_i}{\partial y} & * \\ * & * & * \end{bmatrix}_t + \mathbf{I} \tag{3.9}$$

with U_i and V_i the axial and transversal displacement analytic expressions at $M(x_i, y_i)$ respectively. Note that the knowledge of in-plane displacements only permits to directly recover plane components of the deformation gradient tensor.

Within the small strain decomposition of the deformation gradient, $\mathbf{F}$ is written as:

$$\mathbf{F} = I + \varepsilon + \omega \tag{3.10}$$

with $\boldsymbol{u}(U, V)$ the displacement vector, ε, the small intragranular strain tensor (symmetric part of $\mathbf{grad}(\boldsymbol{u})$) and ω, the small intragranular rotation tensor (antisymmetric part of $\mathbf{grad}(\boldsymbol{u})$):

$$\begin{pmatrix} \varepsilon_{11} & \varepsilon_{12} & \varepsilon_{13} \\ \varepsilon_{21} & \varepsilon_{22} & \varepsilon_{23} \\ \varepsilon_{31} & \varepsilon_{32} & \varepsilon_{33} \end{pmatrix}_t = \frac{1}{2} \begin{bmatrix} 2\dfrac{\partial U_i}{\partial x} & \dfrac{\partial U_i}{\partial y} + \dfrac{\partial V_i}{\partial x} & * \\ \dfrac{\partial V_i}{\partial x} + \dfrac{\partial U_i}{\partial y} & 2\dfrac{\partial V_i}{\partial y} & * \\ * & * & * \end{bmatrix}_t \tag{3.11}$$

$$\begin{pmatrix} \omega_{11} & \omega_{12} & \omega_{13} \\ \omega_{21} & \omega_{22} & \omega_{23} \\ \omega_{31} & \omega_{32} & \omega_{33} \end{pmatrix}_t = \frac{1}{2} \begin{bmatrix} 0 & \dfrac{\partial U_i}{\partial y} - \dfrac{\partial V_i}{\partial x} & * \\ \dfrac{\partial V_i}{\partial x} - \dfrac{\partial U_i}{\partial y} & 0 & * \\ * & * & 0 \end{bmatrix}_t \tag{3.12}$$

To illustrate these derivative analytic operators, the figure 3.14 presents the comparison between ε_{22}, i.e. in the loading direction, calculated from (a) a classical finite difference scheme and (b) by analytic derivation.

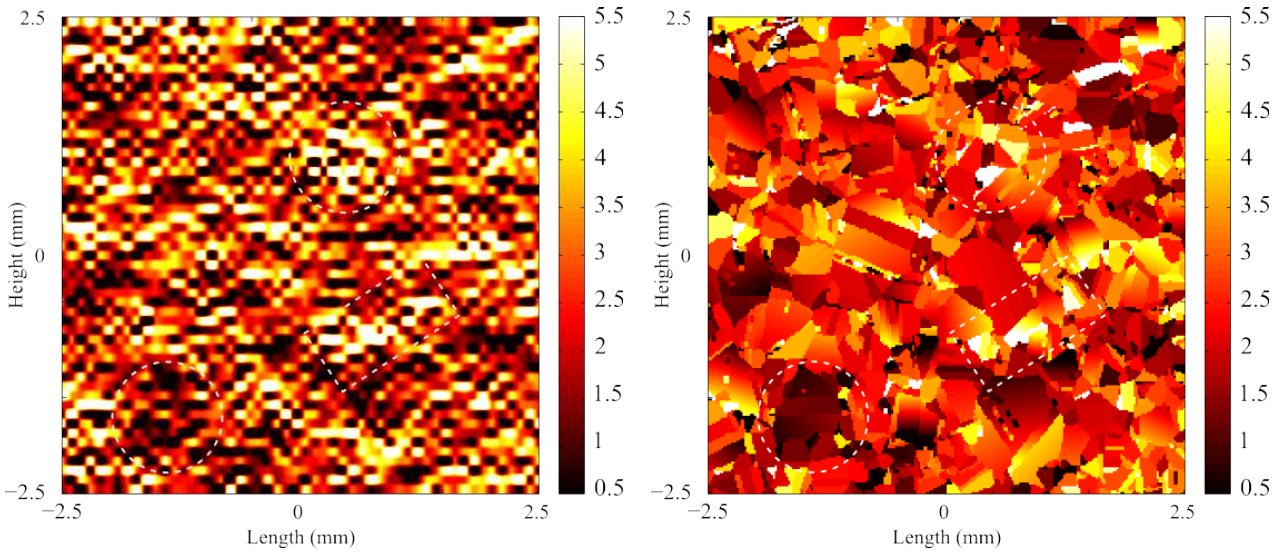

Figure 3.14: Comparison between (a) strain field extract from finite difference method and (b) analytic one (%) both at the end of tensile test (270 MPa of nominal stress)

Obviously, the analytic derivation does not depend any more of the element size contrary to the figure 3.14(a). Concerning the strain distributions, one could precise that in both cases, mean values are identical (2.5% at this time) which is naturally due to the least-square method. However, the standard deviation is significantly reduced in the case of the analytic derivation: 1.15% compared to 1.9% with a finite difference scheme. It could be explained on the one hand by local variations of displacement which have been smoothed and on the other hand, by the fact that analytic derivations are an intragranular one. Indeed, no derivation is performed at grain boundaries whereas finite differences are applied everywhere.One could also underline that the analytic strain field allows us to associate each deformation to its grain and consequently to its crystallographic properties which is quite impossible with the finite difference derivation. Nevertheless, note that similar strain localization can be observed in both fields (white boxed and circled domains).

3.5.2 Thermal operators

The heat flux density vector $\boldsymbol{J}_Q^i$ considered at a point $M(x_i, y_i, z_i)$ and crossing a surface S could be expressed from the Fourier's law as:

$$\boldsymbol{J}_Q^i = -k.\boldsymbol{grad}\,(T) \tag{3.13}$$

with T the absolute temperature and k the material thermal conductivity expressed in $W.m^{-1}.K^{-1}$. Considering now an infinitesimal cubic volume of material crossed in its three direction $(\boldsymbol{x}, \boldsymbol{y}, \boldsymbol{z})$ by the

heat flux density vector $\boldsymbol{J}_Q^i = (J_{Q_x}^i, J_{Q_y}^i, J_{Q_z}^i)$, the local form of the heat flux crossing this elementary volume is:

$$\Phi_i^{ex} = \left(\frac{\partial J_{Q_x}^i}{\partial x} + \frac{\partial J_{Q_y}^i}{\partial y} + \frac{\partial J_{Q_z}^i}{\partial z} \right) \tag{3.14}$$

$$= div\left(-k.\boldsymbol{grad}\left(T\right)\right) \tag{3.15}$$

Finally, considering conductivity as a material constant, the local expression of heat conductive exchanges is:

$$\Phi_i^{ex} = -k\Delta T \tag{3.16}$$

Its in-plane form is the following:

$$\Phi_i^{ex}|_t = -k \left(\left. \frac{\partial^2 T_i}{\partial x^2} \right|_t + \left. \frac{\partial^2 T_i}{\partial y^2} \right|_t \right) \tag{3.17}$$

$$= -2k \left(A_3^g + A_4^g \right)|_t \tag{3.18}$$

Figure 3.15 presents the comparison between the in-plane temperature Laplacian estimated from (a) a finite difference scheme and (b) the analytic expression which conducts to constant values per grain.

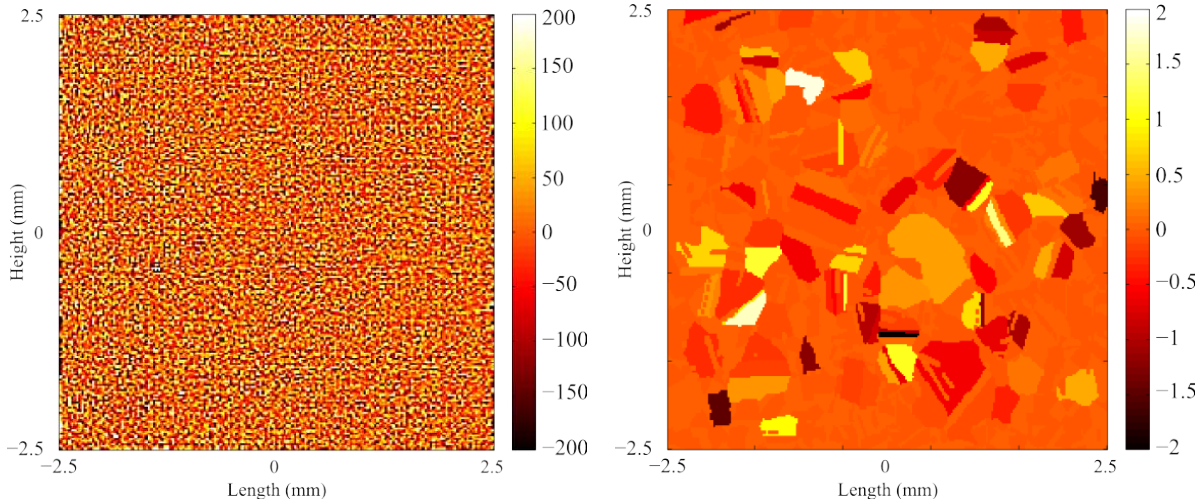

Figure 3.15: Comparison between (a) $\Delta^2 T$ field extract from finite difference method and (b) analytic one (%) both at the end of tensile test (270 MPa of nominal stress)

No link could be observed between 3.15 (a) and (b). The reason is that figure 3.15 (a) is actually the addition of two fields: the 2^{nd} derivation of a smooth temperature field presented on picture 3.11

(b) and the 2^{nd} derivation of a noisy speckle field presented on picture 3.12 (b) whose magnitude is 100 times higher to the first one.

Note (1) that figure 3.15(b) exhibits very high localization in some grains compared to the rest of the microstructure which exhibits a value close to 0 (adiabatic conditions) and (2) that no link has been found between grain shape or grain size and analytic expression of the Laplacian. Consequently the shape and the size of the projection domain do not affect, in appearance, the Laplacian magnitude.

3.5.3 Time derivation

As precise in section 3.3, no spatio-temporal projection has been performed on data set. Here, displacement and temperature time derivation will be performed using a classical finite difference scheme between instants t_{n-1} and t_n. Consequently, the heat production flux evaluated at time t takes the following form:

$$\Phi_i^{pr}|_t = \rho C \left.\frac{\partial T}{\partial t}\right|_t \tag{3.19}$$

$$= \rho C \frac{T_i|_{t_n} - T_i|_{t_{n-1}}}{t_n - t_{n-1}}$$

$$= \rho C \frac{\left[{}^{n}_{n-1}\Delta A_0^g\right] + \left[{}^{n}_{n-1}\Delta A_1^g\right] x_i + \left[{}^{n}_{n-1}\Delta A_2^g\right] y_i + \left[{}^{n}_{n-1}\Delta A_3^g\right] x_i^2 + \left[{}^{n}_{n-1}\Delta A_4^g\right] y_i^2 + \left[{}^{n}_{n-1}\Delta A_5^g\right] x_i y_i}{t_n - t_{n-1}} \tag{3.20}$$

Finally, the analytic in-plane form of the total heat flux at point $M(x_i, y_i, z_i)$ and time t is:

$$\Phi_i|_t = \Phi_i^{pr}|_t + \Phi_i^{ex}|_t \tag{3.21}$$

3.5.4 Inter-granular operators

As there is no asumptions on the continuity between two grains, there is no way to have an analytic derivation on the grain boundary. Nevertheless, intergranular gap of displacement or temperature can be calculated following the method introduced below:

1. Derive the analytical fields (displacement and temperature) using finite difference. On such analytic fields a finite differentiation must be exactly the same than the analytic one exept for the pixel where neighbours are not in the same grain.

2. Derive the analytical fields, only in intragranular domain, using the analytical expressions.

3. Substracting both fields one obtains fields equal to zeros in intragranular domains and reveals the gap of displacement and temperature along each grain contour.

So by this simple procedure it is possible to evaluate during test, displacement and temperature gap at grain boundaries. Figure 3.16 presents the (a) "Inter-granular" estimation of displacement gap

(ΔU_{inter}) as well as (a) "Inter-granular" estimation of temperature gap (ΔT_{inter}) at the end of the test and figure 3.17 presents the micrography of surface.

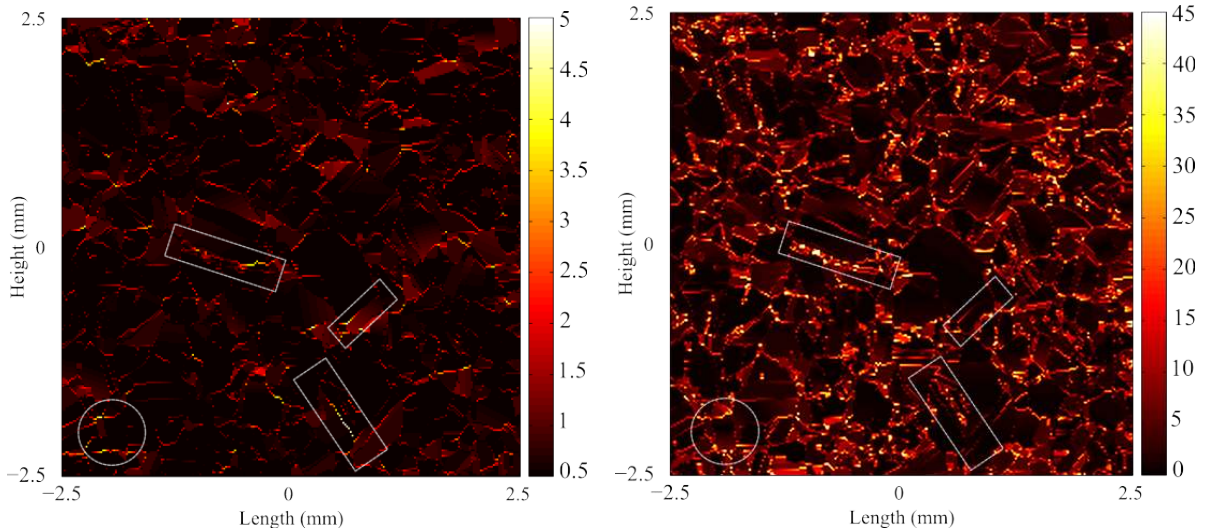

(a) (b)

Figure 3.16: (a) "Inter-granular" gap of displacement (μm) and (b) gap of temperature (mK) both at the end of tensile test (270 MPa of nominal stress)

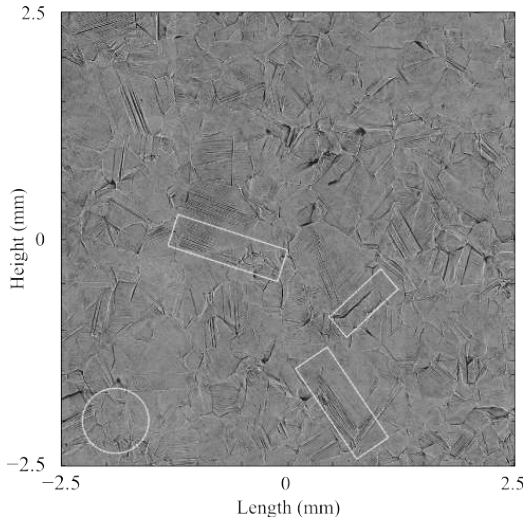

Figure 3.17: micrography of surface after test.

Fields underline some grain boundaries with high magnitude. For displacement field, it reveals grains boundaries where a gap of displacement exist and the magnitude of this gap. It ranges from 0 within grain to 5 μm in white boxed regions. For temperature field, it reveals grain boundaries where the temperature is relatively different from one grain to its neighbour and consequently the level of heat transfert through the grain boundary. It ranges from 0 to 50 mK. Obvisouly levels are very low and probably dependant on the projection method, consequently any interpretation must be done carefully. Neverthless notice that some regions (white boxed ones) reveal an appearante good correlation between micrography of surface, gap of displacement revealed by D.I.C. method then projection, and gap of temperature revealed by Lagrangian thermography then projection.

3.6 Conclusion

In this chapter an original way has been introduced to interpret local field measurements within heterogeneous materials. We consider within mesoscopic analyses that it is more relevant to focus on the smoothing domain than on the complexity of the smoothing function form. Thus, we consider in pratical way that the material could be partitionned in a set of domains in which the physic is basic, i.e. which doesn't required many assumptions or complex mathematical form to fit it. Based on this strong conviction, fullfield measurements are projected on the natural network of polycrystals: the grain structure.
We have shown that a biparabolic base projection per grain could be usefull for kinematic as well as thermal fields. It allows consequently an additive decomposition of thermal and kinematic field in a residu field and projected one.
We have shown that more than 95% and 75% of field elements exhibit a residu which is lower to measurement uncertainty, in displacement and temperature field respectively. Consequently, one could expect that almost the whole physic is conserved. It has also been proved that no specific residu localization exists at grain boundaries, meaning that grain boundary "freedom" doesn't affect the field relevance. It reveals moreover the relevance of such an assumption.
Next, it has been observed that thermal residu is constant during the test and exhibits a speckle aspect confirming that this residu comes from residual unremoved coating effect in calibration method. In opposition, displacement residu exhibits some spots within grains, and it has been observed that its standard deviation increases as the displacement. It seems to evidence any correlations between them, nevertheless no concrete link has been underlined between plasticity development, i.e. development of singularities within intragranular displacement field, and residu from biparabolic projection assumptions. It has been proved consequently the relevance of such projected field as regard of its neglectable deviation from original calibrated fields. In a second part, analytic forms of small strain, small rotation, as well as plane thermal laplacian have been introduced and the great interest of such analytic field in understanding the plastic thermomechanical mechanisms has been underlined. Finally, we have shown that intergranular gap of displacement and temperature could also be estimated, and require to be carefully analysed before any interpretation.

We will use such denoised fields, in the following chapter, to understand local thermomechanical couplings which occur within a polycrystalline metallic material while it undergoes macroscopic monotonic tensile loading. All the experimental fields in our possession and the schematic representation of work done in this part are shown in figure 3.18.

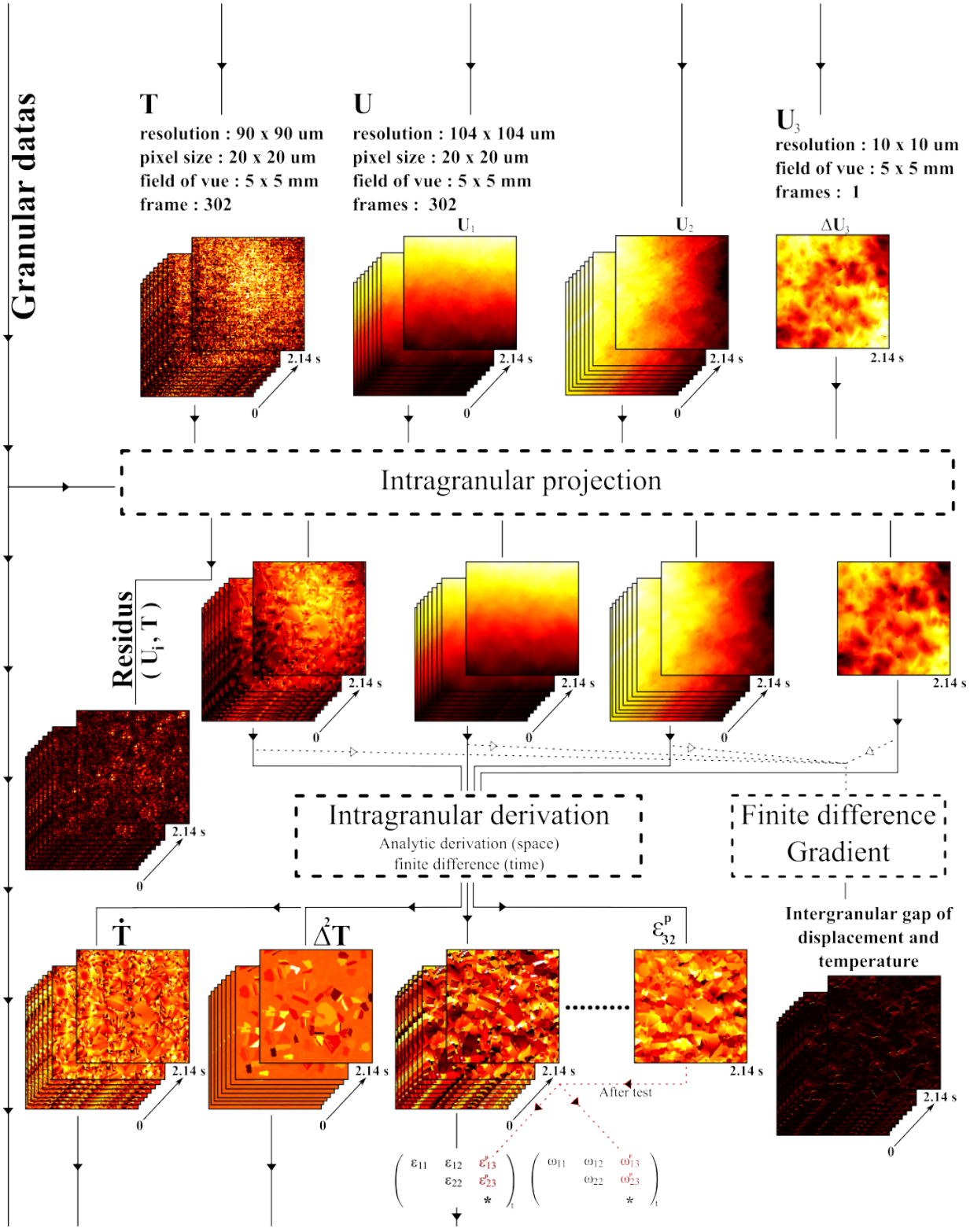

Figure 3.18: Schematic representation of the available multi-fields

Chapter 4

Experimental analysis of thermomechanical couplings

Contents

In the previous chapter, a strategy to denoise experimental thermal and kinematic fields has been proposed. The method adds the structural information of the material (grain pattern) to partition the fields into two additive parts: a continuous field per grain and a residual field. Finally, it allows a concrete dialog, grain by grain, between multiphysic fields such as grain orientation, surface topography, plastic slip systems, slip-band density, kinematic and thermal fields.

The following chapter presents a large range of thermomechanical analysis performed on these fields. It is splitted in three sections: firstly, the macroscopic point of view, secondly the mesoscopic one, i.e. field analyses, and finally the intragranular point of view.

The objective is to go down in scale and to discuss observations and elements which precise the local thermomechanical couplings. Nevertheless, one can already announced that it is not an exhaustive analysis and that some observed mechanisms do not find any explanation. This part is much more an investigation of the relevance of such in-situ full field measurement rather than a complete comprehension tool of the polycrystal.

4.1 Macroscopic elasto-plastic transition

In this section, mean evolution of temperature, strain and nominal stress over the specimen gauge-section are introduced and thermo-elasto-plastic coupling at macroscopic scale is underlined.

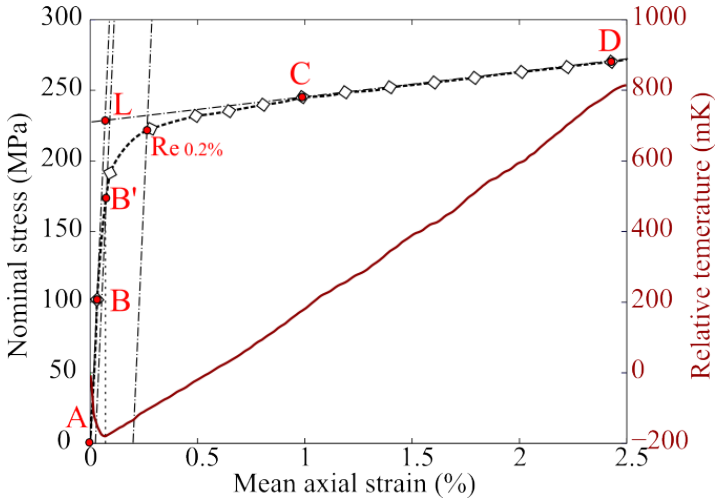

(a)

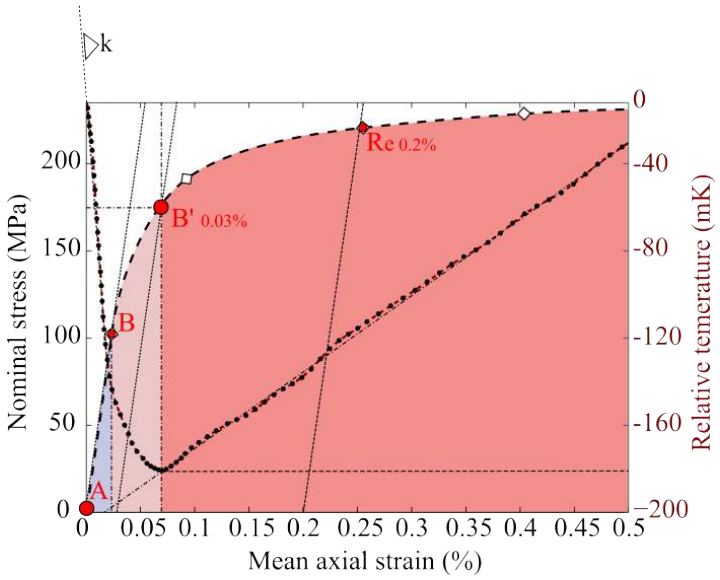

(b)

Figure 4.1: (a) Mean stress-strain and temperature-strain evolution averaged over the specimen gauge-section (5x5mm^2) and (b) a zoom within elastic domain and elasto-plastic transition

Values are averaged over the entire field, i.e. 5x5 mm^2, and reflect therefore the thermomechanical

response of 1776 grains (see chapter 1.1). Figure 4.1 (a) presents the stress-strain as well as temperature-strain curve during the whole test and figure (b) focuses on elastic domain and elasto-plastic transition. Remind that results correspond to a monotonic tensile test with a constant strain rate of $5\text{x}10^{-3}s^{-1}$ up to 270 MPa of nominal stress and 2.5% of total axial strain [Bodelot 2009]. Also reming that the frequency of in-situ kinematic measurements is 7Hz. One of the consequences is that only 3 datapoints have been taken from 0 to 200 MPa (see figure 4.1 (b)). It is consequently hard to estimate, only from kinematic measurements, the end of the linear stress-strain response as well as the elastic modulus. One of the objective of this section is to underline that the macroscopic temperature can solve this problem.

As regards of picture 4.1 (a) and (b), the material seems to deform elastically in a first step up to point B. Note that the linear relation between stress and strain is represented by line A-L in figure 4.1 (a). Then, between B and the conventional yield stress at 0.2%, which is equal to 223 MPa, local plasticity extends and becomes even more generalized up to D. It leads to another linear response of the material from C to D which can be associated to a saturated plastic hardening behavior.
The mean relative thermal evolution, i.e. $\theta = T - T_0$ where T is the absolute temperature and T_0 the initial one, is also presented in figure 4.1. One notes a drop in temperature between points A and B', both located in the conventional elastic domain, followed by a rise between points B' and D. Thermodynamically, it corresponds in a first step, to a thermoelastic coupling and, in a second step, to the effect of a positive dissipation associated with plasticity. This coupled thermomechanical behavior was underlined many years ago [Quinney 1937]. In addition, it is interesting to note that the inflection point in the temperature curve occurs at point B. Indeed, the minimum temperature is reached at B' but the loss of linear relation between temperature and strain, i.e. the appearance of early dissipation occurs earlier at B. Thus this nominal stress level corresponds thermally to the beginning of a deviation from purely elastic behavior. It allows notably to evidence that the loss of linear relation between stress and strain must occur at point B.

In agreement with previous point, picture 4.1 (b) presents the three characteristic domains within thermal response function of strain:

- ***the macroscopic elastic domain*** (blue one, from A to B'). A linear and reversible relation exists between stress, strain and temperature. It is in line with elasticity theory classically accepted as basic in solid mechanics. In addition, within this domain a reversible process between external work and strain energy could be assumed.

- ***microplasticity expension domain*** (pink one, from B' to B). A loss of thermal linearity is observed as well as a loss of linear dependance between stress and strain. It characterises the domain where a decrease of cooling-rate occurs. Concretely, the isentropic power, linked to thermoelastic coupling contribution, becomes to be balanced by the dissipation one (see appendix A.1). Obviously this dissipation is associated to inelastic irreversibilities including, for a great part, microplasticity.

- ***the elasto-plastic domain*** (red one, from B to D). The temperature increases from a minimum. It characterises a global warming of specimen. The dissipation power predominate over

thermoelastic couplings and thermal exchanges, i.e. convection, diffusion.

Both figures, especially 4.1 (b), underline consequently the link between kinetic of macroscopic temperature, i.e. curve slope, thermal magnitude, in particular the minimum, elasticity and an unknown level of microplasticity. This complementarity between temperature and kinematics underlines two interesting aspects of global thermal measurements already emphasized notably in [Lee 1991]. The first one is a more physical definition of plastic yield concept then the ability to identify material parameters.

In this way, let us firstly recall what a yield surface is. From [Michno 1976] in which a large review of yield surface investigations for metals was introduced, three fundamental constituents are presented as necessary to describe the behavior of plastic material under general stress states:

- an initial yield criterion $\mathcal{F}(\boldsymbol{\Sigma}) = \boldsymbol{\Sigma} - \boldsymbol{\Sigma_y} \leq 0$, specifying the threshold stress state before anelasticity appearance. $\boldsymbol{\Sigma}$ is the macroscopic stress tensor and $\boldsymbol{\Sigma_y}$ the yield one.
- an associated flow rule $\dot{\boldsymbol{\varepsilon}}^p = \dot{\lambda}\dfrac{\partial \mathcal{F}(\boldsymbol{\Sigma})}{\partial \boldsymbol{\Sigma}}$, connecting the plastic strain flow to the stress one.
- a hardening rule, specifying the behavior of the yield or flow surface as work hardening progresses.

In addition, a large range of material properties more or less easy to obtain are necessary to complete the flow rules.

Focusing on the first fundamental point (initial yield criterion), we could objectively admit that the concept of lowest yield stress is clearly ambigous at macroscopic scale, since clearly dependent on its definition. Figure 4.2 (a) shows some of the possible definitions which have been used and/or are currently in use. A is the proportional limit, B is a small measurable permanent set, about 10 microstrain, C is the conventional engineering offset of 0.2% strain, D is the point of tangency of stress-strain curve whose the slope corresponds to a multiple of elastic one (for 1.5 time the elastic modulus, this definition is called Johnson's apparent elastic limit), E and F use extrapolation methods (Taylor-Quinney definitions). E neglects the elastic deformation, whereas F includes the elastic deformation.

Figure 4.1 shows that the macroscopic thermal inflection instant is close to the B definition in figure 4.2, i.e. a very small and hardly measurable permanent plastic strain set. Thus, considering macroscopic thermal measurements one could pass from a yield stress concept to a dissipative yield one. The second one seems to provide very accurate results.

According to the tested specimen (see figure 4.1), the thermal loss of linearity appears at 106 MPa and the minimun of temperature, -180 mK, is reached at 172 MPa of nominal stress. According to the elastic slope one notes that 106 and 172 MPa of nominal stress correspond to $\approx 0\%$ and $\approx 0.03\%$ of permanent strain set.

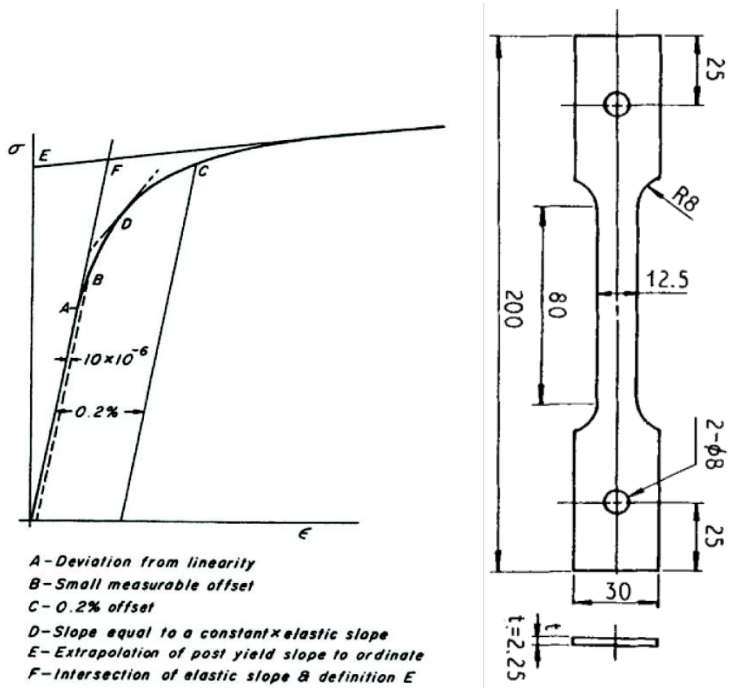

(a) (b)

Figure 4.2: (a) Different definition of plasticity yield [Michno 1976] and (b) dimensions of flat specimens (in mm) used in [Lee 1991].

Let us focus on the appearance of a minimum within the thermal response, i.e. $\approx$ 0.03% of permanent strain set. One could underline that identical results was already found by Lee and Chen in [Lee 1991]. Authors focused on ASTM Wl-8 plate specimen which undergoes uniaxial tensile loading with a strain rate of 1.3x10$^{-4}s^{-1}$. Figure 4.2 (b) presents dimensions of specimen used in this study. One can note that specimen dimensions, specimen shape (toe weld), the strain rate as well as the material is different compared to our study, in particular the conventional yield stress at 0.2% is 602 MPa according to [Lee 1991] compared to 223 MPa in our case. Considering the whole set of fundamental differences between tests performed in [Lee 1991] and in our works, it is very interesting to underline that the permanent deformation observed when the minimum temperature magnitude is reached is similar in both investigations. Indeed, it is 0.03% (see figure 4.1 (b) and [Lee 1991]). It underlines a potential intrinsic relation between the macroscopic yield of dissipation and a specific permanent plastic strain set.
Nevertheless, the minimum temperature reached in [Lee 1991] is -420 mK compared to -180 mK in our case. This point is logical and in line with the Lord Kelvin's equation (see eq. 4.1) which allows to link, in particular, the maximum elastic variation of temperature ΔT_{lim}, material properties and yield

stress Σ_y.

$$\Delta T_{lim} = -\frac{\alpha T_0}{\rho C_v}\Sigma_y = -kE\varepsilon_y \tag{4.1}$$

where ε_y is the strain associated to Σ_y.

Note that this interesting result must be balanced by the relatively poor precision on elastic slope determination. Indeed, as the frequency of in-situ kinematic measurement is low, only two points are located within the macroscopic elastic domain (the origin A and point B in figure 4.1 (b)). Classically, elastic slope identification is done by means of a least squares method on many elastic datapoints. Here, one knows that the elastic slope is somewhere between the line slope (AB) and (AB') (see figure 4.1 (b)). Let us discuss both bounds.

- if one considers line slope (AB) as the elastic one, the lowest temperature magnitude is reached for 0.03% of permanent strain set. Considering this result compared to Lee's ones, it seems that whatever the material the lowest temperature magnitude is reached for constant degree of micro-anelasticity. In this way the thermal measurement would be an intrinsic quantifier of anelasticity magnitude and thus would lead to the identification of an unambiguous macroscopic yield stress, i.e. physical and not phenomenological.

- if one considers line slope (AB') or whatever other intermediate line slope as the elastic one, the lowest temperature magnitude is reached for a permanent strain set which ranges from 0 to 0.03%. In this case, the permanent deformation off-set associated to the lowest temperature magnitude is lower than the one found in [Lee 1991].

In both cases, it shows the ability of a simple bulk temperature measurement to accuratly estimate the lowest yield stress.

In this section, average of fully-coupled thermomechanical fields over the specimen gauge-section have been studied. A strong coupling between macroscopic thermal and kinematic quantities has been emphasized. Three phases have been identified within stress-strain curve as well as temperature-strain curve: (1) linear and reversible relationship exists between each quantity, the Lord Kelvin's formula describes the associated drop of temperature; (2) micro-anelasticity develops and leads to a decrease of the cooling until the temperature reaches a minimum; (3) the specimen undergoes a global warming associated in part to hardening.
Then, it has been shown that the inflection point within thermal response provides an accurate estimation of macroscopic yield stress Σ_y. It assumes that the decrease of specimen cooling-rate reflects the initiation of dissipation associated to local inelastic phenomena. Finally, a comparison with results coming from [Lee 1991] has revealed that the minimum reached by the temperature during a monotonic test occurs for a permanent deformation set lower than $3\text{x}10^{-4}$. An higher frequency of in-situ kinematic measurement would allowed refining this estimation.
The next section goes down in scale, notably to observe how temperature and strain localize at mesoscale.

4.2 Mesoscopic analysis of thermomechanical couplings

In this section, displacements, thermal and strain fields are shown in the same configuration and have the same characteristics. (1) A grid with the same size as the spatial resolution (see chapter 2.1) is superimposed on each field. In this way, one keeps in mind the effective resolution of thermomechanical fields even if in post treatment biparabolic continuous fields within grains has been done. (2) Fields are expressed in deformed configuration in order to underline the fact that presented fields are Lagrangian and not Eulerian, i.e. temperatures, strains, fluxes are associated to material points. note that a scale factor of 15 is applied to improve the displacement visibility. (4) Fields represent a 5x5mm^2 crop of original pictures and are spatially and temporally in phase. Thus fields point the same region at the same time. (3) Finally loading axis is vertical.

Note that the following discussion about kinematic and thermal full-fields is qualitative since fields contain too many informations. In addition, as thermal fields are space and time dependent contrary to kinematic ones, it is obviously impossible to exhibit simple statistics and correlations. Thus the global thermal and deformation process of localization are discussed in a qualitative way. Then, at intragranular scale, some quantitative and local analysis will be done in some grains.

4.2.1 Displacement fields

The figure 4.3 shows the transversal displacement field, noted V, at different steps of loading. The conventional macroscopic stress-strain curve in the right bottom corner precises when each instant appear.
One observes all the way through the test the typical gradient of transversal displacement expected for a monotonic tensile test, i.e. compression by means of the Poisson's effect. Note that ΔV is $\approx 3\mu m$ at 106 MPa of nominal stress and reaches 60 μm at the end of the test. Recall that the uncertainty of measurement, noted e, is widely lower (e=0.04μm). It already allows to estimate the mean transverse strain at the end of the test:

$$\bar{E}_{11} = \frac{\Delta V}{L} \approx 1.2\% \tag{4.2}$$

where $\bar{E}_{11}$ is the mean transversal strain, L=5000 μm is the initial length of studied zone.

Fields exhibit in elastic domain a relatively high heterogeneity grain to grain, in particular at the very beginning of the test (see figure 4.3 (a)). Then, this grain to grain heterogeneity tends to decrease along the deformation path. Nevertheless, the microstructure is still visible in figure 4.3 (e) and seems to play an significant role within the displacement field. Thus, one could already note that the transversal displacement field is far from the one expected for a homogeneous material. In parallel, figure 4.3 (e) shows that the transversal displacement field is different on both sides of the vertical axis of symmetry whereas the field is actually the center region of the specimen gauge-section. Thus the displacement is locally twice more significant on the right side of the microstructure than on the left. It reflects a strong heterogeneity on both side of the specimen-gauge section.

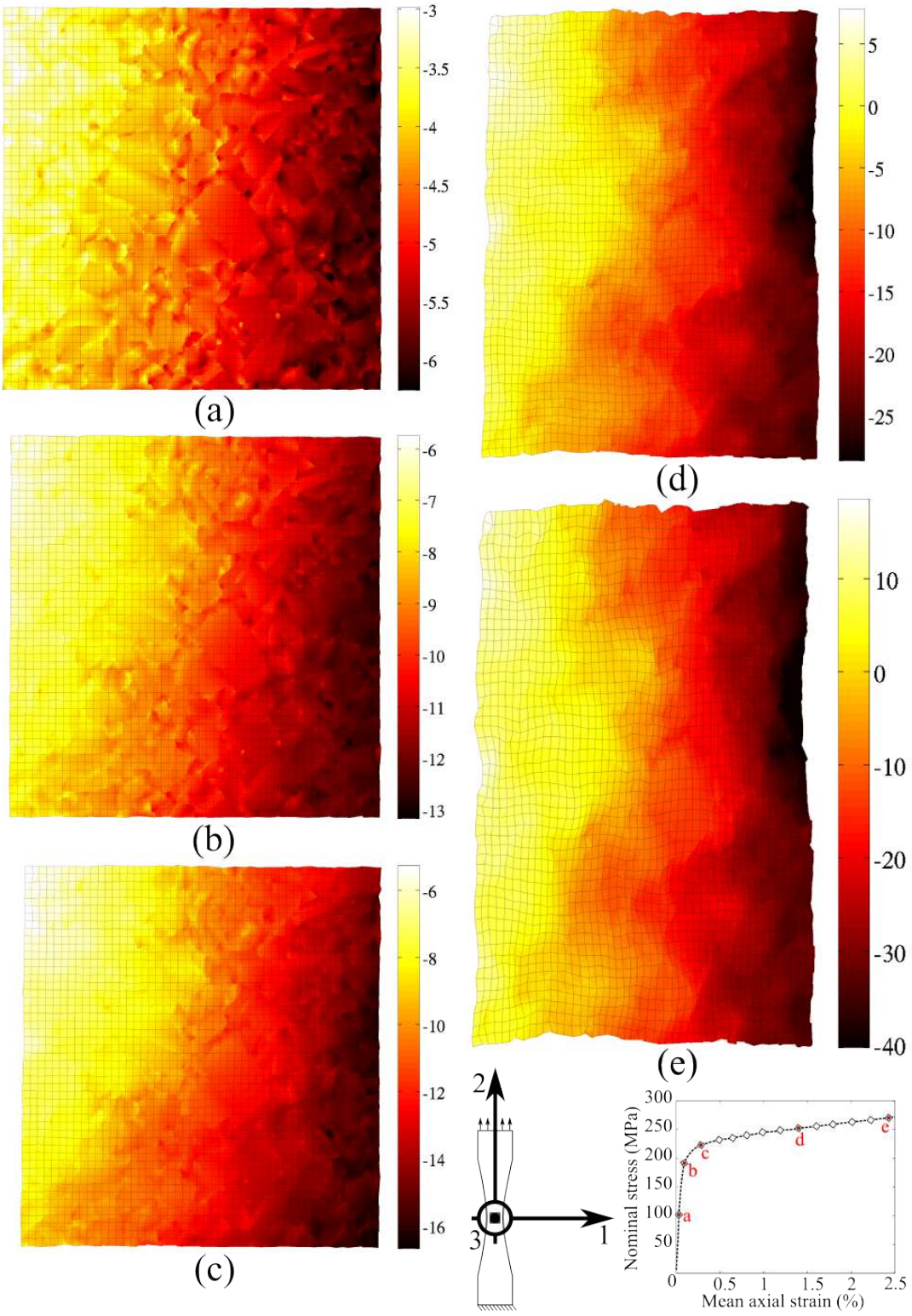

Figure 4.3: Transversal displacement fields V (direction 1) in μm at (a) 106, (b) 191, (c) 220, (d) 252 and (e) 270 MPa of nominal stress

Let us point another important aspect. Figures 4.3 (c) and (d), respectively just before and after the macroscopic elastoplastic transition, exhibit a singular displacement gradient. Indeed typical vertical isovalues of displacement are not obtained, but here, the displacement is not vertically uniform, especially on the left part of specimen gauge-section. It reveals that boundary conditions are potentially unsymmetric between the bottom and the top of the specimen. Nevertheless this unsymmetrical aspect vanishes after a certain level of loading (see figure 4.3 (e)). These observations reveal that the studied monotonic tension test is not totally uniaxial, at least from (a) to (c) in figure 4.3. This analysis must be underlined to avoid any misinterpretation of the fields. Moreover it will not affect the relevance of deeper investigations. Indeed, whatever the macroscopic loading, within a polycrystal, the local deformation path is necessarily fully multiaxial. In the present case, the test is slightly multiaxial at each scale. According to this observation, one could already note that some material parameters can not be identified from nominal stress and axial strain:

- the Poisson's ratio ν. Indeed, within the isotropic linear elasticity framework one classically assumes:

$$\varepsilon = \frac{1+\nu}{E}\sigma - \frac{\nu}{E}\mathrm{tr}\left(\sigma\right)\mathbf{I} \tag{4.3}$$

$$\nu = E\frac{\varepsilon_{11}-\varepsilon_{22}}{\sigma_{11}-\sigma_{22}} - 1 \neq -\frac{\varepsilon_{11}}{\varepsilon_{22}} \tag{4.4}$$

  Thus, as only the nominal stress is known, ν can not be estimated directly.

- the Young's modulus E. Within the same framework:

$$E = \left(\nu+1\right)\frac{\sigma_{11}-\sigma_{22}}{\varepsilon_{11}-\varepsilon_{22}} \neq \frac{\sigma_{11}}{\varepsilon_{11}} \tag{4.5}$$

  Under multiaxial conditions the ratio $\dfrac{\sigma_{11}}{\varepsilon_{11}}$ becomes:

$$\frac{\sigma_{11}}{\varepsilon_{11}} = E\frac{\sigma_{11}}{\left(1+\nu\right)\sigma_{11} - \nu\mathrm{tr}\left(\sigma\right)\mathbf{I}} \tag{4.6}$$

$$= E\frac{\sigma_{11}}{\sigma_{11} - \nu\left(\sigma_{22}+\sigma_{33}\right)} = kE \tag{4.7}$$

Figure 4.4 presents the axial displacement expressed in μm at the same loading instants than the ones introduced in figure 4.3. One observes, all the way through the test, the typical gradient of axial displacement expected for a monotonic tensile test, i.e. almost horizontal isovalues of displacement. The displacement ranges from 380 to 520 μm at 270 MPa of nominal stress thus $\Delta U = 140\mu m$. The mean ultimate deformation is therefore:

$$\bar{E}_{22} = \frac{\Delta U}{L} \approx 2.8\% \tag{4.8}$$

A relative small heterogeneity of axial displacement is observed notably in the elastic domain compared to transversal one.

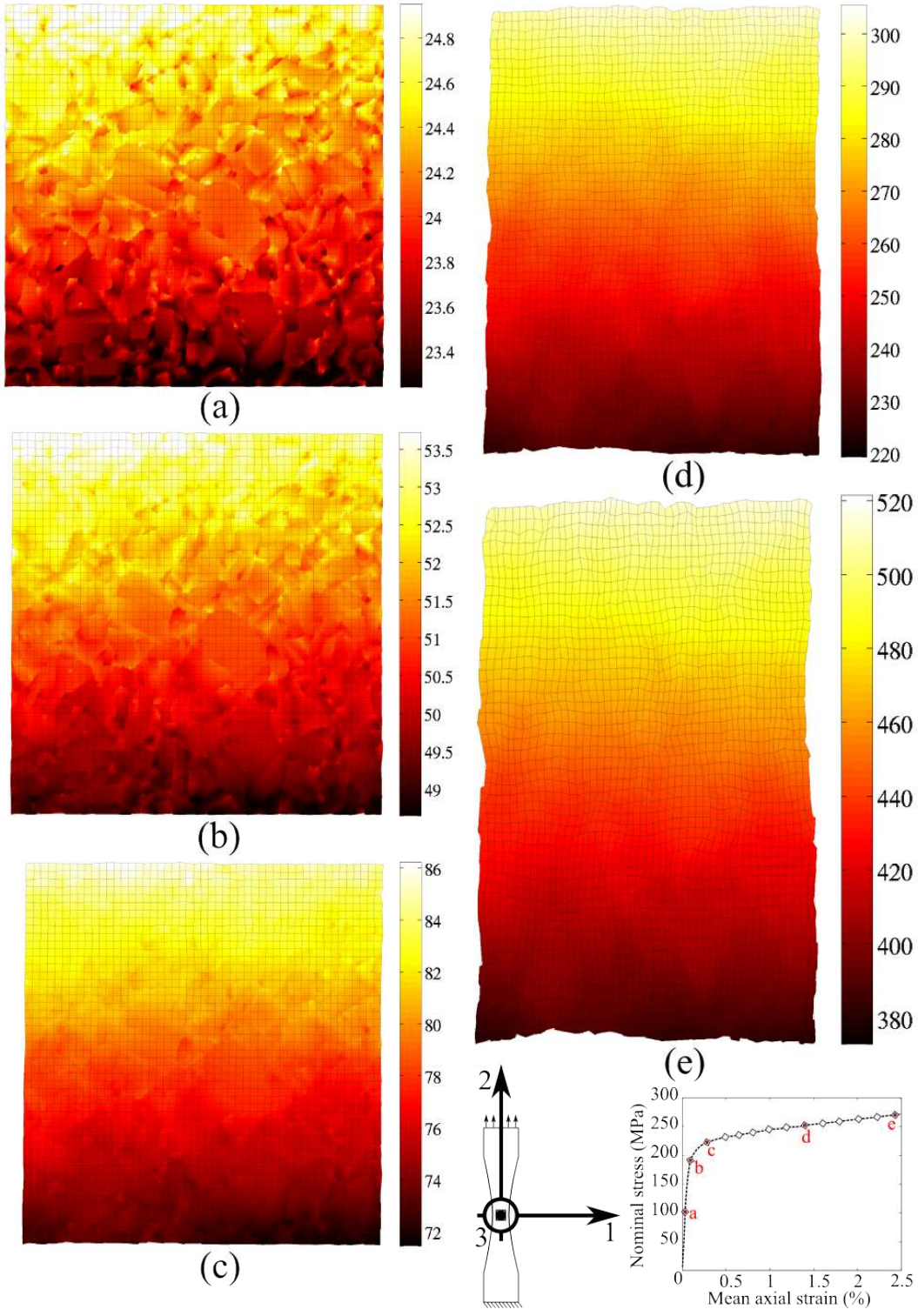

Figure 4.4: Axial displacement fields U (direction 2) in μm at (a) 106, (b) 191, (c) 220, (d) 252 and (e) 270 MPa of nominal stress

Indeed the maximum axial displacement gradient reaches 1 μm and 4 μm in pictures 4.4 (a) and (b) respectively, compared to 2.5 μm and 7 μm observed on picture 4.3 (a) and (b). It reflects a greater heterogeneity of the displacement along the free direction, i.e. the transversal displacement compared to the loading direction. Nevertheless, one could note that, even in axial displacement field (see figure 4.4 (e)), the microstructure plays a non neglectable role. Indeed, especially in the bottom part of the field, one does not see the classical horizontal isovalues of displacement expected for an homogeneous material.

4.2.2 Strain and temperature fields

In this section, strain fields obtained by means of analytic intragranular derivation as well as thermal fields, at different states are presented. These instants correspond to the ones introduced in figure 4.4. The main objective is to observe the strain localization within the material thanks to each component of plane strain tensor and to analyze the associated thermal localization.

4.2.2.1 Elasticity: from E_1 to E_2

Figures 4.5 from (a) to (d) present the axial strain component E_{22}, the transversal strain one E_{11}, the shear strain component E_{12} (in %) and the variation of temperature from equilibrium state $\theta = T - T_0$ (in mK) respectively, at 106 MPa of nominal stress, when the macroscopic temperature inflects (see figure 4.1).

One observes a very heterogeneous response of each strain component which is quite similar for every component in term of standard deviation. In parallel, the temperature exhibits a clear thermal gradient from right (hot) to left part (colder) of the specimen gauge-section. The temperature ranges from -115 to -160 mK ($\Delta\theta$=45 mK).
No clear link could be done between microstructure, strain, and temperature fields. In particular the temperature field exhibits a macroscopic gradient whereas strain fields are heterogeneous at local scale, i.e. grain to grain. It is interesting to note that the temperature is globally higher over the blue dotted line (see figure 4.5 (d)) than below; mean values are -132 mK and -146 mK respectively. Thus grains located over the blue dotted line exhibit a lower cooling rate compared to grains located under the line.

A first explanation could be proposed. In chapter 1.1 a variation of grain size over the specimen-gauge section has been underlined. Over the blue dotted line presented in figure 4.5 (d), the mean grain size is 95 μm whereas under the value is 141 μm. Thus this variation of cooling rate on both sides of the blue dotted line may be due to mean grain size within both domains. Over the blue dotted line, grains are small and grain boundary network is dense and interactions between different intragranular behaviors are numerous. Under the blue dotted line, grains are bigger, grain interaction less numerous.

Then, picture 4.6 presents strain components and temperature at 191 MPa of nominal stress. One could first focus on mean values and standard deviations: (a) (0.096, 0.29), (b) (-0.116, 0.28), (c) (0.012, 0.2) (in %). Thus, the specimen undergoes $\approx 0.1\%$ of axial strain and one could point out a

strain rate increase in some regions compared to the previous state (see figure 4.5). These regions are notably black circled on ε_{22} (see picture 4.6 (a)) as well as on the surface micrography performed after the test (see picture 4.7).

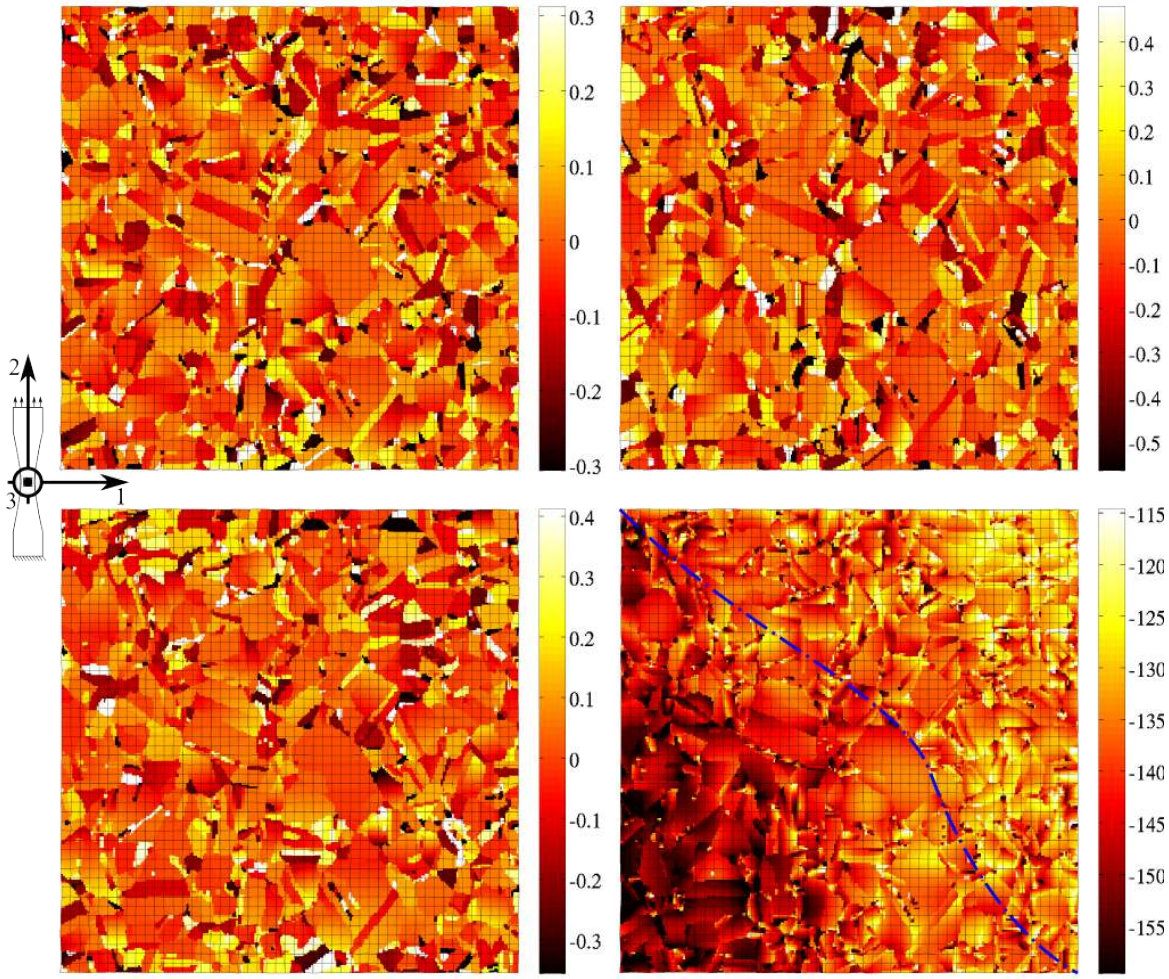

Figure 4.5: Thermomechanical fields at 106 MPa of nominal stress: (a) E_{22} (b) E_{11} (c) E_{12} (%) and (d) T (mK)

The Region denoted by 1 exhibits very intense discontinuities at grain boundaries. They are clearly connected to strain localizations observed in ε_{22} field. Region denoted 2 exhibits intense out-of-plane displacements at twin Σ_3 boundaries (see figure 1.12). This point was already underlined in chapter 1.1. Finally 3, 4, 5 also exhibit appearant strain localizations at grain boundaries as well as intense plastic slip-marks (see figure 4.7).
One underlines here the connection between in-situ strain field measurements and the ultimate surface state of the specimen. In addition, it evidences that many strain localization observed on surface

specimen after the test has initiated very early, since the studied instant (191 MPa of nominal stress) is located in the macroscopic elastic domain.

Then, one notes an increase of intense compressive region within transversal strain component ε_{11}. Moreover, a great part of concerned grains (intense compressive strains) are grouped into a vertical band which is black marked in picture 4.6 (b).

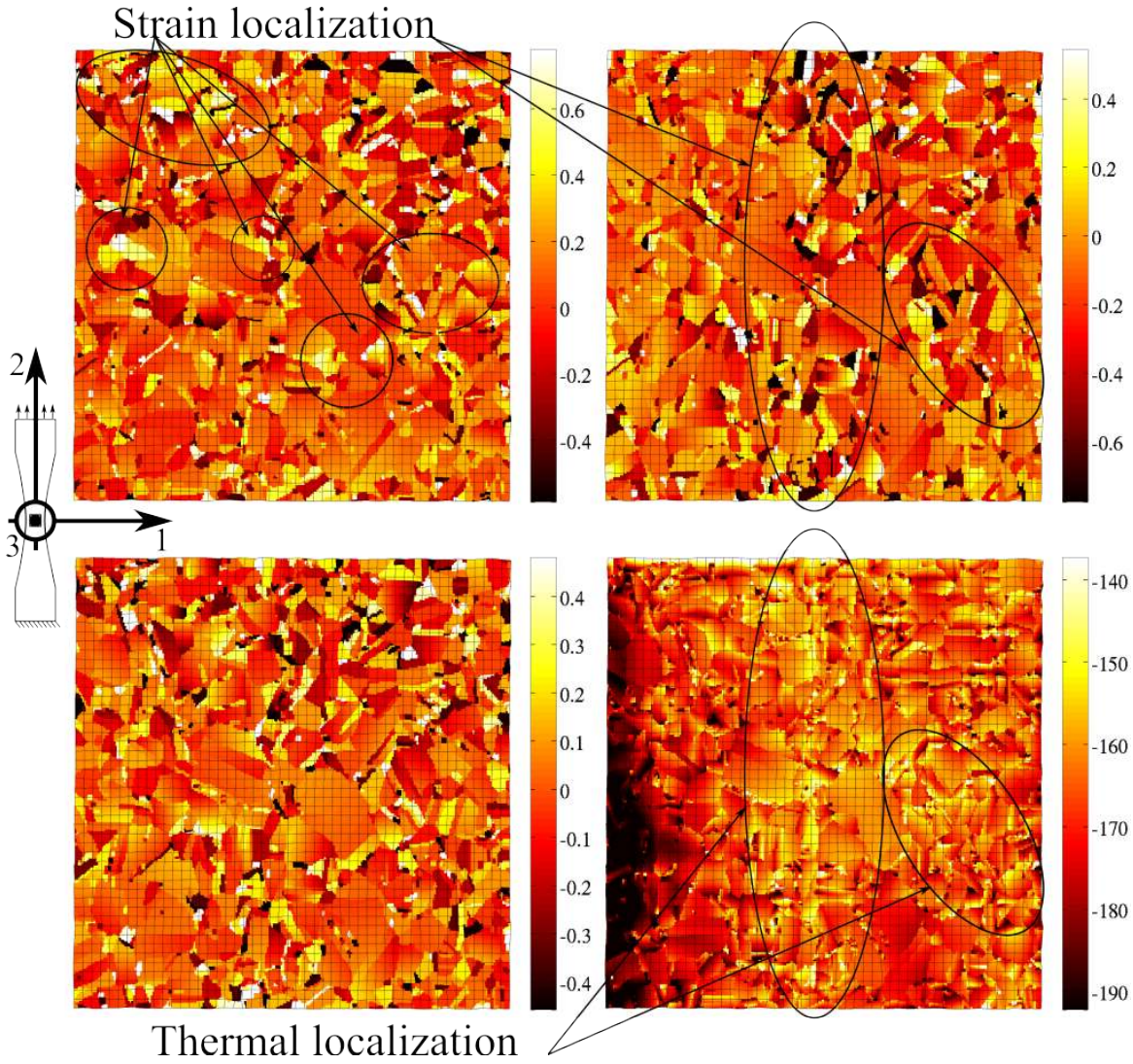

Figure 4.6: Thermomechanical fields at 191 MPa of nominal stress: (a) E_{22} (b) E_{11} (c) E_{12} (%) and (d) T (mK)

Note, this band is precisely located on the vertical symmetry axis of the specimen gauge-section.

By means of Poisson's effect the material is laterally under contraction. It leads in the present case of a high contraction localization on the symmetry axis of the material as well as on its right side. It is interesting to note that this point was already announced when transverse displacement fields were discussed (see figure 4.3). Indeed, one have seen that the displacement field is more important on the right part of the specimen gauge-section than on the left one. One understands that it is related to the concentration of high contraction.

In parallel, the thermal response exhibits a global warning effect as shows on picture 4.1. The mean value is -167 mK and local values range from -192 to -137 mK (ΔT=55mK) (see figure 4.6 (d)). One still observe that the left part of the specimen gauge-section is colder than the rest of specimen. Nevertheless the thermal pattern has changed. Indeed, a thermal localization appears within regions where intense contractions localizations (ε_{11} see 4.6 (b)) are observed. Figure 4.6 (b) and (d) focus on both regions where transversal contractions are intense and temperature localizes. Thermal gradients are slight nevertheless such thermal localization is expected. Indeed, if one focuses on both circled regions (see figure 4.6 (b)), one can note that strains are either positive or negative but magnitudes are widely over the classical limit at 0.2%. It ranges from -0.8 to 0.6 %. Thus local dissipation is expected and the level of dissipation is necessarily higher than the rest of the specimen where strains are more homogeneous and widely lower than 0.2% in absolute values. It is interesting to note that no such slight correlation is observed between ε_{22} (axial strain) and temperature. One can underline a connection between strain localizations, especially contractions due to the Poisson's effect and surface grain microstructure, and thermal localization. Note already that this slight correlation is persistent and more visible for higher stress level as presented in the next section.

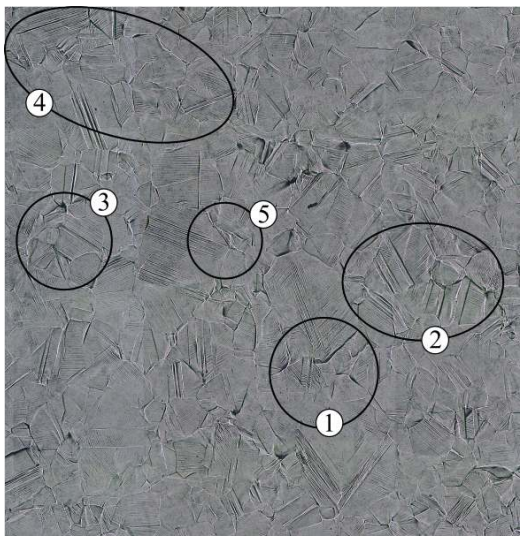

Figure 4.7: Micrography of surface after test with strain localization regions

Some points of the "elastic loading" part may be summarized:
Strain and thermal fields have been observed at two different stress states: 106 MPa and 191 MPa. Both states are located in the macroscopic elastic loading domain. Two main observations have been done. Firstly, strains and temperature are not homogeneous even at such low stress state. Secondly, structural (microstructure), mechanical and thermal heterogeneities are linked. At 106 MPa, a macroscopic thermal gradient has been pointed out. It has been shown that this thermal gradient is potentially associated to a grain size gradient already underlined in chapter 1.1. Nevertheless, this point would required deeper investigations to lead to a clear conclusion. Then, at 191 MPa, a localization of high transverse contraction in the vertical symmetry axis of the specimen gauge-section has been underlined. In parallel, a thermal localization in the same specific band has been evidenced. It reflects a coupling between early strain localization and early dissipation localization. Finally, the comparison with micrography of specimen surface after the test has shown that in-situ strain measurements present similar localizations, that occurred from 106 to 191 MPa.

4.2.2.2 Plasticity: from P_1 to P_2

Figure 4.8 presents experimental strain fields ((a) ε_{22}, (b)ε_{11}, (c) ε_{12}) and (d) the temperature variation from the initial state θ. Fields are taken at P_1 instant, i.e. 220 MPa of nominal stress. The specimen undergoes here a macroscopic plastic deformation. Mean strain values observed within the material surface are 0.25%, -0.17% and 0.06% for ε_{22}, ε_{11} and ε_{12} respectively.

One notes that the transverse strain field ε_{11} in figure 4.8 (b) is notably characterized by a vertical contraction band within its vertical symmetry axis. This band is surrounded by white dotted lines. The appearance of a vertical and central contraction band was already pointed out in the macroscopic elasticity domain (see figure 4.6), but the localization is much more clear in the present case. Thus from 191 to 220 MPa this strain localization has increased.

As it was already presented in section 4.2.1, no symetric phenomena are observed from right to left side of the vertical symmetry axis of the studied area. Indeed on the right side of this median contraction band, one observes a very heterogeneous strain field with high contraction levels whereas strain levels are lower and more uniform on the left side. It is confirmed by the calculation of the mean absolute values of transversal strain over the left and right domain compared to the median. It is 0.19% and 0.29% respectively. Consequently, the left region globally undergoes strain magnitudes lower than 0.2% ($< R_e^{0.2\%}$) while the other side undergoes strain magnitudes close to 0.3%. Thus it is reasonable to think that a great part of grains in the right domain undergo plastic strains whereas a great part of the grains in the left one still potentially undergo elastic or low plastic strains.

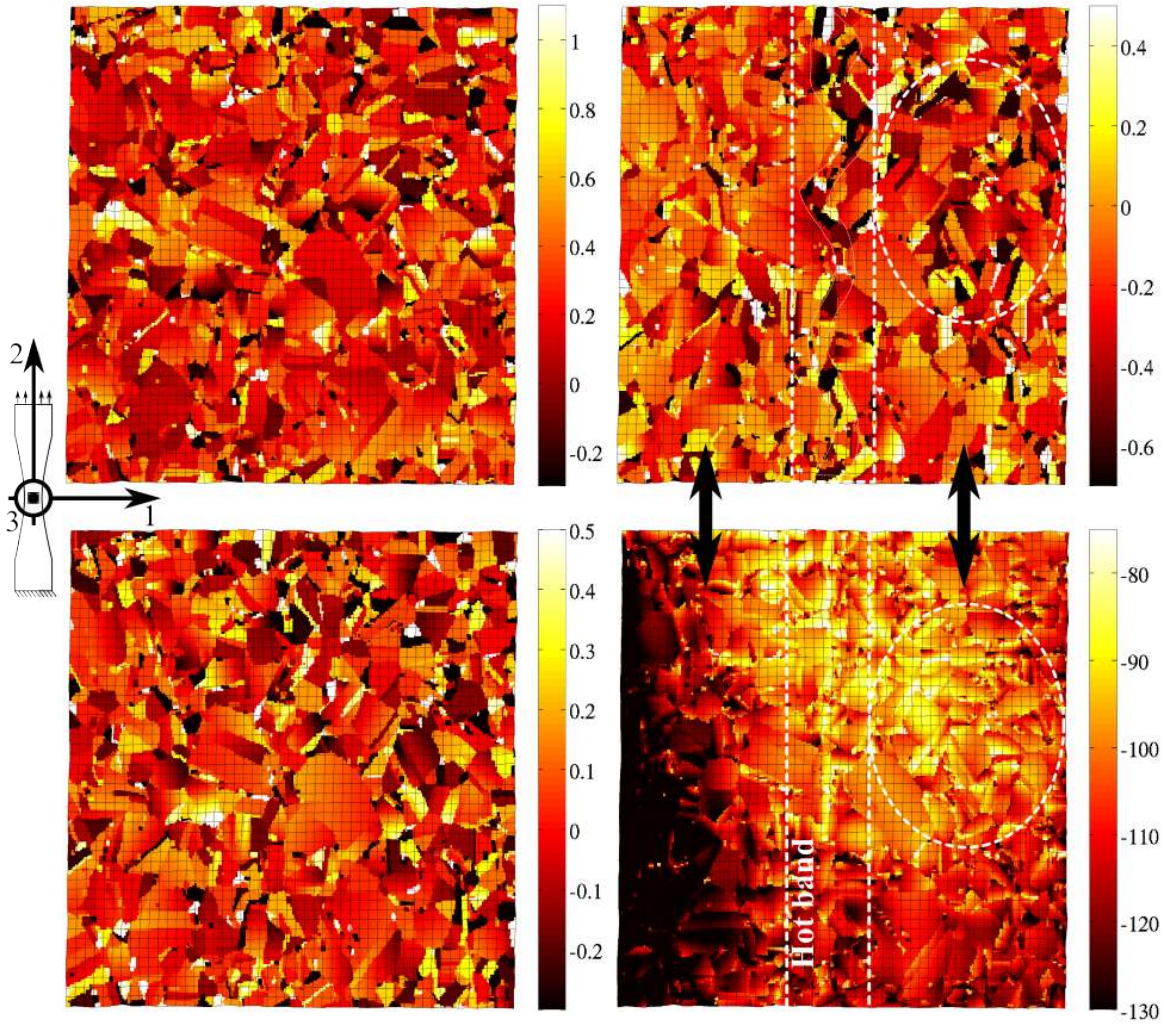

Figure 4.8: Thermomechanical fields at 220 MPa of nominal stress: (a) E_{22} (b) E_{11} (c) E_{12} (%) and (d) T (mK)

Concerning shear strain field ((c) ε_{12}) and axial strain ((a) ε_{22}) one still observe a very high heterogeneity which is also well distributed over the field. Note in axial strain field ((a) ε_{22}) that some grains are still under contraction up to -0.3% while others reach more than 1.1%. Such extremum are only observed in small grains whereas bigger ones exhibit a strain level close to the mean value, i.e. 0.25%.

Figure 4.8 (d) shows that temperature field is also very heterogeneous and connected to the microstructure. The mean value is -110 mK and the field ranges from -170 to -70. Thus a thermal gradient about 100mK is observed. One could clearly identify many correlations with transversal strain field

ε_{11} in (b).

- firstly, a quite intense vertical "hot band" is observed within the center of the specimen gauge-section. It was already observed at lower stress state (see figure 4.6). This "hot band" cross a set of small and apparently elongated grains (see figure 4.8 (b)). It is connected to the compression band observed in transversal strain field ε_{11}.
- secondly, the right top side of the specimen gauge-section exhibits higher temperature than the left side in which the temperature reach a minimum. It is totally in line with previous observations concerning transversal strain field ε_{11}. Indeed, one has seen that the right side of specimen gauge-section undergoes absolute strain levels about 0.3% while the left one undergoes absolute strain levels about 0.2%. Moreover, this correlation is greater within both white dotted circles presented in figures 4.8 (b) and (d) where higher temperature levels and higher contraction levels are localized.

Some points about the mechanical loading part could be summarized:

- The grain size is statistically lower in the top right region of the studied area (see chapter 1.1).
- The high strain levels are localized on the right side of the studied area and the symmetry axis presents a clear localization of contractions. In addition no such localization is observed within the axial strain field ε_{22}. Indeed, high and low strain levels are well distributed (see figure 4.5 (a), 4.6 (a) and 4.8 (a))
- From 0 to 220 MPa the right side of the specimen gauge-section exhibits higher temperature than the other side. At 220 MPa of nominal stress, a correlation between compression strain in ε_{11} field and thermal one is observed.

According to these points one can evidence that the variation of grain size within the specimen gauge-section leads to a localization of high transversal strains in small grain region leading to a specific localization of surface temperature. One points out an obvious thermomechanical coupling between microstructure, kinematics, temperature and also a specific interaction between high negative value of ε_{11} and θ. Thus the grain size, the shape and the "free response" of the grain structure, i.e. transversal strains compared to the loading direction, have a wide influence on the surface thermal field.

Note, in spite of this clear field correlation, it is not possible to evidence the link between ε_{11} and θ in a statistical approach. Indeed, contrary to strain fields, thermal ones are instantaneous and space dependent. Thus the currently dissipative grains but also their neighbors exhibit high local temperatures. Moreover, early strained grain could be in the current instant not dissipate anymore. It points out the great interest to deal with heat sources and not temperature. This point will be discussed in chapter 5.1.

Then, the figure 4.9 presents the same 3 components of strain field (%) and thermal field (mK) at 253 MPa of nominal stress. Note that the strain fields and the thermal one remain the same up to the end of the test, i.e. at 270 MPa of nominal stress. Also note that the colorbar is forced in order to improve the global visibility.

ε_{22} (see figure 4.9 (a)) exhibits a mean value of 1.45%, a standard deviation of 0.72% and ranges from 0 to more than 3.5% in some regions. One notes that the highest strained regions are currently clearly connected to regions where grain boundaries concentrate very high deformation on the surface micrography. This point is evidence by the comparison between figure 4.7 and 4.9 (a), especially in circled regions from A to D. One could point that the four high strain localizations observed in A, B, C and D were not visible at 220 MPa of nominal stress. It reveals a localization of axial strain within these specific set of grains from 220 MPa to 253 MPa. Finally, note that 3% of the surface microtructure maintain a strain level lower than 0.2% which reflects that the axial strain field is still very heterogeneous.
ε_{11} (see figure 4.9 (b)) exhibits a mean value of -0.58%, a standard deviation of 0.59% and ranges from -2 to more than 0.5% in some regions. One can note that grains significantly deformed within ε_{22} field are strongly contracted within ε_{11} one. It reflects the local Poisson's effect. In addition, one notes that the ε_{11} field tends to homogenize compared to the previous state at 220 MPa of nominal stress. Indeed, the central compression band is notably less visible.
ε_{12} (see figure 4.9 (c)) exhibits a symmetric field arround 0 with a mean value of 0.06% and a standard deviation of 0.45%. Extremum are -1 and 1 %.

Figure 4.9 (d) presents a distinct thermal localization within the microstructure. The gradient between the heart of this heat localization and specimen gauge-section boundaries is about 80 mK which underlines the interest of an accurate measurement. This field seems to reflect the contribution of many very local heat sources concentrated within circle 1 and 2. Then a conductive phenomenon through the microstructure up to the specimen gauge-section boundaries seems to lead to this global thermal field shape. Circles 1, 2, 3 and 4 underline the thermal wave front propagation. Note that it is not isotropic. It reflects the impact of boundary conditions on thermal field since there is only 2.5 mm between left or right free boundaries and the center of specimen whereas the distance between specimen heads (on top and bottom) and specimen center is 82.5 mm.
Contrary to previous observations where surface thermal field was apparently only connected to transversal strain field ε_{11}, the current thermal localization seems also to be connected to axial strain field ε_{22}. Indeed, the two more dissipative regions seem to be A and B in the axial strain field (see figure 4.9 (a)). One has seen that these regions are currently localizing high axial strains leading necessarily to current and high dissipation. It seems to be in line with a thermal localization which initiates into and in vicinity of regions A and B (in circle 1 and 2 in figure 4.9 (d)) and then propagates by conduction.

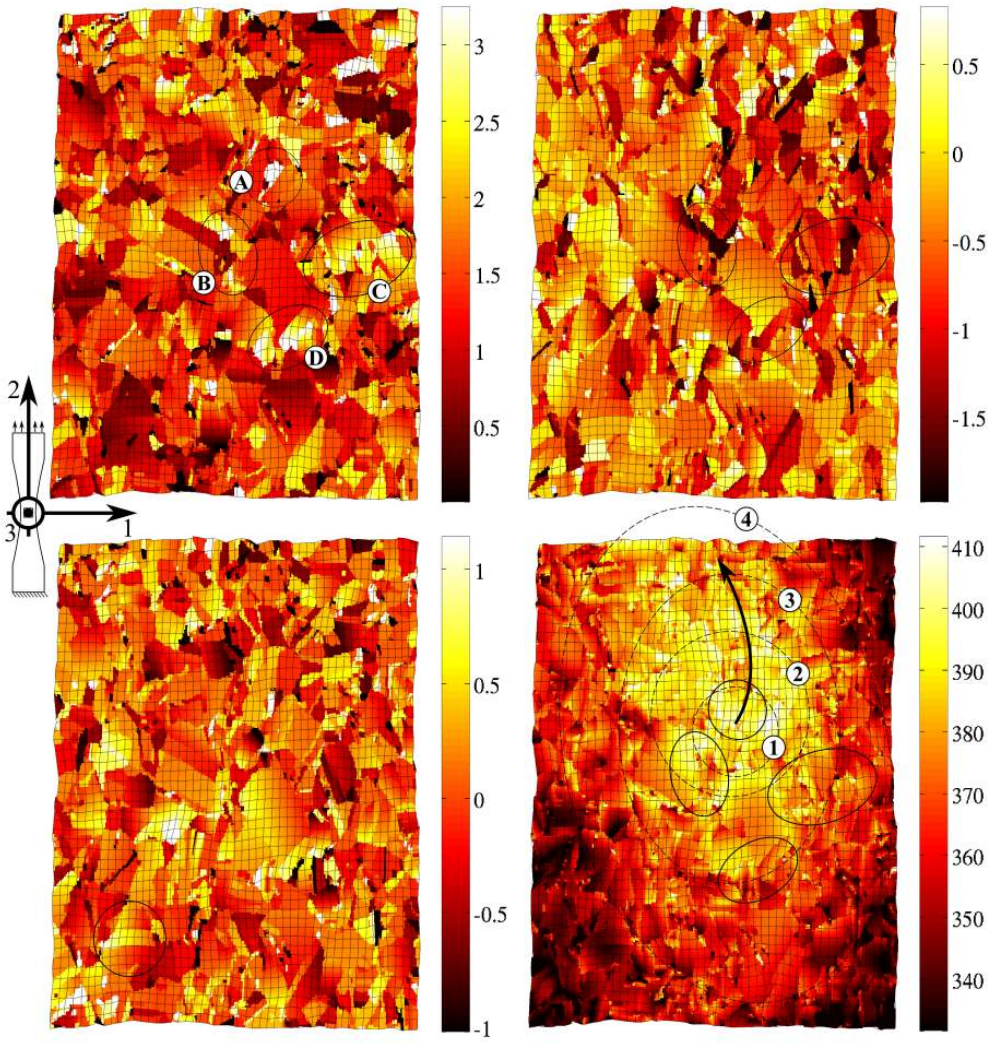

Figure 4.9: Thermomechanical fields at 253 MPa of nominal stress: (a) E_{22} (b) E_{11} (c) E_{12} (%) and (d) T (mK)

4.2.3 Partial conclusion

The strain and thermal fields have been observed during the macroscopic plastic response of the studied sample. Thermomechanical couplings observed in the previous section have been confirmed and a scenario of strain and thermal localization has been proposed. Firstly, an interesting correlation between the low grain size region, the high transverse contraction appearance and surface thermal field has been pointed out. It has been shown that, from 0 to 220 MPa, the thermal surface field is apparently dominated by contractions in the transverse direction. In the present case, such contractions appear in low grain size regions, where the grain boundary network is dense and grain interactions numerous. Finally, from 220 MPa to the end of the test, i.e. 270 MPa of nominal stress, the thermal localization migrates. The thermal field is dominated by current dissipation localized in a limited set of grains and then the thermal wave front propagates through sample boundaries in an non isotropic way. It is due to the distance between specimen gauge-section and free boundaries.
Finally, it has been shown that the connection between thermal field and axial strain is only clearly visible over 220 MPa of nominal stress. It is interesting to note that from 223 MPa the material is over the conventional limit at 0.2% of permanent strain and the macroscopic hardening is quite linear. Thus, one could underline that from 0 to $R_e^{0.2\%}$ the thermal surface field reflects the free response of the microstructure, i.e. its transversal strain field ε_{11}. Then from $R_e^{0.2\%}$ to 2.5% of mean axial strain, i.e. in the linear hardening domain, a relation appears between axial strain and surface thermal field.
Every observation points out on the one hand that measured thermal gradients, even low, are consistent with kinematic fields. It allows the validation of thermal and kinematic measurements [Bodelot 2009] as well as the whole calibration procedure (see chapter 2.1) and intragranular field projection (see chapter 3.1). In another hand, it points out the ability of thermal surface field to reflect the microplasticity activity and also to provide crucial informations about the coupling mechanisms. The analysis of the macroscopic mechanical localization by means of thermal fields was already pointed in some studies, for example [Louche 2001]. Nevertheless, to our knowledges, no such link between microplasticity, microstructure and thermal field has been already established.

4.3 Grain scale

One presents here brief observations of two milimetric grains composed by some twins Σ_3 boundaries.

Figure 4.10 focuses on a grain whose the shear strain ε_{12}, could be easly linked to micrography and profilometry. On the left side, one observes the shear strain ε_{12}, in the center of the surface microgra-

phy and, on the right side, the surface topography. Colored substructure on micrography corresponds to subgrains separated by Σ_3 boundaries.

One notes that the rectangular sub-grain, noted A, exhibits 2 kinds of slip-marks. The system activated on the left part of the subgrain A exhibits intense slip-marks thus underlines high plastic strains. In the opposite, the other side exhibits very few slip-marks thus underlines few plastic strain. This phenomenon is clearly in line with intragranular shear strain field. Indeed, it reaches 1% on left side and ≈0% on right one. The experimental intragranular shear strain reflects consequently the intragranular shear leaded by plastic sliding. It points the relevancy of in-situ kinematic fields even at intragranular scale.
In addition, an intense discontinuity between intragranular fields and neighboring sub-grains is observed. The relevance of this particular result is confirmed by out-of-plane displacement field provided by profilometry. Moreover, one observes a clear connection between activated slip-systems and out-of-plane displacement. Indeed, in the region where both systems cross each other the relief propagates through the grain boundary. This point is visible in the right side of figure 4.10.

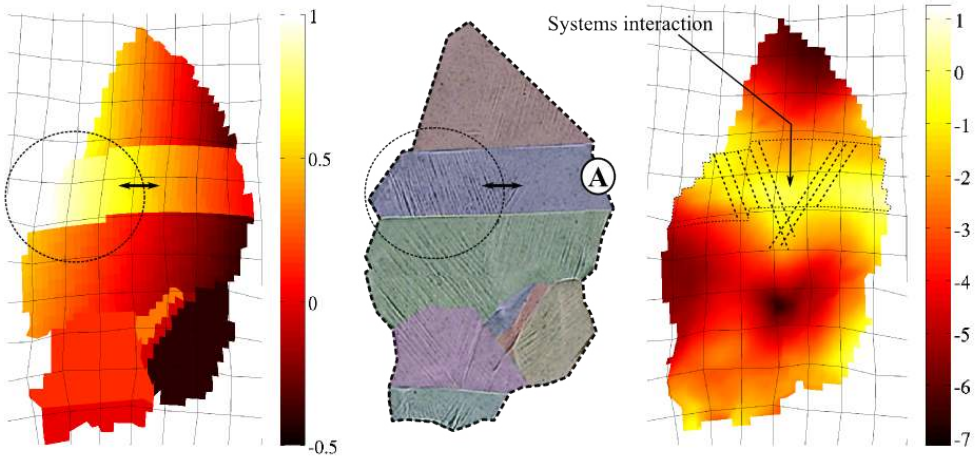

Figure 4.10: Shear strain E_{12} (%), micrograph and out-of-plane displacement (μm) of a grain and its substructure

These observations point out the connection between topography and the grain boundaries, and then the connection between topography and slip-systems. It also underlines that the intragranular projection, regardless of the neighboring grains, reveals the physics of grain boundary behavior. Indeed, one can note that many subgrains are visible in figure 4.10 and the same intragranular projection has been done for every subgrains. Nevertheless, clear discontinuities are not observed at every grain boundaries but only where the surface topography also reveals it. It allows a local validation, at least in the present case, of experimental data treatment hypothesis, especially bilinear intragranular strain field (see figure 4.10 left) and intragranular projection of experimental fields regardless of neighbors.

Picture 4.11 focuses on another millimeter grain composed by some twins. This picture allows the comparison, at 253 MPa of nominal stress, of (a) the shear strain ε_{12} (%), (b) the thermal field (mK) and (c) the surface micrography. This grain is interesting since it is localized at the heart of the heating region (see figure 4.9).
Figure 4.11 (a) emphasizes on one hand, that the subgrain noted A localizes very intense contractions compared to neighbors, even compared to the whole microstructure. Note that its left part exhibits a shear strain close to 0%. In parallel, thermal field (see figure 4.11 (b)) exhibits a very intense heat localization exactly in the same grain and in the same part of it, i.e. at the grain boundary between subgrain noted A and the one noted B. The local interphase is noted I (see figure 4.11 (c)).
One clearly observes in figure 4.11 (b) the thermal wave front propagation from the point I through the subgrains A and B. One also observes that the kinematics of thermal wave front propagation is not similar in both subgrains. In the subgrain A, the temperature ranges from 405 to 345 mK from the left side to the right side of the grain. In the subgrain B (same grain length), the temperature ranges from 405 to 365 mk. This difference of kinematics leads to the appearance of a thermal discontinuity on the left part of both grains. Note that this discontinuity does not exist at point I. It seems that this difference of thermal gradient along each grain is related to the gradient of shear strain. Indeed, in grain A the gradient of shear strain is greater as well as the gradient of temperature. Thus one observes here that, significant discontinuities of temperatures do not occur at every grain boundaries and probably reflect variations of the kinematic of temperature proper to each grain.

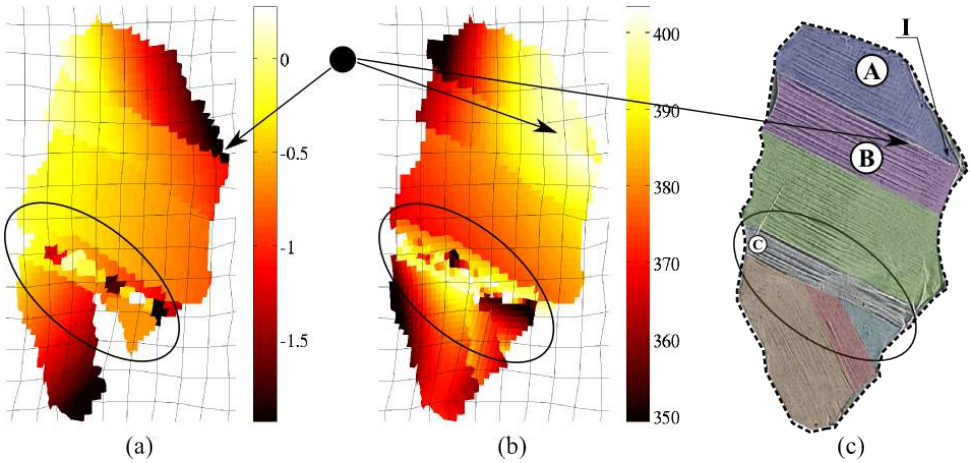

Figure 4.11: Strain field ε_{11} (%), temperature (mK) at 253 MPa of nominal stress and micrograph after test

An other thermal localization is observed in grain C. According to figure 4.11 (c) this subgrain exhibits, with subgrain B, the more intense slip-marks within the studied grain. Temperature and micrography of surface specimen are therefore consistent.

This brief and qualitative observation of local shear strain, temperature, surface micrography and surface topography evidences that intragranular fields are potentially valid for intragranular investigations.

4.4 Plastic flow at intragranular scale

4.4.1 Intragranular kinematic and thermal fields

In the previous section, thermomechanical fields at different instants of loading have been analyzed in order to qualitatively improve the knowledges about the thermomechanical couplings within polycrystalline aggregate. It has been shown that within this complex structure, temperature and strain are strongly connected. One proposes in this section to focus on 4 grains in order to analyze the local strain tensor, the appearance of plasticity and possible relations with thermal fields. Grains are pointed on the surface micrography after the test and on the grain boundary network in figure 4.12 (a) and (b) respectively. Note that it does not consist in an exhaustive investigation of intragranular thermo-elasto-plasticity.

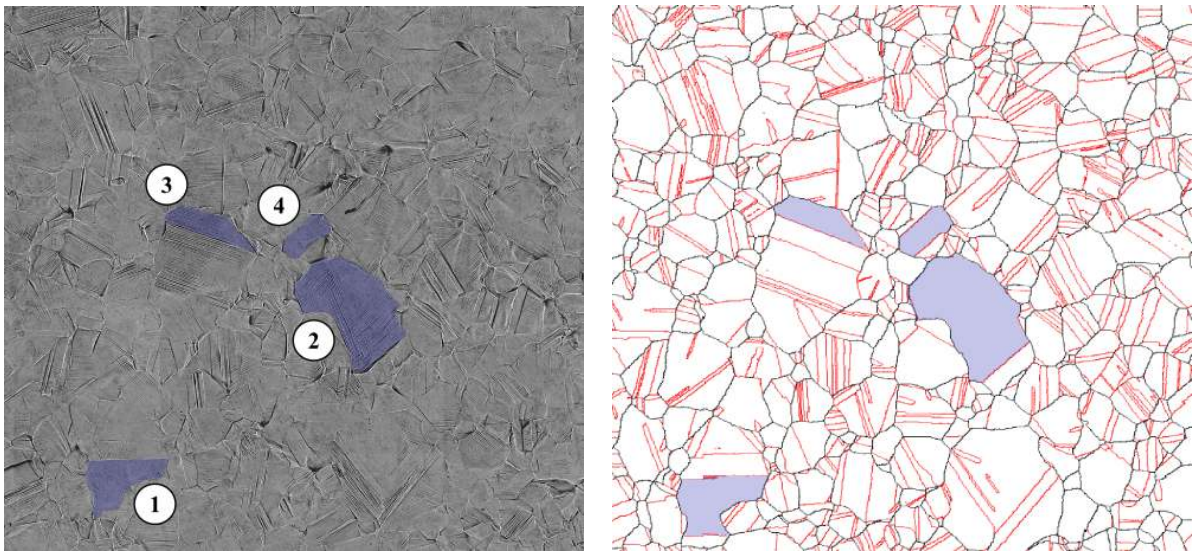

(a) (b)

Figure 4.12: Localization of analysed grain on: (a) the surface micrography after the test and (b) the grain boundary network (in black: ordinary grain boundaries, in red: twin $\Sigma 3$ boundaries

Some grains have been chosen to account for different criteria:

- C_1 **- *grain size***: grains contain enough $100\mu m$x$100\mu m$ regions in order to ensure a great relevance of intragranular data as regard of spatial measurement resolution (see chapter 2.1).

- C_2 - ***plastic mechanism types***: 1 grain exhibits single slip and three others double slip. More grains containing multiple slip have been chosen, on one hand because they are statistically bigger than others (see C_1 constraint), and on the other hand since it allows really to test the accuracy and limits of strain fields. Indeed, one has seen in chapter 3.1 that the intragranular strain fields are bilinear. Thus it cannot capture simultaneously two slip directions and associated gradient of intensity.
- C_3 - ***grain shape and properties***: the 4 chosen grains exhibit very different shape and size. In addition, two of them are surrounded by twin $\Sigma 3$ boundaries.

The entire procedure of analysis as well as the used tools are introduced in this section. Nevertheless, only detailed results concerning one specific grain are presented. A summary of the 4 other grain results is provided and refers to appendix I.1 for more details.

One considers the grain n^{o}1. Table 4.1 presents its statistical data coming notably from the ***SlipEx*** routine introduced in chapter 1.1.
According to table 4.1, its grain surface is 0.16 mm^2 which is widely over the mean one and it is composed by 16 cells of 100x100 μm^2. It allows a great accuracy of intragranular field, according to metrological procedure (see chapter 2.1). It exhibits 2 kind of slip-marks: some makes an angle of 41.08^o compared to the loading direction and corresponds to the C_1 slip-system. For this system, the Schmid factor is 0.294. Remainders marks make an angle of -18.29^o compared to the loading direction and corresponds to the A_6 slip-system. The Schmid factor is 0.269.

In agreement with Schmid theory, i.e. the maximum Schmid factor criterion, one could imagine that the C_1 system activates first and then the A_6 one. Remind that the Schmid theory is verified while the local stress direction remains close to the external one, i.e. while the local triaxiality remains low. Moreover one notes that Schmid factor are significantly low. It points out that the grain is unfavorably oriented for plastic slip. This point is confirmed by the normalized mean slip-mark density, i.e. the mean slip-mark density per grain relatively to the highest density of the global field. Indeed, its normalized density is 42% which is relatively low compared to the rest of the specimen.

size (mm^2)	0.16		
100x100μm^2 cells	16		
normalized slip-mark density (%)	42		
Slip mark orientations (^{o})	41.08	-18.29	
Activated systems	C_1	A_6	
Schmid factors	0.294	0.269	
Crystal orientation (rad)	3.73	0.73	3.19

Table 4.1: Slip-system statistics of grain n^{o}1

Figures 4.13 (a), (b) and (c) present the out-of-plane displacement (μm) measured after test, the slip-mark orientation (^{o}) and the normalized density field of slip-mark (%).

One could first point out a very significant correlation between three quantities. In the center part of the grain, C_1 system is activated within a large intragranular region. In parallel, A_6 system is activated on reduced areas (on the extreme left and on the right shown in figure 4.13 (b) and (c)). Thus, the grain is divided into two parts, where each system acts alone. It is in total agreement and well connected to surface topography (see figure 4.13 (a)) which exhibits a gradient of $\approx$2 μm between both domains. The border is pointed out with a black line. A plateau at $\approx$-5 μm is observed within C_1 domain while a plateau at $\approx$-2 μm is observed within A_6 one. In addition, one could note that the lack of C_1 slip mark observed on the left extremity of the grain in figure 4.13 (b) and (c) is connected to another gradient on the surface relief from -5 to -7 μm (see figure 4.13 (a)).

Such observations evidence a clear connection between slip-system, slip-mark density and surface topography. It is moreover quite impressive to observe that the natural border which divide the grain relief into two parts (see figure 4.13 (a)) perfectly skirts the area where no slip-mark is observed in figure 4.13 (c) and pass from C_1 system border to A_6 one.

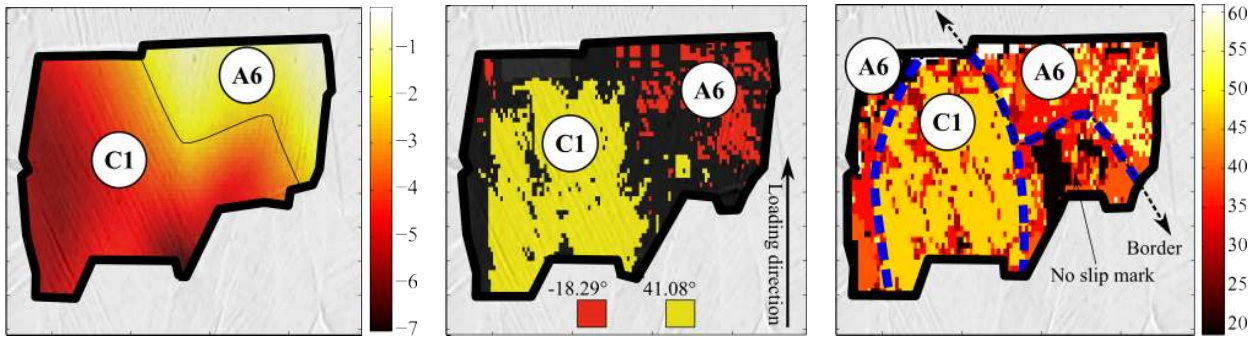

(a) in μm (b) in degree (c) in %

Figure 4.13: (a) Intragranular out-of-plane displacement, (b) slip-marks orientations and (c) normalized slip-mark density as well as associated slip-systems.

The observation of the specimen after the test allows proposing a first scenario. Firstly, the grain has probably undergone plastic strain by means of the slip system C_1 on a large part of its intragranular domain (maximum Schmid factor). Then, plastic strain has initiated on system A_6. The fact that the A_6 system is identified slightly on left grain boundary and on the right one (not at the grain center) allows imaging that the double slip is activated to accommodate incompatible slip on left and right grain boundaries. The initiation of A_6 system leads to a "gap" of out-of-plane displacement at the interface between C_1 and A_6 system. In addition, the fact that the C_1 domain and the region where no slip-mark is observed (see figure 4.13 (c)) are at same altitude evidences that the A_6 plateau has been produced later by the local shear appearance.

Let us now deal with in-situ kinematic and thermal measurement to verify the relevance of the previous scenario.
One focuses on the one hand on the intragranular shear strain, ε_{12}, which is clearly connected to plastic slip activity in the plane $1-2$, i.e. the surface specimen[1], and on the other hand on the intragranular thermal field. Figure 4.14 presents intragranular shear strain (right column in %) and thermal field (left column in mK) at different loading level: 106 (1^{st} row), 191(2^{nd} row), 220 (3^{rd} row) and 253 MPa of nominal stress (4^{th} row). Thus, two first figures rows are taken within the macroscopic elastic domain and the two last ones within macroscopic plastic domain. Black lines follow isovalues to underline gradient orientations.

Let first briefly recall assumptions of kinematic field projection which are detailed in chapter 3.1. Strain fields are bilinear per grain. Thus shear strain field provides two informations: (1) a main shear direction which is the one of its isovalues. Note that this direction is related to slip-marks orientations; (2) a shear intensity trend, fitting at best the variation of shear intensity along neighboring slip-marks.

Firstly, one observes in ε_{12} fields (see figure 4.14 2^{nd} column) a change in isovalue orientations along the deformation path. Firslty, from 106 to 191 MPa of nominal stress, the mean shear strain varies from -0.2 to 0.003 % with a decreasing shear strain gradient from 0.17 to 0.13 %. During this period, isovalues have a fixe angle of $\approx 41^o$ compared to the loading direction. Thus, isovalues of shear strain are oriented as C_1 slip marks (see table 4.1). The microstructure is superimposed on each field to evidence that slip-marks are parallel to shear strain isovalues. Thus one could conclude that from 106 to 191 MPa of nominal stress the grain undergoes single slip due to the activation of the C_1 slip-system. It is totally in line with the previous scenario based on maximum Schmid factor criterion.
Secondly, from 220 to 253 MPa of nominal stress and up to the end of test (not presented here), the mean shear strain varies from 0.05 to 0.1 % with an increasing shear strain gradient from 0.4 to 1 %. During this period, isovalues have a fixe angle of $\approx$-20^o compared to loading the direction. Thus, isovalues of shear strain are oriented as A_6 slip marks (see table 4.1). Thus one could conclude that from 220 MPa of nominal stress to the end of the test, the grain mainly undergoes single shear due to the activation of the A_6 slip-system. The fact that the orientation of shear strain isovalues does not deviate from the A_6 slip-marks orientation evidences that the system C_1 is currently not activated anymore. Otherwise, the orientation of shear strain isovalues is a compromise between both orientations. This second activations remain in line with the previous scenario.

Thus according to in-situ kinematic measurements, one evidences that first slip-system is already activated from 106 MPa of nominal stress. Then between 191 and 220 MPa of nominal stress, a transition has occurred between the first slip-system and the second one. note that 223 MPa corresponds to the macroscopic $R_e^{0.2\%}$. Nevertheless, as the frequency of kinematic measurement is 7Hz (see chapter 2.1), no data has been registered between 0 and 106 MPa of nominal stress as well as between 191 and 220 MPa. Thus, 106 and 220 MPa constitutes the upper bound of C_1 and A_6 yield stress respectively.

[1] 2 loading direction, 1 transversal one and 3 the out-of-plane one

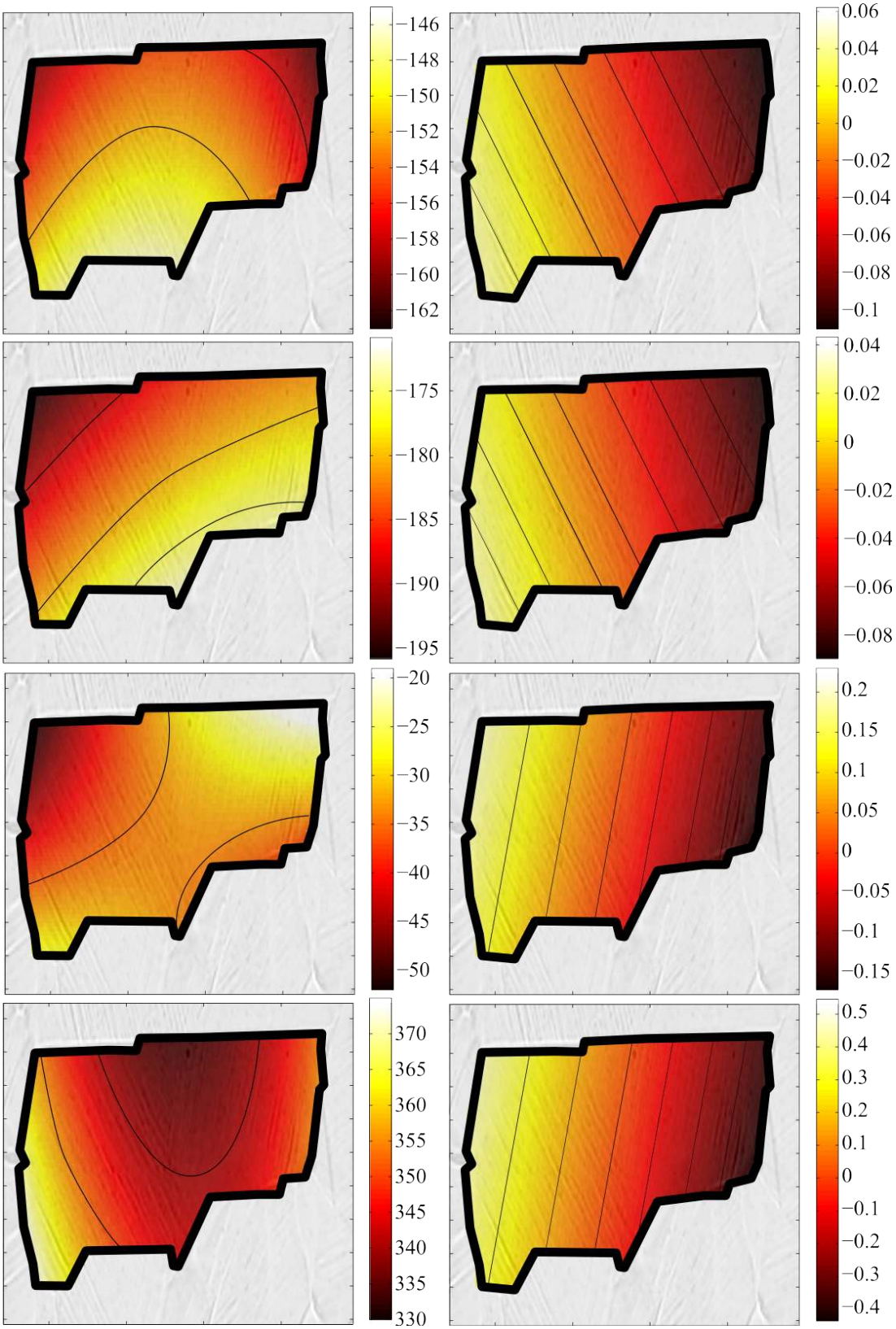

Figure 4.14: Intragranular temperature (left side (mK)) and shear strain ε_{12} (right side (%)) at different instants of loading: 106 - 191 - 220 - 253 MPa

In agreement with previous point, let us estimate the Critical Resolved Shear Stress related to the first activated system from in-situ kinematic measurement. According to figure 4.13 (a), two distinct intragranular domain exist. The left one is more or less related to system C_1 while the right one is related to system A_6.
First, one assumes that the mean plane strain tensor over the domain C_1 (see figure 4.13 (a)) at 106 MPa is $\boldsymbol{\varepsilon}_{106}^{C_1}$ and that 106 MPa corresponds to the C_1 yield stress:

$$\boldsymbol{\varepsilon}_{106}^{C_1} = \boldsymbol{\varepsilon}^e \tag{4.9}$$

where $\boldsymbol{\varepsilon}^e$ is the elastic strain tensor related to C_1 domain. Let us assume now a plane stress assumption to estimate the 3D elastic plane strain tensor noted $\tilde{\boldsymbol{\varepsilon}}^e$. Note that this assumption is necessarily verified on free surface, i.e. specimen surface. Details and equations related to plane stress assumption could be found in 5.2. Finally, let the fourth rank tensor $\tilde{\mathbb{C}}$ be the local elasticity tensor expressed in the specimen reference system (using crystal orientation see section 1.3), $\boldsymbol{\sigma}$ is the stress tensor and $\mathbb{M}^s$ is the Schmid tensor. It gives:

$$\boldsymbol{\sigma} = \tilde{\mathbb{C}} : \boldsymbol{\varepsilon}^e \tag{4.10}$$

$$\tau^s = \boldsymbol{\sigma} : \mathbb{M}^s \tag{4.11}$$

where τ^s is the mean Resolved Shear Stress over the C_1 domain at 106 MPa of nominal stress.

Table 4.2 presents RSS values on each slip-system of the local crystal lattice at C_1 yield stress, i.e. 106 MPa of nominal stress. The table points that C_1 system exhibits the highest RSS (36 MPa) and A_6 system the second more significant (-27 MPa).

A_2	A_3	A_6	B_2	B_4	B_5	C_1	C_3	C_5	D_1	D_4	D_6
6	−20	−27	18	10	−9	36	25	12	−12	−6	−6

Table 4.2: Mean Resolved Shear Stress (RSS) over the C_1 domain at 106 MPa of nominal stress

Many comments could be done on these results:

- It is totally in line with the Schmid theory. First, both maximum Schmid factor systems have the highest Resolved Shear Stress. In addition, C_1 system exhibits higher RSS than A_6 which is in line with the Schmid factor levels. It points out that the local stress tensor is under Schmid assumptions, i.e. the stress field is locally mainly uniaxially oriented as the external loading direction.

- This result is totally in line with specimen surface investigations. Within the C_1 domain, according to figure 4.13 (a) and (b), C_1 system exhibits effectively the highest Resolved Shear Stress. It is necessarily the activated one. According to surface investigation as well as RSS values, the second system is necessarily the A_6 one.

- This result is also in line with the analysis of shear strain isovalues orientation. Indeed, it evidences that the C_1 system is activated at 106 MPa of nominal stress. Thus, the orientation of shear strain isovalues compared to slip-marks allow identifying the activated slip-system.

- Finally, this result is clearly in line with litterature. According to in-situ kinematic measurements, and assuming that 106 MPa of nominal stress correspond to the upper bound of C_1 yield stress, 36 MPa (see table 4.2) corresponds to the upper bound of the material Critical Resolved Shear Stress ($CRSS$). This value is clearly in line with CRSS measured on single crystal of AISI 316L at room temperature. Indeed, in [Feaugas 2009] the author shows that the initial value of CRSS is in the order of 30 MPa.

In addition, such accurate results validates the plane stress assumption, at least within this specific grain as well as the plasticity scenario previously introduced.

In parallel, figure 4.14 presents, in 1^{st} column, the intragranular thermal evolution.
From 106 to 191 MPa, the mean temperature varies from -153 to -181 mK with an increasing gradient from 17 to 25 mK respectively. Then, it ranges from -36 to 347 mK with an increasing gradient from 33 to 45 mK. It points out first, a drop of temperature from 106 to 191 MPa with an increase of intragranular thermal heterogeneities and then, an increase of temperature from 220 to the end of the test also with an increase of intragranular heterogeneities. One shows secondly that thermal intragranular gradient remains very low along the deformation path. Nevertheless, it is interesting to point out in figure 4.14 that the hottest region is firstly located at the bottom of the C_1 domain (activated from 106 to 191 MPa) and then located on right and left grain boundaries, from 220 to 253, where A_6 system is activated. It shows a connection between intragranular thermal gradients and intragranular localization of plasticity.

To understand how the intragranular thermal field could reflect the intragranular elasto-plasticity, the time variation of temperature is analysed. It is important to note that the thermal measurement frequency is originally 140 Hz, i.e. 20 time higher than kinematic one. Thus it necessarilly provides more information.

Figure 4.15 (a) presents the temperature evolution of considered grain during a first part of loading, i.e. from 0 to 200 MPa. One observes successively, the mean decrease and the increase of temperature, and the nominal stress evolution. One could note the 3 kinematic data-points marked on the nominal stress curve. Note, from data-point 2 to 3 (106 to 191 MPa), the figure recalls that the system C_1 is activated (see in-situ kinematic measurement).

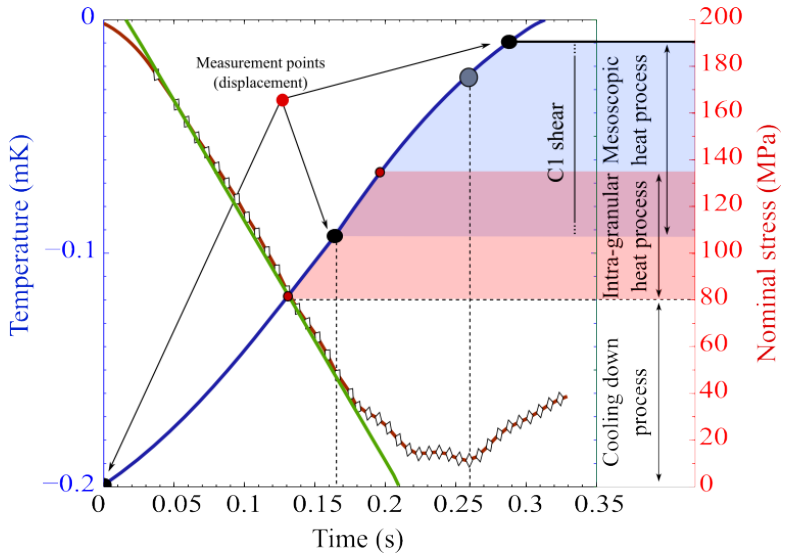

Figure 4.15: Intragranular mean temperature (red - mK), linear regression with Maximum Likehood Method (green) and nominal stress (blue - MPa) from beginning to end of macroscopic elasticity

One has seen in section 4.1 that inflection within macroscopic thermal evolution points out the transition between a perfectly elastic behavior and the appearance of a dissipative mechanisms which tends to increase the temperature. At local scale the problem is more complex. Indeed, the local temperature could deviate from its linear elastic drop because of a dissipation (local plasticity) but it may also be influenced by neighboring dissipation impacting a large domain due a to conductive front. One proposes here to investigate this point.

In this way one deals first with the mean temperature evolution. With the help of the Maximum Likehood Method and a linear regression it is possible to identify the more probable instant when the mean thermal curve looses its linear drop. The green straight line fitting the thermal evolution drop corresponds to the identification. One observes that the mean loss of linearity occurs at 106 MPa of nominal stress reaching -153 mK. Then, the minimum temperature reaches -189 mK at 176 MPa of nominal stress. So, the mean thermal response of the grain provides an crutial information: from 0 to 106 MPa the grain linearly cools-down, then a local or non-local dissipation occurs up to 176 MPa when the grain initiates a heating process. It is interesting to note that 106 MPa corresponds exactly to the initiation of intragranular C_1 system captured by the in-situ kinematic measurement. Note that the stress domain initiated from the loss of thermal linearity is denoted "mesocopic heat process" in figure 4.15.
Then a similar procedure, for thermal yield identification, could be used on each material point of the intragranular domain. It allows accessing the local loss of thermal linearity. Figure 4.16 presents this cartography expressed as a function of the nominal stress.

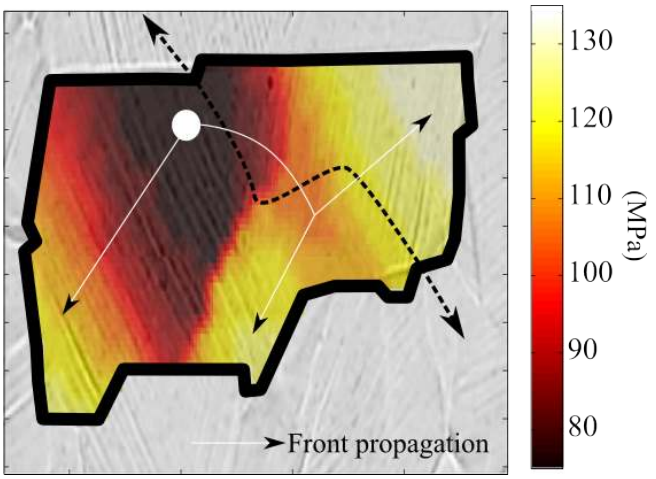

Figure 4.16: intragranular field of thermal inflection appearance expressed as function of nominal stress (in MPa)

One observes that thermal inflection gradually appears within the grain. At 78 MPa of nominal stress, the loss of thermal linearity initiates and propagates in a continuous way in a limited domain. Indeed, toward the left, the thermal inflection propagation front propagates continuously up to 130 MPa when it reaches to left grain boundary. To the right, it is rapidly stopped at ≈100 MPa. The border is very clear. Then it follows the superimposed white arrow and propagates through the other part of the grain. Note that the dotted line which crosses the grain corresponds to the separation between C_1 domain and A_6 one (see figure 4.13 (a)).

The first intragranular loss of thermal drop linearity initiates at 78 MPa of nominal stress within the C_1 domain and then propagates continuously through it (in the left direction). It confirms that the local inflection of temperature is due to intragranular plasticity activity and not to dissipation in a neighboring grain. Thus, figure 4.16 reveals that the first dissipative mechanism has occurred by means of plastic activity on C_1 slip-system. It is in line with previous observations (crystallography, micrography, topography, kinematic). It also reveals that the first C_1 system activation has occured early compared to the upper bound provided by in-situ kinematic measurement. Using the same procedure than previously, in table 4.2, one estimates the associated local value of Critical Resolved Shear Stress which ≈32 MPa, in the material point where the first dissipation appears. This value also is in the same order of magnitude as the one observed for a single crystal of AISI 316L [Feaugas 2009].

Figure 4.16 proposed additional elements to the previous scenario. From 0 to 78 MPa of nominal stress, the entire grain is elastic. It exhibits a uniform drop of temperature. At 78 MPa, the system C_1 is activated within a part of the grain. Local dissipation occurs, and the thermal inflection wave front propagates continuously within the C_1 domain where the behaviour is quite uniform. While the domain C_1 dissipates, the neighboring domain A_6 is still elastic, thus tends to linearly decrease

the local temperature. This gap of thermal behavior may explain why the thermal inflection wave front does not propagates continuously from the C_1 to A_6 domain. Indeed, figure 4.16 reveals at the interface between both domains a discontinuity of thermal response. Note that this discontinuity is not a spatial discontinuity of temperature but a temporal one. Unlike the part of the grain which thermally inflects, the other part still try to linearly decrease up to a critical instant when the elasticity does not balance anymore the dissipation. At this time the inflection wave front propagates. Note that the clear "thermal wall" observed in figure 4.16 does not follow exactly the natural topographic border. Nevertheless, the connection seems obvious. Moreover it is interesting to note that the wave front propagation (toward the right) passes first through the region where no slip-marks are observed in figure 4.13 (b) and (b). It evidences a clear connection between the thermal wave front propagation and the gradient of dissipative behavior, the gradient of surface topography, the gradient of surface state. Finally one notes that the final and finer estimation of Critical Resolved Shear Stress of the studied grain is 32 MPa.

4.4.2 Resolved Shear Stress identification

A brief summary of the results coming from the study of 4 grains detailed in appendix I.1 is proposed.

Figure 4.17 presents intragranular first dissipation appearance observed in 4 grains as a function of the nominal stress. It has been evidenced within intragranular analysis (see appendix I.1 and section 4.4) that the intragranular dissipation threshold exists and allows a fine description of plasticity appearance, notably in terms of intragranular location and slip-system. It also allows the estimation of a local Critical Resolved Shear Stress in agreement with classical results. Finally, it was pointed out that the thermal inflection wave front does not propagate continuously within intragranular domain, especially when multiple slip systems are activated. This point is more clear when slip-bands do not cross each other, i.e. when one slip-system acts mainly in a own intragranular domain. In such case, a specific surface topography has also been observed and interacts probably with temperature propagation. Indeed, when slip-system domains are disconnected (does not cross each other), one has observed that the out-of-plane displacement is clearly connected to these domains and then interface between them is frequently well marked in terms of surface relief.
Figure 4.17 presents, for 4 studied grains, the thermal inflection wave front as well as the CRSS associated to the first dissipation. Note that the grains (a) and (c) exhibit a double plastic shear which does not cross each others, (b) exhibits a double crossing plastic shear, and finally (d) exhibits a single plastic shear.

One observes that for 3 grains, the Critical Resolved Shear Stress estimated from dissipation threshold ranges from 22 to 32 MPa which is in line with literature, notably [Feaugas 2009]. In figure 4.17 (a) and (c), one observes that a clear discontinuity appears in the thermal wave propagation. In both cases it has been related to slip-system domain interface. One could note that, in each studied cases the dissipation threshold is reached in the first activated system. This point has been verified by means of complementary analysis such as slip-marks identification, Schmid theory and in-situ kinematic measurements.

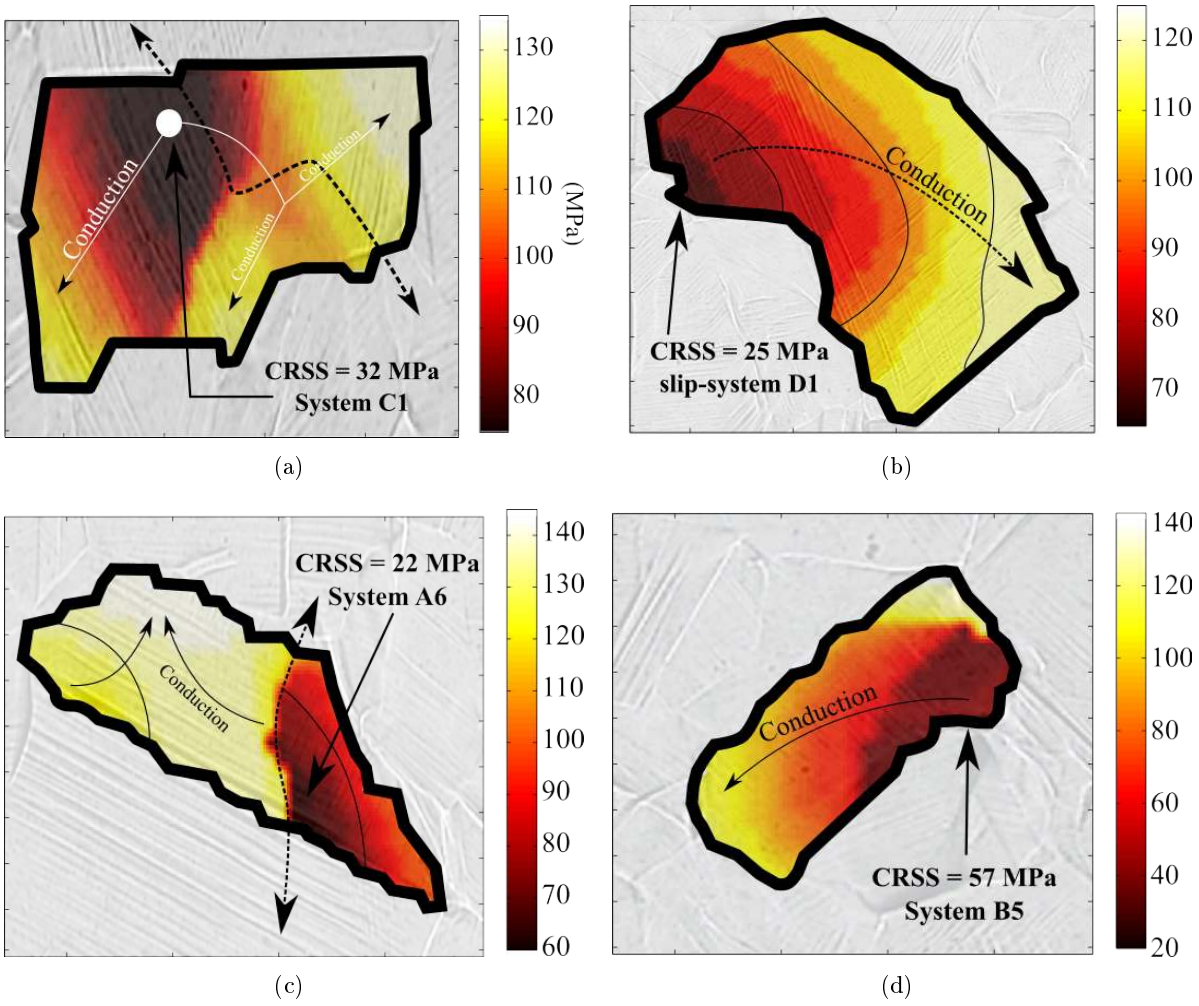

Figure 4.17: Thermal inflection appearance as function of nominal stress for 4 grain and CRSS related to the first dissipation. Grains (a) and (c) exhibit uncrossing double plastic slips, (b) exhibit crossing double plastic slip and (d) single plastic slip.

Finally, one observes in figure 4.17 (c) that the dissipation yield corresponds to a Critical Resolved Shear Stress of 57 MPa, which is about two times higher than previous results. Different cases could be considered:

- the local CRSS experimentally ranges from 20 to 60 MPa in the polycrystal.
- the thermal inflection appears to be due to a conductive phenomenon from the neighboring grain. According to the low density of slip-mark observed within this grain, it is possible that its intrinsic dissipation has not been captured by thermal in-situ measurement.

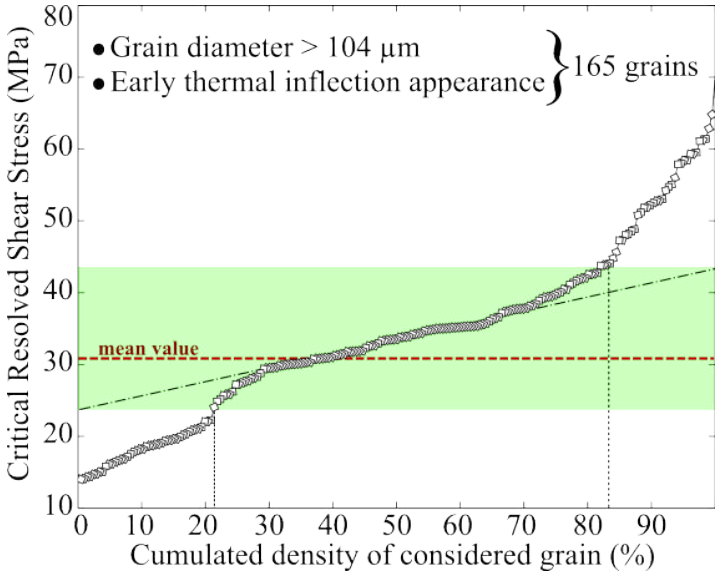

Figure 4.18: Critical Resolved Shear Stress (in MPa) identified at intragranular domain function of the cumulated density of considered grain (in %)

It reveals the key question when studying a local thermal evolution. Contrary to kinematics, the temperature is space dependent. To evidence the relevance of such CRSS identification by means of dissipation threshold one proposes a statistical approach.

To perform an analysis which makes sens, some grains are not considered:

- according to chapter 3.1 one knows that the minimum thermal resolution is 100x100μm^2 for the temperature magnitude and spatial position. Thus every grains whose grain size is lower than such window are not considered.
- once the macroscopic thermal inflection occurs, one could imagine that local inflections are mainly leaded by conduction than by the own local plastic dissipation. According to this point, every grain whose first intragranular thermal inflection appears after the macroscopic one are not considered. Recall that the macroscopic thermal inflection appears at 110 MPa.

Picture 4.18 presents the Critical Resolved Shear Stress identified at intragranular domain function of the cumulated density of considered grains. note that 165 grains match both previous contraints and are considered here. It represents ≈50% of the studied area.
One observes that the identified distribution of CRSS ranges from 14 to 70 MPa, and that the mean value is ≈30 MPa. One also observes a kind of dense plateau from 24 to 44 MPa. It constitutes 60 % of considered grains, i.e. 100 grains. Thus 60 % of grains appropriated for dissipation threshold identification provides a Critical Resolved Yield Stress in the expected magnitude, i.e. about 30 MPa. This results underlines the relevancy of such local and multiphysics investigation.

4.4.3 Partial conclusion

Within this section the intragranular in-situ measurement of temperature and strain field has been discussed. One grain has been studied in details and 3 others are reported in appendix I.1.
The relevancy of intragranular thermal and kinematic fields has been demonstrated and a clear connection between crystallography, activated slip-systems, surface topography, shear strain and temperature has been evidenced. It has been shown that the intragranular transient shear strain and transient temperature variation allow the understanding of crystalline plasticity mechanisms. One has notably observed that when a grain undergoes multiple and distinct plastic slips, the thermal activity is different in each slip domain as well as the surface topography.
Finally, a new method for Critical Resolved Shear Stress identification has been proposed. It is based on a local dissipation threshold. CRSS has been statistically identified over the specimen gauge-section. Obtained levels are in agreement with the litterature.

Chapter 5

Heat source achievement

Contents

The purpose of the present chapter is to go toward the ultimate aim of such investigation of thermo-mechanical coupling within polycrystals: the energy balance achievement at intragranular scale. The chapter is split in three points: (1) the energy balance achievement with an homogenized point of view, i.e. at a macroscopic scale, in order to compare data with some results extracted from the literature; (2) the achievement of energy balance at intragranular scale assuming some "rough" assumptions on thermal exchanges and intragranular stress field; (3) finally, the 2 dimensional intragranular Laplacian of temperature obtained from intragranular projection hypothesis is discussed regarding its associated heat dissipation term, $\rho C_v \dot{T}$ and the second principle of thermodynamics.

5.1 Homogenized energy balance

As it has been precised within the general introduction, the determination of heat source fields within the gauge-section of specimen thanks to energy balance achievement in its local form is one of the ultimate aim of the present work. It has been firstly pass through the analysis of thermomechanical couplings and plasticity mechanisms at such scale. Nevertheless, 3D cases, notably when the scale of observation tends to be lower than characteristic sizes of specimen, impose to make some assumptions, in particular on the form of the heat losses through the specimen or the aggregate boundaries and on the elasto-plastic partition occurring at local scale. In this section, one proposes to deal with homogenized energy balance, i.e. to consider mean quantities over the specimen gauge-section. It will permit to estimate the partition between dissipated and latent energy over the whole specimen gauge-section during the monotonic tensile test and to compare the dissipative behavior of the present material with other studies.

5.1.1 Stored energy partition

Let us first underline that the present material is a polycrystal, thus an heterogeneous material which undergoes incompatible plastic slips and gradient of plasticity ... Within such heterogeneous material, scales transitions are not trivial, in particular concerning energies. Let us deal with a simplified model of two misoriented crystals.

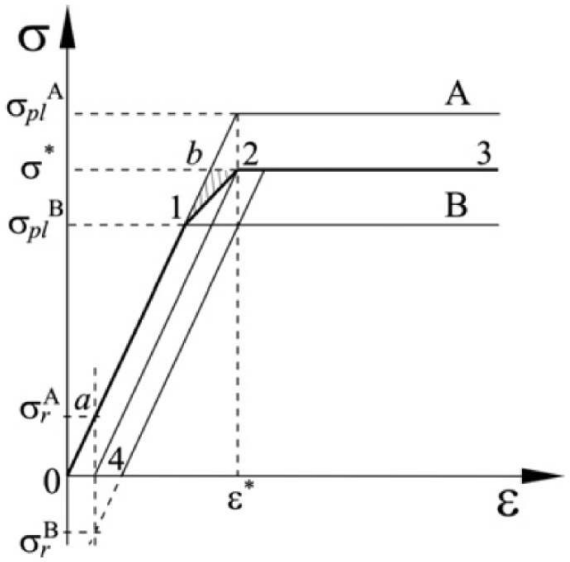

Figure 5.1: Stress-strain relation for two adjacent elastic-perfectly plastic elements (A and B) and associated homogenized response (1, 2, 3) extracted from [Oliferuk 2009]

Figure 5.1 presents the stress-strain response of two adjacent elastic-perfectly plastic elements (A and B) modeled by a finite-element method [Oliferuk 2009]. Each element has its own yield stress noted σ_{pl}^A and σ_{pl}^B respectively. The path 1, 2, 3 presents the homogenized response of both elements. Although the local behavior of both elements is perfectly plastic, the homogenized response exhibits an apparent "hardening" path as soon as A enters the plastic domain. Nevertheless, no hardening occurs but the elastic energy ($1b2$ area on figure 5.1) is stored within the material. This energy is the residual stresses elastic energy, appearing at grain boundaries to accommodate incompatible plastic strain and to preserve the kinematic continuity. If one considers now a local hardening for the elements A and B, an additional energy is stored within each elements corresponding to the hardening energy, physically stored in the form of dislocations and dislocation structures. This simple model underlines the natural partition of stored energy at homogenized scale of a polycristal. A first part is stored within residual stresses elastic energy at grain boundaries and is recovered at the end of a symmetric cycle of loading. Note also that one speaks about stored energy due to third order stresses, i.e. intergranular ones [Diligent 2001]. A second part is stored within hardening occurring at intragranular domain due to local hardening flow and could only be released under recrystallization

conditions (see chapter 0.1). One also speaks about stored energy due to second order stresses, i.e. intragranular ones [Diligent 2001]. Considering finally a real polycrystal, composed by thousands of grains subjected to specific plastic strains, one obtains an homogenized behavior similar to the one of the specimen studied in this work (see figure 5.2), where the area (energy) noted E_{sr} is the sum over the whole grain of the areas noted $1b2$ within figure 5.1. The complementary area of the macroscopic stress-strain curve corresponds consequently to the internal or residual stress field stored energy, noted E_{sr} for Energy Stored due to intergranular Residual stresses. The other part of stored energy is somewhere within the E_a domain and could not be explicitly extracted from the macroscopic stress-strain response [Oliferuk 2009], as the knowledge of the local flow stress is required. To conclude, it is very important to understand that the stored energy estimated through the heat equation (see appendix A.1) with the help of macroscopic temperature, stress and strain is actually the sum of both introduced contributions. Note that the inequality between the macroscopic stored energy and the sum over the whole polycrystal of hardening stored energy has been already underlined by many authors [Mandel 1965, Suquet 1987, Aravas 1990, Oliferuk 2009] and could be written as follow:

$$E_s = \int_{t=0}^{t=T} (< \boldsymbol{a} : \dot{\boldsymbol{\varepsilon}}^p > + < \boldsymbol{\sigma^r} : \mathbb{S} : \boldsymbol{\sigma^r} >) \cdot dt \neq \int_{t=0}^{t=T} < \boldsymbol{a} : \dot{\boldsymbol{\varepsilon}}^p > \cdot dt \tag{5.1}$$

where E_s is the total stored energy per volume unit during the test, $\boldsymbol{a}$ is the thermodynamical force associated to the plastic strain, $\dot{\boldsymbol{\varepsilon}}^p$ the time derivative of plastic strain, $\boldsymbol{\sigma^r}$ the local residual stresses, $\mathbb{S}$ the compliance tensor and $< \bullet >$ means the mean value over the aggregate. In addition, as explained earlier and as it has been shown, for example in [Oliferuk 2009], the homogenized term $E_{sr} =< \boldsymbol{\sigma^r} : \mathbb{S} : \boldsymbol{\sigma^r} >$ could be estimated, under uniaxial condition, from the macroscopic stress-strain response. Thus equation 5.1 becomes:

$$E_s = \int_{t=0}^{t=T} < \boldsymbol{a} : \dot{\boldsymbol{\varepsilon}}^p > \cdot dt + E_{sr} \tag{5.2}$$

where E_{sr} is the complementary area of macroscopic stress-strain curve (see figure 5.2).

5.1.2 Experimental results

Let us recall the heat equation in its local form A.1:

$$\rho C_v \dot{T} - k\Delta T = (\boldsymbol{\sigma} - \boldsymbol{a}) : \dot{\boldsymbol{\varepsilon}}^{\boldsymbol{p}} + T\frac{\partial \boldsymbol{\sigma}}{\partial T} : \dot{\boldsymbol{\varepsilon}}^e \tag{5.3}$$

One can first precise the terms which are effectively measured and the unknowns terms. The temperature and displacement has been measured at intragranular scale during the whole mechanical test and the nominal stress has been provided by tensile machine. Then four terms are known under some assumptions:

- the instantaneous heat dissipation term at intragranular domain: $\rho C_v \dot{T}$. Under the proposed calibration and denoising process, this quantity does not take into account any time variation exceeding $25Hz$ (see chapter 2.1) and any space variations which could not be captured by a biparabolic intragranular field (see chapter 3.1).

- the 2D instantaneous heat losses term at intragranular domain: $-k\Delta^2 T$. This quantity is uniform per grain, assumes an isotropic intragranular conduction and does not take into account any thermal loss at intergranular domain, i.e. grain boundaries, due to intergranular gap of temperature (see chapter 3.1).

- the total plane strain tensor: $\boldsymbol{\varepsilon}$. This quantity does not take into account any space variations which could not be matched by bilinear intragranular field (see chapter 3.1) as well as out-of-plane components.

- the nominal stress: Σ_{yy}. This quantity is a scalar. It does not provide any information about the multiaxiality of the loading and only refer to macroscopic mechanical response of the tested specimen.

Figure 5.2 corresponds to the stress-strain curve during the monotonic tensile test up to 270MPa. Different area are also drawn. They represent deformation energies which act during the deformation process.

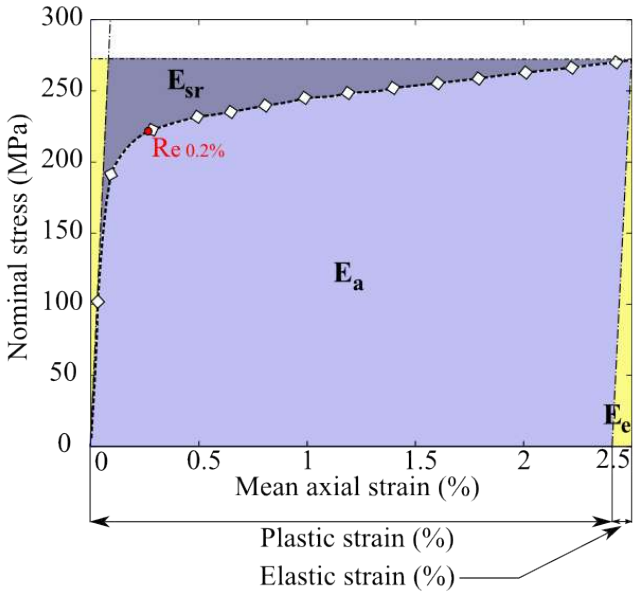

Figure 5.2: Stress/strain curve of A316L stainless steel submitted to monotonic tensile test up to 270MPa as well as definition of deformation energies.

Considering macroscopic stress-strain curve and its associated quantities, i.e. the nominal stress Σ_{yy}, the mean axial strain over the specimen-gauge section $< \varepsilon_{yy} >$ and the associated elastic modulus E, one could first give the expression of macroscopic axial plastic strain ε^p_{yy}:

$$< \varepsilon^p_{yy} >=< \varepsilon_{yy} > - < \varepsilon^e_{yy} >=< \varepsilon_{yy} > - \frac{\Sigma_{yy}}{E} \tag{5.4}$$

Then, considering the Thomson formula [Bever 1973], the thermoelastic coupling power per unit of volume, W_{the}, can be estimated as:

$$W_{the} = T\frac{\partial \boldsymbol{\sigma}}{\partial T} : \dot{\boldsymbol{\varepsilon}}^e \approx -\alpha T tr\left(\dot{\boldsymbol{\Sigma}}\right) \approx -\alpha < T > \dot{\Sigma}_{yy} \tag{5.5}$$

with α the coefficient of linear thermal expansion, $< T >$ the mean absolute temperature over the specimen gauge-section, and $tr\left(\dot{\boldsymbol{\Sigma}}\right)$ the trace of time derivative of macroscopic stress tensor . Note that the final form of thermoelastic coupling power per unit of volume contains two hypothesis: (a) a linear and isotropic elasticity, (b) an homogeneous strain and a uniaxial tensile test. One could already recall that the uniaxiality of loading is not verified in our case, at least during the beginning of the test, it will be necessary to verify the relevance of such assumption.

Then, the "0 dimensional" approach, detailed for example within [Boulanger 2004a], is followed. In this approach, one assumes that heat source distribution is uniform at any time within the specimen gauge part. This could be admitted within a global estimation of heat sources but not a local or microstructural one. Let $\tilde{\theta} =< T > -T_0$ be the variation of the bulk temperature (mean value over the specimen gauge-part) from the initial state for which the bulk temperature is denoted T_0. In this context, and reducing the 3D thermal problem to a "0D" one, one could write:

$$W_{hl} = -k\Delta T = -k\left[\frac{\partial^2 T}{\partial x^2} + \frac{\partial^2 T}{\partial y^2} + \frac{\partial^2 T}{\partial z^2}\right] \approx \rho C_v \frac{\tilde{\theta}}{\tau_{eq}} \tag{5.6}$$

with τ_{eq} a time constant characterizing specific heat losses time. It is interesting to underline that W_{hl} ranges, in our case (see parameters in table 5.1), from -0.013 to $\approx$0.05 $mJ.mm^{-3}$. It is therefore almost neglectable, at homogenized scale, compared to other energy quantities (see figure 5.3). Then, note that it is possible to evidence that τ_{eq} is completely defined thanks to specimen geometry as well as convective exchange coefficients between specimen and the environnement, i.e. the air, and between the specimen and tensile machine heads. The demonstration is done through a step by step simplication of diffusion problem from the 3D to "0D" one. Equation 5.7 presents the full expression of τ_{eq}. The demonstration is for exemple done in [Bodelot 2008].

$$\tau_{eq} = \frac{\rho C_v}{2h\left(\frac{e+l}{el}\right) + \frac{2h^*}{L}} \tag{5.7}$$

with h, h^*, e, l and L the convection coefficient exchange with the air, the tensile machine heads, the specimen gauge-section thickness, width and height respetively. Nevertheless, it is practically quite complicated to measure h^* and finally to solve the analytic form of τ_{eq}. The experimental procedure for direct time constant τ_{eq} determination could be found for exemple in [Vincent 2008]. In his case, τ_{eq} was determined for a A304 stainless steel material which is close to the material used in this study. Thus this value will be exploited here. Every material parameters and material constants are summarise in table 5.1.

As a consequence of the previous assumptions, the stored energy and the dissipated one are estimated at homogenized scale from the following equations:

$$W_s \approx \Sigma_{yy} < \dot{\varepsilon}^p_{yy} > - \left[\rho C_v \left(\frac{\partial < T >}{\partial t} + \frac{\tilde{\theta}}{\tau_{eq}} \right) + \alpha < T > \dot{\Sigma}_{yy} \right] \tag{5.8}$$

$$W_d = W_a - W_s \tag{5.9}$$

E GPa	α K^{-1}	ρ $kg.m^{-3}$	C $J.kg^{-1}.K^{-1}$	τ_{eq} s
210000	1.2x10^{-5}	8000	500	50

Table 5.1: Material parameters for conventionnal AISI 316L stainless steel

Figure 5.3 (a) presents energy quantities whose associated powers has been introduced in equations A.13, 5.5, 5.9 and 5.8. As the legend introduces it, energies are defined as the time integral over the whole monotonic tensile test (see appendix A.1). Figure 5.3 (b) focus on stored energy calculated from the energy balance (see eq. 5.8) noted E_s and from hatched area on picture 5.2 noted E_{sr}. Notations come from equation 5.2. Obtained results are compared to recent works from [Oliferuk 2009].

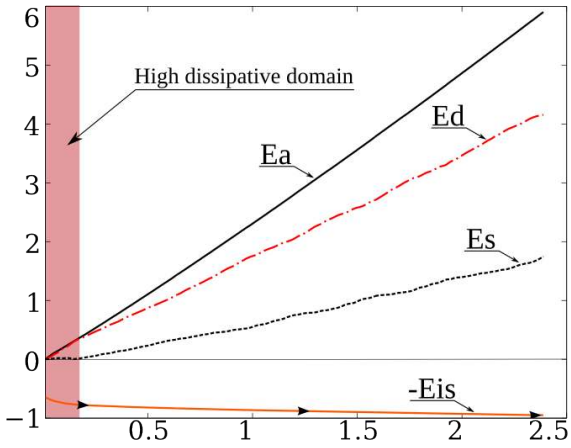

(a) $E_i = \int_{t=1}^{T} W_i . \cdot dt$ in $mJ.mm^{-3}$ with T=test time

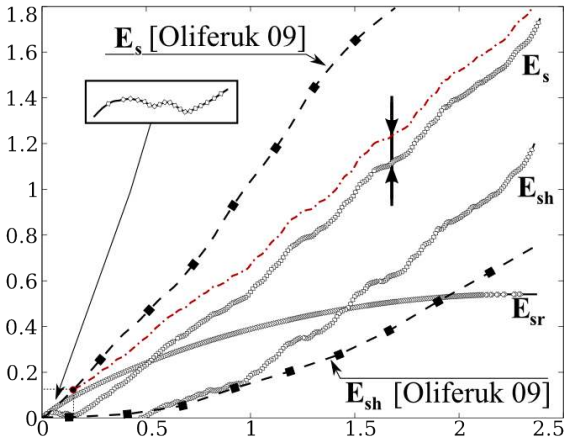

(b) E_s in $mJ.mm^{-3}$

Figure 5.3: (a) E_a total plastic work expended, E_d dissipated into heat, E_s stored in form of dislocations and residual stresses and E_{is} or E_{the} the isentropic energy due to thermoelastic couplings function of axial plastic strain (%). (b) Focus on E_s within our work and comparison with result extracted from [Oliferuk 2009] also as a function of plastic strain (%).

One observes on figure 5.3 (a) an increase of inelastic energy E_a, the dissipative one E_d and the stored one E_s up to 5.90 $mJ.mm^{-3}$, 4.15 $mJ.mm^{-3}$ and 1.75 $mJ.mm^{-3}$ respectively and a quasi constant isentropic energy around -1 $mJ.mm^{-3}$. This last point underlines that the thermoelastic phenomena are significant in elasticity and then become neglectable, notably on such material where the hardening is low (see hardening trend of stress/strain curve on figure 5.2). The picture evidences that a great part of expended inelastic work is converted into heat. Nevertheless, about 30% is progressively stored within the material. This relative great influence of stored energy on early plasticity has been underlined in many works [Bever 1973].
A relatively weird point concerns the very beginning of plasticity. Indeed 5.3 (a) reveals (red domain) that up to 0.18 % (close to $R^e_{0.2\%}$), the entire inelastic expended work is converted into heat. This point is not in line with a currently well admitted point: the ratio of energy storage on expended inelastic one is very significant at the very beginning of plasticity and then decreases to tend toward a saturate state. Chrysochoos evidenced a initial value for ratio $\beta^* = \frac{E_s}{E_a}$ close to 60% [Chrysochoos 1989b]. In our opinion this lack of storage could result from the non uniaxiality of loading. Indeed, one evidenced during the analysis of the displacement field (see chapter 4.1) that the test performed by Bodelot is actually not a perfect uniaxial tensile test, notably in elasticity and micro-plasticity. This point did not lead to misinterpretation in the last chapter since granular loading path are necessarily multiaxial whatever the macroscopic loading type. Nevertheless, in this homogenized achievement of energy balance one has assumed, notably in equation 5.4 that the inelastic expended power could be estimated only through the axial component of stress (the only known) and of strain. Under uniaxial assumption, one could imagine that the effective inelastic plastic power due to a slight multiaxiality is underestimated, notably in early plasticity. As a consequence, the lack of energy storage at the beginning of plasticity may be an underestimation of the total inelastic expended power. Note that the heat power is necessarily well estimated since it is intrinsically related to the bulk temperature and not planar quantities such as strains.

Figure 5.3 (b) focuses on the comparison of energy storage within Oliferuk works[1] also performed on a A316L stainless steel. E_{sh}[2] corresponds to the difference between the total stored energy, estimated from the homogenized heat equation, and E_{sr} the energy stored within internal stresses, estimated from the complementary area (see figure 5.2). One observes on one hand a global good agreement between total stored energies E_s and on the other hand between energies stored in hardening E_{sh}. Table 5.2 presents the following partition of total stored energy.

[1] The curve is drawn from [Oliferuk 2009].
[2] Energy Stored within Hardening

In $mJ.mm^{-3}$ at $\varepsilon^p = 2.5\%$	A316L	
	[Oliferuk 2009] (grain size not specified $\approx 10\mu m$)	Our specimen [Bodelot 2008] (grain size $\approx 120\mu m$)
Total stored energy E_s	3.2	1.75
Energy stored in residual stress field E_{sr}	2.45	0.53
$\frac{E_{sr}}{E_s}$ in %	77	31
Energy stored in hardening E_{sh}	0.75	1.22
$\frac{E_{sh}}{E_s}$ in %	23	69

Table 5.2: Partition of stored energy in parts which act on hardening process and residual stress field within A316L specimen

One observes that the present material stored about 45% less than the one used in [Oliferuk 2009] and the partition of energy is also quite different. Here, 69% of stored energy is stored in intragranular hardening processes whereas only 31% is stored to increase the elastic energy of residual stresses. Within [Oliferuk 2009] one observes more or less the reverse case, i.e. 23% is stored in hardening and 77% in residual stress field. One has to remember that the level of the residual stresses energy is intrinsically linked to the grain size, since greater is the number of grain greater are the potential number of slip incompatibilities at grain boundaries. Consequently, as at early plasticity process the total stored energy is in great part leaded by the grain size and incompatibilities one could imagine that the main difference between both studies is the grain size. As the author does not specify this size, let us assumes a classical A316L whose mean grain size is about $30\mu m$. In this case, it appears totally logical that during early plasticity the small grain material ([Oliferuk 2009]) store more than the "big" grain one ([Bodelot 2008]). Then, the small grain material stores 77% of its total stored energy within residual stress field (at intergranular domain) where as the "big" grain one store 69% in hardening (at intragranular domain).

One could observe in figure 5.3 (b) that a part of the deviation between both total stored energy E_s come from the initial lack of storage at the very begining of plasticity. This initial lack of storage also appears to be in contradiction with E_{sr} curve, since E_s is lower than E_{sr} until 0.5% of plastic strain. It leads to a negative value of E_{sh}, whereas a release of energy does not seem to be possible at such strain level, under such thermal conditions and within a polished material. This point has already been pointed out as being probably due to uniaxiality assumption. The red dotted curve represents our experimental curve translated toward the Oliferuk's one. It shows that if one removes the impact of the lack of storage at the very begining of plasticity, E_s and E_{sr} are in line and the deviation from [Oliferuk 2009] becomes: $\approx -20\%$ up to $\varepsilon^p = 0.75\%$ and $\approx -28\%$ up to $\varepsilon^p = 1.5\%$. Finally, one could also note that the inital plateau within the energy storage variation is actually composed by successive small increases and drops of storage.

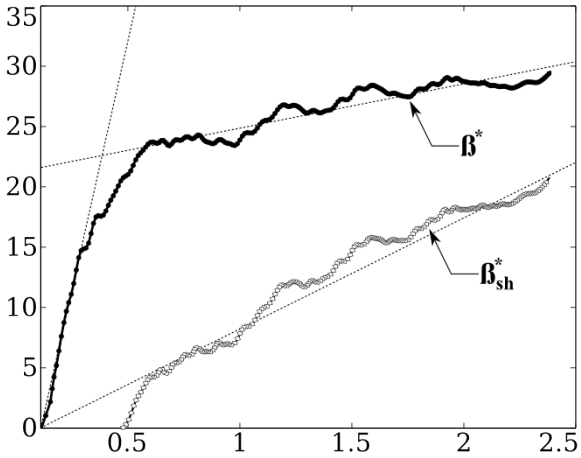

(a) $\beta^* = \frac{E_s}{E_a} = f(\varepsilon^p)$ in % (grain size≈ $120\mu m$)

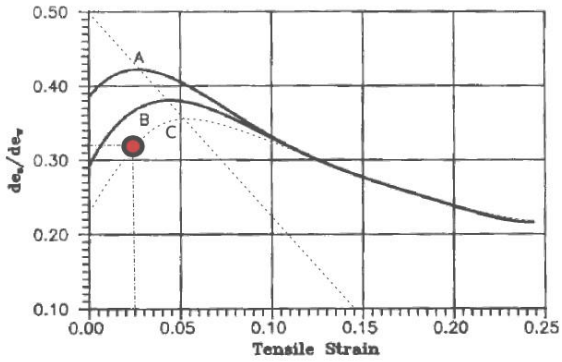

(b) $\beta^* = \frac{E_s}{E_a} = f(\varepsilon^p)$ [Oliferuk 1995] (grain sizes: $A \approx 8\mu m$ and $B \approx 80\mu m$)

Figure 5.4: Ratio of stored energy on expended plastic work function of plastic strain (%) (a) studied specimen and (b) annealed 316L: $A \rightarrow$1h 950^oC and $B \rightarrow$2h 1100^oC and water quenched

Let $\dot{\beta}$ be the ratio between the energy converted into heat and the total extended inelastic one. The factor $\dot{\beta}$ is the Taylor Quinney factor, introduced originally in [Quinney 1937] as β_{int}. Then, in similar way, let $\dot{\beta}^*$ be the ratio between the energy stored within the material and the total extended inelastic one. Using similar notations, figure 5.4 presents the evolution of ratio of stored energy on expended inelastic one, noted β^* in this study, as well as in the previous results extracted from [Oliferuk 1995] on the same material. One also presents here the hardening part of β^*, noted $\beta^*_{sh} = \frac{E_{sh}}{E_a}$.
β^* presented in figure 5.4 (a) reveals three domains: (i) a quasi linear function of plastic strain, from 0 to 0.3%, (ii) a transition phase from 0.3 to 0.6% and finally an other quite linear behavior from 0.6 to 2.5%. Note that 29.6% of inelastic plastic work is stored, and from 0.6% the storing process depends more or less linearly of the plastic strain. In parallel, β^*_{sh} presents almost a linear phase, from 0.5% of plastic strain to the end of test. Its contribution is 20.5% of total expended inelastic work. Thus ≈ 20% of the total inelastic expended energy is stored in the form of local hardening and ≈ 10% is stored to increase the residual stress field energy through grain boundary activities. 5.4 (b) presents an example of β^* evolution for two kind of A316L specimen. The specimen A was annealed 1h at 950^oC and water quenched to produce a homogeneous microstructure with a grain size of $\approx 8\mu m$ whereas the specimen B was annealed 2h at 1100^oC and then water quenched producing a homogeneous microstructure with a grain size of $\approx 80\mu m$. As the specimen used in this study was annealed 2h at 1200^oC and then water quenched producing a mean grain size of $\approx 120\mu m$ (measured from EBSD), one could observe the previously announced increase from 0 to more than 30% at ≈ 2.5% of plastic strain followed by a decrease up to a saturated state. In [Oliferuk 1995], the authors evidence that depending on the grain size, the peak on β^* function is higher in small grain structure and appears also early. Dotted curve C in figure 5.4 (b) presents the linear extrapolation of grain size effect on β^* curve for a grain size of

$120\mu m$, i.e. -15% on pic level for a grain size which is 15 time greater. One observes that under a so "rough" assumption the storage ratio must be in the order of $\approx 32\%$ at 2.5% of plastic strain and the curve must be in its increasing phase. Then, the obtained results are consequently totally in line with Oliferuk's results concerning on the one hand the shape of the curve, i.e. increasing and saturating function up to 2.5% of plastic strain and on the other hand the storage ratio, i.e. $\approx 30\%$. It appears consequently that a linear dependence between the grain size, the β^* ratio at early plasticity (<2.5%) and the level of plastic strain at β^* maximum appearance could be expected within 316L material whose grain size ranges from 8 to $120\mu m$.

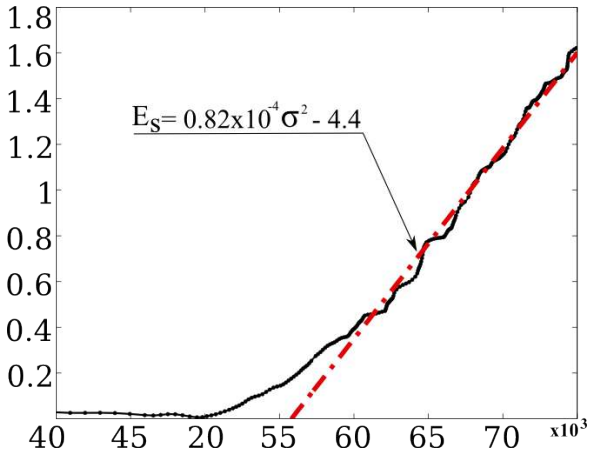

(a) $E_s = f\left(\sigma^2\right)$ in $mJ.mm^{-3}$ and MPa^2 (grain size$\approx$ $120\mu m$)

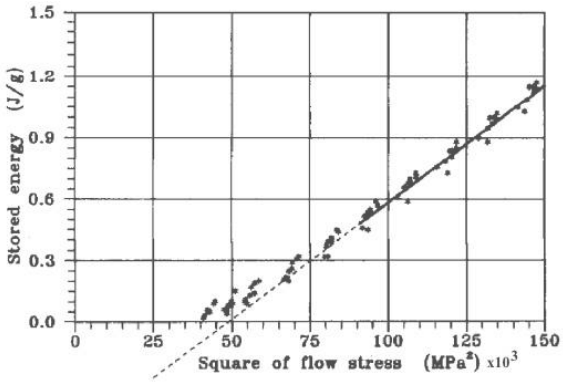

(b) $E_s = f\left(\sigma^2\right)$ in $J.g^{-1}$ [Oliferuk 1997] (grain size$\approx$ $80\mu m$)

Figure 5.5: linear dependence of stored energy fonction of square flow stress during linear hardening: (a) studied specimen [Bodelot 2008] (b) [Oliferuk 1997]

Finally, figure 5.5 presents the variation of stored energy as a function of the square of the macroscopic flow stress, in the case of (a) the studied specimen and (b) a stainless steel specimen with a mean grain size of $\approx 80\mu m$ [Oliferuk 1997]. One could observe the same behavior in both cases, i.e. no energy is stored during elasticity, then at $\approx 50\text{x}10^3$ or 220^2 MPa^2 ($R^e_{0.2\%}$=222 MPa) the stored energy increase toward a linear relationship with the square of the flow stress σ. In the present case, one obtains: $E_s = 0.82\text{x}10^{-4}\sigma^2 - 4.4$. The proportional relationship between flow stress and/or square of flow stress and stored energy has been underlined by many authors. [Bever 1973] summarized many of them. This relation is totally in line with the classically assumed proportionality between σ^2 and the density of dislocation ρ [Bailey 1960, Kuhlmann-Wilsdorf 1983], as well as the proportionality between ρ and E_s [Bever 1973, Nabarro 1987]. One could observe that it exists a degree of hardening when:

$$E_s \propto \rho \propto \sigma^2 \tag{5.10}$$

Oliferuk et al. [Oliferuk 1997] related the non proportionality between stored energy and the square of the flow stress at early plasticity ($< 1\%$) followed by a proportional behavior, to a change in storage mechanism. As previously discussed, these authors propose that during a first step, energy is mainly stored in elastic internal stresses at grain boundaries and, during this step, the stored energy is not proportional to dislocation flow. Then energy is stored in hardening and begins to exhibit a proportional relation with it.

Let us write the theoretical form of proportionality factor linking stored energy and the square of the flow stress in order to discuss the relation underlined in figure 5.5 (a). One classically writes the proportionality relation between the flow stress resolved on shear plane and the associated density of dislocation as follow [Bailey 1960]:

$$\tau = \alpha \mu b \sqrt{\rho} \tag{5.11}$$

with $\tau = m\sigma$ the resolved shear stress, m the Schmid factor [Schmid 1950], μ the shear modulus and b the Burger's vector[3]. Then considering only a storage mechanism in dislocation density [Bever 1973] it follows:

$$E_s = \alpha_s \mu b^2 \rho \tag{5.12}$$

with α_s a constant $\in [1.8, 2.1]$ as considered by Williams for pure Copper, Nickel, Iron and Zirconium materials [Williams 1964]. According to equations 5.12 and 5.11 one could obtain the proportionality relation:

$$E_s = \frac{m^2 \alpha_s}{\alpha^2 \mu} \sigma^2 \approx 0.8\text{x}10^{-4} \sigma^2 \quad \text{with } \sigma \text{ in } MPa \tag{5.13}$$

The slope of the curve in figure 5.5 (a), equal to $0.82\text{x}10^{-4}$, corresponds exactly to the theorical coefficient $\frac{m^2 \alpha_s}{\alpha^2 \mu}$ introduced in equation 5.13. This results confirms the relevance of stored energy estimation at homogenized scale, but also evidences that from 220MPa (see figure 5.5 (a)) the storage mechanism is mainly due to dislocation production. Note that this point is totally in line with β^*_{sh} evolution observed in figure 5.4. Indeed, at 0.5% or $231MPa$ the storage of energy in hardening processes, i.e. based on dislocation or stress flow, initiates. At this moment, its linear trend leads to the global linear trends of $\beta*$. Note finally that the slope of the curve in figure 5.5 (b) is $\approx 1.2\text{x}10^{-4}$ quite similar to our results. As the only remarkable difference between both tested material is the grain size, one could imagine that the small variation between results come from a variation of mechanical properties, here especially the shear modulus.

[3] $\mu \approx 71GPa$, $\alpha^* = 0.3$ in A316L and one assumes $m \approx 0.5$ for polycrystal (see EBSD analysis in chapter 1.1)

An homogenized approach has been used to estimate the global partition between dissipated and stored energy in a A316L specimen submitted to monotonic tensile test up to $270MPa$ and 2.5% of mean axial strain. This approach assumes the uniaxiality of loading as well as the isotropy of mechanical and thermal behaviors, and the homogeneity of heat losses. It has been shown that the specimen gauge-section stored 1.8 $mJ.mm^{-3}$ which represents $\approx 30\%$ of the total inelastic expended work at the end of test and $\approx 70\%$ of the total stored energy which is actually stored in the dislocation network contributing to hardening. It has been shown that the level of stored energy ratio, i.e. $\approx 30\%$ corresponds to a linear extrapolation of previous results obtained in [Oliferuk 1995] for $8\mu m$ and $80\mu m$ mean grains size specimen. It has also been pointed out an initial lack of energy storage. This point has been related to a probable underestimation of inelastic energy due to the assumption of loading uniaxiality. Then, comparing our results with test performed on standard grain size A316L specimen (see [Oliferuk 2009]), it has been shown that grain size has an impact on stored energy level which is currently a classical result, but also on the storage mechanism, i.e. in hardening and/or internal stresses. A first conclusion is, the higher is the grain size, the higher is the ratio of intragranular mechanism, i.e. storage in hardening (dislocations). Finally a linear relationship between the stored energy and the square of the flow stress has been evidenced and the coefficient of proportionality is $0.82\text{x}10^{-4}$. It has been underlined that it perfectly corresponds to $\frac{m^2\alpha_s}{\alpha^2\mu}$ coefficient coming from relation 5.13.

5.2 A local approach of energy balance

This section proposes a simplified way, based on thermomechanical full field measurement, to achieve the energy balance at intragranular scale. It could be seen as a first "rough" estimation of stored energy and β^* field within polycrystals. Nevertheless, it has been pointed out in the previous section that $\boldsymbol{\sigma}$, $\boldsymbol{\varepsilon_p}$ or $\boldsymbol{\varepsilon_e}$ tensors are required and should be estimated with assumptions. Note, in appendix D, that a possible way is proposed to estimate intragranular stress field with the help of intragranular strain "measurement" coupled to the knowledge of grain orientation. The proposed method is based on the geometrical aspect of plastic strain, i.e. plastic strain in a specific grain, with a specific orientation only occurs by shear on a known slip plane. Nevertheless, such method requires the knowledge of the effective 3 dimensional strain tensor, and not only the plane one. One has also seen in the previous section that heat losses energy are, in our case, almost neglectable, then we will consequently assume in first approximation, adiabatic conditions. The approach developed here is in part inspired by the following works [Rittel 1999, Hodowany 2000, Bodelot 2011].

It has been seen that only plane components of strain tensor are provided by plane DIC. In order to use a tensorial approach, one assumes a plane stress state which is verified on the free surface of the specimen and could be propagated through the material since specimen is thin and flat. Let $\boldsymbol{\varepsilon}$, and

$\boldsymbol{\sigma}$ be the 3 dimensionnal strain and stress tensor respectivelly. They are defined under an isotropic elasticity assumption as follow:

$$\left\{ \begin{array}{rcl} \boldsymbol{\sigma} & = & 2\mu\boldsymbol{\varepsilon} + \lambda Tr\left(\boldsymbol{\varepsilon}\right)\boldsymbol{I} \\ \varepsilon_{zz} & = & -\frac{\nu}{1+\nu}\left(\varepsilon_{xx}+\varepsilon_{yy}\right) \end{array} \right. \tag{5.14}$$

with ν the Poisson's coefficient. The additionnal assumptions are the following:

- $\boldsymbol{\varepsilon_e} \to 0$: considering that plastic strain $\boldsymbol{\varepsilon_p}$ prevails in macroscopic plastic domain (see figure 5.2). In addition, as plastic strain is only deviatoric one could approximate it by the deviatoric part of the total strain $\boldsymbol{\varepsilon}$. By neglecting the elastic part of the strain tensor, one also neglects the isentropic power: W_{the} or W_{is}.

- ***linear hardening***: the roughest estimation of local stresses would be to consider a Sachs model, i.e. homogeneous stress assumption. It would lead to an underestimation of the local stresses and consequently significantly overestimate $\dot{\beta}$. It could be notably greater than 1 within some grains. Thus one assumes an heterogeneous stress field based on a local linear hardening, i.e. linearly dependent on total strain $\boldsymbol{\varepsilon}$.

$$\boldsymbol{\sigma} = \boldsymbol{\sigma_y} + \boldsymbol{\sigma_h} \tag{5.15}$$
$$= \boldsymbol{\sigma_y} + H\boldsymbol{\varepsilon} \tag{5.16}$$

  with $\boldsymbol{\sigma_y}$ the uniform local yield stress and H the uniform local hardening modulus. Both are identified on macroscopic stress-strain curve.

- ***adiabatic conditions***: one neglect heat losses, i.e. $k\Delta T \approx 0$.

Following such assumptions the stored power field takes the following form:

$$W_s \approx \boldsymbol{\sigma} : \dot{\boldsymbol{\varepsilon}}^p - \rho C_v \dot{T} \tag{5.17}$$

Then by following the von Mises energy approach, one could underline the following power equivalence:

$$\boldsymbol{\sigma} : \dot{\boldsymbol{\varepsilon^p}} = \sigma_{eq}\dot{\varepsilon}_{eq} \tag{5.18}$$

where the equivalent plastic strain rate is $\dot{\varepsilon}^p_{eq} = \sqrt{\frac{2}{3}\dot{\boldsymbol{\varepsilon}}^p : \dot{\boldsymbol{\varepsilon}}^p}$, the plastic strain is the deviatoric part of strain tensor $\boldsymbol{\varepsilon}^p \approx \boldsymbol{\varepsilon} - \frac{1}{3}Tr\left(\boldsymbol{\varepsilon}\right)$, the equivalent Cauchy stress is $\sigma_{eq} = \sqrt{\frac{3}{2}\boldsymbol{S} : \boldsymbol{S}}$ and the deviatoric part of the Cauchy stress is $S = \boldsymbol{\sigma} - \frac{1}{3}tr\left(\boldsymbol{\sigma}\right)$. The stored energy field is finally estimated through the following equation:

$$W_s \approx \left(\sigma_y + H\varepsilon^p_{eq}\right)\dot{\varepsilon}^p_{eq} - \rho C_v \dot{T} \tag{5.19}$$

The ratio of stored energy field on total anelastic one, noted $\dot{\beta}^*$ becomes:

$$\dot{\beta}^* = \frac{(\sigma_y + H\varepsilon_{eq}^p)\,\dot{\varepsilon}_{eq}^p - \rho C_v \dot{T}}{(\sigma_y + H\varepsilon_{eq}^p)\,\dot{\varepsilon}_{eq}^p} \tag{5.20}$$

with $\dot{T} = \frac{\Delta T}{\Delta t}$ the time derivative field of temperature (experimentally measured) and $\dot{\varepsilon}_{eq}^p = \frac{\Delta \varepsilon_{eq}^p}{\Delta t}$ the time derivative field of equivalent plastic strain (extracted from the deviatoric part of the experimental plane strain tensor). It is important to note that basically, under such adiabatic and other strong assumptions, authors [Rittel 1999, Bodelot 2011] do not directly estimate stored energy but prefer to estimate ratios such as $\dot{\beta}^*$, $\dot{\beta}$ or β ... Nevertheless, when one deals with fields where some regions undergoes small strains, mainly elastic, the term $(\sigma_y + H\varepsilon_{eq}^p)\,\dot{\varepsilon}_{eq}^p \to 0$, especially in our case where the stress field could be locally underestimated due to "rough" assumptions. This means that for low and heterogeneous strain field level, $\dot{\beta}^*$ calculation may not be appropriate.

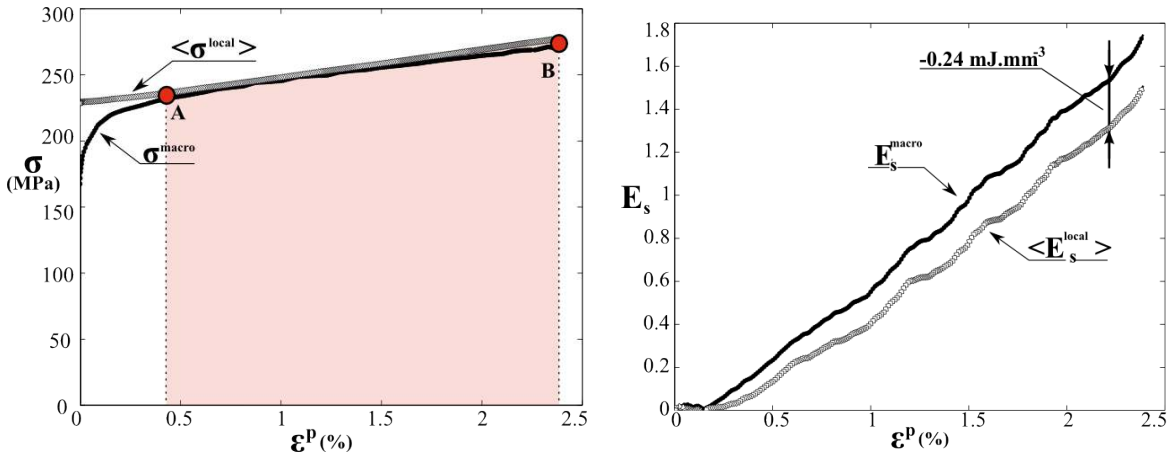

(a) σ and $< \sigma^{local} >$ (b) E_s and $< E_s^{local} >$

Figure 5.6: Comparison between macroscopic (a) stress and (b) stored energy and the average over the field including asumptions 5.18 and 5.19

Figure 5.6 (a) and (b) present firstly the mean value over the specimen gauge-section of stress field as well as the total stored energy field. One could observe that assumptions on local stress field conserve on the one hand the mean stress-strain response of the material during the elasto-plastic phase $(A - B)$ and on the other hand conserve more than 85% of the macroscopic stored energy. The figure 5.6 (b) underlines an underestimation of the total energy balance equal to 0.24 $mJ.mm^{-3}$. This evidences that the estimated local stress field leads to a good estimation of the mean stress value. Nevertheless it slightly underestimates local gradients. Indeed, the underestimation of the mean stored energy comes from the underestimation of local stresses (see equation 5.19) since the term $\rho C_v \dot{T}$ is correctly estimated. As the assumption of stress linearly dependent of plastic strain is certainly valid within grain which undergoes plastic and high plastic strain, one could guess that slight errors are

localized in low strained grains.

Figure 5.7 (a), (b) and (c) presents the total stored energy field E_s, the β^* one as well as the time evolution of stored energy in some grains.

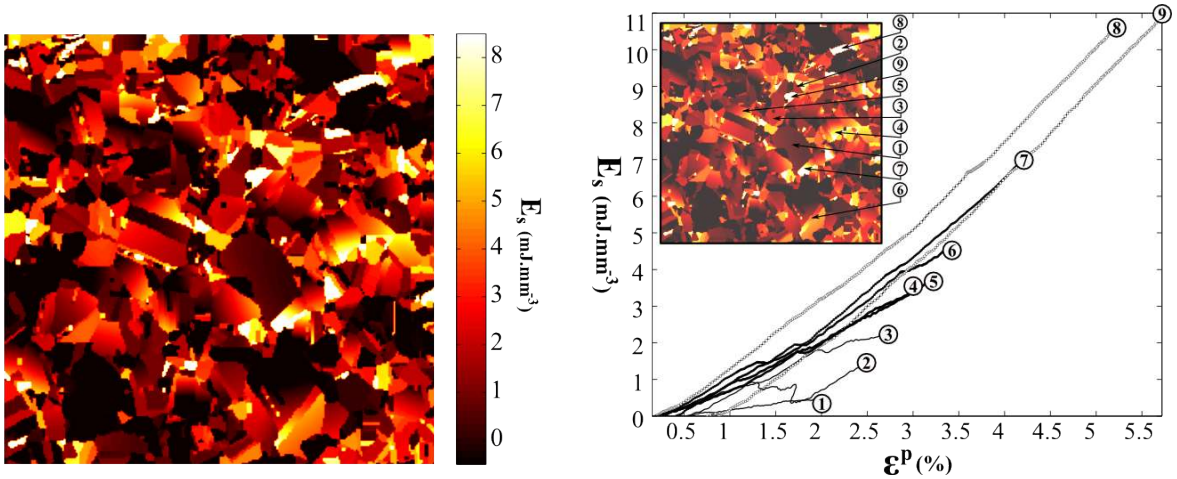

(a) E_s (b) $< E_s >^G$

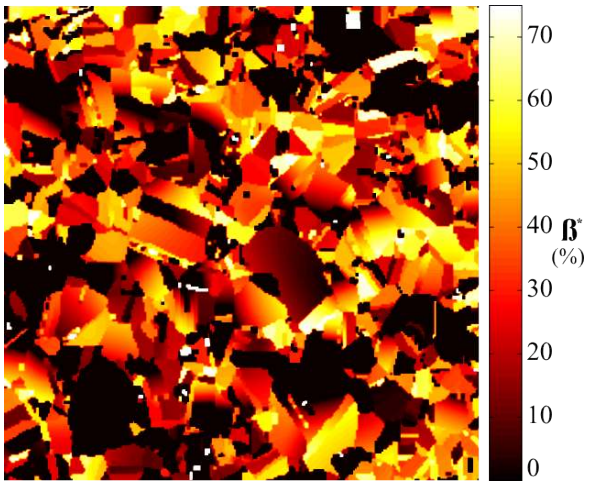

(c) β^*

Figure 5.7: (a) Stored Energy field estimated from A-B part on figure 5.6, (b) local evolution of stored energy function of plastic strain and (c) the ratio of stored energy of anelastic expended one, β^*

One could first observe that some regions exhibit a stored energy and a β^* ratio lower than zero (see 5.7 (a) and (b)). These regions undergo low strain level according to previous observations in chapter 4.1. It points out the relevance of previous explanation concerning the deviation between

macroscopic stored energy evolutions in figure 5.6: the underestimation of mean stored energy over the field presented in picture 5.6 is due in great part to local negative values (errors) of stored energy within low strained regions.
Figure 5.7 (a) presents a stored energy which ranges from ≈ 0 to more than $8mJ.mm^{-3}$ and even reach $12mJ.mm^{-3}$ in few grains. Considering the macroscopic approach performed in section 5.1, where E_s was equal to $1.75mJ.mm^{-3}$, a factor $\in$ [0 - 7] times the mean value is estimated at the granular scale. Figure 5.7 (b) evidences a local quite linear evolution of stored energy as a function of plastic strain. For some grains, this point is nevertheless not verified, notably within grain 2 where a chaotic variation of stored energy is founded. This point may be explained by the localization of the considered grain within the microstructure. Indeed, it is the neighbors of one of the most strained grain which is also the grain which shows the highest storage level. Concerning β^* ratio, picture 5.7 (c) exhibits that the material store between 0 and 75 % of energy. Some large regions present a quasi null β^* ratio. In parallel, figures 5.8 (a) and (b) discuss the distribution of β^* ratio at 2% of plastic strain. In figure (a) the distribution of β^* is plotted and, in figure (b), the variation along the time of β^* density lower than 10%. Figure (a) evidences that $\approx$ 35% of the grains does not store any energy, or few energy ($<$10%) up to 2%. Potentially, two kind of grains could be considered in this group:

- grains which do not undergo any plastic strain or small ones. These grains do not dissipate and do not store any energy (see figure 5.7 (b)) thus β^* tends to such fraction: $\frac{0}{0}$.
- grains which undergo plastic strain but do not store a lot of energy. In other words, grains where plasticity leads to mainly dissipative phenomena.

One could observe that a great part of the microstructure is in these both cases and one observes that the whole set of other grains are almost symmetrically distributed around the 50% of storage ratio. Figure 5.8 (a) also presents macroscopic values of β^*. One observes that the macroscopic value of storage ratio results from a competition between grain which store ($\approx$ 50% at such strain level) and the ones which do not store ($\approx$ 0%) energy.

It reveals that at early plasticity, the macroscopic value of storage may be much more leaded by a parameter α defining the percentage of plastic grains (or plastic inclusions) and a mean value of storage than by a real intrinsic storage rate related to a specific hardening mechanism. It appears consequently as being an interesting indicator of strain localization since depending in part, within heterogeneous material, on the degree of homogeneity of strain field. Nevertheless, following such observation, it seems that the link between macroscopic β^* ratio evolution and mechanisms of plasticity is not direct. Indeed, considering heterogeneous material, macroscopic β^* ratio variation reflect on one hand the kind of storage mechanism, high and then low [Oliferuk 2004], but also the progressive homogenization of strain field which is not necessarily a linear and a continuous phenomenon.

In addition, figure 5.8 (b) shows the evolution between A and B (see figure 5.6 (a)) of the density of grains which store small amount of energy ($<$10%). One observes a decrease of the density from 50 to less than 35% at 2.5% of plastic strain. Thus, the β^* ratio indicate that about 50% of grains did not store at point A ($\varepsilon \approx 0.4\%$) and $\approx$ 35% still are in the same case at 2.5% of strain. It

underlines that the strain field tends toward a more homogeneous state. Nevertheless a high strain localization is still present. This strain localization has initiated during the macroscopic elastic phase in the form of microsplasticity phenomena. Nevertheless, as the following approach does not consider the macroscopic elastic phase we are not able to discuss this point (see figure 5.8 (b) with the dotted line at the beginning of the curve).

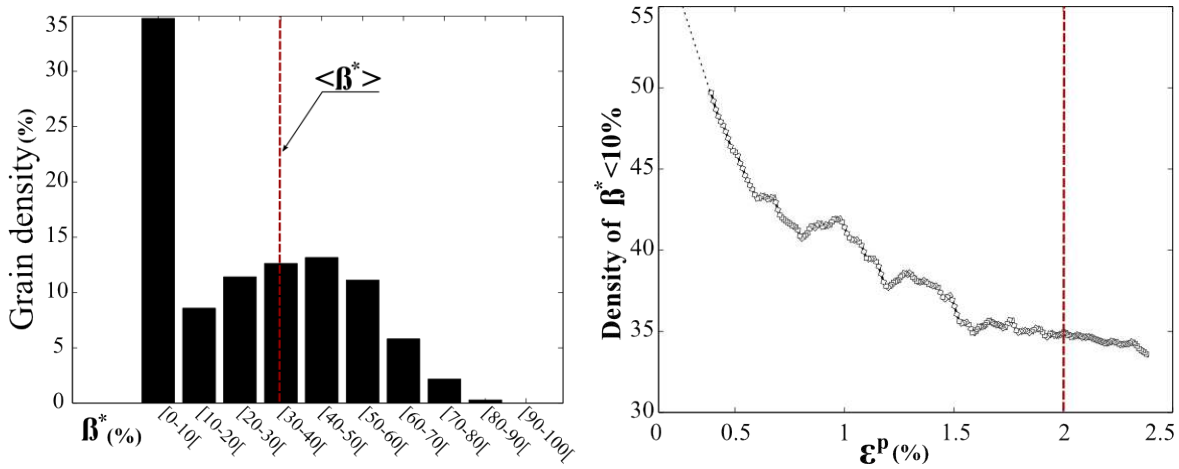

(a) (b)

Figure 5.8: (a) Distribution of β^* ratio at 2% of mean axial plastic strain and (b) Evolution of density of β^* ratio lower than 10% along the $A-B$ deformation path (see figure 5.6 (a))

It is then interesting to study the link between the stored energy or β^* ratio and microstructural elements, notably the surface density of slip-marks and the misorientation investigated within chapter 1.1.

Figures 5.9 presents the mean intragranular β^* ratio per grain as a function of the mean intragranular relative slip-bands density per grain. Each point is a grain of the microstructure. The figure presents a very scattered pattern and no possible link between slip mark density and β^* ratio appears to be obvious. Thus it do not exist a direct relation between slip-band density and the storage ratio and/or stored energy. Nevertheless, even if direct statistical approach do not provide any relevant result, it must exist a relationship between slip-bands (intragranular domain), misorientation (intergranular domain) and stored energy.

Figures 5.10 presents the stored energy, E_s, the β^* ratio, the relative slip-mark density and the mean granular misorientation field respectively, at the end of the test. In addition, different regions are underlined: regions from A to E denote large domains where the stored energy, and the β^* ratio are null or close to zero. The domain F denotes the region where experimentally, the temperature localizes from $\approx$230 MPa to the end of the test. Finally, the domain G denotes, for example, one region where intense out-of-plane displacement has been observed at twin Σ_3 boundaries.

One observes firstly that the β^* ratio field and the stored energy one E_s are in good agreement (see figure 5.10 (a) and (b)). In regions where the stored energy is high, the ratio of stored energy on the the plastic expended one is high and reversely. One observes, in both fields, some large regions where the levels are null or close to zeros which means that these regions have stored only a small amount of energy during the test. Thus one could imagine that a small amount of plasticity is observed in these regions. An observable sign of the plasticity is the relative slip-mark density. One observes in the relative slip-mark density field (see figure 5.10 (c)), that a great part of domains noted A, B, C, D and E exhibit a relative slip-mark density lower than 15%. This point is more obvious in regions B, C and E.

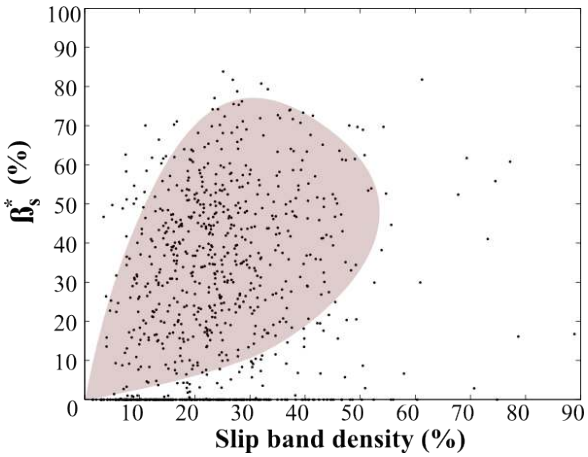

Figure 5.9: intragranular mean β_s^* ratio function of intragranular mean density of slip bands

This shows that a link between the regions that do not store a large amount of energy and regions that do not activate dense and intense slip-marks exist. In addition, this link between low plasticity regions and low β^* ratio ones allows to confirm the interpretation of results presented in figure 5.6. The macroscopic β^* ratio reflects partly the heterogeneity of the deformation field. In the present case, the high density of grain with a low β^* ratio leaded by low strained regions induces an underestimation of the effective mean β^* ratio for plastic strained grain, i.e. ≈50% according to figure 5.6. Thus the homogenization of the deformation field conduct to an increase of the homogenized (macroscopic) β^* ratio. Considering for example results found in [Oliferuk 1995] where the author evidences that the β^* ratio reach a maximum between 35 and 45 % before to decrease, one could imagine that the evolution of the stored energy from 0%, initially, to ≈45% at ≈3% of strain (depending on the grain size) is in part due to the homogenization of the deformation field and not to a intrinsic variation of storage ratio. In other words, at homogenized scale, there is no way to distinguish if the variation of macroscopic β^* ratio is due to its local intrinsic variation as a function of the local plastic strain or if it is due to the competition between a constant β^* ratio about 50% for every plastic grain, whatever the plastic level, and a progressive decrease of the percentage of low strained regions. Here, the second hypothesis seems to be verified. Thus this result asks the following question: is the β^* ratio a material (or crystal)

constant, at least during the stage I of the deformation, since the decrease of β^* ratio observed over the stage II evidence of local variation of the storage rate?

One could nevertheless point out, as presented in the figure 5.9 that the link between low β^* and low slip-marks is not systematic thus not observable statistically. It is moreover the case in region F.

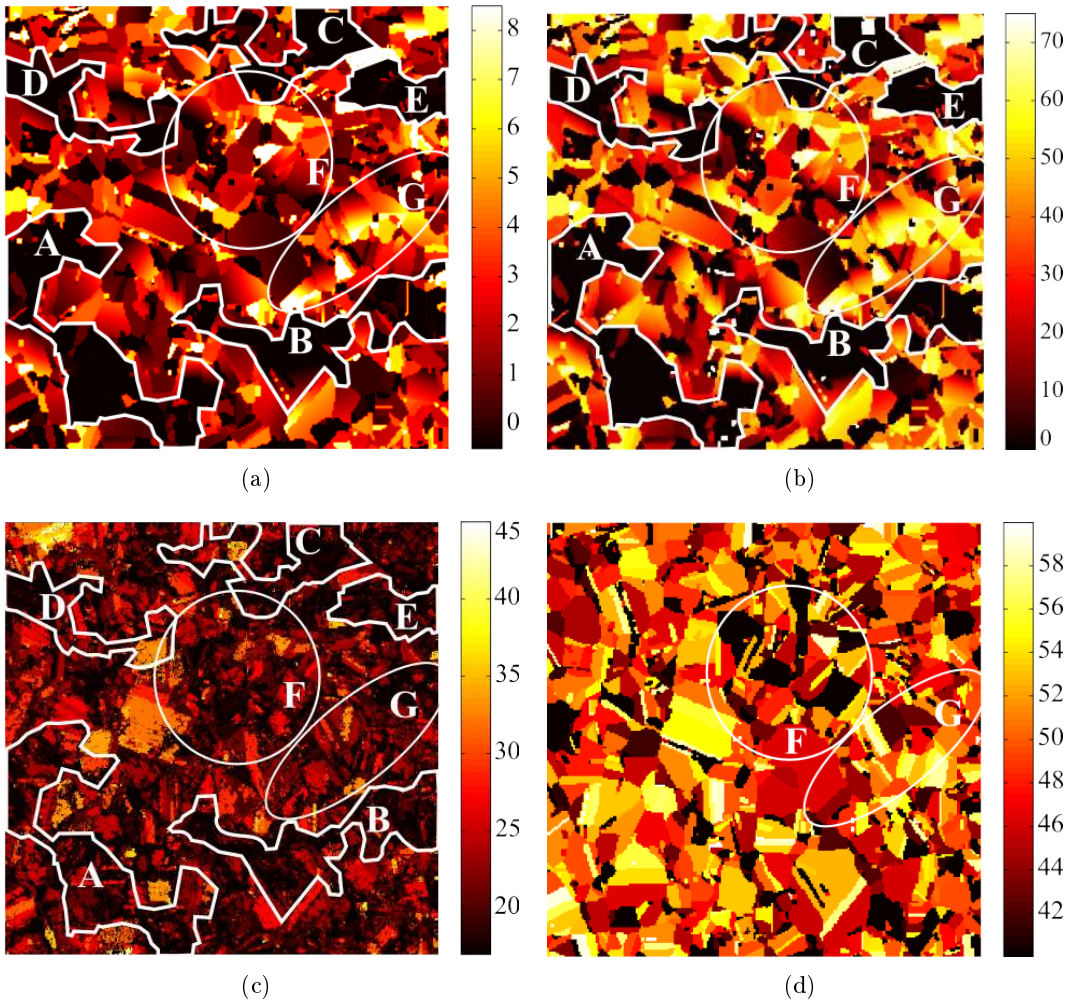

Figure 5.10: (a) stored energy, (b) β^* ratio, (c) relative slip mark density and (d) misorientation

The region F (see circles in figure 5.10) localizes the temperature from ≈230 MPa until the end of the test, thus dissipates a lot compared to other regions, at least during this period, and necessarily stores a large amount of energy, at least locally. Nevertheless, slip-marks are not especially, more numerous or more intense within this region compare to the others. In opposite, it is relatively not important excepted in very small grains. In parallel, this region exhibits in three small grains the larger

amount of stored energy within the polycrystal. Let see the mean granular misorientation field (see figure 5.10 (d)).

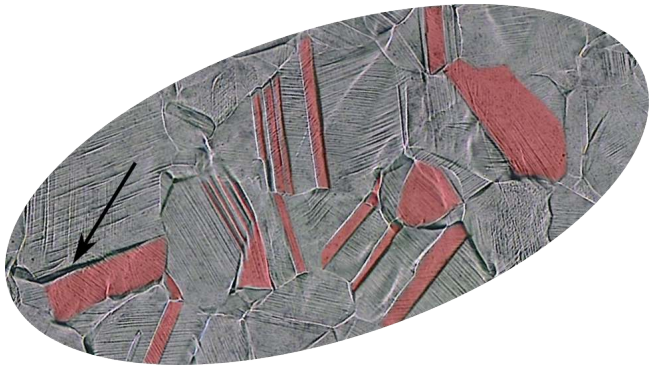

Figure 5.11: micrography of the specimen surface, performed after test. Focus on a region G. Twins (Σ_3 interfaces) are red colored.

One observes that this region concentrates many grains with a relative low misorientation, i.e. $<40^o$, some grains of which the misorientation is about 50% and one grain of which the misorientation is about 60%. Thus the region F has the larger amount of grains which deforms uniformly with their neighbors (few misoriented). One could imagine that this characteristic leads to stronger interactions at grain boundaries. Moreover it has been observed on surface micrography that deformations are, within this region, clearly localized at grain boundaries (see figure 8.7 zoom R_1). This point could explain why a systematic link between stored energy, β^* ratio and slip-marks is not observed. Incompatibilities at grain boundary must play an important role in the energy balance. Moreover the connection between the more heated region and this high density of few misoriented grains can not be fortuitous.

Finally, let us compare the region noted G in figure 5.10 (b) and the figure 5.11. One observes in figure 5.11 that this regions is especially deformed, notably at Σ_3 boundaries. Indeed, one has seen in chapter 1.1 that intense gap of out-of-plane displacement are observed between twins and neighbours, especially in this region. In figure 5.10 (b) this region exhibit a high β^* ratio mainly about 65%, and localized one of the highest level of the field in at its left extremity. The area is pointed in figure 5.11 by an arrow. Thus one observes that the stored energy reaches more than 80% in vicinity of a grain boundary where an intense sliding occurs. These observation seems reflect a strong connection between the storage rate and the grain boundary behavior (sliding).

A local approach has been used to estimate the granular partition between dissipated and stored energy in a A316L specimen submitted to monotonic tensile test up to $270MPa$ and 2.5% of mean axial strain. This approach assumes plane stress condition on specimen surface, a stress field linearly dependent on plastic strain, the predominance of plastic strain in macroscopic plastic domain and adiabatic conditions. It has been shown that the local stored energy level varies from the mean macroscopic value with a factor of 7, and the time evolution is globally linearly dependent of plastic strain. The analysis of β^* ratio allows identifying mainly two kinds of local behavior: (1) a very low storage ratio ($<$15%) within about 30% of grains at 2.5% of plastic strain and (2) a mean storage ratio in the order of 50% within the rest of microstructure. In addition, low storage ratio domains has been correlated to regions with a low slip-mark density. Thus it has been underlined that within early plasticity domain, the macroscopic value of β^* may more reflect the ratio of plastic inclusions within the matrix than an intrinsic ratio of storage. It is consequently an indicator of plastic strain localization. The time variation of the density of grains with a low storage has been studied, and the material tends toward a more homogeneous strain state. Nevertheless, strain localization remains significant. Finally the correlation between slip bands, misorientation and β^* ratio has been studied. Inconclusive statistical results has not been found due to the complex interactions between different mechanisms of storage. Nevertheless it has been shown that most of regions where the β^* ratio is very low correspond to regions where slip-mark density is also very low. In addition some significant β^* level regions correspond to significantly marked and/or misoriented regions especially at twin Σ_3 boundaries. The conclusion remains that a link exists between misorientation, slip-mark density and storage state at intragranular domain. Nevertheless, this link is neither systematic nor direct.

5.3 Local 2D thermal laplacian

As the previous section assumed an adiabatic process for heat exchanges, this section discusses the 2D heat losses energy term within the traditionnal heat equation, $-k \int_{t=0}^{T} \Delta^2 T \cdot dt$.

Figure 5.12 (a) and (b) presents heat production, noted E_{hp}, and 2D heat losses energy, noted E_{hl}, measured from the gauge-section of A316L specimen. These energies are the integral along the whole time test of $\rho C_v \dot{T}$ and $-k\Delta^2 T$ respectively.

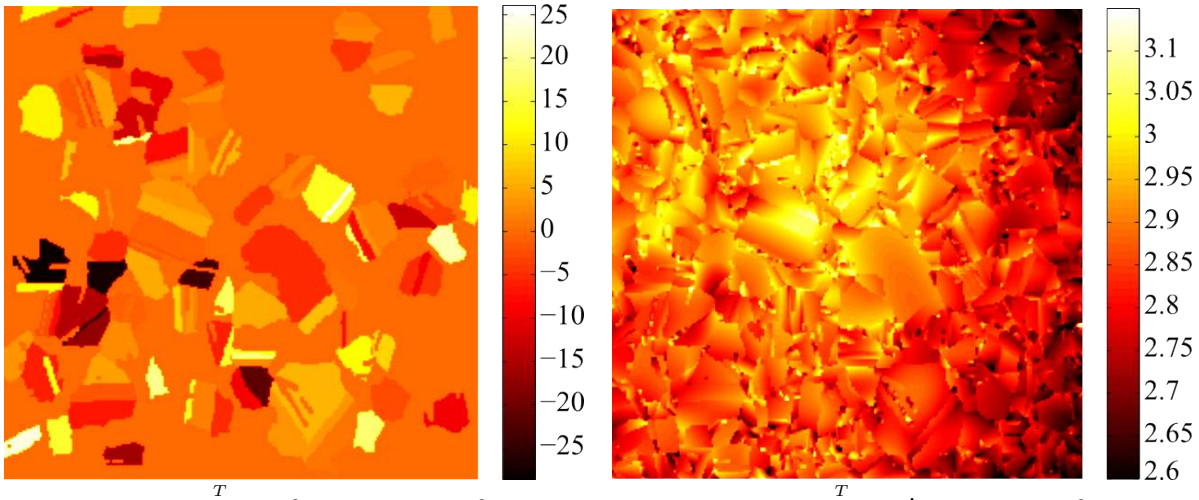

(a) $E_{hl} = \int_{t=0}^{T} -k\Delta^2 T \cdot dt \ (mJ.mm^{-3})$ (b) $E_{hp} = \int_{t=0}^{T} \rho C_v \dot{T} \cdot dt \ (mJ.mm^{-3})$

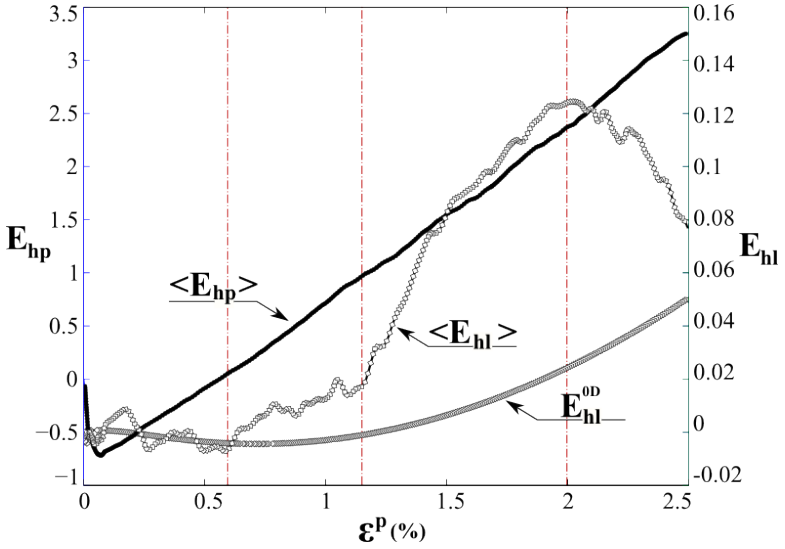

(c) $< E_{hp} >$, $< E_{hl} >$ and E_{hl}^{0D} in $mJ.mm^{-3}$

Figure 5.12: (a) heat source energy produced within A316L flat specimen up to 2.5% of mean axial strain, (b) the associated heat energy lost by conduction through lateral and axial directions and (c) mean values over the specimen-gauge section as well as heat losses energy extract from "0D" approach.

One observes on figure 5.12 (a) that the intragranular heat losses energy ranges from ≈ -30 to 30 $mJ.mm^{-3}$. Table 5.3 presents level distributions within the microstructure.

E_{hl} in $mJ.mm^{-3}$	[-5, 5]	[-10, -5[U]5, 10]	[-30, -10[U]10, 30]
Grain density in %	$\approx 71\%$	$\approx 16\%$	$\approx 12\%$

Table 5.3: Distribution of heat losses energy levels within the surfacic microstructure of tested A316L

Figure 5.12 (c) presents its mean evolution, noted $< E_{hl} >$, function of mean strain. At the end of the test, i.e. the instant corresponding to pictures 5.12 (a) and(b), the mean value of heat losses energy is 0.08 $mJ.mm^{-3}$. Thus although granular high magnitudes are observed in energy field (see figure 5.12 (a)) the mean value of the losses energy remains very low even neglectable compared to mean heat production energy, noted $< E_{hp} >$, also presented in picture 5.12 (c). Indeed, $< E_{hl} >$ ranges from 0 to 0.13 $mJ.mm^{-3}$ while $< E_{hp} >$ ranges from -0.7 to 3.3 $mJ.mm^{-3}$. This low energy magnitude was already pointed out within the section 5.1 where the homogenized heat losses energy was estimated from the term $\rho C_v \frac{\tilde{\theta}}{\tau_{eq}}$. Its is noted E_{hl}^{0D} in picture 5.12 (c) and its value ranges from ≈ -0.01 to ≈ -0.05 $mJ.mm^{-3}$ which is in line with $< E_{hl} >$. However, one could notice that $< E_{hl} >$ significativelly deviate from E_{hl}^{0D} from 0.6% of strain, i.e. the begining of perfect linear hardening (see point A in figure 5.6) and much more from 1.2% of strain. The deviation from E_{hl}^{0D} underlines a deviation from "0D" assumptions, notably the homogeneity of heat sources within the material. Indeed, one observed from the beginning of plasticity that the temperature and thus heat sources are very localized within the gauge-section (see thermal analysis within chapter 4.1). Thus the mean value of heat losses energy and its deviation from homogeneous assumptions reveals a certain relevance of this quantity regarding to observed plasticity mechanisms. It also points the weaknesses of a "0D" approach for low strain regime and especially at 2% of plastic strain where the deviation reaches its maximum. Note that at 2% of plastic strain, $< E_{hl} >$ decrease from 0.13 to 0.08 $mJ.mm^{-3}$ and tends toward E_{hl}^{0D}. It reflects a uniformity of thermal field which could be the result of a decrease of local heat sources activity and/or a uniformity of heat sources.

Let us recall the local form of intrinsic dissipation within continuum mechanics framework (see appendix A.1):

$$d_1 = \rho C_v \dot{T} - k\Delta T - T\frac{\partial \boldsymbol{\sigma}}{\partial T} : \dot{\boldsymbol{\varepsilon}}^e \tag{5.21}$$

From the second principle of thermodynamics (see appendix A.1) one knows that the total dissipation must remain positive, and by extension one classically admits that for every infinitesimal transformation the heat dissipation and the intrinsic one must remain separately positive or null. The present experimental results shown in picture 5.12 (a) and (b), are not consistent with this principle, at least in some grains ($\approx 28\%$ of grains see table 5.3), even if one observes on figure 5.12 (c) that averaged quantities, $< E_{hl} > \; << \; < E_{hp} >$ are consistent with the second principle. Thus, one are locally in view of a infringement of the continuum thermodynamics second principle. A negative value of intrinsic dissipation does not have a physical meaning, especially in our case where no release of energy is expected. Different explanation could be proposed:

- ***space and time treatment have been dissociated***. If one considers heat source appearance,

the Laplacian of the temperature $-\Delta^2 T$, i.e. the local curvature of the surface temperature, will be important only if time derivative of temperature $\dot{T}$ is important. Indeed, if $\dot{T}$ is not important, because of the kinetic of conductive phenomena, the global temperature will increase but the local curvature will remain low and smooth. As the time variation of temperature has been treated on the one hand (low pass filter <25Hz) and the spatial one on the other hand (projection on biparabolic bases per grain) it may be possible that both term $\dot{T}$ and $-\Delta^2 T$ are no more connected.

- ***data treatment as noncontinuous fields***. Thermal fields and kinematic ones have been treated as continuous at intragranular domain regardless of its neighbors. Thus some gaps of temperature exist a grain boundaries. Heat losses energy is defined by $\int_{t=0}^{T} -k\Delta^2 T$ within the continuum mechanics framework, thus intergranular gaps of temperature are not taken into account. Such heat equation may consequently be not appropriate for such thermal field without the treatment of the discontinuities.

- ***variation of temperature along the thickness***. The assumption of uniform temperature within the specimen thickness classically done in thermal analysis is here probably not relevant anymore. Indeed, on the one hand, analysis domains are smaller than the thickness of the specimen and, on the other hand, the present material does not possess columnar grains. Many different grains, with different orientations and strain levels are superimposed along the specimen thickness. Consequently, in the thermal laplacian, the Z component (see equation 5.6), orthogonal to the surface specimen, is missing and could balance and/or translate the 2D heat losses energy level.

One provides here some analysis concerning the three previous points in order to know where the violation of the second thermomechanical principle comes from.

The first point assumes an underestimation of $\rho C_v \dot{T}$, denoted here W_{hp} and thus also of its time integral noted here E_{hp}. Let us consider one material point within the microstructure as well as W_{hp} calculated from time filtered and unfiltered thermal data. One observes in figure 5.13 (a) the comparison between instantaneous heat powers estimated from unfiltered and filtered temperature and in (b) the comparison between associated energy over the whole test. One observes on (a) that the instantaneous energy calculated from unfiltered temperature ranges from ≈-50 to ≈50 $mW.mm^{-3}$ contrary to the one calculated from filtered temperature which ranges from ≈-5 to ≈5 $mW.mm^{-3}$. Thus, it appears that when unfiltered temperature is considered the local and instantaneous $\rho C_v \dot{T}$ term is in the same order that the local $-k\Delta^2 T$ one (see figure 5.12 (a)). Nevertheless, figure 5.13 (b) shows that whatever the temperature used (filtered or not) the energy calculated over the test is almost the same. That means that the low-pass filter has conserved the heat energy of the specimen along its deformation path. Thus whatever the degree of filtering in [25;+∞] Hz range, the local heat energy of the specimen at the end of the test ranges from ≈2.5 to ≈3.5 $mW.mm^{-3}$ and consequently is locally 10 time lower than the heat losses term, E_{hl}.

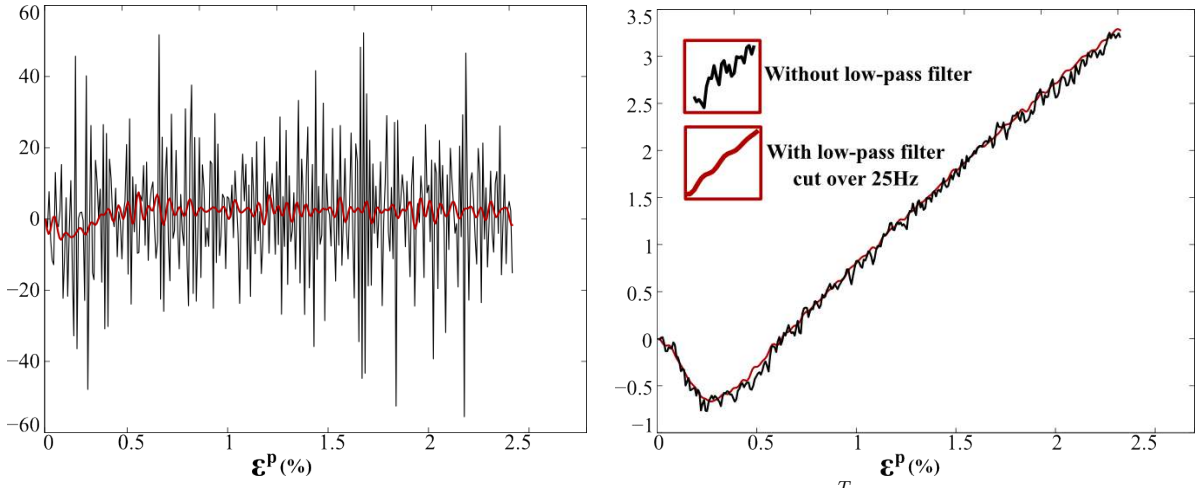

(a) $W_{hp} = \rho C_v \dot{T}$ $(mW.mm^{-3})$ (b) $E_{hp} = \int_{t=0}^{T} \rho C_v \dot{T} \cdot dt$ $(mJ.mm^{-3})$

Figure 5.13: Comparison between filtered and no filtered data on the calcul of (a) heat production power term W_{hp} and (b) heat production energy term E_{hp}

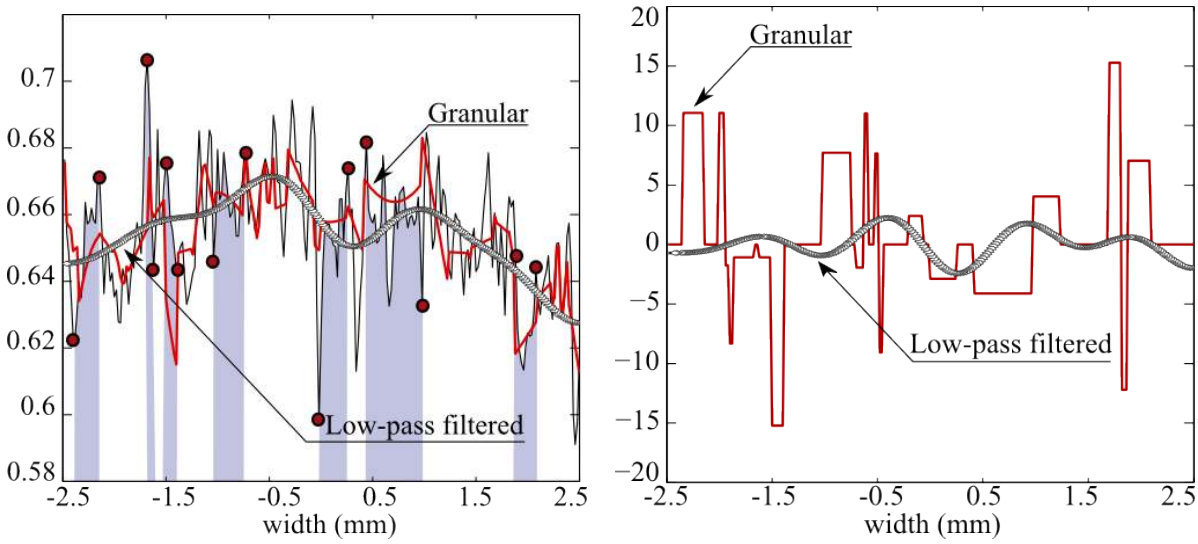

(a) $\theta = T - T_0$ (mK) (b) $W_{hl}(2\%) = -k\Delta^2 T$ $(mW.mm^{-3})$

Figure 5.14: Comparison between raw, granular and low-pass filtered (a) temperature profile and (b) associated intantaneous heat losses power W_{hl} at 2% of mean axial strain

Concerning the second point, the figure 5.14 (a) and (b) present profiles[4] of surface temperature extracted from the thermal field at 2% of mean axial strain as well as the associated 1D heat losses power. Different curves are drawn: the unprojected profile of temperature, the one projected on grain structure and a smooth one, i.e. filtered by a low-pass filter in Fourier space. The last one is build in order to ensure the positivity of local intrinsic dissipation. In other word its local associated heat losses energy $\int_{t=0}^{t=T} -k\Delta T \cdot dt$ is lower than the heat production energy $\int_{t=0}^{t=T} \rho C_v \dot{T} \cdot dt$. Picture 5.14 (a) also presents some grains positions (blue regions). The superimposition of grain boundary on the unprojected thermal field permits to evidence that many grain boundaries exhibit very significant gap of temperature. Red points underline these boundaries. One observes slight variations of temperature at intragranular domain in the order of 15-20 mK and some gaps of temperature up to 80 mK within some grain boundaries. This confirms the assumptions done in the data treatment section (see chapter 3.1), i.e. thermal activity could be very different from one grain to another and thermal grain boundary resistance exist [Kapitza 1941] and seems to be detected. As a thermal boundary resistance exist [Kapitza 1941], thermal field within an intragranular analysis should not be treated as a continuous domain. Note that the projected profile of temperature shows the form of intragranular temperature variation. It takes profit at best of the whole set of intragranular data thanks to the least square method keeping a slight influence of grain boundary discontinuity. Indeed one could underline that after the least square achievement, only a few part of the discontinuity is maintained and in some cases, the discontinuity tends to vanish. Finally, the smooth thermal profile does not take into account any spatial variation lower than 1.2 mm^2, it only reflects a mean local trend of temperature. As projected on a biparabolic basis per grain, the projected thermal profile leads in figure 5.14 (b) to uniform heat losses power per grain. It ranges from -15 to 15 $mW.mm^{-3}$ at 2% of plastic strain and is discontinuous at grain boundaries. In parallel the smooth thermal profile leads to heat losses power which is continuous over the specimen-gauge section and ranges from -2.5 to 2.5 $mW.mm^{-3}$ and is very different from the other one.
To conclude, it exists a degree of thermal filtering when heat losses are in agreement with the second principle of thermodynamic and heat equation in continuum framework. However, in this case, local thermal variations have to be removed, notably every potential thermal discontinuities. Nevertheless it has been evidence within thermal analysis in chapter 4.1 that intragranular quantities extracted from projected field provide relevant results regarding to thermomechanical mechanisms. Thus, the second principle of thermodynamic is ensure in the widely filtered case because the thermal field has been changed to be in line with the thermal response of a homogeneous material. Indeed, the polycrystal aggregate with local thermal resistance, and very local heat sources has been changed in a homogeneous material. In our opinion, first order discontinuities need to be conserved, i.e. grain boundary ones, in order to perform a granular analysis of thermomechanical couplings. In this case the heat equation should be rewritten in a noncontinuous framework even if this conclusion has to be verified.

Within the third point, it is assumed that the origin of heat losses energy misestimation come from the 2D assumption, i.e. uniformity of the thermal field within the specimen thickness. In order to

[4] profile means here a cut of thermal field along one symetry axis of specimen gauge section

discuss this point a model-experiment coupling strategy has been introduced. The model is based on two strong assumptions:

- Heat sources are mainly produced within or between surface grains and thermal evolutions within the specimen thickness are mainly leaded by a conductive phenomenon.

- Thermal properties are isotropic and totally uniform. As we have no idea about the grain boundary network under the surface one assumes here that the conduction is totally uniform and unaffected by microstructure.

A basic heat transfert simulation is conducted on isotropic and uniform numerical model of the same size than specimen-gauge section 5.15. The experimental surface temperature $T(x, y, t)$ is applied as a thermal loading on each element of model face (1). The same mesh as the mesh of data set is used, i.e. 250x250 pixels of $20\mu m^2$ for surface and 10 elements are used for the thickness. Surface flux loadings are applied on the upper, bottom, right and left face of the model (3, 5, 4, 2 respectively). These fluxes are estimated from the Fourier law for conduction phenomena as following:

$$\Phi_x(t) = -\lambda \frac{\Delta T_{(t)}}{\Delta X} \approx -\lambda \frac{\theta(t)}{\Delta X} \tag{5.22}$$

$$\Phi_y(t) \approx -\lambda \frac{\theta(t)}{\Delta Y} \tag{5.23}$$

where $\theta(t) = \bar{T}_{(t)} - T_0$, i.e. the difference between the mean experimental temperature over a segment boundary (top, bottom,right or left) and the external temperature which is approximated by the room and initial specimen temperature T_0. ΔX and ΔY are distances between specimen gauge section segment boundaries and boundaries of specimen (see figure 5.15). λ is the thermal conductivity. Finally, as the model represents only the mid part of the specimen thickness, null thermal exchanges are imposed on the background face (6). Material properties are keeped uniform and constant and values are presented within table 5.4.

The numerical second partial derivative of temperature along the normal direction of surface specimen, $\frac{\partial^2 T}{\partial Z^2}$, is estimated from thermal 3D numerical fields and then its mean value per grain is computed in order to be in agreement with experimental plane thermal Laplacian. The figure 5.16 presents the numerical estimation of heat losses energy along the normal direction at the 2% of plastic strain.

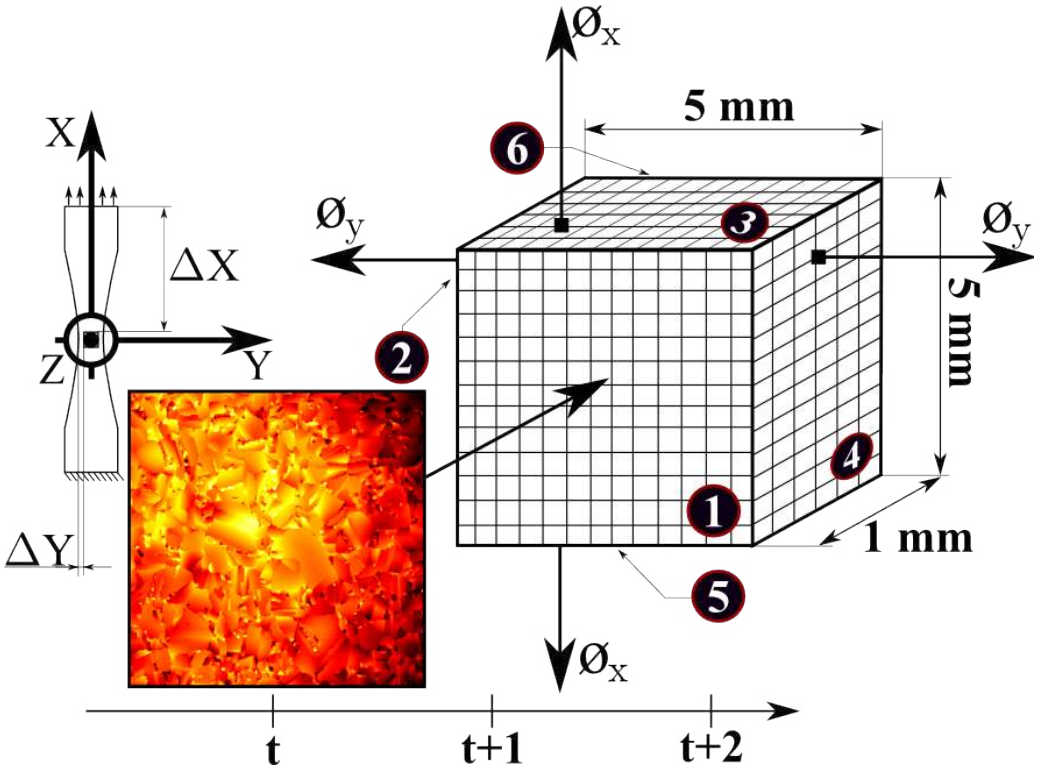

Figure 5.15: Principle of modelling

	A316L
Thermal conductivity λ	15 $W.m^{-1}.K^{-1}$
Density ρ	8000 $kg.m^{-3}$
Specific heat C_v	500 $J.kg^{-1}.K^{-1}$

Table 5.4: Parameters for heat transfert simulation

One observes that under such assumptions the normal component of heat losses energy, i.e. $\int_{t=0}^{T} -k\frac{\partial^2 T}{\partial Z^2}$ is in the order of the plane ones, i.e. $\int_{t=0}^{T} -k\left(\frac{\partial^2 T}{\partial X^2}+\frac{\partial^2 T}{\partial Y^2}\right)$ presented in figure 5.12 (a). Nevertheless, adding this contribution to the 2D one does not reduce the amplitude of total heat losses energy. Thus it still leads to the violation of second principle of thermodynamic.

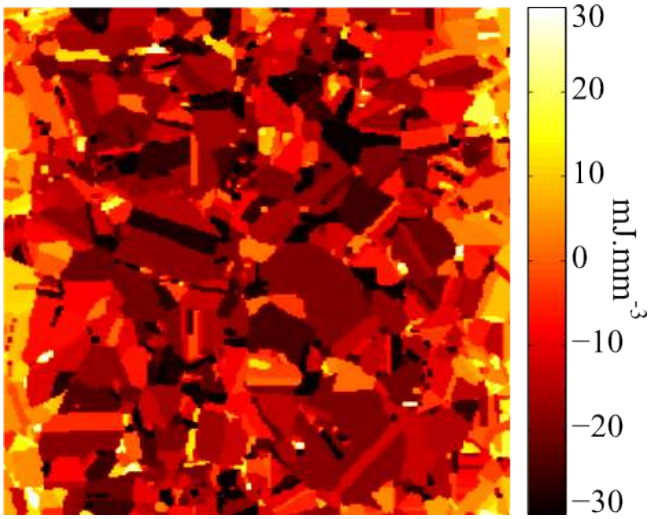

Figure 5.16: Numerical estimation of heat losses energy along the normal direction based on hypothesis of surfacic heat sources and homogeneous and isotropic conduction

The 2D thermal laplacian has been investigated. It has been shown that its local magnitude is not in aggreement with the principle of positivity of the intrinsic dissipation, at least using the heat equation in the continuum mechanics framework. Three hypotheses have been proposed and discussed in order to investigate this point. Mains conclusions are:

1. The decorrelation between time and space in data treatment procedure does not affect the energy balance.
2. The generalization of the heat coupled equation to the treatment of discontinuities seems necessary. Nevertheless this point has not been treated in our study.
3. Further investigation about the difference between 2D and 3D thermal laplacian in the case of none columnar grains and local thermal analysis are necessary. Some complementary results will be proposed in the numerical part 7.1.

Synthesis

The previous chapter has put in light different results coming from experimental investigations. It have been shown that under a specific metrological strategy and then a projection of obtained thermomechanical experimental data within intragranular domain it is possible to investigate many points such as: localization processes and dissipative response at aggregate scale, the thermal propagation through a grain boundary network, the intragranular yield appearance with the help of mechanical and thermal quantities, then the global and intragranular energy balance. During this investigation a clear link has been shown between intragranular plasticity, temperature variation and propagation and it has permit to underline two kind of thermal barriers: the grain boundary and intragranular boundaries between elastic and plastic domains at least close to local elastoplastic transition. Evenif, experimental kinematic and thermal fields come different imaging systems and are estimated through an heavy calibration procedure, it has been prove that final thermomechanical quantities are in phase and in total agreement. Nevertheless some limits of our experimental database in the achievement of mesoscale energy balance have also been shown, notably due to the incapacity of measuring a 3D thermal field as well as a stress field. In order to complete the experimental investigation and to access to complementary data, a numerical strategy is proposed in the next part.

Part III

Coupling model and experiment

Chapter 6

Modelling based on fullfield measurements

Contents

6.1 Introduction

6.1.1 Transition scale

A polycrystalline aggregate is a heterogeneous material where the mechanical properties vary over a characteristic distance (cell size, deformation band, grain...). To model it, a Representative Volume

Element (REV) has to be considered. Classically, it needs to have the proper size, small enough to be macroscopically considered as a material point containing the desired level of physic and large enough to represent the macroscopic material properties and to be numerically efficient. Different levels of modelling could be considered and each of them is related to a characteristic internal length of the material. Figure 6.1.1 presents a schematic scale transition for a polycrystal from the macroscopic structure to the atom.

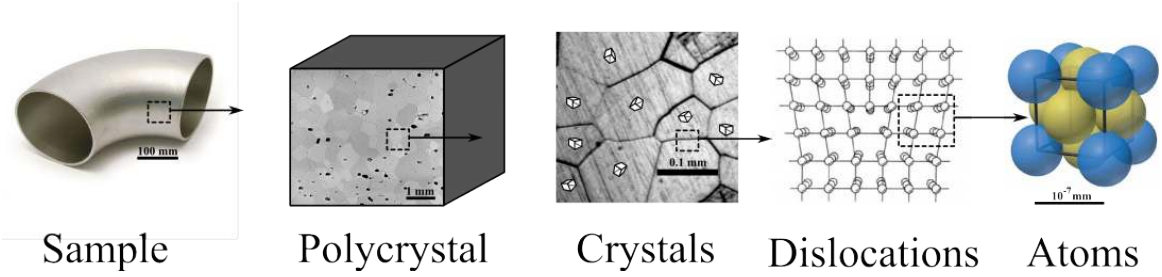

At least, four scales are classically used:

1. ***the macroscopic level***: it represents the mean thermomechanical response of the material generally through phenomenological constitutive laws in the Finite Elements Methods (FEM) framework [Flores 2007]. At such scale, it is difficult to introduce any other structural information than the macroscopic geometry of the sample. Phenomenological constitutive laws are generally identified on "simple" laboratory tests (tension, compression, torsion ...) including simple sensors for the measurements (load cell, extensometers ...). It corresponds to the engineer's scale who has to design components and structures and the main advantage is related to the possibility to apply realistic and quite simple boundary conditions.

2. ***the aggregate level***: it contains from hundreds to thousands grains, classically within a Crystalline Plasticity Finite Element Model ($CPFEM$). Each grain defines an inclusion within the material with its own shape and properties. Constitutive laws could be phenomenological or not, depending on the desired degree of physics and the thermomechanical properties are uniform per grain. These models required the knowledge of physical grain morphologies in 2D, 3D or to use numerical procedure to create fictive grain patterns based or not on experimental measurements and statistics. The main difficulties remains the discretization of the microstructure and the definition of the appropriate mesh [Musienko 2009]. The knowledge of experimental aggregate boundary conditions are also required through experimental field measurements or fictive boundary conditions (periodic, uniform...). Boundary conditions have a wide influence on the mechanical response of the model: no realistic boundary conditions lead to significant errors [Evrard 2010]. This scale is the one of the analysis of strain localization, crack propagation... within polycrystalline structures and leads to a finer description of thermomechanical constitutive laws and relevant variables.

3. ***the dislocations level***: it is often based on Discrete Dislocation Dynamics simulations (DDD).

The principle is to numerically generate dislocations inside a numerical 3D box taking into account physical mechanisms of movement, production and annihilation within a 3D lattice (for F.C.C. material see [Robertson 2001]). Such simulations necessarily required finer experimental observations to be tested. At this scale, the behavior of each individual dislocation segment is modeled to finally improve the understanding of larger discrete population of dislocations, including interaction with obstacles, defects, production flow. It improves the understanding of elementary mechanisms of plasticity appearance and evolution.

4. ***the atoms level***: it is mainly based on Molecular Dynamics (MD). The principle is to simulate the physical movements of atoms and molecules including interaction mechanisms under different conditions of temperature, pressure ...It requires the knowledge of atomic interaction mechanisms, i.e "force fields" and interatomic potentials. It permits notably the understanding of first dislocation nucleation [Chang 2007]. A link between atomic interactions in discrete framework with the concepts of stress and strain in classical continuum mechanics framework has also be proposed [Frankland 2003].

Each internal length requires on the one hand to access to similar experimental observations to model mechanisms and confront results, and on the other hand, the development in parallel of efficient calculation tools. Each modelling level refers to a specific goal, a degree of mechanism comprehension and a desired calculation efficiency. Nevertheless some authors currently combine every modelling level in order to obtain an upper scale procedure (see for example [Chang 2007] where deformations induced by nanoindentation test are simulated from a discrete atomic scale to continuous fields).

6.1.2 Objectives

The experimental field measurements, in terms of crystallographic texture and thermomechanical fields, as presented previously, are at the scale of the aggregate. Thus one focuses now on the polycrystal aggregate model.

1. The first aim consists in observation and understanding. In this way numerical simulations consists in relevant comparative database for a better experimental understanding. Indeed, experimentally, one observes consequences of local mechanical dissipation keeping in mind problems of measurements, resolutions, metrology, smoothing, interpretation, boundary conditions and material properties. In particular, the latter significantly affect the kinematic of the phenomena and consequently the ability to observe and to understand the associated mechanisms. Numerically, the mechanisms of deformation, the local material discontinuities, and the local constitutive laws are introduced and one observes consequently the expected surface fields for a local given and known mechanism. Numerical and experimental databases are consequently complementary ways to analyze the relevance of the experimental database, i.e the relevance of thermal and strain localization related to microstructure, magnitudes, chronology of plastici phenomena, thermal laplacian field shape and levels...

2. The second objective concerns the energy balance. Numerical investigations will introduce a dialog between energy quantities, hardly accessible experimentally, and the localization phenomena.

In this way, the effective energy stored in intragranular hardening is accessible and it is possible to compare it with the one obtained by energy balance. The great interest of thermomechanical simulations is the ability to perform energy balance from surface thermal and mechanical fields, exactly as experimentally, and then to compare to simultaneously unmeasurable quantities such as intragranular plastic strains, stresses, slip systems activity...

To investigate both previous points, i.e to confirm experimental results and to access to complementary unmeasurable fields, one has to simulate the thermomechanical behavior of the previously analyzed polycrystalline aggregate. In this way, one needs to perform 2D or 3D coupled thermomechanical simulations introducing a crystal plasticity framework as well as realistic grain morphology. to our knowledge, no such works have already been published on the ability to polycrystalline model to render local thermal fields thanks to thermomechanical coupled simulations.

6.1.3 Thermomechanical analysis in polycrystalline aggregates

In thermomechanics, authors classically work either with mean-field homogenization techniques, to access notably to mean temperature evolution or Finite Element Method (FEM) to obtain energy fields under purely mechanical modelling. In the first case, the thermomechanical coupling is explicitly introduced through the heat equation. The grain morphology, the microstructure texture, the intergranular behavior are implicitly modeled. The calculation is done through an homogenization procedure. In the second approach, the grain morphology is modeled and allows the estimation of local mechanical fields as well as the intrinsic dissipation, the stored energy, the fraction of stored energy ...

The pure mechanical modelling of polycrystal aggregate is actually more and more mastered. Since about 50 years, very complex theories have been developed within the crystalline plasticity framework [Hutchinson 1964, Asaro 1983, Asaro 1985]. Each of them has been designed to account for several microscales, the presence of heterogeneities, the various population of dislocations, the granular interactions... First simulations based on crystal plasticity are attributed to the pioneering works of Pierce and co-workers [Peirce 1982, Peirce 1983]. A large overview of crystal plasticity modelling could be found within [Roters 2010]. The comparison between experimental and numerical energy balance at granular scale based on such crystalline framework is much more recent, notably due to the complexity in obtaining such experimental database. One can cite for example the works of Saai [Saai 2010]. The author has modeled the mechanical response of a bicrystal subjected to a monotonic tensile test and compared the results to experimental local heat sources evolution. The model uses a finite transformation framework as well as the single crystal dislocation-based constitutive law proposed by Tabourot [Tabourot 1997]. Modeling has been done through the commercial FE code ABAQUS in its explicit form [Dassault-System 2010]. The study notably allowed, to our knowledge, the first intragranular comparison between numerical and experimental energy fields coming from Infrared Thermography. The author emphases the fact that spatial localizations as well as time variations of mean heat losses per grain is captured by the model. Similar studies has been more recently done on oligocrystal specimen (grain number lower than 7 within the analyzed region) [Badulescu 2011]. The 3 dimensional multicrystal sample takes into account the real grain morphology on each sample face and assumes then

a linear interpolation of boundaries through the thickness. The constitutive law was the phenomenological one proposed in [Kalidindi 1992]. Results underline notably a fraction of dissipated energy on inelastic expended one which ranges from 10 to 90 % in different grains and the mean value reach 50% at $\approx 7\%$ of mean axial strain.

For real thermomechanical analysis, analytic and numerical approaches and/or FE method can be considered. A full introduction to coupled thermo-plasticity theory is for example done in [Dillon 1963b] and its implementation within a numerical finite strain analysis could be found in [Simo 1992]. Note that originally, thermo-elastic and then thermo-plastic numerical analysis have been widely developed within a finite strain framework for the modelling of hot metal forming process [Oh 1989]. Nevertheless, the coupling between crystal plasticity and thermomechanical analysis is also recent and is still studied from an homogenized point of view. Here, the homogenization procedure is underlined in contrast with FEM. One could see recent works of Håkansson [Håkansson 2008] where the impact of initial crystallographic texture on the heat generation was studied. In this work, a rate-dependent single crystal model is used within a thermodynamic framework for large deformation. Then isothermal and adiabatic simulations are performed by homogenization of a 400 randomly oriented grains. A Taylor average scheme is used and monotonic as well as low cyclic loading are applied. The framework was inspired from [Hutchinson 1976, Méric 1991, Busso 2005]. The author evidenced notably a great dependence between initial crystallographic texture, i.e Goss, Brass, isotropic one or single crystal and the homogenized temperature variation and fraction of dissipated energy on expended one. In parallel, Vincent [Vincent 2008] worked on the ability of different cyclic plasticity models to predict the thermal and stored energy evolution, also at homogenized scale. The author used notably a micro phenomenological model at granular scale containing isotropic and kinematic variables. The model was the one previously developed in [Cailletaud 1992]. The author shown that its three models, i.e containing non linear-isotropic hardening and either linear kinematic hardening, non-linear kinematic hardening or three non-linear kinematic hardening, provide mechanical cyclic response in agreement with experiments performed on a A304L stainless steel. Every model is then mechanically admissible regarding to a specific database, and thermodynamically admissible also, i.e written in a thermodynamic consistent framework. Nevertheless, thermal and stored energy evolution are significantly different. The author evidenced the need to experimentally and numerically study specimen temperature evolution in order to discriminate energetically and non energetically based model, i.e leading or not to the appropriate partition between stored and dissipated energy. More recently, [Mareau 2011] published works on the interaction between microstructure and dissipative deformation mechanisms under cyclic loading. The aim of this study was to optimize steel microstructure regarding to dissipative mechanisms since it could be responsible of microcrack appearance. Two dissipative mechanisms are assumed: the oscillation of pinned dislocations defined as an anelastic mechanism and the viscoplastic slip of dislocations considered as an inelastic one. Results coming from mean-field approach, introducing local physical crystal plasticity framework, have been compared to self-heating tests [Doudard 2009]. The author emphasized notably that large and well-oriented grains for plasticity are about 30 times more dissipative than other grains and so are preferential sites for microcrack initiation.

From this brief overview one can observe that dissipative aspects of metal regarding of loading or the microstructure is an old addressed problem, widely treated numerically, and one could note that a significant interest on this topic is actually clearly visible, in particular in fatigue. This point is verified whatever the approach, i.e thermomechanical approach within homogenization procedure or mechanical energy balance achievement through Crystal Plasticity Finite Element Method (CPFEM). One also observes that the local thermal modelling within polycrystal aggregate is never done at least in solid mechanical field. A first reason is the absence of experimental studies accessing to local thermal fields. A second reason could be the efficiency of such thermomechanical computation. Indeed, CPFEM are very time consuming because of the multiplicity of internal variables to account for, more or less physics, and the non-linearity of hardening laws. In parallel fully coupled thermomechanical analysis are also time consuming since it requires to solve a coupled problem and boundary conditions are also problematic.

Nevertheless, as we dispose on experimental surface full-field measurements as well as any required crystallographic informations, one presents within this part the study of thermomechanical couplings within polycrystalline FE simulations. In a first chapter, F.E models are introduced and then constitutive laws. In a second chapter numerical field analysis is performed and then numerical energy balance and comparison with experimental results are presented.

6.2 Modeling assumptions and boundary conditions

As Thermomechanical Polycrystal Finite Elements Modeling remains a tricky problem. One presents here some choices which have been done to perform such calculations:

- ***Constitutive laws are basic***. CPFEM[1] remains a complex numerical analysis and a time consuming problem. Thus two options have been chosen:
  - Firstly two frameworks will be studied within this chapter. The first one focuses on a classical elastoplastic constitutive law with a von Mises criterion. The second one focuses on CPFEM, introducing physical plasticity mechanisms at single crystal scale. Both approaches will allow estimating the necessity or not to use a complex physical constitutive law at single crystal scale to represent local thermomechanical couplings.
  - Secondly, both constitutives laws contain basic ingredients for, on the one hand homogenized and phenomenological constitutive law, and on the other hand, crystalline plasticity ones. On one hand a bilinear kinematic hardening with a linear thermoelastic coupling is introduced within intragranular domain. A plastic yield distribution in the sens of von Mises is then implemented based on experimental database to represent the microstructure effect. On the other hand the CPFEM is used. An isotropic hardening based on a viscoplastic dislocation flow is introduced at intragranular domain. Here each grain is characterized by its experimental orientation and a similar isotropic thermoelastic coupling is introduced.

[1] Crystalline Plasticity Finite Element Method

- ***Grains are columnar***, or quasi-2D. Many works have been recently done on the ability to render full 3D numerical microstructure, for exemple, combining a Scanning Electron Microscope (SEM) with a scanning focused ion beam (FIB) [Khorashadizadeh 2011] (destructive method), X-ray diffraction contrast tomography in [Ludwig 2008] (nondestructive method), 3D Voronoi mosaic using statistical information of surface EBSD analysis [Signor 2011] (nondestructive method) or totally random one [Barbe 2001]. A large summary of microstructure models could be found in [Cailletaud 2003]. Here no work is done on a more complex representation of the microstructure than a 3D extrusion of grain-surface morphology, captured by EBSD analysis (see chapter 1.1).

- ***Meshes are regular and no grain boundary properties are considered***. Some authors worked on the grain boundary modelling. In [Musienko 2009], the mains possibilities, notably cohesive elements, adaptative mesh ...are reminded. Within the present study one assumes "zero-width" grain boundary with a displacement continuity. In parallel, grains are modeled as a set of finite elements cubes. This technique makes mesh generation problem quite simple, but provides stair-like grain interfaces.

6.2.1 Polycrystalline Microstructures F.E. Mesh Generation

A ***Matlab*** routine has been developed within this thesis to generate from an Orientation Imaging Microscopy output text file a columnar microstructure mesh compatible with ***Abaqus*** input file formalism. The goal of the mesh generation procedure is to automatically build an input file for ***Abaqus*** simulation, including experimental boundary conditions (see next chapter) and composite properties of polycrystalline material based on crystallographic orientations.

Algorithms are not detailed here but the main steps of the meshing generation procedure are presented. Table 6.1 presents an exemple of OIM output text file for the tested material. (ϕ_1, Φ, ϕ_2) is the triplet of Euler angles. x and y are position of data point and grain I.D. refers to connected datapoint set in which similar orientation is found. It allows to count grains. Algorithm steps are the followings:

ϕ_1	Φ	ϕ_2	x	y	grain I.D.
2.14	0.58	4.64	0.0	0.0	1
↓	↓	↓	↓	↓	↓
2.09	0.56	4.68	140.0	0.0	1776

Table 6.1: Exemple of Orientation Imaging Microscopy output text file

1. read OIM data vector and build a spatial field for each angle and grain ID.

2. create the associated 3D node table as well as element connectivity one. Here, material properties are extruded using a certain number of element along the normal direction of specimen surface.

3. create grain element sets and associated grain properties, notably orientation. The material is treated as a composite containing n different material with n the number of grain.

4. create material properties associated to each grain.

Then, every required information, i.e node positions, element connectivity table, elements sets, material properties ... are written in the ***Abaqus*** input file formalism.

As detailed in the chapter 1.1 the studied material is composed by 1776 grains and the resolution of E.B.S.D. microstructure field is 20x20μm^2 for a field of view of 5x5mm^2. Every field measurement has been projected on similar grid. Keeping in line with experimental database, the crystallographic grid is used as regular mesh for Finite Element Modeling. Figure 6.1 presents the field of view of the studied microstructure as well as a crop of a particular grain with its associated mesh.

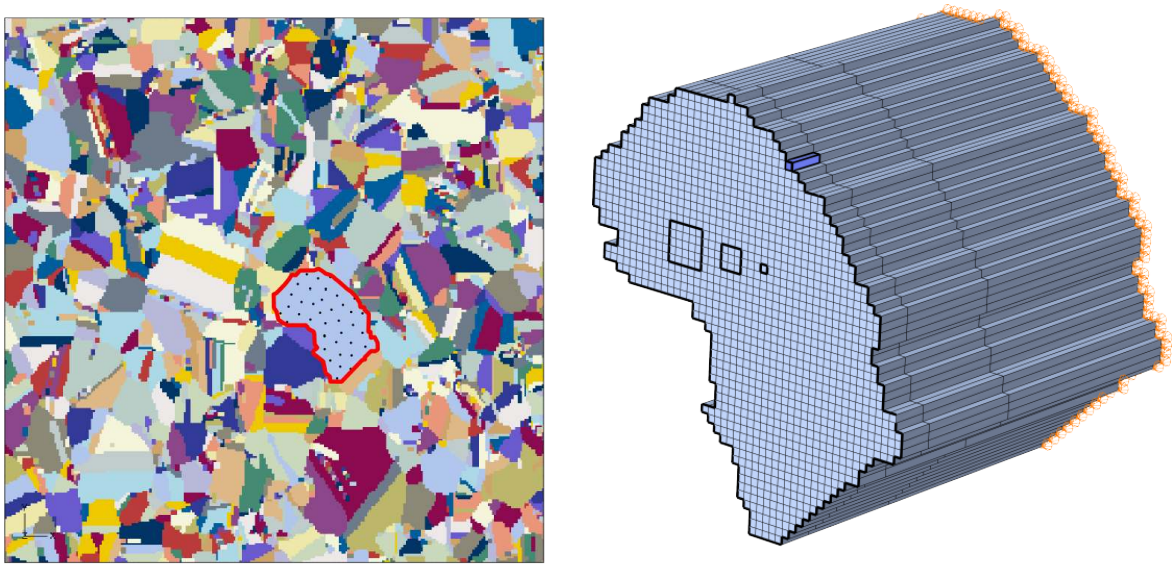

(a) (b)

Figure 6.1: (a) A316L microstructure extracted from E.B.S.D. analysis and (b) crop of one specific grain meshed with 20x20xAμm^3 elements

As shown the figure 6.1, the element thickness, noted A, is not constant in depth. The problem is to obtain the good compromise between the number of elements, the computing convergence, and the relevance of thermal boundary conditions. On the one hand the half thickness of specimen has to be modeled in order to apply symmetrical thermal boundary conditions on the back face to represent the specimen volume for conduction phenomena. On the other hand, within 3D analysis, several elements in the specimen thickness are necessary to improve the calculation convergence because of the multiaxial element distortion introduced by the constitutive law as a function of the loading path.

Finally, depending on the computers (memory, cpus...), it will be necessary to reduce the number of elements. As it is shown in [Petit 2007], 3 layers of elements constitute a good compromise in terms of computing convergence and time calculation when the thickness is close to the grain size. So, 3 layers of elements are at least required for a good convergence, notably within complex loading path (tension-compression). Boundary conditions will be treated in section 6.2.2. Note, for the element surface layer that $A = 80\mu m$, $A = 300\mu m$ for the second and $A = 620\mu m$ for the last.

The FEM is based on solid linear tetrahedral brick elements called $C3D8T$ in Abaqus/Standard. The $C3D8T$ is a coupled temperature displacement element. It consists of a brick with eight nodes, and four degrees of freedom (x, y and z displacements (u_x, u_y, u_z) and temperature). The numerical model contains 187.500 elements (250x250x3) and 1.008.016 associated degree of freedom. In addition, to limit the time simulation, a reduced integration has been chosen. Element used in this way are therefore $C3D8RT$, where R means reduced.

Figure 6.1 (b) points out the fact that some grains, notably the milimetric ones, are well discretized. The mesh resolution ranges from 3 to 4045 elements per grain. Figure 6.1 (b) presents in addition the spatial resolutions. The biggest square (5x5 elements) is equivalent to the experimental kinematic resolution provided by D.I.C. (see chapter 2.1), the second square (3x3 elements) is the minimum experimental thermal resolution, and obviously, the 1x1 element is the E.B.S.D. resolution.

6.2.2 Experimental boundary conditions extraction

Homogeneous or periodic boundary conditions [Barbe 2001, Diard 2002, Guilhem 2011] are often used for FE calculations on grain aggregates. In addition, usually, the displacement boundary conditions are applied by using a linear loading path, i.e. only taking into account the initial and final state [Evrard 2010]. In the present case, a "realistic" approach has been used in terms of boundary conditions, by using experimental kinematic and thermal full-field measurements for the aggregate loading path. This choice is natural for a model-experiment dialog, since neighboring grain behaviors (over the studied area) have a wide influence on the cropped field [Doumalin 2003]. From the numerical point of view, the mean advantage of experimental data treatment procedure which has been developed in previous parts is that every experimental fields are finally expressed in the same configuration, dealing with the same area at the same time, and are interpolated on the same grid (the E.B.S.D. one). It allows on the one hand a direct extraction and then application of experimental measurement to numerical mesh (node by node). On the other hand, it allows a direct comparison between experimental and numerical results.

Applying displacements and temperature at the aggregate boundaries, implies the enforcement of kinematic and thermal Dirichlet boundary conditions at FEM aggregate contour. Both next sections present how such boundary conditions are applied.

6.2.2.1 Kinematical boundary conditions

As described in chapter 2.1, the axial and transversal displacements, noted $U(x, y, t)$ and $V(x, y, t)$ respectively, are known for every node of the EBSD grid and for each experimental time increment. The projection of experimental kinematic field within grains ensures in addition the intragranular continuity as well as the lack of noise of boundary conditions. Applying such regular boundary conditions widely improves the stability of Finite Element problem. This point is classically problematic when one desires the application of the experimental boundary conditions. According to figure 6.1 (b) 4 nodes are considered along the model thickness.

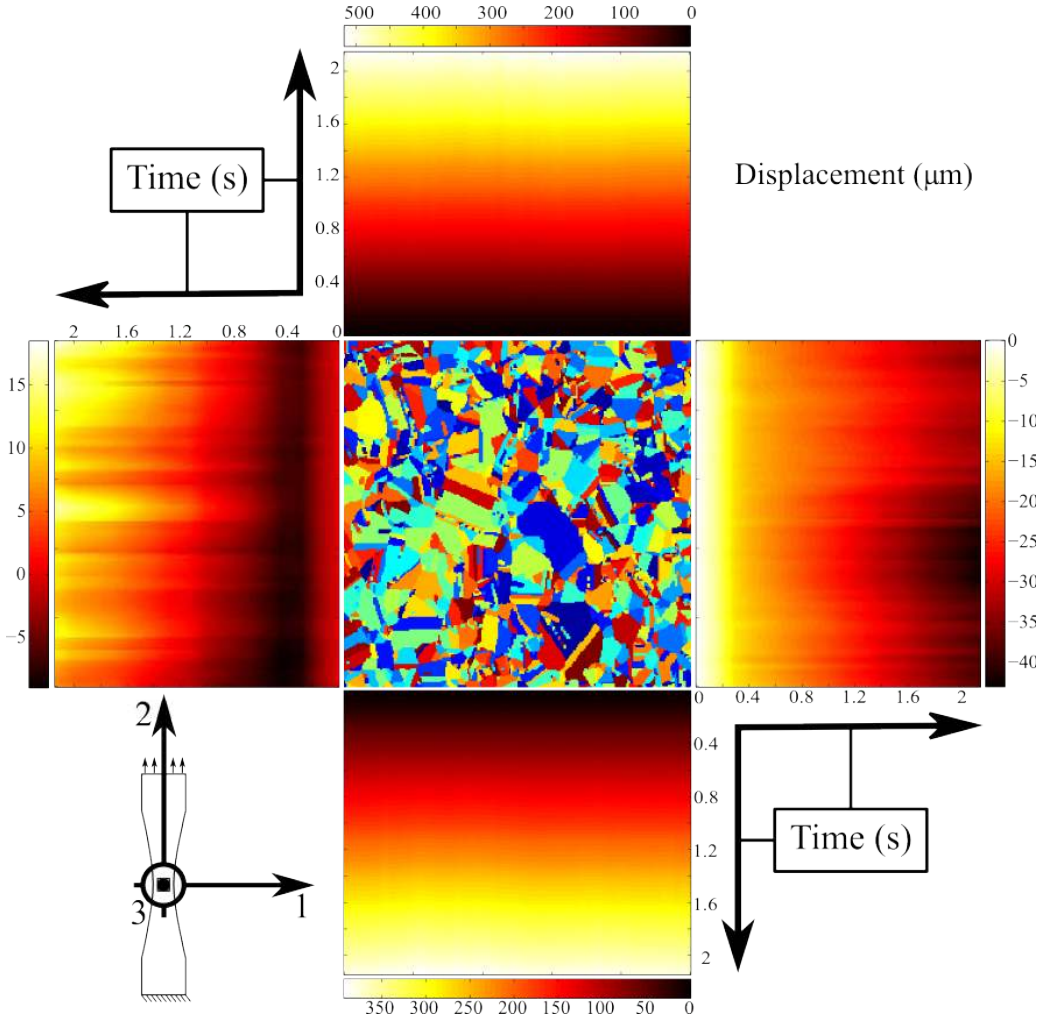

Figure 6.2: Displacement paths, normal to surfaces, applied on boundary conditions of FEM

Let us call $M(x, y, z, t)$ the node at position x, y, z at time t. One assumes here the propagation of U and V displacement along the thickness segment, i.e. $\left[U_{M(x,y,1,t)} = U_{M(x,y,2,t)} = U_{M(x,y,3,t)} = U_{M(x,y,4,t)}\right]$

and $\left[V_{M(x,y,1,t)} = V_{M(x,y,2,t)} = V_{M(x,y,3,t)} = V_{M(x,y,4,t)}\right]$. Such assumption is in agreement with columnar grain structure.
In agreement with previous points, experimental loading paths (U and V) are applied to every node segments of the aggregate contour. Figure 6.2 presents the loading paths applied to contour node. Figure 6.2 only presents the loading normal to the considered surface, i.e. upper and lower face presents $U(x, y, t)$ displacement while right and left one present $V(x, y, t)$ displacement. Colormap presents displacement in μm and loading field presents the propagation of contour loading along the simulation time. One could note that loadings normal to right and left faces are very far from homogeneous boundary conditions.

In addition, the boundary condition $U_{M(x,y,4,t)} = 0$ is applied on the back face (see figure 6.1 (b)) assuming a symmetrical behavior of the specimen.

6.2.2.2 Thermal boundary conditions

As in the previous section, experimental temperature $T(x, y, t)$ is known for each experimental time increment. One assumes here similar assumptions than kinematic ones:

- homogeneity of temperature along the thickness node segment, i.e. $\left[T_{M(x,y,1,t)} = T_{M(x,y,2,t)} = T_{M(x,y,3,t)} = T_{M(x,y,4,t)}\right]$
- Let Φ be the thermal flux boundary condition. Symmetrical or adiabatic boundary conditions are applied on the background face, i.e. $\Phi_{M(x,y,4,t)} = 0$

Finally uniform and constant convective exchanges are applied on the observation face (see figure 6.1). The convection parameter between A316L and the air has been found in literature with a value of 14.6 $W.m^{-2}.K^{-1}$.

One could already point that applying Dirichlet boundary conditions in displacement and temperature to FEM is problematic. Indeed, due to kinematic loading, elements will deform elastically then plastically. Associated to the elasto-plastic deformation, the temperature of elements will vary. The thermomechanical coupling relating deformation and temperature depends on the constitutive law. In parallel, boundary elements exhibit the experimental temperature leading by the effective thermomechanical coupling of the material. Thus numerical thermal field of the aggreate will result from a competition between the thermal response of the FEM model (in the aggregate) and the thermal response of the tested material (at grain aggregate boundaries). If the kinematic and thermomechanical coupling introduced within each Finite Element do not represent exactly the thermomechanical coupling of the tested material, gradient of temperature will necessarily appear from the center to extremities of FE aggregate. Higher is the deviation between experimental and numerical "constitutive law" more important are the thermal gradients. Nevertheless, as for displacements the aggregate thermal boundary conditions must be as realistic as possible representing the dissipative and conductive behavior of neighboring grains (over the field of view). An improved boundary condition management would be to mix Dirichlet ones for displacement and Neumann ones for temperature. It requires to

apply relevant heat losses at aggregate contour. Nevertheless, this point has not been solved within this work.

6.3 Different refinement levels of modelling

6.3.1 Introduction

In recent years, considerable interest has been developed in micromechanical modelling of solids. This interest is due to the heterogeneous character of many materials which play a dominant role in the macroscopic behavior. Many materials are concerned: multiphase fiber and particulate composites, soil, rock, concrete, and various granular materials. classically, the characteristic length of such microstructure is smaller than other characteristic lengths of the problem (see figure 6.1.1). In this case, classical theories of continuum mechanics do not predict any more the local and global response of material. This has lead to the development of many new micromechanical theories for solids (see section 6.1.3).

As precised within the section 6.2, two kinds of modelling are proposed to represent the local heterogeneity of internal variables. Both have different levels of fineness. In a first time, a granular "homogenized" point of view is assumed, i.e. the intragranular stress flow is not based on crystalline plasticity mechanisms but on von Mises approach including a granular distribution of yield stress. In a second time, a granular crystal plasticity framework is used including the effective granular orientation distribution. Actually, both models have been chosen since they correspond to two kinds of basic modelling of heterogeneous material.

Figure 6.3 presents two basic model concepts. Note that the study of such standard case has been developed in detail, for example in [Aravas 1990]. Figure 6.3 (a) represents a structure where every elasto-plastic bar (i.e. grains) possesses the same elastic properties, the same hardening properties but different yield stresses. The plasticity will consequently develop gradually in every bar (or grain) depending on the local yield stress as well as the yield stress of neighboring bars. Figure 6.3 (b) is a structure where every bar have same elastic properties, same hardening properties, same yield stress but different angular orientations relatively to the loading axis. Here the plasticity will develop gradually in every bar depending on the local bar orientation as well as the angle of neighboring bars. Both model introduce the fact that heterogeneous structures such as polycrystals could be modeled in two different ways[2]: (1) by introducing the physical grain orientation as a material heterogeneity (see figure 6.3 (b)) or (2) by using a simplified way which consist in representing this physical grain orientation by a yield stress distribution (see figure 6.3 (a)). Let us begin with the yield stress distribution model.

[2]Homogenization concepts are not presented here

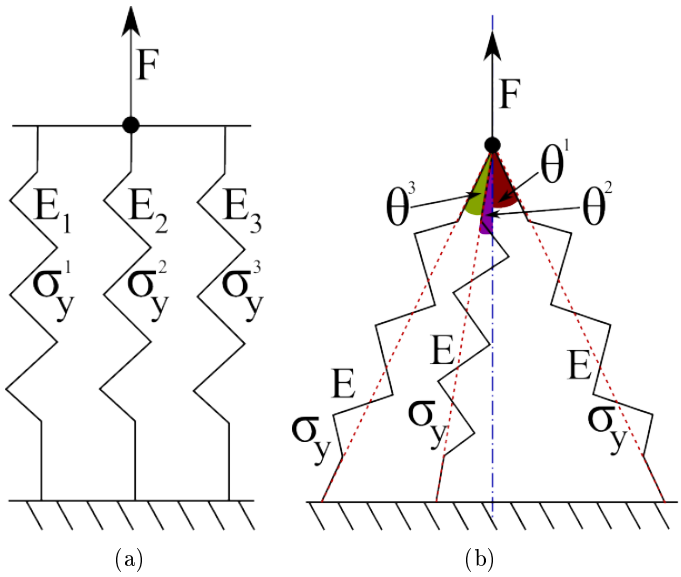

Figure 6.3: Scheme of (a) three parallel bars structure with yield variation and (b) three bars structure with angle variation

6.3.2 Homogenized point of view: thermo-elasto plastic material with linear kinematic hardening

This section introduces a way to estimate, using FE, thermomechanical fields at granular scale of 316L stainless steel keeping a simple description of intragranular plasticity mechanisms. It consists in the modelling of grain orientation field which leads to a natural progressive plastic strain activation by a representative granular yield stress field [Seghir 2012a]. It is based on the analysis of experimental surface strain fields of the tested specimen. This model will be called ***YIELD MODEL*** in the rest of analysis. Let first introduce the constitutive law as well as the associated thermodynamical framework.

6.3.2.1 Constitutive laws and thermomechanical framework

In the following, the Generalized Standard Material framework [Nguyen 1975] is adopted. This framework reduces the construction of the constitutive law to the definition of two potentials: (i) the free energy potential Ψ which describes the local state at every time t and (ii) the dissipation potential ϕ which gives the flow rules of the system according to the 1^{st} and 2^{nd} thermodynamic principles. Ψ is chosen convex quadratic to ensure that the dissipation remains positive for any system variation. In addition, a partition of the total deformation ε into an elastic part ε^e and a plastic part ε^p is assumed. Thus, Ψ is written as a function of three variables: the absolute temperature T, ε^e and ε^p:

$$\varepsilon = \varepsilon^e + \varepsilon^p \tag{6.1}$$

$$\Psi = \Psi\left(T, \varepsilon^e, \varepsilon^p\right) \tag{6.2}$$

The dual thermodynamic variables associated to $\boldsymbol{\varepsilon}^e$ and $\boldsymbol{\varepsilon}^p$ are respectively $\boldsymbol{\sigma}$ and the backstress $\boldsymbol{X}$. Thus:

$$\boldsymbol{\sigma} = \rho\frac{\partial\Psi}{\partial\boldsymbol{\varepsilon}^e} \quad ; \quad \boldsymbol{X} = \rho\frac{\partial\Psi}{\partial\boldsymbol{\varepsilon}^p} \tag{6.3}$$

In the case of an isotropic elasticity, linear thermo-elastic coupling and linear plastic kinematic hardening, the free energy potential Ψ is written [Lemaitre 1994]:

$$\rho\Psi = \left[\frac{1}{2}\left(\lambda \mathrm{tr}\left(\boldsymbol{\varepsilon}^e\right)^2 + 2\mu \mathrm{tr}\left(\boldsymbol{\varepsilon}^{e^2}\right)\right) - (3\lambda+2\mu)\alpha\theta \mathrm{tr}\left(\boldsymbol{\varepsilon}^e\right) + \frac{1}{3}H\,\mathrm{tr}\left(\boldsymbol{\varepsilon}^{p^2}\right)\right] \tag{6.4}$$

with λ and μ the Lamé's coefficients, α the thermal expansion coefficient, $\theta = T - T_0$ with T_0 the initial temperature and H, the hardening modulus. Note that the thermal expansion of the material is assumed to be isotropic. The plastic criterion corresponds to the von Mises yield function which is:

$$\left\{\begin{array}{rcl} f\left(\boldsymbol{\sigma}\right) & = & \sqrt{\frac{3}{2}J_2\left(\boldsymbol{s}-\boldsymbol{X}\right)} - \sigma_y \\ \boldsymbol{s} & = & \boldsymbol{\sigma} - \frac{1}{3}\mathrm{tr}\left(\boldsymbol{\sigma}\right)\boldsymbol{I} \\ J_2\left(\boldsymbol{s}-\boldsymbol{X}\right) & = & \frac{1}{2}\left(\boldsymbol{s}-\boldsymbol{X}\right)\left(\boldsymbol{s}-\boldsymbol{X}\right) \\ \boldsymbol{X} & = & \frac{2}{3}H\boldsymbol{\varepsilon}^p \end{array}\right. \tag{6.5}$$

By derivation of equation (6.4), one obtains the stress $\boldsymbol{\sigma}$ tensor :

$$\boldsymbol{\sigma} = \rho\frac{\partial\Psi}{\partial\boldsymbol{\varepsilon}^e} \quad = \quad \lambda \mathrm{tr}(\boldsymbol{\varepsilon}^e)\boldsymbol{I} + 2\mu\boldsymbol{\varepsilon}^e - 3K\alpha\theta\boldsymbol{I} \tag{6.6}$$

with $3K = 3\lambda + 2\mu$. The total derivative of the stress tensor $\boldsymbol{\sigma}$ could be written:

$$\mathrm{d}\boldsymbol{\sigma} = \frac{\partial\boldsymbol{\sigma}}{\partial\boldsymbol{\varepsilon}^e} : \mathrm{d}\boldsymbol{\varepsilon}^e + \frac{\partial\boldsymbol{\sigma}}{\partial T}\mathrm{d}T \tag{6.7}$$

Thus, taking into account (6.6):

$$\mathrm{d}\boldsymbol{\sigma} = \mathbb{C} : \mathrm{d}\boldsymbol{\varepsilon}^e - 3K\alpha\boldsymbol{I}\mathrm{d}T = \mathbb{C} : (\mathrm{d}\boldsymbol{\varepsilon} - \mathrm{d}\boldsymbol{\varepsilon}^p) - 3K\alpha\boldsymbol{I}\mathrm{d}T \tag{6.8}$$

Moreover, with respect to the 1^{st} and the 2^{nd} thermodynamic principles, the heat coupled equation can be obtained [Maugin 1992] (see appendix A.1):

$$\begin{array}{rl} \rho C_v\dot{T} = & r + div(\boldsymbol{K} : \underline{grad}(T)) + \boldsymbol{\sigma} : \dot{\boldsymbol{\varepsilon}} + \rho T\frac{\partial^2\Psi}{\partial T\partial\boldsymbol{\varepsilon}^e} : \dot{\boldsymbol{\varepsilon}^e} - \rho\frac{\partial\Psi}{\partial\boldsymbol{\varepsilon}^e} : \dot{\boldsymbol{\varepsilon}^e} \\ & + \rho T\frac{\partial^2\Psi}{\partial T\partial\boldsymbol{\varepsilon}^p} : \dot{\boldsymbol{\varepsilon}^p} - \rho\frac{\partial\Psi}{\partial\boldsymbol{\varepsilon}^p} : \dot{\boldsymbol{\varepsilon}^p} \end{array} \tag{6.9}$$

Taking into account the equation (6.3) into the heat coupled equation (6.9), one obtain:

$$\begin{aligned}\rho C_v \dot{T} = \quad & r + div(\boldsymbol{K} : \underline{grad}(T)) + \boldsymbol{\sigma} : \dot{\boldsymbol{\varepsilon}} + \rho T \frac{\partial^2 \Psi}{\partial T \partial \boldsymbol{\varepsilon}^e} : \dot{\boldsymbol{\varepsilon}^e} - \boldsymbol{\sigma} : \dot{\boldsymbol{\varepsilon}^e} \\ & + \rho T \frac{\partial^2 \Psi}{\partial T \partial \boldsymbol{\varepsilon}^p} : \dot{\boldsymbol{\varepsilon}^p} - \boldsymbol{X} : \dot{\boldsymbol{\varepsilon}^p}\end{aligned} \tag{6.10}$$

The term $\rho T \frac{\partial^2 \Psi}{\partial T \partial \boldsymbol{\varepsilon}^p} : \dot{\boldsymbol{\varepsilon}^p}$ corresponds to the thermoplastic coupling, usually linked to phase changes in the material. In the present case, this term is neglected. Thus, the term $\rho T \frac{\partial^2 \Psi}{\partial T \partial \boldsymbol{\varepsilon}^e} : \dot{\boldsymbol{\varepsilon}^e}$ denoted d_{Te}, which corresponds to the thermoelastic coupling, is the only coupling term of the equation. It can be written as follows:

$$d_{Te} = T \frac{\partial \boldsymbol{\sigma}}{\partial T} : \dot{\boldsymbol{\varepsilon}^e} = -3K\alpha T \boldsymbol{I} : \dot{\boldsymbol{\varepsilon}^e} = -3K\alpha T \mathrm{tr}\left(\dot{\boldsymbol{\varepsilon}^e}\right) \tag{6.11}$$

As the expression of the elastic strain under isotropic condition is the following:

$$\boldsymbol{\varepsilon}^e = \frac{1+\nu}{E}\boldsymbol{\sigma} - \frac{\nu}{E}\mathrm{tr}\left(\boldsymbol{\sigma}\right)\boldsymbol{I} + \alpha\left(T - T_0\right)\boldsymbol{I} \tag{6.12}$$

The thermoelastic term is:

$$d_{Te} = -\alpha T tr(\dot{\boldsymbol{\sigma}}) - 9K\alpha^2 T\dot{T} \tag{6.13}$$

By taking into account the heat equation (6.10), one obtains:

$$\rho C_v \dot{T} - div(\boldsymbol{K} : \underline{grad}\,(T)) = r + (\boldsymbol{\sigma} - \boldsymbol{X}) : \dot{\boldsymbol{\varepsilon}^p} - \alpha T \mathrm{tr}\left(\dot{\boldsymbol{\sigma}}\right) - 9K\alpha^2 T\dot{T} \tag{6.14}$$

Different terms could be identified:

- r stands for the external sources.
- $(\boldsymbol{\sigma} - \boldsymbol{X}) : \dot{\boldsymbol{\varepsilon}^p}$ corresponds to the intrinsic dissipation and is generally denoted $\dot{d}$.
- $\boldsymbol{\sigma} : \dot{\boldsymbol{\varepsilon}^p}$ and $\boldsymbol{X} : \dot{\boldsymbol{\varepsilon}^p}$ corresponds to anelastic power and power stored in hardening respectivelly.
- $-\alpha T \mathrm{tr}\left(\dot{\boldsymbol{\sigma}}\right) - 9K\alpha^2 T\dot{T}$ corresponds to the thermoelastic coupling. It is also called isentropic power.

One assumes finally that the conductivity tensor $\boldsymbol{K}$ is isotropic and constant at the specimen scale. Thus $\boldsymbol{K} = k\boldsymbol{I}$ and $div(\boldsymbol{K} : \underline{grad}) = k\Delta T$ where Δ denote the Laplacian function. Then, as external sources are not present in this study, the heat source for, a **thermo-elasto-plastic material** including a **linear and isotropic elasticity**, and a **linear plastic kinematic hardening** is denoted:

$$\dot{\Phi} = (\boldsymbol{\sigma} - \boldsymbol{X}) : \dot{\boldsymbol{\varepsilon}^p} - \alpha T \mathrm{tr}\left(\dot{\boldsymbol{\sigma}}\right) - 9K\alpha^2 T\dot{T} \tag{6.15}$$

$$\dot{\Phi} = \rho C_v \dot{T} - k\Delta T \tag{6.16}$$

The time discretisation and implementation of the following constitutive law in F.E. code ***Abaqus/-standard*** has been done and is developped within the appendix G.1.

6.3.2.2 Yield stress field identification

The objective of this section is to identify a yield stress field able to represent the effective progressive plasticity activation (microplasticity) within the tested material. This identification pass through the knowlege of the constitutive law (see section 6.3.2.1) as well as the experimental ultimate state of deformation of the tested sample. Different point could be underlined:

- H_1: ***uniformity of properties per grain***. One has seen within section 6.2.1 that FEM is treated as a composite material of which every phase shapes correspond to columnar grain coming from surface EBSD analysis. One assumes here that the yield stress is uniform per grain.

- H_2: ***plasticity modelling***. The macroscopic stress Σ necessary for the grain plasticity activation depends, in particular, on the orientation of each grain with respect to the loading axis. At the grain scale, the plastic criterion is generally based on the Schmid theory: $\tau^i \leq \tau_c$ (i=1,...,12 in the case of F.C.C. structure) with the resolved shear stress of the considered slip system $\tau = \mathbf{\Sigma} : \mathbb{D}$, $\mathbb{D} = \frac{1}{2}(\underline{n} \otimes \underline{v} + \underline{v} \otimes \underline{n})$. $\mathbb{D}$ is the symmetric part of the Schmid tensor, $\underline{n}$ the unit normal vector, $\underline{v}$ the unit slip direction vector of the considered slip system (i) (see Chapter 1.1) and τ_c a critical shear stress, commonly supposed constant. As $\mathbb{D}$ is a function of the orientation of each grain, the distribution of grain orientations in the specimen leads to a τ distribution for a given $\mathbf{\Sigma}$. Assumption (H_2) consists in replacing this τ distribution by a σ_y distribution, where σ_y is a von Mises equivalent yield stress as: $\Sigma_{eq} \leq \sigma_y$. This distribution relies on experimental distributions of strains. Schmid theory and its construction will be developed in the next paragraph.

Then, different assumptions are made in order to identify intragranular mechanical and thermal parameters of the FEM. As it was previously introduced, the constitutive law is considered as bilinear: linear elasticity followed by linear hardening. The first assumption is to consider the local scale elastoplastic behavior the same as the macroscopic one in terms of moduli. Therefore, the Young's (E) and hardening (H) moduli are identified on an experimental macroscopic tensile strain-stress curve (see figure 6.4) and their values are respectively $E = 208,000$ MPa (see chapter 4.1) and $H = 1,500$ MPa. Figure 6.4 recall the experimental mean stress-strain response of the tested material as well as the mean strain and thermal evolution.

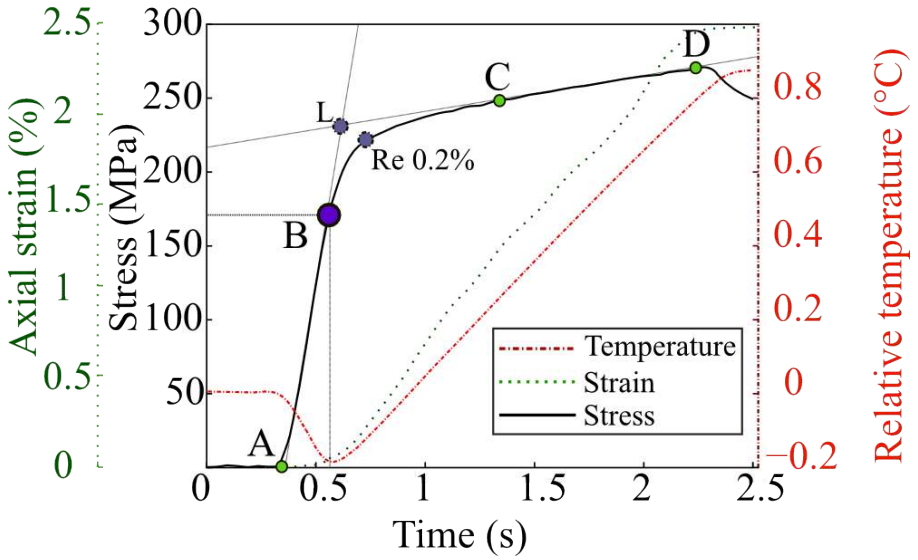

Figure 6.4: Mean values (over the studied area) of thermal, strain and stress fields during monotonic tensile test up to 2.5% mean strain.

A relationship between macroscopic and mesoscopic stresses is also necessary. The transition between the macroscopic and mesoscopic stresses can be described in a general case by the following equation:

$$\boldsymbol{\sigma} = \boldsymbol{\Sigma} - \mathbb{C}^* : \boldsymbol{\varepsilon}^p \tag{6.17}$$

It can then be simplified according to some assumptions, in particular:

- Lin-Taylor's model: $\mathbb{C}^* = \mathbb{C}$
- Sachs's model: $\mathbb{C}^* = 0$

where $\mathbb{C}$ is the stiffness tensor of the bulk and $\boldsymbol{\varepsilon}^p$ the plastic strain at the local scale. An overview is done in [Monchiet 2006]. The first one assumes the homogeneity of the strain $\boldsymbol{\varepsilon}$ in the specimen whereas the second one assumes the homogeneity of the stress $\boldsymbol{\sigma}$. Both homogenized models are popular because they represent respectively an upper and lower bound to the elastoplastic response of the polycrystal [Monchiet 2006]. However, as previously shown in chapter 4.1, the total strain is clearly not homogeneous. Therefore, the Lin-Taylor's model could not be considered here and the Sach's one is chosen. As it is a lower bound of the elastoplastic response of the polycrystal, it will give a first estimate of the local stresses.

Now, as: (i) the experimental total strain field at a fixed macroscopic stress is known (see chapter 4.1), (ii) both elastic and hardening moduli are fixed, (iii) the local stresses are assumed homogeneous and equal to the macroscopic one (Sachs's model), a distribution of equivalent von Mises yield stresses

can be determined (see figure 6.5). The corresponding equations are the following:

$$\begin{cases} {\sigma_y}^g &= \dfrac{E}{E-H}\left[\Sigma - H\varepsilon_\Sigma^g\right] \\ \tau_c &= \mu^g {\sigma_y}^g \end{cases} \tag{6.18}$$

with μ^g the Schmid factor of the considered grain g, Σ the nominal macroscopic axial stress, ε_Σ^g the total strain field in the central studied area at fixed macroscopic stress Σ, τ_c the critical shear stress, which is an intrinsic property of the crystal, and ${\sigma_y}^g$ the field of yield stresses.

The determination of this yield stress field follows three successive steps described below as well as in figure (6.5):

- in order to take into account the generalized plastic state in the studied zone, the mean stress level is taken at 265 MPa, which corresponds to point D in figure (6.4). Then, the experimental corresponding distribution of total strains is plotted in figure 6.5 (a), following the assumption (H_1) that strains are averaged per grain.

- the mean strain per grain in the observed area is linked to a specific ${\sigma_y}^g$ through the bilinear constitutive law and calculated from equation (6.18) and from the values of E, H and Σ (see figure (6.5) (b)),

- the resulting granular distribution of yield stresses is plotted in figure (6.5) (c). This granular yield stress distribution is included between 170 and 265 MPa. This result is qualitatively consistent with the positions of points B and C in figure (6.4), which respectively correspond to the end of the elastic domain and the beginning of perfectly linear plastic domain, i.e. the elasto-plastic transition.

One obtains finally, a uniform intragranular yield stress per grain. This yield stress field ensures each grain to follow an elasto-plastic path from an initial unstressed state to the local ultimate experimental strain state of the tested material. Note that this kind of modelling is based on the knowledge of the ultimate experimental strain state of the sample in opposition to the other model (crystalline plasticity in next section) which is based on the initial crystallographic orientation of each grain.

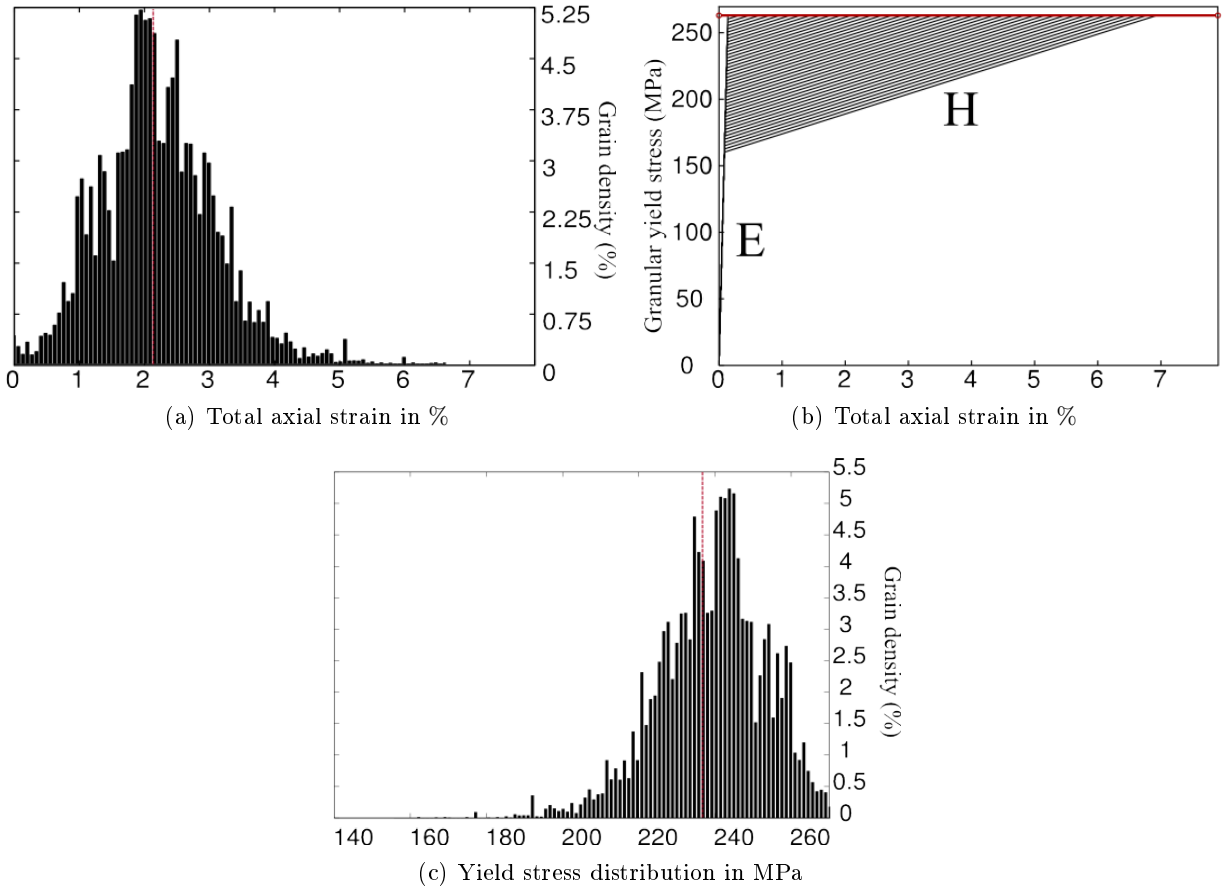

(a) Total axial strain in %

(b) Total axial strain in %

(c) Yield stress distribution in MPa

Figure 6.5: Steps of the determination of the yield stress distribution: (a) experimental granular distribution of absolute strain values, (b) bilinear constitutive law considering a homogeneous stress, (c) resulting granular distribution of yield stresses

Thus, the crystal model ensures the initial state while the yield ensures the final one (at 2.5%). The different thermophysical and material parameters for the present model are summarized in table (6.2).

E (MPa)	H (MPa)	σ_Y (MPa)	ν	lateral aggregate border loading
208,000	1,500	[170; 265]	0.3	experimental conditions (U,V,T)
ρ ($kg.m^{-3}$)	C_v ($J.kg^{-1}.K^{-1}$)	k ($W.m^{-1}.K^{-1}$)	α (K^{-1})	observed face exchanges: h_{air} ($W.m^{-2}.K^{-1}$)
8,000	500	15	$1.65\text{x}10^{-5}$	14.6

Table 6.2: Mechanical and thermal properties of the 316L stainless steel used in the simulation.

In table (6.2), ρ denotes the mass density, C_v the specific heat capacity, k the isotropic conductivity, α the isotropic thermal expansion coefficient, ν Poisson's ratio and h_{air} the convective coefficient between the observed face of specimen and air.

6.3.3 Mesoscopic point of view: crystalline thermo-visco-plasticity and dislocation density based model

This section introduces a way to estimate, using FEM, thermomechanical fields at granular scale of 316L stainless steel using a physical description of intragranular plasticity mechanisms. It consists in a deeper description of numerical integration point (or Gauss point). The integration point is associated to an elementary crystal lattice where physical mechanisms of plastic shear could occur along high atomic density directions. This model will be called ***CRYSTAL MODEL*** in the rest of analysis. Let first introduce the crystal elasto-plastic theory.

6.3.3.1 Introduction to single crystal elasto-plasticity

In crystal plasticity theory, plastic deformation is modeled using the slip system activity concept. It is a physically based plasticity theory that represents the deformation of a metal at the microscale. It is important to note that, in this theory, the continuum framework is keeped even if at such scale the physics is not continuous anymore. Dislocations are assumed to move across the crystal lattice along specific crystallographic planes and directions. When the material is subjected to loading, the magnitude of local stress resolved on a slip plane and along a slip direction initiate and then control the movement, the generation and annihilation of dislocations. Consequently, the material is locally loaded on specific directions, while the volume remains constant. Moreover the crystal lattice could deform elastically while the resolve shear stress does not reach a critical level and also rotates to accommodate the applied loading. Four laws are necessary to describe single crystal elasto-plasticity:

- ***the elastic relation***. It describes the elastic behavior depending on the crystal structure of the considered material.
- ***the kinematic framework***. It describes the partition of strain rate in a elastic and plastic part.
- ***the flow rule***. For intragranular variables, it describes the shear initiation on each system.
- ***the hardening law***. It describes the hardening which occurs on each system after successive loadings.

In the case of polycrystal, an additional component is required: the interaction between such single crystals. It defines how the compatibility is ensured at grain boundaries.

6.3.3.2 Elastic behavior

Elasticity is the physical property of a material that returns to its original shape after loading. Within crystalline material it corresponds to lattice stretching, i.e an increase of distance between atoms which

composes the lattice of crystalline structure. Elastic properties of a material are intrinsically linked to atoms arrangement, i.e atom density in every space direction. Thus by definition, crystalline materials are, at least locally, fundamentally anisotropic. The first important element of single crystal elasto-plasticity modelling is the ability to represent this local anisotropy of elasticity tensor according to the crystalline structure type and the local lattice orientation.
Within elastic domain, most of material exhibit a linear relationship between strain and stress, this point was first stated formally by Robert Hooke in "The true theory of elasticity and springiness [1676]". The resulting linear relationship is known as Hooke's Law. In a generalized manner, i.e 3 dimensionnal case with anisotropic material, the constitutive equation takes the following form:

$$\sigma = \mathbb{C}\varepsilon \tag{6.19}$$

where $\mathbb{C}$ is the fourth rank stiffness tensor which could be write in full tensor notation as:

$$\begin{bmatrix} C_{1111} & C_{1122} & C_{1133} & C_{1123} & C_{1131} & C_{1112} & C_{1132} & C_{1113} & C_{1121} \\ C_{2211} & C_{2222} & C_{2233} & C_{2223} & C_{2231} & C_{2212} & C_{2232} & C_{2213} & C_{2221} \\ C_{3311} & C_{3322} & C_{3333} & C_{3323} & C_{3331} & C_{3312} & C_{3332} & C_{3313} & C_{3321} \\ C_{2311} & C_{2322} & C_{2333} & C_{2323} & C_{2331} & C_{2312} & C_{2332} & C_{2313} & C_{2321} \\ C_{3111} & C_{3122} & C_{3133} & C_{3123} & C_{3131} & C_{3112} & C_{3132} & C_{3113} & C_{3121} \\ C_{1211} & C_{1222} & C_{1233} & C_{1223} & C_{1231} & C_{1212} & C_{1232} & C_{1213} & C_{1221} \\ C_{3211} & C_{3222} & C_{3233} & C_{3223} & C_{3231} & C_{3212} & C_{3232} & C_{3213} & C_{3221} \\ C_{1311} & C_{1322} & C_{1333} & C_{1323} & C_{1331} & C_{1312} & C_{1332} & C_{1313} & C_{1321} \\ C_{2111} & C_{2122} & C_{2133} & C_{2123} & C_{2131} & C_{2112} & C_{2132} & C_{2113} & C_{2121} \end{bmatrix} \tag{6.20}$$

The generalized equation 6.19 leads to 81 $\mathbb{C}_{ijkl}$ stiffness coefficients. Considering, in mechanics the ability to interchange suffixes i and j in σ_{ij}, and suffixes k and l in ε_{kl} thanks to the symmetry properties of these tensors, it is more convenient to use an other notation introduced by Voigt in [Voigt 1928]. It is a contracted matrix notation with single number suffixes instead of pairs. So, $\mathbb{C}_{ijkl}$ could be written as a 6x6 matrix noted $\mathbb{C}_{mn}$ and stiffness coefficients becomes:

ij or kl	11	22	33	23,32	31,13	12,21
	↓	↓	↓	↓	↓	↓
m or n	1	2	3	4	5	6

$$\begin{bmatrix} C_{11} & C_{12} & C_{13} & C_{14} & C_{15} & C_{16} \\ C_{12} & C_{22} & C_{32} & C_{42} & C_{52} & C_{62} \\ C_{13} & C_{23} & C_{33} & C_{43} & C_{53} & C_{63} \\ C_{14} & C_{24} & C_{34} & C_{44} & C_{54} & C_{64} \\ C_{15} & C_{25} & C_{35} & C_{45} & C_{55} & C_{65} \\ C_{16} & C_{26} & C_{36} & C_{46} & C_{56} & C_{66} \end{bmatrix} \tag{6.21}$$

The number of independent coefficients in the 6x6 matrix array could be then reduced from 36 to 21, 13, 9, 6, 5, 3, 2 considering material symmetry, i.e symmetry of atom within lattice. Table 6.3 presents simplification of 6x6 matrix array as function of the crystalline structure type.

In the case of a AISI 316L austenitic stainless steel pollycristalline agregate, F.C.C. structure has to be considered, i.e containing a cubic symmetry. Thus only 3 independent components are required: C_{11}, C_{12} and C_{44}.

Triclinic (21)	Monoclinic (13)	orthotropic (9)	trigonal (6)
●●●●●● ●●●●● ●●●● ●●● ●● S ●	●●●00● ●●00● ●00● ●●0 ●0 S ●	●●●000 ●●000 ●000 ●00 ●0 S ●	●●●●00 ●●∗00 ●000 ●00 ●● S x
tetragonal (6)	**transversely isotropic (5)**	**cubic (3)**	**isotropic (2)**
●●●000 ●●000 ●000 ●00 ●0 S ●	●●●000 ●●000 ●000 ●00 ●0 S x	● ● ● 0 0 0 ● ● 0 0 0 ● 0 0 0 ● 0 0 ● 0 S ●	●●●000 ●●000 ●000 x00 x0 S x

Table 6.3: ● unique component, ● equal components, x components equal to $\frac{(C_{11}-C_{12})}{2}$, S symetry, ● and ∗ opposited components.

One uses parameters identified on a similar material in [Mu 2011]:

[Mu 2011]				
C_{11} (GPa)	C_{12} (GPa)	C_{44} (GPa)	a	ν
248.000	142.000	71.000	1.34	0.3

Table 6.4: Elastic parameters of CPFEM for 316L

with $a = 2\dfrac{C_{44}}{C_{11} - C_{12}}$ the coefficient of anisotropy and ν the Poisson coefficient.

6.3.3.3 Flow rule

The Resolved Shear Stress vector (RSS) τ^s is the projection of the local stress tensor expressed in the global system reference on every possible sliding system s. Its form was introduced by Schmid [Schmid 1950]. The Schmid law takes the following form:

$$\tau^s = \sigma : \mathbb{D}^s \tag{6.22}$$

$$\mathbb{D}^s = \frac{1}{2}\left(b^s \otimes n^s + n^s \otimes b^s\right) \tag{6.23}$$

where σ is the local (at grain) applied stress, n^s the slip plan normal, b^s the slip direction, $\mathbb{D}^s$ is the symmetric part of the Schmid tensor noted $\mathbb{L}^s = b^s \otimes n^s$ and we note here, W^s, its antisymmetric part.

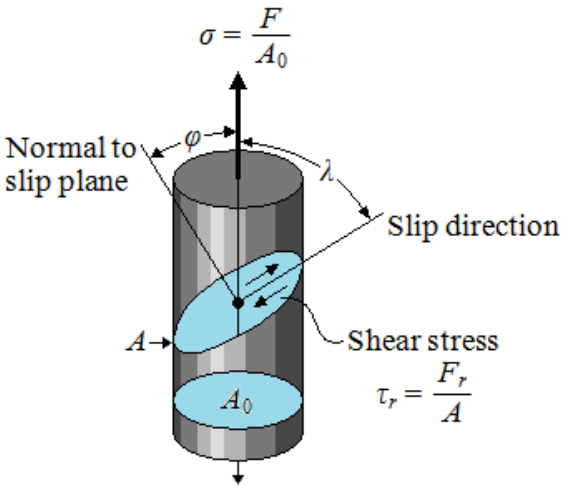

Figure 6.6: Schmid law

Figure 6.6 presents the basic geometrical point of view of the Schmid law[3]. A single crystal is submitted to uniaxial loading equal to $\frac{F}{A_0}$ with F the force and A_0 the initial single crystal section.

[3]for more information refer to chapter 1.1

One could easily find that in this basic case the Schmid matrix $\mathbb{D}^s$ is reduced to a simple composition of crystallographic orientations $cos(\phi)cos(\lambda)$, where λ defines the slip direction angle relative to the force direction and ϕ the normal to the slip plane angle. In a polycrystal, this rule is still verified only if the considered stress σ is the local one, and not the macro one Σ. In this case, no trivial relation exists between Σ and local τ^s because of the local multiaxiality of stress field.

According to the Schmid law, single crystal leaves the elasticity and shear occurs when the Resolved Shear Stress (RSS) on system s is equal to a threshold value, the Critical Resolved Shear Stress ($CRSS$), noted τ_c^s (see section 6.3.3.4). It could basically be written as:

$$\begin{cases} \tau^s < \tau_c^s & \rightarrow \quad \dot{\gamma}^s = 0 \\ \tau^s \geq \tau_c^s & \rightarrow \quad \dot{\gamma}^s \geq 0 \end{cases} \tag{6.24}$$

with $\dot{\gamma}^s$ the slip rate associated to system s. The flow rule introduces a rate-dependent formulation. Classically one uses a viscoplastic formulation derived from the Schmid law. It is more convenient for numerical simulation and consists in a power law [Hutchinson 1976]. The slip rate remains close to zero while τ^s is lower to τ_c^s:

$$\dot{\gamma}^s = \dot{\gamma}_0 \left| \frac{\tau^s}{\tau_c^s} \right|^n \text{sign}\left(\tau^s\right) \tag{6.25}$$

where $\dot{\gamma}_0$ is a reference value of the slip rate and n is the strain rate sensitivity parameter. Table 6.5 presents the parameters used in our simulations [Simonovski 2009]:

[Simonovski 2009]	[Cailletaud 1991]
$\dot{\gamma}_0$ (s^{-1})	n
$3.4\text{x}10^{-6}$	10

Table 6.5: Flow parameters of CPFEM for 316L

6.3.3.4 Hardening rule

When sliding occurs on a specific system, it interacts with different kind of obstacles: additive elements, precipitate, "trees" of the other system "dislocation forest" ... The increasing of dislocation density and these interactions lead to a local material resistance to plastic sliding which results in critical shear stress increasing. In some favorable cases an annihilation processing could occur leading to a decrease of dislocation density storage rate. One experimentally observes the existence of a critical distance between same dislocation systems with opposite sign leading to their annihilation. This processing could conduct to a saturation of hardening and also softening processing. A physically based hardening rule has to take into account these basic mechanisms of dislocation generation and annihilation. It can

take the following generic expression proposed by Mandel [Mandel 1965]:

$$\dot{\tau}_c^s = \sum_u \mathbf{H^{su}} \left|\dot{\gamma}^u\right| \tag{6.26}$$

where H^{su} terms are the components of the hardening matrix. This matrix takes into account the history of slip on the considered system also on the others. Diagonal terms H^{ss} account for the hardening of slip system s due to its own slip activity, also called "self-hardening". Remaining terms, i.e $H^{su}\,|_{s\neq u}$ account for the hardening of system s due to slip activity on the whole set of other systems u, also called "latent-hardening". The form of the hardening matrix depends on the considered physical mechanisms. Note that if the whole H^{su} components are identical, the hardening matrix is reduced to isotropic one.

The generic expression presented in 6.26 is actually derived from the slip resistance or critical revolved shear stress. To account for more physics, its expression could be based on dislocation density. Basically, the total dislocation density could be divided in two parts: statistically stored dislocations ρ_S^s (SSD) which trap each others in a random way and/or are required for compatible deformation of various parts of the crystal [Ashby 1970], and geometrically stored dislocations ρ_G^s (GND) which are required when gradient of plastic shear exists [Cottrell 1964, Ashby 1970]. The expression of total dislocation density is therefore the following:

$$\rho_T^s = \rho_S^s + \rho_G^s \tag{6.27}$$

For simplicity's sake, in the present model only a local point of view is considered. One implicitly assumes that the accumulation of SSD's is the only driving force behind the work hardening. No GND are therefore considered. Note, in a context of cyclic loading or grain size effect study, a non-local approach using GND should be considered to account for more physics [Schwartz 2011]. The form of slip resistance classically used was introduced in [Franciosi 1984] as follows:

$$\tau_c^s = \tau_0 + \mu b \sqrt{\sum_u d^{su}\rho^u} \tag{6.28}$$

where τ_0 is an initial value of Critical Resolved Shear Stress, μ is the shear modulus, b the magnitude of the Burgers vector, d^{su} the interaction coefficients between the slip systems s and u, and ρ^u represents the local density of the Statistically Stored Dislocations on the slip system u. In the case of F.C.C. structure the hardening interaction matrix d^{su} is a 12x12 matrix composed by only 4 d_i independent coefficients due to crystal symmetries [Forest 2004]. Notice d_{su} coefficient identification is still complicated and is classically done using Discrete Dislocation Dynamics simulations [Queyreau 2009]. In practice one uses here a simple form of the matrix which only introduces 2 parameters. d_p characterises the self-hardening ($s = u$) and d_f characterises the latent-hardening ($s \neq u$) [Tabourot 2001].

Then the hardening relation need to be completed by a flow rule for dislocation density on each

system s function of slip rate $\dot{\gamma}^s$. The description of dislocation generation on slip system was first figured out by Frank and Read [Frank 1950]. It takes generally the following form:

$$\dot{\rho}^s = \frac{1}{b}\left(\frac{\sum\limits_u (a^{su}\rho^u)}{L} - 2y_c\rho^s\right)|\dot{\gamma}^s| \tag{6.29}$$

The first terms on the left-hand sides of equation account for dislocation creation $\left[\frac{\sum\limits_u (a^{su}\rho^u)}{bL}\right]$ and the second for dislocation annihilation $\left[\frac{2y_c}{b}\rho^s\right]$. The material parameter y_c associated with annihilation is related to the critical annihilation distance, which is here taken constant. The parameters L is the mean free paths of the mobile dislocations in system s, also assumed to be a constant in the present study. Finally, a^{su} account for geometrical interaction between dislocation density [Forest 2004].
Note that equation 6.29 implies that there exists a saturation in dislocation production which depends on the deformation path, and more precisely on the dislocation quantity accumulated on the whole set of slip system. Note also that the dislocation production rate $\dot{\rho}^s$ depends on the absolute value of slip rate $\dot{\gamma}^s$. That means that this hardening corresponds to an isotropic hardening on each slip direction. Nevertheless, as each slip direction has its own dislocation and yield evolution, the yield surface in spatial domain deforms from an initial sphere (radius = τ_0) to a more complex form.
Then assuming that collinear, coplanar and orthogonal crystal interaction have the same impact on the mean free paths allows reducing the number of a_i unknown up to 4 independent coefficients [Franciosi 1984]. The simplified form of the dislocation density interaction matrix is presented in table 6.6 [Franciosi 1984]:

$a^{su} =$

	A_2	A_3	A_6	B_2	B_4	B_5	C_1	C_3	C_5	D_1	D_4	D_6
A_2	a_1	a_3	a_3	a_3	a_5	a_5	a_3	a_5	a_6	a_3	a_6	a_5
A_3		a_1	a_3	a_5	a_3	a_6	a_5	a_3	a_5	a_6	a_3	a_5
A_6			a_1	a_5	a_6	a_3	a_6	a_5	a_3	a_5	a_5	a_3
B_2				a_1	a_3	a_3	a_3	a_6	a_5	a_3	a_5	a_6
B_4					a_1	a_3	a_6	a_3	a_5	a_5	a_3	a_5
B_5						a_1	a_5	a_5	a_3	a_6	a_5	a_3
C_1							a_1	a_3	a_3	a_3	a_5	a_5
C_3								a_1	a_3	a_5	a_3	a_6
C_5									a_1	a_5	a_6	a_3
D_1										a_1	a_3	a_3
D_4											a_1	a_3
D_6												a_1

Table 6.6: Dislocation density interaction matrix of F.C.C. material (symmetric) [Franciosi 1984]

Hardening parameters used in our simulation are summarized in table 6.7. Note that the initial value of CRSS, τ_0, has been identified experimentally by thermal inflection appearance, in chapter 4.1 and confirmed by literature [Feaugas 2009]. Other parameters have been found from different authors presented above each parameter.

	[Evrard 2010]						[Guilhem 2011, Monnet 2009]			
τ_0 (MPa)	b (mm)	y_c (mm)	L	ρ_0 (mm^{-2})	d_p	d_f	a_1	a_3	a_5	a_6
35	$3.2x10^{-7}$	$3.2x10^{-6}$	33	$1x10^{3}$	0.06	0.004	0.12	0.07	0.14	0.12

Table 6.7: Hardening parameters of CPFEM for 316L

6.3.3.5 Constitutive law and thermodynamic framework

The single crystal elasto-plastic behavior is implemented through a User MATerial subroutine, within a finite strain formalism, in the FE code ***Abaqus/standard***. Then a "Fully" Coupled Thermal-Mechanical Analysis is performed. The User MATerial subroutine has been entirely developed within this work and is inspired from [Huang 1991, Meissonnier 2001, Harewood 2007, Evrard 2008]. Its whole integration is presented in appendix G.2. The Finite strain formalism is also introduced and presented in detail in appendix H.1. This section only recalls the final form of the stress as well as its associated heat source terms.

Let us assume an hypo-elastic constitutive relation as well as the objective Jaumann stress rate and a multiplicative decomposition of the deformation gradient (see appendix H.1). In such a context, the corotational (Jaumann) stress rate take the following form:

$$\overset{\nabla}{\sigma} = \mathbb{C} : \mathbf{D} - \mathrm{tr}\,(D)\,\sigma - \sum_s \dot{\gamma}^s \mathbb{R}^s \tag{6.30}$$

where $\overset{\nabla}{\sigma}$ is the corotational stress rate of Cauchy, $\mathbb{C}$ the tangent modulus expressed in the reference system, $\mathbf{D}$ the total deformation rate and σ the Cauchy stress. Then $\dot{\gamma}^s$ the shear rate on a considered slip-system s. $\mathbb{R}^s$ is detailed within appendix H.1. Then the relation between the corotational Cauchy stress $\overset{\nabla}{\sigma}$ and the Resolved Shear Stress τ^s associated to intragranular crystal lattice orientation is done through the equation 6.22.

As introduced for the yield model, the free energy Ψ is divided into two parts including contributions from thermo-elasticity and strain-hardening. Therefore, the Helmholtz free energy is assumed to be of the form:

$$\Psi\left(\varepsilon^e, \theta, \alpha^i\right) = \Psi^e\left(\varepsilon^e, \theta\right) + \Psi^p\left(\alpha^i\right) \tag{6.31}$$

where α^i are internal variables governing strain-hardening. According to the first and the second ther-

modynamical principles (see appendix A.1) the intrinsic dissipated power $\dot{d}$ and the thermo-mechanical coupling power W_{the} function of the free energy potential Ψ are given by:

$$\dot{d} = \sigma : \dot{\varepsilon}^p - \rho \frac{\partial \Psi}{\partial V^i} \dot{V}^i \tag{6.32}$$

$$W_{the} = \rho T \frac{\partial \Psi}{\partial T \partial V^i} \dot{V}^i \tag{6.33}$$

where V^i is a vector composed by all hardening variables α^i. Second order terms are here neglected since related to plastic phase transformation. One assumes here a single isotropic hardening noted p.

$$\dot{d} = \sigma : \dot{\varepsilon}^p - R\dot{p} \tag{6.34}$$

$$W_{the} = T \frac{\partial \sigma}{\partial T} : \dot{\varepsilon}^e \tag{6.35}$$

where $R = \rho \dfrac{\partial \Psi}{\partial p}$. Finally, by analogy to the formalism introduced in appendix A.1 and in agreement with [Chang 2007] one obtains:

$$\dot{d} = \sum_{s=1}^{s=12} \left[\tau^s \dot{\gamma}^s - \left(\tau_c^s - \tau_0^s \right) \dot{p}^s \right] \tag{6.36}$$

where $\dot{p}^s = |\dot{\gamma}^s|$. Then a weak thermoelastic coupling uncorrelated from the crystalline plasticity framework has been used. In the same spirit than in the thermodynamical yield model, an isotropic thermoelastic coupling from stress to temperature is introduced. The thermoelastic coupling power takes the following form:

$$W_{the} = -3K\alpha T \cdot tr\left(\dot{\boldsymbol{\varepsilon}}^e\right) \tag{6.37}$$

Note that under such loading conditions, i.e. monotonic tensile test up to 2.5% of strain and an associated variation of temperature equal to $\approx 1^o$, the natural thermomechanical coupling lead to non neglectable isentropic power, W_{the}, compared to other power quantities nevertheless the reverse contribution is clearly neglectable. Indeed, the variation of stress due to variation of temperature is in the order of ± 5 MPa. Thus a weak thermomechanical coupling, i.e. the stress involves the temperature, but the temperature does not evolve the stress is totally legitimate. One points here a difference with the yield model where a clear thermodynamic framework was used and Fully Coupled Thermo-Mechanical calculation is done. In practice, a Weak Coupled Thermo-Mechanical analysis is performed by forcing coupled term, $\mathbf{K}_{\theta u}$ and $\mathbf{K}_{u\theta}$, of the Jacobian matrix to be equal to zero (see appendix G.1).

6.4 Conclusion

Two Finite Element models have been developed. Both assume identical geometry and boundary conditions.
The 3D geometry corresponds to the tested specimen gauge-section extruded along the half part of the specimen thickness (5x5x1mm^3). The material is treated as a composite material. It contains 1776 columnar grains related to specimen surface EBSD analysis. The mesh is identical to the EBSD grid as well as the whole set of experimental fields studied within the last part, i.e. the regular mesh where the size is 20x20x80μm^3, 20x20x300μm^3 20x20x620μm^3 for the three layers of element along the thickness (from surface to specimen neutral fiber respectively). In such FEM, the kinematic continuity is fixed at grain boundaries. Experimental axial and transversal displacements and temperatures are applied on the lateral aggregate borders along the deformation path (Dirichlet conditions). Then, a convective exchange is imposed between the observed face and the air while kinematic symmetry and an adiabatic condition are applied on the background face of the model.
Two different constitutive laws are introduced within intragranular domains:
(i) the first one assumes that the distribution of physical grain orientation leading to progressive plasticity activation can be modeled by a distribution of yield stress in the von Mises sense. Then a thermo-elasto-plastic behavior including linear and isotropic thermo-elasticity as well as kinematic linear hardening has been implemented through a User MATerial subroutine within the FE code ***Abaqus/standard***.
(ii) The second one uses the crystalline plasticity framework. The constitutive law accounts for the experimental mean intragranular orientation, a non linear hardening based on dislocation density flow and on a weak thermo-elastic coupling. As for the previous model, the constitutive law has been implemented through a User MATerial subroutine within the FE code ***Abaqus/standard***.
The next chapter deals with the comparison between experimental and numerical results coming from both models.

Chapter 7

Numerical thermomechanical fields

Contents

This section presents results extracted from yield and crystal models. Comparisons with experimental data, in term of displacement, strain, temperature and stress are detailed. Figures 7.1 (a) and (b) recall elastic and hardening parameters considered in both models.

- The first model assumes isotropic elasticity, isotropic and linear thermoelastic coupling and linear kinematic hardening. Elastoplastic parameters, i.e Young E and hardening H moduli, are identified on macroscopic stress-strain curve. The yield stress field is computed from the experimental total strain field at 2% of mean axial strain with a Sachs assumption, i.e. uniform stress field at this instant. Figure 7.1 (a) presents notably the identified yield stress field, uniform per grain as well as schematic representation of intragranular stress flow.

- The second model assumes cubic elasticity, isotropic and linear thermoelasticity coupling and nonlinear isotropic hardening based on dislocation flows. The parameter which leads to the microplasticity is here the grain orientation compared to the loading direction. Figure 7.1 (b) presents the triplet of Euler angle (ϕ_1,Φ,ϕ_2) which defines the entire 3D orientation of each grain.

7.1 Macroscopic values

Let us begin with the comparison between numerical and experimental mean values. Figure 7.2 (a), (b) and (c) present the evolution of stress, strain and temperature respectivelly. Curves correspond

to mean values within the observed area, i.e. 5x5μm regions located in the center of specimen gauge-section. This first comparison allows verifying the relevance of mean thermomechanical response of each model. Recall that no optimization of model parameter has been done to fit experimental curves. Yield model uses locally, Young E and hardening H moduli identified on macroscopic stress-strain curve and crystal model uses parameters founded in literature for similar material. The consequence is that models and experiment don't exhibit exactly the same behavior.

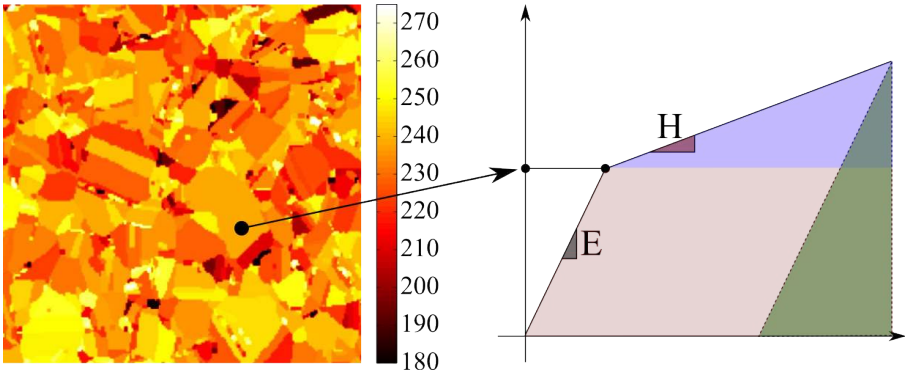

(a) Yield stress map in MPa

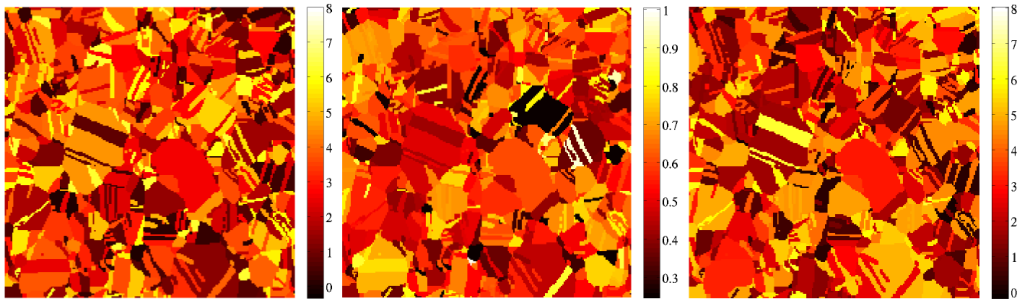

(b) Triplet of Euler angle maps: (ϕ_1,Φ,ϕ_2) in radian

Figure 7.1: Constitutive elements of the intragranular behavior law for (a) yield model and (b) crystalline one.

First, one could note, on figure 7.2 (a), a relatively good agreement between each curve in terms of elastic and hardening behavior. The error does not exceed 6% at the final state of deformation. Nevertheless, one observes that both numerical models exhibit an early plasticity, compared to the experimental one, leading to a deviation from macroscopic elastic domain. This point is observed from 80 MPa. Then both models exhibit a slower plasticity development leading to a later macroscopic elasto-plastic transition and finally, to an overestimation of the mean stress within the aggregate. A comparison between both models shows that the early inelastic phenomena are more progressive within the crystalline model since the elasto-plastic transition appears smoother. Finally, the asymptotic hardening is perfectly linear within yield model, where local linear hardening is assumed, and fluctuates

within the crystal one, where a non-linear hardening based on dislocation flows is assumed. These variations are probably due to the non implicit resolution of the differential system required for non-linear hardening calculation.

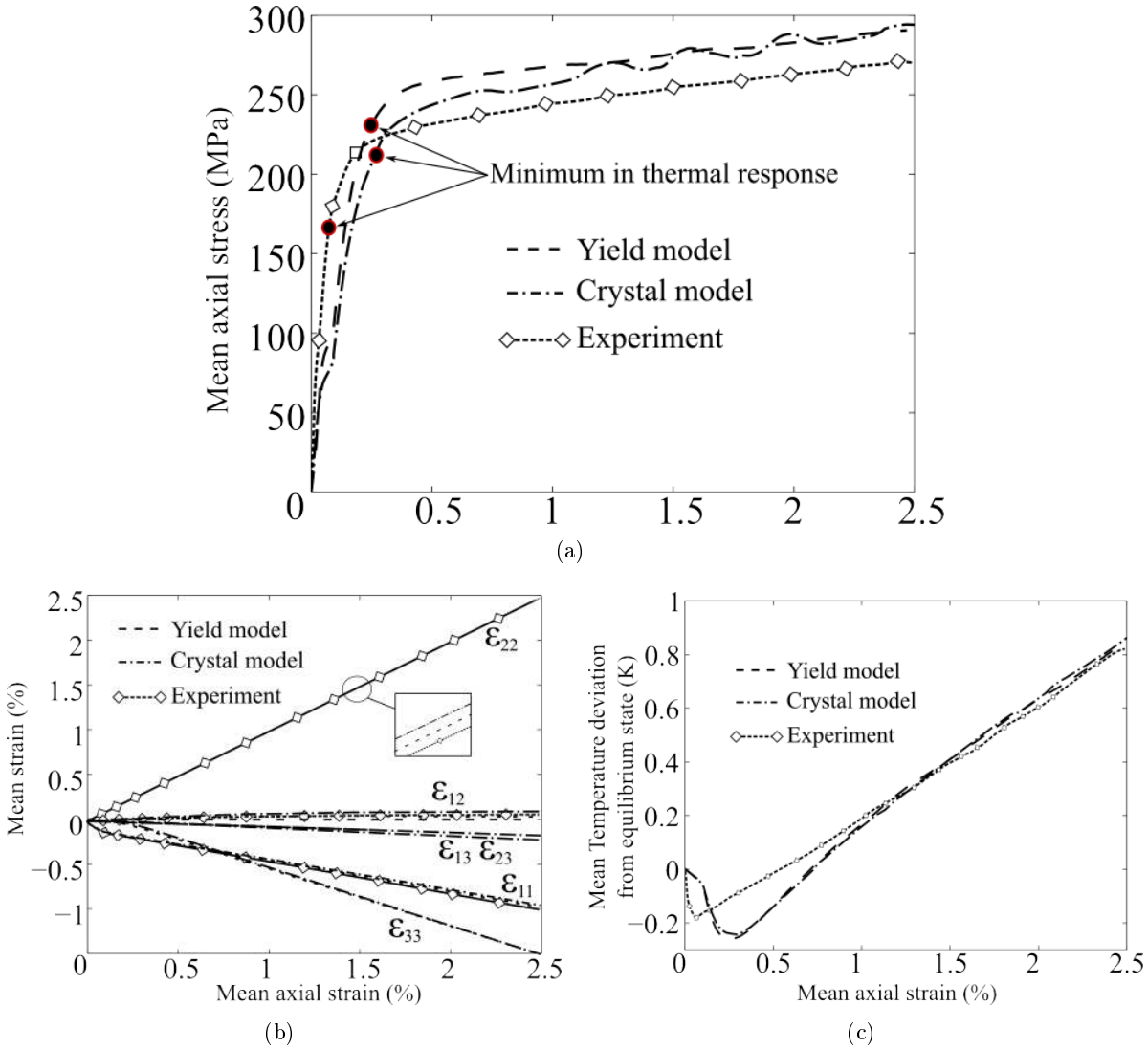

Figure 7.2: Comparison experiment-model of: (a) the experimental nominal stress and mean axial numerical one σ_{22} (MPa) function of mean axial strain (%), (b) experimental and numerical mean axial strains (%) function of test time (s) and (c) the experimental temperature deviation from equilibrium state $\theta = T - T_0$ and mean numerical one (K) function of mean axial strain (%)

This simple macroscopic comparison of purely mechanical behavior also provides informations about the experimental test since experimental boundary conditions are applied to each model. The models

underline the fact that the test is not totally uniaxial especially during the macroscopic elastic phase (up to 200 MPa). Indeed, the stress relaxation observed for each model at 80MPa is numerically due to a multiaxiality of loading. This point is confirmed notably by the level of transversal stress σ_1 not presented here. It confirms experimental analysis done in chapter 4.1. This change in mean axial stress-strain relation was probably not observed experimentally due to the low frequency of kinematic measurement (7Hz). One recalls that experimental data points were linearly interpolated.

Figure 7.2 (b) evidences that both models represent relatively well the mean deformation path, especially ε_{11}, ε_{22}, ε_{12} since others components, i.e ε_{13}, ε_{23} and ε_{33}, are purely numeric. Indeed, in every case, each curve are superimposed. It seems logical since experimental displacement are applied on the aggregate contour, that the mean displacement and strain must be in line. Then, models provide additional information, especially, the out-of-plane strain ε_{33}. For both models mean out-of-plane strain ranges from 0 to ≈-1.5%. It is globally a contraction due to Poisson's effect. One could also note that the mean out-of-plane strain ε_{33} is one third more significant than the transversal strain ε_{11}. This point underlines that the dilatation is not isotropic since different along transversal and normal direction. The dilatation or contraction is easier along the out-of-plane direction compared to the transversal one. This points out the impact of crystalline structure and grain boundaries on the deformation. Indeed, grain are columnar along the out-of-plane direction whereas a grain boundary network ("deformation walls") exist in the plane. It reveals, as expected, that the present models are probably too "soft" along the out-of-plane direction.

Finally, figure 7.2 (c) underlines a deviation between the numerical and experimental thermal inflection appearance. This point is clearly related to the deviation between experimental and numerical stress-strain response. Indeed, it was shown in chapter 4.1 that the experimental thermal inflection appears at 172 MPa of nominal stress. In agreement with stress flows, both models exhibit a thermal inflection about 220 and 230 MPa for crystal and yield model respectively (see figure 7.2 (a)). In parallel, the minimum of numerical temperature is reached at lower magnitude, -0.3 K compared to -0.17 K for experiments. This is also due to the deviation observed on the stress flows. Indeed, the deviation in terms of stress level is about 20 MPa leading to a greater variation of temperature according to the Lord Kelvin formula 4.1.
Then one could note that the numerical thermoelastic behavior may be divided in two phases: firstly, from the beginning of test to the instant where an early change in numerical stress-strain response occurs (about 80 MPa see figure 7.2 (a)), then from this instant to the numerical thermal inflection appearance. Note that in the first phase the slope of temperature variation is low compared to the one observed in second phase. It reflects that from 0 to ≈80 MPa early inelastic phenomena has been occurred leading to an early elasto-plastic behavior. This point is clearly visible at 80 MPa in the figure 7.2 (a) and is connected to the appearance of multiaxial loading as already pointed. Thus drop of temperature due to elasticity is in part balance by early dissipation. Then, from 80 to ≈200 MPa, the behavior is perfectly elastic thus the drop of temperature is more significant. This point is also clearly observed in figure 7.2 (a).

Figure 7.2 (c) also presents a significant deviation between numerical and experimental temperature. This point is visible from 0 to 1.2 % of mean axial strain. Then this deviation vanishes. This deviation is problematic. Indeed, on one hand experimental temperature is applied at the aggregate contour for boundary conditions management. On the other hand, due to its own constitutive law (see figure 7.2 (a)) the FE model exhibit its own temperature. Thus a competition exists between the experimental temperature at aggregate boundaries, and the numerical temperature leaded by the constitutive law of the model. This point underlines a problem already announced at the end of the chapter 6.1. The application of kinematic and thermal Dirichlet conditions is problematic when experimental and numerical thermomechanical behaviors deviate. As a consequence, one could point that a virtual gradient of temperature should appears in the numerical thermal field from 0 to ≈1.2% of mean axial strain between the center and boundary conditions of models (see figure 7.2 (c)). It will lead necessarily to a misestimation of numerical thermal gradients and/or laplacian during this domain of loading. Thus it will have an influence on the numerical energy balance performed in chapter 8.1. Nevertheless, the relation between numerical stress and temperature for both models seems to be in agreement with the relation between experimental stress and temperature. The orders of magnitude are in line.

The main conclusion of this section is a great agreement between both models concerning homogenized quantities. Although no identification has been performed, a good agreement has also been observed between experimental and numerical responses. A slight deviation from experimental stress response leads to a quite significant deviation from the experimental thermal one, especially in elasto-plastic transition, nevertheless the magnitudes are in good agreement. This point will be discussed in the energy balance achievement section 8.1.

7.2 Displacement fields

Figure 7.3 from (a) to (f) present the deviation from experimental displacement field U_1, U_2 and U_3 (from left to right), in the case of yield (upper line) and crystal model (lower line). Results are presented in physical unit, μm, on top of each figure, and in % on bottom. Note that the percent colorbar must be interpreted carefully. Indeed, only the deviation from axial displacement U_2 presents an exact percent colorbar of which the equation is following: $E = 100. \left| \frac{U^{exp}_{2_{(t)}} - U^{num}_{2_{(t)}}}{U^{exp}_{2_{(t)}}} \right|$, with E the deviation in %. As U_1 and U_3 cross the zeros displacement value the percent of displacement is estimate from the mean experimental displacement, as following: $E = 100. \left| \frac{U^{exp}_{i_{(t)}} - U^{num}_{i_{(t)}}}{\bar{U}^{exp}_{i_{(t)}}} \right|$, with $\bar{U}^{exp}_{i_{(t)}}$ a scalar.

Firstly, one has to remember that Dirichlet conditions, i.e experimental displacements U_1 and U_2, are applied as boundary condition on each model. Consequently, for U_1 and U_2 displacement, the deviation tends toward zero close to the boundary condition. Deviation from experimental displacement

far from the boundary conditions of the aggregate depends on the local constitutive law.

The yield model (see figure 7.3 (a), (b) and (c)) presents a mean deviation in the order of 6.99% (±4.49), 0.48% (±0.33) and 22.21% (±17.00) for U_1, U_2 and U_3 respectively.

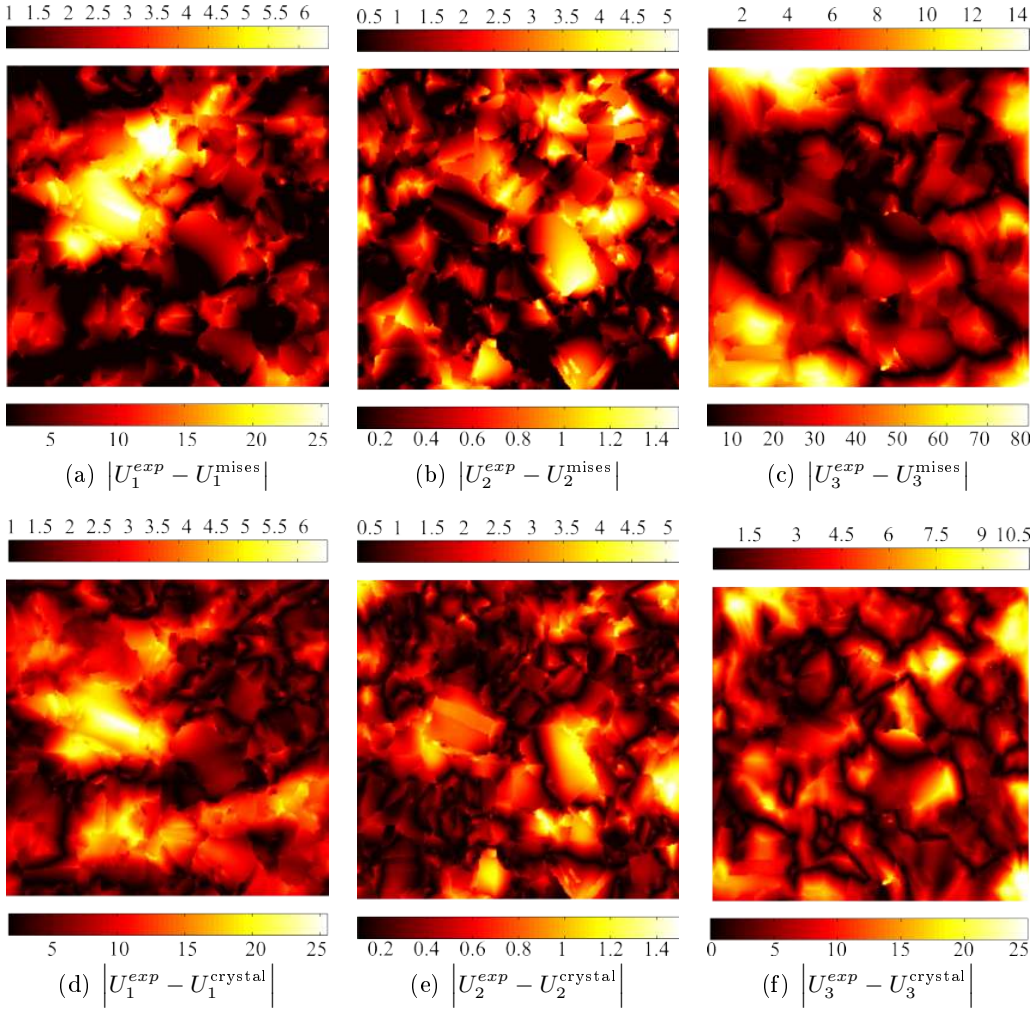

Figure 7.3: Deviation from experimental displacement fields U_1, U_2, U_3 in μm (on top) and in % (on bottom) at 2.5% of mean axial strain. (from a to c) yield model and (from d to f) crystal one.

One could first observe a very good agreement on U_2 displacement field. This agreement is in line with the fact that the yield stress field, leading to a progressive microplasticity, has been identified on the experimental axial strain field ε_{22} and the nominal stress. Peaks of deviation do not exceed 1.5%. Then, one could note that the deviation from transversal displacement U_1 is concentrated in a very limited region. Indeed, more than 79% of the surface specimen exhibits a deviation lower than 10%.

It notably means that the assumed isotropy of behavior, applying same elastic and hardening flow in every spatial direction as well as columnar grain hypothesis, is an appropriate approximation in more than 79% of grains.
Notice, that the region which concentrates from 20 to 25 % of deviation experimentally concentrates small displacements compared to neighboring grains whereas the model predict a progressive and smooth transversal displacement. Consequently, it appears that experimentally, it exists a "hard region" where the transversal displacement is limited compared to neighboring grains and the model does not represents precisely this local behavior. It may be due to a sub-surface contribution, which is not taken into account within the model. One could notice that the deviation is mainly concentrated in the biggest (twinned) grain of the observed area.
To conclude on displacements field, one focus on the out-of-plane displacement U_3. It is the only free surface of the model. Only, 27% of surface specimen exhibits a deviation lower than 10% and contrary to U_2 and U_1 the maximum deviation is obtained close to boundary condition whereas the center of aggregate surface is more or less well represented.

In comparison the crystalline model (see figure 7.3 (d), (e) and (f)) exhibits almost the same deviations from experimental data set concerning U_2 and U_1 displacement in term of deviation intensity, nevertheless a significant difference could be observed on the "free displacement" U_3. Indeed, the mean deviation is about 9% compared to more than 30% for the yield model. Every high deviation spot observed in yield model are here vanished or limited

The analysis of displacement deviation has shown a good agreement between experiment and both models concerning plane displacements. Some limited localizations are observed and are clearly associated to a specific set of grain. Thus the main kinematics is well represented, only some local interactions maybe due to sub-surface grain interactions are missing. The main difference appears on the out-of-plane displacement where crystal model provides a better estimation of experimental surface topography. As it has been shown in chapter 1.1 the experimental surface topography is well connected to grain boundary activity, thus crystal model may increase the degree of freedom of grain boundaries compared to the yield model.

7.3 Strain fields

Figure 7.4 presents the comparison between strain fields ε_{11}, ε_{22} and ε_{33} at 2% of mean axial strain from yield model (1^{st} column) and crystal one (2^{nd} column).
Firstly, one could point out the smoothed aspect of the yield model (1^{st} column) compared to the crystal one. Indeed, while the yield model exhibits long and smooth plastic band localizations with apparent small spots of very high localization, especially on the ε_{22} strain field (see 7.4 (c)), the crystal one reveals more or less the same high localizations with less smoothly strain from one grain to its neighbors. This point is due the intragranular kinematic of each model. Indeed, within the yield model

the interaction between grains is only characterized by a difference of yield stress, defined by a scalar, whereas the crystal model introduces a vectorial difference, defined by a multitude of slip vector combinations. This point was first pointed out by von Mises [von Mises 1928]. He evidenced that a set of five linearly independent slip systems is needed to potentially impose any arbitrary volume-invariant plastic deformation to a crystal structure by the mechanism of crystallographic slip. Thus yield model strain fields are smooth because the intragranular behavior imposes a great compatibility of strain at grain boundaries. In opposite crystal model strain fields underline many variations because the intragranular behavior allows any strain gradient accommodation. If one observes, for example in the picture 7.4 (c), especially the macroscopic strain localization band on the right top of the picture, one could identify 3 main spots of localization (from right to left). One could note that the strain is lower between each spot but exhibits quantitatively the same trend contrary to picture 7.4 (d) where theses spots are connected by significant lower strain areas. Thus both models point the same structural localizations but the crystal model allows variations from grain to grain.

The second observation is in line with the previous one. It concerns strain levels, notably ε_{22}. It ranges from 0.5% to 5% in the crystal model compared to 1.4% to 2.9% in the yield one. Notice that colormaps are a little bit saturated to underline strain variations, i.e. local maximum values are in reality more significant. The yield model does not allow a large deviation from the mean strain. It explains why very closed results were observed on mean values in section 7.1. Crystal and yield model reveal similar localizations, similar mean values but the main difference is the ability of the crystal model to locally deviate from this mean value.

The last point concerns the out-of-plane deformation, i.e ε_{33} (see figure 7.4 (e) and (f)). The crystal model (see figure 7.4 (f)) exhibits a deeper plateau from -1.6 to -2.5% within the white dotted line domain. It is surrounded by a plateau around -1%. Thus the model shows a central region of high contractions surrounded by a lower one. It is interesting to note that this surface topography does not point any similarities with plane strains (see figure 7.4 (b) and (d)) whereas the out-of-plane displacement of yield model is clearly connected to ε_{11} and ε_{22} (see figure 7.4 (a) and (c)). Thu, this is in agreement with the observations done in the last section: the out-of-plane displacement and strain fields are very different in both models.

To point out the relevance of crystal model surface topography, let see the figure 7.5 (a) which presents the experimental out-of-plane displacement measured by profilometry. The contour of deeper plateau domain observed in crystal model (see figure 7.4 (f)) is drawn with a blue dotted line. One note a connection between experimental topography and crystal model out-of-plane deformation, notably in some regions where the compression is the more intense. Experimentally, the compressive plateau is larger than numerically and extends from left bottom corner to right upper one nevertheless crystalline model exhibit similar trends. It evidences the relative ability of the crystal model to represent the free surface kinematics.

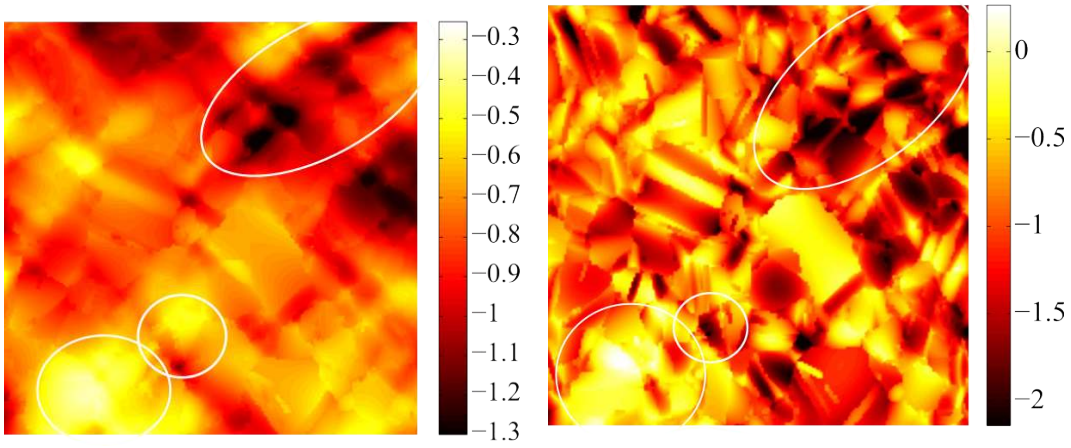

(a) $\varepsilon_{11}^{\text{yield}}$ (b) $\varepsilon_{11}^{\text{Crystal}}$

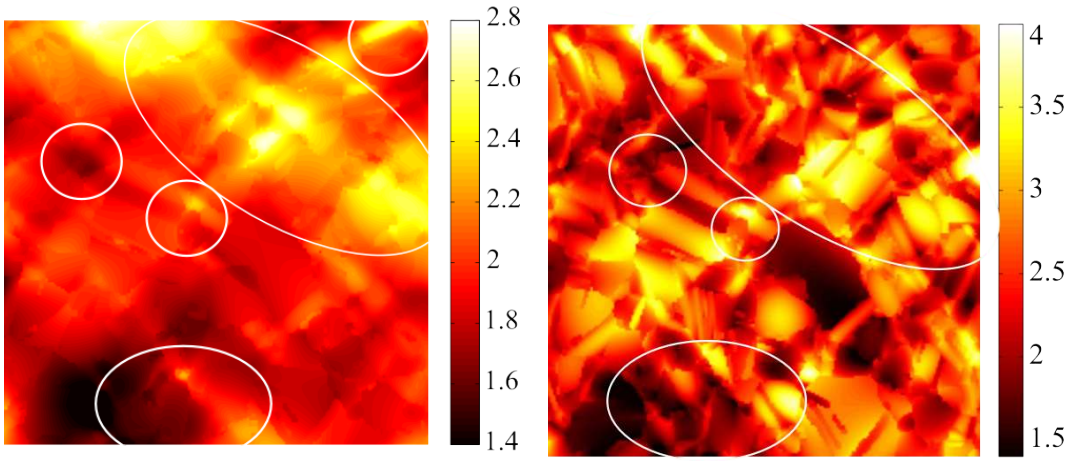

(c) $\varepsilon_{22}^{\text{yield}}$ (d) $\varepsilon_{22}^{\text{Crystal}}$

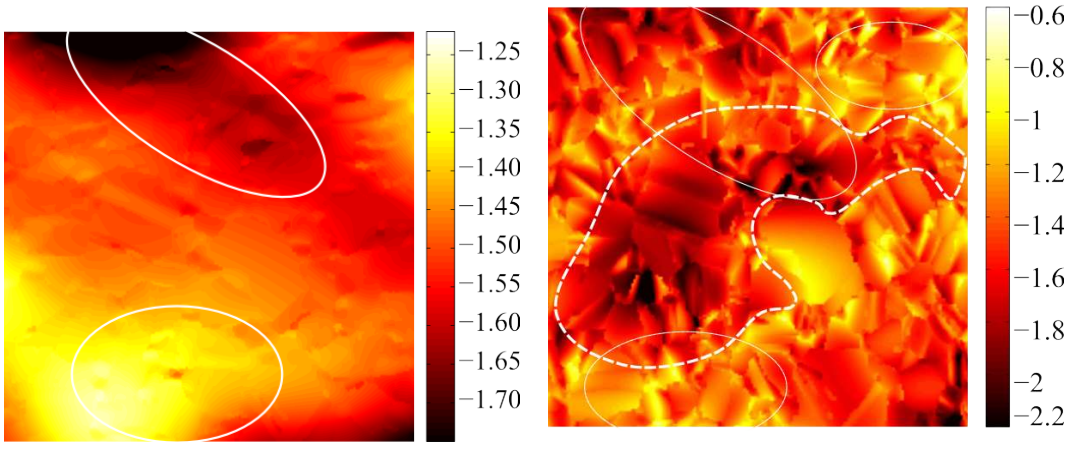

(e) $\varepsilon_{33}^{\text{yield}}$ (f) $\varepsilon_{33}^{\text{Crystal}}$

Figure 7.4: Numerical components of strain tensor at 2% of mean axial strain (in %): 1^{st} column → yield model and 2^{nd} column → crystal model

In consequence one could point out that the experimental surface topography is significantly leaded by surface grain structure as grains are columnar. The ability of the crystal model composed by columnar grains to represent in part the surface topography reveals that the impact of sub-surface structure is second-rate, at least in the tested specimen. The influence of surface grain structure on the experimental surface relief was already pointed in chapter 1.1.

As the surface topography of tested specimen is partially represented by the crystal model one could point that some of its parameters initiate the experimental surface relief:

- the surface grain orientation
- the surface grain shape
- the surface grain size
- the surface grain misorientation

One proposes to confront these fields.
Figure 7.5 (b) and (c) present mean granular misorientation field and the second Euler angle respectively. The first one is a indicator of potential strain incompatibilities while the second is a local indicator of grain orientation especially compared to the direction normal to the specimen surface.
Some slight correlations between both fields and surface topography (see figure 7.5 (a)) seem to appear. Nevertheless, one could already announce that no clear explanation is found.
Firstly, different elements are underlined in figure 7.5 (a): (1) the microtructure, (2) the contour of contractions ε_{33} area observed in crystal out-of-plane strain field (blue dotted line, see 7.4 (f)), some low values of experimental out-of-plane displacement (circles 1, 2 and 3) and the partition between 3 domains. The domains noted A and B localize many regions whose the out-of-plane displacement is $\approx 7\mu m$ while the central domain localizes regions at 0 and negative values of out-of-plane displacement. Let see the three circled regions in figure 7.5 (a). These regions localize clear concentrations of low out-of-plane levels. Grains in circle noted 1 in figure 7.5 (a) has been already pointed in chapter 1.1. Indeed, their second Euler angle (see figure 7.5 (c)), i.e. their out-of-plane orientation exhibit the lowest values of the field and are very close to zero. Thus their crystalline lattice are almost parallel to the surface specimen. One could notice that in three circled regions very low values of second Euler angle are found (see figure 7.5 (c)).
In addition, especially for the circle 1, one observes that the localization of low out-of-plane displacement is connected to a triple grain junction (see figure 7.5 (b)). One observes in figure 7.5 (b) that it is a junction between grains where the mean granular misorientation is very different.

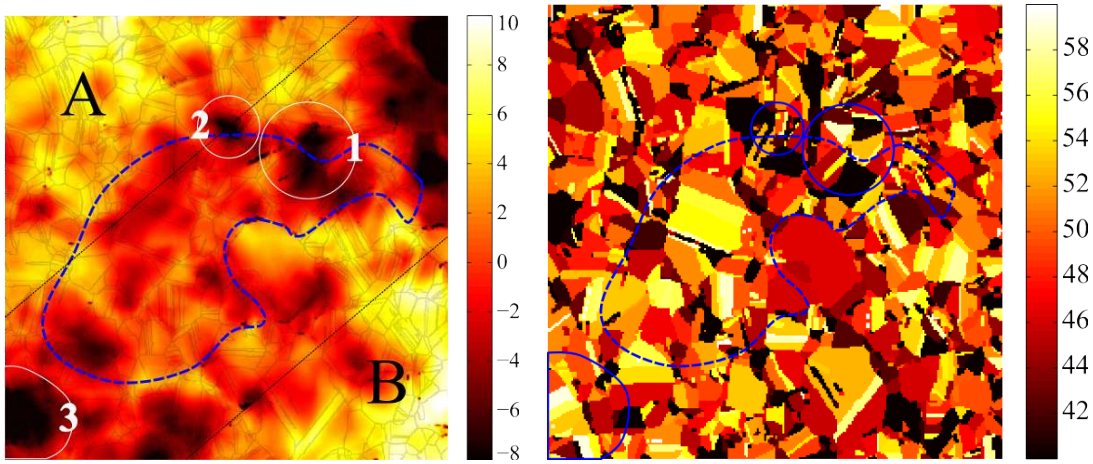

(a) U_3^{exp} in μm (b) $\sum_{\Omega_g} \Delta\theta_{A/B} d\Omega_g$ in degree

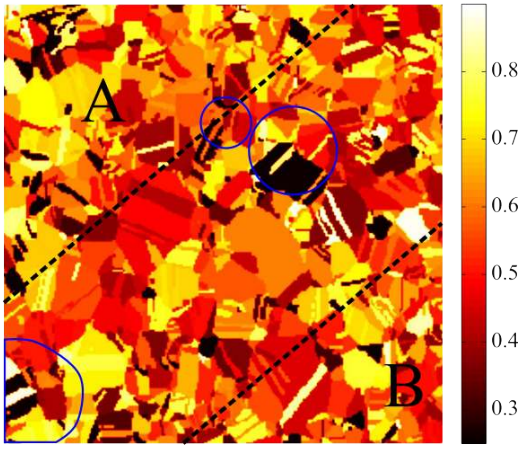

(c) θ_2 in radian

Figure 7.5: (a) Experimental profilometry with the superimposition of: numerical area of compressive ε_{33} strain in blue dotted line. (b) the experimental mean granular misorientation field and (c) the second Euler angle (rad)

Actually, the region is globally surrounded by few misoriented grains, i.e. region which deform uniformly, and concentrate in its center one of the highest misorientation. A similar observation could be done into circle 2. Regions 1 and 2 represent consequently, "hard" regions (set of misoriented grain) surrounded by large "soft" ones (low misoriented set of grain). It could explain, in part, observed out-of-plane localizations in figure 7.5 (a).

Then, let focus on domain A and B in figure 7.5 (c). A slight correlation between second Euler angle Φ and surface topography could be observed. Indeed, one could note notably in domain A that Φ is statistically higher than in the rest of specimen gauge-section. It is 0.59 radians compared to 0.51

in the central domain for example. It is also significant in many grain located into the domain B or close to. The mean value is 0.54 radians. Regarding the great heterogeneity of the microstructure it is difficult to underline clear observations nevertheless; it seems that a great part of low or mean Φ levels are located in the central domain where the surface topography exhibits a dale. In opposite, many high Φ levels are concentrated in domain A and B where the surface relief is significant.

On one hand, one knows that the misorientation could lead the strain localization. On the other hand, it seems reasonable to think that grains with significant Φ angle deforms easily along the out-of-plane direction compared to grains of which the Φ angle tends toward zeros. Thus it seems reasonable to point a relation between the second Euler angle, the misorientation and the topography of specimen surface. Nevertheless, no statistics evidence this point.

Then, let see the strain distributions. Figure 7.6 (a) and (b) presents, the strain distribution of transversal strain (a) ε_{11} and axial one (b) ε_{22}, for each model and for experiment.

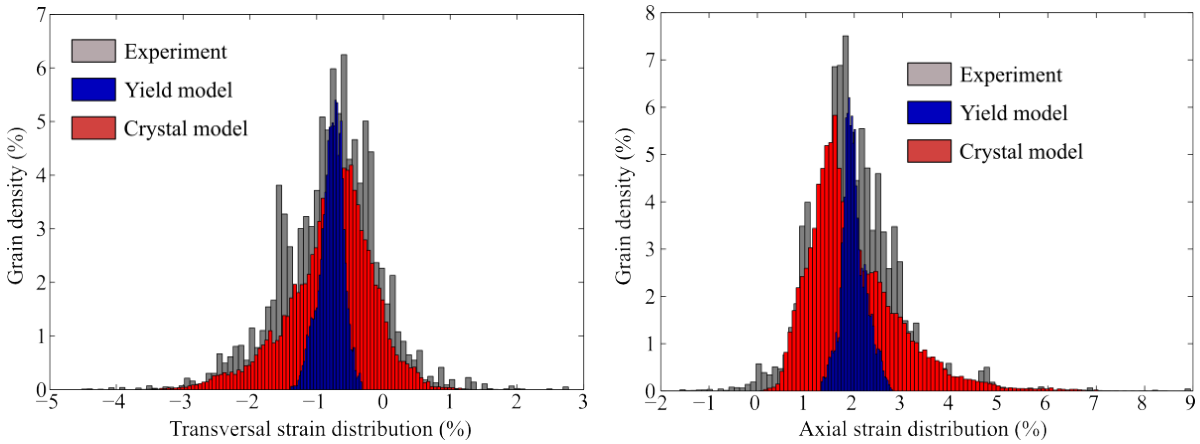

(a) ε_{11} (b) ε_{22}

Figure 7.6: Comparison of numerical and experimental distributions of strain at 2% of mean axial strain (in %)

The yield model does not allow large distributions of strains over the mean value and consequently underestimates the local variation of strain. In opposite, the crystal model fits relatively well the whole field in terms of distribution, extrema, and mean value.
Note that a simpler model was first build to estimate the expected distribution of temperature, energy, strain ... within a polycrystalline aggregate. This work is published in [Seghir 2012a]. The constitutive law is the one of the yield model and the same procedure is used for the distribution of yield stress identification. The difference is that, within this model, the crystallographic texture was not included. Elasto-plastic inclusions were randomly distributed in space. One result of this work is that experimental mean values were well captured by the model. Nevertheless local distributions, notably strains were

widely underestimated. It was pointed out that it could be due to the lack of texture. Indeed, randomly distributed cubic elasto-plastic inclusions could not lead to any real localization. Especially the cubic aspect of inclusions does not account for the grain shape and size which play an significant role within localization processes. Figure 7.6 (a) and (b) shows that adding the crystallographic texture (yield model) does not significantly improve distributions compared to experiment. The main improvement consists in the ability to deal with fields contrary to the model introduced in [Seghir 2012a], nevertheless, one currently knows that improving strain field requires two additional data: the implementation of the crystallographic texture and the implementation of a crystal kinematics.

Numerical strain fields from both models have been discussed and a final comparison between model and experiment has been done. Similar plane strain localizations could be found for the yield and crystal model. Nevertheless, due to its ability to accommodate any strain gradient at grain boundary [von Mises 1928], the crystal model reveals significant gradient of deformation from grain to grain. The comparison between experimental and numerical strain distributions evidences that variations of strain in the crystal model are consistent. In addition the comparison between randomly spaced elasto-plastic inclusion model, yield model and crystal model has allowed pointing out that crystallographic texture as well as crystal kinematics are required to well represent the distribution of strains. It has also been pointed out that the surface topography was in part relatively well represented by the crystal model. It allows to underline that the experimental surface topography observed in chapter 1.1 is actually significantly leaded by the surface grains.
In addition, even if yield and crystal model provide same mean values, fields are totally different in term of localization especially for the out-of-plane strain field. Finally, a comparison between crystallographic orientation, especially second Euler angle, misorientation and surface topography has been done. This comparison reveals a possible relation between high second Euler angle and high surface relief as well as between low second Euler angle and surface dale. Then it has been shown, with the crystal model, that one of the most deformed region (ε_{22} and ε_{33}) is a region surrounded by high density of few misoriented grain and which localized in its center many small and very misoriented grains. Nevertheless no more concrete relation with misorientation has been observed.

7.4 Temperature

7.4.1 Fields

This section deals with the analysis of thermal fields. Figures 7.7 from (a) to (h) present numerical thermal fields at different instant of loading. The two firsts are located in the macroscopic elastic domain while the two others are located in the macroscopic plastic domain. Yield model results are presented in the 1^{st} column and crystal ones in the 2^{nd} column. Note that the surface crystallographic

texture is superimposed.

First, one has to remind the mean variations of temperature presented in picture 7.2 as well as the problematic interaction between experimental thermal boundary conditions and the intrinsic thermal response of models. One has seen that from 0 to ≈0.2% (≈200 MPa) of mean axial strain the mean temperature of the model is higher than the experimental one, and from ≈0.2% to ≈1.2% it is the reverse. It explains results obtained in figures 7.7 (a), (b), (c), (d). Indeed, figures show that whatever the model, a thermal gradient exists: hot in the center of FEM and cold at boundary conditions. One understands that thermal field must be analyzed carefully since both set of field at 80 MPa and 180 MPa, i.e. in the macroscopic elastic domain (see 7.2 (a)), exhibit actually virtual thermal localizations due to boundary condition management. Thus, no interpretation could be done from both first instants since any potential slight micro-dissipation due to microplasticity is vanished by the virtual macroscopic thermal gradient.

Nevertheless, picture 7.7 (e) and (f) shows that when intense local dissipation is produced by plasticity mechanisms, it could clearly be observed. Note that a gradient of temperature still exists between the center and the boundary conditions, but its impact is not enough significant to vanish the intrinsic dissipation of the FEM. Figures 7.7 (e) and (f) shows two important points within the thermomechanical analysis of heterogeneous material: some grains undergo plastic strains then dissipations, whereas other grains still are elastic and tend to go down the temperature. Both models allow us to understand that the bottom left part of specimen is still elastic whereas a region near the center becomes plastic and dissipates a lot. This strain gradient was already visible in axial strain fields. Indeed, in figure 7.4 (d) for example, one has seen that the bottom left part of specimen exhibits low axial strain levels while the heated region in figure 7.7 exhibits strain higher than 4 %. Thermal fields confirm the coupling.

The yield model exhibits a small and circular hot spot and a long colder region on the left. The crystal model reveals a more intense and heterogeneous thermal localization within a larger region impacted by many grains, and a small colder region. Models reveal consequently that surface thermal fields are clearly impacted by the local behavior from the beginning of microplasticity to the end of the test, and that the resulting thermal gradients are in the order of $100mK$ as shown it in figure 7.7 (e), (f), (g) and (h).

These numerical results allow a validation and a better comprehension of experimental thermal fields studied in chapter 4.1:

- numerical thermal gradients are in the same magnitude order than experimentally observed ones (see chapter 4.1).

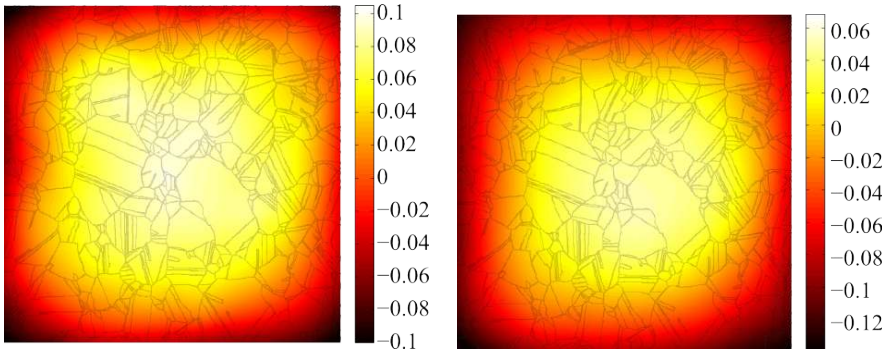

(a) θ in mK at $\sigma_{22} = 80$ MPa

(b) θ in mK at $\sigma_{22} = 80$ MPa

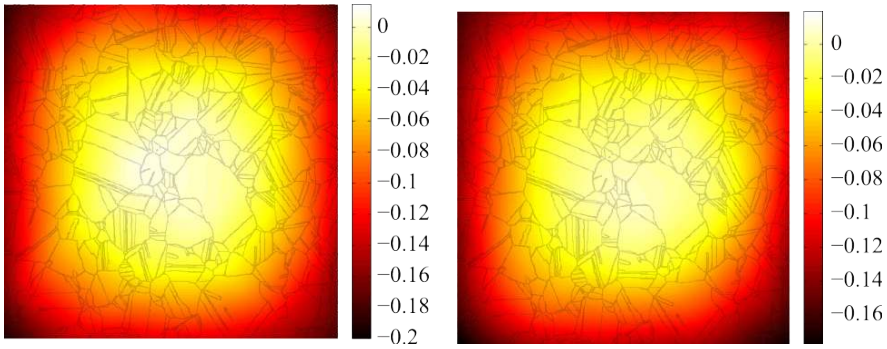

(c) θ in mK at $\sigma_{22} = 180$ MPa

(d) θ in mK at $\sigma_{22} = 180$ MPa

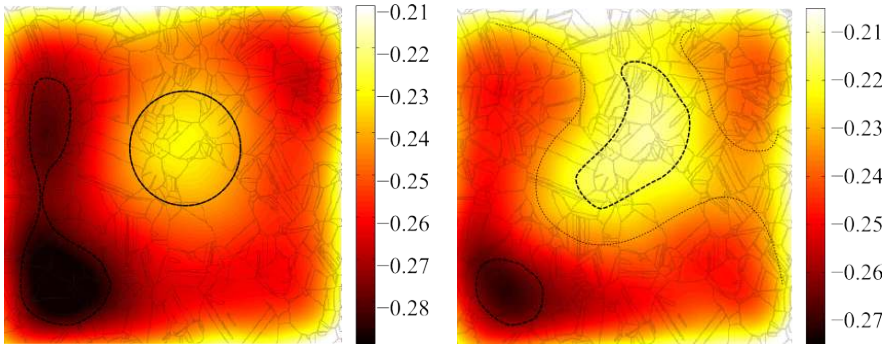

(e) θ in mK at $\sigma_{22} = 220$ MPa

(f) θ in mK at $\sigma_{22} = 220$ MPa

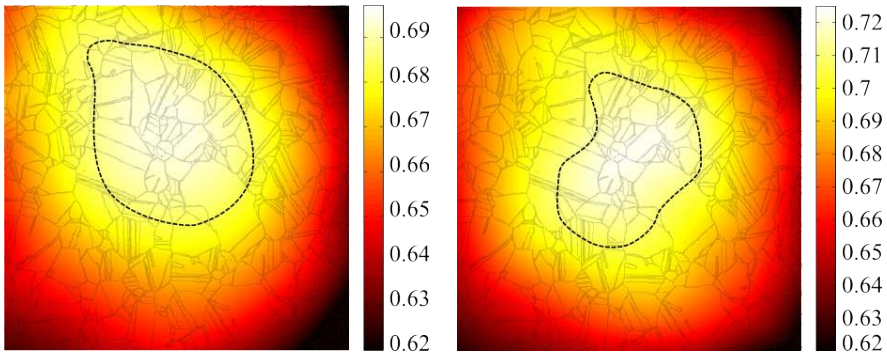

(g) θ in mK at $\sigma_{22} = 270$ MPa

(h) θ in mK at $\sigma_{22} = 270$ MPa

Figure 7.7: Numerical thermal fields $\theta = T - T_0$ (mK) at (a,b) E_1=80MPa, (c,d) E_2=180MPa, (e,f) P_1=220MPa and (g,h) P_2=270MPa for yield model (1^{st} column) and crystal model (2^{nd} column)

- the thermal localization, seen in figure 7.7 (f), occurs exactly in the same set of grain than experimentally (see chapter 4.1). This set of grains also contains the previously discussed region noted 1 in figure 7.5 (a). Thus models evidence that the main thermal localization observed experimentally is effectively linked with plasticity and dissipative mechanisms occurring in a specific set of grain.
  According to previous observations, the set of grain corresponds firstly, to a region where a deep dale is observed on the surface (see figure 7.5 (a)), secondly where axial strains are very intense (see figure 7.4 (d)), thirdly where second Euler angle are very low (see figure 7.5 (c)) and finally where very small misoriented grains are well surrounded by a "soft" region composed by slightly misoriented grains (see figure 7.5 (b)). In addition, one observes in 7.7 (g) and (h) that the early hot spot produced by local micro-plastic strain localizations remains in the same region up to the end of the test, even if the dissipative region extends a little bit. This results is also in line with experimental observations.

- the observed experimental gradient of temperature from left to right part of specimen gauge-section (see figures 4.5 (d), 4.6 (d), 4.8 (d) and 4.9 (d)) is also observed numerically and is clearly not leaded by boundary conditions. According to models (see figure 7.7 (e) and (f)) this gradient of temperature is managed by plasticity mechanisms. While some grains of the specimen-gauge section dissipate leading to a global warming of the sample the left part of the specimen gauge-section still is elastic and tends to decrease the local temperature.

These three points valid every experimental observations and provide some key to understand the mechanisms of localization.

The effective deviation between numerical and experimental thermal fields has been plotted in figure 7.8 (a) and (b) at 2.5% of mean axial strain (end of test). This deviation is shown for yield and crystal model respectively. Firstly, one observes in both cases that model and experiment are quite similar. Whatever the model the deviation is lower than 10%. It evidences that both models well represent the mean and local thermomechanical coupling. No concentrated localization of deviation could be observed which notably means that plastic strain localization are also spatially well represented. Finally, although a small difference is observed between both deviation fields, crystal model is slightly better. The mean thermal deviation with crystal model is 1.8% or 15mK. One could recall that the experiment uncertainty is 30mK. Moreover a great part of the field exhibits a deviation from experiment lower than 2% compared to yield model where the deviation is mainly about 3-4%. One point could be underlined, especially from figure 7.8 (b):

- the tested specimen of stainless steel A316 undergoes a thermomechanical behavior very close to the modeled polycrystalline aggregate. Mesoscopic localization processes are very similar. Only very localized peaks of strain and then temperature 7.8 (b) are underestimated which points possible improvements:
  - introducing a finer description of strain concentration and accommodation at grain boundary, using for example non-local plasticity framework ($GNDs$).

– leaving a continuous framework to introduce the real degree of freedom of free surface grain boundaries, introducing in parallel eventual thermal grain boundary resistancies.

Nevertheless, one could note, at least in the tested case, that non-local plasticity, the discontinuities, subsurface grains ... play a secondary role compared to surface grain structure, size, shape and crystalline kinematics.

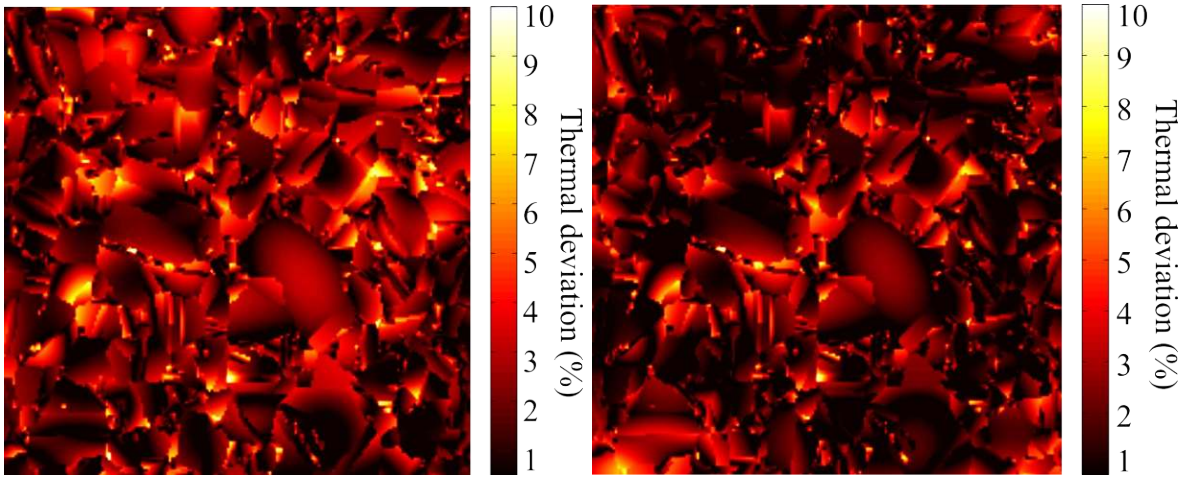

(a) $\Delta T^{yield}_{(2.5\%)}$ (b) $\Delta T^{Crystal}_{(2.5\%)}$

Figure 7.8: Deviation from experimental thermal fields T in % at 2.5% of mean axial strain: (a) yield model and (b) crystal one.

Numerical thermal fields have been investigated. As expected, both models evidence a significant impact of experimental thermal boundary conditions, on numerical fields, in the macroscopic elasticity domain. On the other hand, this impact becomes a second order one when microplasticity occurs. It has been evidenced that the main experimental thermal localization (see chapter 4.1) is mechanically based since models well represent it. This thermal localization of temperature is moreover connected to a set of grain where intense plane strains and specific surface relief are observed (see 7.4 (d) and 7.5 (a)). In parallel, models exhibit also colder regions. It confirms experimental observations and also the fact that this lower dissipative response is connected to the surface grain structure. Finally a deviation lower than 10% and than 2% in a large set of grain between experimental and numerical thermal field has been evidenced, notably for the crystal model. One important conclusion of this section is that the models prove the relevance of measured fields. In spite of the heavy experimental procedure of calibration, intragranular projections ... the measurements lead to a thermal observation which is clearly not due to artifacts but reflects actual mechanisms of plasticity pointed by the models.

7.4.2 Intragranular thermal inflection: case of specific grain

Models have pointed the relevance of experimental observations concerning displacement, strain and thermal fields. The objective of this section is to go deeper at intragranular scale to verify an other experimental observation: the identification of the first intragranular dissipative region with the help of local temperature variation as well as the limitation of dissipative front propagation due to a competition between elastic and plastic intragranular regions.

To perform such analysis one chooses the crystal model which represents intragranular variations and the grain already studied in chapter 4.1. The purpose is not to perform an exhaustive comparison with experiments but to evidence that the phenomenon experimentally observed is clearly not an measurement artifact even at intragranular scale. To realize such a comparison, one needs a grain which numerically exhibits similar slip-system activation than experimentally. The investigated grain is presented in figures 7.9 (a), (b), (c) and (d).

Figures 7.9 (a), (b), (c) and (d) present respectively:

- the propagation of numerical thermal inflection front in millisecond (test time = 2.15s). It is calculated using the same procedure than the experimental one, i.e. by finding the instant when the local variation of numerical temperature deviates from a linear relationship with the local strain. It allows the identification of the first dissipative region within the F.E. grain.
- the systems associated to the maximum numerical Resolved Shear Stress at the end of the test. Numerically different systems are activated simultaneously, classically 4 or 5, and each of them are maximum within different part of the grain. This field allows to observe the numerical predominance of each system within each part of the grain.
- the Resolved Shear Stress level associated to system C_1 in MPa. One presents this field since experimentally, the plasticity and the dissipation are leaded by the plastic activity on this specific system.
- the propagation of experimental thermal inflection front in millisecond. This field allows a direct comparison with numerical field in figure 7.9 (a)

Let firstly deal with numerical observations. Three early dissipation sites are observed in figure 7.9 (a). The two firsts are on left and right grain extremities. In these case, the propagation of thermal inflection front is rapidly stopped. The third one initiates at the bottom region of the grain and then propagates continuously without any constraint through the grain. Here, the total propagation of thermal inflection front required ≈12ms. In parallel one notes that the pattern observed in figure 7.9 (a) is very similar to figure 7.9 (c). Indeed, the thermal inflection front propagates continuously into the region where RSS on system C_1 is high (from 90 to 100 MPa) and quite uniform. In opposite both lateral regions where RSS on system C_1 is relatively low correspond to regions where thermal inflection occurs early and then does not propagate. Thus it seems that the system C_1 has a strong influence on the intragranular thermal activity.

Nevertheless, according to figure 7.9 (b), the C_1 system is numerically not the more activated system and thus does not managed entirely the intragranular plasticity. Actually 5 numerical systems have almost the same level of RSS during the whole test. Figure 7.9 (b) underlines that lateral regions have a great influence of system A_6 and A_3 while the center underlines the system D_1 and D_6. In addition note that the system C_1 has almost the same values of RSS that these systems but as its magnitude is slightly lower (≈-5MPa), it does not appear within figure 7.9 (b). In consequence, numerically 5 systems activates plasticity (A_6, C_1 and A_3, D_1, D_6) whereas only 2 have been observed experimentally (A_6 and C_1). It has necessarily a wide influence on the intragranular thermal field and variation.

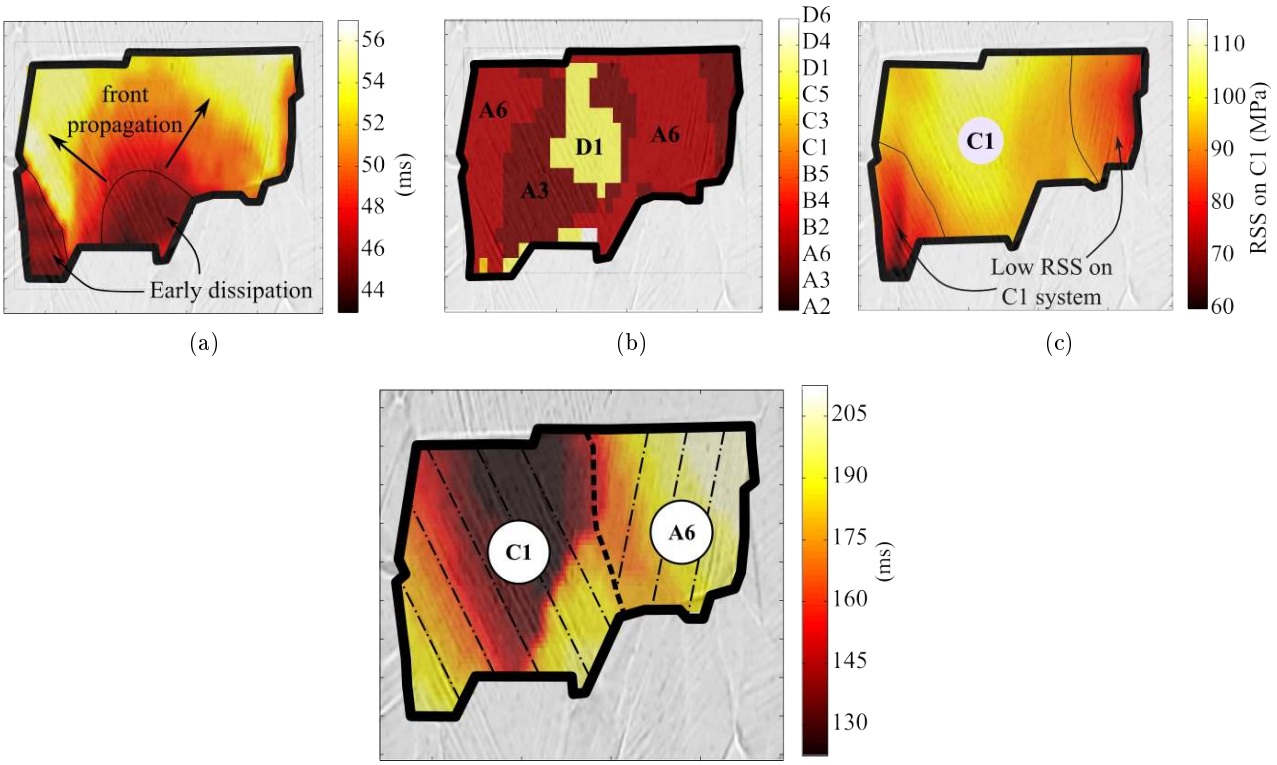

Figure 7.9: (a) the propagation of numerical thermal inflection front in millisecond, (b) the systems associated to the maximum numerical Resolved Shear Stress at the end of the test, (c) the Resolved Shear Stress level associated to system C_1 in MPa (experimentally activated) and (d) the propagation of experimental thermal inflection front in millisecond

Experimentally (see figure 7.9 (d)), one observes that the system A_6 is activated on the left part of grain and C_1 on the other part. One observes that thermal inflection initiate with C_1 system (on top). Then the thermal inflection front does not propagate immediately through the system A_6 which is still elastic (see chapter 4.1). One note that the propagation of thermal inflection front in a great

part of system C_1 spends ≈15 ms but the entire propagation spends ≈80 ms due to the delay between C_1 activation and A_6 one.

Thus one notes that:

- The crystal model well captures the experimental activity of system A_6 on the left part of grain (see figure 7.9 (b)).
- It also captures the late-thermal inflection appearance within this specific system domain relatively to the rest of grain (see figure 7.9 (a) and (d)).
- It captures a significant and uniform activity of system C_1 that is in total agreement with experimental results (see figure 7.9 (c) and (d)). Nevertheless, the model introduces some additional slip-systems (see figure 7.9 (b)).
- Concerning the thermal inflection appearance within C_1 system, a difference between model and experiment may be noted. Experimentally the thermal appearance initiates on top, then propagates and stops. Numerically, it initiates on bottom and then propagate through the grain. No convincing arguments has been found concerning the difference of the first dissipation localization. Nevertheless, one has seen experimentally that when different slip-systems are simultaneously activated and cross each other, no singular variation of temperature is observe anymore. The behavior discontinuities are not enough significant to lead to thermal barriers. Notice that the main difference between the model and the experiment within this grain is: (1) the systems are numerically activated simultaneously whereas they are successively activated experimentally. Thus, numerically there is no clear gradient of response. (2) Numerically, the slip-systems cross each others whereas, experimentally, each slip-system work apparently in its own intragranular domain. It could explains the differences about the dissipation yield appearance.

Nevertheless, it is very interesting to note a great similarity between early experimental plastic (dissipative) region in figure 7.9 (d) (dark region) and numerical gradient of RSS on system C_1 in figure 7.9 (c). Indeed the domain where the RSS reaches its maximum (≈100 MPa) corresponds to the domain where early experimental plasticity has initiated on the same system. Similarly, low numerical RSS on system C_1 correspond to regions where experimentally, thermal inflection appears late. In consequence one could imagine that the model accurately represents the plastic slip activity on system C_1. The activation of multiple slip system and rough grain boundary interactions leads to a slightly different thermal scene.

The crystal model seems to accurately predict the intragranular activity of plastic shear on system C_1 and A_6. In parallel, it reveals the ability to identify the early plastic regions with the help of local surface temperature variations. The model proves here that the experimental and intragranular thermal results introduced in chapter 4.1 and in appendix I.1, are in agreement with the thermomechanical concepts. Thus it evidences the accuracy and the capacity of thermal field measurements.

7.5 Stress fields

One proposes within this section to deal with numerical stress fields. Note that this quantity is still hardly measurable experimentally in an heterogeneous material even if many progresses has been done thanks to X-ray measurements [Singh 1998, Li 2004, Tamura 2005, Weidner 2010]. In [Weidner 2010] the author points out a precision of 10 MPa for 50x50x500 μm^3 silicate minerals specimen.

One observed in section 7.1 that the mean stress-strain relation is globally well represented by each model. Figures 7.10 (a) and (b) introduce firstly mean granular stress-strain relation in the case of yield and crystal model respectively.

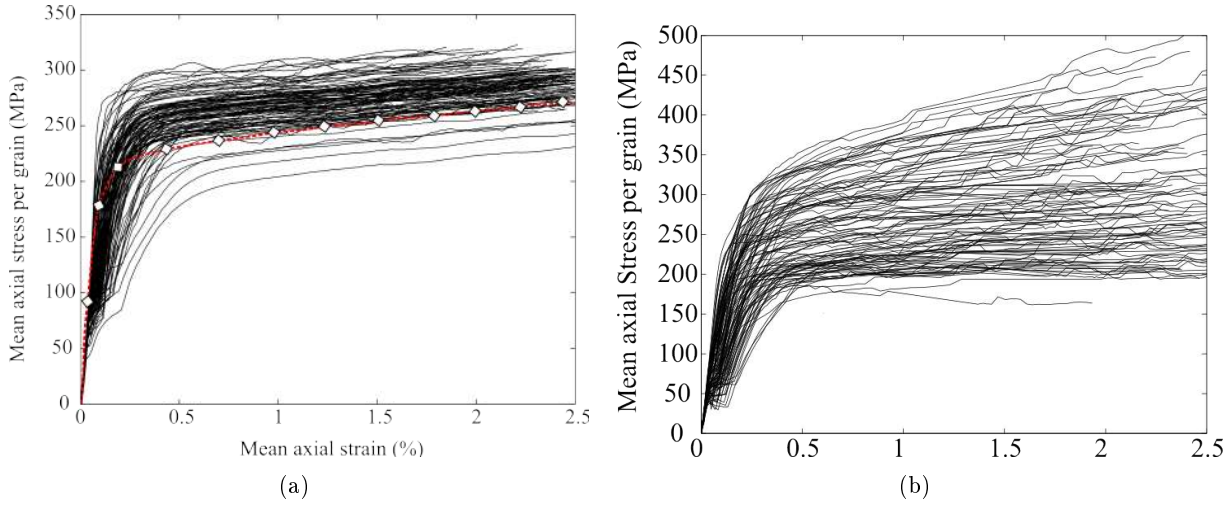

Figure 7.10: Mean granular stress-strain curves: (a) yield model and (b) crystal model

Red and marked curves are mean experimental stress-strain response in the loading axis. One observes in the yield model that the stress level ranges from 225 MPa to 325 MPa at the end of the test, with more than 90% of grain stressed over 270MPa. For the crystal model, the stress distribution ranges from 150MPa to 500MPa. Thus crystal model exhibits a stress distribution of which the standard deviation is 3 times higher than the yield one. This point is in line with respective strain distribution observed in section 7.3. The granular analysis of stress path points out that from 45 MPa, many grains deviate from the perfectly elastic behavior, undergo plastic strain in the direction 2 (axial), $\varepsilon 22$, and then exhibit an elastoplastic behavior up to quasi perfectly plastic one. This observation is verified for both models. As already precise in section 7.1 such stress-strain curve in the loading direction is due to a significant multiaxiality of loading at the very beginning of the test, notably transversal stresses. One also notes that grain which undergo early plastic strain have a significant lower stress level at the end of the test. It is the origin of the large stress distribution amplitude.
An interesting point is the hardening behavior of each model. The yield model exhibits a uniform and constant hardening behavior which is in agreement with its constitutive law, i.e. linear kinematic

hardening. In parallel, the crystal model exhibits a large range of behavior including elastic perfectly plastic behavior and even softening. It points out the interest of the constitutive law (see chapter 6.1). Indeed, a non-linear hardening which decreases when a threshold value of dislocation is reached. Thus it permits to account for the loading path. In the present case, every grain which undergone strong early plasticity storing many dislocations tend toward a saturated state.

Let us now deal with stress fields. Figures 7.11 from (a) to (h) present axial stress field, σ_{22} at different instants of loading. These instants are the same than in previous numerical and experimental analysis. The first column presents results of yield model and the second the crystal one.

Firstly, one could focus on the impact of early plastic grains within yield model, especially in macroscopic elastic domain (see figure 7.11 (a) and (c)). One observes in figure 7.11 (a) that many small grains undergo plastic strain. In these grains the stress state remains low compared to neighbors because of the hardening process. They concentrate very singular value of stresses and the initiation of high stress crossing bands from this plastic inclusions maybe already observed. Then, this local crossing bands propagates and coalesces to produce the pattern observed in figure 7.11 (c), i.e. macroscopic localization bands. Finally, once the elasto-plastic transition is over, i.e. every grain undergo a similar hardening, the field reflects the granular mean response. It corresponds to figure 7.11 (e) and finally (g). This process reflects the clear incapacity of the yield model to accommodate the strong gradients of strain or stress. In parallel, the crystal model presents a very heterogeneous field from 80 MPa of nominal stress. Note that the distribution varies from 10 to 160 MPa at this instant of loading.

One observes, from 80 MPa of nominal stress, with the crystal model, a macroscopic stress localization. Indeed, the band noted H_1 in figure 7.11 (b) and (d) evidences from 80 MPa to 180 MPa a clear concentration of high stresses. In chapter 4.1, the appearance of an experimental hot band within the thermal field was noticed. Experimentally, this hot band was related to an intense contraction band localized into long and thin set of grains. Thus, let us compare the numerical stress field to experimental thermal observations done in chapter 4.1. Figure 7.12 (a) presents the experimental thermal field $\theta = T - T_0$ at 220 MPa of nominal stress.
The figure 7.12 (a) presents the thermal field at 220 MPa since the thermal hot band is here more clear. Nevertheless, it already appears from 180 MPa as in numerical fields (see figure 7.11 (d)). The comparison between the numerical stress field, coming from the mechanical response of the microstructure, and the experimental thermal field proves the existence of a relation between the experimental localization of dissipation and the localization of highly stressed grains. Moreover, it is interesting to notice that the experimental thermal gradients related to such localization are actually of the order of 30-40 mK. Thus, the crystal model points out the accuracy of experimental temperature as well as the existence of a strong thermomechanical coupling even in microplasticity.

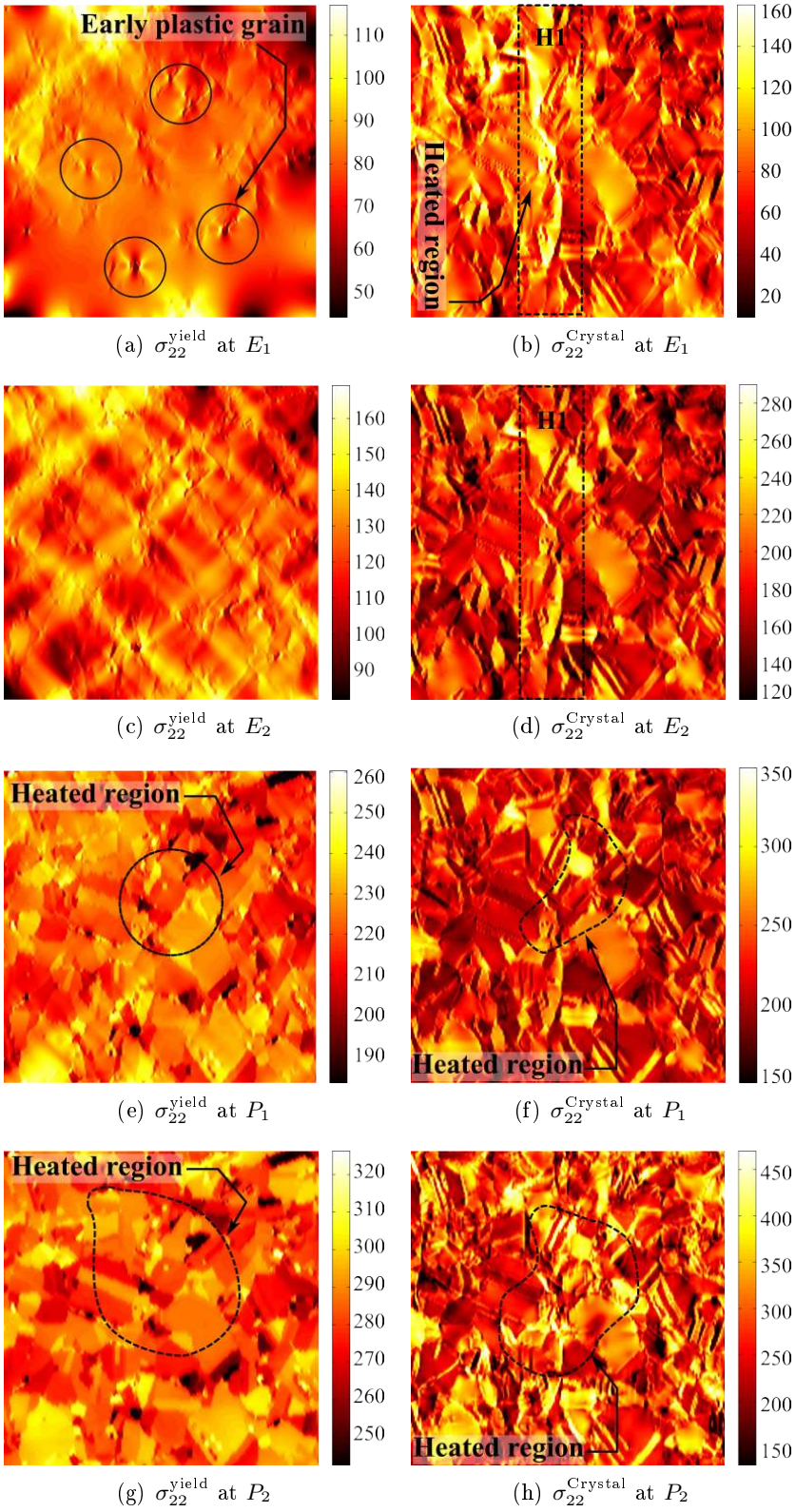

(a) $\sigma_{22}^{\text{yield}}$ at E_1 (b) $\sigma_{22}^{\text{Crystal}}$ at E_1

(c) $\sigma_{22}^{\text{yield}}$ at E_2 (d) $\sigma_{22}^{\text{Crystal}}$ at E_2

(e) $\sigma_{22}^{\text{yield}}$ at P_1 (f) $\sigma_{22}^{\text{Crystal}}$ at P_1

(g) $\sigma_{22}^{\text{yield}}$ at P_2 (h) $\sigma_{22}^{\text{Crystal}}$ at P_2

Figure 7.11: Numerical stress fields σ_{22} (MPa) at (a-b) E_1=80MPa, (c-d) E_2=180MPa, (d-f) P_1=220MPa and (g-h) P_2=270MPa. the 1^{st} column corresponds to yield model and the 2^{nd} to the crystal one.

Then, numerical localization of intensively heated region (see figures 7.7) are pointed out in figures 7.11 (e), (f), (g) and (h). Focusing on crystal model in figure 7.11 (h), one observes that the more heated region localizes the highest axial stress levels as well as the highest stress gradients. Notably, grain boundaries and thin twins are highly stressed. One observes here the clear connection between numerical axial stress field and numerical surface temperature.

Let us now focus on experimental thermal field registered at 253 MPa (close to the end of the test) in figure 7.12 (b). The numerical heat localization is superimposed and figure 7.11 (h) allows the comparison with numerical axial stress field.
One observes that the highly heated region, in the crystal model, matches the experimental one. Same set of grain are concerned. Moreover highly stressed grains or boundaries, in crystal model, are clearly intensively heated experimentally.

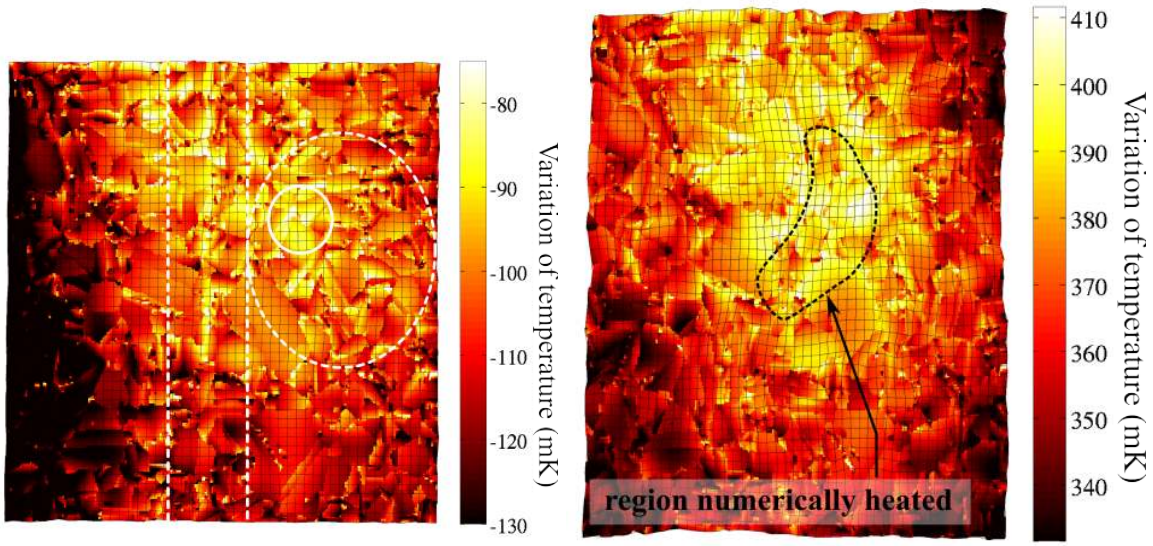

(a) (b)

Figure 7.12: Experimental variation of temperature θ (mK) at (a) 220 MPa and (b) 253 MPa of nominal stress

The numerical stress field from yield and crystal model has been investigated at different instant of loading. A clear correlation has been observed between experimental localization of temperature and the numerical stress field. It allows to conclude that the surface grain texture, used for crystal model, has effectively initiated the main part of dissipative processes observed experimentally. It also points the ability to surface temperature, observed at the appropriate scale, to accurately describe the micro-strain and stress localization processes.

7.6 Conclusion

Within this chapter, numerical fields from yield and crystal model have been investigated and compared to experimental results. The objectives were, on the one hand, to validate every experimental observations which leads to a validation of the entire experimental calibration procedure as well as intragranular projection fields. On the other hand, the objective was to deal with additional fields such as out-of-plane strains, stresses ...

It has been shown that both models present similar thermomechanical results at macroscopic scale and are in line with experimental ones. Then, only the crystal model predicts accurate fields. This point underlines the ability of the crystal model to accommodate large gradients of response from grain to grain compared to the yield one.

It has been shown that the crystal model is able to predict in part the experimental surface topography. Some characteristics of the surface relief has been related to local misorientation and/or crystalline orientation. Nevertheless no convincing and global explanation about the origin of surface topography has been found.

Strain fields are accurately estimated by the crystal model and strain gradients observed experimentally have been validated as well as strain localizations. By coupling numerical stress, temperature and strain fields, it has been proved that every experimental heat localizations observed during the test can be explained by local concentrations of stress and strain. It allows the validation of in-situ experimental measurements and proves the existence of strong thermomechanical couplings even during microplasticity development.

Chapter 8

Numerical energy balance

Contents

The purpose of this chapter is to deal with energy quantities performing energy balance. The main difference with the energy balance performed in experimental part is the knowledge of every internal variables. The stored energy field within dislocation density or hardening is currently accessible, and its comparison with the total macroscopic stored energy can be done. This chapter is divided into two steps: the macroscopic point of vue, and the mesoscopic one.

8.1 Macroscopic point of vue

Within this section only results from the crystalline plasticity model are presented. This choice has been done regarding to the great similarity between homogenized energy quantities of the yield and crystal model.

Let $< i >$ be the average over the specimen-gauge section surface of the quantity i and $\boldsymbol{\varepsilon^p}$, $\boldsymbol{\sigma}$, ΔT the local full 3D, plastic strain and stress tensor, and the local thermal Laplacian respectivelly. As it has been introduced in the chapter 6.1 the isotropic thermoelastic coupling power per unit of volume takes the following form:

$$W_{the} = T\frac{\partial \boldsymbol{\sigma}}{\partial T} : \dot{\boldsymbol{\varepsilon}}^e \approx -3K\alpha T \cdot tr\left(\dot{\boldsymbol{\varepsilon}}^e\right) \tag{8.1}$$

where $tr\left(\dot{\boldsymbol{\varepsilon}}^e\right)$ is the trace of time derivative of elastic strain tensor. Then, according to notations and considering equation A.13 (see chapter 5.1) and 8.1 the homogenized expression of stored power takes the following form:

$$W_s = < \boldsymbol{\sigma} : \dot{\boldsymbol{\varepsilon}}^p > - \left[\rho C_v < \dot{T} > -k < \Delta T > +3K\alpha < T \cdot tr\left(\dot{\boldsymbol{\varepsilon}}^e\right) >\right] \tag{8.2}$$

Let us now deal with energy quantities, i.e. the integral along the whole test time of instantaneous powers. Figure 8.1 (a) presents the homogenized energy balance coming from numerical simulation

using crystal model. Figure 8.1 (b) presents the homogenized stored energy, E_s^{macro} (the time integral of W_s and noted E_s in figure 8.1 (a)), the complementary area of the strain-stress curve E_{sr}^{macro} (see figure 7.2), the difference between both quantities E_{sh}^{macro} and the average over whole energy stored in intragranular hardening $< E_{sh}^{micro} >$. Notice both last energy are expected to be similar since the only difference is the way to access it. The first one, E_{sh}^{macro} is accessed by difference between the total stored energy and the complementary area of stress-strain curve. This is a thermomechanical and homogenized way. The second one, $< E_{sh}^{micro} >$ is accessed by the local stress flow. It is a local and purely mechanical way.

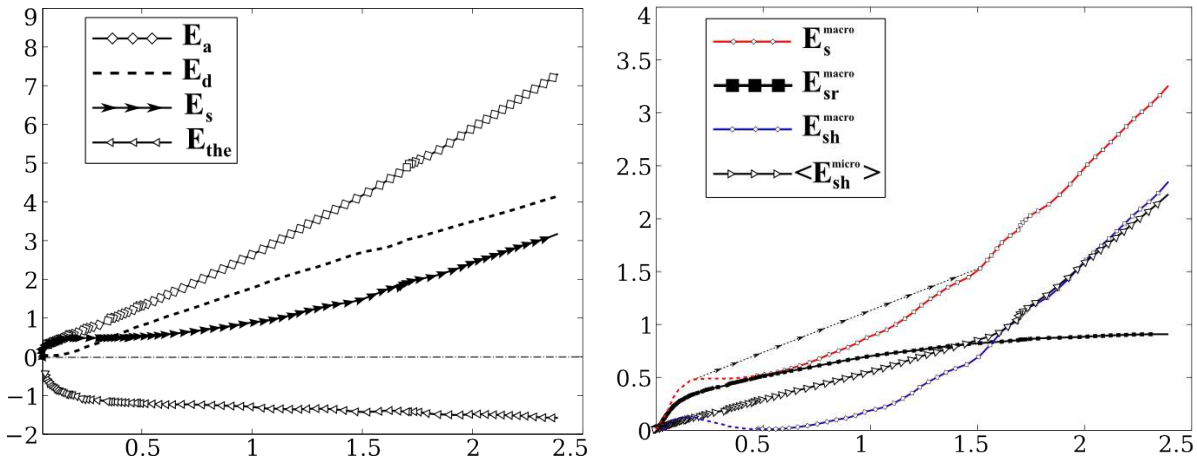

(a) mean axial plastic strain in % (b) mean axial plastic strain in %

Figure 8.1: (a) Evolution of anelastic (E_a), dissipated (E_d), stored (E_s) and isentropic (E_{is}) energy. (b) Evolution of different homogenized stored energy within the material along the monotonic tensile test: total stored E_s^{macro}, stored in residual stresses E_{sr}^{macro}, in hardening E_{sh}^{macro} and average over the intragranular stored energy in dislocation densities $< E_{sh}^{micro} >$.

One observes that the macroscopic anelastic energy E_a ranges from 0 to $\approx 7.2\ mJ.mm^{-3}$ at 2.5 % of plastic strain. In parallel, the dissipated E_d, stored E_s, and isentropic energies E_{the} ranges from 0 to 4.1, 3.1 and -1.6 $mJ.mm^{-3}$ respectivelly. Table 8.1 presents the comparison between numerical and experimental energy data at 2.5 % of plastic strain.
One firslty observes that the crystal model overestimate the anelastic energy compared to experiment and the difference is 1.3 $mJ.mm^{-3}$. This point is explained by the difference between stress-strain curves presented in picture 7.2 where a higher stress-level is reached for the crystal model. One could also observe in table 8.1 that the crystal model dissipates about 57% and stores about 43% of anelastic energy. In comparison, experimental specimen dissipates about 70% and stores about 30%. Thus crystal model dissipates less and stored about $\approx$ 13% more in percentage compared to experimental specimen. Table 8.1 details that it leads to an increase of $\approx$ 10% of hardening stored energy and $\approx$ 3% of residual stresses energy. Thus the main difference between model and experiment, comes from an

overestimation of the intragranular hardening.

		Experiment 5x5x2mm^3 A316L specimen-gauge section (grain size≈ 130μm)		Crystalline plasticity model 5x5x1mm^3 aggregate columnar grains	
		E_i in $mJ.mm^{-3}$	$\frac{E_a}{E_i}$ in %	E_i	$\frac{E_a}{E_i}$
E_a		5.9	100	7.2	100
E_d		4.15	70.3	4.1	56.9
E_s	E_s	1.75	29.6	3.1	43.1
	E_{sr}	0.53	9	0.9	12.5
	E_{sh}	1.22	20.7	2.2	30.6
	$< E_{sh} >$	-		2.2	30.6
E_{is}		-1		-1.6	

Table 8.1: Comparison of the rate of storage in form of hardening and internal stresses between tested A316L specimen and crystal model

One observes in Figure 8.1 (b), that the total stored energy E_s^{macro} estimated from homogenized equation 8.2 increases at the very beginning of the test, then exhibits a kind of plateau and then increases almost linearly up to 3.1 $mJ.mm^{-3}$. In parallel, E_{sr}^{macro}, increases initially as the total stored energy, E_s^{macro}, and then tends toward a saturated state around $0.93mJ.mm^{-3}$. By difference the estimation of energy stored in intragranular hardening, E_{sh}^{macro}, is obtained. It presents a level almost null up to 0.5% of plastic strain and then increases up to $2.18mJ.mm^{-3}$.
Its value is confirmed by the complementary way to estimate energy stored in hardening, the purely mechanical one, $< E_{sh}^{micro} >$. Nevertheless, one could underline that the evolution path is different, especially from 0.25% to 1.6% of mean plastic strain which corresponds to strain domain where the total stored energy rate is low. In consequence, one could note that both ways to estimate the hardening stored energy are not totally consistants. Knowing that the local hardening storage and its mean value $< E_{sh}^{micro} >$ are well calculated as well as the complementary area of stress-strain curve it implies that the total stored energy E_s^{macro} contains some mistakes.
The expected total stored energy evolution, i.e. the sum of $< E_{sh}^{micro} >$ and E_{sr}^{macro} is plotted[1] in order to underline the deviation from the calculated stored energy E_s^{macro}. It point that the macroscopic total stored energy is underestimated from 0.25% to 1.6% of plastic strain. Notice that this strain domain corresponds to the domain where a significant difference exhists between experimental and numerical temperature field (see figure 7.2). Thus the domain where a significant deviation exists between thermal reponse of crystal model and its boundary conditions since experimental temperature is applied at aggregate boundaries. Moreover, one has seen within figures 7.7 that when the thermal boundary conditions and intrinsic thermal response of the model are very different the thermal field is clearly affected by this thermal competition and consequently terms $\dot{T}$, ΔT results from a competition between two mechanics: the crystal model one where the local hardening stored energy $< E_{sh}^{micro} >$

[1] black dotted line with arrows

from, and the experimental one (at boundaries). In our opinion this competition leads necessarily to a misestimation of the macroscopic stored energy E_s^{macro}. In consequence, the plateau in macroscopic stored energy E_s^{macro} evolution appears to be an artefact resulting from an unappropriate management of thermomechanical boundary conditions.
It seems that its real evolution pass through the fictive dotted line builded from the sum of E_{sr}^{macro} and $< E_h^{micro} >$ which are two purely mechanics quantities and consequently unaffected by thermal boundary conditions. Moreover, from the verified aggreement between E_{sh}^{macro} and $< E_{sh}^{micro} >$ from 1.6% of plastic strain, i.e. when thermal boundary conditions are in line with the model, one could underline that the complementary area of the stress-strain curve corresponds to a well estimation of intragranular storage mechanisms. It confirms results coming from [Oliferuk 2009].

An homogenized analysis of energy quantities for the crystal model as well as the comparison with associated experimental results has been done. Results show a good agreement between orders of macroscopic anelastic energy magnitudes as well as evolution. The crystal model stores about 13% more than the tested specimen and the difference mainly results from an increase of hardening stored energy. A finer identification of hardening parameters is required. This point was already pointed during the comparison of macroscopic stress-strain curves. Then both ways in order to estimate the mean energy stored within intragranular hardening have been compared. The way based on thermal fields shows a deviation from effective storage rate due to a the competition between thermal boundary conditions and intrinsic thermal response of the model. One imagines that this error could be removed applying thermal flux boundary conditions (Neumann boundary conditions) to the aggreate instead of direct temperature (Dirichlet boundary conditions) as it was already detail in chapter 6.1. Finally, it has been shown that the complementary area of stress-strain curve reflects effectivelly the mean value of energy stored within residual stresses [Oliferuk 2009]. At least, over the strain domain where the surface thermal field is not disturbed by any boundary condition.

8.2 Energy fields at granular scale

Figures 8.3 and 8.4 introduce respectivelly (a) the heat production energy, (b) the heat energy losses by conduction, (c) the isentropic energy associated to thermoelastic couplings, (d) the anelastic energy, and both part stored energy: (e) the one stored within intragranular hardening and (f) the one stored within residual stresses. Associated equation are done under every figures. Notice that figures present the whole set of energy quantity which composed the classical energy balance such as: "a+b=d-(e+f)-c"

Figure 8.3 presents results coming from yield model while figure 8.4 results coming from crystal model. One could first underline some particular points. Theorically, high thermal heat losses underline regions which have been more heated than the rest of specimen-gauge section during a great part of the test and vice-versa. Thus, it is an intrinsic indicator of local and persistent heated and

anelastic regions. It could also be seen as the indicator of high plastic strained regions. The anelastic energy field provides the same information but coming from a mechanical point of vue whereas the first one points a dissipative aspect. In opposite, high isentropic energy is an indicator of regions where elasticity played a significant role. Thus, high stress levels. One can notably understand here that even if the mean value of heat losses term is very close to 0, as it has been seen in previous section, its field must be representative of persistent plastic gradients and in parallele thermoelastic couplings are representative of stress gradients.

According to both figures 8.3 and 8.4, one could first point 2 aspects depending on the model used (yield or crystal): fields are very different, especially mechanical fields (see (d), (e) and (f)). Then, gradients are much more significant in crystal model nevertheless mean values are closed to yield one. Let us compare and describe each field:

- Both heat production terms (see 8.3 (a) and 8.4 (a)) are very similar concerning the mean value (3.34 and 3.41 $mJ.mm^{-3}$) and the shape. Both exhibits a similar persistent heat localization located close to the center of the specimen gauge section. Nevertheless, the crystal model localization is more heterogeneous which points the appearance of very localized stress concentration compared to the yield model where the stress field is more diffuse. This point has been already pointed in the last section 7.1.

- Within the yield model, heat losses energy (see 8.3 (b)) is localized in two crossing bands (the contour is superimposed in dotted black lines). The same superimposition is done on crystalline field. This energy varies from -1 to 2 $mJ.mm^{-3}$ within the yield model and from -2 to 5 $mJ.mm^{-3}$ within the crystal one. One could note that many localizations are similar in both models. Nevertheless, as already pointed along the numerical part, yield model presents more diffused results. These localizations are surrounded by black circles and will be further discussed regarding to microstructure. One could also notice the same similarities on low energy regions. Thus fields reveal that globally, high plastic strained and dissipative regions are similar in both models. One of the main difference remains the accommodation of such local plastic strain at grain boundary leading to a diffuse or very contrasted field. Same conclusions could be done for anelastic energy (see figures (d)).

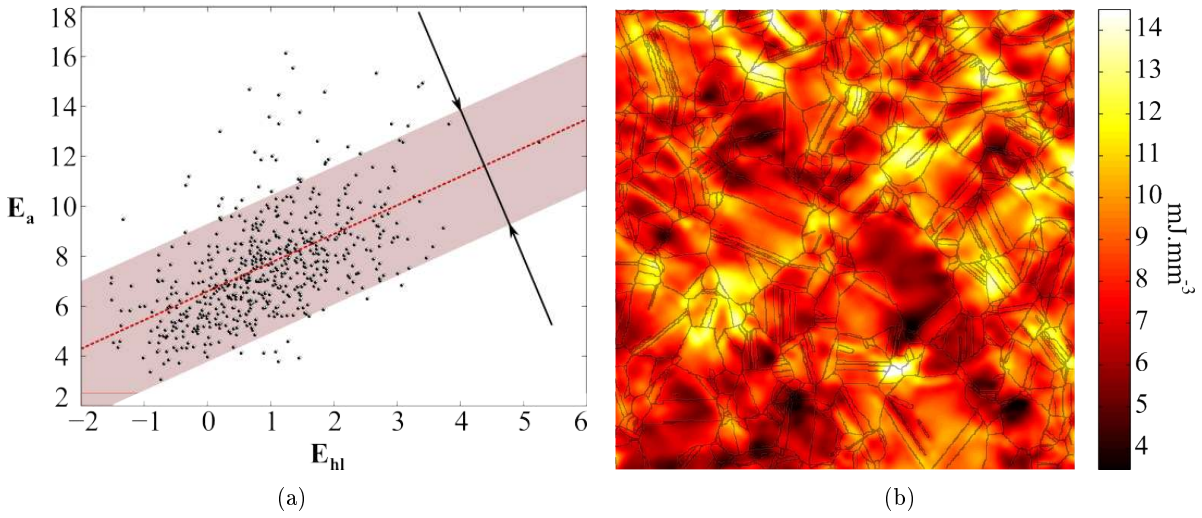

(a) (b)

Figure 8.2: (a) Granular relationship between heat losses energy, E_{hl}, and anelastic energy, E_a within crystal model and (b) estimation of E_a field from equation 8.4 superimposed on grain boundary network

Dealing with heat losses energy, the figure 8.2 (a) presents the relation between the expended anelastic energy of the aggregate and its heat losses by conductions. Figure 8.2 (a) points a linear dependence between E_{hl} associated to the time integral of second spatial derivative of temperature and E_a associated to plastic strain and stress. As one could see in picture 8.4 (b) and (d), fields are very similar, the main difference remains the diffuse aspect of the heat losses energy. The relationship found here, thanks to least square method is:

$$E_a \approx 1.13E_{hl} + 6.54 = aE_{hl} + b\bar{E}_a \tag{8.3}$$

where $\bar{E}_a$ is the mean value of anelastic energy field and a and b are two constants. The straight line shows the least square method identification. Thus, equation 8.3 points the fact that the local anelastic energy field is very close to the sum of its mean value over the field and local heat losses energy variations. Let us denote Σ and E_p the macroscopic value of stress and plastic strain respectivelly. According to notations, equation 8.3 becomes:

$$E_a \approx \int_{t=0}^{T} \left(-ak\Delta^2 T + b\Sigma \cdot E_p\right) \cdot dt \tag{8.4}$$

Equation 8.4 reveals that the local numerical anelastic energy field could be approximated only from the knowledge of the thermal field $T(x, y)$ and the macroscopic value of stress Σ and plastic strain E_p. Keeping in mind that it doesn't exist any trivial ways to experimentally measure the local stress, and plastic strain flow, and consequently to access the local anelastic energy, equation 8.4 underlines a interesting point. Indeed Σ, E_p as well as $T(x, y)$ measurement is currently

managed. Figure 8.2 (b) presents the anelastic energy field estimated from equation 8.4 using $a = 1.13$ (see eq 8.3) and $b = \frac{6.54}{7.21} \approx 0.91$ (see eq 8.3 and figure 8.4 (d)). As announced, taking into account the macroscopic value of anelastic energy and the local variation of heat losses allows a good estimation of local trends of E_a as well as magnitudes.
The present linear relationship is probably due to the linear relation between stress and temperature as well as the linear trend to the local hardening. Nevertheless, under such conditions, i.e. material with a linear hardening, the crystal model shows it must be possible to roughly approach the anelastic energy field with the help of experimental surface thermal field and vice-versa.

- Isentropic energies ranges from 1.2 to 1.45 $mJ.mm^{-3}$ within the yield model and from 0.5 to 3.5 $mJ.mm^{-3}$ within the crystal one. It is hard to precisly compare both field. Nevertheless, one could notice one specific point where both are in disagreement. It concerns twins located within the black boxes. Regarding to its neighbours, the twin exhibit either more energy (yield model), or few isentropic energy (crystal model). Its behavior will be discusted further and compared to its effective one.

- One observes finally the partition of stored energy. E_{sh} ranges from 0 to 2.8 $mJ.mm^{-3}$ in yield model and from 0 to 5.5 $mJ.mm^{-3}$ in crystal one. In parallel, E_{sr} ranges from 0 to 3.5 $mJ.mm^{-3}$ and from 0 to 15 $mJ.mm^{-3}$ in yield and crystal model respectivelly.

E_{sr} provides informations about strain incompatibilities. As frequently pointed they are significant within the crystal model. One observes on both fields (see figures (f)) macro regions where this energy is close to zero, and many of them are similar with both models, notably within grain noted 1 in picture 8.4 (f). Indeed, it is interesting to notice in crystal model that, as expected, E_{sr} is localized at grain boundary or in vicinity to grain boundary within picture 8.4 (f). Then a milimetric grain such as 1 doesn't reveal any E_{sr} at intragranular domain but only at inter one. It shows that the crystal model represents well the physical meaning of E_{sr}, i.e. elastic energy stored at grain boundary, to accommodate incompatible plastic slips.

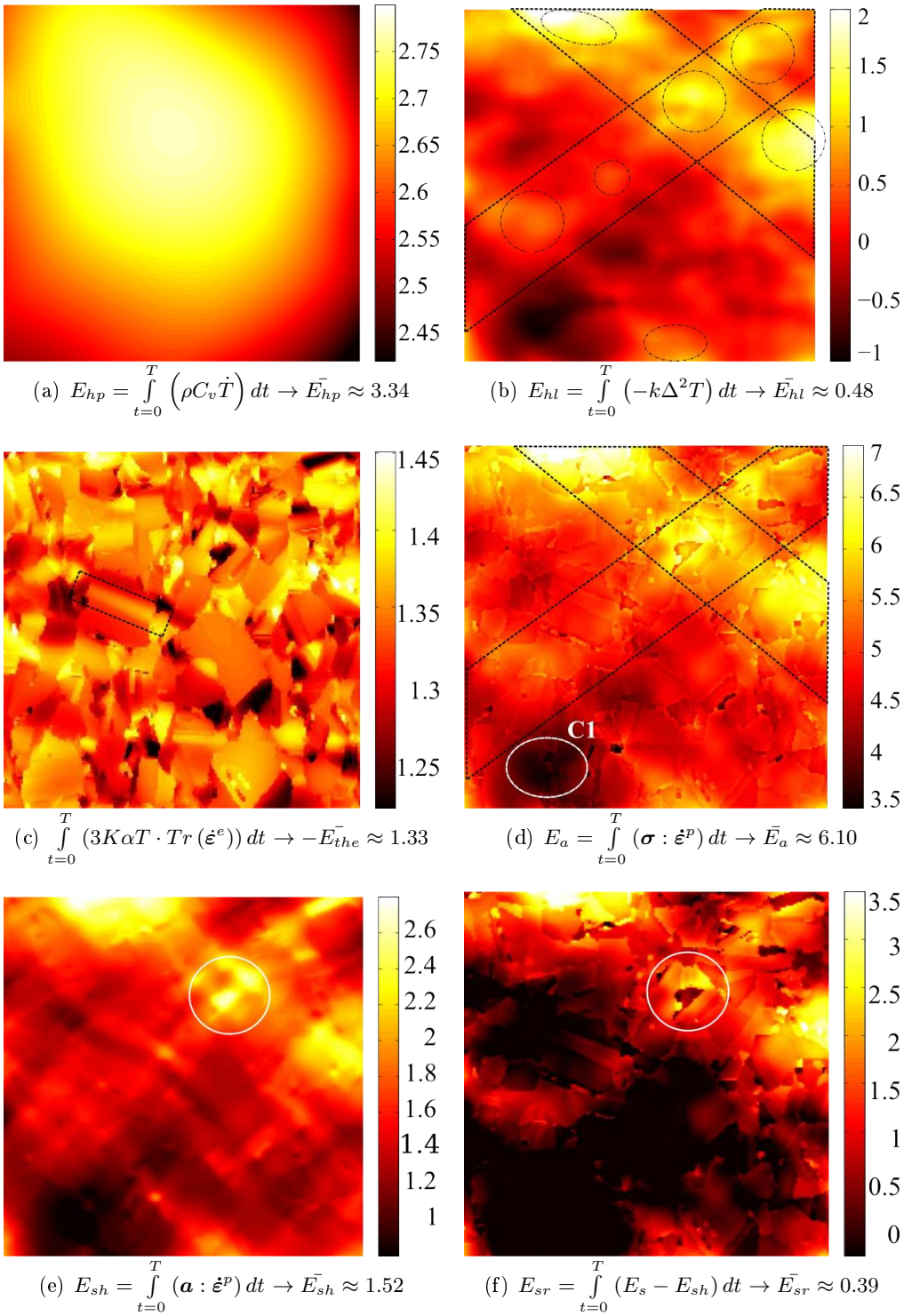

(a) $E_{hp} = \int_{t=0}^{T} \left(\rho C_v \dot{T}\right) dt \rightarrow \bar{E_{hp}} \approx 3.34$

(b) $E_{hl} = \int_{t=0}^{T} \left(-k\Delta^2 T\right) dt \rightarrow \bar{E_{hl}} \approx 0.48$

(c) $\int_{t=0}^{T} \left(3K\alpha T \cdot Tr\left(\dot{\boldsymbol{\varepsilon}}^e\right)\right) dt \rightarrow -\bar{E_{the}} \approx 1.33$

(d) $E_a = \int_{t=0}^{T} \left(\boldsymbol{\sigma} : \dot{\boldsymbol{\varepsilon}}^p\right) dt \rightarrow \bar{E_a} \approx 6.10$

(e) $E_{sh} = \int_{t=0}^{T} \left(\boldsymbol{a} : \dot{\boldsymbol{\varepsilon}}^p\right) dt \rightarrow \bar{E_{sh}} \approx 1.52$

(f) $E_{sr} = \int_{t=0}^{T} \left(E_s - E_{sh}\right) dt \rightarrow \bar{E_{sr}} \approx 0.39$

Figure 8.3: Yield model → Numerical components of uniaxial tensile test energy balance up to 2.5% of mean axial strain (in mW/mm^3): (a) Heat production term, (b) Heat losses term by conduction, (c) isentropic heat source associated to thermoelastic couplings, (d) anelastic strain energy, (e) stored energy in hardening and (f) in residual stresses

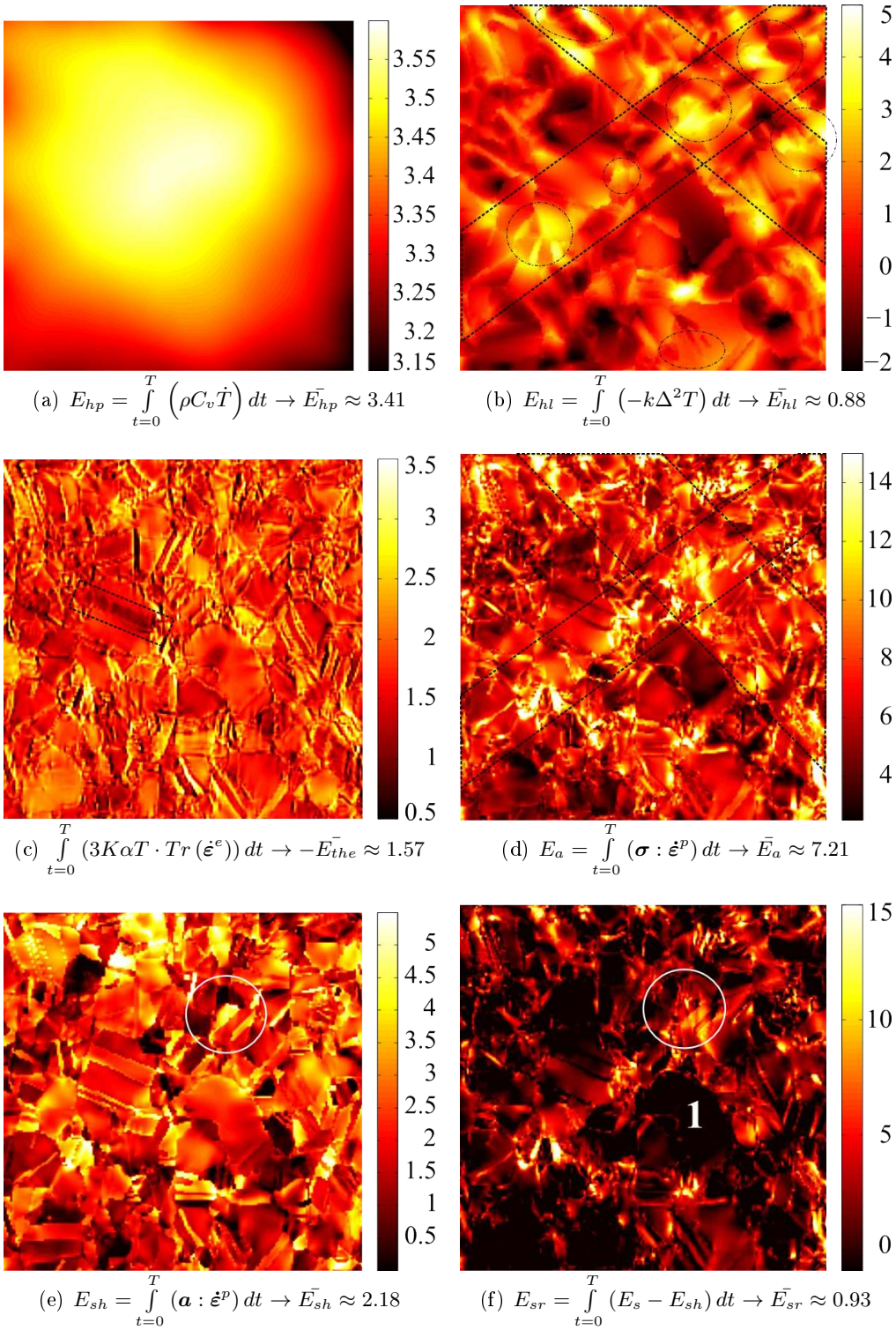

(a) $E_{hp} = \int_{t=0}^{T} \left(\rho C_v \dot{T}\right) dt \rightarrow \bar{E_{hp}} \approx 3.41$

(b) $E_{hl} = \int_{t=0}^{T} \left(-k\Delta^2 T\right) dt \rightarrow \bar{E_{hl}} \approx 0.88$

(c) $\int_{t=0}^{T} \left(3K\alpha T \cdot Tr\left(\dot{\boldsymbol{\varepsilon}}^e\right)\right) dt \rightarrow -\bar{E_{the}} \approx 1.57$

(d) $E_a = \int_{t=0}^{T} \left(\boldsymbol{\sigma} : \dot{\boldsymbol{\varepsilon}}^p\right) dt \rightarrow \bar{E_a} \approx 7.21$

(e) $E_{sh} = \int_{t=0}^{T} \left(\boldsymbol{a} : \dot{\boldsymbol{\varepsilon}}^p\right) dt \rightarrow \bar{E_{sh}} \approx 2.18$

(f) $E_{sr} = \int_{t=0}^{T} \left(E_s - E_{sh}\right) dt \rightarrow \bar{E_{sr}} \approx 0.93$

Figure 8.4: Crystal model → Numerical components of uniaxial tensile test energy balance up to 2.5% of mean axial strain (in mJ/mm^3): (a) Heat production term, (b) Heat losses term by conduction, (c) isentropic heat source associated to thermoelastic couplings, (d) anelastic energy, (e) stored energy in hardening and (f) in residual stresses

Notice within figure 8.4 (f) that the stored energy related to intergranular stresses, exhibits local levels 3 time more significant than stored energy related to intragranular stresses (see figure 8.4 (e)). This point was already visible within anelastic energy field (see figure 8.4 (d)). Nevertheless, as E_{sr} is very localized, the average over the whole field remain lower than the half part of stored energy related to intragranular stresses.

Then focusing on the yield model, one observes that E_{sh}, i.e. energy related to intragranular stresses or hardening, is very similar to E_a and/or E_{hl}. Thus it points a macro-localization while no variation occurs at intragranular domain. In parallel, within the crystal model, E_{sh} appears to ranges from 1 to 5 $mJ.mm^{-3}$ in most of grains and the localization pattern seen, for exemple, in figure 8.4 (f) almost vanish. Some strain localizations, already pointed on figures (b) (d) or (f), still appears but are less visible since every grain localize within a part of its intragranular domain a high and low level of stored energy.

Partial conlusions are:

- the stored energy related to internal stresses accumulated at grain boundaries to accomodate incompatible plastic slips is clearly an indicator of localization network at grain boundary. It must reflect grain interactions where, grain sizes, shapes, and misorientations leads to incompatibilities of behavior. Its value is clearly higher than the other part of stored energy. Nevertheless, studying its mean value [Oliferuk 2009] it appears to be the smallest part of storage since actually related to very localized regions, the grain boundary network.

- the stored energy related to intragranular hardening doesn't account for the structural localization. It is quite similar in every grains and range from 1 to 5 $mJ.mm^{-3}$. This point may be related to the kind of dislocation density used within the model. Indeed, one only uses here Statistically Stored Dislocations. It is a local point of vue of plasticity. Using Geometrically Necessary Dislocations, hardening would integrate an non-local point of vue. Thus intragranular and intergranular incompatibilities would occur and would lead to more significant hardening localizations [Schwartz 2011].

Let us now, focus on the apparantly more deformed region according to micrography of surface specimen. Figure 8.5 presents the micrography of surface of one of the most heated and strained region (see chapter 4.1). This region is the circled one on figures 8.4, 8.3 (e) and (f). Whatever the model, this set of grain localized the stored energy, especially the yield one, and this region seems to be the more deformed region on surface specimen. One could note that whatever the model, areas noted 1 and 7 on picture 8.5 store a lot of energy in form of hardening and few energy in form of intergranular residual stresses. In parallele, areas noted 2, 3, 4, 5 store in form of intergranular residual stresses and few in hardening. Concerning area 1 is high storage of energy at intragranular domain is in line with the slip-mark density since it is the more intense in picture 8.5 (a). In opposite, other grains localize

more at intergranular domain and no intense slip-mark are observed which is in partial agreement with model results.

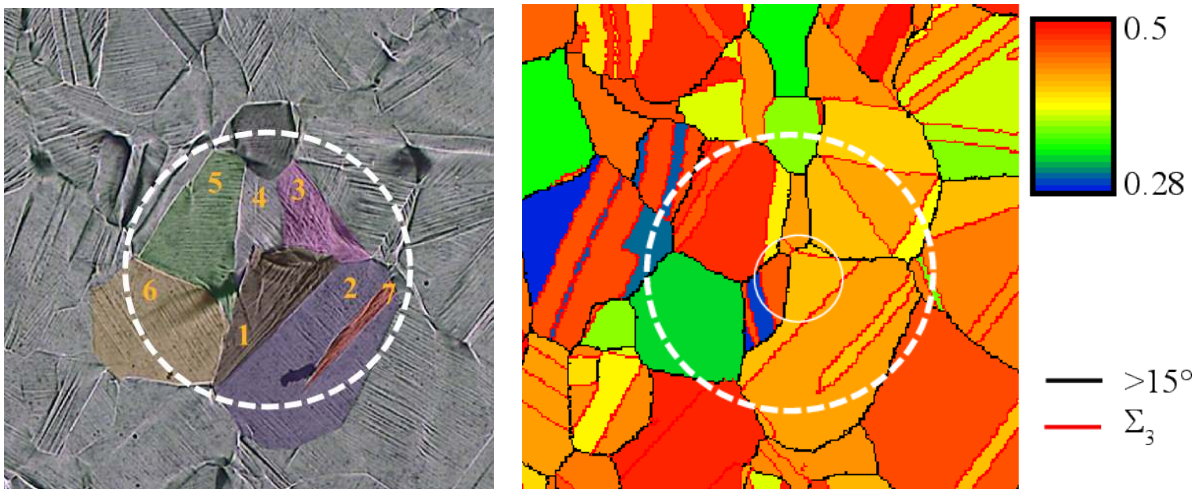

(a) (b)

Figure 8.5: (a) micrography of surface specimen surrounded the appearante more deformed region and (b) the associated maximal Schmid factor field and grain boundary properties

Let us detail the localization of deformation observed within this specific region has well as the entire macro-localization observed within the right upper part of specimen in figures 8.3 (d) and 8.4 (d). Firstly, maximum Schmid factor in figure 8.5 are not especially high, moreover a large range of maximum Schmid factor is observed from 0.28 to 0.5. Secondly, relative slip-mark density is not especially significant compared to other parts of the specimen surface (see chapter 1.1). Nevertheless, as models aslo present such experimental localization, key parameters are necessarily the surface grain orientation (or misorientation) and/or the surface grain shape. Indeed, both models underline that the stress flow is a second order parameter concerning this specific point. In this way, one could first point, as already observed within the whole model, that twin Σ_3 boundaries play an important role within the boundary deformation (see regions 1, 3, 7...8.5). In addition, grain size is here, as in the whole right upper part of specimen gauge-section, statistically lower than the rest of specimen. Indeed it has been shown within chapter 1.1 that the grain size is about $95\mu m$ above the second diagonal[2] of gauge-section compared to about $141\mu m$ below. Thus, the density of twin Σ_3 boundaries as well as every grain interaction are statistically more significant within the right upper part of specimen gauge-section. It could explain in part within figure 8.3 (d) for exemple, why the part above the second diagonal exhibits a significant level of anelastic energy compared to the part below. This point was already pointed within chapter 4.1 when it has been shown that experimental surface temperature was statistically lower within the left bottom part of specimen gauge-section. Previous points allow, in

[2]diagonal which pass from the bottom right corner to the left upper one

part, the understanding of macro-localization within this upper right part of specimen gauge-section but not specifically the significant localization within focused area in figure 8.5. One could recall that the second euler angle is very low within this region. This point has been underlined within chapter 1.1. It underlines a specificity of this set of grain nevertheless, no convincing explanation has been found.

Figure 8.6 present finally, the ratio between hardening stored energy and expended anelastic energy noted β^*_{sh}. Figure 8.6 (a) presents result of the yield model and (b) the crystal one. Let us first deals with the yield model. β^*_{sh} varies between 20 and 40 % and the maximum is obtained within the region previously analysed in figure 8.5 (see area noted 1).

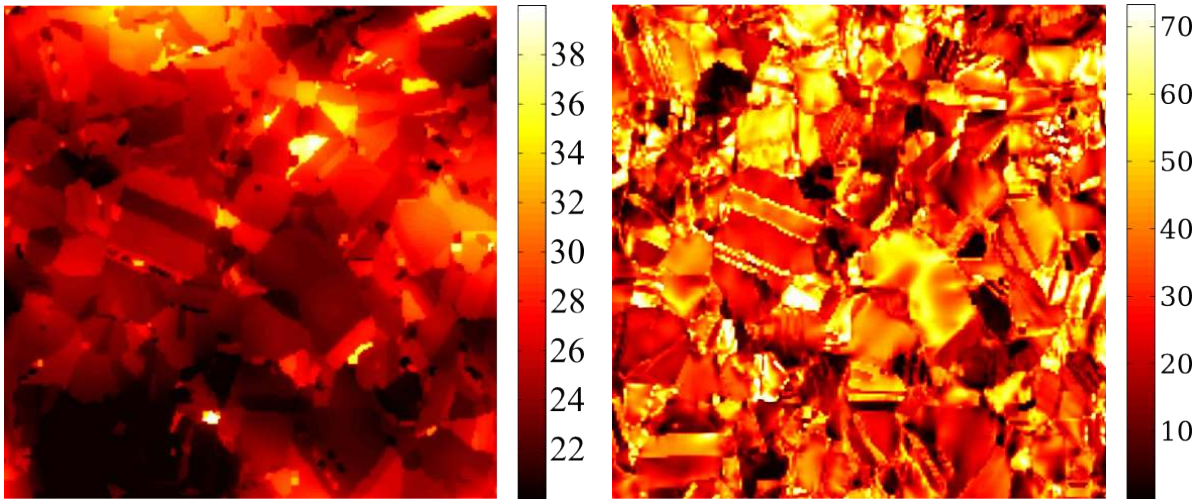

(a) $\beta^*_{sh} = \frac{E_{sh}}{E_a}$ in % (b) $\beta^*_{sh} = \frac{E_{sh}}{E_a}$ in %

Figure 8.6: Crystalline model → Numerical stored energies and β^* ratio up to 2.5% of mean axial strain (in mJ/mm^3): (a) E_{sr}, (b) E_{sh}, (c) β^*_{sh}

Analysed region is also presented in figure 8.7 and a focus is performed on specific regions. According to this map, β^*_{sh} is maximum within region noted R_1. As previsouly announced this region is the region which presents the more important constrast at grain boundary, i.e. significant strain localization. Regions noted R_2, R_3, O_1, O_2, O_3 and O_4 also have a high level of stored energy according to figure 8.6 (a). This comparison between micrography of surface specimen and simulated stored energy allows to put in light that every region where β^*_{sh} is significant correspond to physical region where high strain localization are visible and some grain raveling seems to appear, notably within 0_1, 0_3 and R_3. In parallele, one observes that the ratio is the smallest within region noted C_1. Picture 8.7 evidences the fact that few and not intense slip-marks are present within this region which is totally in line within the β^*_{sh} ratio. This point has already been quantitatively verified by the slip-mark density factor (see chapter 1.1), and the maximal Schmid factor map (see chapter 1.1). The last one has

allowed to underline that the maximal Schmid factor is the lowest within this region and its value is 0.28. Nevertheless a systematic relation between the maximal Schmid factor and β^*_{sh} ratio hasn't been found.

In spite of the fact that the yield model has not been identified as being capable to represent the whole dynamic of observed experimental heterogeneities, the β^*_{sh} ratio reveals that it is able to provide a clear information about the stored energy localization, and its localization is totally in line with micrography of surface specimen. Nevertheless, this field is totally different from the β^*_{sh} ratio observed for the crystal model in figure 8.6 (b). The following presents a field without any clear localization. It could means that evenif the yield model exhibits interesting and clear results the physical aspect of β^*_{sh} ratio field may be not so simple.

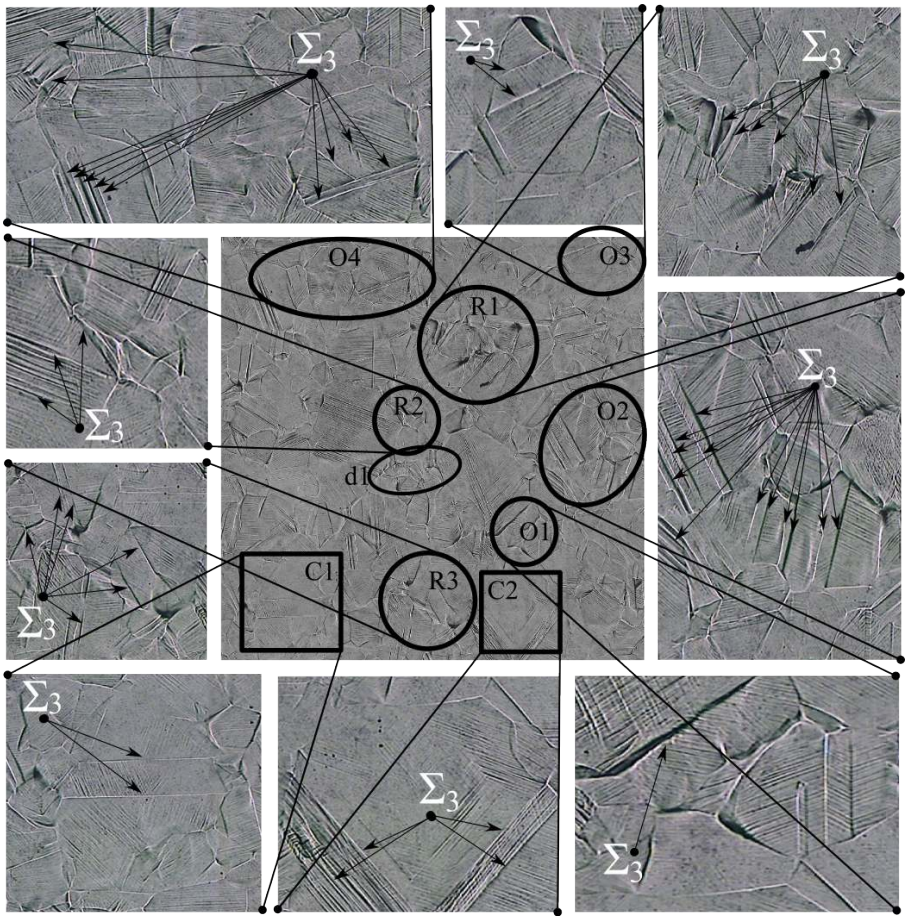

Figure 8.7: Micrography of surface specimen performe after test.

Within figure 8.6 (b) the β^*_{sh} ratio ranges from 0 to more than 70%. The most important localization is located within region noted d_1 on picture 8.7. This region is also marked by important strain localization. Then regions O_2 and O_4 presents also a significant β^*_{sh} ratio. This is notably in agreement

with very intense out-of-plane displacement at Σ_3 boundaries (marked).
According to figure 8.6 (b) and 8.7 Σ_3 boundaries localize a high storage of energy. This point is verified in every regions, notably if one looks at region C_1 and the behavior of the twin surrounded by twin Σ_3 boundaries . It stores about 50% of expendend anelastic energy whereas its neighbours store only $\approx 15\%$. This was not obtain with the yield model. The same observation is done for exemple for well marked twin for which the bottom part is visible in region R_2. This twin was already introduced within figure 8.4 and 8.3 (c). One could note that this twin stores up to 65% of expended anelastic energy, notably at its Σ_3 boundaries whereas neighbours only store about 25%. Slip-mark density is totally in aggreement with this localization of storage since this twin has one of most significant slip-mark density (see Chapter 1.1). Notice both models are not in aggreement concerning this twin. According, for exemple, to thermoelastic coupling in figure 8.3 and 8.4 (c) or β^*_{sh} ratio on figure 8.6 (a) and (b), the yield model predicts within it, a predominance of elasticity (high stresses) and consequently few stored energy whereas the crystalline predict the reverse. The micrography (slip-mark density) of surface specimen evidences that the crystalline model is the more realistic. In addition, according to its intragranular β^*_{sh} ratio its appears clearly that its behavior is mainly leaded by high localization at grain boundaries.

• Focusing on experimental Σ_3 boundaries and their specific mechanical response, i.e. intense out-of-plane displacements, and the aggreement between numerical stored energy, plastic strain ...and Σ_3 localization one could conclude that the crystal model is relevant and more realistic than the other one. One of the reason is the incapability of yield model to make the difference between every type of boundaries. This point has already been pointed and explained in chapter 7.1. It is moreover in aggreement with previous observations, i.e. the crystal model represents a little bit better the experimental planar displacement but also the out-of-plane one (see figures 7.3).
• One could finally note an interesting point. One could imagine that such out-of-plane displacement at grain boundary Σ_3, i.e. grain boundary shear along the out-of-plane direction may be more dissipative than storing mechanism. Nevertheless one have seen experimentally and numerically, that the region O_2 for exemple, was not especially hotter than the rest of specimen during the loading and the β^*_{sh} (numerical) and β^* (experimental) ratio is clearly important within this region (up to 75%). It appears consequently that this kind of interaction stores more than dissipates which was, in our knowledge, not so obvious before such numerical and experimental thermomechanical investigation.

To confirm previous observations, one focus finally on the biggest grain of the microstructure and on an other "big" grain composed by some twins. These grains have already been studied within chapter 4.1. Figure 8.8 presents the comparison between experimental profilometry, slip-mark orientations (slip-systems), relative slip-mark density and the numerical estimation of β^*_{sh} ratio as well as the

micrography of surface underlining grain boundary interactions. Figure 8.8 (c) predicts that the β^*_{sh} is significant mainly within the D_1 slip system region.

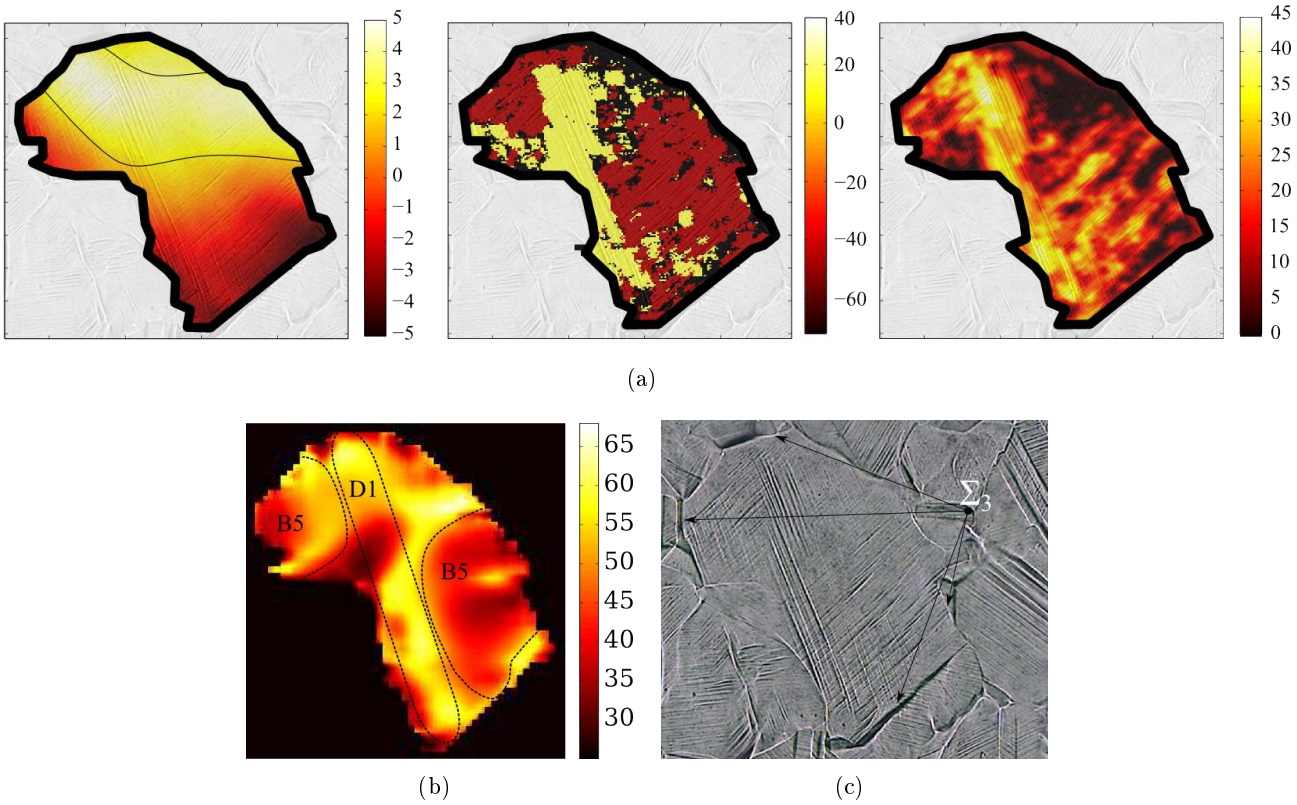

Figure 8.8: (a) Experimental intra-granular profilometry (left side in μm) slip-mark orientations (center in degree) and slip-mark density (right side in %) within grain n^{o}1056, (b) numerical β^*_{sh} ratio and (c) micrography

It is in aggreement with intragranular relative slip-mark density (see (a) right) which exhibits intense slip marks notably at the bottom and top of the D_1 slip-system. In opposite B_5 system store $\approx 20\%$ less. This point is especially clear within the right B_5 domain and it is in aggreement with a lower slip-mark density.
If one recalls results previously discusted within chapter 4.1, one has seen experimentally that the B_5 slip system was activated first, with an important shear on the top part of the grain from ≈ 100 to ≈ 200 MPa in term of nominal stress, i.e. microplasticity, and then the D_1 was activated from 200 MPa to the end of the test (macroplasticity), leading notably to important strain incompatibilities on D_1 region extremities. It is interesting to observe that the numerical β^*_{sh} ratio, at the end of the test, is a clear indicator of this experimental loading path, on one hand because of the slight storage activity within the left top B_5 region, which is in line with a storage at very low strain level, and on the other hand because of a significant storage activity within D_1 domain which is in line with the experimental

persistent plastic activity from 0.2 to 2.5% of plastic strain. Thus, in this grain, the model is able to represent the observed experimental intragranular loading path in term of system, localizations... In addition the ratio of stored energy at intragranular domain on the total anelastic energy seems to be a preferential witness of it.

Figure 8.9 presents finally, the numerical β^*_{sh} ratio, the experimental profilometry and the micrography of surface of a twinned grain. One clearly observes the previously announced interaction between Σ_3 boundaries, within the horizontal twin, the intragranular plasticity, the out-of-plane displacement and the energy storage. Indeed, this twin clearly exhibits a gap of displacement of $\approx 3\mu m$ from neighbours, slip-marks are specifically intense within it, on its left part, and the numerical β^*_{sh} ratio represents the same singular behavior compared with both neighbours. The twins store about 45% of expended anelastic energy whereas neighbours few than 15%. One can understand consequently the local relevance of the crystal plasticity model and the ability to β^*_{sh} ratio to be an indicator of loading path as well as its interaction with some mechanism of deformation notably with Σ_3 boundaries shear, at least within this heat traeated A316L specimen.

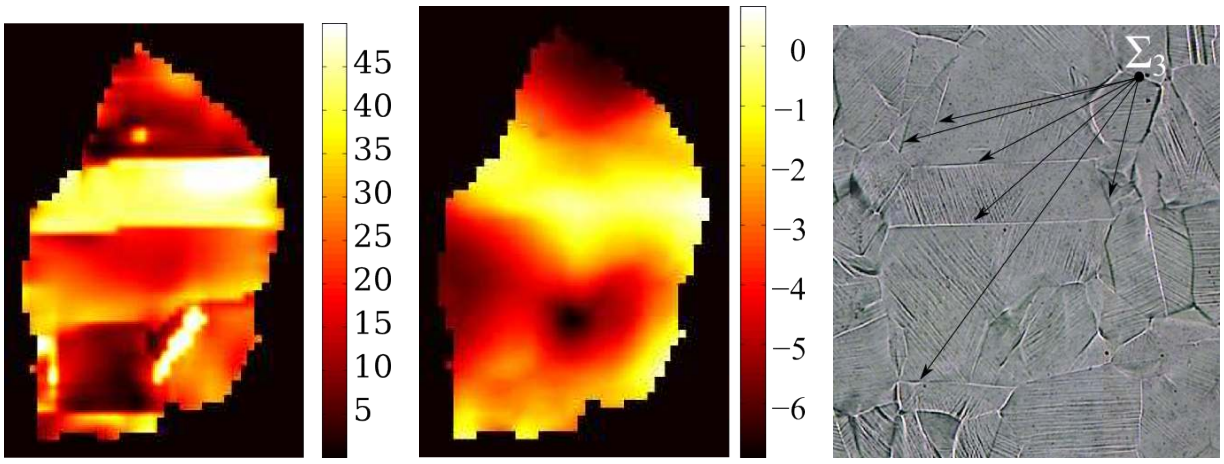

(a) (b) (c)

Figure 8.9: (a) numerical β^*_{sh} ratio (%), experimental prolifometry in μm, and micrography

8.3 Conclusion

A local approach of energy quantities has been done numerically for both yield and crystal models. Energy fields, i.e. the time integral over the whole tensile test of specimen-gauge section powers have been discussed. It has been notice that the heat losses by conduction, i.e. $E_{hl} = \int_{t=0}^{T} \left(-k\Delta^2 T\right) dt$, is a good indicator of persistent plastic and dissipative activities. It clearly reflects the anelastic energy and a linear relationship has been evidenced between both quantities. Then it has been shown that the local anelastic field could be estimated from the knowledge of surface specimen temperature and macroscopic stress Σ and plastic strain E_p. This relationship is here due to the model but may be also expected within material with linear hardening. Then the local partition of stored energy has been discussed. It reveals, especially within the crystal model that the energy stored within residual stresses is localized in the vicinity of grain boundaries and that is a great indicator a region which localized strains. It is an indicator of first order localization, i.e. the one at grain boundary due to compatible or uncompatible relationship between grain orientation. Values are locally up to 5 times the mean stored energy. Then the energy stored within hardening reflects second order localization, i.e. intragranular localization of strain. Nevertheless high and low levels are here distributed in every grain and are closed to the mean value, thus no macroscopic localization is still visible. Coupling numerical field and observations has allowed to evidence that only the crystal model is able to represents plasticity mechanisms and associated storaged energy field evenif stored energy field coming from yield model seemed originally relevant. Finally, β^*_{sh} has been studied. It ranges from 0 to more than 70% within the polycrystalline aggregate. At the scale of the aggregate, it has been shown that the deformation mechanisms at twin Σ_3 boundaries localized maximal values of β^*_{sh} ratio that is in line with very intense deformations observed at Σ_3 boundaries on experimental micrography of surface specimen. At intragranular domain, it has been shown in the biggest grain that the β^*_{sh} ratio is a well witness of deformation path contrary to any other scalar quantity.

General Conclusion

This work focussed on the thermomechanical couplings accompagning micromechanisms of deformation in a A316L austenitic stainless steel polycrystal submitted to a monotonic tensile test up to 2.5% of strain. Two main objectives were the obtaining of physical in-situ fields from raw experimental measurements and the achievement of in-situ energy balances at the mesoscale of the polycrystal aggregate. In this way, a multi-techniques and multi-fields approach has been developped.

Five experimental techniques have been required. Firstly, this study is based on the in-situ raw data captured within the work of Bodelot [Bodelot 2008]. It consists in Gray Level frames registered by a CCD and an IR camera during the monotonic tensile test as well as optical micrography of the surface specimen performed after the test. Then, Orientation Imaging Microscopy technique as well as surface profilometry, both performed after test, have been conducted. To couple, calibrate, and validate these measurements, different tools have been implemented:

1. an automatic procedure for activated plastic slip-system identification on surface micrography,
2. a flux based IR calibration procedure allowing to obtain accurate thermal fields by means of the identification of an apparent emissivity field.
3. a projection method allowing to observe the experimental fields through the natural microstructure of the material,
4. the extension of Finite Element Crystalline Plasticity method to coupled thermomechanical problems including kinematic and thermal experimental boundary conditions.

These different tools allowed us to obtain fully coupled and complementary multi-field data, i.e. expressed in the same initial configuration, at the same instant and interpolated on the same spatio-temporal grid associated to the microstructure. It allows a perfect dialog between experimental in-situ displacements, strains, temperatures, energies, crystallography and activated slip-systems fields but also with numerical fields especially stress, plastic strain and stored energy fields.

Some important assumptions have been done. The first one is the choice of a full biparabolic basis per grain for experimental fields projection, in particular displacements and temperature. It allows to analyse bilinear strain fields per grain as well as the estimation of constant thermal laplacian per grain which corresponds to the assumption of uniform heat losses at grain boundaries. The second one is the choice of the constitutive laws. Two models have been implemented: the first one assumes a bilinear elasto-plastic constitutive law including a linear thermo-elastic strong coupling and a linear kinematic hardening. This model conserves an homogenized plasticity framework. The second one assumes the crystal elasto-plasticity framework based on experimental lattice orientations, a non-linear isotropic and viscoplastic hardening based on dislocation densities, and a linear thermoelastic weak coupling.

Finally, both models include columnar grains since only the surface microstructure is known.

Under such assumptions and taking benefit of the entire range of experimental and numerical fields, different major aspects have been underlined.

1. ***At the field and bulk scale***.

   (a) Previous works, notably [Lee 1991], concerning the ability of the thermal measurement to provide an accurate estimation of the macroscopic yield stress have been confirmed and have been deeper investigated. It results that two dissipation threshold could be introduced. The first one corresponds to the instant when the specimen temperature reaches its minimum. It is related to an off-set of plasticity lower than $3x10^{-4}$. The second corresponds to the instant when the temperature deviates from a linear relationship with the nominal stress. The corresponding off-set of plasticity has not been accuratly estimated but it is significatively lower than 10^{-4}.

   (b) The temperature is heterogeneous from the beginning of the test and localizes differently depending on the loading level. Within the macroscopic elastic domain, the thermal field and its localization are clearly connected to the localization of significant contractions within the aggregate. Then during the macroscopic hardening process, thermal localization are connected to the localization of intense tensile stresses, especially at grain boundaries, in a regions where strong kinematic incompatibilities have been observed. This point has been confirmed by experimental and numerical measurements.

   (c) The experimental stored energy levels as well as its partition into two parts related to hardening and internal stress respectivally, are in aggreement with the literature. Moreover, regarding results from [Oliferuk 2009], a connection between the storage mechanism (hardening or internal stresses) and the grain size has been shown. Large grain seems to store more in intragranular hardening than at intergranular domain, at least in the range of the studied strains.

   (d) The classically assumes linear relation between the stored energy and the square of flow stress has been observed from a certain level of nominal stress. The slope of the linear dependence and its concordance with its theoritical expression proves the predominance of dislocations in the storage process.

   (e) The ratio of stored energy on plastic expended one, called here β^* ratio, increases from 0 to $\approx$30%. It is consequently lower than the one measured in smaller grain structures. Then it has been shown that its increase is partly triggered by the progressive homogenization of the strain field which tends to reduce its fraction of low-strained and dissipative grains.

   (f) Finally, it has numerically been observed that the plastic deformation energy field could be estimated from an off-set and a variation around it. The off-set corresponds to the macroscopic plastic deformation energy, based on the nominal stress and the mean plastic strain while the spatial variation corresponds to the heat losses energy provided by the help of the thermal laplacian.

2. ***At intragranular scale.***

   (a) It has been shown that the experimental intragranular strain fields, especially the shear strain, allows to follow the successive activation of plastic slips. Correlated to the crystal lattice orientation this information allows the estimation of the CRSS of each system.

   (b) The concept of dissipation threshold introduced at a macroscopic scale is also relevant at intragranular scale, at least in early dissipative grains. It has been shown that the early dissipative intragranular region could by detected by means of the time variation of temperature. This point has been confirmed by means of complementary analysis such as shear strain gradient, Schmid theory and crystal lattice orientation.

   (c) It has also been observed that the propagation of the thermal wave front is clearly connected to: the grain boundary in first rate and the intragranular slip-system domain, the surface topography in second rate.

   (d) Finally, it has numerically been observed that the β^*_{sh} ratio[3] is a very interesting indicator of the intragranular loading path compared to any other observed quantities.

The last important result is the validation of a great part of experimental observations in terms of deformation, temperature, localizations by means of the numerical models. This point validates the accuracy of experimental measurements performed by Bodelot [Bodelot 2008] and the relevance of the proposed calibration and projection method as well as the associated assumptions. It finally proves the interest of a local analysis of the temperature and its relevance regarding to the plasticity mechanisms. One could points in addition, that the crystal model[4] has shown that surface grains and their intragranular mechanisms of plastic slip manage in great part the observed fields, since the model does not take into account any sub-surface grain structure, Geometrically Necessary Dislocations, grain boundary behavior ...

From this work different prospects are considered:

1. ***At short- and mid-term.***

   (a) The observations done on a complex polycrystal, in particular the local detection of dissipation threshold and the validation of the Kapitza effect at grain boundary (probably function of the misorientation, the strain level, the grain size) have to be confirmed by complementary tests performed on oligocrystals.

   (b) Some test until fracture are required to follow the strain localization and the energy evolution up to a macroscopic localization and a crack initiation. It would allow to put in light the predominant variables for localization and crack initiation prediction, especially to propose new energy based criteria.

[3] ratio of stored energy related to hardening process on expended energy
[4] based on single crystal theory

(c) The constitutive law, particularly the hardening one, should be improved adding in a first step a kinematic hardening to be able to deals with cyclic loadings which is the ultimate goal.

2. ***At long-term.***

(a) The introduction of a non-local plasticity in order to take into account the intragranular heterogeneity and the influence of grain boundaries. Different ways seem possible as the classical strain gradient plasticity framework, Cosserat media ...

(b) An essential point concerns the modelling of the grain boundaries thermal and mechanical discontinuities which require a particular treatment. A connected question concerns the heterogeneities and the discontinuities of the thermophysics properties.

(c) Some complementary investigation techniques seem to be interesting. The stereocorrelation completed with the framework proposed in appendix D should allow to access to the complete surface 3D strain and stress tensors. An alternative way is the Micro Beam Laue Diffraction. In addition, the different microscopic EBSD based ways presented into the introduction could give local value of stored energy which will be of great interest if compared with the stored energy full field measurements presented in this work.

(d) Finally, it would be interesting to apply the whole framework developed during this thesis to fatigue loadings. In particular, we are interested in the application of such a local approach of thermomechanical couplings to the well known "self heating" test. The main interest is to study the shakedown concept at a microstructural scale as a change in dissipative process. This is a challenging topic.

Bibliography

[Abrivard 2009] G. Abrivard. *A coupled crystal plasticity - phase field formulation to describe microstructural evolution in polycrystalline aggregates during recrystallisation.* PhD thesis, Ecole Nationale Supérieure des Mines de Paris - Mines ParisTech, France, 2009. (Cited on pages 12 and 13.)

[Achenbach 1968] J.D. Achenbach. *The influence of heat conduction on propagating stress jumps.* Journal of the Mechanics and Physics of Solids, vol. 16, no. 4, pages 273–282, 1968. (Cited on page 40.)

[Ait-Amokhtar 2008] H. Ait-Amokhtar, C. Fressengeas and S. Boudrahem. *The dynamics of Portevin-Le Châtelier bands in an 3.2%Mg alloy from infrared thermography.* Materials Science and Engineering: A, vol. 488, no. 1-2, pages 540–546, 2008. (Cited on pages 10, 13 and 27.)

[Akrivoglaz 1969] M.A. Akrivoglaz. Theory of x-ray and thermal-neutron scattering by real crystals. Plenum Press, N. Y., 1969. (Cited on page 19.)

[Allais 1994] L. Allais, M. Bornert, T. Bretheau and D. Caldemaison. *Experimental characterization of the local strain field in a heterogeneous elastoplastic material.* Acta Metallurgica et Materialia, vol. 42, no. 11, pages 3865–3880, 1994. (Cited on page 101.)

[Aravas 1990] N. Aravas, K.S. Kim and F.A. Leckie. *On the Calculations of the Stored Energy of Cold Work.* Journal of Engineering Materials and Technology, vol. 112, no. 4, pages 465–470, 1990. (Cited on pages 161 and 204.)

[Asaro 1977] R.J. Asaro and J.R. Rice. *Strain localization in ductile single crystals.* Journal of the Mechanics and Physics of Solids, vol. 25, no. 5, pages 309–338, 1977. (Cited on page 330.)

[Asaro 1983] R.J. Asaro. *Micromechanics of Crystals and Polycrystals.* vol. 23, pages 1–115, 1983. (Cited on page 196.)

[Asaro 1985] R.J. Asaro and A. Needleman. *Overview no. 42 Texture development and strain hardening in rate dependent polycrystals.* Acta Metallurgica, vol. 33, no. 6, pages 923–953, 1985. (Cited on page 196.)

[Ashby 1970] M.F. Ashby. *The deformation of plastically non-homogeneous materials.* Philosophical Magazine, vol. 21, no. 170, pages 399–424, 1970. (Cited on pages 26 and 217.)

[Atkinson 1988] H.V. Atkinson. *Overview no. 65: Theories of normal grain growth in pure single phase systems.* Acta Metallurgica, vol. 36, no. 3, pages 469–491, 1988. (Cited on page 28.)

[Auld 1973] B.A. Auld. Acoustic Fields and Waves in Solids, volume 2. Wiley-Interscience, New York, 1973. (Cited on page 333.)

[Badulescu 2011] C. Badulescu, M. Grédiac, H. Haddadi, J.D. Mathias, X. Balandraud and H.S. Tran. *Applying the grid method and infrared thermography to investigate plastic deformation in aluminium multicrystal.* Mechanics of Materials, vol. 43, no. 1, pages 36–53, 2011. (Cited on pages 33, 34, 73, 74, 196 and 293.)

[Bailey 1960] J.E. Bailey and P. B. Hirsch. *The dislocation distribution, flow stress, and stored energy in cold-worked polycrystalline silver.* Philosophical Magazine, vol. 5, no. 53, pages 485–497, 1960. (Cited on pages 16, 168, 169 and 293.)

[Barbe 2001] F. Barbe, L. Decker, D. Jeulin and G. Cailletaud. *Intergranular and intragranular behavior of polycrystalline aggregates. Part 1: F.E. model.* International Journal of Plasticity, vol. 17, no. 4, pages 513–536, 2001. (Cited on pages 199 and 201.)

[Barrett 1948] C.S. Barrett. Structure of Metals. McGraw-Hill Book Company, Inc., New York,, 1948. (Cited on pages 12 and 69.)

[Bendada 2004] A. Bendada and M. Lamontagne. *A new infrared pyrometer for polymer temperature measurement during extrusion moulding.* Infrared Physics & Technology, vol. 46, no. 1-2, pages 11–15, 2004. Workshop on Advanced Infrared Technology and Application. (Cited on page 94.)

[Benzerga 2005] A.A. Benzerga, Y. Bréchet, A. Needleman and E. Van der Giessen. *The stored energy of cold work: Predictions from discrete dislocation plasticity.* Acta Materialia, vol. 53, no. 18, pages 4765–4779, 2005. (Cited on page 16.)

[Bergonnier 2005] S. Bergonnier, F. Hild, J.B. Rieunier and S. Roux. *Strain heterogeneities and local anisotropy in crimped glass wool.* Journal of Materials Science, vol. 40, no. 22, pages 5949–5954, 2005. (Cited on pages 58 and 61.)

[Berthel 2007a] B. Berthel. *Mesure thermographiques de champs de dissipation accompagnant la fatigue à grand nombre de cycles des aciers.* PhD thesis, Université Montpellier II - Sciences et Techniques du Languedoc, France, 2007. (Cited on pages 77, 78, 79, 102 and 293.)

[Berthel 2007b] B. Berthel, B. Wattrisse, A. Chrysochoos and A. Galtier. *Thermographic Analysis of Fatigue Dissipation Properties of Steel Sheets.* Strain, vol. 43, no. 3, pages 273–279, 2007. (Cited on pages 16, 22 and 23.)

[Berthel 2008] B. Berthel, A. Chrysochoos, B. Wattrisse and A. Galtier. *Infrared Image Processing for the Calorimetric Analysis of Fatigue Phenomena.* Experimental Mechanics, vol. 48, pages 79–90, 2008. (Cited on pages 9, 14, 22 and 23.)

[Besson 2003] U. Besson. *The distinction between heat and work: an approach based on a classical mechanical model.* European Journal of Physics, vol. 24, no. 3, page 245, 2003. (Cited on page 303.)

[Bever 1973] M.B. Bever, D.L. Holt and A.L. Titichener. *The stored Energy of Cold Work.* Pergamonn, 1973. (Cited on pages 13, 14, 16, 19, 20, 22, 26, 28, 163, 165, 168, 169 and 293.)

[Boas 1948] W. Boas and M.E. Hargreaves. *On the Inhomogeneity of Plastic Deformation in the Crystals of an Aggregate.* Proc. Roy. Soc. A, vol. 193, no. 1032, pages 89–97, 1948. (Cited on page 12.)

[Bodelot 2008] L. Bodelot. *Etude couplées des champs cinématiques et thermiques à l'échelle de la microstructure des matériaux métalliques.* PhD thesis, 2008. (Cited on pages 10, 29, 36, 39, 41, 78, 81, 84, 87, 89, 96, 163, 166, 168, 267, 269, 291, 293, 294 and 325.)

[Bodelot 2009] L. Bodelot, L. Sabatier, E. Charkaluk and P. Dufrénoy. *Experimental setup for fully coupled kinematic and thermal measurements at the microstructure scale of an AISI 316L steel.* Materials Science and Engineering: A, vol. 501, no. 1-2, pages 52–60, 2009. (Cited on pages 10, 29, 40, 73, 75, 76, 77, 85, 86, 94, 125, 143 and 291.)

[Bodelot 2011] L. Bodelot, E. Charkaluk, L. Sabatier and P. Dufrénoy. *Experimental study of heterogeneities in strain and temperature fields at the microstructural level of polycrystalline metals through fully-coupled full-field measurements by Digital Image Correlation and Infrared Thermography.* Mechanics of Materials, vol. 43, no. 11, pages 654–670, 2011. (Cited on pages 29, 30, 73, 85, 92, 170, 172 and 291.)

[Bornert 2009] M. Bornert, F. Brémand, P. Doumalin, J.C. Dupré, M. Fazzini, M. Grédiac, F. Hild, S. Mistou, J. Molimard, J.J. Orteu, L. Surrel, Y. Robert, P. Vacher and B. Wattrisse. *Assessment of digital image correlation measurement errors: methodology and results.* Experimental Mechanics, vol. 49, 2009. (Cited on page 87.)

[Boulanger 2004a] T. Boulanger. *Calorimetric analysis of dissipative and thermoelastic effects associated with the fatigue behavior of steels.* International Journal of Fatigue, vol. 26, no. 3, pages 221–229, 2004. (Cited on pages 14, 163 and 303.)

[Boulanger 2004b] T. Boulanger, A. Chrysochoos, C. Mabru and A. Galtier. *Calorimetric analysis of dissipative and thermoelastic effects associated with the fatigue behavior of steels.* Int. J. Fat., vol. 26, pages 221–229, 2004. (Cited on page 9.)

[Bridier 2005] F. Bridier, P. Villechaise and J. Mendez. *Analysis of the different slip systems activated by tension in a $\alpha\beta$ titanium alloy in relation with local crystallographic orientation.* Acta Materialia, vol. 53, no. 3, pages 555–567, 2005. (Cited on page 57.)

[Brillaud 2002] J. Brillaud and F. Lagattu. *Limits and possibilities of laser speckle and white light image correlation methods: theory and experiments.* Appl Opt, vol. 41, 2002. (Cited on page 87.)

[Bunge 1982] H.J. Bunge. Texture analysis in materials science: Mathematical methods. Butterworths (London and Boston), english ed édition, 1982. (Cited on page 45.)

[Busso 2005] E.P. Busso and G. Cailletaud. *On the selection of active slip systems in crystal plasticity.* International Journal of Plasticity, vol. 21, no. 11, pages 2212–2231, 2005. Plasticity of Heterogeneous Materials. (Cited on page 197.)

[Butler 1989] J.F. Butler and H. Hu. *Channel die compression of aluminum single crystals.* Materials Science and Engineering: A, vol. 114, pages L29–L33, 1989. (Cited on page 12.)

[Cailletaud 1991] G. Cailletaud, V. Doquet and A. Pineau. *Cyclic Multiaxial Behaviour of an Austenitic Stainless Steel: Microstructural Observations and Micromechanical Modelling.* In Fatigue Under Biaxial and Multiaxial Loading, volume 12, 1991. (Cited on page 216.)

[Cailletaud 1992] G. Cailletaud. *A micromechanical approach to inelastic behaviour of metals.* International Journal of Plasticity, vol. 8, no. 1, pages 55–73, 1992. (Cited on page 197.)

[Cailletaud 2003] G. Cailletaud, S. Forest, D. Jeulin, F. Feyel, I. Galliet, V. Mounoury and S. Quilici. *Some elements of microstructural mechanics.* Computational Materials Science, vol. 27, no. 3, pages 351–374, 2003. (Cited on page 199.)

[Chang 1981] Y.W. Chang and R.J. Asaro. *An experimental study of shear localization in aluminum-copper single crystals.* Acta Metallurgica, vol. 29, no. 1, pages 241–257, 1981. (Cited on page 13.)

[Chang 2007] H.J. Chang, H.N. Han and M. Fivel. *Multiscale Modelling of Nanoindentation.* Key Engineering Materials, vol. 345-346, pages 925–930, 2007. (Cited on pages 195 and 220.)

[Charkaluk 2006] E. Charkaluk and A. Constantinescu. *Estimation of the mesoscopic thermoplastic dissipation in High-Cycle Fatigue.* Comptes Rendus Mécanique, vol. 334, no. 6, pages 373–379, 2006. (Cited on page 326.)

[Choi 2004] S.H. Choi and Y.S. Jin. *Evaluation of stored energy in cold-rolled steels from EBSD data.* Materials Science and Engineering: A, vol. 371, no. 1-2, pages 149–159, 2004. (Cited on pages 16, 17, 18, 19 and 293.)

[Chrysochoos 1985] A. Chrysochoos and O. Maisonneuve. *Bilan énergétique en élastoplasticité grandes déformations: Energy balance for elastic plastic deformations at finite strain.* Comptes rendus de l'Académie des sciences, vol. 300, no. 20, pages 985–990, 1985. (Cited on pages 13, 22 and 23.)

[Chrysochoos 1989a] A. Chrysochoos. *Analyse thermomécanique des lois de comportement par thermographie infrarouge.* Revue Phys. Appl., pages 215–225., 1989. (Cited on pages 16 and 293.)

[Chrysochoos 1989b] A. Chrysochoos, O. Maisonneuve, G. Martin, H. Caumon and J.C. Chezeaux. *Plastic and dissipated work and stored energy.* Nuclear Engineering and Design, vol. 114, no. 3, pages 323–333, 1989. (Cited on pages 27, 40, 74, 165 and 303.)

[Chrysochoos 2009] A. Chrysochoos, B. Wattrisse, J.M. Muracciole and Y. El Kaim. *Field of stored energy associated with localized necking of steel.* J. Mech. Mater. Struct., vol. 4, no. 6, pages 245–262, 2009. (Cited on page 13.)

[Clarebrough 1955] L.M. Clarebrough, M.E. Hargreaves, D. Michell and G.W. West. *The Release of Energy during Annealing of Deformed Metals.* Proc. R. Soc. Lond. A, vol. 232, pages 52–270, 1955. (Cited on page 24.)

[Clarebrough 1958] L.M. Clarebrough, M.E. Hargreaves and M.H. Loretto. *The influence of grain size on the stored energy and mechanical properties of copper.* Acta Metallurgica, vol. 6, no. 12, pages 725–735, 1958. (Cited on pages 16, 24, 25, 26 and 293.)

[Cottrell 1964] A.H. Cottrell. The mechanical properties of materials. J. Willey, New York, 1964. (Cited on page 217.)

[Dassault-System 2010] Dassault-System. ABAQUS User's Manual. Version 6.10., 2010. (Cited on pages 196 and 340.)

[Debreceni 1982] P. Debreceni, I. Kirschner and T. Porjesz. *Crystal symmetry effects of the conduction tensor.* Acta physica Academiae Scientiarum Hungaricae, vol. 53, no. 3, pages 395–400, 1982. (Cited on page 40.)

[Delaire 2000] F. Delaire, J.L. Raphanel and C. Rey. *Plastic heterogeneities of a copper multicrystal deformed in uniaxial tension: experimental study and finite element simulations.* Acta Materialia, vol. 48, no. 5, pages 1075–1087, 2000. (Cited on page 31.)

[Diard 2002] O. Diard, S. Leclercq, G. Rousselier and G. Cailletaud. *Distribution of normal stress at grain boundaries in multicrystals: application to an intergranular damage modeling.* Computational Materials Science, vol. 25, no. 1-2, pages 73–84, 2002. (Cited on page 201.)

[Diligent 2001] S. Diligent, E. Gautier, X. Lemoine and M. Berveiller. *Lattice orientation dependence of the stored energy during cold-rolling of polycrystalline steels.* Acta materialia, vol. 49, no. 19, pages 4079–4088, 2001. (Cited on pages 160 and 161.)

[Dillon 1962a] O.W. Dillon. *An experimental study of the heat generated during torsional oscillations.* Journal of the Mechanics and Physics of Solids, vol. 10, no. 3, pages 235–IN1, 1962. (Cited on pages 13, 16 and 23.)

[Dillon 1962b] O.W. Dillon. *An experimental study of the heat generated during torsional oscillations.* J. Mech. Phys. Solids, vol. 10, pages 235–244, 1962. (Cited on page 9.)

[Dillon 1962c] O.W. Dillon. *A nonlinear thermoelasticity theory.* J. Mech. Phys. Solids, vol. 10, pages 123–131, 1962. (Cited on page 9.)

[Dillon 1963a] O.W. Dillon. *Coupled thermoplasticity.* J. Mech. Phys. Solids, vol. 11, pages 21–33, 1963. (Cited on page 9.)

[Dillon 1963b] O.W. Dillon. *Coupled thermoplasticity.* Journal of the Mechanics and Physics of Solids, vol. 11, no. 1, pages 21–33, 1963. (Cited on page 197.)

[Dillon 1966] O.W. Dillon. *The heat generated during the torsional oscillations of copper tubes.* Int. J. Solids Structures, vol. 2, pages 181–204, 1966. (Cited on page 9.)

[Doherty 1997] R.D. Doherty, D.A. Hughes, F.J. Humphreys, J.J. Jonas, D.J. Jensen, M.E. Kassner, W.E. King, T.R. McNelley, H.J. McQueen and A.D. Rollett. *Current issues in recrystallization: a review.* Materials Science and Engineering: A, vol. 238, no. 2, pages 219–274, 1997. (Cited on page 15.)

[Doudard 2004] C. Doudard, Sy. Calloch, F. Hild, P. Cugy and A. Galtier. *Identification of the scatter in high cycle fatigue from temperature measurements.* Comptes Rendus Mecanique, vol. 332, no. 10, pages 795–801, 2004. (Cited on page 16.)

[Doudard 2005] C. Doudard, S. Calloch, P. Cugy, A. Galtier and F. Hild. *A probabilistic two-scale model for high cycle fatigue life predictions.* Fatigue & Fracture of Engineering Materials & Structures, vol. 28, pages 279–288, 2005. (Cited on page 9.)

[Doudard 2009] C. Doudard and S. Calloch. *Influence of hardening type on self-heating of metallic materials under cyclic loadings at low amplitude.* European Journal of Mechanics - A/Solids, vol. 28, no. 2, pages 233–240, 2009. (Cited on page 197.)

[Doumalin 2003] P. Doumalin, M. Bornert and J. Crépin. *Caractérisation de la répartition de la déformation dans les matériaux hétérogènes.* Mécanique & amp; Industries, vol. 4, no. 6, pages 607–617, 2003. (Cited on page 201.)

[Drücker 1951] D.C. Drücker. *A more fundamental approach to stress-strain relations.* pages 487–491, 1951. (Cited on page 9.)

[Dumoulin 2010] S. Dumoulin, H. Louche, O.S. Hopperstad and T. Bø rvik. *Heat sources, energy storage and dissipation in high-strength steels: Experiments and modelling.* European Journal of Mechanics - A/Solids, vol. 29, no. 3, pages 461–474, 2010. (Cited on pages 16, 85 and 293.)

[El Bartali 2009] A. El Bartali, V. Aubin and S. Degallaix. *Surface observation and measurement techniques to study the fatigue damage micromechanisms in a duplex stainless steel.* International Journal of Fatigue, vol. 31, no. 11-12, pages 2049–2055, 2009. (Cited on pages 57, 71 and 87.)

[Evrard 2008] P. Evrard, V. Aubin, Ph. Pilvin, S. Degallaix and D. Kondo. *Implementation and validation of a polycrystalline model for a bi-phased steel under non-proportional loading paths.* Mechanics Research Communications, vol. 35, no. 5, pages 336–343, 2008. (Cited on page 219.)

[Evrard 2010] P. Evrard, A. El Bartali, V. Aubin, C. Rey, S. Degallaix and D. Kondo. *Influence of boundary conditions on bi-phased polycrystal microstructure calculation.* International Journal of Solids and Structures, vol. 47, no. 16, pages 1979–1986, 2010. (Cited on pages 194, 201 and 219.)

[Fargione 2002] G. Fargione, A. Geraci, G. La Rosa and A. Risitano. *Rapid determination of the fatigue curve by the thermographic method.* Int. J. Fatigue, vol. 24, pages 11–19, 2002. (Cited on page 9.)

[Farren 1925] W.S. Farren and G.I. Taylor. *The heat developed during plastic extension of metals.* 1925. (Cited on pages 13, 14, 16, 20, 23, 24, 292 and 293.)

[Feaugas 1999] X. Feaugas. *On the origin of the tensile flow stress in the stainless steel AISI 316L at 300 K: back stress and effective stress.* Acta Materialia, vol. 47, no. 13, pages 3617–3632, 1999. (Cited on page 40.)

[Feaugas 2003] X Feaugas and H Haddou. *Grain-size effects on tensile behavior of nickel and AISI 316L stainless steel.* Metallurgical and Materials Transactions A, vol. 34, no. 10, pages 2329–2340, 2003. (Cited on pages 40, 69 and 70.)

[Feaugas 2009] X. Feaugas and P. Pilvin. *A Polycrystalline Approach to the Cyclic Behaviour of f.c.c. Alloys: Intra-Granular Heterogeneity.* Advanced Engineering Materials, vol. 11, no. 9, pages 703–709, 2009. (Cited on pages 152, 154, 155, 219, 297 and 343.)

[Flores 2007] P. Flores, L. Duchéne, C. Bouffioux, T. Lelotte, C. Henrard, N. Pernin, A. Van Bael, S. He, J. Duflou and A.M. Habraken. *Model identification and FE simulations: Effect of different yield loci and hardening laws in sheet forming.* International Journal of Plasticity, vol. 23, no. 3, pages 420–449, 2007. NUMISHEET2005 Conference. (Cited on page 194.)

[Forest 2004] S. Forest and M. Fivel. Plasticité cristalline et transition d'échelle : cas du monocristal, techniques de l'ingénieur, volume M 4 016. 2004. (Cited on pages 217 and 218.)

[Franciosi 1984] P. Franciosi. *Etude théorique et expérimentale du comportement elastoplastique des monocristaux métalliques se déformant par glissement : Modélisation pour un chargement complexe quasi statique.* PhD thesis, 1984. (Cited on pages 217 and 218.)

[Frank 1950] F.C. Frank and W.T. Read. *Multiplication Processes for Slow Moving Dislocations.* Phys. Rev., vol. 79, no. 4, pages 722–723, 1950. (Cited on page 218.)

[Frankland 2003] S.J.V. Frankland, V.M. Harik, G.M. Odegard, D.W. Brenner and T.S. Gates. *The stress-strain behavior of polymer nanotube composites from molecular dynamics simulation.* Composites Science and Technology, vol. 63, no. 11, pages 1655–1661, 2003. Modeling and Characterization of Nanostructured Materials. (Cited on page 195.)

[Gaussorgues 1989] G. Gaussorgues. La thermographie infrarouge. Principes, technologies, applications. Editions Tec&Doc, 1989. (Cited on page 94.)

[Gerber 2003] P. Gerber, J. Tarasiuk, T. Chauveau and B. Bacroix. *A quantitative analysis of the evolution of texture and stored energy during annealing of cold rolled copper.* Acta Materialia, vol. 51, no. 20, pages 6359–6371, 2003. (Cited on pages 16 and 293.)

[German 1978] R.M. German. *Grain growth in austenitic stainless steels.* Journal Name: Metallography (United States), vol. 11:2, pages 235–239, 1978. (Cited on pages 28 and 40.)

[Godfrey 2005] A. Godfrey, W. Cao, Q. Liu and N. Hansen. *Stored energy, microstructure, and flow stress of deformed metals.* Metallurgical and Materials Transactions A, vol. 36, no. 9, pages 2371–2378, 2005. (Cited on pages 17 and 18.)

[Gordon. 1955] P.P. Gordon. Trans. Amer. Inst. Min. (Metall.) Engrs, vol. 203, page 1043, 1955. (Cited on pages 13, 21 and 22.)

[Guduru 2001] P.R. Guduru, A.J. Rosakis and G. Ravichandran. *Dynamic shear bands: an investigation using high speed optical and infrared diagnostics.* Mechanics of Materials, vol. 33, no. 7, pages 371–402, 2001. (Cited on page 13.)

[Guilhem 2011] Y. Guilhem. *Numerical investigation of the local mechanical fields in 316L steel polycrystalline aggregates under fatigue loading (in french).* PhD thesis, 2011. (Cited on pages 51, 201 and 219.)

[Guzmáin 2009] R. Guzmáin, J. Melández, J.M. Aranda, Y.E. Essa, F. López and J.L. Pérez-Castellanos. *Measurement of temperature increment in compressive quasi-static and dynamic tests using infrared thermography.* Strain, vol. 45, no. 2, pages 179–189, 2009. (Cited on page 28.)

[Hai-peng 2005] Y. Hai-peng, L. Yi-xing and L. Zhen-bo. *Auto detection of wood texture orientation by Radon transform.* Journal of Forestry Research, vol. 16, no. 1, pages 1–4, 2005. (Cited on page 58.)

[Håkansson 2008] P. Håkansson, M. Wallin and M. Ristinmaa. *Prediction of stored energy in polycrystalline materials during cyclic loading.* International Journal of Solids and Structures, vol. 45, no. 6, pages 1570–1586, 2008. (Cited on page 197.)

[Hall 1951] E.O. Hall. *The Deformation and Ageing of Mild Steel: II Characteristics of the Lüders Deformation.* Proceedings of the Physical Society. Section B, vol. 64, no. 9, page 742, 1951. (Cited on pages 50 and 69.)

[Harewood 2007] F.J. Harewood and P.E. McHugh. *Comparison of the implicit and explicit finite element methods using crystal plasticity.* Computational Materials Science, vol. 39, no. 2, pages 481–494, 2007. (Cited on pages 219 and 340.)

[Hazra 2009] S.S. Hazra, A.A. Gazder and E.V. Pereloma. *Stored energy of a severely deformed interstitial free steel.* Materials Science and Engineering: A, vol. 524, no. 1-2, pages 158–167, 2009. (Cited on pages 16, 17 and 19.)

[Hild 2002] F. Hild, B. Raka, M. Baudequin, S. Roux and F. Cantelaube. *Multiscale displacement field measurements of compressed mineral-wool samples by digital image correlation.* Applied optics, vol. 41, no. 32, pages 6815–6828, 2002. (Cited on page 76.)

[Hild 2008] F. Hild and S. Roux. *Correlli Q4: A Software for Finite-element Displacement Field Measurements by Digital Image Correlation, internal report 269.* Rapport technique, LMT Cachan, ENS Cachan, France, 2008. (Cited on pages 78, 87 and 295.)

[Hill 1958] R. Hill. *A general theory of uniqueness and stability in elastic-plastic solids.* Journal of the Mechanics and Physics of Solids, vol. 6, no. 3, pages 236–249, 1958. (Cited on page 9.)

[Hill 1972] R. Hill and J.R. Rice. *Constitutive analysis of elastic-plastic crystals at arbitrary strain.* Journal of the Mechanics and Physics of Solids, vol. 20, no. 6, pages 401–413, 1972. (Cited on page 337.)

[Hodowany 2000] J. Hodowany, G. Ravichandran, A.J. Rosakis and P. Rosakis. *Partition of plastic work into heat and stored energy in metals.* Experimental Mechanics, vol. 40, pages 113–123, 2000. 10.1007/BF02325036. (Cited on pages 16, 170 and 293.)

[Hort 1907] H. Hort. Mitt. ForschArb. Ingenieurw, vol. 41, no. 1, 1907. (Cited on page 17.)

[Huang 1991] Y. Huang. *A user material subroutine incorporating single crystal plasticity in the Abaqus Finite Element program.* Rapport technique, Harvard University Report, MECH 178, 1991. (Cited on pages 219, 329 and 338.)

[Huang 1995] Y. Huang and D. Leu. *Finite element analysis of contact problems for a sheet metal bending process.* Computers and amp; Structures, vol. 57, no. 1, pages 15–27, 1995. (Cited on pages 331 and 332.)

[Huang 1999] Y. Huang and F.J. Humphreys. *Measurements of grain boundary mobility during recrystallization of a single-phase aluminium alloy.* Acta Materialia, vol. 47, no. 7, pages 2259–2268, 1999. (Cited on page 17.)

[Hughes 1980] T.J.R. Hughes and J. Winget. *Finite rotation effects in numerical integration of rate constitutive equations arising in large-deformation analysis.* International Journal for Numerical Methods in Engineering, vol. 15, no. 12, pages 1862–1867, 1980. (Cited on page 340.)

[Hughes 1997] D.A. Hughes and N. Hansen. *High angle boundaries formed by grain subdivision mechanisms.* Acta Materialia, vol. 45, no. 9, pages 3871–3886, 1997. (Cited on page 12.)

[Humphreys 1995] F.J. Humphreys and M. Hatherly. Recrystallization and related annealing phenomena. Pergamon, 1995. (Cited on page 18.)

[Humphreys 2004] F.J. Humphreys and M. Hatherly. Recrystallization and related annealing phenomena. Pergamon, 2004. (Cited on page 12.)

[Hutchinson 1964] J.W. Hutchinson. *Plastic deformation of b.c.c. polycrystals.* Journal of the Mechanics and Physics of Solids, vol. 12, no. 1, pages 25–33, 1964. (Cited on page 196.)

[Hutchinson 1976] J.W. Hutchinson. *Bounds and self-consistent estimates for creep of polycrystalline materials.* Proc. R. Soc. Lond. A., vol. 348, 1976. (Cited on pages 197 and 216.)

[Jahanshahi 1966] A. Jahanshahi. *Quasi-Static Stresses Due to Moving Temperature Discontinuity on a Plane Boundary.* Journal of Applied Mechanics, vol. 33, no. 4, pages 814–816, 1966. (Cited on page 40.)

[Jaoul 1965] B. Jaoul and C. Crussard. Etude de la plasticité et application aux métaux. Dunod, Paris, 1965. (Cited on pages 9 and 12.)

[Kalidindi 1992] S.R. Kalidindi, C.A. Bronkhorst and L. Anand. *Crystallographic texture evolution in bulk deformation processing of FCC metals.* Journal of the Mechanics and Physics of Solids, vol. 40, no. 3, pages 537–569, 1992. (Cited on page 197.)

[Kapitza 1941] P.L. Kapitza. *Heat Transfer and Superfluidity of Helium II.* Phys. Rev., vol. 60, no. 4, pages 354–355, 1941. (Cited on pages 40, 104, 184 and 295.)

[Kasem 2010] H. Kasem, J. Thevenet, X. Boidin, M. Siroux, P. Dufrenoy, B. Desmet and Y. Desplanques. *An emissivity-corrected method for the accurate radiometric measurement of transient surface temperatures during braking.* Tribology International, vol. 43, no. 10, pages 1823–1830, 2010. (Cited on pages 85 and 313.)

[Khorashadizadeh 2011] A. Khorashadizadeh, D. Raabe, S. Zaefferer, G. S. Rohrer, A. D. Rollett and M. Winning. *Five-Parameter Grain Boundary Analysis by 3D EBSD of an Ultra Fine Grained CuZr Alloy Processed by Equal Channel Angular Pressing.* Advanced Engineering Materials, vol. 13, no. 4, pages 237–244, 2011. (Cited on page 199.)

[Kino 1980] G.S. Kino, D.M. Barnett, N. Grayeli, G. Herrmann, J.B. Hunter, D.B. Ilić, G.C. Johnson, R.B. King, M.P. Scott, J.C. Shyne and C.R. Steele. *Acoustic measurements of stress fields and microstructure.* Journal of Nondestructive Evaluation, vol. 1, no. 1, pages 67–77, 1980. (Cited on page 315.)

[Kocks 1981] U.F. Kocks. *Kinematics of nonuniform deformation.* Progress in Material Science, vol. Chalmers Anniversary Volume, 1981. (Cited on page 12.)

[Krapez 2002] J. C. Krapez and D. Pacou. *Thermography detection of early thermal effects during fatigue tests of steel and aluminum samples.* In AIP conference proceedings, volume 615, pages 1545–1552, 2002. (Cited on page 9.)

[Kuhlmann-Wilsdorf 1983] D. Kuhlmann-Wilsdorf and N.R. Comins. *Dislocation cell formation and work hardening in the unidirectional glide of f.c.c. metals I: Basic theoretical analysis of cell walls parallel to the primary glide plane in early stage II.* Materials Science and Engineering, vol. 60, no. 1, pages 7–24, 1983. (Cited on page 168.)

[Lee 1991] H.T. Lee and J.C. Chen. *Temperature effect induced by uniaxial tensile loading.* Journal of Materials Science, vol. 26, no. 21, pages 5685–5692, 1991. (Cited on pages 126, 127, 128, 129, 268 and 296.)

[Lee 2003] H.Y. Lee, J.B. Kim and J.H. Lee. *Thermal ratchetting deformation of a 316L stainless steel cylindrical structure under an axial moving temperature distribution.* International Journal of Pressure Vessels and Piping, vol. 80, no. 1, pages 41–48, 2003. (Cited on page 40.)

[Lekhnitskii 1964] S.G. Lekhnitskii, P. Fern, J.J. Brandstatter and E.H. Dill. *Theory of Elasticity of an Anisotropic Elastic Body.* vol. 17, no. 1, page 84, 1964. (Cited on page 333.)

[Lemaitre 1994] J. Lemaitre and J.L. Chaboche. Mechanics of solids materials. Cambridge University Press, 1994. (Cited on page 206.)

[Lemaitre 2009] J. Lemaitre and J.L. Chaboche. *Mécanique des matériaux solides.* Dunod, 2009. (Cited on page 303.)

[Li 2004] L. Li, D.J. Weidner, J. Chen, M.T. Vaughan, M. Davis and W.B. Durham. *X-ray strain analysis at high pressure: Effect of plastic deformation in MgO.* Journal of Applied Physics, vol. 95, no. 12, pages 8357–8365, 2004. (Cited on page 243.)

[Louche 1999] H. Louche. *Analyse par thermographie infrarouge des effets dissipatifs de la localisation dans des aciers.* PhD thesis, 1999. (Cited on pages 14 and 101.)

[Louche 2001] H. Louche and A. Chrysochoos. *Thermal and dissipative effects accompanying Lüders band propagation.* Materials Science and Engineering: A, vol. 307, no. 1-2, pages 15–22, 2001. (Cited on pages 10, 13, 16, 143, 291 and 293.)

[Louche 2004] H. Louche and L. Tabourot. *Experimental energetic balance associated to the deformation of an aluminum multicrystal and monocrystal sheet.* Mater. Sci., no. Forum 467-470, pages 1395–1400, 2004. (Cited on page 291.)

[Louche 2005] H. Louche, P. Vacher and R. Arrieux. *Thermal observations associated with the Portevin-Le Ch{â}telier effect in an Al-Mg alloy.* Materials Science and Engineering: A, vol. 404, no. 1-2, pages 188–196, 2005. (Cited on pages 27 and 291.)

[Lubliner 1990] J. Lubliner. Plasticity Theory. Macmillan, 1990. (Cited on page 337.)

[Ludwig 2008] W. Ludwig, S. Schmidt, E.M. Lauridsen and H.F. Poulsen. *X-ray diffraction contrast tomography: a novel technique for three-dimensional grain mapping of polycrystals. I. Direct beam case.* Journal of Applied Crystallography, vol. 41, no. 2, pages 302–309, Apr 2008. (Cited on page 199.)

[Lukas 2001] P. Lukas and L. Kunz. *Cyclic slip localisation and fatigue crack initiation in fcc single cristals.* Material Science and Engineering A, vol. 314, pages 75–80, 2001. (Cited on page 9.)

[Lukas 2002] P. Lukas and L. Kunz. *Specific features of high-cycle and ultra-high-cycle fatigue.* Fat. Frac. Engng. Mat. Struct., vol. 25, pages 747–763, 2002. (Cited on page 9.)

[Lukas 2004] P. Lukas and L. Kunz. *Role of persistent slip bands in fatigue.* Phil. Mag., vol. 84, no. 3-5, pages 317–330, 2004. (Cited on page 9.)

[Luong 1995] M. P. Luong. *Infrared thermographic scanning of fatigue in metals.* Nucl. Engng. and Design, vol. 158, pages 363–376, 1995. (Cited on page 9.)

[Luong 1998] M. P. Luong. *Fatigue limit evaluation of metals using an infrared thermographic technique*. Mech. Mat., vol. 28, pages 155–163, 1998. (Cited on page 9.)

[Mackenzie 1958] J.K. Mackenzie. *Second paper on statistics associated with the random disorientation of cubes*. Biometrika, vol. 45, pages 229–240, 1958. (Cited on pages 52 and 53.)

[Magnin 1984a] T. Magnin, J. Driver, J. Lepinoux and L. P. Kubin. *Aspects microstructuraux de la déformation cyclique dans les métaux et alliages C.C. et C.F.C. - I. : consolidation cyclique*. Rev. Phys. Appl., vol. 19, pages 467–482, 1984. (Cited on page 9.)

[Magnin 1984b] T. Magnin, J. Driver, J. Lepinoux and L. P. Kubin. *Aspects microstructuraux de la déformation cyclique dans les métaux et alliages C.C. et C.F.C. - II. : saturation cyclique et localisation de la déformation*. Rev. Phys. Appl., vol. 19, pages 467–482, 1984. (Cited on page 9.)

[Malvern 1969] L.E. Malvern. Introduction to the Mechanics of a Continuum Medium. Prentice-Hall, Englewood Cliffs: NJ, 1969. (Cited on page 337.)

[Mandel 1965] J. Mandel. *Generalisation de la theorie de plasticite de W. T. Koiter*. International Journal of Solids and Structures, vol. 1, no. 3, pages 273–295, 1965. (Cited on pages 161 and 217.)

[Mareau 2011] C. Mareau, V. Favier, B. Weber, A. Galtier and M. Berveiller. *Micromechanical modeling of the interactions between the microstructure and the dissipative deformation mechanisms in steels under cyclic loading*. International Journal of Plasticity, 2011. (Cited on page 197.)

[Maugin 1992] G.A. Maugin. The Thermomechanics of Plasticity and Fracture. 1992. (Cited on pages 206 and 303.)

[Maynadier 2011a] A. Maynadier, D. Depriester, K. Lavernhe-Taillard and O. Hubert. *Thermo-mechanical description of phase transformation in Ni-Ti Shape Memory Alloy*. Procedia Engineering, vol. 10, no. 0, pages 2208–2213, 2011. 11th International Conference on the Mechanical Behavior of Materials (ICM11). (Cited on page 27.)

[Maynadier 2011b] A. Maynadier, M. Poncelet, K. Lavernhe-Taillard and S. Roux. *One-shot Measurement of Thermal and Kinematic Fields: InfraRed Image Correlation (IRIC)*. Experimental Mechanics, pages 1–15, 2011. (Cited on page 74.)

[Meissonnier 2001] F.T. Meissonnier, E.P. Busso and N.P. O'Dowd. *Finite element implementation of a generalised non-local rate-dependent crystallographic formulation for finite strains*. International Journal of Plasticity, vol. 17, no. 4, pages 601–640, 2001. (Cited on pages 219 and 331.)

[Méric 1991] L. Méric, P. Poubanne and G. Cailletaud. *Single Crystal Modeling for Structural Calculations: Part 1 - Model Presentation*. Journal of Engineering Materials and Technology, vol. 113, no. 1, pages 162–170, 1991. (Cited on page 197.)

[Mguil-Touchal 1997] S. Mguil-Touchal. *Une technique de corrélation directe d'images numériques : application à la détermination des courbes limites de formage et proposition d'un critère de striction.* PhD thesis, 1997. (Cited on page 87.)

[Michell 1952] D. Michell, L.M. Clarebrough, M.E. Hargreaves and G.W. West. *The stored Energy of Cold Work.* Proc. Roy. Soc. A, vol. 215, page 507, 1952. (Cited on page 13.)

[Michell 1957] D. Michell and F.D. Haig. *Investigation of the annealing of deformed nickel powder by X-ray and stored energy measurements.* Philosophical Magazine, vol. 2, no. 13, pages 15–32, 1957. (Cited on pages 16 and 293.)

[Michno 1976] M.J. Michno and W.N. Findley. *An historical perspective of yield surface investigations for metals.* International Journal of Non-Linear Mechanics, vol. 11, no. 1, pages 59–82, 1976. (Cited on pages 126 and 127.)

[Mineur 2000] M. Mineur. *Conditions locales d'amorçage des fissures de fatigue dans un acier inoxydable de type 316L : aspects cristallographiques (EBSD).* PhD thesis, Université de Poitiers, France, 2000. (Cited on page 46.)

[Miroux 1999] B. Bacroix A. Miroux and O. Castelnau. *Simulation of the orientation dependence of stored energy during rolling deformation of low carbon steels.* Modelling and Simulation in Materials Science and Engineering, vol. 7, no. 5, page 851, 1999. (Cited on page 28.)

[Monchiet 2006] V. Monchiet, E. Charkaluk and D. Kondo. *Plasticity-damage based micromechanical modelling in high cycle fatigue.* Comptes Rendus Mécanique, vol. 334, no. 2, pages 129–136, 2006. (Cited on page 209.)

[Monnet 2009] G. Monnet. *A crystalline plasticity law for austenitic stainless steel.* 2009. (Cited on pages 19 and 219.)

[Morabito 2007] A.E. Morabito, A. Chrysochoos, V. Dattoma and U. Galietti. *Analysis of heat sources accompanying the fatigue of 2024 T3 aluminium alloys.* International Journal of Fatigue, vol. 29, no. 5, pages 977–984, 2007. (Cited on page 14.)

[Mu 2011] P. Mu. *Study of crack initiation in low-cycle fatigue of an austenitic stainless steel.* PhD thesis, 2011. (Cited on pages 214 and 215.)

[Mughrabi 1983] H. Mughrabi. *Fatigue crack initiation by cyclic slip irreversibilities in high cycle fatigue.* In Fatigue mechanisms : advances in quantitative measurement of physical damage - ASTM STP 811, pages 5–45, 1983. (Cited on page 9.)

[Murr 1975] L.E. Murr. Interfacial phenomena in metals and alloys. 1975. (Cited on page 18.)

[Musienko 2009] A. Musienko and G. Cailletaud. *Simulation of inter- and transgranular crack propagation in polycrystalline aggregates due to stress corrosion cracking.* Acta Materialia, vol. 57, no. 13, pages 3840–3855, 2009. (Cited on pages 194 and 199.)

[Nabarro 1987] F.R.N. Nabarro. Theory of crystal dislocations. Dover Publications, New York, 1987. (Cited on page 168.)

[Needleman 1988] A. Needleman. Rev. Phys. Appl. (Paris), vol. 23, no. 4, pages 585–593, 1988. (Cited on page 13.)

[Nguyen 1975] Q.S. Nguyen and B. Halphen. *Sur les matériaux standard généralisés.* Journal de Mécanique, vol. 14, pages 39–63, 1975. (Cited on page 205.)

[Nguyen 1977] Q.S. Nguyen. *On the elastic plastic initial-boundary value problem and its numerical integration.* International Journal for Numerical Methods in Engineering, vol. 11, no. 5, pages 817–832, 1977. (Cited on page 326.)

[Nguyen 2000] Q.S. Nguyen. *Stabilité et mécanique non linéaire.* Revue Française de Génie Civil, vol. 4, no. 1, page 149, 2000. (Cited on page 303.)

[Oh 1989] S.I. Oh, T. Altan and S. Kobayashi. *Metal Forming and the Finite Element Method.* 1989. (Cited on page 197.)

[Oliferuk 1985] W. Oliferuk, S.P. Gadaj and M.W. Grabski. *Energy storage during the tensile deformation of Armco iron and austenitic steel.* Materials Science and Engineering, vol. 70, pages 131–141, 1985. (Cited on pages 10, 13, 16 and 293.)

[Oliferuk 1993] W. Oliferuk, W.A. Świątnicki and M.W. Grabski. *Rate of energy storage and microstructure evolution during the tensile deformation of austenitic steel.* Materials Science and Engineering: A, vol. 161, no. 1, pages 55–63, 1993. (Cited on pages 16, 22, 23 and 293.)

[Oliferuk 1995] W. Oliferuk, W.A. Świątnicki and M.W. Grabski. *Effect of the grain size on the rate of energy storage during the tensile deformation of an austenitic steel.* Materials Science and Engineering A, vol. 197, no. 1, pages 49–58, 1995. (Cited on pages 15, 24, 25, 26, 40, 167, 170, 176 and 297.)

[Oliferuk 1996] W. Oliferuk, A. Korbel and M.W. Grabski. *Mode of deformation and the rate of energy storage during uniaxial tensile deformation of austenitic steel.* Materials Science and Engineering A, vol. 220, no. 1-2, pages 123–128, 1996. (Cited on pages 26 and 27.)

[Oliferuk 1997] W. Oliferuk, A. Korbel and M.W. Grabski. *Slip behaviour and energy storage process during uniaxial tensile deformation of austenitic steel.* Materials Science and Engineering A, vol. 234-236, pages 1122–1125, 1997. (Cited on pages 168 and 169.)

[Oliferuk 2001] W. Oliferuk, A. Korbel and W. Bochniak. *Energy balance and macroscopic strain localization during plastic deformation of polycrystalline metals.* Materials Science and Engineering A, vol. 319-321, pages 250–253, 2001. (Cited on pages 16 and 293.)

[Oliferuk 2004] W. Oliferuk and M. Maj. *Effect of pre-strain direction on energy storage process during tensile deformation of polycrystal.* Materials Science and Engineering A, vol. 387-389, pages 218–221, 2004. (Cited on pages 26, 27 and 174.)

[Oliferuk 2009] W. Oliferuk and M. Maj. *Stress-strain curve and stored energy during uniaxial deformation of polycrystals.* European Journal of Mechanics - A/Solids, vol. 28, no. 2, pages 266–272, 2009. (Cited on pages 16, 160, 161, 164, 165, 166, 170, 252, 258, 268, 293, 297 and 299.)

[Padilla 2011] H. Padilla, J. Lambros, A. Beaudoin and I. Robertson. *Spatiotemporal Thermal Inhomogeneities During Compression of Highly Textured Zirconium.* Experimental Mechanics, vol. 51, pages 1061–1073, 2011. 10.1007/s11340-010-9425-4. (Cited on pages 13, 27 and 29.)

[Peirce 1982] D. Peirce, R.J. Asaro and A. Needleman. *An analysis of nonuniform and localized deformation in ductile single crystals.* Acta Metallurgica, vol. 30, no. 6, pages 1087–1119, 1982. (Cited on pages 196 and 335.)

[Peirce 1983] D. Peirce, R.J. Asaro and A. Needleman. *Material rate dependence and localized deformation in crystalline solids.* Acta Metallurgica, vol. 31, no. 12, pages 1951–1976, 1983. (Cited on pages 196 and 329.)

[Peirce 1984] D. Peirce, C.F. Shih and A. Needleman. *A tangent modulus method for rate dependent solids.* Computers amp; Structures, vol. 18, no. 5, pages 875–887, 1984. (Cited on page 326.)

[Perrin 2010] C. Perrin, S. Berbenni, H. Vehoff and M. Berveiller. *Role of discrete intragranular slip on lattice rotations in polycrystalline Ni: Experimental and micromechanical studies.* Acta Materialia, vol. 58, no. 14, pages 4639–4649, 2010. (Cited on page 57.)

[Petit 2007] P Petit. *Etude du comportement d'un acier inoxydable duplex à l'échelle de la microstructure.* PhD thesis, 2007. (Cited on page 201.)

[Poncelet 2007] M. Poncelet. *Multiaxialité, hétérogénéités intrinsèques et structurales des essais d'autoéchauffement et de fatigue à grand nombre de cycles.* PhD thesis, 2007. (Cited on page 78.)

[Pron 2004] H. Pron and C. Bissieux. *Focal plane array infrared cameras as research tools.* QIRT Journal, vol. 1, no. 2, pages 229–240, 2004. (Cited on page 81.)

[Queyreau 2009] S. Queyreau, G. Monnet and B. Devincre. *Slip systems interactions in α-iron determined by dislocation dynamics simulations.* International Journal of Plasticity, vol. 25, no. 2, pages 361–377, 2009. (Cited on page 217.)

[Quinney 1937] H. Quinney and G.I. Taylor. *The emission of latent energy due to previous cold working when a metal is heated.* 1937. (Cited on pages 13, 125, 167, 292 and 325.)

[Rajmohan 1997a] N. Rajmohan, Y. Hayakawa, J.A. Szpunar and J H Root. *The determination of orientation-dependent stored energy using neutron diffraction.* Physica B: Condensed Matter, vol. 241-243, no. 0, pages 1225–1227, 1997. (Cited on pages 16, 19 and 293.)

[Rajmohan 1997b] N. Rajmohan, Y. Hayakawa, J.A. Szpunar and J.H. Root. *Neutron diffraction method for stored energy measurement in interstitial free steel.* Acta Materialia, vol. 45, no. 6, pages 2485–2494, 1997. (Cited on page 19.)

[Ranc 2008] N. Ranc and D. Wagner. *Experimental study by pyrometry of Portevin-Le Châtelier plastic instabilities Type A to type B transition.* Materials Science and Engineering: A, vol. 474, no. 1-2, pages 188–196, 2008. (Cited on pages 13, 27 and 94.)

[Rao 1990] A.R. Rao. A taxonomy for texture description and identification. Springer-Verlag New York, Inc., New York, NY, USA, 1990. (Cited on page 58.)

[Read 1950] W.T. Read and W. Shockley. *Dislocation Models of Crystal Grain Boundaries.* Phys. Rev., vol. 78, no. 3, pages 275–289, 1950. (Cited on page 17.)

[Resk 2010] H. Resk. *Influence de la structure métallurgique des soudures en acier inoxydable austénitique sur le contrôle non destructif par ultrasons.* PhD thesis, Ecole Nationale Supérieure des Mines de Paris - Mines ParisTech, France, 2010. (Cited on pages 14 and 15.)

[Rice 1976] J.R. Rice. *The localization of plastic deformation.* pages 207–220, 1976. (Cited on page 9.)

[Rittel 1999] D. Rittel. *On the conversion of plastic work to heat during high strain rate deformation of glassy polymers.* Mechanics of Materials, vol. 31, no. 2, pages 131–139, 1999. (Cited on pages 170 and 172.)

[Rittel 2010] D. Rittel and S. Osovski. *Dynamic failure by adiabatic shear banding.* International Journal of Fracture, vol. 162, no. 1, pages 177–185, 2010. (Cited on pages 10 and 27.)

[Robertson 2001] C. Robertson, M.C. Fivel and A. Fissolo. *Dislocation substructure in 316L stainless steel under thermal fatigue up to 650 K.* Materials Science and Engineering: A, vol. 315, no. 1-2, pages 47–57, 2001. (Cited on page 195.)

[Rosakis 2000] P. Rosakis, A. J. Rosakis, G. Ravichandran and J. Hodowany. *A thermodynamic internal variable model for the partition of plastic work into heat and stored energy.* J. Mech. Phys. Solids, vol. 48, pages 581–607, 2000. (Cited on page 10.)

[Roters 2010] F. Roters, P. Eisenlohr, L. Hantcherli, D.D. Tjahjanto, T.R. Bieler and D. Raabe. *Overview of constitutive laws, kinematics, homogenization and multiscale methods in crystal plasticity finite-element modeling: Theory, experiments, applications.* Acta Materialia, vol. 58, no. 4, pages 1152–1211, 2010. (Cited on page 196.)

[Saai 2007] A. Saai. *Modèle physique de la plasticité d'un cristal métallique CFC soumis à des chargements alternés: Contribution à la définition d'une modélisation multiéchelles de la mise en forme des métaux.* PhD thesis, 2007. (Cited on pages 31 and 293.)

[Saai 2010] A. Saai, H. Louche, L. Tabourot and H.J. Chang. *Experimental and numerical study of the thermo-mechanical behavior of Al bi-crystal in tension using full field measurements and micromechanical modeling.* Mechanics of Materials, vol. 42, no. 3, pages 275–292, 2010. (Cited on pages 16, 31, 32, 73, 75, 76, 196 and 293.)

[Sabatier 2002] L. Sabatier. *Apport des techniques d'analyse locale EBSD et AFM à l'étude de l'émergence des bandes de glissement induites par fatigue dans l'acier inoxydable 316L. Influence de couches minces.* PhD thesis, 2002. (Cited on page 46.)

[Sachs 1928] G. Sachs. *Zur ableilung einer fleissbedingung.* Z. Ver. Dtsch. Ing., vol. 72, pages 734–736, 1928. (Cited on page 11.)

[Schlosser 2007] P. Schlosser, H. Louche, D. Favier and L. Orgéas. *Image Processing to Estimate the Heat Sources Related to Phase Transformations during Tensile Tests of NiTi Tubes.* Strain, vol. 43, no. 3, pages 260–271, 2007. (Cited on page 291.)

[Schmid 1924] E. Schmid. *Yield point of a crystals: critical shear stress law.* In: Proc. 1st Int. Congr. Appl. Mech., page 342, 1924. (Cited on pages 11 and 12.)

[Schmid 1950] E. Schmid and W. Boas. Plasticity of crystals with special reference to metals. F.A. Hughes (London), 1950. (Cited on pages 169 and 215.)

[Schreier 2009] O.J. Schreier and M.A. Sutton. Image correlation for deformation, motion and shape measurements: basic concepts, theory and applications. 2009. (Cited on page 309.)

[Schwartz 2011] J. Schwartz. *Approche non locale en plasticité cristalline: application à l'étude du comportement mécanique de l'acier 316LN en fatigue oligocyclique.* PhD thesis, 2011. (Cited on pages 217 and 258.)

[Seghir 2012a] R. Seghir, L. Bodelot, E. Charkaluk and P. Dufrénoy. *Numerical and experimental estimation of thermomechanical fields heterogeneity at the grain scale of 316L stainless steel.* Computational Materials Science, vol. 53, no. 1, pages 464–473, 2012. (Cited on pages 205, 234 and 235.)

[Seghir 2012b] R. Seghir, J-F Witz, E. Charkaluk and P. Dufrénoy. *Improvement of thermomechanical full-field analysis of metallic polycrystals using crystallographic data.* Mechanics & Industry, vol. 13, no. 06, pages 395–403, 2012. Giens 2011. (Cited on page 101.)

[Seghir 2013] R. Seghir, J-F Witz, L. Bodelot, E. Charkaluk and P. Dufrénoy. *An improved lagrangian thermography procedure for the quantification of the temperature fields within polycrystals.* Quantitative InfraRed Thermography, vol. 10, no. 1, pages 74–95, 2013. (Cited on page 73.)

[Signor 2011] L. Signor, J. Dumoncel, P. Villechaise and M. Gueguen. *Simulations 3d d'aggregats polycristallins reconstruits par approche type cao.* In 10e colloque national en calcul des structures: CSMA - Giens (France), 2011. (Cited on page 199.)

[Simo 1985] J.C. Simo and R.L. Taylor. *Consistent tangent operators for rateindependant elastoplasticity.* Compu. Meth. Appl. Mech. Engng, vol. 48, pages 101–118, 1985. (Cited on page 326.)

[Simo 1992] J.C. Simo and C. Miehe. *associative coupled thermoplasticity at finite strains: formulation, numerical analysis and implementation.* Comput. Methods Appl. Mech. Eng., vol. 98, 1992. (Cited on page 197.)

[Simonovski 2009] I. Simonovski and L. Cizelj. *The Influence of the Grain Structure Size on Microstructurally Short Cracks.* Journal of Engineering for Gas Turbines and Power, vol. 131, no. 4, page 42903, 2009. (Cited on page 216.)

[Singh 1998] A.K. Singh, C. Balasingh, Ho kwang Mao, Russell J. Hemley and Jinfu Shu. *Analysis of lattice strains measured under nonhydrostatic pressure.* Journal of Applied Physics, vol. 83, no. 12, pages 7567–7575, 1998. (Cited on page 243.)

[Smith 1990] R. A. Smith. *The Versailles railway accident of 1842 and the first research into metal fatigue.* In Fatigue 90, vol. 4, pages 2033–2041. Birmimgham: Materials and Component Engineering Publications, 1990. (Cited on page 9.)

[Stanley 1969] J.K. Stanley and A.J. Perrotta. *Grain growth in austenitic stainless steels.* Metallography, vol. 2, no. 4, pages 349–362, 1969. (Cited on page 28.)

[Suquet 1987] P. Suquet. Elements of homogenization theory for inelastic solid mechanics. In Homogenization Techniques for Composite Media. Sanchez-Palencia, E. and Zaoui, A., springer, berlin édition, 1987. (Cited on page 161.)

[Suresh 1998] S. Suresh. Fatigue of materials – second edition. Cambridge University Press, Cambridge, 1998. (Cited on page 9.)

[Sutton 1995] A.P. Sutton and R.W. Balluffi. Interfaces in Crystalline Materials. Clarendon Press, Oxford, 1995. (Cited on page 54.)

[Tabourot 1997] L. Tabourot, M. Fivel and E. Rauch. *Generalised constitutive laws for f.c.c. single crystals.* Materials Science and Engineering: A, vol. 234-236, pages 639–642, 1997. (Cited on page 196.)

[Tabourot 2001] L. Tabourot. *Vers une vision unifiée de la plasticité cristalline.* PhD thesis, 2001. (Cited on page 217.)

[Tamura 2005] N. Tamura, H.A. Padmore and J.R. Patel. *High spatial resolution stress measurements using synchrotron based scanning X-ray microdiffraction with white or monochromatic beam.* Materials Science and Engineering: A, vol. 399, no. 1-2, pages 92–98, 2005. Measurement and Interpretation of Internal/Residual Stresses. (Cited on page 243.)

[Taylor 1934] G.I. Taylor and H. Quinney. *The latent energy remaining in a metal after cold working.* Proc. R. Soc., vol. A413, pages 307–326, 1934. (Cited on pages 13, 20, 23, 24 and 292.)

[Taylor 1938] G.I. Taylor. *Plastic strains in metals.* J. Inst. Metals, vol. 62, page 307, 1938. (Cited on page 11.)

[Truesdell 1955] C. Truesdell. *Hypo-Elasticity.* Indiana Univ. Math. J., vol. 4, no. 1, pages 83–133, 1955. (Cited on page 337.)

[Vacher 2003] P. Vacher. *Apport des techniques de corrélation d'images en mécanique: analyses de déformations et numérisations 3D.* PhD thesis, 2003. (Cited on page 87.)

[Villechaise 2002] P. Villechaise, L. Sabatier and J.C. Girard. *On slip band features and crack initiation in fatigued 316L austenitic stainless steel: Part 1: Analysis by electron back-scattered diffraction and atomic force microscopy.* Materials Science and Engineering: A, vol. 323, no. 1-2, pages 377–385, 2002. (Cited on pages 43 and 57.)

[Vincent 2008] L. Vincent. *On the ability of some cyclic plasticity models to predict the evolution of stored energy in a type 304L stainless steel submitted to high cycle fatigue.* European Journal of Mechanics - A/Solids, vol. 27, no. 2, pages 161–180, 2008. (Cited on pages 27, 163 and 197.)

[Voigt 1928] W. Voigt. Lehrbuch Der Kristallphysik. B.G. Teubner, Leipzig, Germany, 1928. (Cited on pages 213 and 332.)

[von Mises 1928] R. von Mises. *Mechanik der plastischen Formänderung von Kristallen.* Zeitschrift für angewandte Mathematik und Mechanik, no. 8, pages 161–185, 1928. (Cited on pages 11, 13, 230 and 235.)

[Wattrisse 2002] B. Wattrisse, J.M. Muracciole and A. Chrysochoos. *Thermomechanical effects accompanying the localized necking of semi-crystalline polymers.* Int. J. Therm. Sci., vol. 41, pages 422–427, 2002. (Cited on pages 13 and 27.)

[Weidner 2010] D.J. Weidner, M.T. Vaughan, L. Wang, H. Long, L. Li, N.A. Dixon and W.B. Durham. *Precise stress measurements with white synchrotron x rays.* Rev. Sci. Instrum., vol. 81, page 013903, 2010. (Cited on page 243.)

[Williams 1964] R.O. Williams. *the increase in internal energy of copper crystals during deforming at 25 ^{o}c.* Acta Met., vol. 12, no. 6, 1964. (Cited on page 169.)

[Winther 2004] G. Winther, X. Huang, A. Godfrey and N. Hansen. *Critical comparison of dislocation boundary alignment studied by TEM and EBSD: technical issues and theoretical consequences.* Acta Materialia, vol. 52, no. 15, pages 4437–4446, 2004. (Cited on page 58.)

[Witz 2008] J. Witz, S. Roux, F. Hild and J.B. Rieunier. *Mechanical Properties of Crimped Mineral Wools: Identification From Digital Image Correlation.* Journal of Engineering Materials and Technology, vol. 130, no. 2, page 21016, 2008. (Cited on page 58.)

[Wu 2005] J. Wu, Wray P.J., Garcia C.I., H.U.A. Mingjian and Deardo A.J. *Image Quality Analysis: A New Method of Characterizing Microstructures.* ISIJ International, vol. 45, no. 2, pages 254–262, 2005. (Cited on page 18.)

[Zehnder 2000] A.T. Zehnder, P.R. Guduru, A.J. Rosakis and G. Ravichandran. *Million frames per second infrared imaging system.* Rev. Sci. Instrum., vol. 71, no. 10, pages 3762–3768, 2000. (Cited on pages 13 and 28.)

[Zhou 2007] W. Zhou and Z.L. Wang. Scanning microscopy for nanotechnology: techniques and applications. Springer, 2007. (Cited on pages 18, 47 and 58.)

Extended abstract (French)

Introduction générale

La sollicitation de matériaux métalliques sous conditions de chargements cycliques conduit à l'apparition de micro-fissures, leurs propagation et leurs coalescence aboutissant finalement à la ruine complète du matériau ou de la structure considérée et cela sans que des signes macroscopiques avant-coureurs de défaillance mécanique puissent être clairement perçu. Ce domaine de recherche, que l'on nomme classiquement la "fatigue des matériaux", est au coeur des problèmes industriels depuis la fin du 19$^{\text{ème}}$ siècle, et fait toujours l'objet d'une recherche active. En effet, les principales difficultés liées à l'étude de ce type de sollicitation réside d'une part dans les faibles amplitudes de chargement misent en jeux, et d'autre part dans l'aspect microstructural de ses mécanismes ce qui nécessite d'en étudier les causes, les indicateurs et les conséquences d'un point de vue local et physique, s'appuyant sur des démarchent multi-échelles tant d'un point de vue théorique, expérimental que numérique.
Une voie pertinente pour étudier ces micromécanismes de déformation semble être celle de la thermomécanique. Comme cela a été montré depuis plusieurs décennies, durant la déformation plastique des métaux, une grande partie du travail plastique est dissipée sous forme de chaleur tandis que le reste demeure latent au sein du matériau. Cette portion d'énergie stockée au sein du matériau est associée à l'accommodation de la microstructure, à la création de défauts, de structures de dislocation et constitue donc probablement un indicateur pertinent au regard des processus de localisation de la déformation et de l'endommagement. Certains auteurs ont ainsi montré que les mesures thermiques et l'évaluation des sources de chaleur pouvaient, sous chargement monotone, fournir un certain nombre d'informations cruciales sur les phénomènes de localisation macroscopiques : (1) bandes de Lüders [Louche 2001], (2) dissipation plastique au sein d'agrégats Al [Louche 2004], (3) localisation Portevin Le Châtelier [Louche 2005], et (4) transformation de phase localisée au sein d'alliage Nitinol à mémoire de forme [Schlosser 2007]. Il semble alors possible de déterminer les zones où se développent favorablement la plasticité et l'endommagement grâce à l'information thermique et dans certains cas grâce à l'évolution de l'énergie bloquée au sein du matériau pendant le processus de déformation. Dans le cas des polycristaux, et de manière plus générale au sein des matériaux fortement hétérogènes, les mesures de champs cinématiques et thermiques sont complexes ainsi que l'ensemble des traitements de données nécessaires à la réalisation d'un bilan d'énergie puisqu'ils sont alors associés à des phénomènes de microplasticité, i.e. peu dissipatifs et extrèmement localisés. L'objet de cette étude est l'observation, la compréhension et la modélisation de ce type précis de phénomène dissipatif.

Ce travail s'incrit dans le continuité du travail de L. Bodelot [Bodelot 2008, Bodelot 2009, Bodelot 2011] qui a développé au sein de ce laboratoire, un nouveau protocole expérimental de mesures couplées insitu de champs cinématiques et thermiques à l'échelle des grains d'un acier inoxidable AISI 316L. S'appuyant sur les données expérimentales issuent de ces travaux [Bodelot 2008], et plus particulièrement un essai de traction monotone à faible niveau de déformation, ainsi que sur de nombreuses mesures

complémentaires telles que la mesure de texture cristallographique locale, la mesure profilométrique mais aussi la simulation numérique, l'objectif de ce travail est ainsi de:

- développer des outils d'analyse de microstructure pertinents.
- d'étudier, au regard de la microstructure sollicitée, les couplages thermo-mécaniques opérant durant la transition élasto-plastique puis conduisant à un état de plasticité localisée et cela pour des déformations n'excédant pas 2.5%. Cette limite en déformation permettra d'appréhender notre capacité à pouvoir étudier de manière expérimentale les phénomènes peu dissipatifs et plus complexes tels que la microplasticité au sein d'un essai de fatigue à $\pm 1\%$ de déformation.
- établir un premier bilan d'énergie à une échelle mésoscopique, c'est à dire celle du grain.
- développer les simulations numériques adaptées et nécessaires à l'estimation de variables internes encore difficilement mesurables telles que l'énergie bloquée, les contraintes...

Après une partie introductive sur les mécanismes de déformation, le stockage d'énergie associé et l'historique des techniques utilisées afin de pouvoir l'estimer, ce manuscrit se décompose en trois parties. Premièrement, l'essai étudié, le matériau ainsi que les techniques de mesures sont présentés. La microstructure après essai est analysée au travers de mesures E.B.S.D., profilométriques, micrographiques ainsi qu'à l'aide d'un outil automatique d'analyse de bandes de glissement développé à cet effet. Ensuite, la seconde partie est dédiée à l'étude des champs thermomécaniques in-situ. Une technique originale dédiée à la projection des données expérimentales sur la microstructure de surface est présentée et discutée. Enfin, les couplages inter- et intragranulaires sont investigués et de premiers bilans d'énergies à l'échelle mésoscopique sont réalisés. Finallement, dans une dernière partie, des simulations numériques d'agrégats polycrystallins sont conduits afin d'estimer un certain nombre de variables internes, de discuter les observations expérimentales mais aussi de réaliser des bilans d'énergies numériques permettant ainsi un véritable dialogue entre modèle et expérience.

Partie I

Au tout début du siècle dernier, les processus de déformation et nottament l'écrouissage faisait l'objet de nombreux questionnements. La voie proposée par Farren et Taylor [Farren 1925, Taylor 1934, Quinney 1937] fut d'étudier les différentes énergies misent en jeu au cours des processus de déformation et nottament la part stockée au sein du matériau, principalement associée à la création de réseaux de dislocations et de défauts. Cette variable interne, associée de manière intrinsèque à ce qu'on appelle macroscopiquement l'endommagement et la plasticité, a depuis fait l'objet de nombreuses recherches. Trois voies se sont développées:

- l'approche "microscopique" : où l'énergie stockée est estimée en s'appuyant sur son origine physique, i.e l'observation des réseaux de dislocations, la création de défauts, l'évolution des orientations granulaires et plus généralement toutes les transformations du réseau cristallin. De ces études, de nombreux modèles, pour la plupart empiriques, ont pu être développés de manière

à relier le stockage d'énergie à ces quantités microstructurales [Rajmohan 1997a, Gerber 2003, Choi 2004].

- l'approche "thermomécanique globale ou macroscopique" : où l'énergie stockée est estimée à partir de bilans d'énergies dont l'échelle d'interêt est lié à la technique utilisée. Tout d'abord globale (calorimètre) [Farren 1925], puis macroscopique avec l'émergence de la mesure de champs infrarouges [Chrysochoos 1989a, Hodowany 2000, Louche 2001, Berthel 2007a, Dumoulin 2010] permettant d'accéder à une information spatiale et temporelle des phénomènes dissipatifs mais tout en restant limitée en résolution de part les capacités des imageurs infrarouges.

- l'approche "multi-échelle" : où les auteurs se sont intéressés à la comparaison systématique entre les transformations microstructurales et le bilan d'énergie, vue comme une signature globale d'un ensemble de mécanismes irréversibles locaux [Michell 1957, Clarebrough 1958, Bailey 1960, Bever 1973, Oliferuk 1985, Oliferuk 1993, Oliferuk 2001, Oliferuk 2009, Saai 2010]. L'influence du trajet de chargement, de la taille de grain ainsi que du type de mécanisme de déformation sur le stockage globale a pu être notamment mis en évidence.

Cette étude s'inscrit dans la continuité de cette dernière approche avec pour ambition, la réalisation de bilans d'énergies à l'échelle de la microstructure permettant ainsi un dialogue privilégié entre les différents paramêtres microstructuraux et la variation de quantités thermomécaniques à la même échelle telles que les déformations, la température, les énergies... Fort de quelques études similaires notamment sur un bi-crystal d'aluminium [Saai 2007, Saai 2010], et sur un oligocrystal d'aluminium [Badulescu 2011], la singularité réside ici dans le fait que l'objet de celle-ci est un véritable polycrystal, i.e. contenant plus de 1700 grains en surface. Cela nous permet simultanément une étude des mécanismes de plasticité locaux ainsi que les effets de structure associés.

Partie II

Essai et matériau

Le cas traité au sein de cette étude, issue de [Bodelot 2008], est un essai de traction monotone piloté en déplacement jusqu'à une contrainte nominale de 270MPa et une déformation axiale de 2.5%. La vitesse de déformation est de $5\text{x}10^{-3}$ s^{-1} conduisant à une variation moyenne de température au cours de l'essai de $\approx 1^{o}C$. L'échantillon étudié est une éprouvette d'acier inoxidable AISI 316L traité thermiquement afin d'obtenir une taille de grain de $118\mu m$ en moyenne au sein de la zone utile de l'éprouvette.
Différentes mesures sont effectuées:

- une mesure couplée de champs cinématiques et thermiques in-situ : les champs visibles et infrarouges sont obtenues simultanément, sur la même face de l'éprouvette et cela tout au long de l'essai à des résolutions conformes à celle de la microstructure.

- une mesure d'orientation cristalline E.B.S.D. après essai : l'analyse met en évidence $\approx$1700 grains en surface dont le diamètre varie entre 20 et $800\mu m$. 80% de la surface étudiée contient

des grains dont la surface est supérieure à la résolution des imageurs et notamment 20 grains ont un diamètre supérieur à $400\mu m$ ce qui permet d'envisager une analyse intragranulaire fine des champs thermomécaniques. En outre, le matériau n'est pas texturé mais montre cependant un gradient de taille de grain de part et d'autre de la zone utile probablement dû à la trempe.

- une mesure profilométrique de la topographie de surface après essai : le matériau, initialement polit au micron met en évidence après essai des gradients de déplacements hors plan de l'ordre de $20\mu m$ ce qui traduit une forte activité de la surface libre. Cette topographie est clairement associée à la microstructure et révèle notamment d'importants sauts de déplacements aux joints de type Σ_3 qui représentent en outre 57% des joints de grains au sein de la zone utile.

- une mesure de micrographie de surface après essai : un outil automatique de détection de bandes de glissement ainsi que des systèmes de glissement associés est mis au point spécifiquement pour étudier ce type de micrographie. Il se base sur la transformée de Radon et l'identification intragranulaire de l'orientation ainsi que de la densité des lignes de glissement. Au travers de cet outil, la surface met en évidence une forte hétérogénéité liée à la densité de bandes de glissement ce qui traduit un champ de déformation tout aussi hétérogène. On note que certaines régions mettent en évidence une densité de bandes de glissement relativement très faible. La microstructure montre principalement du glissement simple et double (57% et 29%) ce qui traduit une déformation finale se situant entre le stade I et II.

Techniques de mesure et métrologie

Les données correspondant aux mesures de champs visibles et infrarouges issues de la thèse de L. Bodelot [Bodelot 2008] sont reprises dans leur état brute et une stratégie de calibration et de traitement est proposée.

Concernant les données infrarouges, une calibration pixel à pixel en flux est effectuée de manière à pouvoir considérer l'émissivité effective du corps noir étalon et celle de l'éprouvette. La réponse de chaque detecteur en fonction du flux thermique émis par le corps noir est approchée par des fonctions polynomiales d'ordre 6 dans la gamme 405 - 465 $W.mm^{-3}$. Une incertitude de mesure inférieure à 30 mK est mise en évidence pour une résolution spatiale limitée à $90\text{x}90\mu m^2$ (3x3 pixels) ainsi qu'une fréquence temporelle limitée à 25Hz.
Une décomposition du flux thermique émis par l'éprouvette afin de remonter à une calibration locale de la température est proposée. Elle repose sur l'hypothèse que ce flux, en condition de non chargement, peut être décomposé de manière additive en un flux basse fréquence et fixe dans le repère de la caméra lié aux éventuelles réflexions ainsi qu'en un flux haute fréquence et fixe dans le repère de l'éprouvette lié aux variations d'émissivité locales. Ce dernier est associé au revetement apposé sur l'éprouvette afin de permettre l'utilisation d'outils de corrélation d'images. Une cartographie initiale du champ d'émissivité est identifiée et permet d'approcher plus finement les champs thermiques tout au long de l'éssai, considérant donc que celle-ci reste constante dans des conditions de faibles déformations et faibles variations de température.

Correli^{Q4} [Hild 2008] est utilisé pour remonter aux champs cinématiques. Des fenêtres de corrélation de 16x16 pixels sont choisies conduisant à une résolution cinématique de 104x104μm^2 ainsi une incertitude de mesure de 4x10$^{-2}\mu m$. La fréquence d'acquisition est de 7hz. Les champs de déplacement ainsi obtenus permettent de remonter aux champs de température dans la configuration lagrangienne.

Finalement, l'ensemble des champs cinématiques et thermiques sont interpolés en espace à la résolution de la cartographie EBSD de l'éprouvette et en temps à la fréquence du signal thermique. L'ensemble des données, cartogaphie EBSD après essai, champs cinématiques et thermiques in-situ sont par conséquent exprimés dans la configuration lagrangienne, et recallés en temps et en espace.

Partie III

Projections de champs fondées sur la cristallographie

Une voix originale dans le traitement et l'interprétation des champs cinématiques et thermiques est introduite.

Elle consiste en une projection grain à grain des champs in-situ à l'aide des données cristallographiques en surface du matériau. Une minimisation au sens des moindres carrés est effectuée grain par grain sur une base polynomiale d'ordre 2 permettant une première approche mésoscopique des phénomènes intragranulaires. L'ordre 2 en déplacement est choisi de manière à identifier une déformation intragranulaire de type bilinéaire, conforme à une hypotèse mésoscopique de glissement simple. L'ordre 2 en température est choisi de manière à identifier des sources thermiques constantes par grain, ce qui est associé à un hypothèse d'instantanéité de la conduction intragranulaire.

Il est montré, respectivement en déplacement et en température, que 95% et 75% des champs projetés entrainent un résidu, par rapport aux champs initiaux, inférieur aux incertitudes de mesures précédement décrites. Il est aussi montré que le résidu ne se concentre pas aux joints de grains, comme on aurait pu le craindre, ce qui confirme par ailleurs la légitimité d'imposer un degré de liberté cinématique et thermique aux joints de grains. Thermiquement, il est montré que le résidu est globalement stationnaire durant l'essai ce qui permet de supposer qu'une telle projection affine le travail déjà opéré par la calibration au travers de la cartographie d'émissivité.

Finalement, la projection permet l'expression analytique des champs de déplacement et température et de leurs dérivés, déformations et flux, ainsi que l'analyse de sauts de déplacement et de température aux joints de grains [Kapitza 1941].

Analyse expérimentale des couplages thermomécaniques

Les moyennes des champs de déplacement et de température sont analysées au sein de la zone utile de l'éprouvette.

Trois phases sont alors mises en évidence: (1) une relation linéaire existe entre les différentes quantités et la température décroit, (2) La micro-anélasticité se développe et conduit à une diminution du refroidissement. Cela se traduit par une inflexion de la température, (3) L'éprouvette subit un réchauffement global dû en partie à la plasticité macroscopique. Il est montré que l'inflexion thermique permet une estimation pertinente du seuil de plasticité macroscopique, vu comme le début des phénomènes inélastiques et dissipatifs. Ceci est en accord avec les travaux de Lee [Lee 1991] et semble montrer que la température atteint un minimum pour une déformation permanente de $3\text{x}10^{-4}$.

Les champs sont ensuite analysés au cours de l'essai.

Les couplages thermomécaniques sont observés et un scénario de localisation est proposé. Il est observé de 0 à 220 MPa (soit pour $\sigma < R_e^{0.2\%}$), que le champ de température de surface est associé à de fortes contractions dans la direction transverse à la direction de sollicitation. De tels contractions sont notamment observées dans les régions où la taille de grain est statistiquement plus faible.
De 220 MPa à la fin de l'essai, les micro-localisations thermiques migrent vers une localisation macroscopique de la température. Celle-ci est visiblement associée à un ensemble de grains où la déformation axiale est très importante (>5%).

Ces observations mettent en évidence l'aptitude de tels mesures à renforcer la connaissance des micro-mécanismes de déformation au sein des polycrystaux et des matériaux hétérogènes en général.

Ecoulement plastique intragranulaire

Différents grains de taille millimétrique sont analysés. Les champs cinématiques, thermiques, profilométriques ainsi que les densités intragranulaires de bandes de glissement sont étudiés de manière à établir un scénario de propagation intragranulaire de la plasticité.

L'inflexion intragranulaire des champs de température est identifiée en chaque pixel des grains de manière à identifier une cartographie spatio-temporelle de celle-ci. Elle permet d'identifier avec précision les zones où les phénomènes dissipatifs débutent puis la manière dont le front d'inflexion se propage au sein de la matière. Ces mesures thermiques sont en accord avec les micrographies de surface faites après essai dans lesquelles on peut identifier les systèmes qui se sont activés au cours de la déformation ainsi que leur localisation au sein du grain. Un lien fort est mis en évidence entre la topographie de surface est le front de propagation thermique. Il nous éclaire sur la connection entre mécanismes de plasticité, hétérogénéité dissipative temporelle et topographie de surface.

En parallèle, l'orientation des isovaleurs de déformation de cisaillement au cours de l'essai permet de suivre l'activation des différents systèmes. Cette information est corrélée à la fois à la thermique et à la théorie de Schmid au travers de la connaissance à posteriori des systèmes activés.

Finalement, la confrontation de ces différentes informations ainsi que l'hypothèse selon laquelle l'inflexion thermique est associée au début de la plasticité permet d'identifier un seuil de plasticité

local ainsi que la contrainte critique résolue associée ($CRSS$). L'éprouvette met statistiquement en évidence une contrainte résolue critique de ≈30 MPa au sein de 165 grains, ce qui est en accord avec des études menées sur monocristaux [Feaugas 2009]

Bilan d'énergie expérimental

Une approche homogeneisée a d'abord été étudié afin d'estimer la partition globale entre l'énergie dissipée et stockée au sein de l'éprouvette et au cours d'une déformation de 2.5%. La zone utile de l'éprouvette stocke 1.8 mJ.mm^{-3} ce qui représente ≈30% de l'énergie anélastique de déformation. Environ 70% de cette énergie est stoquée dans l'écrouissage tandis que le reste est associé à des contraintes résiduelles (incompatibilités de déformations). Ces résultats sont cohérents avec des résultats issus de [Oliferuk 1995, Oliferuk 2009]. Une première conclusion est que plus les grains sont gros, plus la part de stockage dans l'écrouissage intragranulaire est importante relativement à celle associée aux contraintes résiduelles. Finalement, une relation linéaire entre énergie stockée et le carré de contrainte nominale est confirmée.

Dans un second temps, une approche locale est étudiée. Cette approche est basée sur une hypothèse de contraintes planes, d'une relation linéaire, en plasticité macroscopique, entre la déformation plastique est la contrainte nominale et de conditions adiabatiques. Il est montré, dans ces conditions, que l'énergie stockée locale est jusqu'à 7 fois supérieure à sa valeur moyenne au sein de la zone utile de l'éprouvette. L'analyse du ratio de l'énergie stockée sur l'énergie anélastique totale met en évidence 2 comportement au sein du matériaux. (1) Un faible niveau de stockage (<15%) est observée dans 30% des grains tandis que le reste de l'éprouvette stocke environ à hauteur de 50%. Ces comportements ont pu dans certains cas être confirmés par les densités de bandes de glissement observées en surface de l'éprouvette après essai.
La variation locale de le proportion de stockage ainsi que l'augmentation progressive de la quantité de grain stockant de plus en plus d'énergie au cours de la déformation est en relation avec la valeur du ratio moyen. Il met en évidence que celui-ci est bien plus le reflet d'un état de localisation global qu'un indicateur intrinsèque du niveau de stockage local.
Finalement, les joints de grains de type Σ_3 semblent dans de nombreux cas localiser plus fortement le stockage. Ceci est lié aux incompatibilités.

Finalement, l'estimation du laplacien 2D de la température est présentée et ses incohérences en termes de niveaux locaux sont analysées. 3 hypothèses sont investiguées : (1) l'impact de la décorrélation entre le traitement spatial et temporel des champs de température, (2) l'impact du terme du laplacien dans la direction hors plan et (3) l'aptitude de l'équation couplée de la chaleur dans le cadre de la thermomécanique des milieux continues à étudier un champ de température discontinu.

Partie IV

Des modélisations basées sur des mesures de champs

Deux modélisations élements finis sont développées. Elles reposent toutes les deux sur la même microstructure ainsi que sur les mêmes conditions aux limites mais intégrent un comportement différent. La géométrie 3D ($2D^{\frac{1}{2}}$) correspond à celle de la zone utile ($5x5mm^2$) de l'éprouvette étudiée et la microstructure provient d'analyses EBSD de surface. La géométrie contient 1776 grains extrudés. Le maillage est régulier en surface et progressif selon l'épaisseur. Il correspond à la résolution de la cartographie EBSD, i.e. 20x20x(80, 300, 620)μm^3. Le modèle impose, en outre, la continuité cinématique aux joints de grains.
Les conditions aux limites correspondent, en déplacement et en température, à celles mesurées expérimentalement tout au long de l'essai (conditions de dirichlet) et sont extrudées selon l'épaisseur. Ensuite les échanges convectifs entre l'air et la surface de l'éprouvette sont modélisés au travers d'une constante de convection.

Deux lois de comportement sont implémentées : (1) la première modélise la distribution d'orientations cristallines à l'aide d'une distribution de seuils de plasticité au sens de von Mises. Ensuite un comportement thermo-élasto-plastique incluant un écrouissage cinématique linéaire est introduit. (2) le suivant, plus proche des véritables mécanismes, utilise un cadre de plasticité cristalline. La loi de comportement prend en compte la véritable orientation cristalline de chaque grain et repose sur un écrouissage non linéaire function de l'évolution des densités de dislocations. Finalement, un couplage thermomécanique faible est introduit.
Les deux lois sont implémentées au sein d'une User's MATerial dans le code calcul ABAQUS.

Champs thermomécaniques numériques

Dans un premier temps, les quantités moyennes sont analysées. Un bon accord entre les deux modèles et les données expérimentales est observé quant aux quantités cinématiques, thermiques ainsi que la contrainte nominale.

Ensuite, les champs numériques et expérimentaux sont confrontés.
Premièrement, des localisations de déformation semblables entre les deux modèles et cohérentes avec les champs expérimentaux sont observées. Le modèle à dislocations montre toutefois de meilleurs résultats notamment concernant les déplacements hors plan qui sont en accord avec la topographie de surface observée sur l'éprouvette après essai.
Deuxièmement, les champs numériques de température sont en parfait accord avec ceux observés sur éprouvette. Un écart inférieur à 10% entre les champs est mis en évidence. Par ailleurs, la présence d'une localisation thermique précoce semblable à celle observée expérimentalement est mise en évidence. Celle-ci prend nécessance dans le même ensemble de grains, validant ainsi les observations expériementales ainsi que l'origine mécanique de celle-ci. Les mêmes observations sont faites quant aux régions relativement plus froides.

finalement, les champs de contrainte numériques sont analysés. On observe une claire connection entre ces champs de contrainte, inobservables experimentalement, et les champs de température de surface, notamment, des micro-localisations de température associées à des concentrations de contraintes

Ces observations permettent en conclusion de mettre en évidence l'aptitude des champs de température de surface, observés à la bonne échelle, à décrire les mécanismes de micro-déformation ainsi que les localisations de contraintes.

Bilans d'énergies numériques

Dans un premier temps, une démarche homogénéisée est présentée.
Le modèle à dislocation montre un stockage de ≈13% supérieur à celui observé expérimentalement. Cette augmentation est principalement associée au stockage liée à l'écrouissage intragranulaire. Cela semble indiquer qu'une meilleure identification des paramètres d'écrouissage doit être menée. Il est en outre montré que l'aire complémentaire à la courbe contrainte déformation correspond effectivement à l'énergie stockée dans les contraintes residuelles [Oliferuk 2009]. Finalement, les conditions aux limites de type Dirichlet sont analysées et des conditions aux limites en flux thermiques sont proposées afin de corriger l'impact de la température expérimentale aux bords du modèle sur les températures calculées au sein de celui-ci à partir de la loi de comportement.

Dans un second temps, un bilan d'énergie numérique est mené sur les champs de la même manière que celui réalisé classiquement expérimentalement. La spécificité réside ici dans le fait que toutes les quantités nécessaires au bilan d'énergie sont connues. On observe alors que l'énergie stockée dans les contraintes résiduelles est localisée aux joints de grains. Elle semble donc être un indicateur pertinant de la localisation de la déformation. Elle est en outre largement supérieure en amplitude à l'énergie stockée dans l'écrouissage, mais cependant beaucoup plus localisée. Cela démontre notamment que l'étude de sa valeur moyenne est insufisante dans le cadre d'analyses fines puisque relativement très faible en valeur. L'énergie stockée dans l'écrouissage intragranulaire semble à contrario ne pas représenter les localisations structurelles. Il est relativement similaire de grain à grain et varie entre 1 et 5 $mJ.mm^{-3}$. Ceci doit cependant être interprété au regard des choix de modélisation qui ne prennent pas en compte l'impact d'une plasticité non locale et de densités de dislocations géométriquement nécessaires.

Finalement, le ratio entre énergie stockée et énergie de déformation plastique est analysé. Il varie de 0 à 70% au sein de la microstructure. Ceci confirme les observations expérimentales mettant en évidence que ce ratio n'est ni une constante matériaux ni une quantité négligeable au sein du bilan d'énergie.

Conclusions générales

Différents développements ont été menés afin d'utiliser au mieux les mesures de champs cinématiques et thermiques dans le cadre de l'analyse des couplages thermomécaniques au sein des polycristaux soumis à de faibles niveaux de déformation. De nombreuses analyses ont été menées afin d'approfondir la compréhension des micro-mécanismes de déformation ainsi que leurs signatures thermiques. Enfin, une modélisation de l'agrégat étudié a été présentée et permet de confirmer les observations expérimentales et enrichit la compréhension de certains phénomènes.

A court terme, de nombreuses analyses des mécanismes élementaires doivent être menées sur monocristaux et bi-crystaux afin de confirmer de nombreuses observations, telles que l'effet Kapitza. En outre des essais à rupture doivent être menés. Du point de vue modélisation, l'implémentation d'un écrouissage cinématique permettant l'analyse de sollicitations cycliques doit être envisagé.

A moyen terme, la modélisation des joints de grains semble être cruciale. Les mesures de champs stéréoscopiques semblent être une évolution nécessaire dans l'étude du tenseur de déformation intragranualaire et en outre le bilan d'énergie intégrant des sauts de déplacement et de température doit être envisagé.

Appendices

Appendix A

A dissipative framework for the metals

The purpose of this appendix is to evidence the link between temperature, dissipation, and heat through the heat equation. As the experimental estimation of a "mesoscopic" mechanical dissipation is not direct, an adapted technic consists in the infrared thermography which supposes to separate the different heat sources [Boulanger 2004a, Chrysochoos 1989b]. This requires to precise a relevant thermodynamic framework.

A.1 Continuum thermodynamics

A practical framework for the thermomechanical study of the deformation of continuum media is the Continuum Thermodynamics and in the present case the Thermodynamics of Irreversible Processes. Many references synthesize this framework and its hypothesis. One can cite [Maugin 1992, Nguyen 2000, Besson 2003, Lemaitre 2009].

Let consider a domain Ω with a boundary denoted $\partial\Omega$ of a continuum media. Let E be its internal energy and e its specific internal energy defined as :

$$E = \int_{\Omega} \rho \cdot e \cdot dV,$$

K is its kinetic energy :

$$K = \frac{1}{2} \int_{\Omega} \rho \cdot \vec{v} \cdot \vec{v} \cdot dV$$

and Q the heat quantity received by Ω :

$$Q = \int_{\Omega} r \cdot dV - \int_{\partial\Omega} \vec{q} \cdot \vec{n} \cdot ds \tag{A.1}$$

The first term of the right of this last expression corresponds to the heat quantity created in Ω and the second term to the heat quantity received by conduction through the boundary $\partial\Omega$. Let $P_{(x)}$ be the power brought by external forces :

$$P_{(x)} = \int_{\Omega} \vec{f} \cdot \vec{v} \cdot dV - \int_{\partial\Omega} \vec{q} \cdot \vec{n} \cdot ds$$

With the previous notations, on one hand, the first principle of thermodynamics can be classicaly writen as follow :

$$\frac{d}{dt}(E+K) = P_{(x)} + Q$$

On the other hand, the work-kinetic energy theorem stipulates that :

$$\frac{dK}{dt} = P_{(x)} + P_{(i)}$$

where $P_{(i)}$ is the power brought by internal forces of Ω. The first principle can be then written as:

$$\frac{d}{dt}(E) = -P_{(i)} + Q$$

By defining a volumic power brought by internal forces of Ω, $p_{(i)}$

$$P_{(i)} = \int_{\Omega} p_{(i)} \cdot dV$$

a local form of the first principle can be obtained by applying the Ostrogradsky theorem on the equation (A.1) :

$$\rho \cdot \dot{e} = -p_{(i)} + r - div\,(\vec{q}) \tag{A.2}$$

By using the same notations and equation (A.1), the second principle of thermodynamics can be stated as:

$$\frac{dS}{dt} \geq \int_{\Omega} \frac{r}{T} dV - \int_{\partial\Omega} \frac{\vec{q}\cdot\vec{n}}{T} dS$$

Assuming the existence of an entropy specific density s such as :

$$S = \int_{\Omega} \rho \cdot s \cdot dV,$$

one can find the local expression of the second principle

$$\rho \cdot \frac{ds}{dt} + div\left(\frac{\vec{q}}{T}\right) - \frac{r}{T} \geq 0 \tag{A.3}$$

Combining equations (A.2) and (A.3), one can obtain the following inequality :

$$\rho \cdot \left(T\frac{ds}{dt} - \frac{de}{dt}\right) - p_{(i)} - \frac{\vec{q}}{T} \cdot \vec{grad}(T) \geq 0 \tag{A.4}$$

The function Ψ is defined as the specific free energy. This is the Legendre transformation of the internal energy e versus s :

$$\Psi = e - Ts \ , \ \Psi = \Psi(T, \boldsymbol{\alpha_j}) \tag{A.5}$$

where the $\boldsymbol{\alpha_j}$, $(j = 1, 2, \ldots, n)$ are the complementary internal state variables. One can easily deduce:

$$s = -\frac{\partial \Psi}{\partial T} \tag{A.6}$$

and

$$\frac{d\Psi}{dt} = \frac{\partial \Psi}{\partial T}\dot{T} + \frac{\partial \Psi}{\partial \boldsymbol{\alpha_j}}\dot{\boldsymbol{\alpha}}_{\boldsymbol{j}} \ , \ (j = 1, 2, \ldots, n) \tag{A.7}$$

Then, by using the equation (A.5), the inequality (A.4) becomes the *Clausius Duhem* inequality:

$$-\rho \cdot \frac{\partial \Psi}{\partial \boldsymbol{\alpha_j}}\dot{\boldsymbol{\alpha}}_{\boldsymbol{j}} - p_{(i)} - \frac{\vec{q}}{T} \cdot \vec{grad}(T) \geq 0 \ , \ (j = 1, 2, \ldots, n) \tag{A.8}$$

The next interesting step in this framework consists in the expression of the local coupled thermal equation. As e is defined as a function of Ψ, T and s (see equation (A.5)), using the relations (A.6) and (A.7), one can write the following relation

$$\begin{aligned} \frac{de}{dt} &= \frac{d\Psi}{dt} + T\frac{ds}{dt} + s\dot{T} \\ &= \frac{\partial \Psi}{\partial T}\dot{T} + \frac{\partial \Psi}{\partial \boldsymbol{\alpha_j}}\dot{\boldsymbol{\alpha}}_{\boldsymbol{j}} + T\left(\frac{\partial s}{\partial T}\dot{T} + \frac{\partial s}{\partial \boldsymbol{\alpha_j}}\dot{\boldsymbol{\alpha}}_{\boldsymbol{j}}\right) - \frac{\partial \Psi}{\partial T}\dot{T} \\ &= \frac{\partial \Psi}{\partial \boldsymbol{\alpha_j}}\dot{\boldsymbol{\alpha}}_{\boldsymbol{j}} - T\left(\frac{\partial^2 \Psi}{\partial T^2}\dot{T} + \frac{\partial^2 \Psi}{\partial \boldsymbol{\alpha_j}\partial T}\dot{\boldsymbol{\alpha}}_{\boldsymbol{j}}\right) \end{aligned} \tag{A.9}$$

Therefore the expression of the local coupled thermal equation derived directly of the local form of the first principle (A.2) :

$$\begin{aligned} \rho \cdot \dot{e} &= -p_{(i)} + r - div\,(\vec{q}) \\ &= \rho \cdot \left(\frac{\partial \Psi}{\partial \boldsymbol{\alpha_j}}\dot{\boldsymbol{\alpha}}_{\boldsymbol{j}} - T\left(\frac{\partial^2 \Psi}{\partial T^2}\dot{T} + \frac{\partial^2 \Psi}{\partial \boldsymbol{\alpha_j}\partial T}\dot{\boldsymbol{\alpha}}_{\boldsymbol{j}}\right)\right) \ , \ (j = 1, 2, \ldots, n) \end{aligned}$$

By using the conduction equation :

$$\vec{q} = -\boldsymbol{K} \cdot \vec{grad}(T),$$

and using the specific massic heat $C_v = -T\dfrac{\partial^2 \Psi}{\partial T^2}$ and deducing from the virtual power principle in the context of small perturbations that $p_{(i)} = -\boldsymbol{\sigma} \cdot \dot{\boldsymbol{\varepsilon}}$, one can obtain the local coupled thermal equation :

$$\begin{aligned} \rho C_v \dot{T} = \ & r + div(\boldsymbol{K} \cdot \vec{grad}(T)) \\ & + \left(\boldsymbol{\sigma} : \dot{\boldsymbol{\varepsilon}} + \rho T \frac{\partial^2 \Psi}{\partial T \partial \boldsymbol{\alpha_j}}\dot{\boldsymbol{\alpha}}_{\boldsymbol{j}} - \rho \frac{\partial \Psi}{\partial \boldsymbol{\alpha_j}}\dot{\boldsymbol{\alpha}}_{\boldsymbol{j}}\right) \ , \ (j = 1, 2, \ldots, n) \end{aligned} \tag{A.10}$$

It seems interesting to underline that this expression (A.10) is completely independant of the choice of a constitutive law. In the case of no coupling between the mechanical and thermal material

behaviours, the previous expression is the classical heat equation : the heat quantity ρC_v necessary to elevate the temperature of the considered solid is equal to the heat supply r arised by the conduction effects. In the case of the coupling, at the heat supply r is added mechanical heat sources, decomposed in a heat supply part $\boldsymbol{\sigma} : \dot{\boldsymbol{\varepsilon}}$, a stored part $-\rho\dfrac{\partial \Psi}{\partial \boldsymbol{\alpha}}\dot{\boldsymbol{\alpha}}$ and a thermomechanical term $\rho T\dfrac{\partial^2 \Psi}{\partial T \partial \boldsymbol{\alpha}}\dot{\boldsymbol{\alpha}}$.

A.2 The mesoscopic constitutive law

Two kind of state variable exist:

- observable variables which fully described a reversible system. This is the cas of T, the absolute temperature and ε, the global strain.
- internal variables which take into account the internal hystory of system. We assume here a simple additive partition of the total strain ε in an elastic part (reversible) ε^e and a plastic part (irreversible) ε^p

Based on this assumption, let us assume that the specific free energy Ψ only depends on T, $\boldsymbol{\varepsilon^e}$, $\boldsymbol{\varepsilon^p}$ and $p = \displaystyle\int_0^t \sqrt{\dot{\boldsymbol{\varepsilon}}^p : \dot{\boldsymbol{\varepsilon}}^p}dt$, the equivalent plastic strain. Thus:

$$\Psi = \Psi(T, \boldsymbol{\varepsilon^e}, \boldsymbol{\varepsilon^p}, p)$$

In addition, an isotropic hypothesis is taken for the R.E.V. (Representative Elementar Volume), so the thermal conduction tensor is equal to $\boldsymbol{K} = k \cdot \boldsymbol{I}$, where $\boldsymbol{I}$ corresponds to the isotropic identity fourth rank tensor, and the conduction equation becomes :

$$\vec{q} = -k \cdot \vec{grad}(T),$$

In this case, the equation (A.10) takes the following form

$$\begin{aligned} \rho C_v \dot{T} = \quad & r + k\Delta T + \left(\boldsymbol{\sigma} : \dot{\boldsymbol{\varepsilon}} + \rho T \frac{\partial^2 \Psi}{\partial T \partial \boldsymbol{\varepsilon^e}} \dot{\boldsymbol{\varepsilon^e}} - \rho \frac{\partial \Psi}{\partial \boldsymbol{\varepsilon^e}} \dot{\boldsymbol{\varepsilon^e}}\right) \\ & + \left(\rho T \frac{\partial^2 \Psi}{\partial T \partial \boldsymbol{\varepsilon^p}} \dot{\boldsymbol{\varepsilon^p}} - \rho \frac{\partial \Psi}{\partial \boldsymbol{\varepsilon^p}} \dot{\boldsymbol{\varepsilon^p}}\right) \end{aligned} \tag{A.11}$$

with ΔT is the Laplacian of temperature. As the associated thermodynamical forces of $\boldsymbol{\varepsilon_e}$ and $\boldsymbol{\varepsilon_p}$ are $\boldsymbol{\sigma}$ and $\boldsymbol{a}$, the following expression are obtained:

$$\boldsymbol{\sigma} = \rho \frac{\partial \Psi}{\partial \boldsymbol{\varepsilon^e}} \; ; \boldsymbol{a} = \rho \frac{\partial \Psi}{\partial \boldsymbol{\varepsilon^p}}$$

So finally, the heat coupled equation can be simplified as:

$$\rho C_v \dot{T} - r - k\Delta T = (\boldsymbol{\sigma} - \boldsymbol{a}) : \dot{\boldsymbol{\varepsilon^p}} + T\left(\frac{\partial \boldsymbol{\sigma}}{\partial T}\dot{\boldsymbol{\varepsilon^e}} + \frac{\partial \boldsymbol{a}}{\partial T}\dot{\boldsymbol{\varepsilon^p}}\right) \tag{A.12}$$

The first mechanical term $d_1 = (\boldsymbol{\sigma} - \boldsymbol{a}) : \dot{\boldsymbol{\varepsilon}^p}$ corresponds to the intrinsic dissipation and the two other terms $d_{Te} + d_{Tp} = T\left(\frac{\partial \boldsymbol{\sigma}}{\partial T}\dot{\boldsymbol{\varepsilon}^e} + \frac{\partial \boldsymbol{a}}{\partial T}\dot{\boldsymbol{\varepsilon}^p}\right)$ define the thermomechanical couplings, respectively thermoelastic denoted by d_{Te} and thermoplastic denoted by d_{Tp}. One can remark that those different dissipative terms correspond to mechanical heat sources.

In the case of metallic material which undergoes limited strains at room temperature, two additionnal assumptions could be done:

- In the case of traditionnal test, the external heat sources are absent and therefore $r = 0$.
- The stress tensor $\boldsymbol{a}$ is associated to the hardening law of the cristal and implicitely to the microstructural state of the material. While the temperatures induced by the loading are low, one can admit that the temperatures variations have no influence on this microstructural state and also on the $\boldsymbol{a}$ tensor. Therefore $T\frac{\partial \boldsymbol{a}}{\partial T}\dot{\boldsymbol{\varepsilon}^p} = 0$ and the thermoplastic dissipative term d_{Tp} can be neglected.

The heat equation becomes:

$$\rho C_v \dot{T} - k\Delta T = (\boldsymbol{\sigma} - \boldsymbol{a}) : \dot{\boldsymbol{\varepsilon}^p} + T\frac{\partial \boldsymbol{\sigma}}{\partial T}\dot{\boldsymbol{\varepsilon}^e} \tag{A.13}$$

Equation A.13 allows basically, integrating the desired term, to exhibit six interesting quantities:

$$E_{Hp} = \rho C_v \int\int \dot{T} \cdot dt \cdot dV \tag{A.14}$$

$$E_{Hl} = -k \int\int \Delta T \cdot dt \cdot dV \tag{A.15}$$

$$E_a = \int\int (\boldsymbol{\sigma} : \dot{\boldsymbol{\varepsilon}^p}) \cdot dt \cdot dV \tag{A.16}$$

$$E_b = \int\int (\boldsymbol{a} : \dot{\boldsymbol{\varepsilon}^p}) \cdot dt \cdot dV \tag{A.17}$$

$$E_c = \int\int d_1 \cdot dt \cdot dV \tag{A.18}$$

$$E_{the} = \int\int T\frac{\partial \boldsymbol{\sigma}}{\partial T}\dot{\boldsymbol{\varepsilon}^e} \cdot dt \cdot dV \tag{A.19}$$

$$\tag{A.20}$$

With E_{Hp}, E_{Hl}, E_a, E_s, E_c and E_{the} the heat energy produced during the whole test, the heat energy lost by conduction, the plastic work, the stored energy, the dissipated energy by heat and the energy of thermoelastic coupling respectivally. Notice the last term is also frequently noted E_{is} as isentropic energy. One could note that the energy balance achievement, notably at granular scale, means be able measure 3D temperature field T, total strain $\boldsymbol{\varepsilon}$ as well as the elastoplastic partition.

Appendix B

Digital Image Correlation (DIC)

A complete explanation of Digital Image Correlation and its applications could be found in [Schreier 2009].

To recover the displacement field of an image compared to a reference one, the picture is divided in sub square pictures, called Zone Of Interest (ZOI). Each sub picture must be found in deformed picture. The ZOI displacement corresponds to the bidimensionnal displacement of a gray level signal. Thus, the signal within the deformed ZOI, $g(x)$, corresponds to the reference signal, $f(x)$, subjected to a displacement $u(x)$, so $f(x-u(x))$. The optical flow is expressed as follows:

$$g(x) = f(x - u(x)) + b(x) \tag{B.1}$$

where $u(x)$ is a unknown bidimensionnal displacement, x the coordonnate vector et b the noise. It is generally neglected compared to the magnitude of f and g. Then, the procedure consists in the minimisation of F in the meaning of least square method, with F the norme of difference between $f(x-v)$ and $g(x)$ where v is a test displacement. It could be expressed as the following system:

$$\begin{cases} F(v) = \|g(x) - f(x-v)\|^2 \\ \min\limits_{v} [F(v)] \end{cases} \tag{B.2}$$

with $\|F(v)\|^2 = \int\limits_{-\infty}^{+\infty} |F(v)|^2 \cdot dx$, the quadratic norm, i.e:

$$\|F(v)\| = \int\limits_{-\infty}^{+\infty} |g(x) - f(x-v)|^2 \cdot dx \tag{B.3}$$

This function tends to it minimum, 0, without noise ($b(x) = 0$) when $v = u$. Practically, the minimisation problem detailed in equation B.2 is equivalent to the maximisation of a functionnal $\Phi(v) = g \bullet f$ compared to v. $g \bullet f$ is the intercorrelation product of functions f and g. It follows:

$$\min_{v} [F(v)] = \max_{v} [\Phi(v)] = \int\limits_{-\infty}^{+\infty} g(x) f(x-v) \cdot dx \tag{B.4}$$

The calcul of intercorrelation product B.4 is done in Fourier space using Fast Fourier Transform (FFT).

B.4 becomes finally:

$$\max_{v} \left[\Phi(v)\right] = \max_{v} \left[FFT^{-1}\left(FFT(g)\overline{FFT(f)}\right)\right] \tag{B.5}$$

where $\overline{A}$ means the conjugate complexe.

Appendix C

InfraRed Thermography (IRT)

The InfraRed thermography (IR) allows the measurement of radiative energy emitted by an object. Indeed, every body of which the temperature is higher than 0 K, emit an electromagnetic radiation. In the particular case of a so called, Black Body, i.e a body of which emitted radiation only depends on its temperature (it doesn't reflect any incident radiations), the radiative power per surface and wave length, also called spectral exitance, is given by the Planck's law:

$$M_{e\lambda}(\lambda, T) = \frac{2\pi hc^2\lambda^{-5}}{exp\left(\frac{hc}{\lambda kT}\right) - 1} \quad \text{in } W.m^{-3} \tag{C.1}$$

T = Absolute temperature of the blackbody in K h = Planck's constant (6.626x10^{-34} Js)
c = Speed of light (2.998x10^{8} ms^{-1})
k = Boltzmann's constant (1.381x10^{-23} JK^{-1})
λ = Wavelength in m

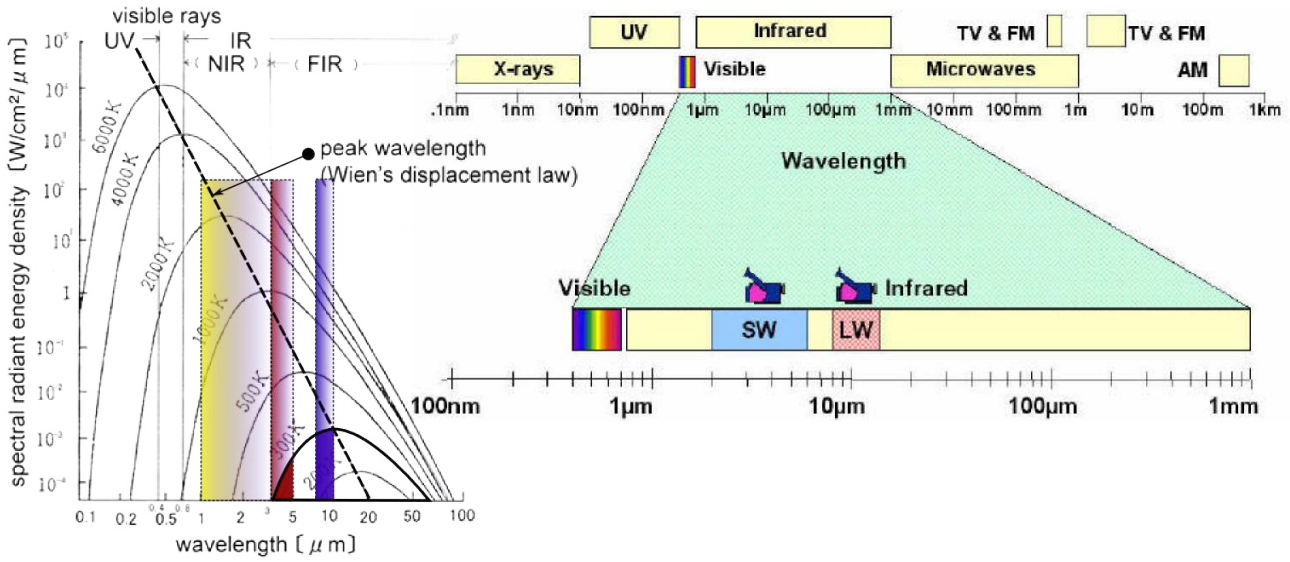

Figure C.1: Planck's law and electromagnetic spectrum

Figure C.1 shows the representation of the Planck's law for different temperatures from 200 to 6000 K (sun surface temperature), with in parallel the total electromagnetic spectrum. One could first note

that visible wave lengths only represent a small part of the total spectrum (from 0.4 to 0.8 μm). When wave lenghts increase and temperature decrease one crosses the infrared domain, in opposite, when wave lengths decrease and temperature rises, one crosses the ultraviolet domain. Three domains are colored on left picture and are also visible on right one. Theses domains are three ranges observed by existing IR cameras. One talks about three categories: Short Wavelenghts (SW) from 1 to 3 μm, Medium Wavelengths from 3 to 5 μm and Long Wavelengths (LW) from 8 to 12 μm. So depending on the temperature of the observed body or application, one has to choose the appropriate camera. One also understands, thanks to left picture, that it is currently not possible to observe the entire radiative spectrum of a body, notably at room temperature, i.e $\approx 300K$. Indeed, considering a body at $\approx 300K$, the left draw on picture C.1 shows that a Medium Wavelength camera capture $I = \int_{\lambda=3}^{5} (M_{e\lambda} \cdot d\lambda) \cdot S$ which corresponds to the red area, Long Wavelengths camera capture $I = \int_{\lambda=8}^{12} (M_{e\lambda} \cdot d\lambda) \cdot S$ which corresponds to the blue area and finally, Short Wavelenghts camera doesn't capture anything. S is the observed surface.

This observation underlines two important aspects of InfraRed Thermography:
• one does not measure temperature, one only measures a small part of radiative flux emitted by the body. Recover the thermal field passes necessary through a calibration procedure.
• the choice of IR camera must be leaded by researched informations, either the accuracy of thermal absolute value, or the accuracy of variation of temperature. Indeed in the case of mechanical tests where the temperature exhibits low variation around the room temperature, the MW and LW cameras will be very sensitive to thermal variation and absolute temperature respectively. This point is easily understandable regarding the red and blue area localization within 300 K in left picture C.1.

Let consider now, a "GreyBody", i.e. a body which absorbes only a part α of incident radiation, reflects only a part ρ and transmits a part τ. At thermodynamic equilibrium, energy conservation implies that the energy emitted by radiation, reflection and transmition to the external environnement be equal to absorbed energy. It leads to the following expression:

$$\alpha(\lambda) + \rho(\lambda) + \tau(\lambda) = 1 \tag{C.2}$$

Moreover, if the body is opaque, that is the case of any metallic specimen, one could assume that $\tau(\lambda) = 0$. Note ε the emission term which balance the absorbtion one α.

$$\rho(\lambda) = 1 - \varepsilon(\lambda) \tag{C.3}$$

with, $\varepsilon(\lambda)$ called the emissivity of the body. Equation C.3 allows finally establishing the form of the

apparent thermal flux Φ:

$$\Phi = \Phi_e + \Phi_r \quad (C.4)$$

$$= \varepsilon_{obj}\Phi_{obj} + (1 - \varepsilon_{obj})\Phi_{env} \quad (C.5)$$

where, Φ_e, Φ_r, ε_{obj}, Φ_{obj}, and Φ_{env} are the emitted flux, the reflected one, the emissivity of the body, its effective flux due to its own surfacic temperature and the flux radiated by the environnement due to the room temperature. Notice that this expression remains valid while the transmition properties of the atmosphere is equal to 1.

Integrating the Planck's law along wavelengths, it is then possible to establish the link between the effective flux of the body Φ_{obj} (in $W.mm^{-2}$) and its surfacic temperature. It is called the Stefan-Boltzmann law. Following it, the apparent thermal flux Φ takes the following form:

$$\Phi = \varepsilon_{obj}\sigma T^4 + (1 - \varepsilon_{obj})\Phi_{env} \quad (C.6)$$

where, σ is the Stefan-Boltzmann constant ($5.670400\text{x}10^{-8}\ Js^{-1}m^{-2}K^{-4}$) and T the absolute temperature of surface body.

This part underlines two other important aspects of InfraRed Thermography:
• the determination of the surfacic temperature of specimen passes through the knowledge of its emissivity. In the case of specimens which exhibits a variation of surfacic properties, i.e roughness for exemple, the unknown becomes an emissibity field. If one desires measure gradients of temperature at the same characteristic scale than surfacic "imperfections", the determination of the emissivity map becomes crutial. We will see that our study is exactly in this case. As numerous material properties are temperature dependent, one could ad that if the body temperature variation is important, the unknown becomes an emissibity field calibrated at different temperature. It is still a challenging problem for researcher how works on contact problem such as thermal analysis of hot spots within braking systems [Kasem 2010].
• The knowledge of the surfacic temperature also passes through the determination of reflections from environnement which could drastically affect the measurement, especially when the emissivity of the observed body deviates significantly from 1 (ex: aluminium). One proposes in chapter 2.1 a way to identify emissivity map as well as reflection one.

Appendix D

What about internal variables?

It has been shown that the measurement of relevant intragranular total strain and thermal fields and the estimation of a mean value per grain of the 2D thermal Laplacian which are the essential ingredient of a granular energy balance achievement, is possible. The relevance of the thermal and kinematic quantities compared to the plasticity mechanisms as well as the limits of a 2D temperature measurement in the estimation of its 3D Laplacian. For the complete achievement of energy balance, the estimation of stress or plastic strain field remains a challenging topic. Indeed in the basic formulation of the heat equation, one could underline three essential elements: the temperature field, the total strain field and the elasto-plastic partition in order to determine on the one hand, the stress field and on the other hand the plastic strain field.

The purpose of this very short section is to open a new way to an intragranular stress field measurement. Note that this part does not provide any results, but propose a comment on the ability to obtain granular stress fields when the granular total strain field as well as the grain orientation is known. Let us first try to summarize some techniques about the stress field measurement. Different non destructive methods could be considered:

- *Acoustic measurements*: the velocity of an acoustic wave which travels through a stressed solid depends on the strain state and hence the stress state of the solid. This dependence is known as the elastoacoustic effect. This technique was used for stress fields measurement in the case of uniaxial test in [Kino 1980].
- *XRD method* X ray method residual stress field.

These techniques take profits of the physical properties of plasticity, in term of atomistic lattice change during irreversible processes. Unfortunately, when one only knows the total strain tensor at the macroscale, its plastic part could not be easily determined. Nevertheless, when one access to the granular total strain field, its plastic part is characterized by the specific plane slip mechanisms, in particular directions[1], and these 2 parameters are known a priori and a posteriori:

1. a priori: the Schmid theory provides a good prediction of slip plane activity in F.C.C. structure which undergoes low strain levels ($<10\%$).
2. a posteriori: tools which have been developed during this work for the automatic determination of slip mark orientations and then slip system activities with the help of micrography of the

[1] more easily while only one slip system is activated

surface specimen performed after the test. E.B.S.D analysis permits then a good a posteriori determination of the granular slip system direction and orientation.

Let us partition the granular total strain tensor, noted here ε^g:

$$\varepsilon^g = \varepsilon^g_s + \varepsilon^g_d \tag{D.1}$$

with ε^g_s and ε^g_d the spheric and deviatoric part of the total granular strain tensor respectively. As plasticity is strain mechanism with no volume changes, we assume that ε^g_s could be noted ${\varepsilon_{\mathbf{e1}}}^g$. It is a part of total granular strain tensor which only contain elasticity. Equation D.1 becomes:

$$\begin{aligned} \varepsilon^g &= \varepsilon^g_{e1} + \varepsilon^g_d & \text{(D.2)} \\ &= \varepsilon^g_{e1} + \mathbf{P}_\alpha \tilde{\varepsilon}^g_d \mathbf{P}^T_\alpha & \text{(D.3)} \end{aligned}$$

with $\tilde{\varepsilon}^g_d$ the granular deviatoric strain tensor expressed in the slip system base $B_1(n,b,w)$, n the normal to the slip plane, b the slip direction, and w the vector which completes the direct orthonormal basis (see figure D.1). $\mathbf{P}_\alpha$ is the transformation matrix which permits to pass from B_1 to B_0, i.e. a combination of the α^{th} part of the Schmid tensor $\mathbb{D}^\alpha = \frac{1}{2}\left(n^\alpha \otimes b^\alpha + b^\alpha \otimes n^\alpha\right)$, α the activated slip system and the rotation matrix associated to the grain orientation $\mathbf{R}$.

$$\mathbf{P}_\alpha = R\mathbb{D}^\alpha \mathbf{R}^T \tag{D.4}$$

The granular deviatoric strain tensor expressed in B_0, $\tilde{\varepsilon}^g_d$ could finally be divided into two parts: $\tilde{\varepsilon}^g_{e2}$

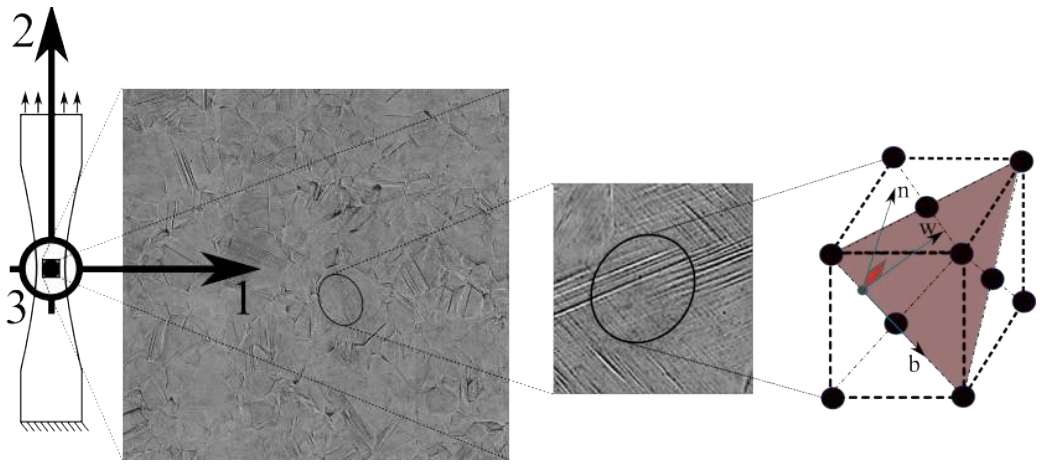

Figure D.1: Scale transition from polycrystal reference system $B_0(1,2,3)$ to the lattice and activated slip-system one $B_1(n,b,w)$

associated to the remaining elastic strain and $\tilde{\varepsilon}^g_p$ associated to the plastic part of strain tensor. The

total strain tensor takes finally the following form:

$$\varepsilon^g = \underbrace{\left[\varepsilon_{\mathbf{e1}}{}^g + P_\alpha \tilde{\varepsilon}^g_{e2} P^T_\alpha\right]}_{\varepsilon^g_e} + \underbrace{\mathbf{P}_\alpha \tilde{\varepsilon}^g_p \mathbf{P}_\alpha{}^T}_{\varepsilon^g_p} \tag{D.5}$$

with,

$$\begin{aligned} \tilde{\varepsilon}^g_d &= \tilde{\varepsilon}^g_{e2} + \tilde{\varepsilon}^g_p \\ \begin{bmatrix} a & b & c \\ d & e & f \\ g & h & i \end{bmatrix} &= \begin{bmatrix} a & 0 & c \\ 0 & e & f \\ g & h & i \end{bmatrix} + \begin{bmatrix} 0 & b & 0 \\ d & 0 & 0 \\ 0 & 0 & 0 \end{bmatrix} \end{aligned} \tag{D.6}$$

One assumes here that the plastic strain is activated in a known direction and on a known plane. Once the granular deviatoric strain tensor $\tilde{\varepsilon}^g_d$ is expressed in the relevant base B_0, regarding to plasticity mechanism, $\tilde{\varepsilon}^g_p$ could be reduced to shear stress in the (b,w) plane. If one denote $\mathcal{Z}$ a function which permits the additive decomposition of $\tilde{\varepsilon}^g_d$, the local plastic strain becomes:

$$\tilde{\varepsilon}^g_p = \mathcal{Z}\left(\tilde{\varepsilon}^g_d\right) \tag{D.7}$$

One could finally write the granular stress field as follow:

$$\sigma^g = \tilde{\mathbb{C}} : \varepsilon_e \tag{D.8}$$

$$= \tilde{\mathbb{C}} : \left[\varepsilon^g - \mathbf{P}_\alpha \mathcal{Z}\left(\tilde{\varepsilon}^g_d\right) \mathbf{P}_\alpha{}^T\right] \tag{D.9}$$

with $\tilde{\mathbb{C}}$ the elasticity matrix rotated in B_0 with the help of R and σ^g, the classical Cauchy stress field within the grain g. At intragranular scale, σ^g is consequently, a combination of the total granular strain tensor and its deviatoric part expressed through a ***structure tensor*** noted $\mathbf{P}_\alpha$.

This granular stress field determination is in the same spirit than the whole approach proposed within our works, i.e. by introducing additional information, notably about texture, within the analysis of the mechanical and thermal fields, and deals with quantities associated to a specific physics. In our opinion, the key is to consider the material, and the whole set of complementary informations to finally devide the complex material into independent subdomains which incorporate basic physic mechanisms of strain. This subdomain is, in first approach, the single crystal (grain).

Actually, one admits that the presented framework does not solve the problem of stress field determination but only changes the problem:

1. one assumes here that the stress field could be recovered only thanks to kinematic field measurements done with an appropriate spatial resolution and the knowledge of the microstructure as well as grain orientations. Nevertheless, the kinematic field measurement have to be done in 3 dimensions, in order to recover the full total granular strain tensor ε^g. Some tests have been done

in the present work in order to confirm the relevance of such approach. Nevertheless, we only have access to 2D total granular strain tensor. The complexity of the loading path, especially in elasticity (multiaxiality of deformation), does not permit to use some basic assumptions such as plane stress, or plane strain in order to complete unknown components of strain tensor. For that matter, it will be shown in the next chapter, thanks to a numerical approach, that we are not at all in theses basic kind of loading conditions.

2. an hypothesis of simple slip is taken. Indeed, while the grain is loaded by only one slip system, the ***structure tensor***, $\mathbf{P}_\alpha$ is relevant for the elasto-plastic partition. If the plastic activity is stopped on the α^{th} system and begins on the β^{th} one, one could build the associated ***structure tensor***, $\mathbf{P}_\beta$ which permits also solve the problem. Nevertheless, if two or more system are activated simultaneously, the Cauchy stress becomes a linear combination a different terms as:

$$\sigma^g = \tilde{\mathbb{C}} : \left[\varepsilon^g - a\mathbf{P}_\alpha \mathcal{Z}\left(\tilde{\varepsilon}_d^g\right) \mathbf{P}_\alpha{}^T + b\mathbf{P}_\beta \mathcal{Z}\left(\tilde{\varepsilon}_d^g\right) \mathbf{P}_\beta{}^T + \ldots + n\mathbf{P}_\lambda \mathcal{Z}\left(\tilde{\varepsilon}_d^g\right) \mathbf{P}_\lambda{}^T\right] \tag{D.10}$$

with coefficient (a, b, c, ldots, n) the effective part of plastic strain on associated shear strain components. There is not unicity of the solution, but under some additional assumptions, such a problem could be solve by optimization method.

Appendix E

Slip-system EXtraction (SLIPEX)

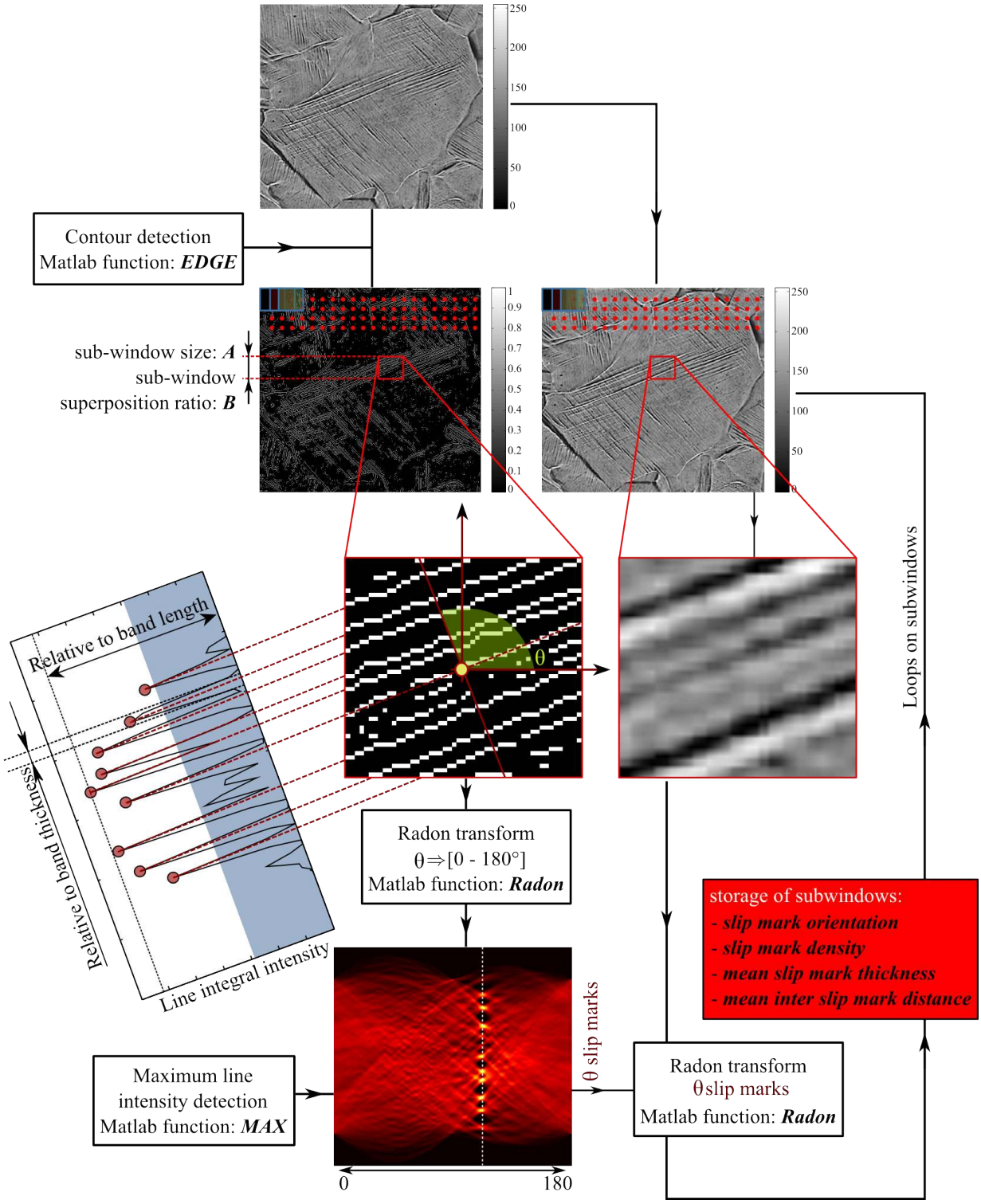
Contour detection
Matlab function: EDGE
sub-window size: A
sub-window
superposition ratio: B
Relative to band length
Relative to band thickness
Line integral intensity
θ
Radon transform
θ⇒[0 - 180°]
Matlab function: Radon
Maximum line
intensity detection
Matlab function: MAX
θ slip marks
0
180
Radon transform
θslip marks
Matlab function: Radon
storage of subwindows:
- slip mark orientation
- slip mark density
- mean slip mark thickness
- mean inter slip mark distance
Loops on subwindows

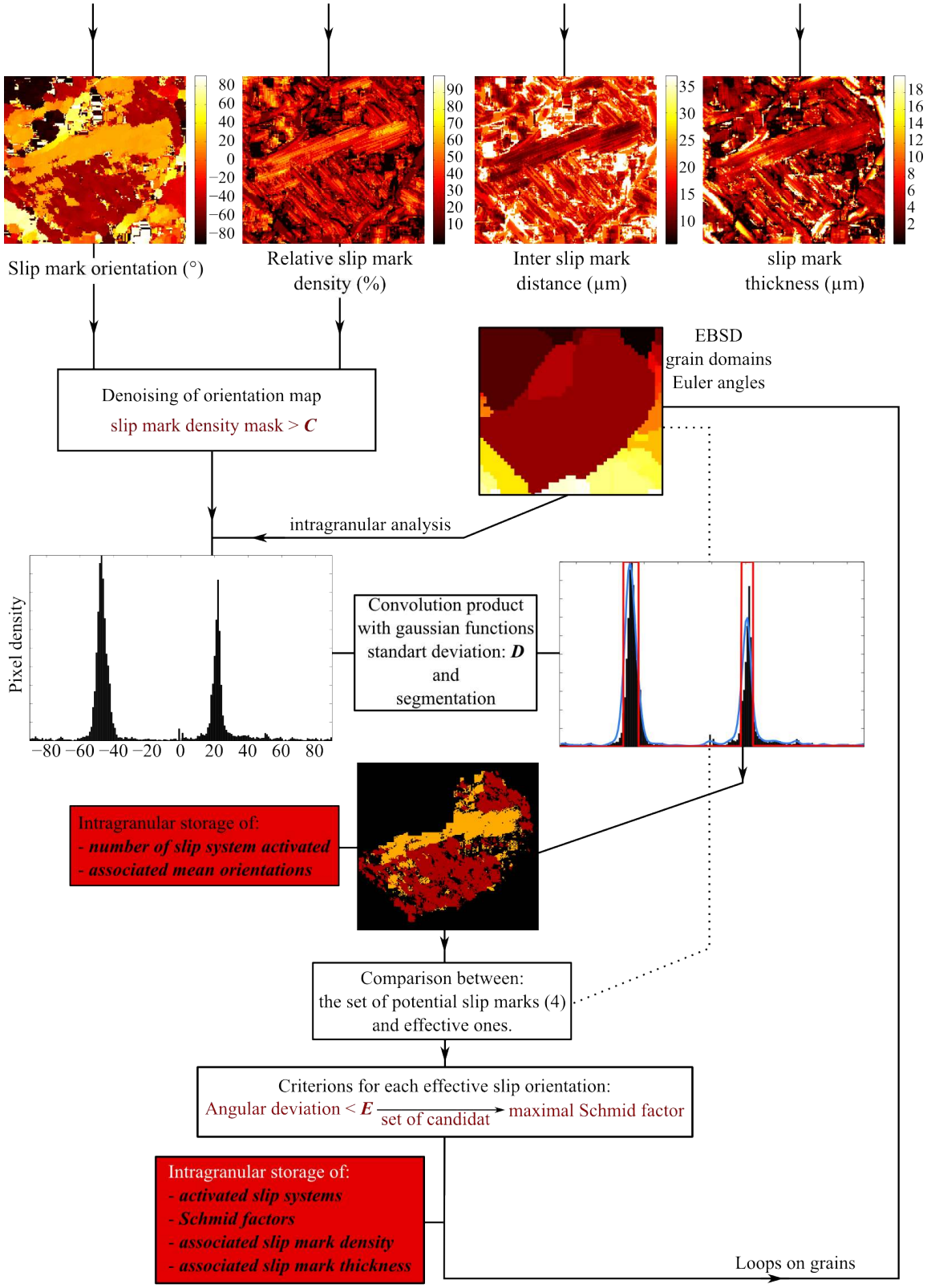
Slip mark orientation (°)
Relative slip mark density (%)
Inter slip mark distance (µm)
slip mark thickness (µm)
Denoising of orientation map
slip mark density mask > C
EBSD grain domains Euler angles
intragranular analysis
Pixel density
Convolution product with gaussian functions standart deviation: D and segmentation
Intragranular storage of:
- number of slip system activated
- associated mean orientations
Comparison between:
the set of potential slip marks (4) and effective ones.
Criterions for each effective slip orientation:
Angular deviation < E
set of candidat
maximal Schmid factor
Intragranular storage of:
- activated slip systems
- Schmid factors
- associated slip mark density
- associated slip mark thickness
Loops on grains

Appendix F

Crystal symmetry operators

Cubic crystalline lattice such as FCC or FC contain 24 symmetries related to 24 symmetry operators noted $\mathbf{O}_i$. It corresponds to:

- the identity
- the nine 90^o rotation about axis group <100>, i.e [100], [010], [001]
- the six 180^o rotation about axis group <110>, i.e [110], [101], [011], [$\bar{1}$10], [10$\bar{1}$], [0$\bar{1}$1]
- the eight 120^o rotation about axis group <111>, i.e [111], [$\bar{1}$11], [1$\bar{1}$1], [11$\bar{1}$]

$$\mathbf{O}_1 = \begin{pmatrix} 1 & 0 & 0 \\ 0 & 1 & 0 \\ 0 & 0 & 1 \end{pmatrix} \quad \mathbf{O}_2 = \begin{pmatrix} 1 & 0 & 0 \\ 0 & \bar{1} & 0 \\ 0 & 0 & \bar{1} \end{pmatrix} \quad \mathbf{O}_3 = \begin{pmatrix} 0 & 1 & 0 \\ 0 & 0 & 1 \\ 1 & 0 & 0 \end{pmatrix} \quad \mathbf{O}_4 = \begin{pmatrix} 0 & \bar{1} & 0 \\ 0 & 0 & \bar{1} \\ 1 & 0 & 0 \end{pmatrix}$$

$$\mathbf{O}_5 = \begin{pmatrix} \bar{1} & 0 & 0 \\ 0 & \bar{1} & 0 \\ 0 & 0 & \bar{1} \end{pmatrix} \quad \mathbf{O}_6 = \begin{pmatrix} 1 & 0 & 0 \\ 0 & 0 & 1 \\ 0 & \bar{1} & 0 \end{pmatrix} \quad \mathbf{O}_7 = \begin{pmatrix} 0 & 0 & \bar{1} \\ \bar{1} & 0 & 0 \\ 0 & 1 & 0 \end{pmatrix} \quad \mathbf{O}_8 = \begin{pmatrix} 0 & 1 & 0 \\ 1 & 0 & 0 \\ 0 & 0 & \bar{1} \end{pmatrix}$$

$$\mathbf{O}_9 = \begin{pmatrix} 0 & 0 & \bar{1} \\ 0 & 1 & 0 \\ 1 & 0 & 0 \end{pmatrix} \quad \mathbf{O}_{10} = \begin{pmatrix} 0 & \bar{1} & 0 \\ 1 & 0 & 0 \\ 0 & 0 & 1 \end{pmatrix} \quad \mathbf{O}_{11} = \begin{pmatrix} 0 & 0 & \bar{1} \\ 0 & 0 & 1 \\ \bar{1} & 0 & 0 \end{pmatrix} \quad \mathbf{O}_{12} = \begin{pmatrix} \bar{1} & 0 & 0 \\ 0 & 0 & 1 \\ 0 & 1 & 0 \end{pmatrix}$$

$$\mathbf{O}_{13} = \begin{pmatrix} \bar{1} & 0 & 0 \\ 0 & 1 & 0 \\ 0 & 0 & \bar{1} \end{pmatrix} \quad \mathbf{O}_{14} = \begin{pmatrix} \bar{1} & 0 & 0 \\ 0 & \bar{1} & 0 \\ 0 & 0 & 1 \end{pmatrix} \quad \mathbf{O}_{15} = \begin{pmatrix} 0 & 1 & 0 \\ 0 & 0 & \bar{1} \\ \bar{1} & 0 & 0 \end{pmatrix} \quad \mathbf{O}_{16} = \begin{pmatrix} 0 & 0 & 1 \\ 0 & \bar{1} & 0 \\ 1 & 0 & 0 \end{pmatrix}$$

$$\mathbf{O}_{17} = \begin{pmatrix} 0 & 0 & 1 \\ 0 & 1 & 0 \\ \bar{1} & 0 & 0 \end{pmatrix} \quad \mathbf{O}_{18} = \begin{pmatrix} 0 & 1 & 0 \\ \bar{1} & 0 & 0 \\ 0 & 0 & 1 \end{pmatrix} \quad \mathbf{O}_{19} = \begin{pmatrix} 0 & 0 & \bar{1} \\ 1 & 0 & 0 \\ 0 & 1 & 0 \end{pmatrix} \quad \mathbf{O}_{20} = \begin{pmatrix} 0 & \bar{1} & 0 \\ \bar{1} & 0 & 0 \\ 0 & 0 & \bar{1} \end{pmatrix}$$

$$\mathbf{O}_{21} = \begin{pmatrix} 1 & 0 & 0 \\ 0 & 0 & \bar{1} \\ 0 & 1 & 0 \end{pmatrix} \quad \mathbf{O}_{22} = \begin{pmatrix} 0 & 0 & 1 \\ 1 & 0 & 0 \\ 0 & 1 & 0 \end{pmatrix} \quad \mathbf{O}_{23} = \begin{pmatrix} 0 & 0 & 1 \\ \bar{1} & 0 & 0 \\ 0 & \bar{1} & 0 \end{pmatrix} \quad \mathbf{O}_{24} = \begin{pmatrix} \bar{1} & 0 & 0 \\ 0 & 0 & \bar{1} \\ 0 & \bar{1} & 0 \end{pmatrix}$$

Appendix G

Numerical implementations

G.1 Yield model

In order to perform numerical simulations based on the finite element (FE) method, Abaqus 6.5. commercial package is chosen along with its Abaqus/standard implicit solver. In this code, fully thermomechanical coupled calculations were introduced to solve forming processes problems where the variations of temperature are mainly leaded by plastic dissipation. Therefore thermoelastic coupling is not included in the code and the definition of the partition between dissipated and stored energies is relatively poor, basically based on the β_{int} ratio of Taylor and Quinney [Quinney 1937]. It is therefore necessary to implement the previous model as a User-defined stress update algorithm, denoted UMat in Abaqus and written in Fortran 77. At each loading increment and for each integration point, the FE code provides the mechanical quantities and the strain increment to the UMat which updates the stresses and all internal variables. Then the UMat computes the mechanical and thermal tangent moduli as well as the coupled moduli, and finally the thermal and plastic strain increments. This scheme introduces a non-symmetric jacobian matrix:

$$\begin{pmatrix} \mathbb{K}_{uu} & \boldsymbol{K}_{u\theta} \\ \boldsymbol{K}_{\theta u} & K_{\theta\theta} \end{pmatrix} \begin{Bmatrix} \Delta \underline{u} \\ \Delta T \end{Bmatrix} = \begin{Bmatrix} \underline{R}_u \\ R_\theta \end{Bmatrix} \tag{G.1}$$

where $\mathbb{K}_{uu}$, $\boldsymbol{K}_{\theta\theta}$, $\boldsymbol{K}_{\theta u}$, $K_{u\theta}$ denote the assembly of the local tangent stiffness [1]. Local tangent stiffness are defined in relations (G.2) (1, 2, 3, 4) respectively. Details about their calculation can be found in [Bodelot 2008].

$$\begin{cases} \dfrac{\partial \Delta \boldsymbol{\sigma}}{\partial \Delta \boldsymbol{\varepsilon}} &= \mathbb{C} - 2\mu \dfrac{\partial \Delta \boldsymbol{\varepsilon}^p}{\partial \Delta \boldsymbol{\varepsilon}} \\ \dfrac{\partial \Delta \boldsymbol{\sigma}}{\partial \Delta T} &= -3K\alpha \boldsymbol{I} \\ \dfrac{\partial \Delta \dot{\Phi}}{\partial \Delta \boldsymbol{\varepsilon}} &= (\boldsymbol{\sigma} - \boldsymbol{X}) \dfrac{\partial \Delta \boldsymbol{\varepsilon}^p}{\partial \Delta \boldsymbol{\varepsilon}} - \alpha T \boldsymbol{I} : \dfrac{\partial \Delta \boldsymbol{\sigma}}{\partial \Delta \boldsymbol{\varepsilon}} \\ \dfrac{\partial \Delta \dot{\Phi}}{\partial \Delta T} &= -9K\alpha^2 T \end{cases} \tag{G.2}$$

[1] Following the Abaqus notations, the different stiffness $\mathbb{K}_{uu}$, $\boldsymbol{K}_{\theta\theta}$, $\boldsymbol{K}_{\theta u}$, $K_{u\theta}$ corresponds to the assembly of the local tangent stiffness *DDSDDE*, *DDSDDT*, *DRPLDE*, *DRPLDT* for each integration point

The incremental form of the equations (6.8) and (6.15) are[2]:

$$\Delta\boldsymbol{\sigma} = \mathbb{C} : (\Delta\boldsymbol{\varepsilon} - \Delta\boldsymbol{\varepsilon}^p) - 3K\alpha\boldsymbol{I}\Delta T \tag{G.3}$$

$$\Delta\dot{\Phi} = (\boldsymbol{\sigma} - \boldsymbol{X}) : \frac{\Delta\boldsymbol{\varepsilon}^p}{\Delta t} - \alpha T \mathrm{tr}\left(\frac{\Delta\boldsymbol{\sigma}}{\Delta t}\right) - 9K\alpha^2 T\frac{\Delta T}{\Delta t} \tag{G.4}$$

In this incremental problem, the resolution consists in the determination of the plastic strain increment $\Delta\boldsymbol{\varepsilon}^p$ eventually induced by a firstly supposed purely elastic stress tensor increment. This plastic strain increment has then to verify the consistency condition (Kuhn-Tucker condition) and the normality rule, which are respectively written:

$$\begin{cases} \dot{f}(\boldsymbol{\sigma}) = 0 \\ \Delta\boldsymbol{\varepsilon}^p = \dot{\lambda}\dfrac{\partial f}{\partial\boldsymbol{\sigma}}\Delta t \end{cases} \tag{G.5}$$

The calculation of $\Delta\boldsymbol{\varepsilon}^p$ is here based on the radial return mapping method firstly developed by [Nguyen 1977] and [Simo 1985]. More details about this problem can be found in [Charkaluk 2006]. The proposed implementation is time implicit in displacement and time explicit in temperature and the coupled non linear system is solved by a Newton method.

G.2 Crystalline model

We will see in this section that behavior law equations constitute a differential system which needs to be integrate. At each iteration, time increment Δt as well as deformation gradient $\mathbf{F}$ are known, then the goal is to calculate the evolution of Cauchy stress σ and temperature T, as well as internal variables such as shear strain on each slip system (s) γ^s, the density of statistically stored dislocation (SSD) ρ^s and the lattice rotation matrix $\mathbf{R}$.

As, the crystal plasticity constitutive theory and its associated thermodynamic frameworks are not provided as standard in any of commercially available finite element analysis software, it is therefore necessary to implement the theory in the form of a User-defined stress update algorithm. We have defined a subroutine which uses the finite element code ABAQUS/standard, an implicit solver, written in Fortran 77. It implements the model in term of stress update algorithm which is called at each integration point, for each time increment during a finite element simulation.

The stress update algorithm use here the "rate-tangent modulus" scheme of [Peirce 1984] to derive the visco-elasto-plastic forward gradient modulus relating the increment of shear strain $\Delta\gamma^s$ on system s to those of Resolved Shear Stress (RSS) $\Delta\tau^s$ or Cauchy stress $\Delta\sigma$ and Critical Resolved Shear Stress (CRSS) τ_c^s. Finally, time integration scheme involved the solution of the non-linear equation G.10 for the incremental slip system shear strain using the Newton-Raphson method. Consequently, it constitutes a non-linear implicit equation as the increment of Resolved Shear Stress $\Delta\tau^s$, and current

[2]Following the Abaqus notations, $\Delta\dot{\Phi}$ correspond to RPL.

strengh τ_c^s are functions of $\Delta\gamma^s$.

We presents here main steps of non-linear system building.

G.2.1 Estimation of shear strain increment

One defines the increment of shear strain in slip system (s) within the time increment Δt by:

$$\Delta\gamma^s = \gamma^s_{(t+\Delta t)} - \gamma^s_{(t)} \tag{G.6}$$

Considering the **Mean value theorem** one could write: $\exists\theta \in [0,1]$ so $t+\theta\Delta t \in [t, t+\Delta t]$ such that:

$$\dot{\gamma}^s_{(t+\theta\Delta t)} = \frac{\gamma^s_{(t+\Delta t)} - \gamma^s_{(t)}}{(t+\Delta t) - t} \quad \Leftrightarrow \quad \Delta\gamma^s = \dot{\gamma}^s_{(t+\theta\Delta t)}\Delta t \tag{G.7}$$

and employing a linear interpolation for $\dot{\gamma}^s$ evolution within the small time increment Δt:

$$\Delta\gamma^s = \left((1-\theta)\,\dot{\gamma}^s_{(t)} + \theta\dot{\gamma}^s_{(t+\Delta t)}\right)\Delta t \tag{G.8}$$

The parameter θ ranges from 0 to 1. $\theta = 0$ and $\theta = 1$ corresponds to limits cases: the first one corresponds to a simple forward Euler time integration scheme. It is an explicit time integration scheme. The second represents backward integration (implicit formulation). Between both limits equation solution is approximate thanks to a linear interpolation at an intermediate state. Results presented in this document will use an intermediate θ parameter: $\theta = 0.5$. It leads to a good compromise between stability, robustness and accurancy since it corresponds to a minimum in term of approximation error.

At time t, $\dot{\gamma}^s_{(t)}$ is provided by the flow rule. The effective slip rate $\dot{\gamma}^s_{(t+\Delta t)}$ is approximate with the help of a first order Taylor expansion about the current state.

Abseil

first order Taylor expansion: case of 2 variables functions

considering $\underline{X} = (x, y)$, $\underline{A} = (a, b)$, $\nabla f(\underline{A})$ the gradient of f expressed in $\underline{A}$ and $H(\underline{A})$ the Hessienne's matrix expressed in $\underline{A}$:

$$H(\underline{A}) = \begin{pmatrix} \frac{\partial^2 f}{\partial x^2}(\underline{A}) & \frac{\partial^2 f}{\partial x \partial y}(\underline{A}) \\ \frac{\partial^2 f}{\partial y \partial x}(\underline{A}) & \frac{\partial^2 f}{\partial y^2}(\underline{A}) \end{pmatrix}$$

$$f(\underline{X}) = f(\underline{A}) + \nabla f(\underline{A})(\underline{X} - \underline{A}) + \tfrac{1}{2}(\underline{X} - \underline{A})^T H(\underline{A})(\underline{X} - \underline{A}) + o(||\underline{X} - \underline{A}|\,|^2)$$

One assume that the slip rate $\dot{\gamma}^s$ is mainly a function of two variables: the Resolved Shear Stress (RSS) and the critical one (CRSS), consequently $\dot{\gamma}^s_{(t+\Delta t)}$ takes the following form:

$$\begin{aligned} \dot{\gamma}^s_{(t+\Delta t)} &= \dot{\gamma}^s_{(t)} + \left(\left.\frac{\partial \dot{\gamma}^s}{\partial \tau}\right|_t \left.\frac{\partial \dot{\gamma}^s}{\partial \tau_c}\right|_t \right) \begin{bmatrix} \Delta\tau \\ \Delta\tau_c \end{bmatrix} \\ &\quad + \frac{1}{2}(\Delta\tau \Delta\tau_c) \left[\begin{array}{cc} \frac{\partial^2 \dot{\gamma}^s}{\partial \tau^2} & \frac{\partial^2 \dot{\gamma}^s}{\partial \tau \partial \tau_c} \\ \frac{\partial^2 \dot{\gamma}^s}{\partial \tau_c \partial \tau} & \frac{\partial^2 \dot{\gamma}^s}{\partial \tau_c^2} \end{array} \right]_t \begin{bmatrix} \Delta\tau \\ \Delta\tau_c \end{bmatrix} + o(\Delta\tau\Delta\tau_c)^2 \qquad \text{(G.9)} \\ &= \dot{\gamma}^s_{(t)} + \left.\frac{\partial \dot{\gamma}^s}{\partial \tau}\right|_t \Delta\tau + \left.\frac{\partial \dot{\gamma}^s}{\partial \tau_c}\right|_t \Delta\tau_c \\ &\quad \underbrace{+ \frac{1}{2}\left(\left.\frac{\partial^2 \dot{\gamma}^s}{\partial \tau^2}\right|_t \Delta\tau^2 + \left.\frac{\partial^2 \dot{\gamma}^s}{\partial \tau_c^2}\right|_t \Delta\tau_c^2 + \cancel{\Delta\tau_c \Delta\tau \left.\frac{\partial^2 \dot{\gamma}^s}{\partial \tau_c \partial \tau}\right|_t} \right) + o(\Delta\tau\Delta\tau_c)^2}_{2^{nd} \text{ order}} \end{aligned}$$

Combining equations G.8 and G.10 one could finally write the shear strain increment as:

$$\Delta\gamma^s = \left[\dot{\gamma}^s_{(t)} + \theta \left(\left.\frac{\partial \dot{\gamma}^s}{\partial \tau^s}\right|_t \Delta\tau^s + \left.\frac{\partial \dot{\gamma}^s}{\partial \tau_c^s}\right|_t \Delta\tau_c^s \right) \right] \Delta t \qquad \text{(G.10)}$$

where a subscript after a vertical bar is used to denote the time at which the rate is evaluated.

G.2.2 Expression of slip resistance increment

As introduced earlier, the rate-dependent, viscoplastic single crystal theory, as presented in [Peirce 1983] or [Huang 1991] and employed in several works, is used. It is implemented in the formulation through a power-law that relates the resolved shear stress τ^s to the slipping rate $\dot{\gamma}^s$ on each slip system (s),

$$\dot{\gamma}^s = \dot{\gamma}_0 \left| \frac{\tau^s}{\tau_c^s} \right|^n \text{sign}\left(\tau^s\right) \tag{G.11}$$

Considering $X^s = \dfrac{\tau^s}{\tau_c^s}$ equation G.10 becomes:

$$\begin{aligned} \Delta\gamma^s &= \left[\dot{\gamma}^s_{(t)} + \theta \left. \frac{\partial \dot{\gamma}^s}{\partial X^s} \right|_t \left(\left. \frac{\partial X^s}{\partial \tau^s} \right|_t \Delta\tau^s + \left. \frac{\partial X^s}{\partial \tau_c^s} \right|_t \Delta\tau_c^s \right) \right] \Delta t & \text{(G.12)} \\ &= \left[\dot{\gamma}^s_{(t)} + \left. \frac{\partial \dot{\gamma}^s}{\partial X^s} \right|_t \frac{\theta}{\tau^s_{c_{(t)}}} \left(\Delta\tau^s - X^s_{(t)} \Delta\tau_c^s \right) \right] \Delta t & \text{(G.13)} \end{aligned}$$

One could observe that the estimation of $\Delta\gamma^s$ at $t + \Delta t$ only depends on $\Delta\tau^s$ and $\Delta\tau_c^s$ expressed at $t + \Delta t$ remaining parts being directly estimate at time t thanks to Taylor expansion.

According to assumed slip resistance formula one could write:

$$\dot{\tau}_c^s = \frac{\mu b}{2} \frac{\sum\limits_u \left(d^{su} \dot{\rho}^u \right)}{\sum\limits_w \left(d^{sw} \rho^w \right)} \tag{G.14}$$

introducing the dislocation density flow rule within G.14 on could expressed the slip resistance increment as:

$$\begin{aligned} \Delta\tau_c^s &= \dot{\tau}_c^s \Delta t & \text{(G.15)} \\ &= \sum_u \left[\frac{\mu d^{su}}{2 \sum\limits_w \left(d^{sw} \rho^w \right)} \left(\frac{\sum\limits_w \left(a^{uw} \rho^w \right)}{L} - 2 y_c \rho^u \right) \right] \Delta\gamma^u \text{sign}\left(\dot{\gamma}^u\right) & \text{(G.16)} \\ &= \sum_u \mathbf{H^{su}} \Delta\gamma^u \text{sign}\left(\dot{\gamma}^u\right) & \text{(G.17)} \end{aligned}$$

Equation G.13 becomes:

$$\Delta\gamma^s = \left[\dot{\gamma}^s_{(t)} + \left. \frac{\partial \dot{\gamma}^s}{\partial X^s} \right|_t \frac{\theta}{\tau^s_{c_{(t)}}} \left(\Delta\tau^s - \sum_u X^s_{(t)} \mathbf{H^{su}} \text{sign}\left(\dot{\gamma}^u\right) \Delta\gamma^u \right) \right] \Delta t \tag{G.18}$$

G.2.3 Expression of Resolved Shear Stress increment

With the help of Schmid's rule introduced in section 6.3.3.3 one could write:

$$\dot{\tau}^s = \frac{\partial \left(\sigma : \mathbb{D}^s\right)}{\partial t} \tag{G.19}$$

with $\mathbb{D}^s$ the Schmid tensor, i.e the symmetric part of the orientation tensor $\mathbb{M}^s = b^s \otimes n^s$. With the help of relation established within finite strain formalism (see appendix H.1), one could show that the time derivation of Resolved Shear Stress could be written as:

$$\dot{\tau}^s = \mathbb{R}^s : \mathbf{D}^e \tag{G.20}$$

with $\mathbb{R}^s = \mathbb{C} : \mathbb{D}^s + \mathbb{W}^s\sigma - \sigma\mathbb{W}^s$, and $\mathbf{D}^e$ the symmetric rate of stretching tensor. We recommend to interested readers the reference [Asaro 1977] for more informations about step calculations.
Finally, the Resolved Shear Stress increment takes the following form:

$$\begin{aligned}
\Delta\tau^s &= \dot{\tau}^s\Delta t && \text{(G.21)}\\
&= \mathbb{R}^s : \mathbf{D}^e\Delta t && \text{(G.22)}\\
&= \mathbb{R}^s : \left(\mathbf{D} - \sum_u \dot{\gamma}^u\mathbb{D}^u\right)\Delta t && \text{(G.23)}\\
&= \mathbb{R}^s : \mathbf{D}\Delta t - \sum_u \mathbb{R}^s\mathbb{D}^u\Delta\gamma^u && \text{(G.24)}
\end{aligned}$$

So, introducing this equation within equation G.13, the non linear implicit equation for shear strain increment $\Delta\gamma^s$ becomes:

$$\begin{aligned}
\Delta\gamma^s &= \dot{\gamma}^s_{(t)}\Delta t + \\
&\quad \left.\frac{\partial\dot{\gamma}^s}{\partial X^s}\right|_t \frac{\theta\Delta t}{\tau^s_{c_{(t)}}}\left(\mathbb{R}^s : \mathbf{D}\Delta t - \sum_u \left[\mathbb{R}^s : \mathbb{D}^u - X^s_{(t)}\mathbf{H^{su}}\text{sign}\left(\dot{\gamma}^u\right)\right]\Delta\gamma^u\right)
\end{aligned}$$

Considering $\mathbb{Q}^s = \left.\frac{\partial\dot{\gamma}^s}{\partial X^s}\right|_t \frac{\theta\Delta t}{\tau^s_{c_{(t)}}}\mathbb{R}^s$, and, $\mathbf{N}^{su} = \delta^{su} + \mathbb{Q}^s : \mathbb{D}^u - \left.\frac{\partial\dot{\gamma}^s}{\partial X^s}\right|_t \frac{\theta\Delta t}{\tau^s_{c_{(t)}}}X^s_{(t)}\mathbf{H^{su}}\text{sign}\left(\dot{\gamma}^u\right)$ one obtains:

$$\sum_u \mathbf{N}^{su}\Delta\gamma^u = \dot{\gamma}^s_{(t)}\Delta t + \mathbb{Q}^s : \mathbf{D}\Delta t \tag{G.25}$$

The slip increments can finally be expressed in terms of quantities at time t as:

$$\left\{\begin{array}{lcl} \Delta\gamma^u & = & \left(\dot{f}^u + \mathbb{F}^u : \mathbf{D}\right)\Delta t \\ & \text{where} & \\ \dot{f}^u & = & \sum_u (\mathbf{N^{su}})^{-1}\dot{\gamma}^s_{(t)} \\ \mathbb{F}^u & = & \sum_u (\mathbf{N^{su}})^{-1}\mathbb{Q}^s \end{array}\right. \tag{G.26}$$

The numerical increment $\Delta\gamma^s$ is consequently the solution of this differential system.

G.2.4 Tangent modulus

Elements presented in this section are a summary of the full explanation of material Jacobian matrix calculation founded in [Meissonnier 2001]. As introduced in this paper, the derivation of the material Jacobian matrix or tangent modulus, Stiffness matrix associated to Cauchy stress, i.e $\frac{\partial \mathbf{\Delta}\sigma}{\partial \mathbf{\Delta E}}$ must be accurately determined to achieve an accurate correction to the incremental kinematics. It plays a fundamental role in the rate convergence nevertheless its calculation requires some tensorial algebra knowledges, as presented here:

Let $\mathbf{F_E}$ denotes a second order tensor function of strain $\mathbf{E}$, $\mathbf{A}$, $\mathbf{B}$ $\mathbb{C}$ ordinary ones with appropriate rank.

$$\left[\begin{array}{rcl} \dfrac{\partial\left[\mathbb{C} : \mathbf{F_E}\right]}{\partial \mathbf{E}} & = & \mathbb{C} : \dfrac{\partial \mathbf{F_E}}{\partial \mathbf{E}} \\ \dfrac{\partial\left[\mathbf{B}\left(\mathbf{A} : \mathbf{F_E}\right)\right]}{\partial \mathbf{E}} & = & \left[\mathbf{B}\otimes\mathbf{A}\right] : \dfrac{\partial \mathbf{F_E}}{\partial \mathbf{E}} \end{array}\right] \tag{G.27}$$

With $\mathbf{A} : \mathbf{B} = \sum_{i,j}\left[A_{ij}B_{ij}\right]$ means the double contraction, $(\mathbf{A}\otimes\mathbf{B})_{ijkl} = A_{ij}B_{kl}$ means the tensor product.

According to this brief abseil of tensorial algebra one could establish the incremental form of the tangent modulus $\dfrac{\partial\Delta\sigma}{\partial\Delta\mathbf{E}}$. It is function of the corotational stress increment of which the definition is consistent with F.E. code ABAQUS for finite deformation analysis [Huang 1995]:

$$\begin{array}{rcl} \Delta\sigma & = & \overset{\nabla}{\sigma}\Delta t \\ \Delta\sigma & = & \mathbb{C} : \Delta\mathbf{E} - \sigma\left(\mathbf{I} : \Delta\mathbf{E}\right) - \sum_s \mathbb{R}^s\Delta\gamma^s \\ & = & \mathbb{C} : \Delta\mathbf{E} - \sigma\left(\mathbf{I} : \Delta\mathbf{E}\right) - \sum_s \mathbb{R}^s\left[\dot{f}^s\Delta t + \mathbb{F}^s : \mathbf{D}\Delta t\right] \\ & = & \mathbb{C} : \Delta\mathbf{E} - \sigma\left(\mathbf{I} : \Delta\mathbf{E}\right) - \sum_s \mathbb{R}^s\left[\dot{f}^s\Delta t + \mathbb{F}^s : \Delta\mathbf{E}\right] \end{array} \tag{G.28}$$

So,

$$\frac{\partial \Delta\sigma}{\partial \Delta \mathbf{E}} = \mathbb{C} - \mathbb{C}^{tr} - \overline{\mathbb{C}} \tag{G.29}$$

with $\mathbb{C}^{tr}$ and $\overline{\mathbb{C}}$ are geometric contributions to the global stifness matrix associated with the volume change and strain rate respectively. Expressed here in Voigt notation [Voigt 1928] each fourth rank tensor could be write as:

$$\mathbb{C}^{tr} = \sigma \otimes \mathbf{I} = \begin{bmatrix} \sigma_1 & \sigma_1 & \sigma_1 & 0 & 0 & 0 \\ \sigma_2 & \sigma_2 & \sigma_2 & 0 & 0 & 0 \\ \sigma_3 & \sigma_3 & \sigma_3 & 0 & 0 & 0 \\ \sigma_4 & \sigma_4 & \sigma_4 & 0 & 0 & 0 \\ \sigma_5 & \sigma_5 & \sigma_5 & 0 & 0 & 0 \\ \sigma_6 & \sigma_6 & \sigma_6 & 0 & 0 & 0 \end{bmatrix} \tag{G.30}$$

$$\overline{\mathbb{C}} = \sum_s (\mathbb{R}^s \otimes \mathbb{F}_s) \tag{G.31}$$

For more information we suggest to refer to [Huang 1995].

G.2.5 Updating internal variables

Following the equation G.17 one obtains:

$$\begin{aligned} \tau^s_{c_{(t+\Delta t)}} &= \tau^s_{c_{(t)}} + \Delta\tau^s_c \\ &= \tau^s_{c_{(t)}} + \sum_u \mathbf{H^{su}} \Delta\gamma^u \text{sign}\left(\dot{\gamma}^u\right) \end{aligned} \tag{G.32}$$

Then equation G.23 leads to:

$$\begin{aligned} \tau^s_{(t+\Delta t)} &= \tau^s_{(t)} + \Delta\tau^s \\ &= \tau^s_{(t)} + \mathbb{R}^s : \left(\mathbf{D}\Delta t - \sum_u \mathbb{D}^u \Delta\gamma^u\right) \\ &= \tau^s_{(t)} + \mathbb{R}^s : \left(\Delta\mathbf{E} - \sum_u \mathbb{D}^u \Delta\gamma^u\right) \end{aligned} \tag{G.33}$$

where E denotes the true or logarithmic strain[3] used in ABAQUS in the case of finite strains. According to equation 6.29, the current density of Statiscally Stored Dislocation becomes:

$$\begin{aligned}\rho^s_{(t+\Delta t)} &= \rho^s_{(t)} + \Delta\rho^s \\ &= \rho^s_{(t)} + \frac{1}{b}\left(\frac{\sum\limits_u a^{su}\rho^u}{L} - 2y_c\rho^s\right)\Delta\gamma^s \text{sign}\left(\dot{\gamma}^s\right)\end{aligned} \tag{G.34}$$

Then, denoting $\overset{o}{\sigma}_{(t)} = STRESS$ in ABAQUS notation, the current stress takes the following form:

$$\begin{aligned}\sigma_{(t+\Delta t)} &= \overset{o}{\sigma}_{(t)} + \Delta\sigma \\ &= \overset{o}{\sigma}_{(t)} + \mathbb{C} : \Delta\mathbf{E} - \overset{o}{\sigma}_{(t)}\text{tr}\left(\Delta\mathbf{E}\right) - \sum_s \mathbb{R}^s\Delta\gamma^s\end{aligned} \tag{G.35}$$

Finally, crystalline lattice base vectors could be updating by:

$$\Delta B^s = \left[\Delta\mathbf{E} + \Delta\omega - \sum_s \Delta\gamma^s\mathbb{L}^s\right]B^s \tag{G.36}$$

$$\Delta N^s = -N^s\left[\Delta\mathbf{E} + \Delta\omega - \sum_s \Delta\gamma^s\mathbb{L}^s\right] \tag{G.37}$$

G.2.6 Rotation of fourth-order stiffness tensor

As each grain has its own orientation and the differential system to solved is expressed in the global referential system, the stiffness tensor needs to be rotated from granular to global base. The base change formula for stiffness or elasticity tensor $\mathbb{C}$ is:

$$\mathbb{C}^*_{ijkl} = \mathbf{R}_{ip}\mathbf{R}_{jq}\mathbb{C}_{pqrs}\mathbf{R}_{kr}\mathbf{R}_{ls} \tag{G.38}$$

where $\mathbb{C}^*$ and $\mathbb{C}$ are the stiffness tensor in the transformed and original axes, respectively and $\mathbf{R}$ the rotation matrix. Equation G.38 is not convenient for practical calculation because it introduces fourth-order tensor operation. So, it is efficient to deal with a 6x6 matrix for the stiffness tensor and its associated second-order rotation tensor as introduced for exemple in [Lekhnitskii 1964] or [Auld 1973]. Equation G.38 becomes:

$$\mathbf{C}^* = \mathbf{KCK^{-1}} \tag{G.39}$$

[3] $E = ln\left(\frac{l}{L}\right)$ with the final length l and the initial length L of the material line.

with,

$$\left\{\begin{array}{rcl} \mathbf{K} & = & \left[\begin{array}{cc} \mathbf{K^1} & 2\mathbf{K^2} \\ \mathbf{K^3} & \mathbf{K^4} \end{array}\right] \\ K^1_{ij} & = & (R_{ij})^2 \\ K^2_{ij} & = & R_{ij_1} R_{ij_2} \\ K^3_{ij} & = & R_{i_1 j} R_{i_2 j} \\ K^4_{ij} & = & R_{i_1 j_1} R_{i_2 j_2} + R_{i_1 j_2} R_{i_2 j_1} \\ i_1 & = & i+1 \text{ if } i+1 \leq 3 \text{ else } i_1 = i+1-3 \\ i_2 & = & i+2 \text{ if } i+2 \leq 3 \text{ else } i_2 = i+2-3 \end{array}\right. \tag{G.40}$$

Appendix H

Finite strain formalism and crystal stress flow

H.1 Kinematics

The kinematics of finite strains describes the process where a body originally in a reference state, $A \in \mathbb{R}^3$, is deformed to the current state, $B \in \mathbb{R}^3$, by a combination of externally applied forces and displacements over a period of time, Δt. One chooses the perfect single crystal as reference state.

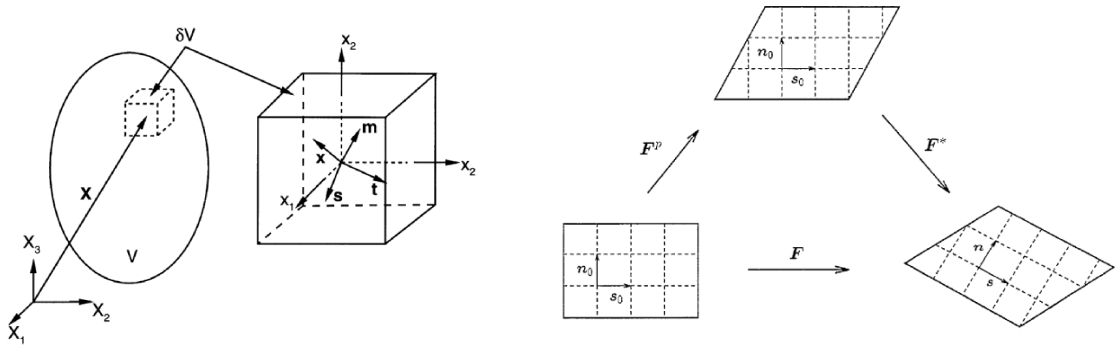

Figure H.1: (a) granular reference system (b) deformation of single crystal [Peirce 1982]

Pictures H.1 (a) and (b) present two mains elements of elasto-plastic deformation within crystal. On one hand, the lattice orientation of each grain is characterized by the orientation of a normal n^s to slip plane s and the orientation of the slip direction b^s within this plane during the whole deformation path (see H.1 (a)). Here n_0^s and b_0^s are unit vectors where subscript 0 means the initial configuration of the lattice. On the other hand, one assumes that the deformation of this infinitesimal volume could be divided in an elastic and plastic contribution (Cf H.1 (b)), where $\mathbf{F}^p$ denotes a purely plastic deformation, i.e irreversible shear in the same reference system than the global one. It is called isoclinic configuration. This takes into account the fact that purely plastic deformation does not affect the crystal lattice. Then $\mathbf{F}^e$ denotes an elastic deformation, i.e reversible stretching and rotation of lattice. n^s and b^s are slip plane normal and direction respectively after deformation.

The δV volume is here an infinitesimal volume of a single crystal structure which undergoes mechanical loadings. Let us consider X the coordinate of the gravity center of this volume element in its initial configuration and x the ones in the deformed configuration. The deformation gradient associated to the displacement U such as: $U(X,t) = x(X,t) - X$, is noted $\mathbf{F}$ and could be write as:

$$\mathbf{F} = \frac{\partial x(X,t)}{\partial X} \tag{H.1}$$

or function of displacement vector U:

$$\mathbf{F} = \mathbf{I} + \frac{\partial U}{\partial X} \tag{H.2}$$

where $\mathbf{I}$ is the second rank identity tensor and $\dfrac{\partial U}{\partial X}$ the displacement gradient. Notice that within small strains framework, one could define the infinitesimal strain tensor as $\varepsilon = \dfrac{1}{2}\left(\dfrac{\partial U}{\partial X} + \dfrac{\partial U}{\partial X}^T\right)$ and the infinitesimal rotation tensors as $\omega = \dfrac{1}{2}\left(\dfrac{\partial U}{\partial X} - \dfrac{\partial U}{\partial X}^T\right)$.

The velocity gradient tensor $\mathbf{L}$, associated to the deformation gradient one, takes the following form:

$$\mathbf{L} = \frac{\partial \dot{x}(X,t)}{\partial x(X,t)} = \frac{\partial \dot{x}(X,t)}{\partial X}\frac{\partial X}{\partial x(X,t)} = \dot{\mathbf{F}}\mathbf{F}^{-1} \tag{H.3}$$

Notice that the symetric part of the velocity gradient tensor: $\mathbf{D} = \frac{1}{2}\left(\mathbf{L} + \mathbf{L}^T\right)$ is called the deformation or stretching rate tensor and its antisymetric part: $\mathbf{W} = \frac{1}{2}\left(\mathbf{L} - \mathbf{L}^T\right)$ is called spin tensor.

One adopt here a multiplicative partition of deformation gradient such as:

$$\mathbf{F} = \mathbf{F}^e\mathbf{F}^p \tag{H.4}$$

In this way, one could deduce:

$$\mathbf{L} = \dot{\mathbf{F}}^e\mathbf{F}^{e^{-1}} + \mathbf{F}^e\dot{\mathbf{F}}^p\mathbf{F}^{p^{-1}}\dot{\mathbf{F}}^{e^{-1}} \tag{H.5}$$

$$\mathbf{L} = \mathbf{L}^e + \mathbf{F}^e\mathbf{L}^p\dot{\mathbf{F}}^{e^{-1}} \tag{H.6}$$

One consequently understand that the total velocity gradient tensor associated to this elasto-plastic deformation is the sum of an elastic component $\mathbf{L}^e$, expressed in current configuration, and a plastic one $\mathbf{L}^p$, calculated in an intermediate configuration (isoclinic: i.e identical to crystalline configuration) and then moved in current configuration. Equation H.6 evidence the schematic decomposition introduced within figure H.1.

As already announced, within the isoclinic (intermediate) configuration the velocity gradient is associated to plastic slip between different atomic planes. According to Schmid theory one could

conclude that the plastic part of velocity gradient is the resultant of each slip rate and takes the following form:

$$\mathbf{L}^p = \sum_s \dot{\gamma}^s \mathbb{L}^s \quad \text{with} \quad \mathbb{L}^s = n^s \otimes b^s \tag{H.7}$$

$\mathbb{L}^s$ is frequently called the Schmid tensor. Identically to previous step one could define the symetric part of plastic velocity gradient as being $\mathbf{D}^p = \sum_s \dot{\gamma}^s \mathbb{D}^s$ with $\mathbb{D}^s = \frac{1}{2}\left(n^s \otimes b^s + b^s \otimes n^s\right)$ and the antisymetric part as $\mathbf{W}^p = \sum_s \dot{\gamma}^s \mathbb{W}^s$ with $\mathbb{D}^s = \frac{1}{2}\left(n^s \otimes b^s - b^s \otimes n^s\right)$. To conclude, one could finally write the total deformation rate as:

$$\mathbf{D} = \mathbf{D}^e + \mathbf{D}^p = \mathbf{D}^e + \sum_s \dot{\gamma}^s \mathbb{D}^s \tag{H.8}$$

$$\tag{H.9}$$

H.2 Constitutive relations

An hypo-elastic constitutive relation is used. This concept was originally proposed by Truesdell in [Truesdell 1955]. Hypo-elasticity is a generalization of the theory of nonlinear elasticity and states in which the stress rate is determined by the current stress and the rate of deformation. Basically, one has:

$$\dot{\sigma} = f\left(\sigma, \mathbf{D}\right) \tag{H.10}$$

$$\tag{H.11}$$

Following [Hill 1972] one use a stress rate related to the elastic part of strain rate $\mathbf{D}^e$ by:

$$\overset{\nabla}{\sigma}{}^* = \mathbb{C}^* : \mathbf{D}^e \tag{H.12}$$

with $\mathbb{C}^*$ the natural tensor of elastic moduli which is appropriate for the corotational rate of Cauchy stress ($\overset{\nabla}{\sigma}{}^*$) and $\overset{\nabla}{\sigma}{}^*$ the corotational stress rate of Cauchy formed on axes which spin with the lattice. This is an objective stress rate, i.e. independent of the referenc esystem. Indeed, contrary to stress, the stress rate is dependent of the configuration. Then it is necessary to use an objective form of stress rate, taking into account the material rotation. Mathematically, an infinite number of objective rates can be defined [Malvern 1969], nevertheless only some well-known rates are used widely in the literature, the Jaumann, Green-Naghdi, Oldroyd or Truesdell ones, for more details, interested reader could refer to [Lubliner 1990]. In our case, let us define two quantities: (1) the Jaumann stress rate of Cauchy stress which rotates with the crystal lattice $\overset{\nabla}{\sigma}{}^*$ and (2) the Jaumann stress rate formed on

axes rotating with the material $\overset{\nabla}{\sigma}$ [Huang 1991]:

$$\dot{\sigma} = \overset{\nabla}{\sigma} + \mathbf{W}\sigma - \sigma\mathbf{W} \tag{H.13}$$

$$\overset{\nabla}{\sigma^*} = \overset{\nabla}{\sigma} + (\mathbf{W} - \mathbf{W}^e)\,\sigma - \sigma\,(\mathbf{W} - \mathbf{W}^e) \tag{H.14}$$

with $\mathbf{W}$ the total spin tensor and $\mathbf{W^e}$ the lattice part, i.e the rotation rate between the current and the isoclinic configuration (see figure H.1). $\dot{\sigma}$ is the ordinary time-rate of σ following the material element and σ the Cauchy (or "true") stress tensor. Table H.2 presents key points for implementation of a such stress rate under the F.E. code ***Abaqus***.

Nevertheless, the F.E. code requires the calculation of the Cauchy or "true" stress tensor. One presentes here some elements helping the understanding of the ordinary time-rate of σ using the Logarithmic strain in the case of updated Lagrangian scheme. If Updated Lagrangienne scheme is used the position x a time t is equivalent to the reference one X:

$$\mathbf{F}_t = \frac{\partial x}{\partial X} = \mathbf{I} \rightarrow det\,(\mathbf{F}) = J = 1 \tag{H.15}$$

consequently, $\tau = J\sigma = \sigma$. Then in a similar way to equation H.12 and H.14 the material rate of the Kirchoff stress $\overset{\nabla}{\tau^*}$ can be related to its corresponding objective Jaumann rate as follows:

$$\overset{\nabla}{\tau^*} = \mathbb{C} : \mathbf{D}^e = \dot{\tau} - \mathbf{W}^e\tau + \tau\mathbf{W}^e \tag{H.16}$$

with $\mathbb{C}$ the tangent modulus appropriate for Jaumann rate of Kirchoff stress, and $\mathbf{D}^e$ the elastic part of strain rate. Then taking into account the time derivative of Kirchoff stress $\dot{\tau}$:

$$\dot{\tau} = \dot{\tau}\sigma + J\dot{\sigma} = \mathrm{tr}\,(D^e)\,\sigma + \dot{\sigma} = \mathrm{tr}\,(D)\,\sigma + \dot{\sigma} \tag{H.17}$$

and then combining equation H.17 andH.13, one could establish:

$$\mathbb{C} : \mathbf{D}^e = \mathrm{tr}\,(D)\,\sigma + \overset{\nabla}{\sigma^*} \tag{H.18}$$

Notice that $\mathbb{C}$ is expressed in the reference system configuration and not on the material (lattice) one. Consequently it will be necessary to move the elastic properties from the lattice reference system to the reference one. Section G.2 details how to rotate such a fourth order tensor. The elasto-plastic constitutive relation between Cauchy stress rate and local slip rate associated to slip systems takes the

following form:

$$\begin{array}{rcl} \overset{\nabla}{\sigma^*} & = & \mathbb{C} : \mathbf{D}^e - \mathrm{tr}\,(D)\,\sigma \\ & \Updownarrow & \\ \dot{\sigma} & = & \mathbb{C} : (\mathbf{D} - \mathbf{D}^p) - \mathrm{tr}\,(D)\,\sigma + (\mathbf{W} - \mathbf{W}^p)\,\sigma - \sigma\,(\mathbf{W} - \mathbf{W}^p) \\ & = & [\mathbf{W}\sigma - \sigma\mathbf{W}] + \mathbb{C} : \mathbf{D} - \mathrm{tr}\,(D)\,\sigma - [\mathbb{C} : \mathbf{D}^p + \mathbf{W}^p\sigma - \sigma\mathbf{W}^p] \\ & \Updownarrow & \\ \overset{\nabla}{\sigma} & = & \mathbb{C} : \mathbf{D} - \mathrm{tr}\,(D)\,\sigma - \sum_s \dot{\gamma}^s \mathbb{R}^s \end{array} \tag{H.19}$$

with $\mathbb{R}^s = \mathbb{C} : \mathbb{D}^s + \mathbb{W}^s\sigma - \sigma\mathbb{W}^s$. Notice that the physical meaning of $\mathrm{tr}(D)$ is the dilatation strain rate.

To finish, the lattice deformation and rotation is fully characterized by the vector B^s, oriented along the slip direction of system s in deformed configuration by:

$$B^s = \mathbf{F^e} b^s \tag{H.20}$$

and the vector N^s, normal of system s in the deformed configuration by:

$$N^s = N^s \mathbf{F^{e^{-1}}} \tag{H.21}$$

It leads to the expression of lattice deformation and rotation rate:

$$\dot{B}^s = \dot{\mathbf{F}}^{\mathbf{e}} b^s = \mathbf{L^e}\dot{\mathbf{F}}^{\mathbf{e}} b^s$$

$$\left\{ \begin{array}{rcl} \dot{B}^s & = & \mathbf{L^e} B^s \\ & \text{and} & \\ \dot{N}^s & = & -N^s \mathbf{L^e} \\ & \text{with} & \\ \mathbf{L^e} & = & \left[\mathbf{D} + \mathbf{W} - \sum_s \dot{\gamma}^s \mathbb{L}^s\right] \end{array} \right. \tag{H.22}$$

The implementation of consitutive law has been done within the F.E. code ***Abaqus*** in its implicit version (***ABAQUS/standard***). Several points need consequently to be keeped in mind [Dassault-System 2010]:

- ABAQUS/standard uses by default, the Jaumann rate as objective stress rate (see eq. H.13). It is relatively easy to implement and it leads to symmetric tangent moduli.
- it uses Updated Lagrangian scheme when a finite strain formulation is required, i.e for the calculation of state at time $t + \Delta t$ the reference configuration is assumed to be the one at time t and not at t_0. When calculation is done from original configuration, the scheme is called Total Lagrangian one. This procedure allows keeping small strain increments. Within this framework, the deformation used is the Logarithmic one; $E = ln(U)$ with its associated Kirchoff stress tensor $\tau = J\sigma$, where $J = det\,(\mathbf{F})$.
- the material is treated as being based in a fixed global coordinate system.
- in the case of finite-strain problems the stress tensor has already been rotated to account for rigid body motion in the increment before User's subroutine for behavior law definition is called, so that only the corotational part of the stress integration should be done in the UMat[1], so $\overset{\nabla}{\sigma}\Delta t$.
- in finite-strain problems the strain components have been rotated to account for rigid body motion in the increment before UMAT is called and are approximated by logarithmic strain. In addition, if thermal expansion is included in the same material definition, the strains passed into UMAT are the mechanical strains only (that is, the thermal strains computed based upon the thermal expansion coefficient have been subtracted from the total strains)
- the necessary Jacobian matrix of the constitutive model is defined as $\dfrac{\partial \Delta\sigma}{\partial \Delta\varepsilon}$, where ε and $\Delta\sigma$ are the strain and stress increments. According to previous points $\Delta\sigma$ is the increment of corotationnal part of stress: $\Delta\sigma = \overset{\nabla}{\sigma}\Delta t$. Then, Abaqus updates itself the stress as the following scheme:

$$\sigma_{(t+\Delta t)} = \Delta\sigma + \Delta R\sigma\Delta R^T \tag{H.23}$$

with ΔR, the amount by which the stress and strain arrays have been rotated between the end of the previous increment and the start of the current one. It is calculated using the Hughes-Winget algorithm [Hughes 1980]

$$\Delta\mathbf{R} = \left(\mathbf{I} - \frac{1}{2}\Delta\omega\right)^{-1}\left(\mathbf{I} + \frac{1}{2}\Delta\omega\right) \tag{H.24}$$

$\mathbf{I}$ is the identity matrix and $\Delta\omega$ the incremental form of $\mathbf{W}$ [Harewood 2007].

Appendix I

Intragranular dissipative and plastic threshold

This appendix investigates the intragranular couplings between local temperature and elasto-plasticity mechanisms in 3 specific grains. Are discussed:

- the surface intragranular observations of post-tested sample.
- the intragranular shear strain, and notably its isovalues orientation along the deformation path. It provides a kinematic estimation of developped plasticity mechanisms.
- the intragranular temperature, and notably its localisation along the deformation path. It provides a thermal estimation of instantaneous plastic localization.
- the intragranular variation of temperature, especially the loss of local linearity within the elastic drop. It provides a thermal estimation of first dissipation appearance.

I.1 Grain n^{o}2

Table I.5 presents grain surface statistics. In parallel, figure I.1 presents intragranular fields of out-of-plane displacement in μm, slip-band orientations in degree and normalized slip-mark density in %. It is the density of slip-mark relatively to the highest level found in the whole surface.
The studied grain is the biggest of the surface microstructure. It is composed by 54 cells of 100x100μm^2. Its normalized slip-density is significant relatively to the rest of the surface microstructure, especially in a specific band where the normalized slip-mark density reach 67% (see figure I.1). Texture analysis allows to evidence that 2 plastic systems have been activated: D_1 with a Schmid factor of 0.339 which corresponds to the red domain in picture I.1 (b), and B_5 with a Schmid factor of 0.296 which corresponds to yellow domain in picture I.1 (b).

size (mm^2)	0.5392		
100x100μm^2 cells	54		
normalized slip-mark density (%)	58		
Slip mark orientations (^{o})	21.40	-46.76	
Activated systems	B_5	D_1	
Schmid factors	0.296	0.339	
Crystal orientation (rad)	2.63	0.61	3.03

Table I.1: Slip-system statistics of grain n^{o}2

According to maximum Schmid factor criterion, one could imagine that the D_1 system was activated first and then the B_5 system. In addition, according to normalized slip-mark density, one observes that the shear on B_5 system was predominant. Then one could point that intense material discontinuities (not presented here) has been observed on its grain boundaries, especially on top and bottom part of shear band B_5. Notice that these discontinuities occurs at twin Σ_3 boundaries. It is in line with previous observation done in chapter 1.1.

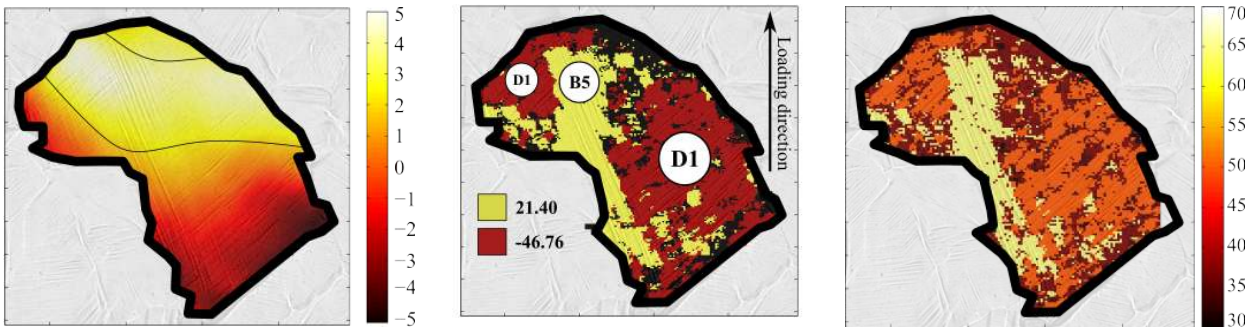

(a) in μm (b) in degree (c) in %

Figure I.1: (a) Intragranular out-of-plane displacement, (b) slip-marks orientations and (c) normalized slip-mark density as well as associated slip-systems.

Then, one observes in figure I.1 a significant gradient of out-of-plane displacement through the grain. It ranges from -5 to 5 μm cutting the grain into two parts. Nevertheless, contrary to the grain n^{o}1 analysed in section 4.4, no clear connection appears between slip-band domains and surface topography. The fact that the slip pattern is more complex, i.e. systems cross each others, may explain this point.

Let analyse now, in-situ kinematic and thermal fields.
Figure I.2 presents intragranular temperature (left side) and shear strain ε_{12} (right side) at 106, 191, 230 and 253 MPa of nominal stress. Notice these instants correspond to E_1, E_2, P_1 and P_2 introduced

in chapter 4.1. Black thin lines precise isovalues in order to underline gradient orientations.
normalized

As for grain n^{o}1, One observes in ε_{12} field a change in isovalues orientation along the deformation path. From 106 to 191 MPa, the mean shear strain ranges from 0.02 to 0.04 % with an increasing gradient from 0.05 and 0.1 % respectively. During this period, isovalues orientation remain fixe and make an angle of -46^o compared to the loading direction. It reflects the plastic activity of system D_1. The superimposed microstructure allows to confirm that from 106 to 191 MPa D_1 system is activated. It is in line with the maximum Schmid factor criterion. Then from 220 MPa to 253 MPa and to the end of the test (not presented) shear strain isovalues make an angle of 21^o compared to loading direction. It reflects exactly the activaty of system B_5. As there is no deviation between shear strain isovalues and B_5 slip-marks one could image that the system D_1 is not active anymore during this period.

Thus, in-situ kinematic measurements, in agreement with Schmid theory, allows to conclude that from 106 to 191 MPa the grain undergo plastic strain by meaning of D_1 system. In addition, the shear strain intensity (see figure I.2 1^{st} and 2^{nd}) shows that the more intense shear occurs in the top part of the grain. It corresponds to the top left D_1 domain observed in figure I.1 (b). Then, from 191 to 220 MPa, a plastic transition occurs from D_1 to B_5 system. Finally, this system remains active up to the end of the test. This point confirms observations done on normalized slip-mark density (see figure I.1 (c)). Indeed, slip-mark density is widely more intense within the B_5 slip-band. It is in agreement with shear occuring at high strain level (from 0.2 to 2.5%) compared to the other system and during a longer period. To conclude, for similar reason than the ones exposed in section 4.4, 106 and 220 MPa of nominal stress constitute the upper bounds of D_1 and B_5 yield stress respectivelly.

According to this point, let us estimate the Resolved Shear Stress acting on every slip-systems of the lattice at 106 MPa. Table I.2 presents the Shear Stress resolved on 12 crystallograpic slip-systems. The procedure to obtain this quantity is similar to the one used in section 4.4.

A_2	A_3	A_6	B_2	B_4	B_5	C_1	C_3	C_5	D_1	D_4	D_6
22	15	−7	8	−11	−19	−3	4	−7	35	30	4

Table I.2: mean Resolved Shear Stress (RSS) over the grain at 106 MPa of nominal stress

One observes that the Resolved Shear Stress is maximum on system D_1 and be worth $35MPa$. One notes that it is in agreement with previous observations and Schmid theory. Thus, 35 MPa is an upper bound of the D_1 Critical Resolved Shear Stress which is very similar to the value found for grain n^{o}1, i.e. 36 MPa. It also in agreement with experimentally observed critical value for single crystal of A316L [Feaugas 2009]. The value of B_5 system is -19 MPa which is lower than system A_2. Nevertheless, in-situ kinematic observations as well as slip-system identifications have shown that B_5 is effectivelly the second activated system. Thus, a significant rise of the RSS associated to this system is expected (from 106 to 220 MPa of nominal stress), especially compared to other second potential systems as A_2.

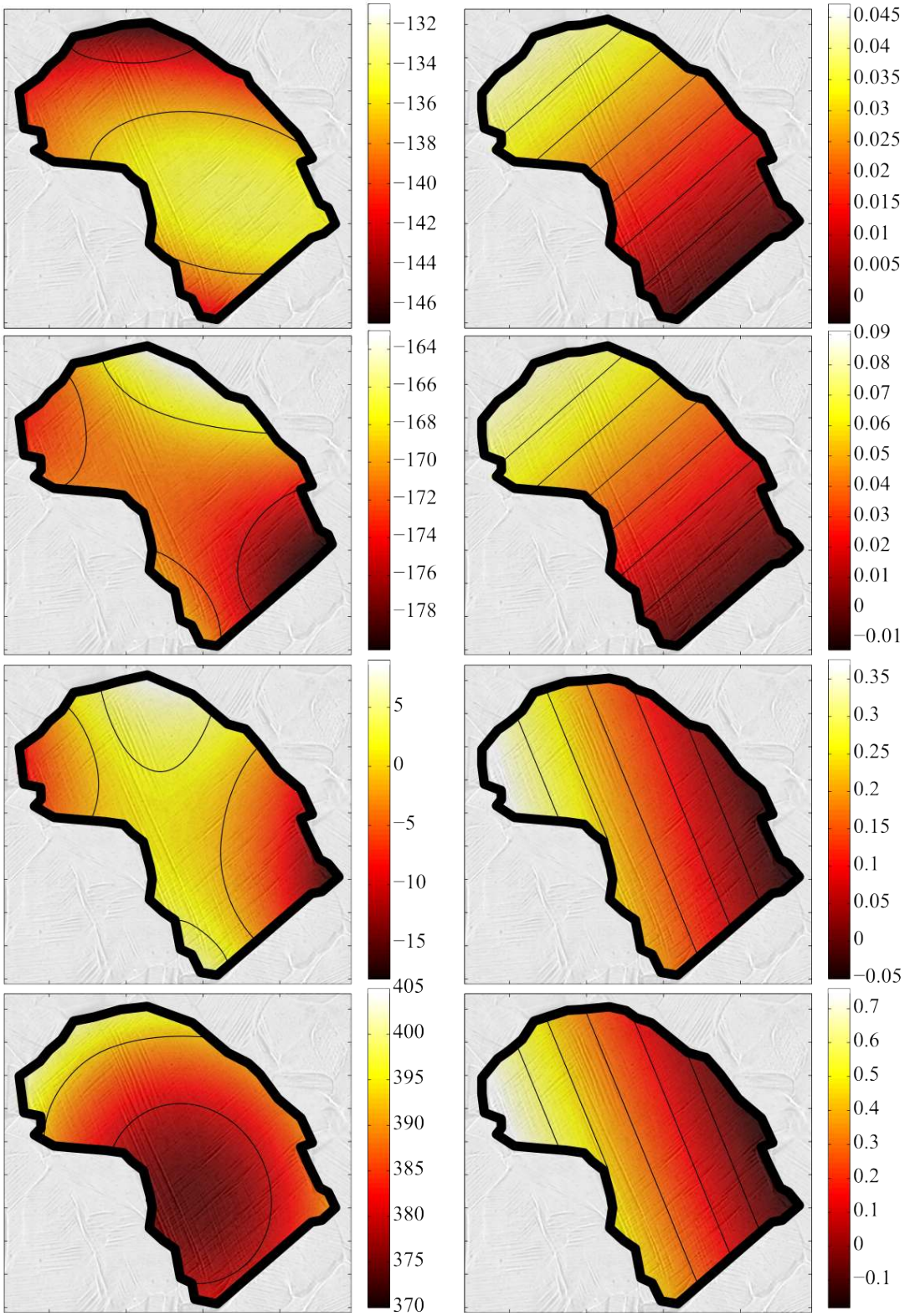

Figure I.2: Intragranular temperature (left side (mK)) and shear strain ε_{12} (right side (%)) at different instant of loading: 106 - 191 - 220 - 253 MPa

Let us now, deal with intragranular thermal fields. From 106 to 191 MPa of nominal stress, the mean temperature varies from -138 to -171 mK with a constant gradient of 16 mk.

Then, from 220 to 253 MPa of nominal stress, it ranges from 0 to 384 mK with an increasing gradient from 25 to 70 mK. Notice that the intragranular gradient is here, compared to grain n^{o}1, quite significant and could be considered with interest. From 106 to 191 MPa of nominal stress, the more hot region pass from the center of the grain to the top right. Then at 220 MPa a hot band is observed. Notice that it crosses the grain as the B_5 slip-band (see figure I.1 (b)). Finally, the center of the grain becomes the colder region and the whole top grain boundary localize the highest temperatures.

Let focus on the "hot band" which crosses the grain from top right to bottom left. One could first point that this pattern is observed in parallel of the activation of system B_5 (see shear strain in figure I.2). Actually, this pattern is observed 4 times during the 190 - 230 MPa period (not presented here), and disapears very quickly. Table I.1 summarises the loading level and the duration of such specific pattern within intragranular thermal field.

Nominal stress	199 MPa	222 MPa	227 MPa	230 MPa
Duration	20 ms	35 ms	29 ms	31 ms

Table I.3: Properties of B_5 "hot band" appearance

The "hot band" is observed from 199 MPa to 230 MPa, and persists about 29ms at each appearance. According to the clear connection between the "hot band" shape, location, orientation and slip-band B_5 (see figure I.1), as well as the appearance of such thermal localization while B_5 system initiates plastic slip, one could imagine that both phenomena are associated. In this case, it means that the experimental intragranular thermal gradients captures successive plastic activations within the B_5 slip-band. It also means that the yield stress related to system B_5 appears slightly before the found upper bound (220 MPa). 199 MPa would be a finer estimation.

Finally, figure I.3 (a) presens the mean intragranular thermal variation as well as the nominal stress during macroscopic elastic domain. The green straight line corresponds to the best fit of thermal linear drop. One observes that the intragranular thermal inflection, i.e. loss of linearity, appears at 106 MPa reaching -138 mK, and the minimum value is -174 mK at 172 MPa. Thus, from 106 MPa the grain exhibits a mesoscopic heating process (see figure I.3 (a)). In parallel, the system D_1 is active.
Figure I.3 (b) presents the local loss of thermal linearity as function of nominal stress. One observes that the thermal inflection appears gradually through the grain. Indeed, the first dissipation occurs within the top left part of the grain. Then the thermal inflection wave front propagate continuously up to the opposite grain boundary. It is interesting to notice that the first dissipation occurs in the D_1 domain (see figure I.1), especially where the shear strain is initially the more intense. Indeed, one have seen in figure I.2 at 106 MPa, that the plastic slip activity of system D_1 is captured by kinematic measurement and the shear strain level is 0.045% in the top left corner and tends toward zeros in the

rest of the grain.
Figure I.3 (b) is consequently in total agreement with kinematic measurements and the first thermal inflection observed in figure I.3 (b) is effectivly due to the local first plastic activity of system D_1.
The nominal stress is locally equal to 69 MPa and corresponds to a Critical Resolved Shear stress of 24 MPa. It is slightly lower than the value found in section 4.4 but remains in the expected order. One could finally point (refer to figure I.3 (a)) that from 0 to 69 MPa of nominal stress, the grain undergo a cooling down process (elasticity), then from 69 to 125 MPa the grain exhibits a progressive heating process (microplasticity). Then, the whole grain exhibits an increasing temperature.

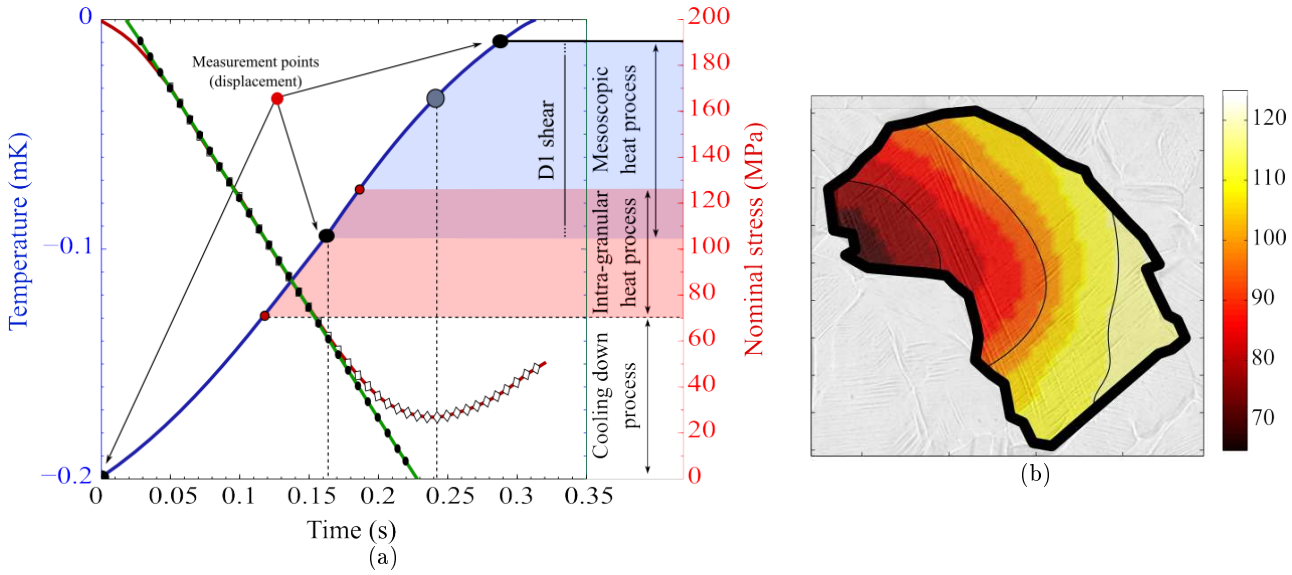

Figure I.3: (a) Intragranular mean temperature (red - mK), linear regression and Maximum Likelihood (green) and nominal stress (blue - MPa) from beginning to end of macroscopic elasticity and (b) intragranular field of thermal inflection appearance expressed as function of nominal stress (in MPa)

Summary

The grain n^o2 has been investigated. This grain reveals 2 activated systems (D_1 and B_5 in F.C.C. structure). Intragranular shear strain and thermal field are in total agreement about the loading path and thermal fields allow finer plastic yield identification. In agreement with Schmid theory, D_1 system is activated first from 69 to ≈199 MPa of nominal stress, then B_5 system is activated up to the end of the test (270 MPa). The Critical Resolved Shear Stress related to D_1 system has been estimated about 25 MPa which is in the order of expected magnitude for AISI 316L single crystal. Finally, successive specific "hot bands" has been observed while the plastic slip initiated on system B_5. It seems evidence that intragranular shear is captured by in-situ measurements.

I.2 Grain n^{o}3

Firstly, note that the present grain is surrounded on bottom and left part by twin Σ_3 boundaries (see figure 4.12 (b)). These boundaries exhibit a high contrast on micrography (see 4.12 (a)) which reveals significant steps of out-of-plane displacement at grain boundaries. It must play a significant role in dissipative response of the grain and its environnement.

Table I.4 presents surface grain statistics and figure I.4 presents the out-of-plane displacement in μm, the slip-band orientations in degree and finally the normalized slip-mark density in %.

size (mm^2)	0.138		
100x100μm^2 cells	14		
normalized slip-mark density (%)	55		
Slip mark orientations (^{o})	-68.1	38.2	
Activated systems	B_5	A_6	
Schmid factors	0.4303	0.4306	
Crystal orientation (rad)	4.59	0.497	1.687

Table I.4: Slip-system statistics of grain n^{o}3

The grain surface is 0.138 mm^2, i.e. composed by 14 cells of 100x100μm^2. Its normalized slip-mark density is 55% and ranges up to 65% in a limited domain (see figure I.4 (c)).

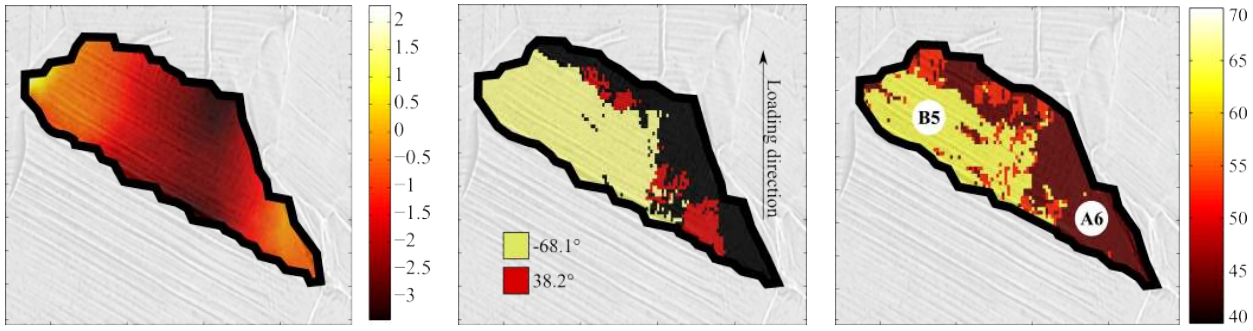

(a) in μm (b) in degree (c) in %

Figure I.4: (a) Intragranular out-of-plane displacement, (b) slip-marks orientations and (c) normalized slip-mark density as well as associated slip-systems.

Thus, relatively to the rest of the microstructure, it makes part grains significatively sheared. Slip-mark analysis has revealed that it activates 2 slip systems: A_6 and B_5 associated to a Schmid factor of 0.4306 and 0.4303 respectively. In the present case, the first activated system is not necessarilly the A_6. Indeed, the Schmid factor difference is too low to imagine a scenario based on the maximum

Schmid factor criterion. In-situ observations are consequently required.

Then, one observes in figure I.4 (b) and (c) that A_6 system (in red) exibits a low slip-mark density compared to the other system and it is located in a limited part of the grain, mainly in the right bottom. The major part of grain (left top part) exhibits B_5 slip-marks. This point is clearly in line with surface topography presented in figure I.4 (a). Indeed, the out-of-plane displacement exhibits two plateau at $\approx 0 \mu m$ where A_6 and B_5 systems are activated and a clear drop up to -3.5μm exactly at the interface between both systems. Thus, both slip-systems have their own intragranular domain and are separated by a natural topographic barrier. According to previous observations, one could already imagine that this specific gradient of topography is associated to specific gradient of surface temperature (see section 4.4).

Figure I.5 presents intragranular temperature (1^{st} column) and shear strain (2^{nd} column) at different instants of loading: 106 and 191 MPa of nominal stress, both located in macroscopic elastic domain. 220 and 253 MPa are located in macroscopic plastic domain.
One observes in figure I.5 that shear strain isovalues are oriented as B_5 slip-marks at 106 MPa (see superimposed micrography), and then in an intermediate orientation between B_5 and A_6 slip-marks at 191, 220 and 253 MPa. Notice, at 253 MPa isovalues orientation tends again toward B_5 slip-marks ones. This point is totally in line with Schmid factors presented in table I.4. Indeed as both systems has a very similar Schmid factor, they possess a similar trendy to initiate the plastic shear. Contrary to previous analysed grain, one are here in view of double shear. Notice the system B_5 is nevertheless the predominant one. This point is totally in line with slip-mark density (see figure I.4 (c)).

In the case of double or multiple shear and such bilinear strain field, the identification of yield stress is very delicate contrary to previous analysis. Indeed, as isovalues orientations turn arround both slip-marks ones, according to relative shear intensity, the yield could be accurately identify.

Let deal with thermal intragranular fields. it presents a very specific localization from 106 MPa of nominal stress to the end of the test. At 106 MPa , highest thermal values are observed on top part of grain which is the region where shear is the most significant at this instant (0.042%). Then, at each other instants, the pic of temperature is localized on right part of the grain. It systematically corresponds to the region where shear strain is the more intense. Thus a clear connection appears between high temperature localization and high shear strain localization. In addition, one could point that the specific thermal gradient observed at from 191 MPa of nominal stress to the end of the test is clearly connected to previous observations done on the surface topography and slip-system domains. Indeed, one has seen in figure I.4 (a) and (c) that the A_6 system domain is located on right part of the grain while the B_5 system domain is located on left part. In addition, the interface between both regions is characterised by a significant drop of out-of-plane displacement. Thus, intragranular thermal field evidences, in Figure I.5, that a persistent thermal gradient exist between both detailed domains.

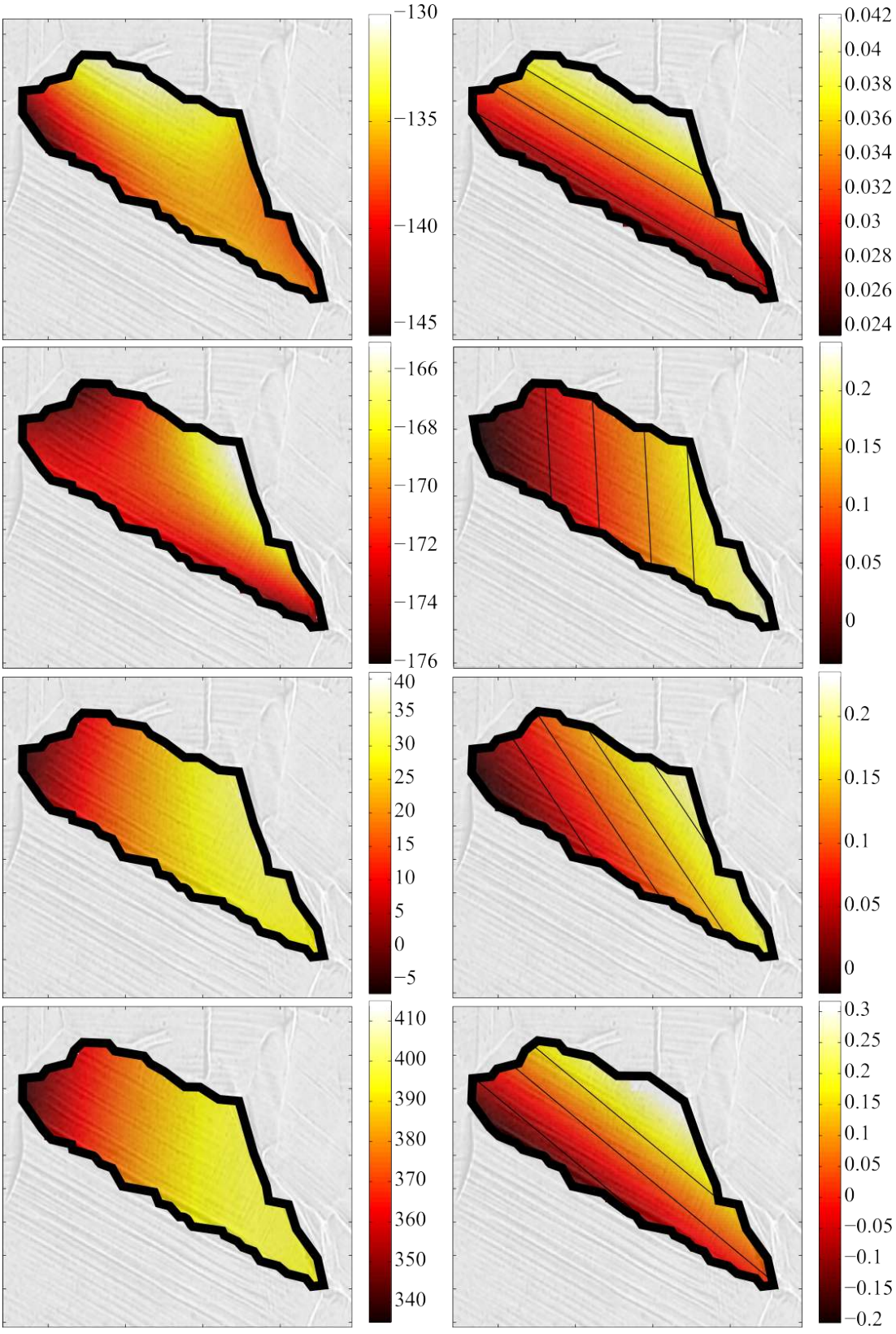

Figure I.5: Intragranular temperature (left side (mK)) and shear strain ε_{12} (right side (%)) at different instant of loading: 106 - 191 - 220 - 253 MPa

Figure I.6 presents the thermal deviation between the mean temperature over the A_6 domain (right part to minimum value of out-of-plane displacement in figure I.4) and the B_5 one (left part) along the test. A clear trends is observed and the deviation tends to stabilize about 8 mK at the end of test. Indeed, from low strain levels, A_6 system domain is more hot than the B_5 one, and the deviation persists. Actually, the deviation is very low, nevertheless, one uses here mean deviations over large domains which increase the accuracy of results.

Finally, the ultimate question is: is the thermal gradient is due to persistent gradient of plasticity and thus dissipation and/or the specific topography observed on surface acts as a thermal barrier which limits the thermal wave front propagation from A_6 to B_5 domain?

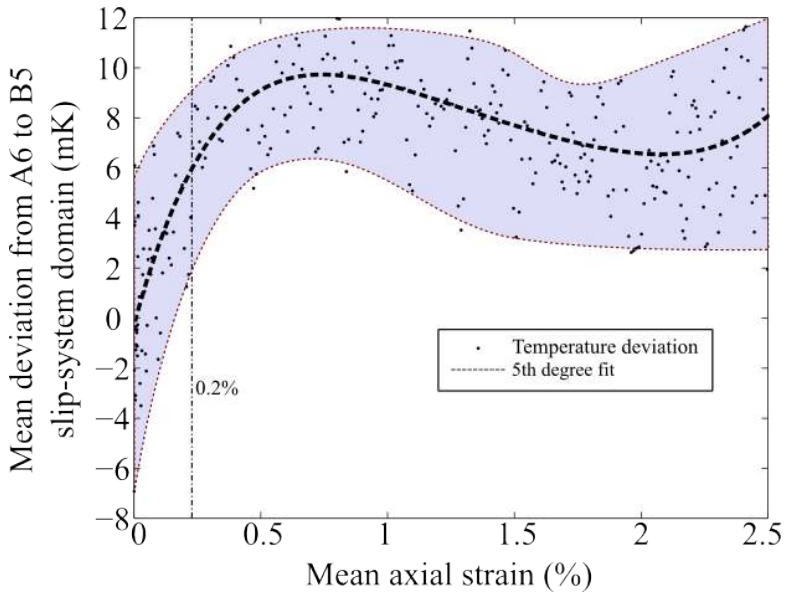

Figure I.6: Mean temperature deviation from A_6 to B_5 slip-mark domains

Let deal with the first intragranular thermal inflection in order to propose a deformation scenario. Picture I.7 (a) presents the mean temperature evolution from 0 to 200 MPa of nominal stress as well as nominal stress variation. One observes at mesoscale that the thermal inflection appears at 121 MPa and the minimum is reached at 167 MPa. Notice it is widely late compared to results found in previous grains. Picture I.7 (b) presents the same analysis performed at local scale. One observes that the first thermal inflection occurs at 60 MPa of nominal stress. Then the thermal inflection wave front propagates continuously through the A_6 domain. Finally, at 120 MPa, the thermal inflection appears in B_5 domain and then propagate continuously.

One recalls that profilometric analysis of final surface state, slip-system identification and in-situ thermal measurements are totally independent. It is therefore very impressive to observe that the time

variation of temperature, especially the loss of linearity exhibits a clear barrier for thermal inflection wave front propagation exactly at the interface between both activated systems, and at the location where a significant drop of topography occurs. According to figure I.7 (b), the first thermal inflection is due to local dissipation which initiate in the system A_6 and a physical thermal barrier exhists at both slip-ssytems interface.

In consequence, grain n^{o}3 exhibits a cooling down process (elasticity) from 0 to 60 MPa of nominal stress, then A_6 system initiate and locally dissipate. The associated Critical Resolved Shear Stress is 22 MPa. From 60 to 145 MPa the whole part of the grain deviate from the linearity. No results allow the identification of B_5 yield stress, nevertheless, final shear strain state evidences its predominance.

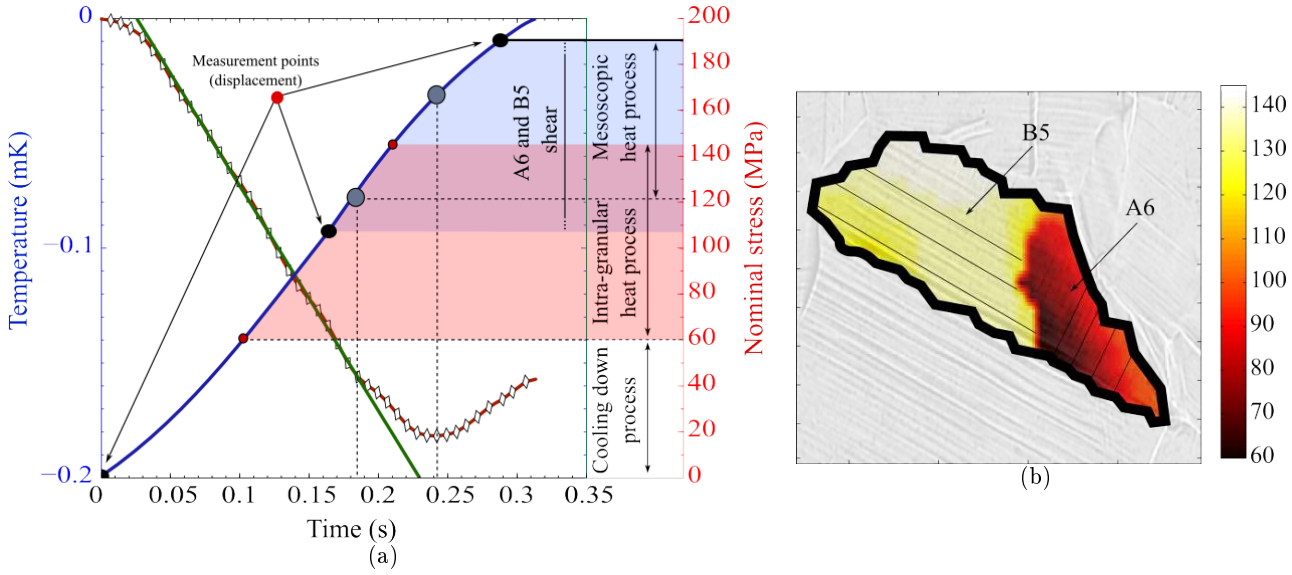

Figure I.7: (a) Intragranular mean temperature (red - mK), linear regression and Maximum Likelihood (green) and nominal stress (blue - MPa) from beginning to end of macroscopic elasticity and (b) intragranular field of thermal inflection appearance expressed as function of nominal stress (in MPa)

Summary

The grain n^o3 has been investigated. It reveals 2 activated systems (A_6 and B_5 in F.C.C. structure). Shear strain has revealed a competition between both system (double shear) which is in line with the low deviation between both Schmid factors. Intragranular fields has revealed that A_6 system is activated first, at 60 MPa of nominal stress. It correspond to CRSS of 22 MPa. One notes that thermal fields has allowed to discriminate the plastic activity of system A_6 whereas the bilinear intragranular kinematic couldn't. It points the complementarity of both information. Finally, a concrete link between slip-band interface, surface topography and thermal propagation has been observed.

I.3 Grain n^{o}4

The present grain is choosen since it is located at the center of the most heated region during the test. In addition, contrary to previous analysed grain, it exhibits single shear.
Table I.8 presents slip-system statistics and figure I.8 the out-of-plane displacement in μm, the slip-mark orientations in degree and finally the normalized slip-mark density in %. According to table I.8, the grain surface is 0.095 mm^2, i.e. composed by 9 100x100μm^2 cells. It is the smaller studied grain. It exhibits a relatively low normalized slip-mark density about 35 %. Texture analysis reveals only one activated slip system: B_5 corresponding to a high Schmid factor of 0.483. One could also note that the grain is surrounded in great part by twin Σ_3 boundaries which have leaded to a relatively intense out-of-plane displacement gradient at its boundaries (see picture 4.12 (a) and (b)).

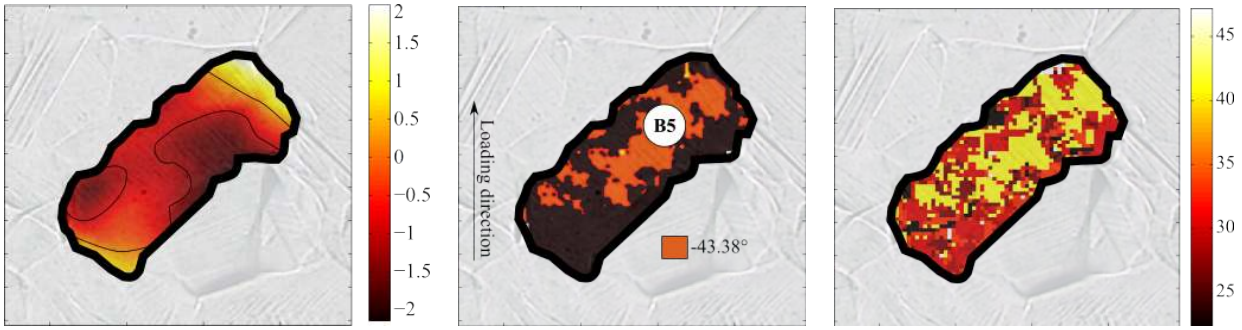

(a) in μm (b) in degree (c) in %

Figure I.8: (a) Intragranular out-of-plane displacement, (b) slip-marks orientations and (c) normalized slip-mark density as well as associated slip-system.

size (mm^2)	0.0952		
100x100μm^2 cells	9		
normalized slip-mark density (%)	35		
Slip mark orientations (^{o})	-43.38		
Activated systems	B_5		
Schmid factors	0.483		
Crystal orientation (rad)	4.59	0.497	1.687

Table I.5: Slip-system statistics of grain n^{o}4

In addition, one shows in figure I.8 (a) that the out-of-plane displacement ranges from -2 to 2 μm and exhibits 3 distinct regions. One could note that regions where the out-of-plane displacement is close to 0 seems to be connected to regions where lower slip-marks density is observed (see figure I.8 (b) and (c)).

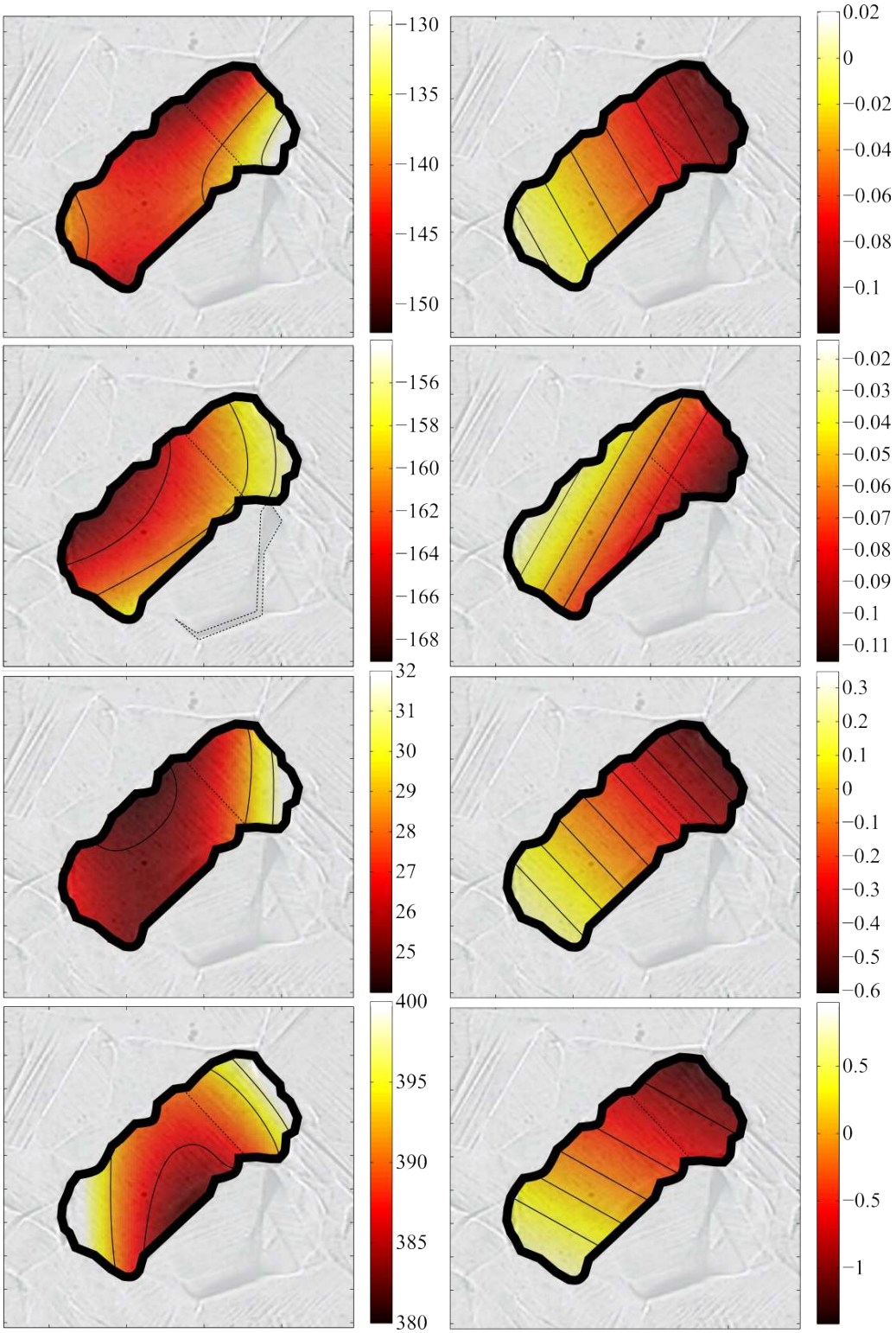

Figure I.9: Intragranular temperature (left side (mK)) and shear strain ε_{12} (right side (%)) at different instant of loading: 106 - 191 - 220 - 253 MPa

Pictures I.9 presents the intragranular thermal and shear strain field at different instant of loading: 106, 191, 220 and 253 MPa of nominal stress. Contrary to previous grains, one could note that shear strain isovalues orientation doesn't remain parallel to B_5 slip-mark one, exepted at 191 MPa. Slip-mark orientation is underlined with dotted lines. Thus, contrary to other analysis, no direct correlation could be done between slip system activity and intragranular shear strain.

Nevertheless, one could point the clear connection between thermal localization and shear strain one. From 106 to 220 MPa, the highest magnitude of shear strain are observed close to the right grain extremity. In parallel, highest temperature level are also located in the same area. Finally, at 253 MPa the shear strain tends toward a symmetrical state from left to right boundaries. Indeed, on the left, the shear strain is ≈1 % while it is ≈1.2 % on the right. In parallel, the thermal gradient exhibits the same pattern. Left and right boundaries exhibit highest thermal magnitudes while the center is colder. This point is in line with the value of shear strain at this region, i.e. ≈0 %. If one focus on thermal field at 191 MPa, a strong incompatibility of deformation is observed in vicinty of the studied grain. The well deformed boundary is pointed with a dotted line. One observes that this well deformed boundary is connected to the grain where high shear strain magnitudes as well as thermal localization are observed. It seems evidence that the strain and thermal localization occuring in the grain is due to incompatibilities of deformation at this specific interface.

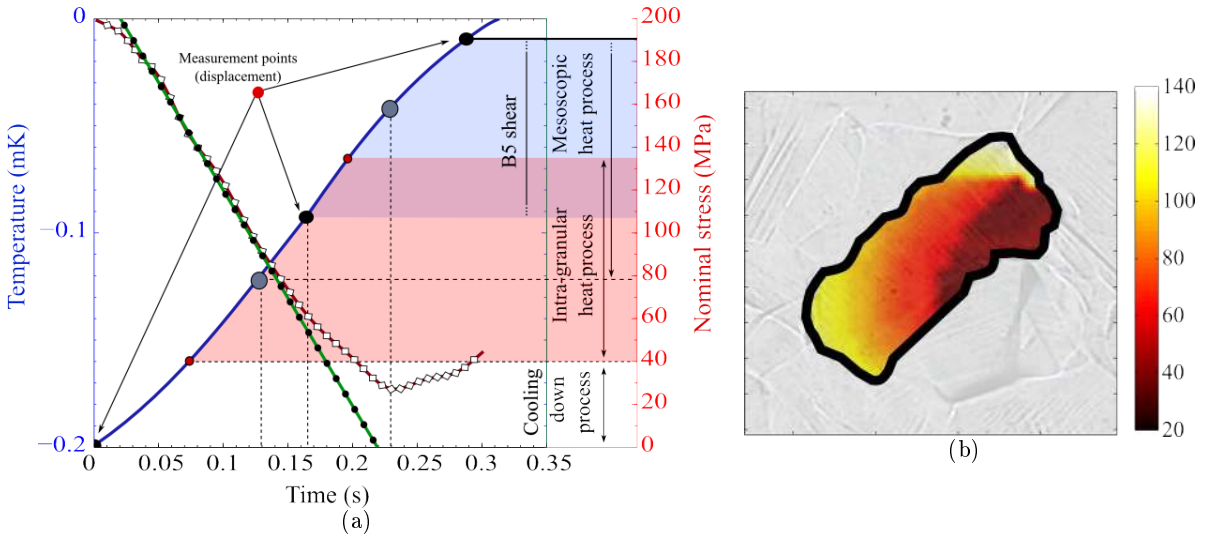

Figure I.10: (a) Intragranular mean temperature (red - mK), linear regression and Maximum Likelihood (green) and nominal stress (blue - MPa) from beginning to end of macroscopic elasticity and (b) intragranular field of thermal inflection appearance expressed as function of nominal stress (in MPa)

Finally, in the same way than in previous analysis, figure I.10 (a) and (b) presents mean variation of temperature as well as its loss of linearity and the field of local thermal inflection appearance as function of the nominal stress. One observes in figure I.10 (a) that the loss of linearity in mean tem-

perature curve appears very early compared to previous analysed grains. It appears at 79 MPa. One observes in figure I.10 (b) that it corresponds to a local first inflextion about 35 MPa of nominal stress. Thus one could note that the grain makes part of first dissipative grains within the whole structure. In addition, as expected one observe that the dissipation initiate at right grain boundary. This point is in line with, the surface micrography where a specific grain boundary deformation is visible, the in-situ kinematic measurements where shear strain localizes in this regions and finally thermal gradients.

Finally notice that the first dissipation allow the estimation to the associated Critical Resolved Shear Stress. In the present case its value is 57 MPa which is higher than other values found; about 20-30 MPa. It may imply that the observed dissipation is not associated to intragranular hardening but, dissipation of the neighboring grain, or intergranular dissipation due grain boundary shear.

Abstract

“Experimental and numerical investigation of thermomechanical couplings and energy balance in metallic polycrystals”

Strain localization and damage criteria of materials and structures are commonly based on a dissipative framework and this work investigates the thermomechanical couplings accompanying the deformation micromechanisms. It is partly based on experimental data obtained previously in the laboratory by Bodelot for a A316L austenitic stainless steel polycrystal. This work takes profit of a multi-technique approach combining, in particular, in-situ kinematic and thermal fields measurements as well as Orientation Imaging Microscopy, profilometry and surface micrography. Different tools have been developed (1) to automatically identify the activated slip systems directly from the surface micrography, (2) to approach the surface emissivity field allowing an accurate determination of the thermal fields with a 30 mK precision, (3) to project raw experimental fields on the microstructure and (4) to allow the modeling of the polycrystal aggregate and its real thermomechanical boundary conditions by using a crystal plasticity framework within the Abaqus FE code. It has notably been shown that the temperature variations provides an easy and accurate estimation of the macroscopic yield stress at the specimen scale as well as the determination of the Critical Resolved Shear Stress at the intragranular scale. In addition, the local kinematic measurements allow the in-situ identification of the activated slip systems. Experimental and numerical energy balances have been conducted and a great influence of the polycrystalline heterogeneity on the energy storage mechanism has been underlined. The proposed methods would help improving physical based dissipative criteria for damage analysis.

Key words: stored energy, thermomechanical couplings, crystalline plasticity, Quantitative InfraRed Thermography, Digital Image Correlation.

Résumé

“Étude expérimentale et numérique des couplages thermomécaniques, et bilan d'énergie au sein des polycristaux métalliques”

Les critères de localisation et d’endommagement sont généralement basés sur un cadre dissipatif et ce travail s’intéresse aux couplages thermomécaniques accompagnant les micromécanismes de déformation. Il repose en partie sur des données expérimentales obtenues précédemment dans le laboratoire par Bodelot pour un polycristal d’acier A316L. Ce travail tire profit d'une combinaison de techniques différentes, en particulier de mesures in situ de champs cinématiques et thermiques ainsi que de l’Orientation Imaging Microscopy, de la profilométrie et d’une micrographie de surface. Différents outils ont été développés afin (1) d'identifier automatiquement les systèmes de glissement activés, (2) d’estimer l’émissivité de la surface permettant ainsi une détermination des champs thermiques avec une précision de 30 mK, (3) de projeter les champs bruts expérimentaux sur la microstructure et (4) de permettre la modélisation du polycristal et de ses conditions aux limites thermomécaniques réelles dans un cadre de plasticité cristalline dans le code EF Abaqus. Il a notamment été montré que les variations de température fournissent une estimation précise et aisée de la limite d'élasticité macroscopique ainsi que la détermination de la contrainte de cisaillement critique à l'échelle granulaire. En outre, les mesures cinématiques ont permis l'identification des systèmes de glissement activés. Des bilans énergétiques expérimentaux et numériques ont été réalisés et une grande influence de l'hétérogénéité polycristalline sur les mécanismes de stockage d’énergie a été soulignée. Les méthodes proposées contribueront à améliorer les critères d’endommagement basés sur un cadre dissipatif.

Mots clés: Énergie stockée, Couplages thermomécaniques, Plasticité cristalline, Thermographie InfraRouge Quantitative, Corrélation d'image numérique.